WEATHER-RELATED GEO-HAZARD ASSESSMENT MODEL FOR RAILWAY EMBANKMENT STABILITY

A Thesis Submitted to the College of
Graduate Studies and Research
in Partial Fulfilment of the Requirements for the Degree of

Doctor of Philosophy

in the
Department of Civil and Geological Engineering
University of Saskatchewan
Saskatoon, Saskatchewan
Canada

By
Gilson de Farias Neves Gitirana Jr.

Permission to use

In presenting this thesis in partial fulfillment of the requirements for a Postgraduate degree from the University of Saskatchewan, I agree that the Libraries of this University may make it freely available for inspection. I further agree that permission for copying of this thesis in any manner, in whole or in part, for scholarly purposes may be granted by the professor or professors who supervised my thesis work or, in their absence, by the Head of the Department or the Dean of the College in which my thesis work was done. It is understood that any copying or publication or use of this thesis or parts thereof for financial gain shall not be allowed without my written permission. It is also understood that due recognition shall be given to me and to the University of Saskatchewan in any scholarly use which may be made of any material in my thesis.

Requests for permission to copy or to make other use of material in this thesis in whole or part should be addressed to:

Head of the Department of Civil and Geological Engineering
University of Saskatchewan
Saskatoon, Saskatchewan, Canada, S7N 5A9

ABSTRACT

The primary objective of this thesis is to develop a model for quantification of weather-related railway embankments hazards. The model for quantification of embankment hazards constitutes an essential component of a decision support system that is required for the management of railway embankment hazards. A model for the deterministic and probabilistic assessment of weather-related geo-hazards (W-GHA model) is proposed based on concepts of unsaturated soil mechanics and hydrology. The model combines a system of two-dimensional partial differential equations governing the thermo-hydro-mechanical behaviour of saturated/unsaturated soils and soil-atmosphere coupling equations. A Dynamic Programming algorithm for slope stability analysis (Safe-DP) was developed and incorporated into the W-GHA model. Finally, an efficient probabilistic and sensitivity analysis framework based on an alternative point estimate method was proposed. According to the W-GHA model framework, railway embankment hazards are assessed based on factors of safety and probabilities of failures computed using soil property variability and case scenarios.

A comprehensive study of unsaturated property variability is presented. A methodology for the characterisation and assessment of unsaturated soil property variability is proposed. Appropriate fitting equations and parameter were selected. Probability density functions adequate for representing the unsaturated soil parameters studied were determined. Typical central tendency measures, variability measures, and correlation coefficients were established for the unsaturated soil parameters. The inherent variability of the unsaturated soil properties can be addressed using the probabilistic analysis framework proposed herein.

A large number of hypothetical railway embankments were analysed using the proposed model. The embankment analyses were undertaken in order to demonstrate the application of the proposed model and in order to determine the sensitivity of the factor of safety to the uncertainty in several input variables. The conclusions drawn from the sensitivity analysis study resulted in important simplifications of the W-GHA model. It was shown how unsaturated soil mechanics can be applied for the assessment of near ground surface stability hazards. The approach proposed in this thesis forms a protocol for application of unsaturated soil mechanics into geotechnical engineering practice. This protocol is based on predicted unsaturated soil properties and based on the use of case scenarios for addressing soil property uncertainty. Other classes of unsaturated soil problems will benefit from the protocol presented in this thesis.

ACKNOWLEDGEMENTS

No matter how much knowledge I can gather, I have no hope of finding scientific answers for the most important, the spiritual matters. I pray for the Almighty God for enlightenment and I thank Him for all his blessings.

I would like to acknowledge some of the people that have provided support during the past years. Their support was essential for the completion of this work, directly and indirectly.

First of all, my dearest wife Lílian Virgínia Pôrto for her constant support and love.

My family. In particular my mother, Maria Amélia de Vasconcelos and my father Gilson Gitirana Sr.; Daniela, André, Isabella, and Gabriel; my departed grandparents Genes and Maria Gitirana, and Armando and Terezinha de Vasconcelos. My family-in-law. Sárya, Laézio, Leandro, Márlon, Laura, and my departed grampa-in-law, Adélio do Prado.

My supervisor, Dr. Del Fredlund. Without his support and encouragement this work would be much harder to complete. Professor Fredlund has offered friendship and an example of character and dedication. I hope to have learned his lessons and to have been a worthy student.

The members of my advisory committee, Dr. Dennis Pufahl, Dr. Gordon Sparks, and Dr. Charles Maule. I would like to express my appreciation for the help and suggestions provided throughout my Ph.D. program.

The faculty and staff at the Department of Civil and Geological Engineering. In special to Dr. Lal Samarasekera, Joanne Skeates, Cynthia Hanke, and Melissa Zink.

All my friends and colleagues in Saskatoon and back in Brazil. It's hard to do justice to all of them, but I would like to mention the following names in no special order: Paula, Luizinho, and Paloma Pereira; Marie-Diane and Natalie Clarke; Luciene Marçal and family; Mônica and Stan Benke; Barroncas family in Manaus; Barroncas family in Brasília; José Camapum de Carvalho;

Murray Fredlund; JoAnne Fredlund; Rob Thode; Hung Vu; Hung Pham; Elsa Tan; Nader Ebrahimi; and Abdoreza Pessaran.

Mr. Robert Nelson, from PDE Solutions Inc. I would like to express my appreciation for the constant and always prompt support provided.

The help provided by Ha Pham with the development of an early version of the dynamic programming code presented in this thesis is acknowledged.

Part of the models proposed in this thesis was further tested by Dennys R. Oliveira and Carlos C. Brito as part of their Masters thesis, under the co-supervision of me and Dr. José Pereira, from the University of Brasília, DF, Brazil. Their dedication and hard work is acknowledged.

My departed friend, José Henrique Feitosa Pereira, presented me with the opportunity to come to the University of Saskatchewan and to meet Dr. Fredlund. José was my supervisor during my Masters research and became one of my best friends. I'm certain that this thesis has José's touch and I hope to have made him proud.

The financial support from the following private and governmental organizations is acknowledged:

CNPq – Conselho Nacional de Desenvolvimento Científico e Tecnológico, Brazil.
Bolsa de doutorado pleno no exterior, Processo 200370/00-6.

CPR – Canadian Pacific Railway Company.
Collaborative Research and Development Grant

NSERC – Natural Sciences and Engineering Research Council of Canada.
Collaborative Research and Development Grant

Saskatchewan Highways and Transportation

To *Lílian*

And

To the memory of *José Henrique Feitosa Pereira*, 1958✯ – 2003✞

TABLE OF CONTENTS

Chapter 3 – *Theory for the Assessment of Embankment Stability Hazards Considering Weather Conditions*

Chapter 4 – Implementation and Verification of Numerical Models

Chapter 5 – Statistical Assessment of Unsaturated Soil Properties

Chapter 6 – *Analysis of Hypothetical Railway Embankments and Sensitivity Analysis*

LIST OF TABLES

LIST OF FIGURES

Chapter 1

Introduction

1.1 PROBLEM BACKGROUND

Weather-related geo-hazards are a major concern for the railway industry in Canada. The financial losses that result from derailments and delays amount to millions of dollars every year. The safety exposure of employees and the public is also a concern. The railway industry faces a serious dilemma; namely, the industry operates networks with tens of thousands of kilometres, crossing several types of geographical terrain, soil, and weather conditions from coast to coast (see the CPR network on Fig. 1.1). It is extremely difficult to protect and/or remediate every site under risk. At the same time, risks must be managed in an affordable manner.

The geo-hazards affecting the Canadian railway networks can be classified into several categories, as shown in Fig. 1.2. The primary focus of this thesis is on embankment failure hazards. Most geo-hazards, including embankment failures, are triggered by severe weather conditions and the increase in pore-water pressures. Railway subgrades composed of "moisture-sensitive" alluvial deposits are frequent and reflect the limited construction capabilities and understanding of soil characteristics at the time of construction (Transportation Safety Board, 1997). Railway embankments were constructed as early as the turn of the century. As a result, safety risks are found at numerous sections of Canadian railways that can be exposed to high levels of precipitation, rapid melt of snow pack, or drainage disruption.

Most aspects of current Railways' geotechnical hazard programs are reactive in nature (Transportation Safety Board, 1997). Reactive management programs are not intended to prevent occurrences but to restore operations after eventual occurrences. Economic and safety

factors have prompted the Canadian Railways to pursue proactive hazard programs (Mackay and Bunce, 2001). Beaver control, culvert inspections, and adoption of modern construction standards are some of the acknowledged proactive measures that can be implemented.

While there is a general understanding of the factors involved in railway embankment failures, a proactive hazard management system for embankment failures has not yet been developed and implemented. The main factor hindering the development of such hazard management system is the lack of an appropriate *model of hazard quantification*. A judicious implementation of a proactive hazard management program requires a *model of hazard quantification* that can provide a measure of embankment stability. Without a *model of hazard quantification* it is not possible to determine where and when hazard management actions must be taken. Railway resources can be rationalized by determining where and when management actions are required and the appropriate action "intensity".

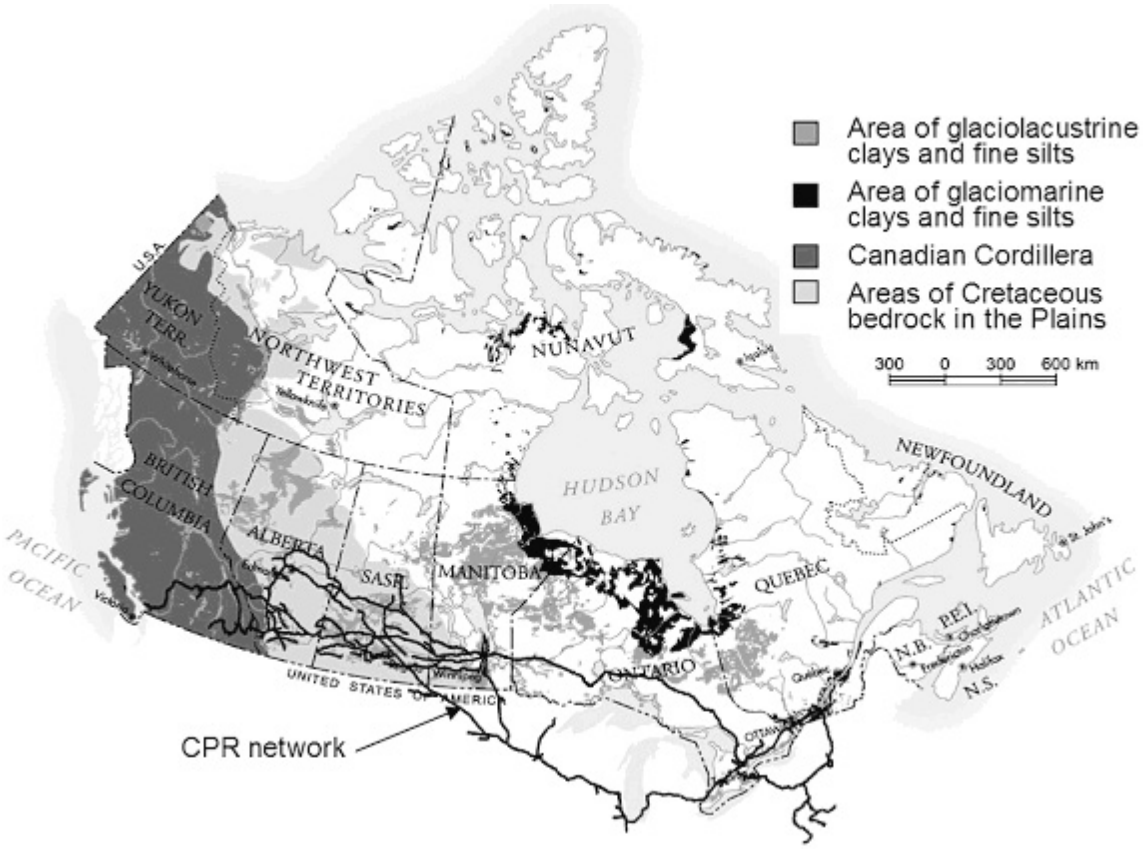

Figure 1.1 Canadian Pacific Railway network and main landslide areas according to the type of terrain (terrain data from Office of Critical Infrastructure Protection and Emergency Preparedness, 2001).

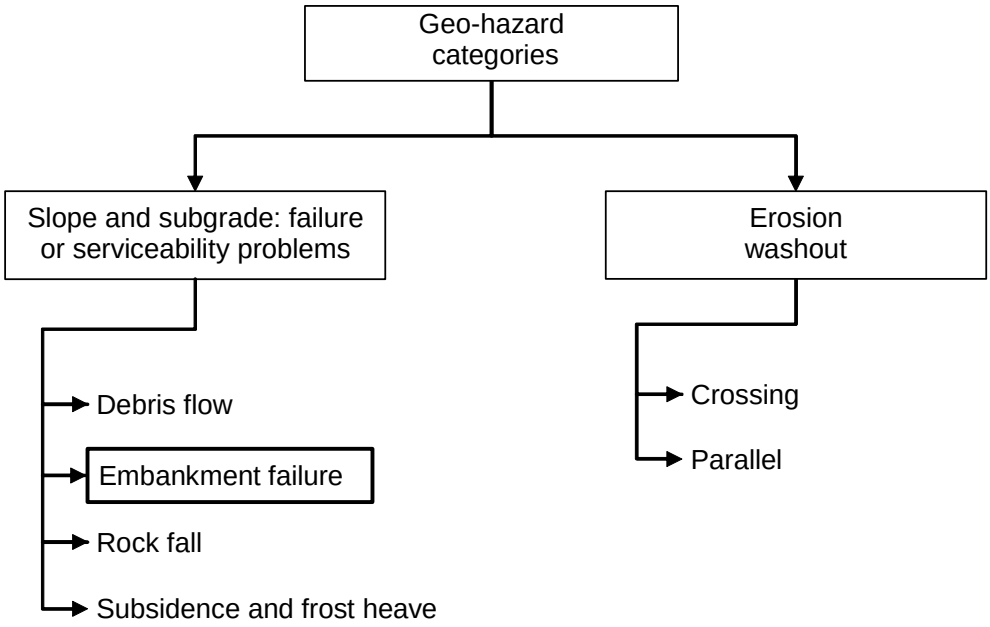

Figure 1.2 Categorization of geo-hazards.

The quantification of weather-related geo-hazards requires the ability to model the complex influence of weather and ground conditions on the embankment stability and to take into account the inherent soil parameter uncertainty. To this date, existing geotechnical and hydrological concepts have not been combined in an appropriate and feasible manner to quantify railway embankment hazards. *Probabilistic analysis* is widely accepted as the appropriate approach for geotechnical hazard assessment (Ang and Tang, 1975, Whitman, 1984, Harr, 1987, Becker, 1996a, Duncan, 2000). However, probabilistic approaches have not been extended to the unsaturated soil conditions generally found in railway embankments. There is a need for a methodology for considering the uncertainty of nonlinear unsaturated soil properties. There is also a need to determine how existing geotechnical and hydrological concepts can be combined and effectively employed in the assessment of railway embankment hazards.

1.2 ASSESSMENT OF WEATHER RELATED GEO-HAZARDS

A *hazard assessment model* is an essential component of a proactive management model for embankment hazards. A hazard management model consist of a *decision support system*, which is generally defined as a computational model that processes data and presents it in a manner that the user can make decisions more easily (Spraghe and Carlson, 1982). Figure 1.3 presents the

components of a conceptual management model for railway embankment hazards and the role of a *hazard assessment model*. According to Fig. 1.3, a hazard management model is composed of a *hazard assessment model* and a *decision making process*. The development of a *hazard assessment model* for embankment hazards can be considered a geotechnical discipline issue, while the cost-benefit analyses considered in the decision making process pertain to other areas within management and economic sciences (IUGS Working Group on Landslides, 1997).

Figure 1.3 suggests that the *decision making process* requires not only the quantification of geo-hazards, but also the assessment of the vulnerability (for computing risks), the establishment of acceptable risk levels and the selection of a collection of managing actions available. Several techniques for assessing vulnerability and selecting acceptable risk levels are available (Whitman, 1984 and Becker, 1996a) and a number of management actions can be taken, as presented in the previous section. However, the quantification of embankment hazards represents a major obstacle towards the management of railway embankment hazards.

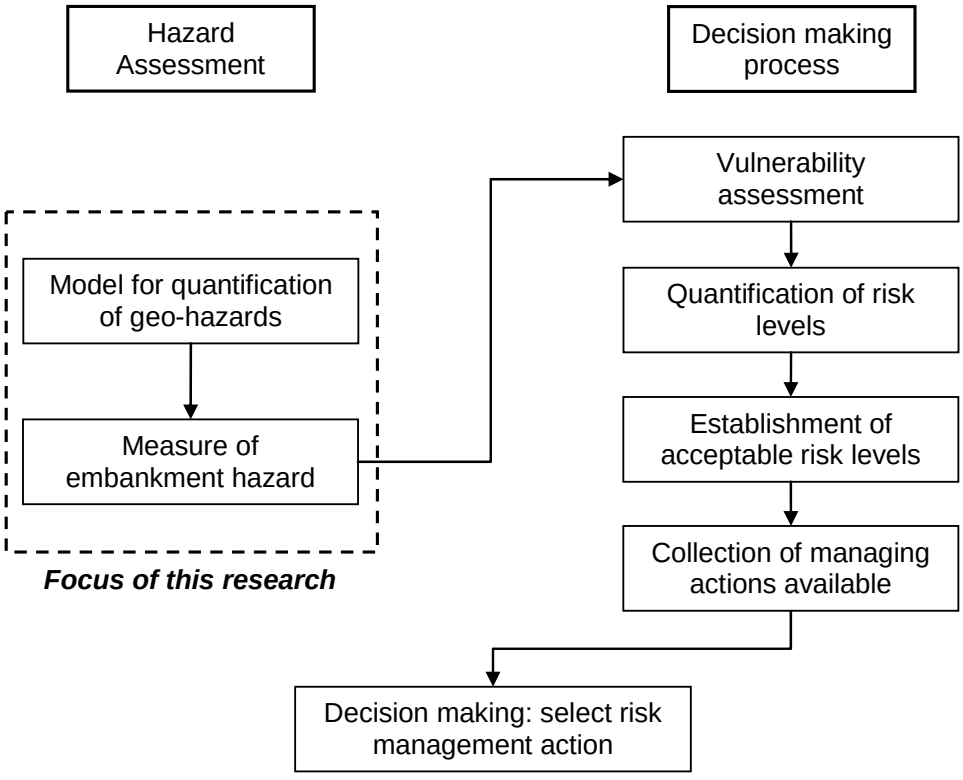

Figure 1.3 Components of a conceptual decision support system for the management of railway embankment hazards.

The development of a model for quantifying embankment hazards is a challenging task. Railway hazard assessment models can be developed and implemented at various scales. It is possible to focus on specific areas that have a high potential for becoming unstable and attempt to monitor the stability of specific embankments. It is also possible to produce a rather crude and yet appropriate hazard assessment for a whole region of the railway network with the aid of a geographic information system, GIS. This study focuses on the former scale (i.e., the assessment of hazards in a local scale). Besides being applied to specific areas, a local scale hazard assessment model can also be considered the first step towards the assessment of hazards on a regional scale. Simplifications required by larger scale management systems must be founded on the mechanisms associate with local scale embankment failures.

Unsaturated soil mechanics provides a powerful theoretical background for the quantification of weather-related geo-hazards. Embankment failure hazards are a function of the near ground surface soil characteristics and state. The near ground surface soil is generally unsaturated. Embankment hazards are strongly related to the reduction in soil suction and shear strength at the near ground surface soil. Soil suction and shear strength varies according to the amount of water stored in the soil. On the other hand, the amount of water within the soil is a function of the soil properties and the antecedent weather conditions.

The near ground surface unsaturated soil behaves as a dynamic system that interacts with the atmosphere and the deeper layers of soil. Several coupled phenomena take place within the near ground surface soil and affect the amount of water stored in the soil. These coupled phenomena can be modelled using fundamental laws of physics (e.g., conservation of momentum, mass, and energy) and constitutive relationships for unsaturated soils. Soil-atmosphere interaction must also be considered, including infiltration, evaporation, and runoff.

Figure 1.4 illustrates in a qualitative manner the relationship between the amount of water stored in the soil and the embankment hazard level. The soil comprising an embankment can be viewed as a “water tank”. The relationship between the amount of water in the soil and the soil suction is given by the soil-water characteristic curve. The soil-water characteristic curve works as a gauge, indicating the water level within the “water tank”. The water level presented in Fig. 1.4 is a function of antecedent weather conditions. The water level increases after precipitation events, and retreats during dry periods. Therefore, both precipitation events and evaporation periods must be considered for the establishment of the water level at any point in time.

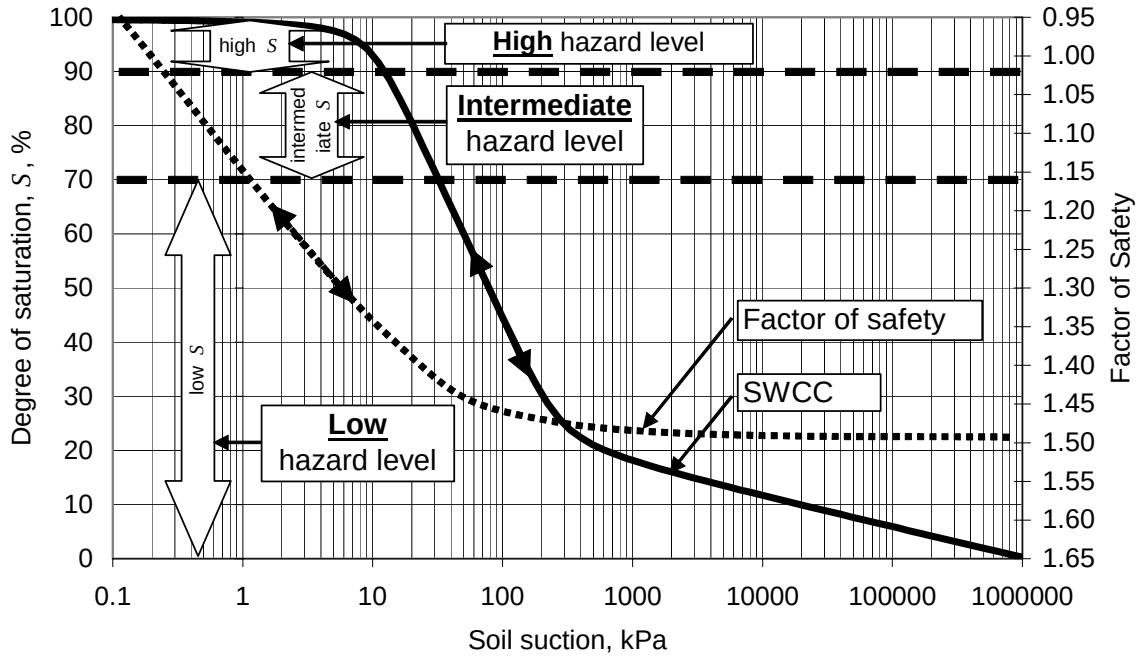

Figure 1.4 SWCC as a water level and embankment hazard gauge (intervals of degree of saturation and factor of safety are arbitrary).

The embankment hazard level, here represented as an arbitrary function of the *factor of safety*, F_s, varies according to the water level shown in Fig. 1.4. A low water level corresponds to higher suction, higher shear strength, and results in a lower level of hazard (higher F_s). Higher water levels produce lower soil suction, lower shear strength, and a greater hazard level (lower F_s). A rigorous model for assessment of embankment hazards must reflect the "water tank" concept presented in Fig. 1.4.

1.3 RESEARCH OBJECTIVES AND SCOPE

The primary objective of this thesis is to develop a model for the local scale quantification of weather-related railway embankment hazards. As explained in Figure 1.3, the model for quantification of embankment hazards constitutes an essential component of a decision support system that is required for the management of railway embankment hazards.

The scope of this thesis is limited to a theoretical study. Most embankment geometries can be reduced to a two-dimensional plane strain condition. Therefore, the models proposed herein are

limited to two-dimensional conditions. The environmental influences considered in this research are limited to infiltration and evaporation, but the framework developed must allow future extension to consider freeze-thawing cycles and water uptake due to plant transpiration.

The assessment of risks (i.e., the combination of a hazard measure and potential consequences) is beyond the scope of this thesis. The establishment of acceptable risk levels and the selection of management actions available are not considered herein. The scope established for this research does not imply that the assessment of risks, establishment of acceptable risk levels, and selection of management actions are not important. Subsequent studies must be carried out preferably with the direct aid of engineers and decision makers from the Railways in order to define appropriate acceptable risk thresholds, establish management actions, and implement the resulting hazard management model.

1.4 RESEARCH METHODOLOGY

The research focus of this thesis is the application of unsaturated soil mechanics concepts for the quantification of railway embankment hazards. A number of methodological steps were established and are prerequisite for the fulfillment of the primary objective described in the previous section. The methodological steps are as follows:

(i) Mechanistic soil modelling: Identification of the physical processes and soil variables that control the behaviour of the near ground surface soil comprising a railway embankment and establishment of a theoretical model based on unsaturated soil mechanics concepts;

(ii) Mechanistic soil-atmosphere modelling: Identification of the physical processes and variables associated with soil-atmosphere interaction and establishment of an appropriate theoretical model;

(iii) Probabilistic modelling: Establishment of a probabilistic framework for the assessment of embankment hazards that is capable of addressing the inherent uncertainty associated with nonlinear unsaturated soil property functions;

(iv) Numerical modelling and model verification: Development and verification of numerical and analytical models based on the deterministic and probabilistic hazard assessment theory developed in the previous steps. The numerical and analytical models are required

for the implementation of the proposed hazard assessment model;

(v) Data collection and statistical assessment of input parameters: Establishment of a methodology for the statistical assessment of unsaturated soil property uncertainty and the statistical assessment of parameter uncertainty using the proposed methodology and a database of soils;

(vi) Analysis of typical railway conditions and sensitivity analysis: Analysis of case scenarios designed to demonstrate the application of the proposed hazard quantification model to typical railway conditions. The case scenarios should also be designed to analyse the sensitivity of the factor of safety to the parameters controlling the stability of railway embankments and identify the most and less important parameters.

The research methodology established herein was designed in order to overcome hurdles associated with the application of unsaturated soil mechanics into engineering practice. First, there is a need to unify unsaturated soil theories and hydrological concepts. Both disciplines have not been developed in a combined way and relatively little focus has been given to the application of weather boundary conditions in unsaturated soil problems (Wilson, 1990).

Secondly, the determination of unsaturated soil properties represents the main challenge towards the implementation of unsaturated soil mechanics into routine practice (Fredlund, 2002). Laboratory tests for unsaturated soils are laborious and time consuming (Fredlund and Rahardjo, 1993). Alternatively, approximate methods for the prediction of unsaturated soil property function provide a feasible alternative approach for the implementation of unsaturated soil mechanics (Fredlund, 2002). Most predictive models are based on the grain-size distribution and/or on the soil-water characteristic.

The special circumstances associated with the use of predicted unsaturated soil properties result in the need for an unsaturated soil mechanics protocol adequate for embankment hazard assessment and routine geotechnical engineering. An unsaturated soil mechanics protocol must accommodate the uncertainty of unsaturated soil properties through a formal probabilistic framework. Such probabilistic framework can be based on the analysis of formally established “case scenarios”. The probabilistic framework envisaged herein would be a formal version of the “what-if” approach proposed by Fredlund (2002).

1.5 THESIS OUTLINE

This thesis is organised in seven chapters and five appendices. The present chapter has introduced the railway embankment stability problem. A description of the types of geo-hazards of concern was presented, along with an overview of how unsaturated soil mechanics may potentially be employed in the quantification of weather-related geo-hazard. Finally, the objectives and scope of the thesis were presented. The following paragraphs present a concise description of the contents of the remaining chapters and thesis appendices:

Chapter 2 presents a literature review covering diverse aspects of the geo-hazard assessment problem. A concise review of derailments caused by embankment failures is presented in order to illustrate the typical derailment conditions. A review of moisture, heat, and soil-atmospheric flow models available is presented. A review of method of stability analysis applicable to the railway embankment stability is also presented. Finally, probabilistic methods that can be used for the assessment of geo-hazards are reviewed.

Chapter 3 presents the theory developed for the assessment of weather-related geo-hazards. A hazard assessment model (W-GHA model) is developed. First, an overall description of the model is provided, showing its individual components and the manner how the components are connected. Next, each individual component is presented in detail. The components of the W-GHA models are the following: (i) model for coupled heat and moisture flow; (ii) equations for the soil-atmospheric coupling; (iii) model for quantification of embankment stability; and (iv) probabilistic and sensitivity analysis framework. A concise description of method of prediction of unsaturated soil property function is also presented, in connection with the W-GHA model.

Chapter 4 presents the development and implementation of numerical and analytical models for the solution of the W-GHA model. The implementation of the W-GHA model is presented for each of the individual model components. The solution of simple problems is presented, in order to verify the proposed models.

Chapter 5 presents the statistical assessment of unsaturated soil properties. A methodology for the statistical assessment of unsaturated soil property uncertainty is developed. Typical central tendency values and variability of unsaturated soil properties are obtained based on the soil textural classification and using a database of soils.

Chapter 6 presents the analysis of typical embankment conditions and sensitivity analyses. Case scenarios were designed in order to demonstrate the application of the proposed model to typical railway conditions and to identify the properties and physical processes that have greater and lesser importance for the assessment of weather-related geo-hazards. A series of typical problems covering a wide range of conditions is considered. Scenarios where failure occurs and does not occur are shown for a number of geometry configurations, soil types, initial conditions, and atmospheric conditions.

Chapter 7 presents the conclusion and recommendation of future studies.

Appendix A presents a concise description of probability density functions used throughout this thesis.

Appendix B presents the numerical models developed for the solution of the W-GHA model.

Appendix C presents a new class of soil-water characteristic curve equations, developed in connection with the W-GHA model.

Appendix D presents the soil data sampled for the statistical analysis of unsaturated soil properties and the results of the descriptive statistics for the properties.

Appendix E presents the output data obtained from the W-GHA model and corresponding to the case scenarios presented in Chapter 6. The factors of safety obtained are presented for each property case scenario.

Chapter 2

Literature Review

2.1 GENERAL

The objective of this chapter is to present a review of railway embankment failure occurrences and to review the theories available for assessment of weather-related geo-hazards. Section 2.2 presents a description of some derailments reported in the literature that were triggered by embankment failures. These derailments provide some understanding on the nature of the geo-hazards affecting the Canadian railway industry. The typical embankment, soil, and weather conditions associated with embankment failures are identified.

Section 2.3 presents a concise overview of decision analysis and traditional reliability-based approaches that can be used for assessing geo-hazards. Section 2.4 deals with theories available for the deterministic quantification of embankment stability hazards. A detailed review of mechanistic approaches for the prediction of moisture movement in saturated/unsaturated soils and soil-atmosphere coupling is presented. Liquid water and water vapour flow mechanisms are considered, along with thermal coupling. Soil-atmosphere models are presented for infiltration, evaporation, and runoff. Section 2.4 also presents a review of methods for the quantification of embankment stability. Several stability analyses approaches are described and compared.

Section 2.5 presents a review of reliability-based slope engineering approaches and a detailed review of the probabilistic methods available for the analysis of functions of random variables. The theoretical basis of each probabilistic method is described and the methods are compared in terms of their accuracy and computational requirement. Finally, Section 2.6 presents a summary of the chapter.

2.2 DERAILMENTS ON CANADIAN RAILWAYS DUE TO EMBANKMENT FAILURES

This section presents evidences found in the literature showing the significance of weather-related geo-hazards to the Canadian railway system. A series of derailments caused by embankment/subgrade failures are described herein. A close look at these derailments provides an insight into the typical weather, drainage, embankment geometry, and soil conditions associated with embankment failures.

Several detailed reports of derailment investigations are provided by the Transportation Safety Board of Canada (TSB). The TSB, an independent Canadian federal agency created by an Act of Parliament in 1990, holds a legal mandate to advance safety in the marine, pipeline, rail, and aviation modes of transportation. The TSB conducts investigations on major occurrences and publishes investigation results and safety recommendations. Only a small portion of the derailments reported to the TSB are investigated. However, the Board also provides general statistics about all the derailments reported, including those derailments subject of investigation. A summary of the statistics available to this date will be presented.

2.2.1 *Derailment statistics*

The importance of geo-hazards to the Canadian railway industry can be illustrated by using derailment statistics. Figure 2.1 presents the number of main-track derailments reported to the Transportation Safety Board of Canada until 1994 (Transportation Safety Board, 1994) combined with data from the following years (Transportation Safety Board, 2001). A 'main track' is defined as a track extending through yards and between stations whereas a 'non-main track' is composed mostly of sidelines and yards. Figure 2.1 shows that Canadian main-track derailments have declined by almost a factor of three between 1980 and 1988, followed by a roughly level trend thereafter, despite a peak of derailments on 1996.

Many issues raised after the official inquiry into the derailment at Mississauga (November 10, 1979) were addressed in the 1980-1988 period, markedly contributing to the decline in derailments. Several important advances are noteworthy; namely, improvements in the installation, repair, and defect detection procedures for rails; gradual elimination of straight-plate wheels and friction bearings (substituted by roller bearings); improved marshalling requirements; increased number of hot box detectors; and adoption of rigorous government safety regulatory enforcement and inspection programs (Transportation Safety Board, 1994).

The series of initiatives taken during the eighties can be considered as essentially exhausted after 1988, explaining in part why the number of derailments have somewhat levelled thereafter.

More detailed rail occurrence statistics, including non-main track data, are provided by the Transportation Safety Board starting in 1992. Figure 2.2 presents the total number of derailments classified by assigned factors, along with the number of fatalities and injuries caused by derailments from 1992 to 2001. Geometry/roadbed factors are closely related to geo-hazards whereas equipment factors are associated to mechanical failures and defects (Transportation Safety Board, 2001). Action factors are related to inappropriate train and track operation.

Figure 2.2 shows that the number of fatalities and injuries caused by derailments can be considered small when compared to the numbers of fatalities and injuries associated with crossing and trespasser accidents, which reaches the hundreds annually (not shown in the figure). The high number of derailments suggests a potentially high financial impact. Clear trends for the entire period are non-existent, but the trend is roughly level as shown in Fig. 2.2. One important observation is that cross-section geometry and roadbed factors have a significant contribution to the number of derailments, demonstrating the importance of geo-hazards for railway safety.

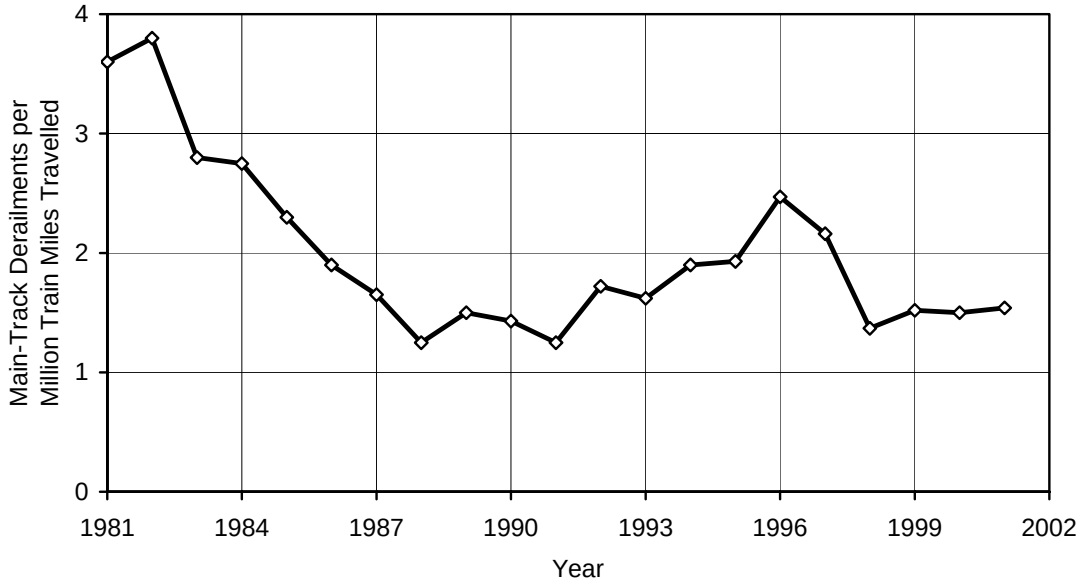

Figure 2.1 *Main-track* derailment data provided by the Transportation Safety Board of Canada (1994 and 2001).

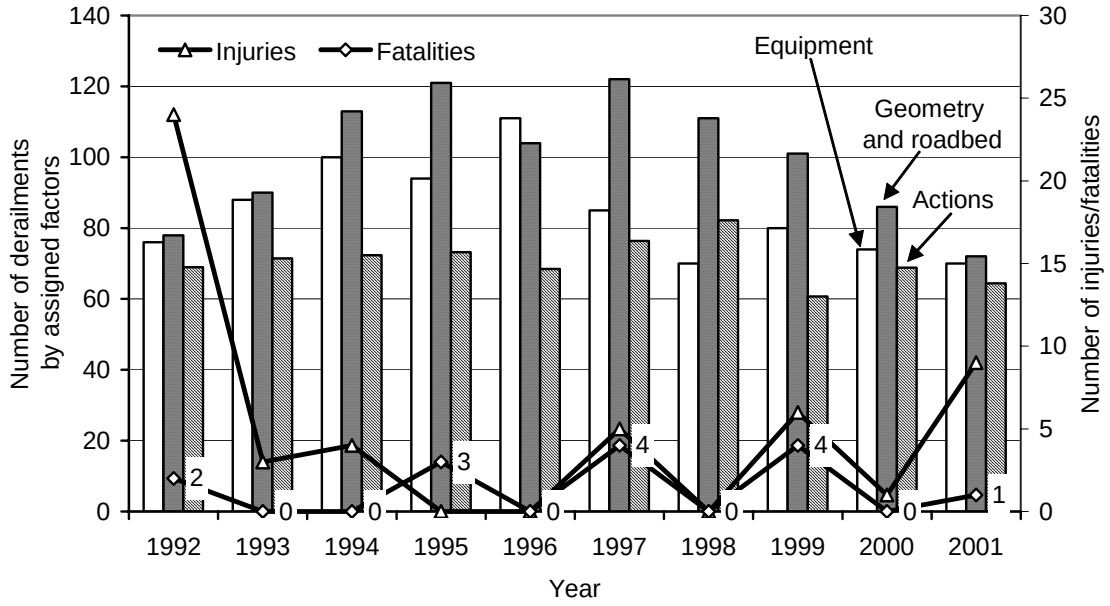

Figure 2.2 *Main*- and *non-main* track derailments by assigned factors and injuries/fatalities due to derailments (data from Transportation Safety Board of Canada, 2001).

2.2.2 *Occurrences involving embankment failure*

Detailed reports from the TSB on derailment investigations are dated since 1991. The derailments investigated have different causes, but are frequently related to crossing accidents, collisions, rail defects/deterioration and embankment/roadbed failure. The focus here will be given to derailments caused by embankment/roadbed failures.

Caramat derailment, 1992

The first report about an occurrence caused by subgrade failure corresponds to an accident that occurred in July, 1992 (Transportation Safety Board, 1997, occurrence No. R92T0183). The derailment involved a Canadian National Railway (CN) freight train. The train encountered a collapsed subgrade at Mile 135.0 of CN's Caramat Subdivision near Nakina, Ontario. The train traveled onto the suspended portion of track and plummeted into a pond (see Fig. 2.3). As a result, two crew members were killed and a third sustained serious injuries. According to the Transportation Safety Board (1997), the roadbed failure was caused by a sudden draw down of the water of the pond from a breached beaver dam. It was found that the roadbed had been built over glaciolacustrine silt and peat at the turn of the century. The saturated silt had become unstable as a result of the rapid draw down of water. The track remained intact and suspended over the depression. Therefore, the Automatic Block Signal System (ABS) was unable to detect the failure.

Figure 2.3 Caramat derailment: west end of derailment site showing grade slump (Transportation Safety Board, 1997).

Kinghorn derailment, 1994

In April 25, 1994, a CN freight train encountered a large roadbed depression at Mile 89.7 of the Kinghorn Subdivision at Orient Bay, Ontario (Transportation Safety Board, 1995). The roadbed failure caused the derailment of two locomotives and 15 loaded cars. The train included 2 locomotives, 79 loaded and 8 empty cars, weighed approximately 8,421 tons and was 1,540 meters in length. Three employees sustained injuries as a result of the derailments. The Transportation Safety Board (1995) determined that water infiltrating into the subgrade resulted in the subgrade becoming saturated to a level higher than previously experienced. As a result, the subgrade became unstable and slumped, leaving a large depression under the track. The water that infiltrated the subgrade originated from a build-up caused by a partially blocked culvert. The subgrade was composed of glaciolacustrine silts and clays. The Transportation Safety Board (1995) did not report weather data to indicate whether or not severe weather conditions could have contributed to the subgrade failure.

Conrad derailment, 1997

The derailment that occurred in 1997 near Conrad, British Columbia, presents interesting information linking railway embankment collapse to severe weather conditions (Transportation Safety Board, 1998a). In March 26, 1997, a CN train encountered a large roadbed depression and derailed at Mile 106.15 of the Ashcroft Subdivision, near Conrad, BC (see Fig. 2.4). Both crew members were fatally injured and fourteen freight cars and two locomotives were damaged beyond repair. Approximately 365 meters of main track and siding was destroyed. The train included 2 locomotives, 72 loaded cars and 5 empty cars. It weighed approximately 4,850 tons and was about 1,700 meters in length. The TSB determined that a large volume of run-off from melting snow cover and high seasonal precipitation was not captured and carried away as intended by the drainage system above the adjacent Trans-Canada Highway (see Fig. 2.5). The overlapping nature of the highway fills, as shown in Fig. 2.5, created a contiguous groundwater flow path into the railway fills. Infiltrated water moved through the highway fills, increasing pore-water pressures and destabilizing the railway subgrade. The Transportation Safety Board (1998a) pointed out that factors contributing to the embankment failure included the presence of 'moisture-sensitive' alluvial deposits in the bottom area of the railway subgrade. The highway embankment and railway embankment were at an approximate 1.5H:1.0V slope.

Figure 2.4 Conrad derailment (Transportation Safety Board, 1998a).

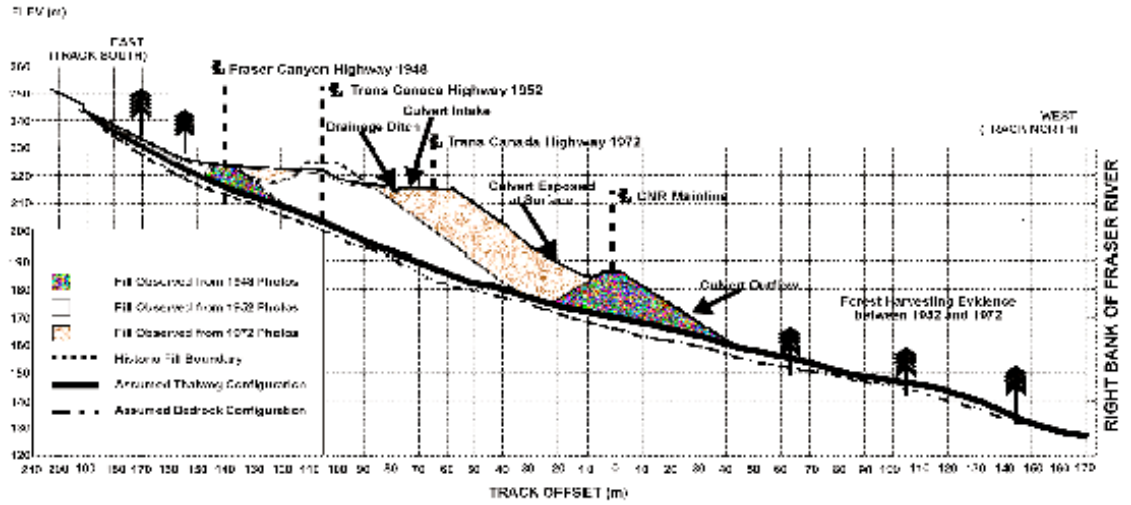

Figure 2.5 Conrad derailment: embankment cross-section (Bruce Geotechnical Consultants Inc., 1997, cited by Transportation Safety Board, 1998a).

The Transportation Safety Board (1998a) presented precipitation data from the Conrad area. The report indicates that snow had accumulated in Conrad from November 16, 1996 to January 1st, 1997, when the precipitation turned to rain. January 1997 was the wettest January on record, with 240.7 mm of rainfall recorded at the Vancouver International Airport. February did not produce any abnormal levels of precipitation. Based on the Lytton 2 weather station, 13 km north of Conrad, thawing began in the middle of February. On March 1st, 1997, the second heaviest one-day rainfall in 59 years occurred, with 47.2 mm of rain recorded at the Vancouver International Airport. On March 18, 1997, 48.4 mm of rain was recorded at the same station and more than 20 mm of rain fell each day on March 17, 1997 and March 19, 1997. According to the Transportation Safety Board (1998a), the 1,327.0 mm of precipitation recorded between October 1996 and March 1997 makes it the wettest six months in 59 years. In addition to the antecedent rainfall, the winter snow pack of approximately 55 cm suddenly began to melt between 17 and 19 of March. The melting rate reached 5 cm/day on 25 March.

Evans and Savigny (1998), cited by Transportation Safety Board (1998a), presented a geotechnical engineering report on the Conrad derailment. According to the report, two landslides were observed. The first landslide, which caused the derailment, was a smaller failure on the west side of the siding fill. Under elevated pore-water pressures, low to non-plastic silts in the foundation of the subgrade initiated the first failure. The first failure event exposed the original railway fill, which was loose and saturated at the lower portion. This fill then slipped away in retrogressing shallow slumps until the loose, saturated original fill was eliminated. The

extent to which the slides retrogressed was found to be related to the level of the water table and the loose compaction of the original railway embankment fill. A slope stability analysis indicated that the railway fill was stable when the water table was located in the alluvial deposits beneath the fills. In summary, the weather and geotechnical data from the Conrad derailment clearly shows that this occurrence was caused by a combination of severe weather conditions and poor soil conditions. The data also suggests that the antecedent weather conditions played an important role on the stability of the railway embankment.

Parry Sound derailment, 1997

The results of an investigation on another derailment related to increase in pore-water pressures are presented by the Transportation Safety Board (1998b). On April 7, 1997, 4 locomotives and 14 cars derailed after a CPR train plunged into a depression in the track at Mile 44.8, Parry Sound Subdivision, near Pointe au Baril, Ontario. One crew member sustained serious injury and two had minor injuries. The train was 914 m long, weighed about 2,380 tons, and was hauling 2 loaded cars and 46 empty cars. The roadbed collapse occurred on a section of an embankment consisting of loose sand fill. The embankment was 140 m long, 15 m high, and with side slopes of 1.5H:1.0V.

The subgrade failure was caused by build up of pore-water pressure as a result of a beaver dam and the rapid melting of snow during the two weeks prior to the derailment. The loose state of the sand fill was viewed as a contributing factor in the subgrade failure. The track remained intact and suspended over the depression, allowing the Automatic Block Signal System (ABS) to continue to function as the train approached the area of failure. A geotechnical investigation on the failure circumstances conducted by CPR concluded that the dynamic loading of the embankment by the train may have also contributed to the slide (Transportation Safety Board, 1998b). However, the TSB observed that the trajectory and scatter pattern of train wreckage indicated that the failure occurred before the train crossed the embankment. The TSB recommended an evaluation of the current track continuity warning system that was not able to detect the roadbed failure. Evaluations and sponsoring of research on alternative methods of detection of roadbed failures were recommended.

Kingston derailment, 1997

Transportation Safety Board (1998c) presents a report on a derailment on May 6, 1997, caused by an embankment failure triggered by saturation of the weak clays under the subgrade at Mile

34.55, Kingston Subdivision, near Coteau, Quebec. The train was approximately 323 m long and weighed about 1,000 tons. The failure caused the derailment of 2 locomotives and the first 12 of 20 cars. Two crew members received minor injuries and approximately 82 m of track was destroyed. The railway embankment consisted of 3 m of crushed rock ballast and gravel roadbed over 11 m of a variety of clays. The collapse was attributable to the presence of weak clays under the subgrade and water saturation from several sources including surface water migration through the railway embankment. The total precipitation recorded between April 18, 1997 and May 5, 1997, was 114.4 mm, an amount higher than normal. The investigation found that the subgrade collapsed under the moving train and that a blockage of either the culvert or siphon, with the resultant high water level next to the embankment, may have contributed to the failure. The Board recommended the identification of locations where the railway embankments were constructed over materials vulnerable to loss of strength when saturated and the assessment of the adequacy of the existing drainage systems for these locations. The Board also recommended the implementation of a monitoring program to detect embankment instability due to soil saturation.

Nelson derailment, 1998

Transportation Safety Board (2000a) presented another occurrence illustrating the potential instability of silty fills when subject to saturation. On May 31, 1998, a CPR freight train encountered a roadbed depression at Mile 59.1 on the Nelson Subdivision near Creston, British Columbia. Three locomotives and eight gondola cars derailed (Fig. 2.6). There were no injuries. Approximately 46 m of track was destroyed. The train included 3 locomotives, 31 loaded cars and 58 empty cars, was approximately 1,585 m long and weighed about 5,400 tons. The railway embankment slip surface left a void approximately 27 m long and 5 m deep. The Board determined that the amount of precipitation recorded for the week before the derailment was 111.2 mm at Goatfell (Mile 45.6). This amount of weekly precipitation has a return period higher than 100 years. According to the investigation results, the materials consisted of glaciolacustrine silts forming the matrix of glacial and colluvial deposits in the vicinity of the site. The Board determined that the track failed due to saturation and failure of the subgrade fill. The contributing factors to the occurrence were the record rainfall, the poor performance of the drainage system, the steep side hill slope, and the high susceptibility of the subgrade fill material to changes in water content.

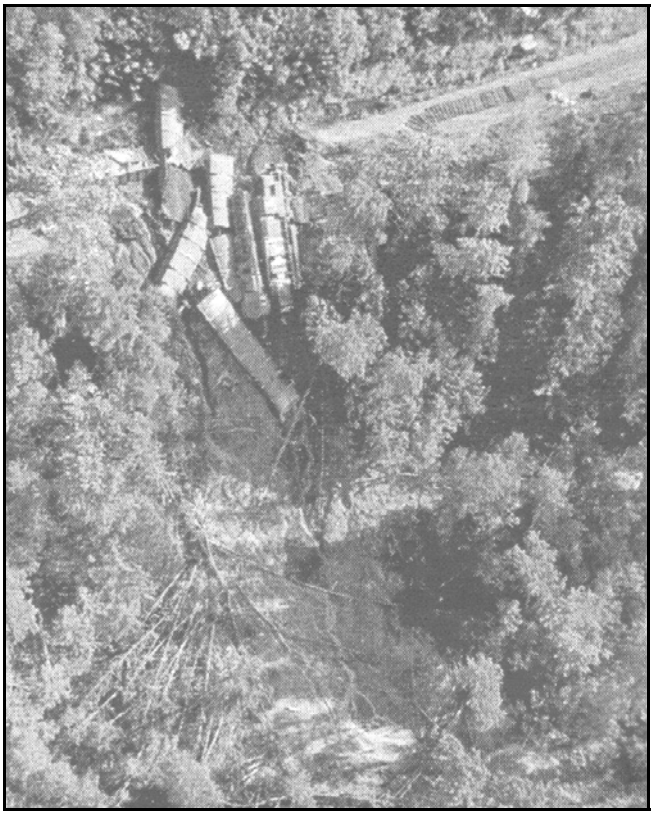

Figure 2.6 Nelson derailment (Transportation Safety Board, 2000a).

Keewatin derailment, 1999

Another investigation involving a roadbed failure caused by severe weather conditions is presented by Transportation Safety Board (2000b). On June 26, 1999, a CPR train encountered a roadbed depression at Mile 5.3 of the Keewatin Subdivision near Keewatin, Ontario. Eight freight cars derailed. There was minor track and equipment damage but no injuries and no dangerous goods were involved. The train was approximately 1,920 m long and weighed about 8,600 tons. The train was powered by 2 locomotives and comprised 102 cars, 62 loaded. The weather station at Kenora Airport reported that a total of 137 mm of rain fell between 4:20pm on June 25 and 2:30am on June 26. The highest intensity of rain (71 mm) occurred between 7:00pm and 1:00am. The average intensity over a 12-hour period was 11.45 mm/h. At the point of the derailment, the subgrade embankment was approximately 6 m high and was built of local sand and silt materials. Based on the investigation results, the Transportation Safety Board (2000b) concluded that heavy rainfall during the 11 hours before the derailment saturated the subgrade embankment, causing the track structure to fail. It was found the drainage system did not provide the proper channelling for the excess water to flow under the subgrade because the south ditch was blocked and culverts were plugged.

2.2.3 *Summary of occurrences, TSB recommendations, and research required*

Table 2.1 presents a summary of the derailments caused by embankment/subgrade instability presented in the previous section. These occurrences serve as an indication of the main factors involved in embankment instabilities. Based on these occurrences, the TSB has issued a number of recommendations. Among other things, the TSB has recommended that a collaborative program be established by the Department of Transport with the objective of identifying potential locations of incipient failure where main track has been laid over weak sediments or where waters adjacent to main track may be subject to rapid draw down. Restricted speeds have been recommended for trains traversing those sites identified as most vulnerable to failure caused by draw down of adjacent waters. The Board also recommended that corrective measures be identified and implemented to increase soil stability with an acceptable factor of safety at locations identified as being vulnerable to terrain slump.

Transportation Safety Board (1997) recommended a review of the adequacy of current roadbed design criteria for laying roadbed over peat, silt, or other weak sediments. This recommendation reflects the significant role played by these types of sediments. In reaction to the Board recommendation concerning the design criteria for roadbed construction, the Minister of Transport advised that future design and construction be carried out in accordance with applicable engineering standards. The railways have undertaken corrective measures to alleviate the problem of beaver activity near railway tracks, but little has been accomplished in response to soil weakness identification, bank stabilization or warning systems development. Part of the difficulties in undertaking these measures is due to the diversity of weather and terrain conditions that must be considered and the complexity associated with quantifying hazards.

The quantification of weather-hazards must take into account both weather and ground conditions. The challenging task of quantifying weather-related geo-hazards involves the establishment of a measure of hazard intensity, the identification of the relevant physical processes involved, the identification of the relevant variables related to these physical processes, and finally, the development of a way of implementing the hazard quantification model. Once such system is in place, acceptable risk levels must be established. Such levels also require the assessment of potential hazard consequences that vary from site to site and depend of the type of goods being transported.

Table 2.1 Summary of some derailments in Canada during the 1990's caused by embankment and subgrade failure.

Derailment location and date	Soils	Geometry	Antecedent Conditions	Causes of failure
July, 1992 Mile 135.0, Caramat subdivision, near Nakina, ON	Glaciolacustrine silts and peat	N/A	N/A	Sudden draw down of water due to a breached beaver dam
April 25, 1994 Mile 89.7, Kinghorn subdivision, Orient Bay, ON	Glaciolacustrine silts and clays	N/A	N/A	Subgrade saturation
March 26, 1997 Mile 106.15, Ashcroft Subdivision, near Conrad, BC	Alluvial low to non-plastic silts	1.5H:1.0V	1,327 mm of precipitation in the antecedent 6 months (59 years high) and more than 20 mm/day in the three days before failure	Severe weather conditions, improper drainage system, and the presence of 'moisture-sensitive' alluvial deposits
April 7, 1997 Mile 44.8, Parry Sound Subdivision, near Pointe au Baril, ON	Loose silty sand	15 m high, 90 m wide base, 1.5H:1.0V	Rapid melting of snow cap during the two weeks prior to the derailment	Build up of pore-water pressure as a result of a beaver dam and infiltration
May 6, 1997 Mile 34.55, Kingston Subdivision, near Coteau, Quebec	Gravel roadbed over weak clays	14 m high	Precipitation between April 18 and May 5 was 114.4 mm	Saturation of the weak clays under the subgrade and poor drainage
May 31, 1998 Mile 59.1, Nelson Subdivision, near Creston, BC	Glaciolacustrine silty materials	Steep side hill	Precipitation during week before the derailment was 111.2 mm (Return period: 100 year)	Saturation of the subgrade fill due to severe weather conditions and poor drainage
June 26, 1999 Mile 5.3, Keewatin Subdivision, near Keewatin, ON	Sand and silt materials	6 m high	Average intensity over the antecedent 12-hour period was 11.45 mm/h	Saturation of the subgrade fill due to severe weather conditions and poor drainage

2.3 MODELLING APPROACHES

There are two main approaches available for the modelling and assessment of railway embankment hazards; namely, the decision analysis approach and the traditional reliability-based approach. This section presents a concise overview of both modelling approaches, indicating their main advantages and limitations.

2.3.1 *Decision analysis*

Decision analysis theory provides not only a modelling tool for decision making, but also a "decision analysis process" (Clemen, 1996). The decision analysis process is based on four main steps; namely, (i) framing; (ii) modelling and data collection; (iii) model evaluation; and (iv) decision. These four main steps form a cycle that must be followed and repeated a number of times. The lessons learned from a first complete cycle must be used as a starting point for a second analysis. Posterior analysis cycles serve for the test and refinement of modelling ideas, variables, etc.

During the framing phase the problem is formulated. In order to formulate the "right problem" a problem statement must be produced, along with a list of objectives, decisions, and uncertainties. Based on this information, it is possible to create an *influence diagram* and a *decision tree* that serves as the basis of the quantitative model. A traditional *decision analysis* approach involves a team formed by the decision-maker, an evaluation team, and information experts. Information experts have the best available data, experience, and judgement relevant to specific topics and issues relevant to evaluation.

Two fundamental tools traditionally used in *decision analysis* were mentioned in the previous paragraph; namely, the *influence diagram* and the *decision tree* (Applied Decision Analysis LLC., 1998). The *influence diagram* is a graphic representation of the elements in a decision problem and the relationships among them. *Decision trees* display the time of the events in the model and a discrete representation of the uncertainties. Figure 2.7 presents an exceptionally simplified and merely illustrative *influence diagram* and *decision tree* for a slope stability problem. Not all variables are included. A decision model is composed of uncertain variables, certain variables, decisions, and a system performance variable. Figure 2.7a represents the uncertain components using circles. Uncertain variables are considered in the calculation by using discrete measurements, represented by the tree branches. The system performance variable is often represented in monetary values, but additional variables may be considered,

using multi-attribute decision analysis procedures (Bunn, 1984). Figure 2.7b shows that three branches were used for all three uncertain variables, resulting in 27 evaluations of the performance variable (i.e., the factor of safety). The number of evaluations of the performance variable is given by the total number of branches at the end of the *decision tree* and increases sharply as the number of uncertain variables increases. The number of branches is given by n^m, where n is the number of branches adopted for each variable and m is the number of uncertain variables.

The modelling and data collection phase has four steps; namely, (i) build a deterministic model; (ii) conduct deterministic sensitivity analysis; (iii) assess probability distributions; (iv) build the full probabilistic decision model. The deterministic model gives the outcome value to any scenario in the *decision tree*. It can be as simple as a table of values or as complex as a numerical model. The sensitivity analyses serves to determine what uncertainties have a significant impact on the outcome and prioritise analysis efforts. Next, available data, experience, history, and forecasts can be used to access the probability distribution of the most important variables. The final step is to build the probabilistic model. The *influence diagram* and *decision tree* must be modified in order to incorporate the probabilistic distributions of the most important parameters.

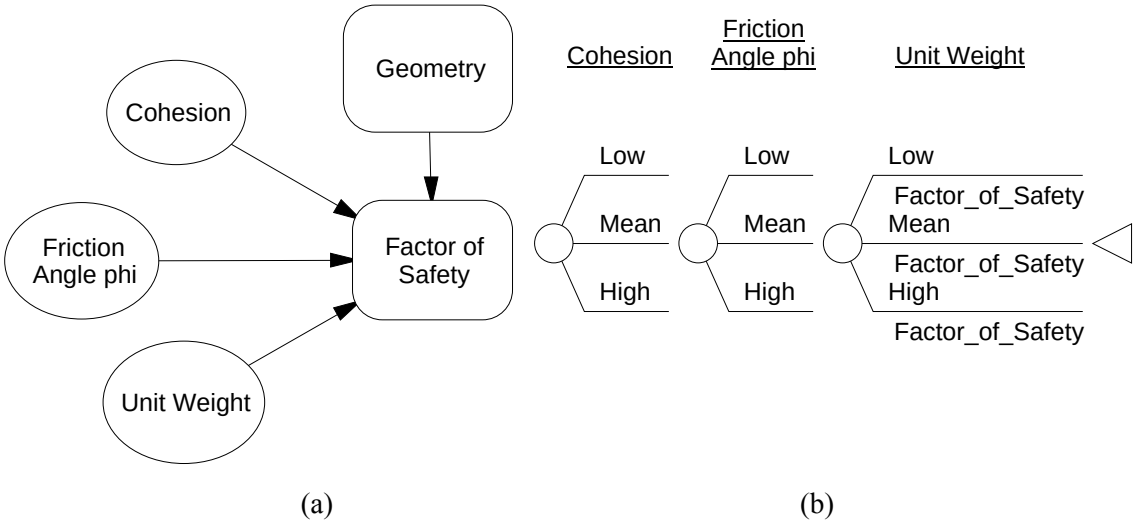

Figure 2.7 A simple decision analysis model for slope stability: (a) Influence diagram; (b) Decision tree.

During the analysis and evaluation phase the decision analysis model is applied to the problem and its performance is examined. Sensitivity analyses may be carried out in order to explore possible refinements to the model. This process must be repeated until a thorough understanding of the decision strategy is attained. The results of a decision analysis and evaluation may be analysed using policy trees, the risk profile graph. Finally, a decision can be made based on the modelling results and lessons.

The *decision analysis* framework provides useful techniques for the assessment of embankment hazards, but some of the traditionally used tools may not be considered appropriate. The decision analysis cycle described above provides a systematic approach for modelling. However, *influence diagrams* and *decision trees* may result in unfeasibly long computation times. The quantification of embankment hazards involves a large number of components and random variables. *Influence diagrams* and *decision trees* can be considered adequate only if the function adopted for quantifying hazards is simple enough or based on expert information. However, the quantification of embankment hazards involves complex and numerous phenomena that cannot be assessed based on simple expert information. A rigorous, quantitative model for hazard assessment often requires large computational effort and numerical analyses.

2.3.2 *Traditional reliability-based approach*

Reliability-based approaches have been widely used in geotechnical design (Harr, 1987). Reliability-based approaches provide a way of incorporating parameter uncertainty into the modelling process. Reliability-based approaches are based on a probabilistic method of computation of the probability density function of the performance variable (e.g., the *factor of safety*). Several methods of probabilistic analysis are reviewed later in this chapter. Measures of reliability are defined based on the central tendency and variability of the performance variable (Whitman, 1984). Several reliability measures can be adopted, including the *reliability index*, and the *probability of failure*.

Some of the available probabilistic methods require considerably less computations when compared to the *decision tree approach*. The *reliability-based approaches* may be more adequate when complex models are required for the computation of the performance variable. A combination of an efficient probabilistic method and the *decision analysis cycle* provides a more adequate and feasible method for embankment hazard assessment.

2.4 MECHANISTIC MODELS FOR THE PHENOMENA ASSOCIATED WITH EMBANKMENT STABILITY

Section 2.2 presented evidence of the role played by soil-atmosphere fluxes and ground conditions on the occurrence of derailments in the Canadian railway system. In order to quantify the geo-hazards of concern in this thesis, pore-water pressure changes within a railway embankment must be predicted as a function of weather conditions. Water flow mechanisms associated with both the infiltration and the removal of water from the ground surface through evaporation must be considered as both flow mechanisms affect antecedent conditions. The effect of the predicted pore-water pressure changes to the stability of an embankment must also be quantified. This section presents a literature review on mechanistic theories for (i) the analysis of flux in saturated/unsaturated soils, (ii) theories for the quantification of soil-atmosphere fluxes, and (iii) theories for the quantification of slope stability. These theories are termed *mechanistic* because these methods are based on continuum mechanics approaches.

2.4.1 *Models for moisture and heat movement in saturated/unsaturated soils*

The quantification of changes in water content and pore-water pressures within an embankment requires the combination of geotechnical and hydrogeology concepts. The hydrological cycle is one of the most fundamental concepts of hydrology and hydrogeology sciences and serves to characterize the behaviour, occurrence, and transformations of water in the environment (Horton, 1933, Linsley et al., 1949). From an engineering point of view, the hydrological cycle can be summarised as presented in Fig. 2.8. According to Eagleson (1970), the hydrological cycle consists of the "*circulation of water from the oceans, through the atmosphere, then reaching the continents, and the return of water after its retention at several locations to the oceans by surface and subsurface flow and in part through the atmosphere*." A whole cycle can also be complete without passing through some of the hydrological cycle components. For instance, water may move between land and atmosphere, without passing through the oceans.

Various water transport processes presented in Fig. 2.8 may take place on or within a railway embankment. Part of the water made available by the atmosphere reaches the embankment surface as precipitation, snow pack and icepack melting, and throughfall. A fraction of the water that reaches the embankment surface infiltrates. The fraction of water not reaching the embankment surface and/or not infiltrating into the embankment returns to the atmosphere as evaporation, sublimation (from the ice pack), or reaches streams, lakes, and rivers as runoff.

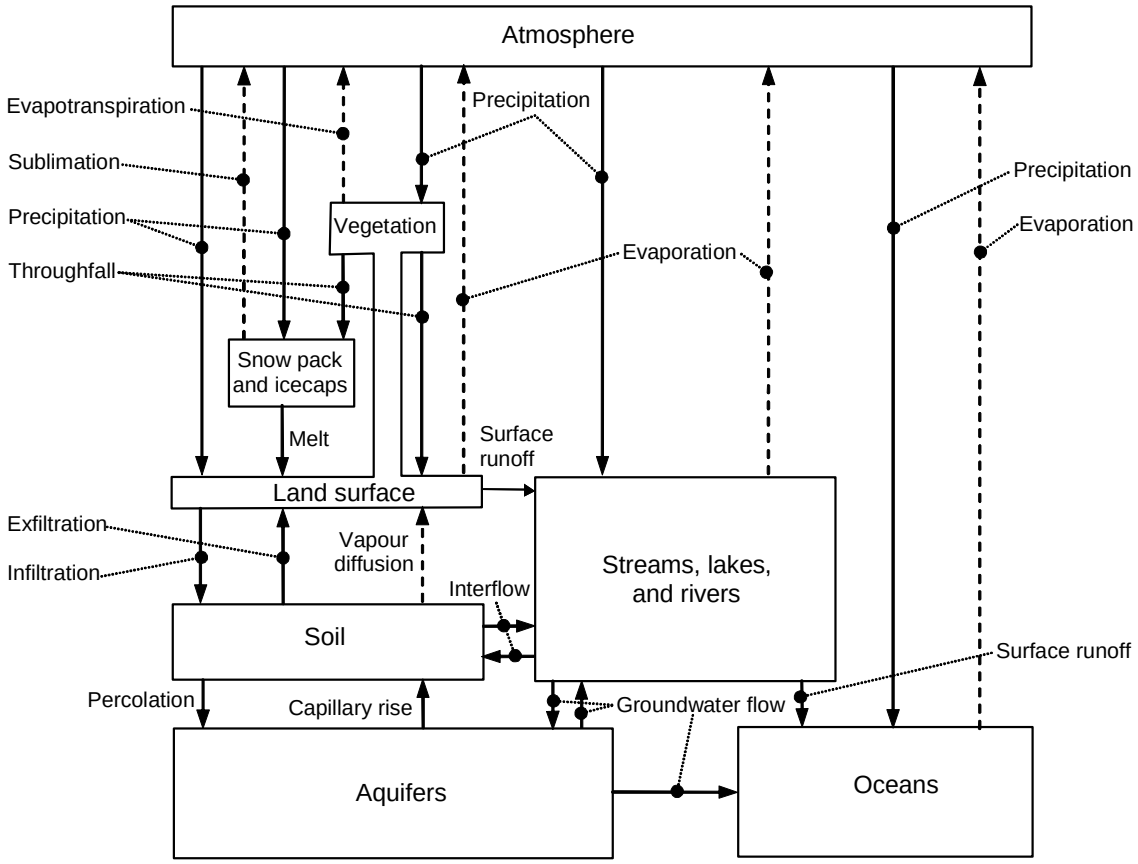

Figure 2.8 Hydrological cycle (modified from Eagleson, 1970).

Figure 2.8 indicates also the manner whereby moisture crosses the embankment surface, moving between the atmosphere and the soil comprising the embankment. The soil-atmosphere moisture transfer components indicated by Eagleson (1970) are exfiltration, infiltration, and vapour diffusion. The identification in separate of the vapour diffusion component indicates that the term exfiltration includes only flow of moisture as liquid water. Finally, Fig. 2.8 indicates that the embankment moisture may reach the groundwater. The inverse process may also take place, with groundwater moving upwards.

The flow of water in saturated/unsaturated soils and the soil-atmosphere fluxes have been studied by different areas of science. The different perspectives have led to the use of different driving potentials, the consideration of different number of soil phases, and the consideration of the effect of additional coupling, such as heat flow. The understanding and modelling of moisture flow problems consists of the definition of constitutive laws for the rate of flow of each phase and the use of fundamental laws of physics, such as the law of conservation of mass and

energy. Two distinct mechanistic approaches to the analysis of moisture flow in soil can be found in the literature. The first and simpler approach considers that the flow of moisture occurs only in liquid form. The second approach incorporates both liquid water and water vapour flow along with heat flow. Historical advances on these two main approaches are described in the following sections.

2.4.1.1 *Liquid water flow*

Darcy's law (1856) is one of the first known equations proposed to describe the flow of water in saturated soils. Darcy's law states that the flow of water is directly proportional to the total head gradient and introduces a property called coefficient of permeability, or hydraulic conductivity. The one-dimensional form of Darcy's law can be written, for the vertical direction, as follows:

$$v_y^w = -k^w \frac{\partial h}{\partial y} \tag{2.1}$$

where:

v_y^w	=	Darcy's flow in the *y*-direction (i.e., macroscopic, specific discharge);
k^w	=	coefficient of permeability;
h	=	total head;
h	=	$u_w/\gamma_w + y$;
y	=	Elevation with respect to an arbitrary datum;
u_w	=	pore-water pressure;
γ_w	=	unit weight of water;
$\partial/\partial y$	=	derivative with respect to the *y*-direction.

Equation 2.1 was extended to unsaturated soil flow by Buckingham (1907). Matric potential was used instead of total head and the coefficient of permeability was assumed as varying with water content (i.e., coefficient of permeability decreases for decreasing water content). Later, Richards (1928) re-wrote Buckingham's equation using total head as the driving potential. Richards (1931) combined the equation of conservation of mass of water and the flow law in order to obtain an equation governing the transient one-dimensional flow of water in saturated/unsaturated soils. This equation, commonly referred as Richard's equation, is written as follows:

$$\frac{\partial}{\partial y}\left[k^{w}(\theta)\frac{\partial h}{\partial y}\right]=\frac{\partial \theta}{\partial t} \tag{2.2}$$

where:

$k^w(\theta)$ = coefficient of permeability, function of θ;

θ = volumetric water content;

θ = V_w/V;

$\partial/\partial t$ = derivative with respect to time, t.

For steady state conditions in an isotropic and saturated soil Richard's equation reduces to the well-know Laplace equation. Graphical procedures known as flow nets have been used in the past for the solution of the Laplace equation (Casagrande, 1937 and Cedergren, 1977). The flow net technique has been used to solve both confined and unconfined flow. Numerical techniques are required in order to solve the more general form of Richard's equation, for transient flow in unsaturated/saturated soils. The finite difference method and the finite element method are the two most popular numerical techniques used to solve Richard's equation.

Terzaghi (1943) presented the theory of consolidation for saturated soils. The consolidation theory is based on the combination of Darcy's law, the equation of conservation of mass of water, and the volume change of the saturated soil. Terzaghi's one-dimensional formulation is summarised by the following equation:

$$\frac{k^{w}}{m_{v}\gamma_{w}}\frac{\partial^{2}u_{w}}{\partial y^{2}}=\frac{\partial u_{w}}{\partial t} \tag{2.3}$$

where:

m_v = coefficient of volume change for the saturated soil.

Philip and de Vries (1957) presented an alternative equation for the flow of moisture in saturate/unsaturated soils, expressed in terms of volumetric water content. This formulation provided improvements in terms of numerical stability because gradients of θ are considerably smaller than gradients of h. However, the equation proposed by Philip and de Vries (1957) is not appropriate for engineering applications because it neglects the gravimetric potential. In addition, the formulation using the water content as main variable cannot handle heterogeneous

soils and layered systems.

Lam et al. (1987) presented and equation similar to Richard's equation, but extended to two-dimensional conditions. It was assumed that the permeability coefficient of an unsaturated soil can be assumed a function of the volumetric water content or the matric suction. The proposed equation is as follows:

$$\frac{\partial}{\partial x}\left(k_x^w \frac{\partial h}{\partial x}\right) + \frac{\partial}{\partial y}\left(k_y^w \frac{\partial h}{\partial y}\right) = m_2^w \gamma_w \frac{\partial h}{\partial t} \tag{2.4}$$

where:

m_2^w = coefficient of water volume change with respect to matric suction;
k^w_x = coefficient of permeability in the *x*-direction;
k^w_y = coefficient of permeability in the *y*-direction.

Equation 2.4 was solved by Lam et al. (1987) using the finite element method. The analysis of several hypothetical cases showed good agreement with traditional flow net solutions. Lam et al. (1987) pointed out that the numerical solution of Eq. 2.4 produces more complete solutions for unconfined flow. Relatively arbitrary assumptions regarding the position of the water table are no longer required when Eq. 2.4 is used along with appropriate boundary conditions.

2.4.1.2 *Liquid-vapour flow and heat coupling*

The formulations for liquid water flow neglect the moisture movement when the soil is relatively dry. Formulations based on both liquid and vapour flow are required for the prediction of pore-water pressure changes within a railway embankment subjected to alternating periods of infiltration and evaporation. The flow of vapour is usually idealized as a direct function of vapour pressure gradients. The vapour pressure can be written as a function of the water potential in the soil and the temperature. As a result, gradients in temperature need to be determined. The theories for liquid water and water vapour flow found in the literature typically include a heat transfer coupling.

Several heat and moisture flow models can be found in the literature. Most early studies were presented by soil scientists and focused on identifying the mechanisms of moisture movement in soils. Buckingham (1907) presented a study of moisture movement and evaporation from soil

surfaces under arid and humid atmospheric conditions. Buckingham (1907) found that the rate of evaporation from a moist soil surface decreased with time and that the evaporation rate for arid atmospheric conditions was initially higher than in humid conditions, but at later stages would become lower. Later, Boyoucos (1915) presented a study focusing on the effect of thermal gradients on moisture flow within a closed system. Qualitative interpretations of the heat-moisture flow coupling were presented. The role of vapour flow was found to be insignificant though. Smith (1943) presented a critical study of Boyoucos (1915) work. Smith (1943) proposed that the lower than expected magnitude of vapour flow found by Boyoucos (1915) could be a result of an effect of evaporation and condensation on the capillary action and suggested that vapour flow could be considerable.

Gurr et al. (1952) conducted thermal moisture transfer experiments in soils within closed systems and using salt tracer techniques. Salt was placed at the cold end of the specimens. It was found that salt was carried to the hot end after a thermal gradient was imposed for a certain time. According to Gurr et al. (1952), vapour moved from the hot end of the specimens and condensed at the cold end. Eventually, the increase in moisture content at the cold end produced a reversed moisture path. In addition to this semi-quantitative explanation, Gurr et al. (1952) pointed out the role of the permeability of the soil with respect to both water and vapour.

Rollins et al. (1954) presented a summary of previous research work on moisture and heat flow, along with experimental results of flow tests under thermal gradients and analytical studies. A cyclic moisture flow due to the flow of vapour and liquid water was identified, similar to the findings of Gurr et al. (1952). Analyses of vapour flow showed that the computed values were one sixth of the experimental results. Rollins et al. (1954) concluded that either the values of diffusivity and/or tortuosity were wrong or some other additional moisture transfer mechanism was taking place.

Philip and de Vries (1957) presented a macroscopic and phenomenological model for coupled heat and moisture flow that reflects the most accepted concepts developed up to that in time. Two one-dimensional equations where proposed, the first for the moisture flow and the second equation for the heat flow. The equations are based on continuity of water mass and heat energy and make use of Fick's (for vapour flow) and Darcy's law (for liquid flow), along with Lord Kelvin's thermodynamic vapour pressure equation. The equations proposed are as follows:

$$\nabla \cdot \left(D_T \nabla T\right) + \nabla \cdot \left(D_\theta \nabla \theta\right) + \frac{\partial k^w}{\partial y} = \frac{\partial \theta}{\partial t} \tag{2.5}$$

$$\nabla \cdot \left(\lambda \nabla T\right) - L\nabla \cdot \left(D_{\theta vap} \nabla \theta\right) = C\frac{\partial T}{\partial t} \tag{2.6}$$

where:

D_T	=	thermal moisture diffusivity (liquid and vapour);
T	=	temperature;
D_θ	=	isothermal moisture diffusivity (liquid and vapour);
λ	=	apparent thermal conductivity;
L	=	latent heat of vaporization;
$D_{\theta vap}$	=	isothermal vapour diffusivity;
C	=	volumetric heat capacity of the soil.

Equation 2.5 governs moisture flow (both liquid water and water vapour) driven by gradients of both volumetric moisture content and temperature. Equation 2.6 governs heat flow driven by conduction and heat consumption due to vaporization/condensation (latent heat). Several simplifying assumptions were considered in Eqs. 2.5 and 2.6. The liquid phase was assumed to have uniform chemical properties and to move under capillary and adsorptive forces. Vapour flow by diffusion was assumed to take place only on the air-filled pores. The pore-air pressure was assumed uniform and constant. Local thermodynamic equilibrium was assumed and heat flow by radiation was neglected.

Philip and de Vries (1957) observed that the diffusivity of moisture could be separated into two components, one corresponding to flow of water vapour and the other corresponding to flow of liquid water. It was also observed that the vapour diffusivity controls the overall rate of moisture flow under relatively dry conditions, whereas the liquid water diffusivity dominates under relatively wet conditions. Additionally, Philip and de Vries (1957) explained why vapour flow larger than expected had been previously observed by several researchers. The relatively high vapour flow was due to higher temperature gradients within soil pores. These higher gradients were theoretically reproduced by using appropriate thermal conductivity functions. Philip and de Vries (1957) where successful in identifying and modelling the most important mechanisms associated with coupled moisture and heat flow in saturated/unsaturated soils, but some limitations where pointed out. Among the main limitations, hysteresis was not considered,

total volume change of the soil was not considered, the formulation was limited to homogeneous and isotropic media, and freezing and thawing processes were not considered.

Philip and de Vries (1957) formulation has been tested against laboratory and field data and subjected to further theoretical examination by several other researchers. Reasonably good agreement between experimental and simulated data was obtained in some but not all cases. Some of these research results are presented by Aitchinson et al. (1965), Cassel et al. (1969), Jury and Miller (1974), Jackson et al. (1975), Dempsey (1978), Sophocleous (1979), and Milly (1984), among others. According to de Vries (1987), the natural soils variability and difficulties in measuring moisture and temperature gradients, and limitations of the theory are some of the reasons for eventual difficulties in comparing theoretical and measured data.

The equations proposed by Philip and de Vries (1957) cannot be considered adequate for geotechnical engineering applications because they do not consider the gravimetric potential and are limited to homogeneous and isotropic media. Systems formed by layers of different soils cannot be modelled by the equations proposed by Philip and de Vries (1957). In addition, the formulation does not take into account for total volume change and the influence of changes in total stresses. Therefore, volume change problems cannot be addressed by this theory. The formulation is not able to compute pore-air changes, making the theory inadequate for certain conditions were the pore-air cannot be immediately drained.

In order to overcome some of the limitations of the Philip and de Vries (1957) theory, Fredlund and Hasan (1979) presented a theory of one-dimensional consolidation of unsaturated soils following the geotechnical engineering approach taken by Terzagui (1943) for saturated soils. The individual behaviour of the air and water phases was considered. Therefore, both the air and the water phases were assumed as distinct phases that can flow according to separate gradients. Most of the basic assumptions adopted were the same of those adopted by Terzagui (1943) for saturated soils. The air phase was considered continuous. Two partial differential equations were proposed, for the air and water phases, as follows:

$$-C_a \frac{\partial u_w}{\partial t} + c_v^a \frac{\partial^2 u_a}{\partial y^2} = \frac{\partial u_a}{\partial t} \tag{2.7}$$

$$-C_w \frac{\partial u_a}{\partial t} + c_v^w \frac{\partial^2 u_w}{\partial y^2} = \frac{\partial u_w}{\partial t} \tag{2.8}$$

where:

C_a = interactive pressure constant associated with the air phase;

u_a = air pressure;

c_v^a = coefficient of consolidation for the air phase;

C_w = interactive constant associated with the water phase;

c_v^w = coefficient of consolidation for the water phase.

Dakshanamurthy and Fredlund (1980) extended the work of Fredlund and Hasan (1979) for non-isothermal conditions by considering the flow of heat. The three partial differential equations governing the flow of water, air, and heat were solved using the principle of superposition. The interaction between the air and water phases was considered through a pore-pressure parameter, $B_{aw} = \Delta u_a / \Delta u_w$. The pore-water pressure was adjusted using the pore-pressure parameter B_{aw}. The pore-air pressure was adjusted according to the temperature using the ideal gas law. Later, Dakshanamurthy and Fredlund (1981a) presented a fully coupled solution for the equations proposed by Dakshanamurthy and Fredlund (1980).

Dakshanamurthy and Fredlund (1981b) presented a new set of equations, incorporating the flow of vapour to the partial differential equations. The proposed equations are as follows:

$$C_a \frac{\partial u_w}{\partial t} + C_T \frac{\partial T}{\partial t} + c_v^a \frac{\partial^2 u_a}{\partial y^2} = \frac{\partial u_a}{\partial t} \qquad (2.9)$$

$$C_w \frac{\partial u_a}{\partial t} + c_{vl}^w \frac{\partial^2 u_w}{\partial y^2} + c_{vv}^w \frac{\partial^2 p_v}{\partial y^2} = \frac{\partial u_w}{\partial t} \qquad (2.10)$$

$$\alpha \frac{\partial^2 T}{\partial y^2} = \frac{\partial T}{\partial t} \qquad (2.11)$$

where:

C_T = interactive thermal constant associated with the air phase;

c_{vl}^w = coefficient of consolidation for the liquid water phase;

c_{vv}^w = coefficient of consolidation for the water vapour phase;

p_v = partial water vapour pressure;

α = thermal diffusivity factor, function of the thermal conductivity and heat capacity.

Wilson (1990) and Wilson et al. (1994) presented a one-dimensional soil-atmosphere model that combines moisture and heat flow equations (including latent heat) and formulations to couple the soil flow and the atmosphere forcing conditions. Heat energy consumption due to vaporization and condensation was incorporated into the formulation. The model was developed with focus on evaporative fluxes, but the equations are applicable to both infiltration and exfiltration. Wilson (1990) presented a rigorous derivation of the governing equations and developed a finite difference model for the solution of the proposed equations. The numerical model considered the air phase to be continuous and in contact with the atmosphere. Good agreement was observed between the numerical model solution and laboratory results of a sand column drying test. The set of equations proposed by Wilson (1990) are as follows:

$$C_w^1 \frac{\partial}{\partial y}\left(k^w \frac{\partial h}{\partial y} \right) + C_w^2 \frac{\partial}{\partial y}\left(D_v \frac{\partial p_v}{\partial y} \right) = \frac{\partial h}{\partial t} \tag{2.12}$$

$$\frac{\partial}{\partial y}\left(\lambda \frac{\partial T}{\partial y} \right) - L_V \left(\frac{\overline{u}_a + p_v}{\overline{u}_a} \right) \frac{\partial}{\partial y}\left(D_v \frac{\partial p_v}{\partial y} \right) = C_V \frac{\partial T}{\partial t} \tag{2.13}$$

where:

C_w^1	=	coefficient associated with consolidation due to liquid flow;
C_w^2	=	coefficient associated with consolidation due to vapour flow;
D_v	=	diffusion coefficient of the water vapour through soil;
λ	=	thermal conductivity;
L_v	=	latent heat of vaporization;
C_V	=	apparent volumetric specific heat.

Later, Joshi (1993) presented a one-dimensional finite element model for the solution of the equations proposed by Wilson (1990). The numerical model reproduced the column drying test results by Wilson (1990) with reasonable agreement. The numerical model developed by Joshi (1993) took approximately 1% of the running time and half of the elements required by the finite difference model developed by Wilson (1990).

Tratch et al. (1995) extended the theoretical and numerical models proposed by Wilson (1990) to include plant transpiration. The models were extended through the incorporation of a sink term to the moisture flow partial differential equation. The amount of water uptake was obtained using the equations proposed by Ritchie (1972), a triangular water uptake distribution, and a

plant limiting factor. A laboratory experiment was conducted, using a column of silt with a vegetation cover. Experimental and simulation results agreed well and showed the significance of the transpiration flux term.

A two-dimensional extension of the framework established by Wilson (1990) and subsequent researchers appears to be appropriate for geotechnical engineering applications and could be used as the basis for a two-dimensional formulation to model the flow of moisture in a railway embankment. While the partial differential equations proposed by Wilson (1990) appear appropriate, several inconsistencies can be pointed out in terms of the solution approach proposed and in terms of the definition of boundary conditions. For instance, Wilson et al. (1994) suggests that natural boundary conditions could be partitioned in terms of vapour and liquid flow but does not present a theoretical justification. Lord Kelvin's equation is proposed by Wilson et al. (1994) to couple water and heat flow equations, but the coupling approach is not described. A number of developments are required in order to model the flow of water in a railway embankment, such as the formulation of two-dimensional governing equations and the establishment of appropriate two-dimensional boundary conditions. A coupling approach clearly defined must also be established for the water flow and heat flow equations.

2.4.2 *Equations for soil-atmosphere interaction*

The changes in pore-water pressure and moisture content within a railway embankment are a function of the flow of moisture through the soil-atmosphere boundary. In order to compute the changes in pore-water pressure within an embankment, the equations presented in the previous section require boundary conditions to reproduce the soil-atmosphere interaction. The soil-atmosphere boundary conditions depend mostly on three main components; namely, evaporation, precipitation, and runoff. There are several propositions in the literature for computing the three main components of soil-atmosphere flux. The next sections will present a concise description of the most important formulations available.

2.4.2.1 *Evaporation*

Evapotranspiration is the process whereby water from either wet surfaces or plant leaves is brought to a vapour state through heat transfer (Veihmeyer, 1964, Linsley, Kohler and Paulhus, 1949). Evaporation takes place from free water surfaces and non vegetated soil surfaces, while transpiration is related to vaporization of water through plants. Although some other factors may interfere, the evaporation mechanism from soil surfaces is basically the same as in free

water surfaces. Railway embankments may have vegetated surfaces. Nonetheless, only evaporation will be considered in this literature review and in the general framework for hazard assessment provided in this thesis. This section presents the fundamental concepts related to evaporation, some of the most relevant models, and a historical review of the major scientific breakthroughs on the subject.

The understanding of the process of evaporation has developed significantly since the 1940's. Most studies focused on evaporation from free water surfaces, but some extensions to evaporation from soil surfaces where developed. Three conditions are required for the process of evaporation to occur, as described by Penman (1948), Veihmeyer (1964), Baver et al. (1972), and Hillel (1982). Firstly, a continuous supply of energy must be available for the latent heat of vaporization. The net all-wave radiation, R_n, is typically the most important energy supply. Secondly, the vapour pressure of the atmosphere above the evaporating surface must be less than the vapour pressure at the soil surface. The vapour pressure is proportional to the amount of vapour molecules in a unit volume of air and can be interpreted as a measure of concentration of vapour. If the vapour in the air is not removed and an energy source keeps the kinetic energy of the liquid water molecules high enough, evaporation will continue until the vapour pressure in the surrounding air reaches a value equal to the vapour pressure at the evaporating surface. The first two conditions required for evaporation to occur determine the *potential evaporation*, *PE*, and are controlled by micro-meteorological factors such as long and short wave radiation, humidity, air temperature and wind speed.

Penman (1948), Veihmeyer (1964), Baver et al. (1972), and Hillel (1982) explained that the third condition required for evaporation to occur is the existence of a continual supply of water to the evaporating surface. In the case of a free water surface, the supply of water is related to the depletion of the water body. For a soil surface, the supply of water is controlled by subsurface conditions such as soil type, moisture content, and groundwater. Gardner (1958) observed that the shallower the water table, the higher the evaporation rate. For a shallow and constant water table, a steady state flux can occur, with the water being removed through the surface and with a constant water content profile. In the absence of a shallow water table, evaporation starting from a wet condition is a variable process. It takes place in three stages; namely, constant-rate stage, falling-rate stage, and low-rate stage (see Fig. 2.9). During the constant-rate stage, the evaporation rate from soil is equal to that from a free water surface in the same micro-meteorological conditions and is controlled mainly by the *potential evaporation*. In the falling-

rate stage, the evaporation rate is less sensitive to the *potential evaporation*, and is dictated only by the water transmission properties of the soil. In the low-rate stage, a few centimetres of soil surface dry out to air relative humidity and water is lost slowly as vapour movement through the dry layer. Therefore, an embankment surface may experience the three drying stages during dry periods when the water table is relatively deep.

There are several methods of direct and indirect measurement of evaporation. Among the direct methods, the "class A" evaporation pan in one of the most widely used for free water surfaces. Lysimeter are typically used for soil surfaces. Unfortunately, edge effects limit the applicability of lysimeters. There are also a large number of indirect methods, using empirical, semi-empirical and physical approaches. Most of the indirect methods of determination of evaporation were developed for free water or wet soil surfaces and have limited applicability to non-wet soil surfaces. Nevertheless, the methods developed for free water surfaces serve as a reference for the evaporation of soil surfaces. The indirect methods are based on different approaches, using different physical concepts. Barry (1969) explained that the major approaches to the estimation of evaporation and evapotranspiration can be classified as: (i) aerodynamic equations; (ii) energy-budget equations; and (iii) combination methods, involving the use of both the above approaches.

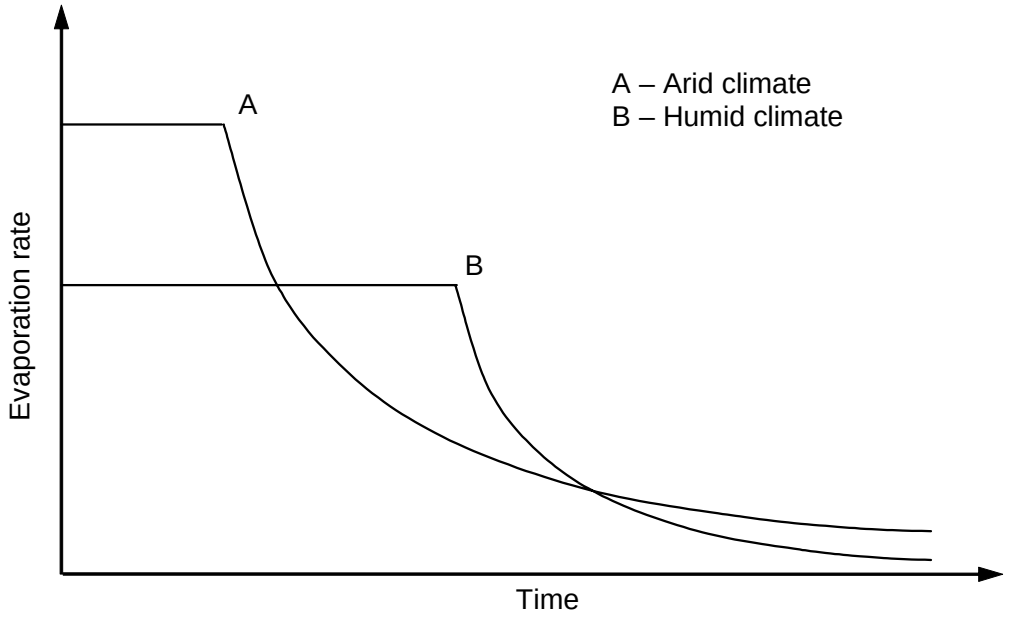

Figure 2.9 Evaporation rate versus time on a soil surface for different climates (modified from Hillel, 1971).

Table 2.2 Equations for the indirect calculation of potential and actual evaporation rate (*PE* and *AE*, respectively).

Method (1)	Equation (2)	Eq. # (3)	Input parameters (4)
Dalton type equation	$PE = B(p_{vsat} - p_v^{air})$	2.14	B = a transmission function which depends on the mean wind speed and turbulent mixing; p_{vsat} = surface saturation vapour pressure; p_v^{air} = vapour pressure at the near ground surface air.
Water mass conservation	$PE = P - R$, mm/day	2.15	P = precipitation, mm/day; R = runoff, mm/day.
Energy budged (Bowen ratio)	$PE = \frac{Q_n}{\rho_w L_V (1+R)}$, m/s	2.16	Q_n = net radiation, J/m^2 s; ρ_w = water density, kg/m^3; L_V = latent heat of vaporisation, J/kg; R = Bowen ratio.
Mass transfer Rohwer (1931)	$PE = 0.44(1+0.118u)(p_v - p_v^a)$, mm/day	2.17	u = wind speed, miles/h; p_v = evaporating surface vapour pressure; p_v^a = vapour pressure above the surface;
Aerodynamic equation Thorntwaite and Holzman (1942)	$PE(x_0, y_0) = Cu_2^{0.76} x_0^{0.88} y_0 (p_v - p_v^{a'})$, mm/day	2.18	x_0, y_0 = evaporating area, m; C = constant related to the temperature; u_2 = wind speed at 2 m, miles/day; p_v = vapour pressure at the surface; $p_v^{a'}$ = vapour pressure above surface unaffected by evaporation.
Thornthwaite (1948)	$PE = 1.6\left(\frac{L}{12}\right)\left(\frac{N}{30}\right)\left(\frac{10T_a}{I}\right)^a$, cm/month	2.19	L = length of daylight, hours; N = number of days during the month; T_a = mean monthly air temperature, ^{o}C; a=6.75·10$^{-7}I^3$–7.71·10$^{-5}I^2$–1.79·10^{-2}I–0.492 $I = \Sigma^{12}_{month=1}(T_a / 5)^{1.514}$.
Combined method Penman (1948)	$PE = \frac{\Gamma Q_n + \eta E_a}{\Gamma + \eta}$, m/s	2.20	Γ = slope of the saturation vapor pressure versus temperature curve, mmHg/^{o}F; Q_n = net radiation at the surface, m/s; η = psychrometric const., 0.27 mmHg/^{o}F; $E_a = 0.35(1 + 0.15W_w)(p_{vsat}^{air} - p_v^{air})$, m/s; W_w = wind speed, km/h; p_v^{air} = near surface air vapour pressure.
Blaney and Criddle (1950)	$PE = (0.457T + 8.13)p$, mm/day	2.21	T = mean daily temperature, ^{o}C; p = mean annual fraction of day that is in daylight.
Jensen and Haise (1963)	$PE = (0.025T + 0.078)\frac{R_s}{59}$, mm/day	2.22	T = air temperature, ^{o}C; R_s = incident solar radiation, mm/day.
Penman-Monteith Monteith (1965)	$PE = \frac{1}{\lambda}\left[\frac{\Gamma A + \rho_a c_p D / r_a}{\Gamma + \eta(1 + r_s / r_a)}\right]$, MJ/m^2 day	2.23	Γ, η = same as in Penman (1948), kPa/^{o}C; $A = R_n - G$, MJ/m^2 day; ρ_a = air vol. heat capacity, MJ/m^3 ^{o}C; c_p = vapour pressure deficit, kPa; D = fraction of day that is in daylight; r_s, r_a = canopy and aerodynamic resistances to vapour transfer, day/m.

Priestley-Taylor (1972)	$PE = \alpha \frac{\Gamma}{\Gamma + \eta}(R_n - G)$, mm/day	2.24	α = empirical constant; Γ, η = same as in Penman (1948); R_n = net radiation, mm/day; G = soil heat flux, mm/day.
Hargreaves (1985)	$PE = 0.0023 S_0 \sqrt{\delta_T}\,(T + 17.8)$, mm/day	2.25	S_0 = extraterrestrial radiation, mm/day; δ_T = difference between the mean monthly maximum and minimum temperature, ^oC; T = temperature, ^oC.
Modified Penman (Wilson, 1994)	$AE = \frac{\Gamma Q_n + \eta E_a}{\Gamma + \eta A}$, m/s	2.26	Γ, Q_n, η, W_w, p_v^{air} = as in Penman (1948); $E_a = 0.35(1 + 0.15W_w)p_v^{air}(B - A)$, m/s; $A = 1/RH$; $B = 1/RH_{air}$; RH = relative humidity at the surface; RH_{air} = relative humidity of the air.
Limiting function (Wilson et al., 1997)	$AE = PE \frac{p_v - p_v^{air}}{p_{vsat} - p_v^{air}}$ $= PE\left[\frac{RH - \left(p_{vsat}^{air} / p_{vsat}\right)RH_{air}}{1 - \left(p_{vsat}^{air} / p_{vsat}\right)RH_{air}}\right]$	2.27	AE = actual evaporation; p_v = vapour pressure at the soil surface; p_v^{air} = vapour pressure at the near ground surface air; p_{vsat}^{air} = saturation vapour pressure at the near ground surface air; p_{vsat} = surface saturation vapour pressure; RH, RH_{air} = same as in Wilson (1994).

Table 2.2 presents an overview of some of the well known methods in chronological order. This summary is by no means exhaustive, but shows that there are a large number of equations available, following different approaches. A detailed review of most of the equations presented in Table 2.2 can be found in Wilson (1990). Each equation presented in Table. 2.2 have its advantages and disadvantages. Most equations are used for calculating the *potential evaporation*, *PE*, which corresponds to the evaporation rate from a surface given that a continual supply of water to the evaporating surface exists.

Equation 2.20, proposed by Penman (1948), is one of the most popular equations for indirectly determining *potential evaporation*. Equation 2.20 combines a Dalton type formulation (Eq. 2.14) with the heat budget equation, Eq. 2.16. With the combination of both methods, the temperature at the evaporating surface is no longer required. The equation proposed by Penman (1948) uses only routine weather data, but incorporates the effect of several important factors, such as, relative humidity of the air, air temperature, net solar radiation, and wind speed. Penman (1948) presents some comparisons between observed and computed values of evaporation, for water and wet soil surfaces (both vegetated and not). The results agreed reasonably, with some small differences due to the surface albedo. However, it is important to note that the experiments carried out with soil had a constant source of water keeping the soil at saturated or near saturated conditions. Therefore, these tests did not serve as a verification of Penman's equation for soils at relatively dry conditions. Linsley et al. (1958) points out that Penman's equation overestimates the evaporation rate for low winds and humid conditions and

underestimates the evaporation rate for windy and dry conditions.

The only equations presented in Table 2.2 that consider unsaturated soil surface conditions are Equations 2.26 and 2.27. These equations are used for calculating the *actual evaporation*, *AE*, from soil surfaces. Equation 2.26, proposed by Wilson (1994), is a modified version of the equation proposed by Penman (1948). Wilson (1994) included the dry soil conditions in the Penman formulation by replacing the water surface vapour pressure by the soil surface vapour pressure. The soil vapour pressure can be related to the soil suction and soil water content by using Lord Kelvin's equation. The soil suction at the soil surface can be obtained by combining Eq. 2.26 or 2.27 and a moisture transfer model, such as Eqs. 2.12 and 2.13. Wilson et al. (1997) presented a more general approach by using a *limiting function* that can be combined with any direct or indirect value of *potential evaporation*. Equations 2.26 and 2.27 were experimentally tested by Wilson (1990) using thin soil layer drying experiments and a sand column drying test, with reasonable results. The equations proposed by Wilson (1990) and Wilson et al. (1997) are based on a sound theoretical basis. The combination of Eqs. 2.26 or 2.27 and moisture and heat movement partial differential equations provides a method for computing evaporative fluxes from saturated/unsaturated soils.

2.4.2.2 *Infiltration and runoff*

Infiltration is the process whereby water enters the soil through the soil-atmosphere boundary. The sources of water available for infiltration can be from rain, snow melt, or irrigation. According to the hydrological cycle presented in Fig. 2.8, part of the water from precipitation may be intercepted or may turn into runoff. Surface retention includes interception, depression storage, and evaporation during a precipitation event, but does not include that water which is temporarily stored en route to the streams.

Infiltration produces a downward flux that changes the water content with depth. Horton (1933) showed that during a period of constant precipitation, the rate of infiltration decreases with time. Horton (1933) showed also that there is a limiting curve that gives the maximum infiltration rate along the time, assuming that there is always water available to be infiltrated (see Fig. 2.10). The driving potential responsible for the infiltration of water is the total head gradient between the wetting front and the soil surface. Considering that the total head is constant at the soil surface, if the wetting front is advancing, the total head gradient is reducing. This explains in part why the rate of infiltration decreases with time (Koorevaar et al., 1983). If the amount of

precipitation minus interception is higher than the maximum rate obtained from the limiting curve, runoff takes place. When there is plenty of water available for infiltration, the infiltration rate follows the limiting function along the time, until a constant rate is reached. This constant rate is called *infiltration capacity*. According to Rubin et al. (1964) cited by Freeze and Cherry (1979), the infiltration capacity is equal to the saturated coefficient of permeability, k^w_{sat}.

There are several theories for the computation of the amount of infiltration. Two main approaches are available, the first using empirical equations and the second using saturated/unsaturated moisture flow theory. The most common empirical equations were proposed by Kostiakov (1932), Horton (1933), and Holtna (1961). The equation proposed by Kostiakov (1932) establishes a relationship between the infiltration rate and time using the following function:

$$I = I_0 t^{-\alpha} \tag{2.28}$$

where:

I = infiltration rate;

I_0 = the initial infiltration rate;

α = empirical constant experimentally determined for the site of interest.

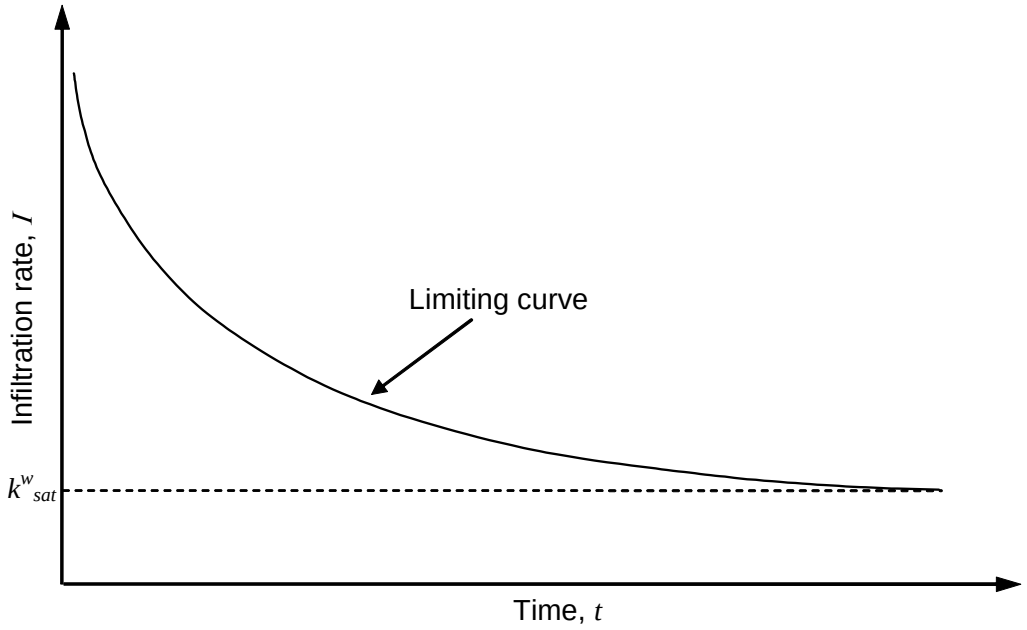

Figure 2.10 Infiltration rate versus time (Horton, 1933 and Koorevaar et al., 1983).

Horton (1933) proposed a popular empirical equation that is based on three parameters. The equation is as follows:

$$I = f_c + (f_0 - f_c)e^{-\beta t} \tag{2.29}$$

where:

f_c = the infiltration capacity;
f_0 = the maximum infiltration rate;
β = the rate of decrease of the infiltration rate.

Equations 2.28 and 2.29 merely try to reproduce the shape and main features identified in the limiting infiltration curve. The equations proposed by Green and Ampt (1911) and by Philip (1957) incorporate some physics into the infiltration rate equations. The Green and Ampt (1911) model is based on Darcy's equation and is based on the infiltration in deep homogeneous reservoirs with a homogeneous initial water content distribution. A well defined wetting front is assumed, with the soil saturated beyond the wetting front. Green and Ampt (1911) proposed the following analytical solution:

$$I = k_{sat}^{w}\left[1 + \frac{(n - \theta_i)S_f}{D}\right] \tag{2.30}$$

where:

n = the soil porosity;
θ_i = the initial volumetric water content;
S_f = the soil suction at the wetting front;
D = cumulative depth infiltrated.

Philip (1957) proposed an analytical solution of the water flow equation that is based on a finite difference solution. The proposed equation for the infiltration rate is as follows:

$$I = \frac{C}{2}t^{1/2} + F \tag{2.31}$$

where:

C = the field capacity;

F = a constant related to the gravity driving mechanism.

The infiltration rate can also be computed in a rigorous manner, by modelling the internal moisture flow combined with boundary conditions that represent the precipitation and drainage conditions. Freeze and Cherry (1979) present some analyses using Richard's equation and the finite difference method, with excellent results. The results are in qualitative agreement with the shape of the limiting curve presented in Fig. 2.10. The approach presented by Freeze and Cherry (1979) is similar to the general approach for computing evaporation, presented in the previous section in the sense that internal water flow equations are combined with appropriate boundary conditions. In fact, both precipitation and evaporative boundary conditions can be combined and solved along with water flow differential equations. This approach results in a comprehensive analysis that is able to handle alternating infiltration and exfiltration boundary conditions.

2.4.3 *Methods of stability analysis*

Section 2.2 presented several derailment occurrences caused by embankment/roadbed failures triggered by severe weather conditions. The previous sections presented approaches available in the literature for computing pore-water pressure changes according to the weather conditions. The prediction of soil moisture and pore-water pressure changes is a fundamental step towards the quantification of embankment stability. Nevertheless, a measure of stability must be selected that takes into account the pore-water pressures within a railway embankment, the shear strength of the soil, and the failure mechanism.

Embankment stability can be quantified using several methods of stability analysis. The major stability analysis methods can be classified in four categories; namely, (i) *slip lines methods*; (ii) *limit equilibrium methods* (LEM); (iii) *limit analysis methods* (LAM); and (iv) *displacement-based finite element methods*. The main criterion for establishing the above categories is the manner how failure is defined by each method. Though most methods of stability analysis have certain elements of the LAM framework, not all requirements of a *limit analysis* solution are met by the other procedures (Chen, 1975). Hence, independent categories of stability analysis methods can be established.

The *limit equilibrium method* is by far the most popular stability analysis approach available, due to its simplicity. Considerable design experience has been accumulated using the LEM. For

these reasons, this literature review will be focused on *limit equilibrium methods*. The typical railway embankment stability problems can be reduced to two-dimensional, plane strain problems. Therefore, only two-dimensional *limit equilibrium methods* will be considered herein.

Numerous *limit equilibrium methods* of two-dimensional slope stability analysis have been proposed to this date. The set of concepts and assumptions pertaining to each method often overlaps, making their categorization difficult. Nevertheless, Fig. 2.11 presents a tentative categorization. The three main categories presented in Fig. 2.11 were established based on the most distinguishable aspect of each approach. Existing combinations of the three main approaches were not indicated in Fig. 2.11. The LEMs consist in the search of a failure mechanism (i.e., a critical slip surface) that gives a minimum value of the overall *factor of safety*, F_s (Fig. 2.12). The classical definition of overall F_s is as follows: *factor of safety is the factor by which the shear strength must be reduced to bring the soil mass into a state of limit equilibrium along a given slip surface* (Coulomb, 1773). The shear strength of the soil required to compute F_s can be calculated based on the extended Mohr-Coulomb failure criteria for saturated/unsaturated soils and the total stress and pore-water pressure distributions.

Several *methods of slices* are shown in the first branch of Fig. 2.12. In order to calculate the *factor of safety*, a slipping wedge is divided in slices and equations of static equilibrium are applied to the slipping wedge as a whole and to each of the slices. Figure 2.11 indicates what equilibrium equations are satisfied by a number of methods. Different combinations of moment, vertical, and horizontal equilibrium can be found in the literature. Several trial slip surfaces with an assumed shape, usually circular, are analysed in order to find the minimum *factor of safety*. If a circular slip surface is assumed, a grid of centres can be defined and the radius varied at each centre. The same procedure can be used for composite slip surfaces (Fredlund, 1981). The static equilibrium equations solved by the *method of slices* disregard the soil stress-strain behaviour and gives no consideration to the ratio of horizontal and vertical stresses, K_0. The *method of slices* is also incapable of determining the mechanism of failure. Therefore, the shape of the slip surface must always be assumed. Fredlund and Krahn (1977) and Fredlund (1984) present detailed literature reviews about the historical developments related to the *methods of slices* and the most popular methods proposed.

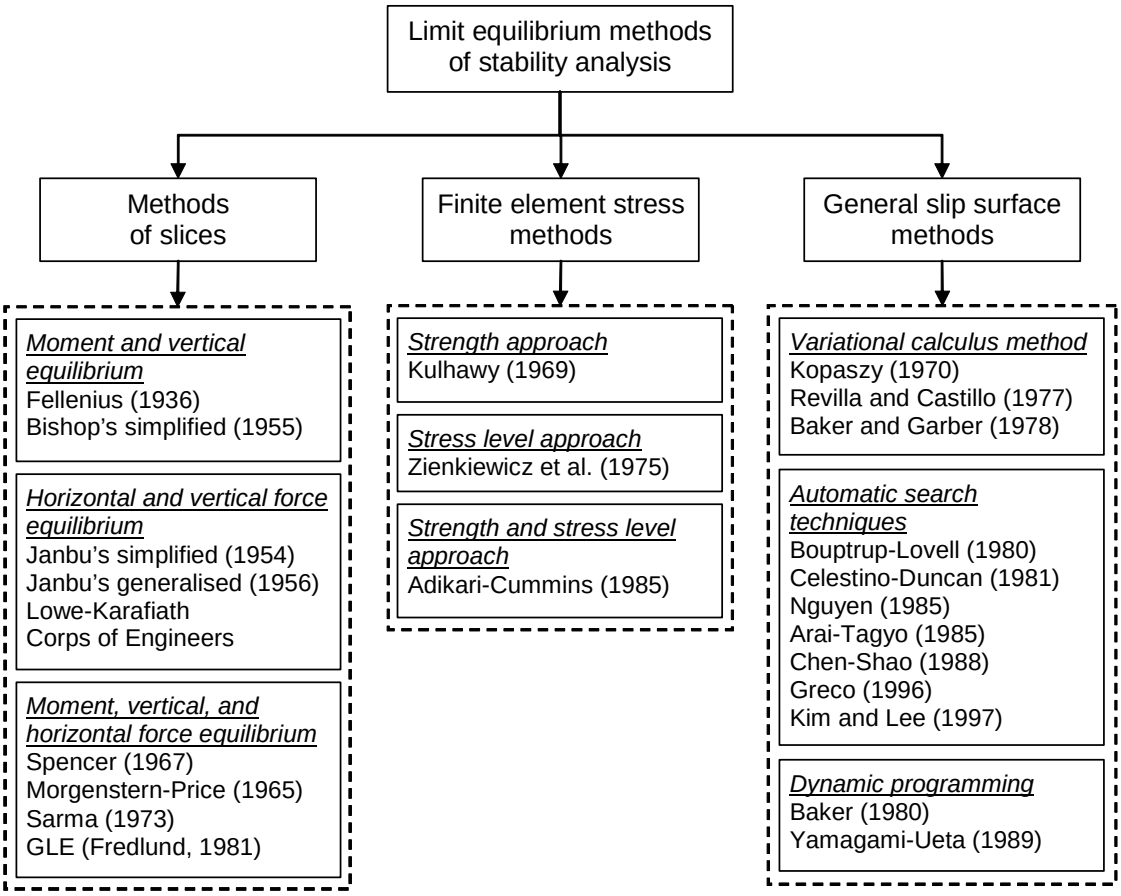

Figure 2.11 Categorisation of common limit equilibrium methods of stability analysis.

The *finite element stress methods*, presented in the second branch in Fig. 2.11, use a finite element stress distribution in order to compute the factor of safety. The stresses along any trial slip surface are obtained from the stress distribution calculated by solving numerically the partial differential equations governing static equilibrium. The calculation of stress distributions using the finite element method allows the incorporation of the mechanical behaviour of the soil (i.e., the stress-strain behaviour) and boundary conditions in the analysis. Several trial slip surfaces must be analysed in order to find the minimum factor of safety. However, the failure mechanism (i.e., the slip surface shape) must be assumed. Kulhawy (1969) introduced the *finite element stress method* and defined the *factor of safety* as the ratio of the sum of the resisting and acting forces along the trial slip surface. Later, several other methods were proposed, using alternative definitions for the *factor of safety*.

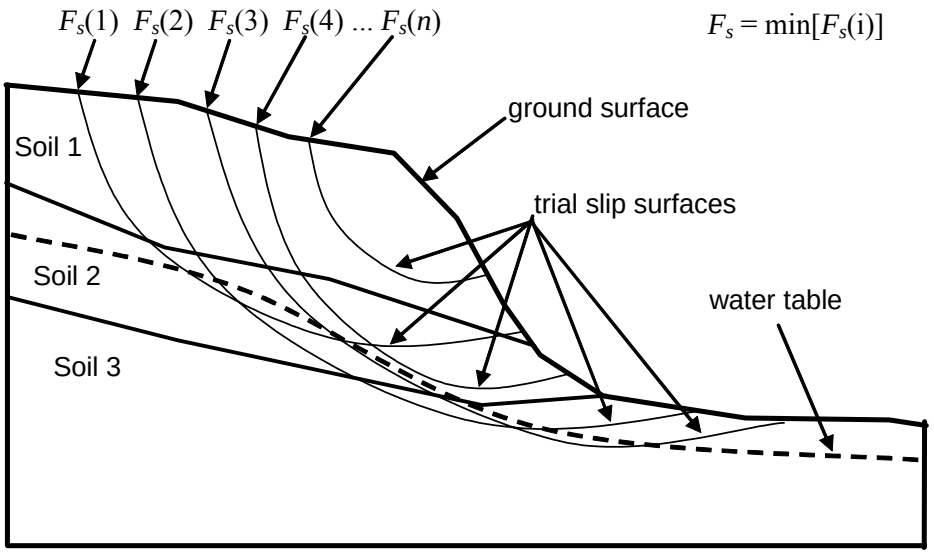

Figure 2.12 Limit equilibrium methods of stability analysis.

The actual failure mechanism often deviates from circular arc shapes traditionally assumed. This has motivated the development of general methods of slope stability analysis that are capable of determining the location and shape of the critical slip surface, and the corresponding factor of safety. The third branch in Fig. 2.11 presents such general methods, termed herein *general slip surface methods*. The earliest *general slip surface method* was based on variational calculus (Kopacsy, 1957). *Variational calculus* solutions were pursued by several researchers, with limited success. Other noteworthy general slip surface approaches proposed use *random search* techniques (Carter, 1971 and Boutrup and Lovell, 1980), the *alternating variable method* (Celestino and Duncan, 1981), and several general mathematical optimization methods. These methods did not achieve wide acceptance due to their lacking theoretical background and the considerable computational requirements, as will be presented next.

A third type of general slip surface method, called *dynamic programming method*, was proposed by Baker (1980). Unlike the other *general slip surface* approaches, the *dynamic programming method* has a solid theoretical basis and a relatively simple formulation that has been verified against other slope stability analysis methods (Pham et al., 2001). The assessment of transient stability conditions requires repeated computations of *factor of safety* for several time steps. The availability of an automated search procedure becomes advantageous for such conditions.

The next sections will present a concise description of advances in the use of finite element

stress fields in slope stability, followed by a review of historical developments regarding *general slip surface methods*. Detailed literature reviews of methods of slices can be found elsewhere (Fredlund and Krahn, 1977 and Fredlund, 1984) and will not be presented herein.

2.4.3.1 *Finite element stress methods of stability analysis*

Bishop (1952), La Rochelle (1960), and Wright et al. (1973) among others, have pointed out that the stresses calculated along a slip surface using the *methods of slices* do not agree with the actual stresses. A superior alternative to the *method of slices* is the use of the finite element method to solve the partial differential equations governing static equilibrium. Kulhawy (1969) introduced the use of finite element stress fields in slope stability analysis, assuming a linear elastic behaviour. Kulhawy (1969) proposed a definition of overall *factor of safety*, here called *strength approach*. Alternative definitions for the *factor of safety* have been proposed. Table 2.3 presents a summary of the equations for F_s available.

Several researchers investigated the approach first proposed by Kulhawy (1969). Wright (1969) observed that the values of the overall factor of safety obtained using Kulhawy's approach were approximately 3% higher than those obtained by the Bishop's Simplified method of slices (Bishop, 1955). Higher values of local factors of safety were observed near the ends of the slip surface and smaller values were observed in the middle of the slip surface. Wright et al. (1973) stated that the *finite element stress method* should be superior to conventional *methods of slices* because arbitrary assumptions are employed in the *method of slices*, the factor of safety is assumed to be equal for all slices, and some *methods of slices* do not satisfy all conditions of equilibrium (see Fig. 2.11). Wright et al. (1973) showed, based on cases studied, that the difference in the overall *factor of safety* calculated using the *methods of slices* and the *finite element stress method* could be as high as 8%. It was also found that the difference in *factor of safety* increases with an increase in the value of Poisson's ratio.

Zienkiewicz et al. (1975) proposed an alternative equation for the *factor of safety* to be used in the *finite element stress method* (see Table 2.3). The equation proposed by Zienkiewicz et al. (1975) is similar to the equation proposed previously by Resendiz (1974) in the sense that both equations use deviatoric stresses to define F_s. The equation for F_s proposed by Zienkiewicz et al. (1975) is usually called *stress level approach*. Zienkiewicz's equation leads to high values of F_s when compared against other approaches. The equation proposed by Resendiz (1974) has not received considerable interest.

Table 2.3 Equations for the overall factor of safety in finite element stress analyses.

Method (1)	Equation (2)	Eq. # (3)
Kulhawy (1969)	$F_s = \frac{\sum_{i=1}^{n} \tau_{f_i} \Delta L_i}{\sum_{i=1}^{n} \tau_i \Delta L_i}$	2.32
Zienkiewicz et al. (1975)	$F_s = \frac{\sum_{i=1}^{n} \Delta L_i}{\sum_{i=1}^{n} \frac{(\sigma_1 - \sigma_3)_i}{(\sigma_1 - \sigma_3)_{f_i}} \Delta L_i}$	2.33
Chowdhury (1978)	i) $\int_L \frac{\tau_f}{F_s} dL = \int_L \tau dL$;	2.34
	ii) $F_s = \frac{\int_L \tau_f \, dL}{\int_L \tau dL}$;	2.35
	iii) $F_s = \frac{1}{L} \int_L \frac{\tau_f}{\tau} dL$.	2.36
Adikari and Cummins (1985)	$F_s = \frac{\sum_{i=1}^{n} \tau_{f_i} \Delta L_i}{\sum_{i=1}^{n} \frac{(\sigma_1 - \sigma_3)_i}{(\sigma_1 - \sigma_3)_{f_i}} \tau_{f_i} \Delta L_i}$	2.37

where:

F_s = factor of safety; n = total number of slip surface segments; τ_{fi} = the shear strength (shear stress at failure) on the slip surface segment i; ΔL_i = slip surface segment length; τ_i = the shear stress acting on the slip surface segment i; $(\sigma_1 - \sigma_3)_{fi}$ = deviatoric stress at failure on the slip surface segment i; $(\sigma_1 - \sigma_3)_i$ = deviatoric stress acting on the slip surface segment i; L = total length of the slip surface; τ_f = shear strength; dL = infinitesimal length along the slip surface; τ = acting shear stress.

Chowdhury (1978) presents an interesting comparison of the definitions of overall *factor of safety*. The equations considered by Chowdhury (1978) are presented in Table 2.3. Equation 2.34 is similar to the equation used in conventional *methods of slices*, and assumes that F_s has the same value at all points along the slip surface. Chowdhury (1978) points out that the factor of safety as defined in Eq. 2.34 losses meaning when the overall F_s is significantly higher than unity because the value of F_s is constant along the slip surface only when the slope is near failure. The second equation (Eq. 2.35) is similar to the equation proposed by Kulhawy (1969). Chowdhury (1978) states that F_s defined by Eq. 2.35 assumes a more realistic meaning than Eq. 2.34 when the overall factor of safety is greater than unity. The third equation (Eq. 2.36) defines F_s as the average of the local factors of safety along the slip surface. Equation 2.36 is very sensitive to local factors of safety and fails to give a meaningful measure of the overall stability of the slope when small regions with significantly higher than the average values of F_s exist.

Adikari and Cummins (1985) revived the discussion about appropriate definitions for F_s. The stability of Blue Rock Dam in Victoria, Australia, was analysed using finite element stress and the equations for factor of safety proposed by Kulhawy (1969), Zienkiewicz et al. (1975), and a newly proposed equation (Eq. 2.37 in Table 2.3), here called *strength and stress level approach*. Equation 2.37 is a combination of Eqs. 2.32 and 2.33. Bishop's Simplified method of slices (Bishop, 1955) was also used in the analyses, for comparison. The results showed that the factor of safety found using Kulhawy's equation (Eq. 2.32) was generally close to that obtained using the Bishop's Simplified method. The F_s values obtained using Zienkiewicz's equation (Eq. 2.33) were significantly higher than the F_s values obtained using Kulhawy's equation and Bishop's method. Finally, the newly proposed F_s equation (Eq. 2.37) produced F_s values close to those obtained using Zienkiewicz's equation in most cases.

Further studies on the *finite element stress method* were presented by Farias and Naylor (1996), Fredlund and Scoular (1999), and Krahn (2003). These studies were focused mainly on the applicability of the methods and/or focused on further comparisons. Farias and Naylor (1996) proposed a mixed formulation based on the approach proposed by Kulhawy (1969), but making use of the displacement field in order to determine the development and location of the failure surface. Farias and Naylor (1996) presented an important contribution in terms of the finite element model sensitivity and the use of appropriate numerical procedures. Fredlund and Scoular (1999) presented a parametric study using the approach proposed by Kulhawy (1969) and varying the shear strength parameters, Poisson's ratio and pore-water pressure. Fredlund and Scoular (1999) presented also comparisons with the GLE method (Fredlund et al., 1981), concluding that the Kulhawy's approach gave satisfactory results in terms of the value of F_s.

Krahn (2003) discussed the applicability of the *finite element stress method* and the limitations of the *methods of slices* due to the approximation of the stresses at the base of the slices. Krahn (2003) concluded that the *finite element stress method* is a powerful approach and that its main difficulty is the lack of experience with the method in geotechnical engineering practice. It is important to note that the advent of powerful problem solving environments, such as FlexPDE (PDE Solutions, 2003), makes the use of the *linear finite element stress method* as simple and as quick as the use of the *methods of slices*, with the advantage of the greater rigorousness (Gitirana Jr. and Fredlund, 2003a).

2.4.3.2 *General slip surface methods*

The *general slip surface methods* are procedures for determining the location and shape of the critical slip. The general *slip surface methods* are often regarded as "exact" or "complete" solutions, particularly when finite element stress fields are used. The use of the terms "exact" and "complete" is due to the generality of such solutions. This section presents a concise literature review of the three categories of *general slip surface methods* presented in Fig. 2.11.

Variational calculus method

The early *general slip surface methods* were based on variational calculus (Kopacsy, 1957). The variational calculus method is based on the definition of the slip surface as a functional of coordinates $y(x)$. Variational calculus is used to minimise the load of rupture associated with the $y(x)$ functional. The formulation makes use of the same type of equilibrium equations used in the *method of slices*. The equilibrium equations are solved for the *factor of safety* and the equation obtained is solved using variational analysis. The shape and location of the critical slip surface are completely determined, along with the corresponding factor of safety.

Further studies on the *variational calculus method* were done by Revilla and Castillo (1977), Ramamurthy et al. (1977), and Baker and Garber (1978) among others. Revilla and Castillo (1977) combined the variational calculus with the Janbu's Simplified method (Janbu, 1954). The comparison against Taylor's method (Taylor, 1948) showed that the *factor of safety* determined using variational calculus was significantly lower in some cases. Baker and Garber (1978) improved the work of Kopacsy (1957) by introducing two new functionals related to the slip surface definition. The formulation was extended for non-homogeneous anisotropic properties, general pore-water pressure distributions, and general external loads. Based on the analysis of homogeneous slopes, Baker and Garber (1978) showed that the shape of the slip surface should be log-spiral for rotational modes of failure and planar for translational modes of failure. This result cannot be extended to heterogeneous and layered slopes.

The *variational calculus method* captured little interest afterwards, mostly because of its mathematical complexity. Additionally, de Josselin de Jong (1981) refuted the variational calculus approach by pointing out that the functionals used to define the failure surface are of a degenerate (Petrov, 1968) nature and possess no minimum. Among the few researchers that continued to study the variational calculus approach are Leshchinsky (1990), Leshchinsky and Huang (1992a and 1992b), and Ugai and Leshchinsky (1995). Leshchinsky et al. proposed the

use of a user defined slip surface, instead of the degenerate functional present in the previous formulations. While this modification removes the mathematical inadequacy pointed out by de Josselin de Jong (1981), the shape of the slip surface is no longer part of the solution.

Automatic search techniques

Automatic search techniques rely on the flexibility of the search procedure adopted and do not have sounding and "fail-proof" theoretical bases. The *random search method*, one of the first *automatic search techniques*, was introduced by Boutrup and Lovell (1980). The critical slip surface was formed by linear segments defined by points of a search grid. The random search consisted of the generation of random angles between consecutive segments and the minimization of the factor of safety. The technique was combined with Bishop's Simplified method (Bishop, 1955) and the Janbu's Simplified method (Janbu, 1954). Boutrup and Lovell (1980) found that slip surfaces with kinks and convex shapes would be occasionally found and recommended the use of fine search grids in order to overcome this problem.

Celestino and Duncan (1981) introduced the *alternating variable method*. The optimization process consists in the shifting of points defining the trial slip surface (Fig. 2.13). Each point must be shifted at a time, until its optimum position is located. The *alternating variable method* was combined with Spencer's method (Spencer, 1967) to analyse the stability of Birch dam (Oklahoma, USA). The optimum position of each point was determined by a quadratic interpolation for the rate of change in F_s due to the point shifting. Celestino and Duncan (1981) recommended the use of small shift increments, in order to avoid numerical instability.

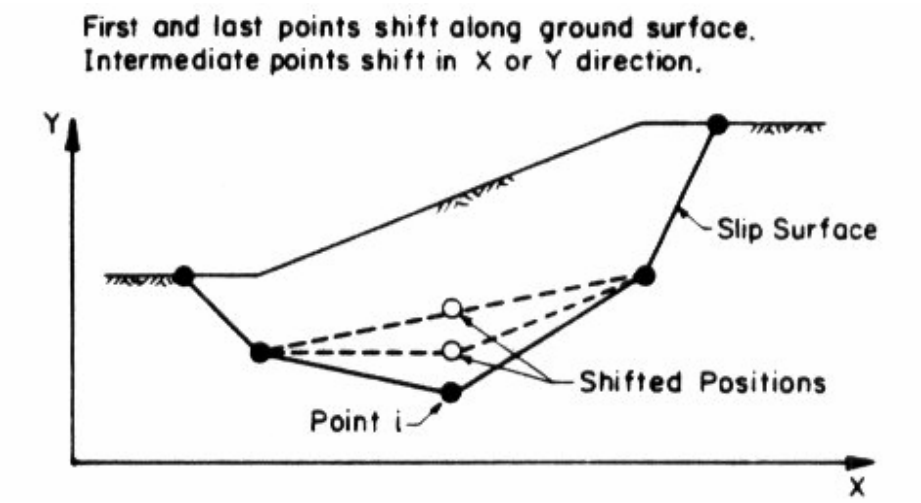

Figure 2.13 Shifting points defining the slip surface (Celestino and Duncan, 1981).

Several *general slip surface methods* were proposed in the 1980's. Nguyen (1985) introduced the use of *simplex method* (Spendley et al., 1962). The case of the Birch Dam (Oklahoma, USA) was again analysed, with satisfactory results. Arai and Tagyo (1985) employed the conjugate gradient method developed by Fletcher and Reeves (1964) in the optimization of the slip surface. Li and White (1987) presented a study on existing *general slip surface methods* and proposed improvements to the *alternating variable method* proposed by Celestino and Duncan (1981).

Greco (1988) and Yamagami and Ueta (1988a) presented comprehensive comparisons considering most of the existing *general slip surface methods*. The study presented by Greco (1988) considered the *simplex method*, the *alternating variable method*, and the *conjugate gradient method*, among others. The difference in performance between the examined methods was found to be insignificant. Greco (1988) also concluded that all the examined methods merely yielded local rather than global minimums. The study presented by Yamagami and Ueta (1988a) involved the *simplex method*, the *conjugate gradient method*, the *Davidon-Fletcher-Powell method*, and the *Broyden-Fletcher-Golfarb-Shanno method*. The *Broyden-Fletcher-Golfarb-Shanno method* provided the best results in terms of computing time. Yamagami and Ueta (1988a) also found that the several methods yielded similar results in the case of homogeneous slopes but significant differences were found in the case of layered slopes. Lastly, the authors stated that all examined methods provided local rather than global minimums.

Research on *general slip surface methods* continued throughout the 1990's. de Natale (1991) proposed improvements to the approach proposed by Nguyen (1985), in order to reduce the amount of computer work. The simplex technique proposed by Nelder and Mead (1965) was used. It was stated that the minimization technique yielded a global minimum provided that the search area actually contained the global minimum. Greco (1996) proposed the use of the *Monte-Carlo method* for locating the critical slip surface. The analyses of several examples were presented using the proposed method and other available optimization methods. Greco (1996) pointed out that the proposed method could be considered as an *ad hoc* method because of the poor theoretical background. It was also suggested that the analysis should be started from different trial slip surfaces in order to ensure that the global minimum was found.

Zhou (2001) proposed a new *general slip surface method* based on a *critical slip field* consisting of a family of slip surfaces having maximum value of unbalanced thrust forces at exit points on the slope boundary. Critical slip surfaces corresponding to several exit points had to be

determined. Janbu's Simplified method (Janbu, 1954) and Morgenstern-Price (1965) were used to calculate stresses along the slip surface. Based on several case studies and comparisons against other optimization methods, it was concluded that the proposed method approximated rather than searched for the position of the critical slip surface.

Dynamic programming

Dynamic programming is a general method of minimisation of additive multi-stage functionals, initially proposed by Bellman (1957). Baker (1980) proposed the use of the *dynamic programming method*, pointing out its sound theoretical basis. In order to use the dynamic programming technique, Baker (1980) divided the slope analysis problem in stages and state points, as shown in Fig. 2.14. The procedure did not include any restriction to the critical slip surface shape. The dynamic programming method was combined with the Spencer method (Spencer, 1967) for the calculation of stresses along the slip surface and the corresponding factor of safety. Baker (1980) introduced an *auxiliary function* in order to minimize the *factor of safety*. Several case studies including homogeneous and layered slopes were presented. Results obtained by the proposed method were compared with those of the Bishop's simplified method (Bishop, 1955) and the GLE method (Fredlund and Krahn, 1977), with good results.

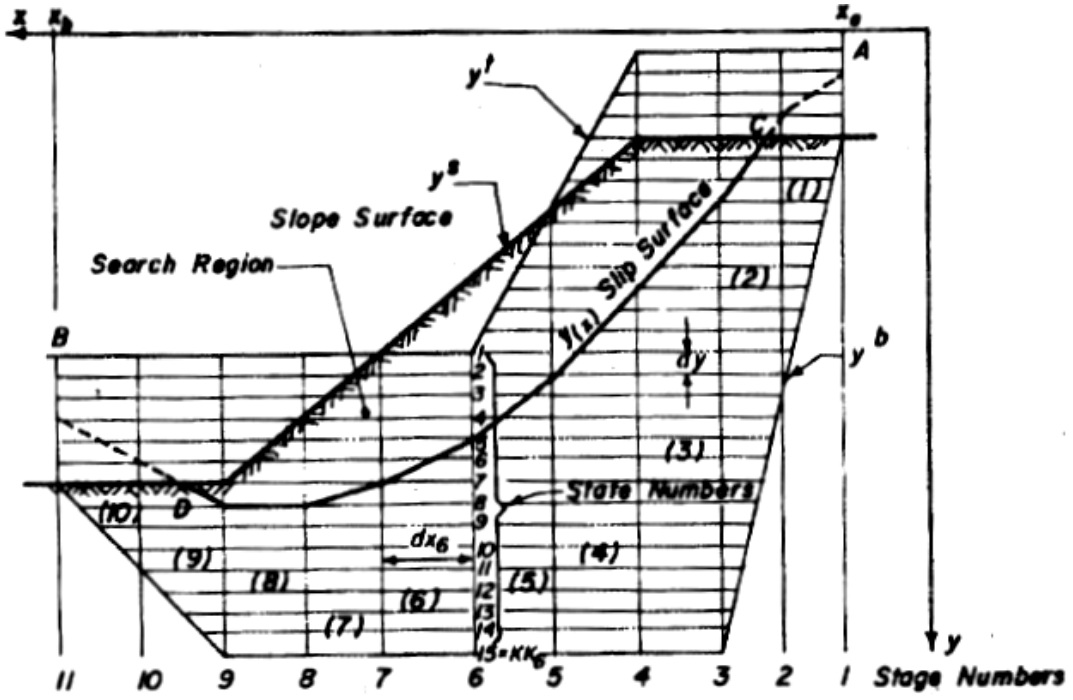

Figure 2.14 The analytical scheme of Baker's approach (Baker, 1980).

The *dynamic programming method* of slope stability was the subject of several recent studies (Talesnick and Baker, 1984, Yamagami and Ueta, 1988a, Zou et al., 1995, Pham, 2002, and Gitirana Jr. and Fredlund, 2003a). Talesnick and Baker (1984) present the analyses of four test embankments using the procedure proposed by Baker (1980). The results presented by Talesnick and Baker (1984) where in disagreement with the observed critical slip surfaces and the factors of safety determined previously by La Rochelle et al. (1974) and Blondeau et al. (1977). Talesnick and Baker (1984) questioned the field techniques of failure observation and pointed out that the observed failure mode was not in agreement with the expected failure mode.

Yamagami and Ueta (1988b) proposed the combination of the *dynamic programming method* with finite element stress fields. The procedure was able to determine the position and shape of the slip surface and the corresponding factor of safety, while taking into account the static equilibrium and the soil stress-strain behaviour throughout the soil mass. Assumptions regarding the relationship between interslice forces were no longer required because normal and shear stresses were determined using the finite element method. Two examples were solved using the proposed method. The results were compared with those produced by the Bishop's Simplified (1955) method. In spite of the roughness in the shape of the critical slip surface determined, the applicability of the proposed method appeared promising.

Zou et al. (1995) developed a modified dynamic programming procedure to search for the critical slip surface. The procedure presented by Zou et al. (1995) was similar to the method proposed by Yamagami and Ueta (1988b) but the critical slip surface could contain the linear segment connecting two state points located in the same stage. A test embankment built in Nong Ngoo Hao site (Bangkok, Thailand) was analyzed. The result showed that the location of the critical slip surface was close to the actual failure surface observed in the field. A comparison between the present method and the generalized limit equilibrium wedge analysis method (Giam, 1989) was also made with good results.

Pham et al. (2001), Pham (2002), Gitirana and Fredlund (2003a), and Brito et al. (2004) presented detailed studies on the applicability of the *dynamic programming method* combined with finite element stress fields. Several slopes where analysed, with varying geometries, pore-water pressure conditions, and soil properties. Pham (2002) proposed a restriction to the acting shear stresses that are acceptable in the optimization procedure. According to this so-called *kinematical restriction*, slip surface segments whose acting shear stresses have the same

direction as the failure direction should be discarded during the optimization procedure. The results of these studies indicated that the value of F_s obtained using the proposed solution is strongly dependent on the value of Poisson's ratio. Comparison against conventional *methods of slices* showed that the values of F_s could be higher or lower than the values of F_s obtained with the dynamic programming solution, depending on the Poisson ratio value. The *dynamic programming method* provided similar results when compared with conventional LEMs.

2.5 PROBABILISTIC METHODS FOR THE ASSESSMENT OF EMBANKMENT STABILITY

The application of probabilistic approaches to geotechnical problems has been widely advocated during the past three decades (Ang and Tang, 1975, Vanmarcke, 1977, Whitman, 1983, Harr, 1987, Christian et al., 1992, Becker, 1996a and 1996b, Whitman, 2000, Duncan, 2000, among many others). A superior assessment of embankment stability is possible if the uncertainties involved are taken into account in an explicit, quantitative manner. Uncertainties associated with input variables, such as shear strength and hydraulic properties, results in uncertainty in the *factor of safety*, F_s. The uncertainty in F_s can be assessed through the analysis of different "case scenarios", or using a measure of safety that takes into account the uncertainty in F_s, such as the *probability of failure*. The *probability of failure*, P_f, is generally defined as the probability of the factor of safety being less than 1 (shaded areas in Fig. 2.15).

The two probability density functions (p.d.f.s) presented in Fig. 2.15 make the case for incorporating uncertainty into the assessment of embankment stability. From a traditional deterministic standpoint, a slope with an expected factor of safety $E[F_s] = 1.5$ is safer than a slope with $E[F_s] = 1.2$. The expected or mean values of F_s correspond to a certain extent to the stability measure used in deterministic analyses. The two scenarios presented in Fig. 2.15 show that the p.d.f. with higher $E[F_s]$ has a higher probability of failure. Therefore, $E[F_s]$ alone may provide incomplete or even misleading information about the stability of an embankment.

Foundation design codes have been rewritten in order to accommodate probabilistic concepts (Becker, 1996b). Becker (1996a) presents a review of reliability-based foundation design approaches and describes the motivations for the use of probabilistic methods. The implementation of unsaturated soil mechanics into the assessment of geo-hazards must rely on predicted soil properties. The relatively high uncertainties associated with predicted soil

properties provide additional motivation for the adoption of probabilistic approaches. A formal probabilistic framework based on the analysis of "case scenarios" may provide a new protocol, appropriate for unsaturated soils engineering practice.

Probabilistic approaches in geotechnical engineering require (i) the establishment of methods of characterisation of soil property variability, (ii) the development of a method of reliability analysis, and (iii) the establishment of acceptable risks. Soil property variability can be quantified using conventional statistical tools. Acceptable risk levels can be established by decision makers, based on the historic frequency of disasters, or based on calibration approaches using previous successful designs (Becker, 1996a). Several reliability analysis methods are available in the literature. Reliability analysis methods must be selected based on their accuracy and computation requirements. The following sections will present a concise literature review of reliability analysis methods that can be used for the assessment of railway embankment hazards.

2.5.1 *Reliability analysis methods*

A probabilistic method that yields the probability density function of the *factor of safety* is required in order to quantify weather-related geo-hazards. A literature review of the probabilistic methods available is presented herein. Four probabilistic methods are described; namely, the Monte Carlo simulation, the Taylor series method, the Point Estimate method, and the Moment-matching method.

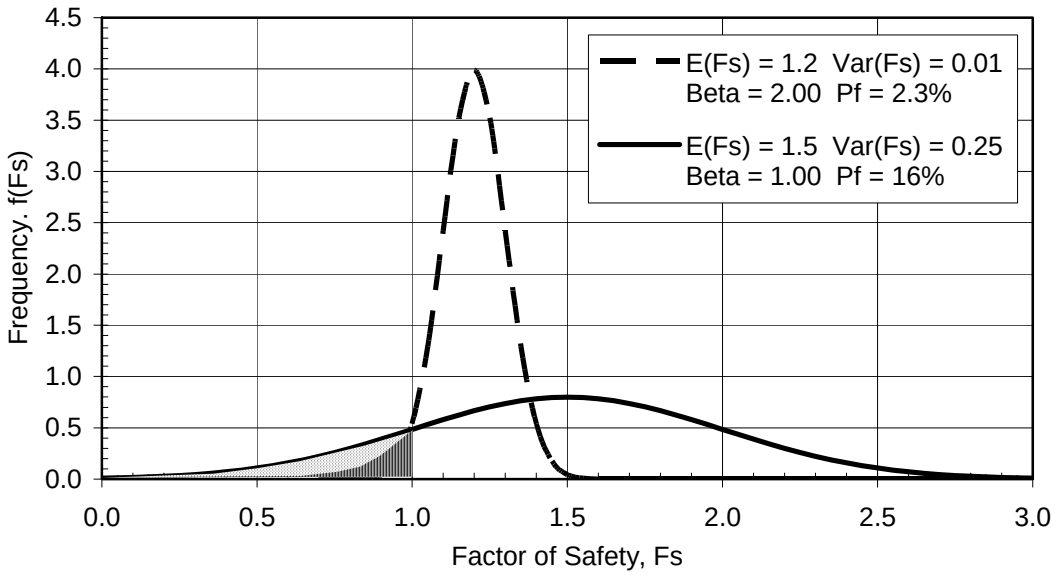

Figure 2.15 Probability density function of the factor of safety, F_s, and probability of failure, P_f.

2.5.1.1 *Monte Carlo method*

According to Harr (1987), the *Monte Carlo method* was first developed by Hammersley and Handscomb (1964). Figure 2.16 presents a flow chart for the *Monte Carlo method*. According to Fig. 2.16, several sets of values of n input random variables $X = (x_1, x_2, \ldots, x_n)$ must be randomly generated. The sets of random input variables X are obtained using random number generators that produce the selected probability density function. Each randomly generated set must be used to calculate a realisation of $F_s(X)$. The realisations of $F_s(X)$ are then used to define the probability density function of $F_s(X)$.

It is important to note that unbiased random number generators are required in order to perform an unbiased *Monte Carlo* simulation. Hahn and Shapiro (1967), presents a summary of random number generators for a series of probability density functions. A detailed discussion about equations for the generation of random numbers can be found in Rubinstein (1981).

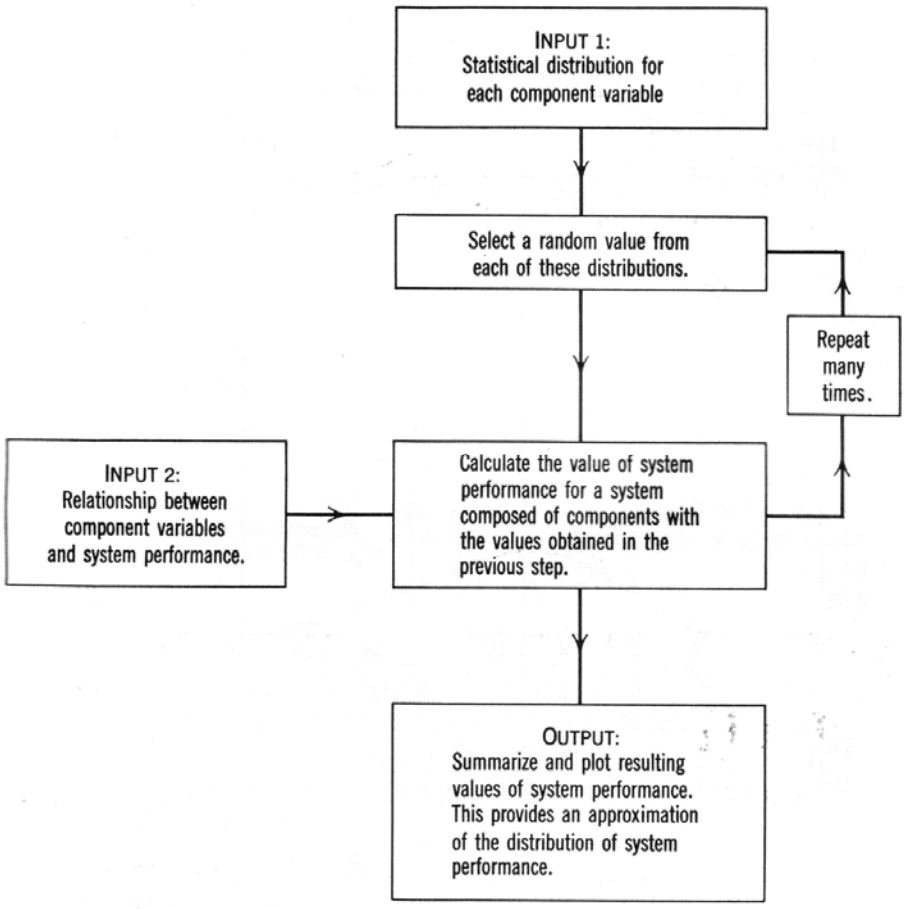

Figure 2.16 Flow chart of Monte Carlo method (Hahn and Shapiro, 1967).

The *Monte Carlo* simulation method requires a large number of trials (i.e., evaluations of F_s). Theoretically, the larger the number of trials in the simulation, the more precise will be the final answer. Harr (1987) presents the following equation for the number of *Monte Carlo* simulations required to achieve a given accuracy:

$$N = \left[\frac{d^2}{4\varepsilon^2} \right]^m \tag{2.38}$$

where:

N	=	number of Monte Carlo trials required;
d	=	confidence coefficient for normal distribution (Table 2.4);
ε	=	maximum allowable system error, equal to the complement of the confidence level;
m	=	number of random input variables.

Table 2.4 Confidence coefficients for normal distribution.

ε, %	10	5	4.55	2	1	0.5	0.27	0.1	0.01	0.006
d	1.64	1.96	2.00	2.33	2.58	2.81	3.00	3.29	3.89	4.00

Hahn and Shapiro (1967) points out that the *Monte Carlo method* has a more intuitive appeal that other available methods. Another advantage is the fact that the method precision can be calculated using equations such as Eq 2.38. In addition, the *Monte Carlos method* is flexible, and can accommodate different probability density functions and correlated variables. Unfortunately, the large number of trials required limits the applicability of the *Monte Carlo method*. The *Monte Carlo method* is impractical in analyses that involve Finite Element models due to the large computation time of each trial. For instance, a *Monte Carlo* simulation with 99% of confidence requires 16,641 trials if the problem has one variable (Harr, 1987). If the problem has *m* variables, the number of trials increases geometrically, according to the power *m*.

2.5.1.2 *Taylor series method*

The *Taylor series method* provides an approximate approach for obtaining the first few moments of the probability density function of a function of random variables, such as the *factor of safety*, $F_s(X)$. The symbol X represents a collection of n random variables $x_1, x_2, \ldots, x_n$. Unlike the

Monte Carlo method, the *Taylor series method* does not provide the complete probability density function of $F_s(X)$. Therefore, the p.d.f of F_s must be assumed for the computation of P_f.

The *Taylor series method* consists of expanding the function of random variables $F_s(X)$ about the expected values of the n input random variables, $E[x_1]$, $E[x_2]$,..., $E[x_n]$, using a multivariate Taylor series. Hahn and Shapiro (1967) showed that an equation for the first moment of $F_s(X)$, $E[F_s(X)]$ (i.e., the expected value), can be obtained by taking expected values of the Taylor expansion of $F_s(X)$ about $E(x_1)$, $E(x_2)$, ..., $E(x_n)$, as follows:

$$E[F_s(X)] = F_s(E[x_1], E[x_2], ..., E[x_n]) + \frac{1}{2}\sum_{i=1}^{n}\frac{\partial^2 F_s}{\partial x_i^2}Var[x_i] + \sum_{\substack{i \\ i<j}}\sum_{j}\frac{\partial^2 F_s}{\partial x_i \partial x_j}Cov[x_i, x_j] \qquad (2.39)$$

where:

$Var[x_i]$ = $E[(x_i - E[x_i])^2]$ is the variance of x_i;

$Cov[x_i, x_j]$ = $E[(x_i - E[x_i])(x_j - E[x_j])]$ is the covariance between x_i and x_j.

The function $F_s(X)$ was expanded using terms up to the second order. The derivatives of F_s with respect to x_i must be evaluated at the expected values of x_i, $E[x_i]$. The second moment of the probability density function of F_s, $Var[F_s(X)]$, can be obtained using a similar approach and considering that $Var[F_s(X)] = E[F_s(X)^2] - \{E[F_s(X)]\}^2$:

$$\begin{aligned} Var[F_s(X)] = &\sum_{i=1}^{n}\left(\frac{\partial F_s}{\partial x_i}\right)^2 Var[x_i] + 2\sum_{\substack{i \\ i<j}}\sum_{j}\left(\frac{\partial F_s}{\partial x_i}\right)\left(\frac{\partial F_s}{\partial x_j}\right)Cov[x_i, x_j] \\ &+ \sum_{i=1}^{n}\left(\frac{\partial F_s}{\partial x_i}\right)\left(\frac{\partial^2 F_s}{\partial x_i^2}\right)\mu_3[x_i] + \sum_{\substack{i \\ i\neq j}}\sum_{j}\left(\frac{\partial F_s}{\partial x_i}\right)\left(\frac{\partial^2 F_s}{\partial x_j^2}\right)E[(x_i - E[x_i])(x_j - E[x_j])^2] \\ &+ 2\sum_{\substack{i \\ i\neq j}}\sum_{j}\left(\frac{\partial F_s}{\partial x_i}\right)\left(\frac{\partial^2 F_s}{\partial x_i \partial x_j}\right)E[(x_i - E[x_i])^2(x_j - E[x_j])] \\ &+ 2\sum_{i}\sum_{\substack{j \\ i\neq j\neq s}}\sum_{s}\left(\frac{\partial F_s}{\partial x_i}\right)\left(\frac{\partial^2 F_s}{\partial x_j \partial x_s}\right)E[(x_i - E[x_i])(x_j - E[x_j])(x_s - E[x_s])] \end{aligned} \qquad (2.40)$$

where:

$\mu_3(x_i)$ = $E[(x_i - E[x_i])^3]$ is the third central moment, related to the skewness.

Equations for the third and fourth central moments of $F_s(X)$ can be obtained in a similar manner. Ditlevsen (1981) presented similar equations. In order to simplify the computations, Harr (1987) advocates the use of a *first-order, second-moment* approximation (FOSM) as follows:

$$E[F_s(X)] = F_s[E[x_1], E[x_2], ..., E[x_n]] \tag{2.41}$$

$$Var[F_s(X)] = \sum_{i=1}^{n}\left(\frac{\partial F_s}{\partial x_i}\right)^2 Var[x_i] + 2\sum_{\substack{i \\ i<j}}\ \sum_{j}\left(\frac{\partial F_s}{\partial x_i}\right)\left(\frac{\partial F_s}{\partial x_j}\right) Cov[x_i, x_j] \tag{2.42}$$

The last term of Eq. 2.42 can be eliminated when the input random variables are uncorrelated. The use of the *first-order, second-moment* equation provides a good approximation if $F_s(X)$ is a linear function of x_i. The greater the nonlinearity of F_s, the greater the errors in the computation of $E[F_s(X)]$ and $Var[F_s(X)]$.

Several researchers have employed the FOSM approximation in geotechnical engineering analyses. Sandroni and Sayão (1993) presented the use of Eqs. 2.41 and 2.42 to the probabilistic analysis of slope stability. The variables assumed as uncertain were the unit weight, the soil cohesion, the tangent of the friction angle, and the water table elevation. Sandroni and Sayão (1993) proposed the calculation of the derivatives of factor of safety based on a 10% increment of the input random variables, as follows:

$$\frac{\partial F_s}{\partial x_i} = \frac{F_s(E[x_i] + 0.1 \times E[x_i]) - F_s(E[x_i])}{0.1 \times E[x_i]} \tag{2.43}$$

where:

F_s = the factor of safety, computed using any slope stability approach;

x_i = the uncertain variables.

The FOSM equations require only n+1 evaluations of F_s when Eq. 2.43 is employed. Sandroni and Sayão (1993) pointed out that the contribution of each of the uncertain variables to the coefficient of variation of the factor of safety, $Var_{xi}^{F_s}$, can be obtained as follows:

$$Var_{x_i}[F_s] = \left(\frac{\partial F_s}{\partial x_i}\right)^2 Var[x_i] \Bigg/ \sum_{i=1}^{n}\left(\frac{\partial F_s}{\partial x_i}\right)^2 Var[x_i] \tag{2.44}$$

Farias and Assis (1998) present further studies on the FOSM method, considering two different slopes. The results indicate that the FOSM approximation gives similar results when compared to the Point estimated method (Rosenblueth, 1975). Using different variations for the set of input random variables, $\delta E[x_i]$, Farias and Assis (1998) observed that the derivatives of $F_s(X)$ were roughly constant. Unfortunately, this observation is not general and cannot be extended to different problems. The computation of the derivatives of $F_s(X)$ remains the primary obstacle towards the use of the *Taylor series method* for embankment stability assessment.

2.5.1.3 *Point estimate method*

The term *Point Estimate method* (PEM) refers to the category of probabilistic methods for calculating the moments of a function of random variables that are based on the calculation of $F_s(X)$ at pre-determined values of X. The pre-determined values of X are combined with corresponding "weights" or discrete probabilities. Most PEM approaches are based on two-point estimates (i.e., two values for each x_i), but references to third- and higher-order point estimates can be found in the literature (Harr, 1987).

Evans (1967, 1972) proposed an early PEM for independent random variables. However, the first popular PEM approach is generally credited to Rosenblueth (1975, 1981). Rosenblueth (1975) proposed a two-point PEM for correlated variables in which the joint probability density function of X was assumed to be concentrated at points in the 2^n hyperquadrants of the space defined by X. A univariated formulation was presented as the basis of the more general, multivariate equations. The moments of the set of two estimate points were matched to the three first central moments of the input variables by solving the following system of equations:

$$\begin{cases} p_1 + p_2 = 1 \\ x_1 p_1 + x_2 p_2 = 0 \\ x_1 p_1^2 + x_2 p_2^2 = Var[x] \\ x_1 p_1^3 + x_2 p_2^3 = \gamma_1[x]\{Var[x]\}^{3/2} \end{cases} \tag{2.45}$$

where:

$\gamma_1[x]$ = $\mu_3[x] / \{Var[x]\}^{3/2}$ is the skewness of x;

$\mu_3[x]$ = is the third central moment of x.

The unknowns of the system of equations (Eq. 2.45) are the estimate points and concentrated

probabilities (x_1, x_2, p_1, and p_2). Rosenblueth (1975, 1981) presented the following solution for the system of moment-matching equations:

$$x_{1,2} = E[x] + \sqrt{Var[x]}\left[\gamma_1[x]/2 \mp \sqrt{1+(\gamma_1[x]/2)^2}\right] \tag{2.46}$$

$$p_{1,2} = \frac{1}{2}\left[1 \mp \sqrt{1-\frac{1}{1+[\gamma_1[x]/2]^2}}\right] \tag{2.47}$$

The first few moments of the univariated function $F_s(x)$ were obtained directly from the definition of the central statistical moments of $F_s(x)$. The following equations are obtained for the three first moments of $F_s(x)$, considering that the estimate points are equivalent to the continuous p.d.f. of F_s, as illustrated in Fig. 2.17:

$$E[F_s(x)] \doteq p_1 F_s(x_1) + p_2 F_s(x_2) \tag{2.48}$$

$$Var[F_s(x)] \doteq p_1 p_2 [F_s(x_1) - F_s(x_2)]^2 \tag{2.49}$$

$$\gamma_1[x]\sqrt{Var[F_s(x)]} \doteq (p_2 - p_1)[F_s(x_1) - f(x_2)] \tag{2.50}$$

where:

$\doteq$ = "equal to, except for higher-order terms."

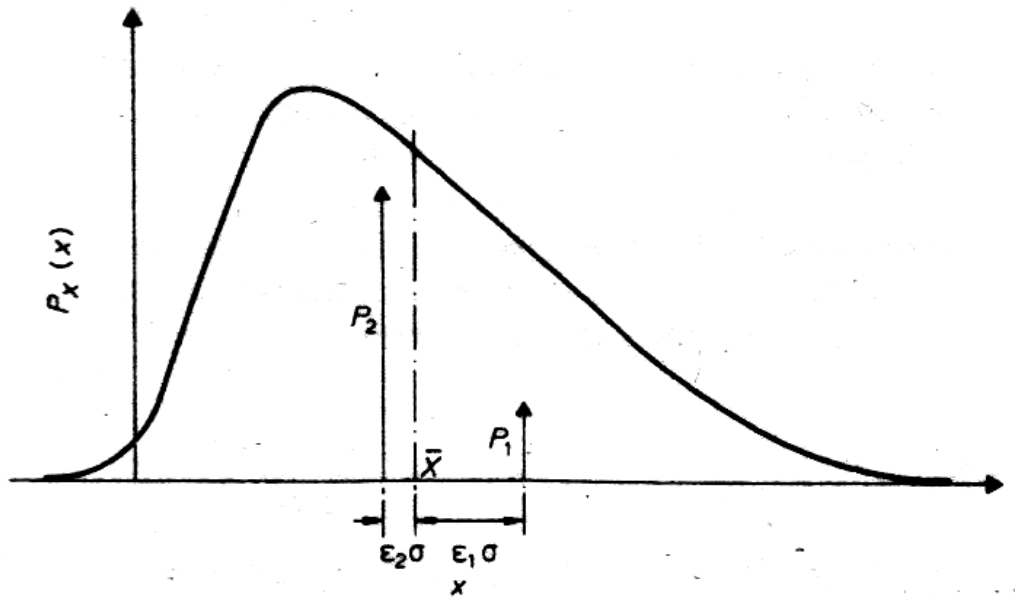

Figure 2.17 Concentrations of a probability density function (Rosenblueth, 1981).

When $\gamma_1[x] = 0$ the expressions for x_1, x_2, p_1, and p_2 are simpler:

$$x_{1,2} = E[x] \mp \sqrt{Var[x]} \tag{2.51}$$

$$p_1 = p_2 = 1/2 \tag{2.52}$$

$$E[F_s(x)] \doteq (1/2)[F_s(x_1) + F_s(x_2)] \tag{2.53}$$

$$Var[F_s(x)] \doteq (1/4)\left[F_s(x_1) - F_s(x_2)\right]^2 \tag{2.54}$$

Rosenblueth (1981) pointed out that a univariated two-point approximation of $E[F_s(x)]$ based on three moments (Eq. 2.48) has an accuracy that is equivalent to that of a third order *Taylor series* approximation (i.e., errors equivalent to the fourth order term). Equations 2.49 and 2.53 are of second order and Eqs. 2.50 and 2.54 are of first order. Rosenblueth (1975) introduced also the *n*-point estimate for univariated functions. Analytical equations for a three-point estimate of a symmetrical function $F_s(x)$ were provided. It was pointed out that the larger the number of estimate points, the more accurate is the procedure.

Rosenblueth (1975 and 1981) presented a generalisation of the univariated procedure, for a multivariate analysis, using two-point estimates. Rosenblueth (1981) proposed the use of a superabundant number of estimate points and the procedure used the assumption of symmetric p.d.f.s. Figure 2.18 presents the estimate points and weights for a function of two random variables. The term σ_i corresponds to $\{Var[x_i]\}^{1/2}$ and ρ is the correlation coefficient between x_1 and x_2. When the variables are correlated or uncorrelated, the moments are matched up to the second-order and third-order moments, respectively. The proposed equations take the following form for a function of three random variables:

$$E[F_s(X)] = p_{+++}F_s(X)_{+++} + p_{++-}F_s(X)_{++-} + ... + p_{---}F_s(X)_{---} \tag{2.55}$$

$$Var[F_s(X)] = E[\{F_s(X)\}^2] - \{E[F_s(X)]\}^2 \tag{2.56}$$

$$F_s(X)_{\pm\pm\pm} = F_s(E[x_1] \pm \sqrt{Var[x_1]}, E[x_2] \pm \sqrt{Var[x_2]}, E[x_3] \pm \sqrt{Var[x_3]}) \tag{2.57}$$

$$p_{+++} = p_{---} = (1/2^3)(1 + \rho_{12} + \rho_{23} + \rho_{31}) \tag{2.58}$$

$$p_{++-} = p_{--+} = (1/2^3)(1 + \rho_{12} - \rho_{23} - \rho_{31}) \tag{2.59}$$

$$p_{+-+} = p_{-+-} = (1/2^3)(1 - \rho_{12} - \rho_{23} + \rho_{31}) \tag{2.60}$$

$$p_{+--} = p_{-++} = (1/2^3)(1 - \rho_{12} + \rho_{23} - \rho_{31}) \tag{2.61}$$

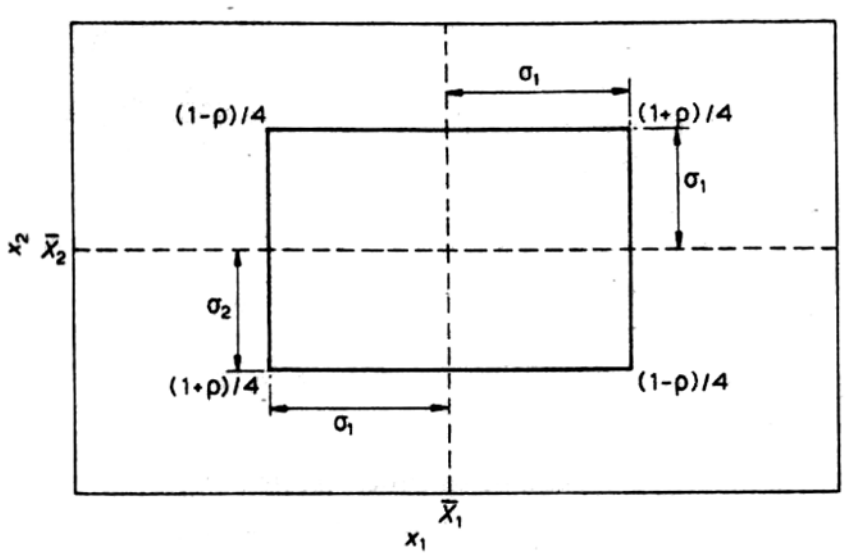

Figure 2.18 Concentrations for a function of two random variables considering $\gamma_1[x] = 0$ (Rosenblueth, 1981).

Equations 2.55 to 2.61 have permutation elements that can be extended easily for any number of n variables. The number of evaluations of $F_s(X)$ is 2^n. This number may become excessive if a large number of random variables are being considered and if each evaluation of $F_s(X)$ involves time consuming computations (e.g., when finite element numerical analyses are involved). Nevertheless, the number of evaluations of $F_s(X)$ may be significantly lower than the number required by a Monte Carlo simulation.

Lind (1983) proposed an alternative point estimate method that requires a reduced number of evaluations of $F_s(X)$. The approach proposed by Lind (1983) was derived from the covariance matrix. The chosen estimate points are located near the centre of each face of the hypercube whose corners are the estimate points proposed by Rosenblueth (1975, 1981). The first two moments of the input random variables are matched by Lind's formulation. The method is exact for linear systems, and approximate for nonlinear systems.

Harr (1987) presents an overview of the method introduced by Rosenblueth (1975, 1981) and a number of applications. Later, Harr (1989) presented a procedure similar to Lind's (1983), but derived from the correlation matrix. The estimate points were defined based on a diagonalized form of the correlation matrix, which was obtained based on the eigenvalues and eigenvectors of the correlation matrix. Harr (1989) observed that the correlation matrix K could be represented by a hypersphere of radius $n^{1/2}$, centered at the expected values of the input random variables.

The two estimate points proposed correspond to the point where each eigenvectors intercepts the hypersphere, $x_{\pm}$:

$$x_{ij\pm} = E[x_i] \pm e_{ij}\sqrt{Var[x_i]}\sqrt{n} \tag{2.62}$$

where:

e_{ij}	=	the ij component of the normalised eigenvector of K;
i	=	the random variable number and also the eigenvectors matrix column number, 1, …, n;
j	=	eigenvectors matrix row number, 1, …, n.

The weights used for the computation of the expected value of $F_s(X)$ are all equal to $1/n$. For the calculation of the variance of $F_s(X)$, the weight used for each pair of $x_{\pm}$ is equal to the corresponding eigenvalue divided by n. The approach proposed by Harr (1989) requires only $2n$ evaluations of $f(x)$, using $2n$ sets ($x_{1j\pm}$, $x_{2j\pm}$,… $x_{nj\pm}$). Unfortunately, the formulation requires computations of eigenvalues, while other point estimate approaches are based on simple calculations that can be easily performed on spreadsheets.

Li (1991, 1992) introduced a new theory based on point estimates and the Gauss quadrature. The alternative PEM presented by Li (1991, 1992) accommodates univariated and multivariate functions of correlated and skewed random variables. The univariated equation is as follows:

$$E[F_s(x)] = w^{+}F_s(x^{+}) + w^{0}F_s(E[x]) + w^{-}F_s(x^{-}) \tag{2.63}$$

where:

$x^{\pm}$	=	$E[x] + \alpha^{\pm}\sqrt{Var[x]}$;
$w^{\pm}$	=	$1/[\alpha^{\pm}(\alpha^{\pm} - \alpha^{\mp})]$;
w^{0}	=	$1 - w^{+} - w^{-}$;
$\alpha^{\pm}$	=	$(1/2)[\gamma_1[x] \pm \sqrt{4\gamma_2[x] - 3\{\gamma_1[x]\}^2}]$ for a 4th order approximation;
$\alpha^{\pm}$	=	$(1/2)[\gamma_1[x] \pm \sqrt{\{\gamma_1[x]\}^2 + 4}]$ for a 3rd order approximation;
$\alpha^{\pm}$	=	± 1 for a 2nd order approximation;

$\gamma_1[x]$ = $\mu_3[x]/\{Var[x]^{3/2}\}$ is the skewness of x;

$\gamma_2[x]$ = $\mu_4[x]/\{Var[x]^{2}\}$ is the kurtosis proper of x;

μ_3 and μ_4 = the third and fourth central moments of x, respectively.

The inspection of the univariated equations proposed by Li (1991, 1992) shows that the proposed estimate points (x, w) produce moments matching the input moments up to the fifth order for the 4th order approximation. The equations proposed by Li (1991, 1992) force the mid point at $E[x]$ for any $\gamma_1[x]$ and $\gamma_2[x]$ while the position of the mid point is part of the solution in the three-point equations proposed by Rosenblueth (1975) and are not equal to $E[x]$ if $\gamma_1[x] \neq 0$.

Li (1991, 1992) proposed a formulation for multivariate functions $F_s(X)$ considering correlated variables x_i. The solution was obtained by combining a polynomial approximation of $F_s(X)$ and the approximation for univariated functions (i.e., Eq. 2.63). The proposed equation is as follows:

$$E[F_s(X)] = \left(1 - \frac{3n}{2} + \frac{\delta}{2} + \sum_i w_i^0\right) F_s(E[x_1], E[x_2], ..., E[x_n]) + \sum_i \left[(w_i^+ - \delta_i + 1) F_s(x_i^+) + w_i^- F_s(x_i^-)\right] + \sum_{i<j} F_s(x_i^+, x_j^+)\delta_{ij} \quad (2.64)$$

where:

i = 1, 2, …, n with n being the number of x_i input variables;

δ = $\Sigma_i \delta_i = \Sigma_i \Sigma_j \delta_{ij}$;

δ_{ij} = $\rho_{ij}/(\alpha^+_i \alpha^+_j)$ if $i \neq j$ and 1 if $i = j$;

ρ_{ij} = the correlation coefficient between x_i and x_j;

$F_s(x_i^{\pm})$ = $F_s(E[x_1], E[x_2], ...E[x_{i-1}], x_i^{\pm}, E[x_{i+1}], ..., E[x_n])$;

$F_s(x_i^+, x_j^+)$ = $F_s(E[x_1], E[x_2], ...E[x_{i-1}], x_i^+, ..., E[x_{j-1}], x_j^+, ..., E[x_n])$;

w^-, w^0, w^+, x^-, and x^+ = as defined in Eq. 2.63 for the 4th, 3rd, and 2nd order univariate polynomial approximations.

Li (1992) observed that the variance of $F_s(X)$ can be computed using Eq. 2.64, replacing $F_s(X)$ by $\{ F_s(X) - E[F_s(X)]\}^2$, and making use of the computed value of $E[F_s(X)]$. According to Li (1992), Eq. 2.64 is more accurate than the 2-point approximation proposed by Rosenblueth (1975) when the former is based on a 4th order polynomial approximation. If a 3rd and/or 2nd order approximation is used, the accuracy is the same as using Rosenblueth (1975) method.

When $n > 3$ the number of evaluations required by the equations proposed by Li (1992) are lower then the number require by Rosenblueth (1975).

Dai et al. (1993) evaluated the use of the PEM in geotechnical engineering and stability analyses. The results of probabilistic slope stability analysis using the Monte Carlo method and the equations proposed by Rosenblueth (1975) were compared. The Morgenstern-Price method of slices was used in the evaluation of the factor of safety. Parametric analyses demonstrated that the effect of the correlation coefficient between friction angle and cohesion is not significantly large. The authors recommended the use of the Rosenblueth (1975) method, saying that the number of evaluation required by the Monte Carlo method is significantly higher.

Panchalingam and Harr (1994) presented a new PEM for multivariate functions of correlated and skewed random variables. The method was presented as an extension of the PEM proposed by Rosenblueth (1975). Panchalingam and Harr (1994) presented a discussion about the uniqueness of point estimate approximation. The point estimate method proposed involves $2n + 2^n$ unknowns, where n is the number of input random variables. The term $2n$ corresponds to the number of estimate points and 2^n corresponds to the weights. The proposed solution is based on the following estimate points and weights, p:

$$\{E[x_1] + (-1)^{d_1} F_1 \sqrt{Var[x_1]}, E[x_2] + (-1)^{d_2} F_2 \sqrt{Var[x_2]}, ..., E[x_n] + (-1)^{d_n} F_n \sqrt{Var[x_n]}\} \qquad (2.65)$$

$$p_{\pm\pm,...,\pm} = p_{1\pm} p_{2\pm}, ..., p_{3\pm} + (-1)^{d_1} (-1)^{d_2} a_{12} p_{12} + ... + (-1)^{d_{n-1}} (-1)^{d_n} a_{n-1n} p_{n-1n} \qquad (2.66)$$

where:

d_i = 0 or 1;

F_i = $\left(p_{i+} / p_{i-}\right)^{0.5}$ if $d_i = 1$ and $\left(p_{i-} / p_{i+}\right)^{0.5}$ if $d_i = 0$;

p_{i+} = $0.5[1 \pm \sqrt{1 - 1/(1 + (\gamma[x_i]/2)^2)}]$;

p_{i-} = $1 - p_{i+}$;

a_{lm} = $\rho_{lm} (p_{l+} p_{l-} p_{m+} p_{m-})^{0.5}$;

p_{lm} = $p_{1\pm} p_{2\pm} ... p_{k\pm} ... p_{n\pm}$ ($k \neq l$ and $k \neq m$);

L = 1, 2,…, $n - 1$;

M = $l + 1$, $l + 2$,…, n;

ρ_{lm} = the correlation coefficient between x_l and x_m.

All possible permutations of n +'s and −'s are considered for the definitions of the estimate points. Equation 2.66 implicitly assumes that the weights are concentrated at the corners of a hyperprism of an n-dimensional space defined by the input random variables. The system solution is rendered determinate by means of this assumption. The new PEM requires 2^n evaluations of $F_s(X)$, the same number of evaluations by Rosenblueth (1975).

Chang et al. (1995) presented an interesting comparison study of some PEMs. Three PEMs were compared; namely, Rosenblueth (1975, 1981), Harr (1987), and Harr (1989). The input random variables were assumed normally distributed. The three methods were evaluated for different numbers of random variables and different functions $F_s(X)$. The results indicated that the method proposed by Harr (1989) yielded comparable, if not better performance than the other two methods.

Tsai and Franceschini (2003) addressed the issue of solution uniqueness in point estimate approximations. The authors present a multivariate PEM based on Rosenblueth (1975) univariated two-point approximation. The multivariate equation was derived by combining the univariated moment-matching equations up to the third moment and a polynomial approximation of $F_s(X)$. The equation presented is identical to the equation presented by Li (1991, 1992) for the case of a 3rd order polynomial approximation. Tsai and Franceschini (2003) pointed out that the presented equation (i.e., the equation originally proposed by Li, 1991, 1992) provides a unique solution for the point estimate problem.

The accuracy of the numerous PEMs presented herein increases as the number of input moments used increases. On the other hand, the accuracy of each approach is not proportional to the number of evaluations of $F_s(X)$. For instance, the equations proposed by Li (1991, 1992) provide a comparably accurate approximation while requiring considerably less evaluations than the PEM proposed by Rosenblueth (1975, 1981). The amount of information required and efficiency must be considered for the selection of the most appropriate PEM.

2.5.1.4 *Moment matching method*

The moment matching method is based on the use of discrete probability distributions that match the moments of the input random variables. Moment-matching discrete probability distributions were developed by Miller and Rice (1983) as a manner of translating continuous probability distributions into discrete distributions for use in decision and risk analysis. The equations used

to match the moments are identical to the equations presented by Rosenblueth (1975). However, the manner how the point estimates are used is distinct. The approach is based on three steps:

(i) replace the probability density function of the input random variables by moment-matching discrete distributions;
(ii) compute the statistical moments of the probability distribution of the outcome (i.e., F_s) using the decision tree method; and
(iii) choose and adjust a probability density function matching the moments of F_s.

Smith (1993) presented a review of some of the available methods for establishing discrete approximations of a probability density functions. Miller and Rice (1983) made the case for the use of the moment matching method, showing that it produces higher accuracy when compared to the *bracket median method*, *bracket mean method*, and *extended Pearson-Tukey method*. The discrete moment matching distribution is formed by n "sampled points", determined by the following system of $2N - 1$ equations:

$$\mu_k(x) = \int_{-\infty}^{\infty} x^k f(x)dx = \sum_{i=1}^{N} p_i x_i^k \quad \text{for } k = 0, 1, 2, \ldots 2N-1 \tag{2.67}$$

where:

$\mu_k(x)$	=	k^{th} raw moment of the probability density function of x;
$f(x)$	=	probability density function;
p_i	=	probability of the i^{th} sampled point;
x_i	=	value of the i^{th} sampled point;
N	=	number of sampled points.

The moment matching method proposed by Miller and Rice (1983) produces moments of $F_s(X)$ identical to those obtained using the Rosenblueth (1975) method when the input variables are uncorrelated. The moment matching approach using decision trees requires the same number of evaluations of $F_s(X)$ required by the method proposed by Rosenblueth (1975). Nevertheless, the moment matching approach produces a complete, discrete frequency distribution of $F_s(X)$, while the PEMs produce the moments of $F_s(X)$ only. The main disadvantages of the moment matching method are the absence of an explicit way of considering correlation between the input random variables and the large number of evaluations of $F_s(X)$ required.

2.6 CHAPTER SUMMARY

This chapter presented a review of derailment investigation reports available and the theories available for assessment of weather-related geo-hazards. A summary of some derailments caused by embankment/subgrade failures was presented in Section 2.2. The main factors involved in the weather-related derailments were identified. The main factors are severe weather conditions, poor drainage conditions, and the presence of moisture sensitive deposits, such as silts and weak clays. It became apparent that the methods of quantification of weather-related geo-hazards must take into account both weather and ground conditions.

Section 2.4 presented a detailed review of mechanistic approaches that can be employed in the quantification of weather-related hazards. Several models for the prediction of heat and water flow in unsaturated soils, soil-atmosphere coupling, and stability analysis were reviewed. It was found that the one-dimensional water flow and soil-atmosphere model proposed by Wilson (1990) provides a comprehensive framework that can be used as the basis for a two-dimensional model for the flow of water in a railway embankment. However, there is a need for an extension of the governing equations and atmospheric conditions, considering the two-dimensional conditions of railway embankments. Theoretical issues associated with the manner in which soil-atmospheric fluxes are partitioned as liquid and vapour flow must also be addressed.

Several methods of stability analysis applicable to railway embankments were reviewed. The approaches available in the literature appear to provide varying accuracies. It was found that general slip surface methods, such as *dynamic programming*, provide more complete solution for quantifying embankment stability. Most importantly, the *dynamic programming* method allows the computation of *factors of safety* in an automatic manner.

Section 2.5 presented a review of reliability-based approaches applicable to the assessment of geo-hazards. The literature review showed that the stability of a railway embankment can be assessed based on the factor of safety and its probability density function. A series of probabilistic models available for the study of functions of random variables was presented. The advantages and disadvantages of each probabilistic method were explored. Point Estimate methods were found to give significantly higher accuracy at the cost of fewer evaluations. Nevertheless, it was found that the most popular methods, such as the Rosenblueth (1975) and Moment-matching approaches require an unfeasible amount of computations of factor of safety and that more efficient approaches must be pursued.

Chapter 3

Theory for the Assessment of Embankment Stability Hazards Considering Weather Conditions

3.1 GENERAL

This chapter presents the theoretical development of a model for the assessment of weather-related railway embankment stability hazards, henceforth referred as "*W-GHA model*" (Weather-Related Geo-Hazard Assessment model). The proposed model combines the stability analysis of railway embankments with the analysis of the effects of weather conditions on the embankment pore-water pressures. A rigorous soil-atmosphere flow model for two-dimensional conditions is formulated, considering flow of liquid water, water vapour, and heat. Soil-atmospheric boundary conditions appropriately reflecting weather conditions are presented. An optimization procedure based on the *Dynamic Programming* method and Finite Element stress fields is presented for the determination of embankment factors of safety during transient flow. Ultimately, the thermo-hydro-mechanical behaviour of the saturated/unsaturated soil comprising a railway embankment is represented by a system of partial differential equations. Deterministic and probabilistic models where developed using a *Decision Analysis* framework. The systematic problem-solving approach is one of the main benefits of using Decision Analysis.

The chapter is divided in six sections. The present section introduces the W-GHA model and gives a general explanation of the chapter structure. Section 3.2 presents an overview of the decision analysis model for weather-related geo-hazards. The objectives, means, and

alternatives of the railway industry are laid out according to a Decision Analysis framework. The third section, 3.3, presents the deterministic core of the W-GHA model, also referred to as the model of problem structure. The objectives and roles of each model component are presented along with the manner of how the model components are connected. The theoretical development of the three major model components is presented; namely, (i) the partial differential equations governing the thermo-hydro-mechanical soil behaviour; (ii) the weather-related boundary conditions; and (iii) optimization technique model for stability analysis based on *Dynamic Programming*. Section 3.4 presents methods for the assessment of unsaturated soil properties functions based on simple soil data. These property assessment methods are required in order to implement the W-GHA model. Section 3.5 presents the techniques employed for the probabilistic and sensitivity analyses. The techniques employed are based on an *alternative point estimate* method. Finally, Section 3.6 presents a summary of the chapter.

3.2 DECISION ANALYSIS FRAMEWORK FOR THE ASSESSMENT OF WEATHER-RELATED GEO-HAZARDS

The assessment and management of weather-related geo-hazards for railway embankments requires deterministic and probabilistic analyses, which can be developed within a *Decision Analysis* framework. *Decision Analysis* provides a structure for a systematic examination of difficult situations. According to Clemen (1996), there are four basic sources of difficulty in decision analysis. These are: (i) problem complexity; (ii) inherent uncertainty of the situation; (iii) presence of multiple objectives; and (iv) existence of different perspectives that can lead to different conclusions.

In order to quantify weather-related geo-hazards, complex multidisciplinary elements of geotechnical and hydrological engineering need to be brought together. In addition, there are inherent uncertainties due to soil properties and weather conditions. Therefore, the two first sources of difficulty in decision analysis (i and ii above) play a significant role in the assessment of geo-hazards. The third source of difficulty listed above can be considered to be 'not important' if the analysis of geo-hazards is kept sufficiently narrow. All objectives depend on the minimization of geo-hazards. The minimization of geo-hazards can be expressed in terms of the single objective to maximize the factor of safety for the problem at hand. Difficulties due to different perspectives should be of relatively minor importance, as long as broadly accepted geotechnical engineering approaches are undertaken.

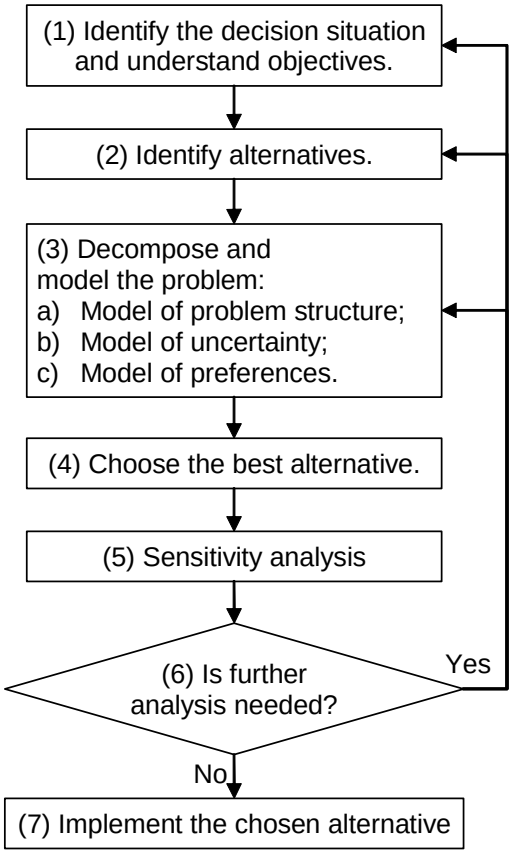

Figure 3.1 A *Decision Analysis* process cycle (modified from Clemen, 1996).

A typical *Decision Analysis* flowchart has seven steps (Fig. 3.1). The first two steps in the *Decision Analysis* cycle, 'identification of decision situations' and 'identification of alternatives' are presented in this section. Step number three, 'decomposition and modelling' is presented later, along with a sensitivity analysis framework. The choice of a best alternative (i.e., step 4 in Fig. 3.1) can be based on a measure of safety against embankment failure. Given the alternatives simplicity, the problem is similar to a *reliability-based* analysis problem.

3.2.1 *Identification of railway objectives and means*

Clemen (1996) offers guidelines for the identification of objectives and means in Decision Analysis. This portion of the decision modelling process is often referred as 'brainstorming". Figure 3.2 describes the fundamental objectives' hierarchy for the railway, for the context considered herein. The maximization of the railway system performance can be considered to be the most fundamental objective. Minimization of financial losses, injuries, loss of life, and the release of dangerous goods are objectives to be reached as part of the most fundamental objective. Finally, the objectives in the lower hierarchical places are the minimization of each

type hazard. The hazard may be caused by mechanical or geotechnical failure, or improper human action. This thesis focuses on embankment failure hazards, but offers a framework where the remaining geo-hazards can be incorporated. The widely used global *factor of safety* concept will be used to quantify embankment stability hazard levels. Debris flows, rock falls, and volume change problems may require different hazard quantification parameters.

The identification of the means available to deal with geo-hazards is less straightforward. Figure 3.3 presents the *means-objectives* network for the railway system. The means to maximize the railway system performance are numerous, and only a few are presented in the figure in order to keep the context of the problem from becoming excessive. Two distinct types of means can be identified; namely, reactive and proactive means. As geo-hazard assessment techniques were not available in the past, the rail industry needed to invest most of its resources on reactive methodologies. As the knowledge and understanding of geo-hazards develops, new proactive methodologies become an option. The following can be considered some of the most important means towards the implementation of proactive methodologies; namely, (i) the identification and characterization of hazards; (ii) use of real-time monitoring and warning systems; and (iii) decision support systems. The triggering event for embankment failures is typically associated with severe weather conditions. The problem of embankment failures has a dynamic, transient nature, and real-time monitoring systems would appear to provide a logical course of action towards the development of a proactive methodology.

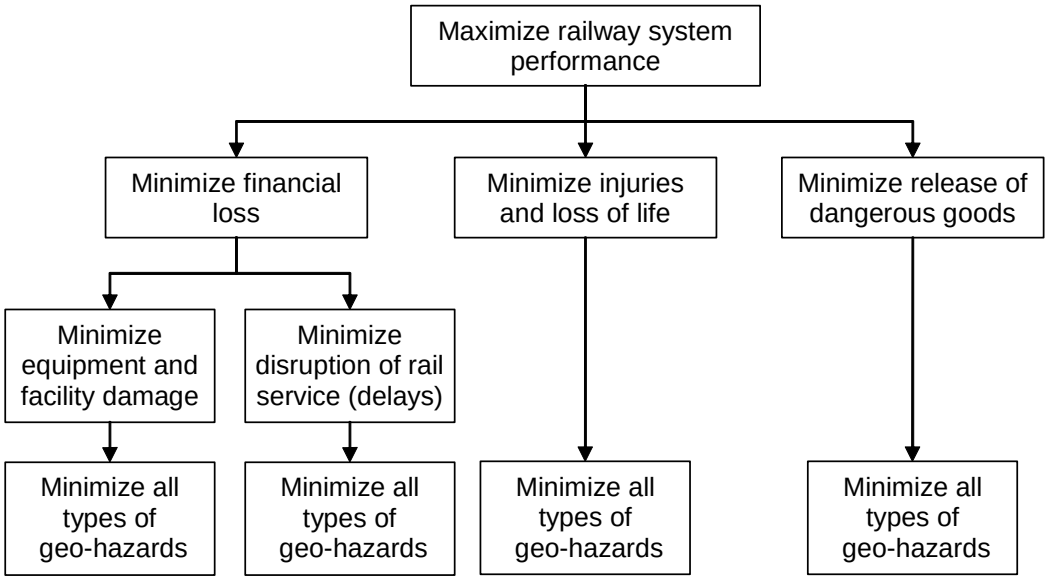

Figure 3.2 Fundamental objectives hierarchy of the W-GHA model.

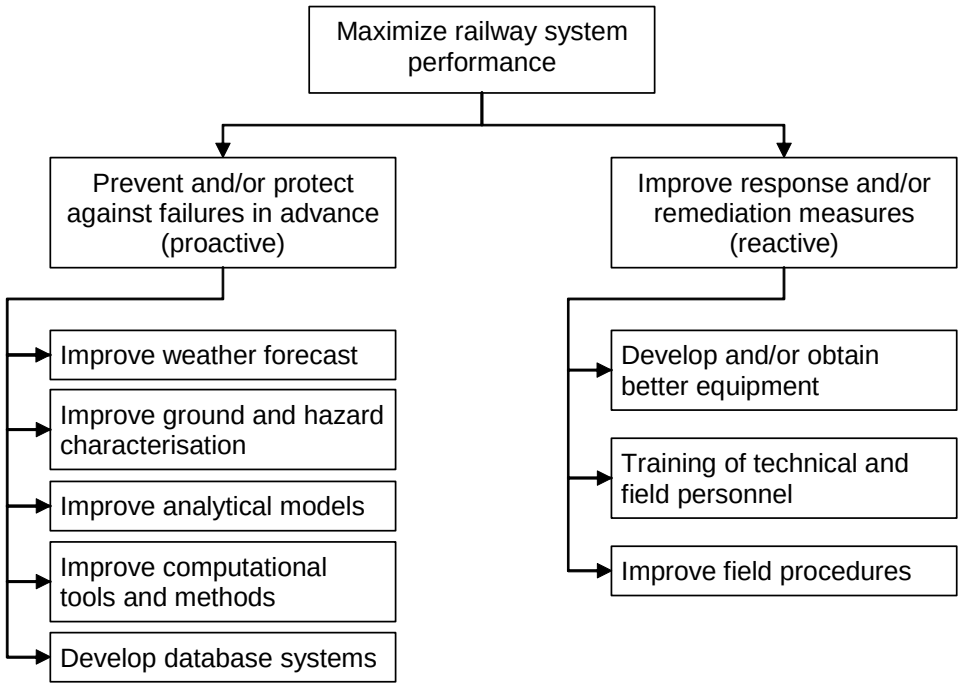

Figure 3.3 Means-objectives network of the W-GHA model.

3.2.2 *Identification of railway alternatives*

The decision at hand has two possible alternatives; namely, to take action or not take action. The question of whether or not action needs to be taken is of paramount importance in the management of a railway system. The ability to identify high-level hazards along the railway would render considerable savings. By taking safety measures, loss of equipment can be prevented and the safety of the railway workers increases, reducing the number of injuries and the chance of fatalities. A major concern to the railway companies is the frequent service disruption caused by accidents along the track, and in this case, delays could be reduced.

The two generic alternatives (i.e., to take action or not take action) are considered herein. However, different hazard levels and conditions would require different actions. Stronger actions must be taken for greater risks and different actions must be taken for different hazard characteristics. Details regarding the railway system management and considerations of types of actions to be taken are issues that must be addressed by the railway managers and *Decision Makers*. Specific alternatives can be considered using the proposed framework.

3.3 MODEL OF PROBLEM STRUCTURE

The deterministic modelling of railway embankment stability represents the most complex part of developing the W-GHA model. A traditional geotechnical engineering approach is used herein in the sense that the stability of railway embankments is idealized as a function of the stress state (i.e., net stress and pore-water pressure) and the shear strength along a critical slip surface within the earth mass. The *factor of safety*, F_s, is defined using an optimization technique as that factor by which the shear strength must be reduced to bring the mass into a state of limit static equilibrium along a given slip surface and is used as a measure of stability.

The W-GHA model is based on a series of partial differential equations governing the thermo-hydro-mechanical behaviour of the saturated/unsaturated soil system. Appropriate boundary conditions to account for evaporation, precipitation, and runoff are given. The manner in which the pore-water pressure and total stress distributions are used to determine the embankment stability is explained later.

3.3.1 *W-GHA model components*

Figure 3.4 illustrates the environmental factors affecting the stability of an embankment. Changes in the stress state distribution and shear strength within the soil mass take place in response to moisture fluxes at the soil-atmosphere boundary. In order to determine the moisture flux and changes in pore-water pressure in the soil, partial differential equations (PDEs) governing the flow of moisture must be combined with appropriate boundary conditions and solved for the period of time under consideration. The PDE governing the flow of heat must also be solved since the amount of liquid water flow and water vapour flow depends on the temperature, which in turn, changes according to the energy available at ground surface. Special procedures to determine the amount of run-off and actual evaporation are also required. The total stress distribution and the shear stress acting along a particular slip surface are obtained by solving the PDEs governing static equilibrium of forces.

The W-GHA model incorporates the influence of soil-atmosphere moisture fluxes on the stability of an embankment according to the flowchart presented in Figure 3.5. An essential component of the model is the *Dynamic Programming* algorithm for stability analysis. The algorithm is used to determine critical conditions and the corresponding factors of safety F_s at any time, t. In order to determine critical conditions, the net stress distribution at $t = t_i$ and the corresponding pore-water pressure distribution, u_w, at $t = t_i$ are required. The pore-water pressure

distribution is determined by solving two-dimensional partial differential equations governing transient moisture and heat flow. The initial pore-water pressure and temperature distributions, u_{w0} and T_0, are also required. Realistic functions for the amount of precipitation and potential evaporation are combined with the moisture and heat flow analysis to determine the transient net soil-atmosphere boundary flux.

In order to determine the embankment stability, the pore-water pressure distribution must be sampled at several pre-determined times, $t = t_i$. The degree of saturation within the soil mass and the soil unit weight distribution are computed as functions of the pore-water pressure distribution (i.e., using the SWCC). For each of the chosen sampling times, the partial differential equations governing static equilibrium are solved using the soil unit weight distribution and external loads. Finally, the Dynamic Programming optimization algorithm uses the net stress and pore-water pressure distributions to determine the location and shape of the critical slip surface and the corresponding factor of safety. It is assumed that the development of a critical slip surface is sufficient to compromise the railway safety. Even if the initial slip surface does not reach the track, subsequent failures may compromise it.

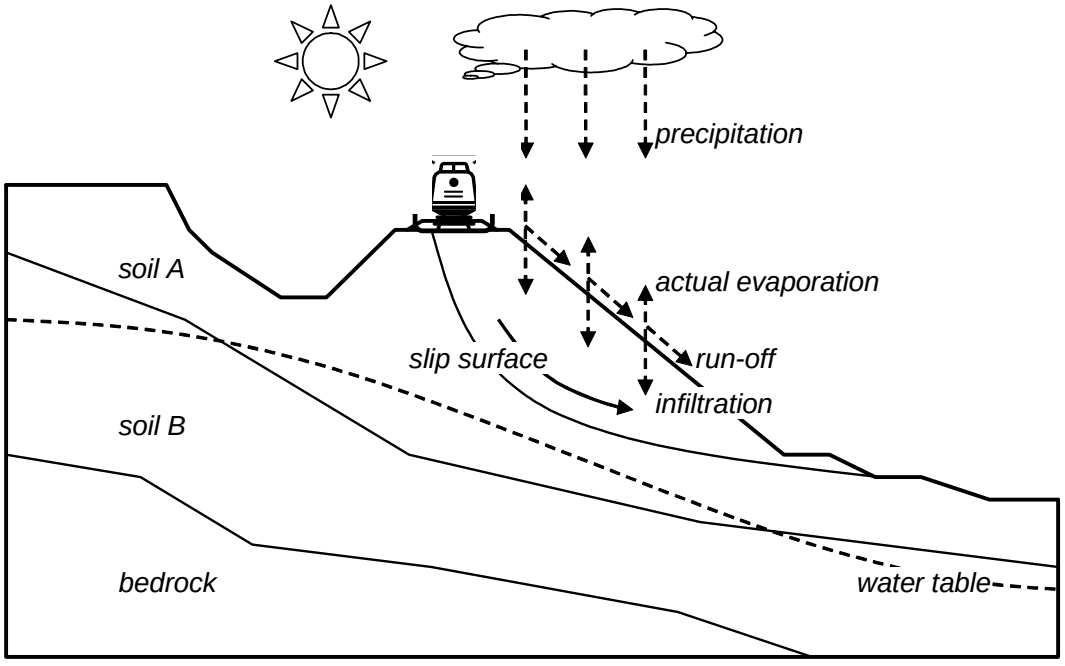

Figure 3.4 Factors affecting the stability of an embankment.

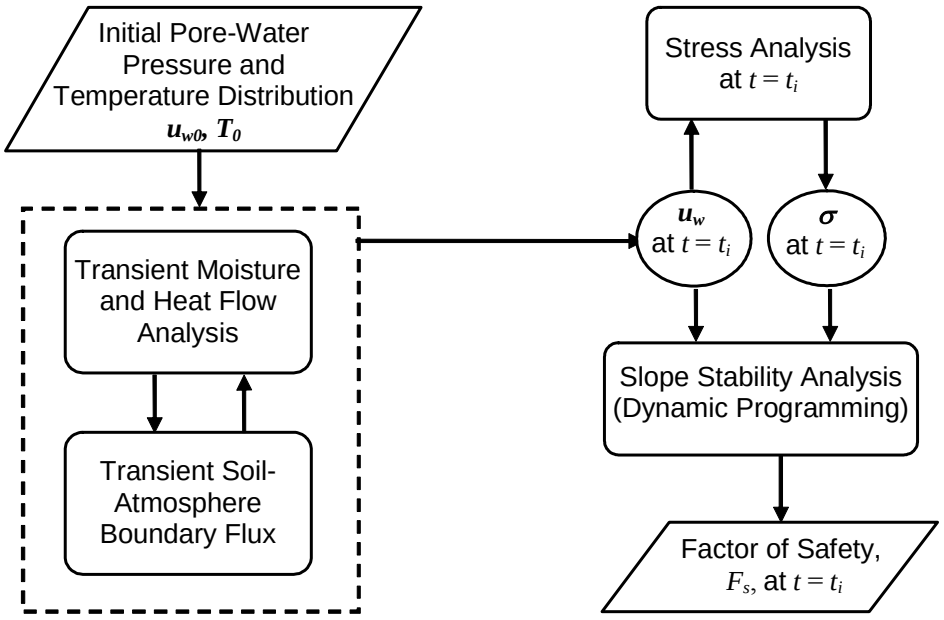

Figure 3.5 W-GHA model flowchart.

Uncertainties related to soil properties and weather conditions are considered by the W-GHA model through a frequency (or probabilistic) analysis. The probabilistic model consists of using a point estimate approach base on a moment-matching technique. The frequency distribution of the random variables considered as uncertain is used as input. As a result, the problem is reduced to a number of case scenarios. The probability of the embankment becoming unstable is assessed based on the statistical moments of the *factor of safety* and assuming a probability density function for F_s.

3.3.2 *Partial differential equations governing soil behaviour*

The hydro-thermo-mechanical behaviour of the soil comprising a railway embankment can be represented by a system of partial differential equations (PDEs). These equations are obtained using a traditional continuum mechanics approach and appropriate state variables. The broadly accepted stress state variables; namely, net stress ($\sigma - u_a$) and matric suction ($u_a - u_w$), are used (Fredlund and Morgenstern, 1977), where σ is the total stress, u_a is the pore-air pressure, and u_w is the pore-water pressure. The displacement state variables are the horizontal and vertical displacements, u and v (x- and y-direction, respectively), and the change in volume of water and air in a referential volume. The PDEs governing (i) static force equilibrium, (ii) flow of moisture, and (iii) flow of heat are obtained from basic continuity and equilibrium laws, combined with constitutive laws that describe soil behaviour.

The computation of changes in water content and pore-water pressure distributions within an embankment form an essential step towards to the assessment of weather-related geo-hazards. Atmospheric forcing conditions produce internal moisture flow and changes in the pore-water pressures within the embankment. The internal flow makes moisture available for evaporation and/or allows precipitation to infiltrate the embankment. Neglecting either evaporation or infiltration may lead to unrealistic pore-water pressure predictions as both are important components of the net soil-atmosphere flux. The importance of taking into account evaporative fluxes is particularly evident in arid and semi-arid regions where the annual amount of evaporation is greater than precipitation (Fredlund and Rahardjo, 1993). Keeping account of evaporative fluxes is also important in other types of climate where the rate of evaporation is comparable to the rate of precipitation.

Moisture moves through soils driven by gradients of total head and/or partial pressures for each of the moisture phases (i.e., both liquid water and water vapour). The ratio between the flow of liquid water and water vapour depends mainly on the *temperature* and degree of saturation of the soil. Consequently, the transient temperature gradients need to be determined and heat transfer must be taken into account when simulating the flow of moisture (Philip and de Vries, 1957 and Wilson et al., 1994). Several physical processes are involved in the analysis of moisture and heat flow. In order to obtain the equations governing heat and moisture transfer, constitutive flow laws and water volume change constitutive laws are combined with the mass and heat conservation equations. Appropriate equations for the soil-atmosphere flux boundary conditions are required. The two-dimensional PDEs used herein are extensions of the one-dimensional formulations presented by Philip and de Vries (1957) and Wilson et al. (1994).

3.3.2.1 *Conservation and flow of moisture (vapour and liquid water)*

A series of assumptions form the backdrop for the equation for the flow of liquid water and water vapour in soils. The main assumptions are as follows:

(i) the soil phases are individually continuous and therefore can be described using a continuum mechanics approach;
(ii) the air phase is in permanent contact with the atmosphere;
(iii) osmotic pressure gradients are negligible at "low" matric suctions ($u_a - u_w < 1500$ kPa);
(iv) local thermodynamic equilibrium between the liquid water and water vapour phases exists at all times at any point in the soil;

(v) temperature within the soil remains below the boiling point and above the freezing point of water at all times;

(vi) dissolution of air into the liquid water phase is neglected;

(vii) hysteretic behaviour of the soil-water characteristic curve can be approximated by taking the logarithmic average between the main drying and main wetting curves.

The equation of conservation of mass for the water phase can be derived by taking the rate of flux of water mass in and out of a representative elemental volume (REV) and equating the difference to the rate of change of water mass within the REV with time (Fig. 3.6). Two types of water mass flow must be considered; namely, mass flux of liquid water, q^w; and mass flux of water vapour within the air phase, q^v. Considering flow only in the *x*- and *y*-directions (i.e., two-dimensional flow), the following mass conservation equation is obtained:

$$-\frac{\partial}{\partial x}(q_x^w + q_x^v) - \frac{\partial}{\partial y}(q_y^w + q_y^v) = \frac{1}{V_0}\frac{\partial M_w}{\partial t} \tag{3.1}$$

where:

q_i^w = flux rate of mass of liquid water in the *i* direction per unit of total area, kg/(m^{2}s);

q_i^v = flux rate of mass of water vapour within the air phase in the *i* direction per unit of total area, kg/(m^{2}s);

M_w = mass of water within the representative elemental volume, kg;

V_0 = total volume of the elemental volume, $V_0 = dxdydz$, m^3;

t = time, s.

The mass flux of liquid water in saturated/unsaturated soils can be described by using a generalisation of Darcy's Law (Bear, 1972), where the driving mechanism is the total head gradient and the hydraulic conductivity varies with matric suction, ($u_a - u_w$). The generalised Darcy's law can be written as follows:

$$\begin{aligned} q_x^w &= -\rho_w k^w \frac{\partial h}{\partial x} = -\rho_w k^w \frac{\partial (u_w/\gamma_w + y)}{\partial x} \\ q_y^w &= -\rho_w k^w \frac{\partial h}{\partial y} = -\rho_w k^w \frac{\partial (u_w/\gamma_w + y)}{\partial y} \end{aligned} \tag{3.2}$$

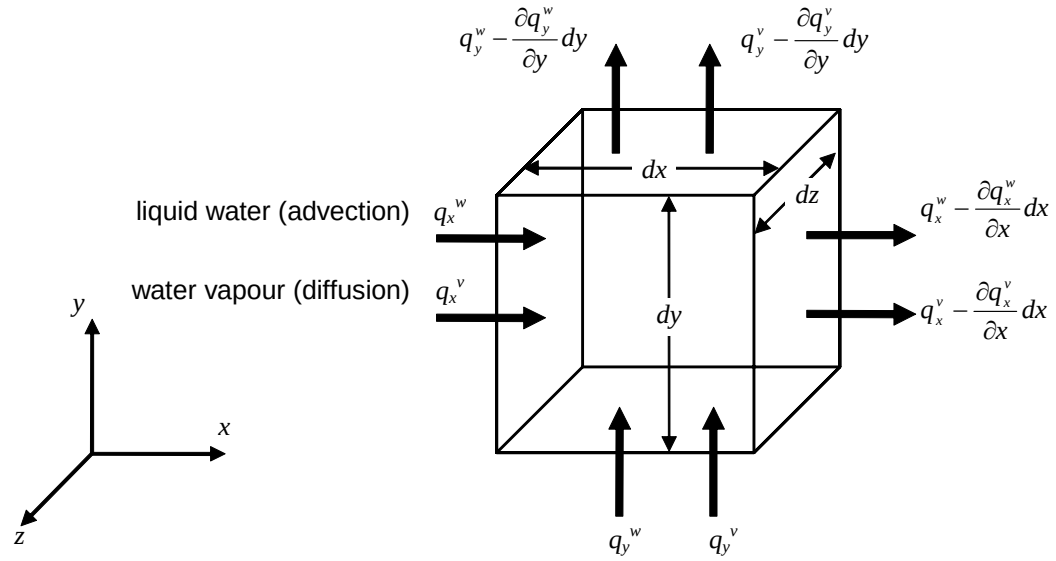

Figure 3.6 Soil representative elemental volume and water mass fluxes.

where:

ρ_w	=	density of water, ≈ 1000.0 kg/m^3;
k^w	=	hydraulic conductivity, $k^w = f(u_a - u_w)$, m/s;
h	=	hydraulic head, m;
u_w	=	pore-water pressure, kPa;
γ_w	=	unit weight of water, ≈ 9.81 kN/m^3;
y	=	elevation, m.

Water vapour flow takes place by two mechanisms. Water vapour may move independently from the air phase, driven by gradients in its concentration. Water vapour may also move along with the air phase that moves driven by gradients in the total pressure of the bulk air phase. The mass flux of water vapour and water vapour within the bulk air may be described by a modified form of Fick's law (Philip and de Vries, 1957 and Dakshanamurthy and Fredlund, 1981a):

$$q_x^v = -D^v \frac{\partial C_v}{\partial x} - \frac{\rho_v}{\rho_a} D^a \frac{\partial C_a}{\partial x} = -D^{v*} \frac{\partial p_v}{\partial x} - \frac{\rho_v}{\rho_a} D^{a*} \frac{\partial \overline{u}_a}{\partial x}$$
$$q_y^v = -D^v \frac{\partial C_v}{\partial y} - \frac{\rho_v}{\rho_a} D^a \frac{\partial C_a}{\partial y} = -D^{v*} \frac{\partial p_v}{\partial y} - \frac{\rho_v}{\rho_a} D^{a*} \frac{\partial \overline{u}_a}{\partial y} \qquad (3.3)$$

where:

D^v	=	molecular diffusivity of vapour in air, $0.229\times10^{-4}(1+T/273.15)^{1.75}$, m^2/s;

D^a = coefficient of transmission of air, $D^a \approx D^v$ (Wilson, 1990);

T = temperature, K;

C_v, C_a = concentration of water vapour and air, respectively, in terms of the mass of vapour per unit volume of soil, $C_v = \rho_v(1 - S)n$, $C_a = \rho_a(1 - S)n$;

S = degree of saturation, $S = V_w/V_v$;

n = porosity, $n = V_v/V_0$;

V_w, V_v = volume of water and voids in the elemental volume, respectively, m^3;

ρ_v = density of the water vapour, $\rho_v = W_v p_v/(RT)$, kg/m^3;

ρ_a = density of the bulk air phase, $\rho_a = W_a \bar{u}_a/(RT)$, kg/m^3;

W_v, W_a = molecular weight of water vapour and pore-air, respectively, kg/kmol;

p_v = partial pressure of water vapour, kPa;

$\bar{u}_a$ = total pressure in the bulk air phase, $u_a + u_{atm}$, kPa;

u_a = pore-air pressure, kPa;

u_{atm} = atmospheric pressure, 101.325 kPa;

R = universal gas constant, 8.314 J/(mol.K);

D^{v*} = $(1 - S)nD^v W_v / RT$, (kg.m)/(kN.s);

D^{a*} = $(1 - S)nD^a W_a / RT$, (kg.m)/(kN.s).

The term ρ_v/ρ_a in Eq. 3.3 gives the fraction of water vapour present in the pore-air. Neglecting any gradients in atmospheric pressure and assuming the air phase is continuous and in direct contact with the atmosphere, gradients of u_a will be equal to gradients in the partial pressure of water vapour, p_v. Therefore, Eq. 3.3 can be re-written as follows:

$$q_x^v = -D^{v*}\frac{\partial p_v}{\partial x} - \frac{p_v}{\bar{u}_a}D^{v*}\frac{\partial p_v}{\partial x} = -\frac{\bar{u}_a + p_v}{\bar{u}_a}D^{v*}\frac{\partial p_v}{\partial x}$$
$$q_y^v = -D^{v*}\frac{\partial p_v}{\partial y} - \frac{p_v}{\bar{u}_a}D^{v*}\frac{\partial p_v}{\partial y} = -\frac{\bar{u}_a + p_v}{\bar{u}_a}D^{v*}\frac{\partial p_v}{\partial y} \qquad (3.4)$$

In order to obtain the partial differential equation that governs the conservation and flow of liquid and vapour water through soils the flow law equations (Eqs. 3.2 and 3.4) and a water volume change constitutive equation are combined with the continuity of water mass equation (Eq. 3.1). Considering the reference volume V_0 constant, the water phase and the soil structure incompressible, and assuming that the pore-air pressure is constant, the following equation is obtained:

$$\frac{\partial}{\partial x}\left[k^{w}\frac{\partial\left(u_{w}/\gamma_{w}+y\right)}{\partial x}+\frac{\overline{u}_{a}+p_{v}}{\overline{u}_{a}}\left(\frac{D^{v^{*}}}{\rho_{w}}\frac{\partial p_{v}}{\partial x}\right)\right]$$
$$+\frac{\partial}{\partial y}\left[k^{w}\frac{\partial\left(u_{w}/\gamma_{w}+y\right)}{\partial y}+\frac{\overline{u}_{a}+p_{v}}{\overline{u}_{a}}\left(\frac{D^{v^{*}}}{\rho_{w}}\frac{\partial p_{v}}{\partial y}\right)\right]=\frac{\partial(nS)}{\partial t} \qquad (3.5)$$

where:

n = soil porosity;

S = degree of saturation, obtained from the soil-water characteristic curve.

As will be shown in the next section, it is convenient to replace the gradients of p_v in Eq. 3.5 by gradients of temperature, T. Based on the thermodynamic theory of soil moisture (Edlefsen and Anderson, 1943), p_v can be expressed as a function of the total potential of the liquid pore-water, ψ, and temperature. Assuming local thermodynamic equilibrium, such function is as follows:

$$p_{v}=p_{vsat}e^{\frac{-\psi g W_{v}}{\gamma_{w}R(T+273.15)}} \qquad (3.6)$$

where:

p_{vsat} = saturation vapour pressure of the soil water at temperature T, kPa;

ψ = $(u_a - u_w) + \pi$, (i.e., matric suction plus osmotic suction);

ψ = total potential of the liquid pore-water, kPa;

g = acceleration of gravity, 9.81 m/s^2;

W_v = molecular weight of water, 0.018016 kg/mol;

γ_w = unit weight of water, ≈ 9.81 kN/m^3;

R = universal gas constant, 8.314 J/(mol×K);

T = temperature, ^{o}C.

Some terms from Eq. 3.6 require further explanation. Values of saturation vapour pressure, p_{vsat}, are well established and depend primarily on the vapour temperature. Values of p_{vsat} experimentally obtained by Kaye and Laby (1973) for various temperatures are presented in Fig. 3.7 along with a best fit curve that can be used as a continuous representation of the data-set. Figure 3.8 presents a plot of the relationship between p_v, ψ, and T, obtained using Eq. 3.6 and the best-fit equation presented in Fig. 3.7. The limits of the curves presented in Fig. 3.8 are the saturation vapour pressure for ψ = 0 kPa and zero vapour pressure for $\psi \approx 1\times10^{6}$ kPa. Figure 3.7 shows that changes in p_v due to changes in ψ are negligible when ψ < 1500 kPa.

The total potential of the liquid pore-water, ψ, from Eq. 3.6, is termed "total suction" when its value is positive. The values of ψ are traditionally plotted as a function of the degree of saturation (or some other water content measure), forming the plot that is known as the soil-water characteristic curve. It has become conventional practice to plot soil-water characteristic curves using matric suction data for $(u_a - u_w) < 1500$ kPa and total suction data otherwise. Fredlund (2002) presents a detailed justification for why this apparently inconsistent approach is adequate in geotechnical engineering practice. Capillary effects dominate in the "low" suction range, while osmotic potential becomes of importance in the "high" suction range. Quoting Fredlund (2002), "*it is anticipated that this* [the above manner] *will continue to be the manner in which the soil-water characteristic curve is plotted and utilized in geotechnical engineering*". The plot of the SWCC combining matric and total suction was adopted throughout this thesis.

A relationship between the gradients of p_v and the gradients of the other two variables, ψ and T, can be determined by deriving Eq. 3.6. The following equation is obtained:

$$\nabla p_v = \frac{g W_v p_v}{\gamma_w R(T + 273.15)} \left(\frac{\psi}{(T + 273.15)} \nabla T - \nabla \psi \right) \qquad (3.7)$$

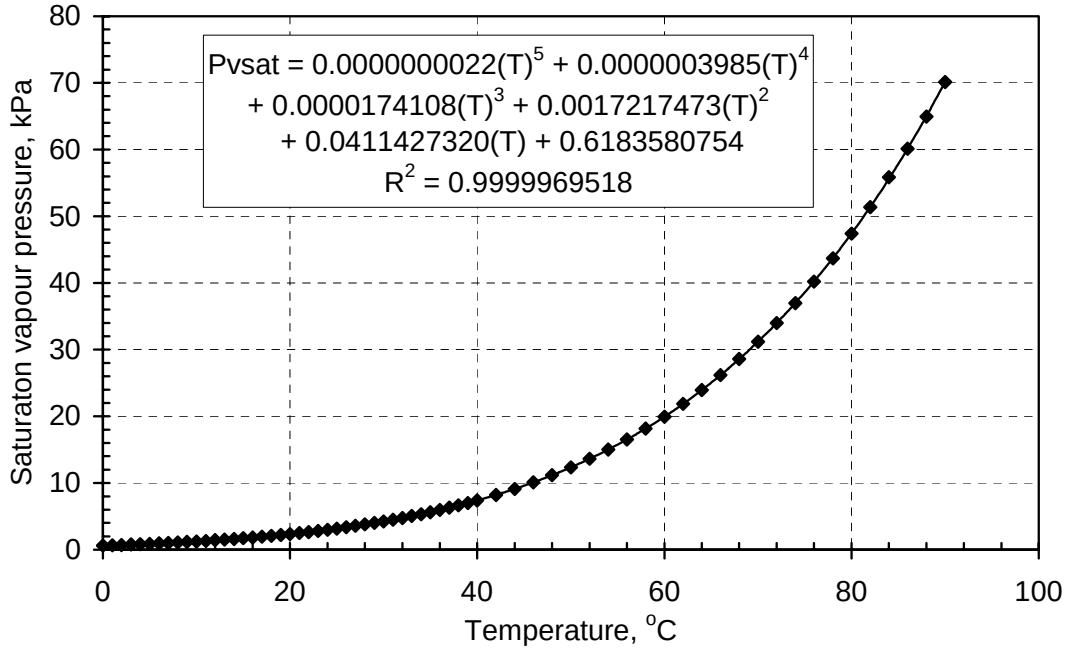

Figure 3.7 Experimental data for saturation soil vapour pressure versus temperature (Kaye and Laby, 1973) and best fit curve.

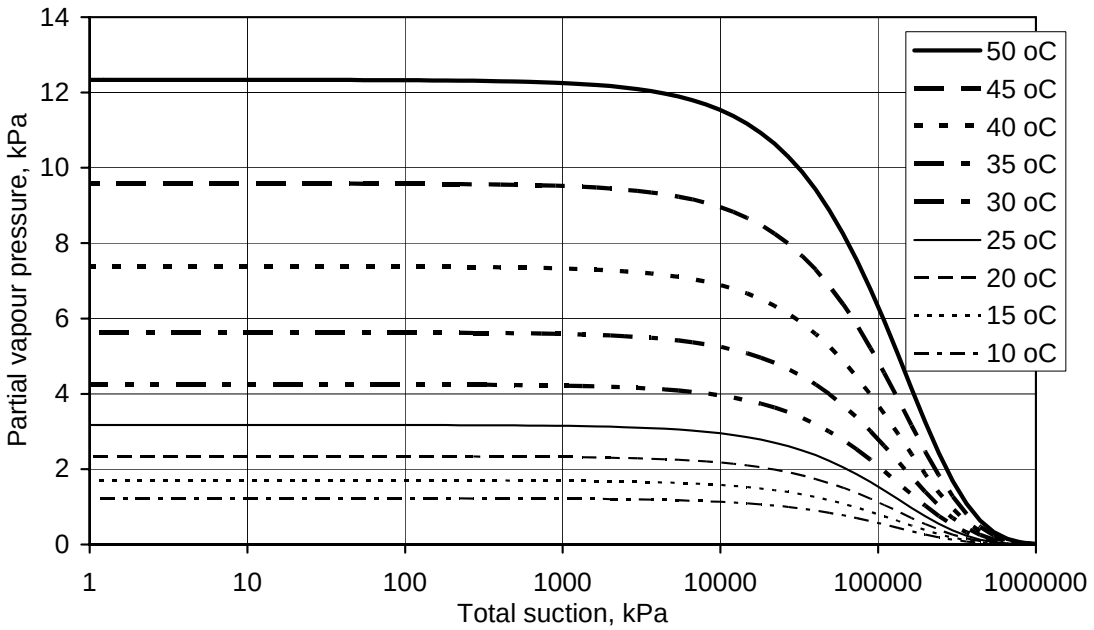

Figure 3.8 Relation between partial vapour pressure, total suction, and temperature.

In order to make Eqs. 3.6 and 3.7 consistent with the convention adopted for the SWCC, the water potential, ψ, in Eqs. 3.6 and 3.7 will be assumed as equal to the soil suction obtained from the SWCC and will be represented by the term $(u_a - u_w)$. According to this convention, the term $(u_a - u_w)$ corresponds to the total suction for soil suctions larger than 1500 kPa. Assuming that the pore-air phase is in contact with the atmosphere ($u_a = 0$), Eq. 3.7 can be written as follows:

$$\nabla p_v = \frac{g W_v p_v}{\gamma_w R(T + 273.15)} \left(\nabla u_w - \frac{u_w}{(T + 273.15)} \nabla T \right) \qquad (3.8)$$

The PDE governing moisture flow can be modified using Eq. 3.8 in order to express gradients of p_v as function of the gradients of u_w and T. As a result, Eq. 3.5 can be re-written as follows:

$$\begin{aligned} &\frac{\partial}{\partial x}\left[\left(\frac{k^w + k^v}{\gamma_w} \right) \frac{\partial u_w}{\partial x} - \frac{k^v}{\gamma_w} \left(\frac{u_w}{T + 273.15} \right) \frac{\partial T}{\partial x} \right] \\ &+ \frac{\partial}{\partial y}\left[\left(\frac{k^w + k^v}{\gamma_w} \right) \frac{\partial u_w}{\partial y} + k^w - \frac{k^v}{\gamma_w} \left(\frac{u_w}{T + 273.15} \right) \frac{\partial T}{\partial y} \right] = \frac{\partial (nS)}{\partial t} \end{aligned} \qquad (3.9)$$

where:

k^v = vapour conductivity; and

$$k^v = \frac{\bar{u}_a + p_v}{\bar{u}_a} \frac{gW_v p_v}{R(T+273.15)} \frac{D^{v*}}{\rho_w}, \text{ m/s.}$$

Equation 3.9 is the final PDE governing the flow of moisture by liquid water and water vapour flow. Temperature gradients required to render this equation solvable can be obtained by solving a PDE governing conservation of thermal energy. Three unsaturated soil property functions can be identified in Eq. 3.9; namely: the hydraulic conductivity, the vapour conductivity, and the soil-water characteristic curve. These soil properties functions vary with soil suction, and therefore, the PDE is physically non-linear.

3.3.2.2 *Conservation and flow of heat*

Heat transfer in soils occurs by three mechanisms, namely: conduction; convection; and latent heat due to phase change. Heat transfer by convection of the pore-fluid in soils is considerably smaller than conductive heat transfer (Milly, 1984) and therefore neglected for the problem at hand. In terms of changes of phase, the present concern is relative to vaporization/condensation. Considering these conditions, the heat transfer in soils may be modelled using a modified Fourier equation (Dakshanamurthy and Fredlund, 1981a). The modified Fourier equation is based on the conservation of heat within a REV (Fig. 3.9), which is written as follows:

$$-\frac{\partial}{\partial x}(h_x^c + h_x^l) - \frac{\partial}{\partial y}(h_y^c + h_y^l) = \frac{1}{V_0}\frac{\partial (Q_h)}{\partial t} \qquad (3.10)$$

where:

q_i^c = heat flux rate by conduction in the *i* direction per unit of total area,J/(m^{2}s);

q_i^l = flux rate of latent heat in the *i* direction per unit of total area, J/(m^{2}s);

Q_h = heat within the representative elemental volume, J.

The conductive heat flow, q_i^c, can be written as a function of the thermal conductivity of the soil and the temperature gradient, as follows:

$$q_x^c = -\lambda \frac{\partial T}{\partial x}, \quad q_y^c = -\lambda \frac{\partial T}{\partial y} \qquad (3.11)$$

where:

λ = thermal conductivity, $\lambda = f(u_a - u_w)$, J/(m s ^{o}C).

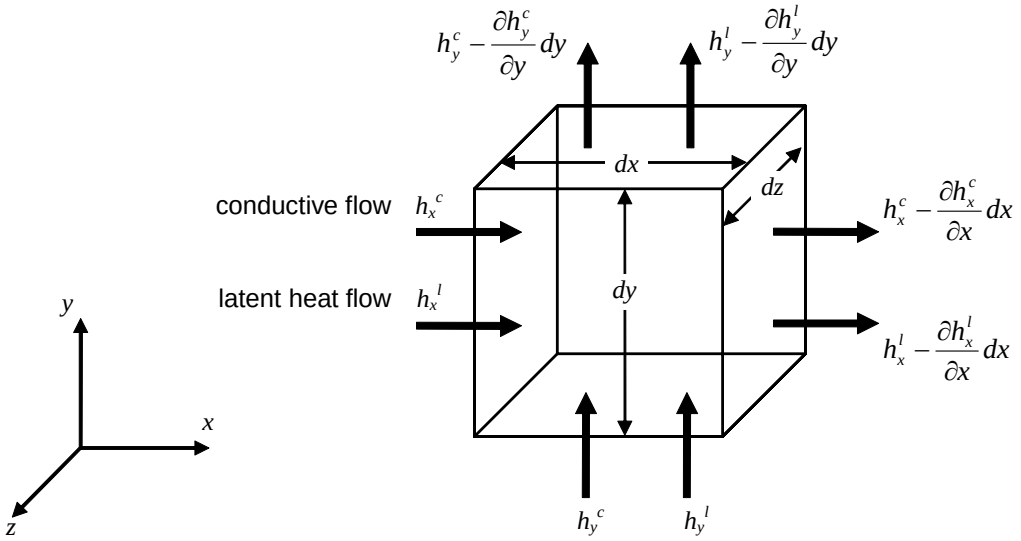

Figure 3.9 Soil representative elemental volume and heat fluxes.

The latent heat flow can be obtained by multiplying the latent heat of vaporization/condensation, L_V, by the amount of vapour flow, given by Eq. 3.4. In order to obtain the partial differential equation that governs the conservation and flow of heat through soils, the equation of conservation of heat (Eq. 3.10) must be combined with the heat flow equations (Eqs. 3.4 multiplied by L_v, and Eqs. 3.11). Furthermore, the total amount of heat within the REV must be written as a function of the volumetric specific heat of the soil. The following results:

$$\frac{\partial}{\partial x}\left(\lambda\frac{\partial T}{\partial x}+L_V\frac{\overline{u}_a+p_v}{\overline{u}_a}D^{v*}\frac{\partial p_v}{\partial x}\right)+\frac{\partial}{\partial y}\left(\lambda\frac{\partial T}{\partial y}+L_V\frac{\overline{u}_a+p_v}{\overline{u}_a}D^{v*}\frac{\partial p_v}{\partial y}\right)=\zeta\frac{\partial T}{\partial t} \tag{3.12}$$

where:

T = temperature, ^{o}C;

L_V = latent heat of vaporization/condensation, $4.187\times10^3\times(591-0.51\times T)$, J/kg;

ζ = volumetric specific heat of soil, $\zeta=\gamma_{nat}\,c=f(u_a-u_w)$, J/(m^3 ^{o}C).

Expressing the gradients of partial vapour pressure in Eq. 3.12 in terms of gradients of pore-water pressure and temperature (using Eq. 3.8), the following PDE is obtained:

$$\begin{aligned}&\frac{\partial}{\partial x}\left[\left(\lambda-L_V k^v\frac{\rho_w}{\gamma_w}\frac{u_w}{T+273.15}\right)\frac{\partial T}{\partial x}+L_V k^v\frac{\rho_w}{\gamma_w}\frac{\partial u_w}{\partial x}\right]\\&+\frac{\partial}{\partial y}\left[\left(\lambda-L_V k^v\frac{\rho_w}{\gamma_w}\frac{u_w}{T+273.15}\right)\frac{\partial T}{\partial y}+L_V k^v\frac{\rho_w}{\gamma_w}\frac{\partial u_w}{\partial y}\right]=\zeta\frac{\partial T}{\partial t}\end{aligned} \tag{3.13}$$

Equation 3.13 is the final PDE governing the flow of heat. Equation 3.13 must be solved in a coupled manner, along with Eq. 3.9. The primary variables are u_w and T. These two PDEs can be solved using some numerical approximations, such as the *Finite Element* and the *Finite Difference* methods. Two new unsaturated soil property functions can be identified in Eq. 3.13; namely: the thermal conductivity function and the volumetric specific heat. These soil properties functions also vary with soil suction, rendering the PDE physically non-linear. All of the above-mentioned unsaturated soil property functions bear a relationship to the SWCC.

3.3.2.3 *Static equilibrium of forces and stress-strain relationship*

The PDEs governing static equilibrium of forces can be obtained by considering the equilibrium of forces acting upon a REV of soil (Chou and Pagano, 1992). For the two-dimensional case, equilibrium in the *x*- and *y*-directions must be considered. The forces are expressed in terms of stresses and infinitesimal areas. The equilibrium equations, in Cartesian coordinates, are:

$$\begin{aligned} \frac{\partial \sigma_x}{\partial x} + \frac{\partial \tau_{xy}}{\partial y} + b_x &= 0 \\ \frac{\partial \tau_{xy}}{\partial x} + \frac{\partial \sigma_y}{\partial y} + b_y &= 0 \end{aligned} \tag{3.14}$$

where:

σ_i = normal stress acting on the *i* plane, on the *i* direction;

τ_{ij} = shear stress acting on the *i* plane, on the *j* direction;

b_i = body force acting on the *i* direction.

Equation 3.14 respects the rotational equilibrium, since the stress tensor was considered symmetrical. Combining the equilibrium equations with Hooke's generalised stress-strain law, and expressing the strain in terms of small displacements (*u* and *v* for the *x*- and *y*-directions, respectively), the following PDEs are obtained for the *x*- and *y*-directions:

$$\frac{\partial}{\partial x}\left[D_{11}\frac{\partial u}{\partial x} + D_{12}\frac{\partial v}{\partial y}\right] + \frac{\partial}{\partial y}\left[D_{44}\left(\frac{\partial u}{\partial y} + \frac{\partial v}{\partial x}\right)\right] = 0 \tag{3.15}$$

$$\frac{\partial}{\partial x}\left[D_{44}\left(\frac{\partial u}{\partial y} + \frac{\partial v}{\partial x}\right)\right] + \frac{\partial}{\partial y}\left[D_{12}\frac{\partial u}{\partial x} + D_{11}\frac{\partial v}{\partial y}\right] + \gamma_{nat} = 0 \tag{3.16}$$

where:

D_{11} = $E(1-\mu)/[(1+\mu)(1-2\mu)]$;

D_{12} = $E\mu/[(1+\mu)(1-2\mu)]$;

D_{44} = $E/[2(1+\mu)]$;

E = Young modulus, kPa;

μ = Poisson ratio;

γ_{nat} = body force acting in the *y*-direction (vertical);

γ_{nat} = $\gamma_s(1-n)+\gamma_w nS$, kN/m^3;

γ_s = specific weight of soil particles, kN/m^3.

Though Hooke's law may not result in the best prediction of displacements in some cases, Scoular (1997) has shown that the stress field results are not significantly influenced by the stress-strain law employed. Different stress-strain laws give essentially the same results for the stress fields within homogeneous soil masses (i.e., without contacts between different materials). The railway geo-hazards of concern herein are assumed to be characterised by the embankment overall stability, which depends primarily on the stress distributions. Therefore, the use of Hooke's generalised law is considered appropriate for its simplicity.

Total volume change due to changes in pore-water pressure is neglected in Eqs. 3.15 and 3.16. If total volume change due to changes in pore-water pressure is to be determined, the relationship between total volume change and pore-water pressure would have to be considered and Eqs. 3.15 and 3.16 should be solved in a coupled manner with Eqs. 3.9 and 3.13. The primary variable of interest in the W-GHA model is the change in pore-water pressure and net stresses in response to the atmospheric boundary conditions. Therefore, the equilibrium-moisture flow coupling was assumed as not essential. This may not be the case for soils with large volume change characteristics, such as expansive and collapsible soils (Pereira, 1996).

3.3.3 *Weather-related boundary conditions*

The partial differential equations governing the conservation of moisture and heat require boundary conditions associated with atmospheric forcing conditions. The net soil-atmosphere moisture flux is a function of precipitation, actual evaporation, run-off, and the pore-water pressures at the ground surface. The heat flow at the soil-atmosphere boundary is a function of the net radiation available at ground surface and the latent heat of evaporation. Appropriate equations to represent these boundary conditions are presented in this section.

3.3.3.1 *Net soil-atmosphere moisture flux*

The net soil-atmosphere moisture flux is a function of some of the key components of the hydrology cycle; namely, precipitation, actual evaporation, and run-off. Horton (1933) presented and overview of the commonly identified components of the slope hydrological cycle. Other components, such as depression storage, interception, and plant transpiration, are not considered herein, but could also be included in the formulation. The combination of precipitation, actual evaporation, and runoff can produce a net soil-atmosphere flux resulting in either infiltration (positive flux) or exfiltration (negative flux). The net soil-atmosphere moisture flux can be determined by the following water balance equation:

$$NF = P\cos\alpha - AE - R \tag{3.17}$$

where:

NF	=	net moisture flux, m/s;
P	=	precipitation, m/s;
α	=	ground surface angle (zero if horizontal), radians;
AE	=	actual evaporation, m/s;
R	=	runoff, m/s.

The soil-atmosphere net moisture flux components are illustrated in Fig. 3.10. The net moisture flux, NF, corresponds to a natural (i.e., flux) boundary condition. The amount of precipitation, P, is a "known" input obtained from weather data. The term $\cos\alpha$ multiplying P was included based on the assumption that precipitation reaches the ground surface in a vertical trajectory and based on the fact that precipitation is typically measured on a horizontal surface (see Fig. 3.10). The terms AE and R are assumed not to be a function of the orientation of the ground surface. However, AE and R are a function of weather parameters and of the soil suction at the soil-atmosphere boundary. As a result, the net moisture flux is an unknown that must be computed by simultaneously solving the net soil-atmosphere moisture flux boundary condition and the PDEs governing the movement of moisture and heat.

As described by Hillel (1982), three conditions are required for the process of evaporation to occur. Firstly, a continuous supply of energy must be available for the latent heat of vaporization (typically, the net all-wave radiation, R_n). Secondly, the vapour pressure of the atmosphere above the soil surface must be less than the vapour pressure at the soil surface.

Thirdly, a continual supply of water to the site of evaporation is required. The first two conditions determine the *potential evaporation*, *PE*, and are controlled by micro-meteorological factors such as long and short wave radiation, humidity, air temperature and wind speed. The third condition for evaporation is controlled by subsurface conditions such as soil type, moisture content, and groundwater. Therefore, the amount of actual evaporation is a function of *potential evaporation*, *PE* (i.e., the amount of evaporation for a saturated surface under a given atmospheric condition), the soil surface conditions, and the availability of water.

The flow of moisture towards the soil surface under "wet conditions" occurs primarily by liquid water movement. As the soil dries, vapour transfer takes over. A decrease in water content at the soil surface corresponds to an increase in soil suction. As soil suction increases, a larger amount of energy is required to remove water from the soil surface. Wilson (1990) showed that the actual evaporation from a soil surface can be determined by using a measure of potential evaporation combined with a limiting function. This limiting function reflects the decrease in actual evaporation as soil suction at the soil-atmosphere boundary is increased:

$$AE = PE\frac{p_v - p_v^{air}}{p_{vsat} - p_v^{air}} = PE\left[\frac{RH - \left(p_{vsat}^{air} / p_{vsat}\right)RH_{air}}{1 - \left(p_{vsat}^{air} / p_{vsat}\right)RH_{air}}\right] \tag{3.18}$$

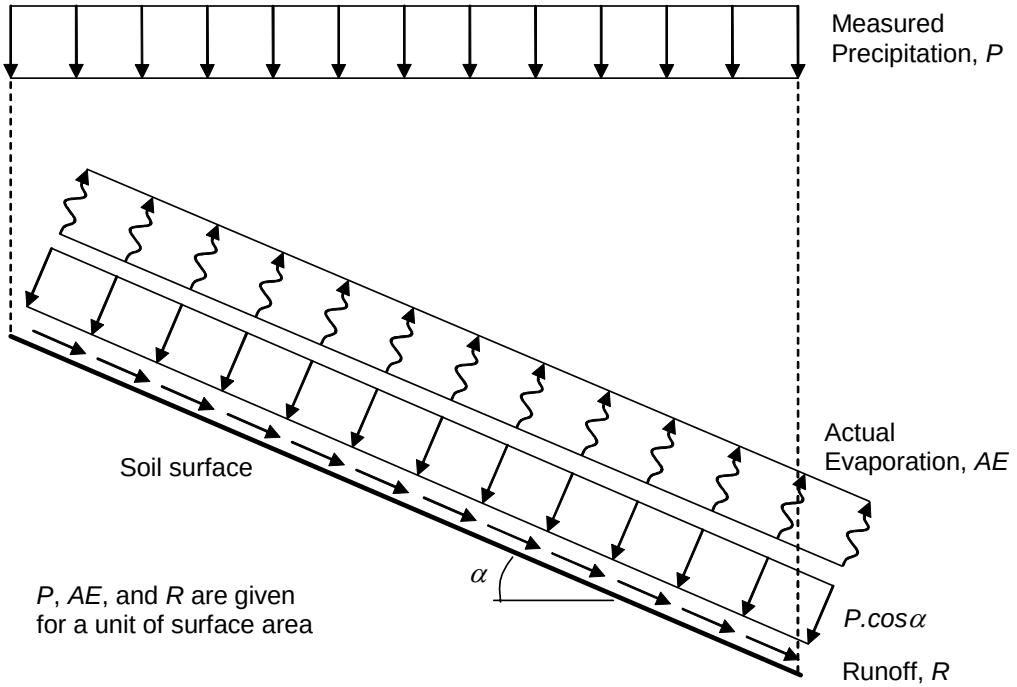

Figure 3.10 Soil-atmosphere moisture flux components.

where:

RH = p_v/p_{vsat}, is the relative humidity at the soil surface, given by Eq. 3.6;

p_v^{air} = vapour pressure in the air near the ground surface, kPa;

p_{vsat}^{air} = saturation vapour pressure in the air near the ground surface, kPa;

RH_{air} = relative humidity of the air near the ground surface;

According to Eq. 3.6, as soil suction increases, *RH* decreases until it reaches zero for a value of suction approximately equal to $1x10^6$ kPa. Equation 3.18 shows that as the relative humidity *RH* decreases, *AE* decreases until it approaches zero when the relative humidity approaches zero. If a direct measure of potential evaporation, *PE*, is not available, it is possible to use one of the several equations available in the literature to calculate *PE* based on weather data. The equation proposed by Penman (1948) is one of the most widely used equations, giving reasonable results and relying on simple weather data. The Penman equation combined with the limiting function presented by Wilson (1990) can be written as follows:

$$AE = \frac{\Gamma Q_n + \eta E_a}{\Gamma + \eta A} \tag{3.19}$$

where:

Γ = slope of the saturation vapor pressure versus temperature curve at the mean temperature of the air, mmHg/^{o}F;

Q_n = net radiation available at the surface, m/s;

η = psychrometric constant, 0.27 mmHg/^{o}F;

E_a = $f_v p_v^{air} (B - A)$, m/s;

f_v = $0.35(1 + 0.15W_w)$;

W_w = wind speed, km/h;

p_v^{air} = vapour pressure in the near the soil surface air;

A = $1/RH$;

B = $1/RH_{air}$.

The net moisture flux at the soil-atmosphere boundary can be determined once the amount of precipitation is known and the parameters of the *AE* equation are obtained. The third component of the water balance at the soil surface, runoff, can be computed in an interactive way. If the embankment being analysed has an efficient drainage system, any runoff water will be removed

from the ground surface. In this case, the amount of net moisture flux, *NF*, should not produce pore-water pressures at ground surface higher than zero. The following set of equations is used to represent this condition:

$$NF = \begin{cases} P\cos\alpha - AE & : \text{if } P\cos\alpha - AE > 0 \text{ and } u_{ws} < 0 \\ EF(0 - u_{ws}) & : \text{if } P\cos\alpha - AE > 0 \text{ and } u_{ws} \geq 0 \\ P\cos\alpha - AE & : \text{if } P\cos\alpha - AE \leq 0 \end{cases} \tag{3.20}$$

where:

u_{ws} = pore-water pressure at the surface, kPa;

EF = large number.

If the multiplier *EF* tends to infinity, the area flux boundary condition $NF = EF(0 - u_{ws})$ becomes mathematically equivalent to the node value boundary condition $u_w = 0$. Therefore, the boundary condition using the flux $EF(0 - u_{ws})$ is an alternative to switching the type of boundary condition when the pore-water pressure at the soil surface reaches zero. Equation 3.20 has been implemented in FlexPDE using conditional functions built into the software. Runoff may take place when the value of $P\cos\alpha - AE$ is larger then the saturated hydraulic conductivity. The amount of runoff corresponds to the difference between the water available, $P\cos\alpha - AE$, and the amount of infiltration computed using Eq. 3.20.

3.3.3.2 *Heat flow*

The amount of heat flow through the soil-atmosphere boundary depends on the availability of heat energy (mostly in the form of solar radiation) and the amount of heat being removed from the soil by evaporation. The heat flow at the ground surface must be in accordance with the following energy balance equation:

$$H = Q_n - AE \tag{3.21}$$

where:

H = heat flux at the soil surface, W/m^2;

Q_n = net radiation available at the soil surface, W/m^2;

AE = actual evaporation, W/m^2.

Actual evaporation, AE, may be converted from usual units (m/s) to W/m^2 by multiplying its value by the latent heat of vaporization (MJ/kg) and by the soil density (kg/m^3), AE[W/m^2] = $1\times10^{-6}\times AE$[m/s] $\times L_V$[MJ/kg] $\times \rho_w$[kg/m^3]. Geothermal gradients were neglected. The heat flux H must be applied as a natural (flux) boundary condition.

The net radiation, Q_n, reaching the ground surface is composed by short-wave and long-wave radiation. The amount of short-wave radiation corresponds to the radiation that comes from the sun, that is not absorbed by the atmosphere and clouds, and that is not reflected back to space by the atmosphere, the clouds, and the earth itself. Estimates of long-wave radiation reaching the earth must take the amount radiated by the atmosphere towards the earth and subtract it by the amount of radiation emitted by the earth itself towards the atmosphere and the space. Oke (1970) provides a fairly comprehensive summary of the energy budget at the ground surface, considering mean values on global annual basis.

3.3.4 *Embankment stability using an optimization technique*

Section 3.3.2 and 3.3.3 dealt with the computation of the transient stress state (i.e., pore-water pressure and total stress) within a railway embankment. PDEs governing the thermo-hydro-mechanical behaviour of the soil comprising a railway embankment were presented, along with boundary conditions required in order to incorporate the effect of weather conditions in the transient stress state distribution throughout the embankment. Changes in the water content and in stress state produce changes in the stability of railway embankments, potentially causing embankment failures and derailments. This section presents the theory for quantifying near-ground surface stability as a function of the shear strength properties of the soil comprising a railway embankment and as a function of the stress state computed using the PDEs and soil-atmospheric boundary conditions proposed in the previous sections.

Chapter 2 presented a literature review of available methods for quantifying embankment stability. Two main approaches were identified; namely, the conventional limit equilibrium methods of slices, and the *Dynamic Programming Method* (DPM). Conventional limit equilibrium methods are usually combined with an assumption regarding the shape of the critical slip surface. Nevertheless, numerous well established analytical procedures using conventional limit equilibrium methods are available. The DPM represents an important theoretical breakthrough in that the slip surface shape restrictions are significantly relaxed, therefore allowing for a superior prediction of the failure mechanism. The combined use of finite element

stress fields further enhances the analysis by providing means of incorporating into the slope stability analysis more realistic boundary conditions, soil stress-strain properties, and stress history. Little human interference in the analysis process is required; once the problem geometry, boundary conditions, material properties, and search grid are established, the solution algorithm does not require any further external interference (Gitirana Jr. and Fredlund, 2003a). Unfortunately, only a reduced number of analytical procedures using the DPM exist, with their applicability limited by the relatively narrow testing published.

The input requirements of the DPM combined with FE stress fields are quite similar to those of conventional limit equilibrium methods. The stress-strain constitutive parameters and the boundary conditions are the only additional parameters that must be selected. The use of problem solving environments, such as FlexPDE, can make stress-strain analyses as simple as traditional limit equilibrium procedures. If a linear constitutive law is adopted in the stress analysis, the computational time can be shorter than that of conventional limit equilibrium codes (Pham et al., 2001, Gitirana Jr. and Fredlund, 2003a). The characteristics of the DPM combined with FE stress fields are particularly desirable for the W-GHA model because all analyses are reduced to the solution of a series of partial differential equations. This section lays out the theory on which the DPM of slope stability is based.

3.3.4.1 *Optimization procedure*

Figure 3.11 presents the analytical scheme for stability analysis using the Dynamic Programming Method, DPM, adapted from Yamagami and Ueta (1988b). The procedure is based on the assumption that the critical slip surface can be approximated by "*n*" linear segments. Each linear segment connects two *state points* located at two successive *stages*. The *search grid* consists of a collection of *state points* lying on "*n*+1" *stages*. A relatively coarse search grid is superimposed on the geometry shown in Figure 3.11. The dynamic programming procedure is used to determine a continuous assemblage of segments that corresponds to a minimum overall factor of safety. In order to quantify the overall stability, a *factor of safety*, F_s, along a slip surface is defined in its discrete form as:

$$F_s = \frac{\sum_{i=1}^{n} R_i}{\sum_{i=1}^{n} S_i} = \frac{\sum_{i=1}^{n} \tau_{f_i} \Delta L_i}{\sum_{i=1}^{n} \tau_i \Delta L_i} \tag{3.22}$$

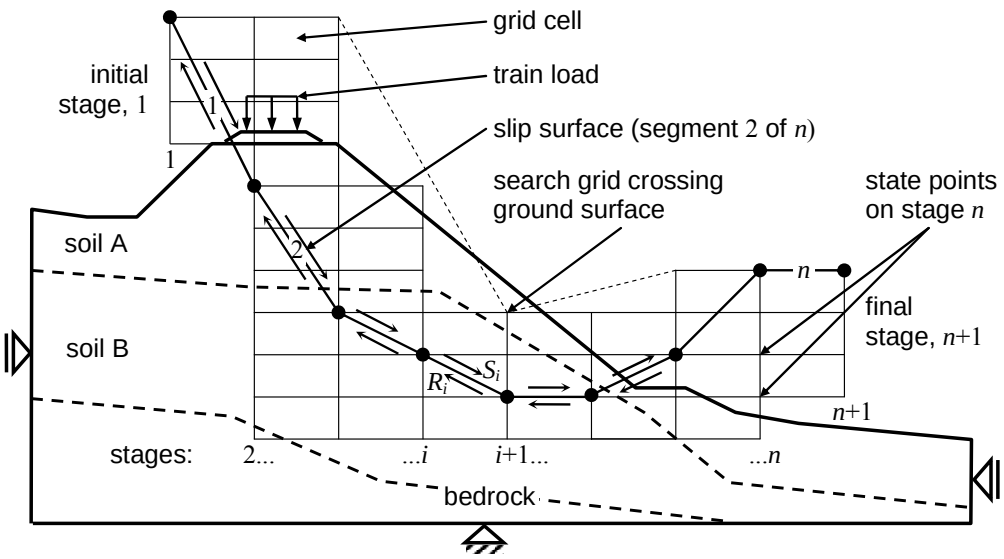

Figure 3.11 The analytical scheme for stability analysis using Dynamic Programming.

where:

n	=	total number of segments;
R_i	=	resisting force of the soil along the i^{th} segment, kN/m;
S_i	=	shear force acting along the i^{th} segment, kN/m;
τ_{fi}	=	shear strength of the soil along the i^{th} segment, kPa;
ΔL_i	=	length of the i^{th} segment, m;
τ_i	=	shear stress along the i^{th} segment, kPa.

The shear strength, τ_f, is function of the total stress and pore-water pressure. Equations for the prediction of the unsaturated shear strength will be presented in the following section. This definition of factor of safety (i.e., considering the limit equilibrium of forces on the entire slip surface and not at each segment or slice), is slightly different than that of the conventional limit equilibrium methods. Nevertheless, the unique characteristic of the DPM lies in the manner in which the shape and position of the critical slip surface is obtained, along with the corresponding minimum F_s. The dynamic programming method can only be applied to *additive functionals* (i.e., functions of the form $Y = \Sigma[a \cdot y_i + b]$). Therefore, in order to minimize the non-additive functional, F_s, the following additive functional is introduced (Baker, 1980):

$$G = \sum_{i=1}^{n} (\tau_{f_i} \Delta L_i - F_s \tau_i \Delta L) \tag{3.23}$$

In order to minimise G, the *optimal function*, H, is used. $H_{i+1}(j)$ is defined as the minimum value

of G between any *state point* [i, j] and the initial *stage*, j = 1. According to the *principle of optimality* (Bellman 1957), the optimal function at a posterior stage, $H_{i+1}(j)$, is a function of the optimal function at the prior stage, $H_i(k)$, as follows:

$$H_{i+1}(j) = \min\left[H_i(k) + DG_{i+1}(j,k)\right] \tag{3.24}$$

where:

i	=	1, n;
j	=	1, $NP(i+1)$;
k	=	1, $NP(i)$;
$NP(i)$	=	number of *state points* on *stage* i;
$DG_{i+1}(j,k)$	=	$\tau_{f_i}\Delta L_i - F_s\tau_i\Delta L$.

The optimization scheme described by Eq. 3.24 is presented in Fig 3.12. The term $DG_{i+1}(j, k)$ corresponds to the "cost" of passing between the state points [i+1, j] and [i, k], and is termed the *return function*. The principle of optimality establishes that the optimal function at each state point of a posterior stage corresponds to the minimum value amongst all the sums of the optimal functions at each state point of the prior stage and the "cost" of passing between the state points [i+1, j] and [i, k]. Bellman (1957) presents a rigorous examination of the principle of optimality.

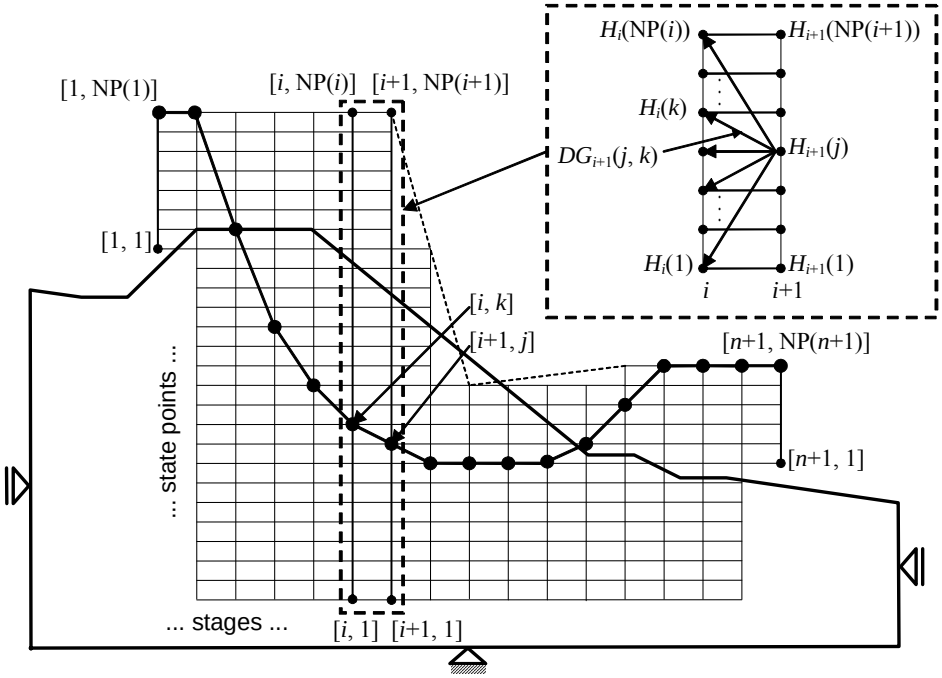

Figure 3.12 Optimum functions: detail showing two adjacent stages.

The principle of optimality implies in a sequential computation that starts on the first stage and walks towards the last stage. At the initial stage, the value of the optimal function, $H_1(k)$, must be set equal to zero. The search for the optimal function $H_{i+1}(j)$ must be repeated for each state point in each stage, up to the last stage, n+1. The ultimate minimum value of G corresponds to the minimum value of H at n+1, min[$H_{n+1}(j)$]. The optimal path that defines the critical slip surface is found by connecting the optimal state points, traced back from the final stage to the initial stage. The value of F_s is given an assumed value for the first slip surface computation and is replaced by the newly obtained F_s. This process must be repeated until F_s converges to a unique value while respecting an error tolerance.

The search grids presented in Figs. 3.11 and 3.12 observe certain rules (Gitirana Jr. and Fredlund, 2003a). The state points at the initial and final states (1 and n+1) must all be above the ground surface in order for the slip surfaces to form a complete wedge of soil. There must be state points at the intermediate stages both above and below the ground surface, giving freedom for the slip surface to find its most critical position without grid restrictions. Finally, the search grid must cross the ground surface somewhere along the intermediate stages in order to force slip surfaces to cross the ground surface. It's important to emphasize that the dynamic programming search procedure is not merely a random search. Random walk theories are subjected to limitations due to lack of flexibility in the procedure and poor theoretical basis. Conversely, the dynamic programming search procedure has a sound theoretical basis.

3.3.4.2 *Shear strength and stresses within the DPM search grid*

The shear strength, normal stress, pore-water pressure, and acting shear stress must be known at all *state points* in order to solve Eqs. 3.23 and 3.24. These variables can be calculated based on the finite element stress field, finite element pore-water pressure field, shear strength parameters, and orientation angle of the plane. The stress field is obtained by solving the PDEs governing static equilibrium. The pore-water pressure field is determined by solving the PDEs governing moisture movement along with appropriate soil-atmospheric boundary conditions. If a regular DP *search grid* formed by rectangular grid cells is used (such as those in Figs. 3.11 and 3.12), it is convenient to interpolate the values of the variables involved on a regular *data grid* coinciding with the *search grid*. The variables interpolated are the stress state, pore-water pressure, and shear strength parameters. The *data grid* must extend beyond the area of the soil domain, overlapping the entire area enclosed by both the *search grid* and the soil domain. A value of zero must be assigned to the values of the variables on grid points not overlapping the soil mass.

Figure 3.13 presents how the variables on any segment connecting two state points can be calculated from the data grid. The value of a variable along a segment was assumed as equal to the value interpolated at the centre of the segment. If a segment crosses more than one *grid cell*, the value of the variables must be interpolated at the centre of each "sub-segment" within each *grid cell*. The interpolation can be performed using *Lagrange* interpolation functions for linear quadrilateral elements. The subscripts "*c*" in Fig. 3.13 indicate that each variable lies on the sub-segment centre. Besides the shear strength parameters, the following variables must be interpolated at the centre of the trial sub-segments: σ_x, σ_y, τ_{xy}, and u_w. The normal stress, σ_n, and shear stress, τ, acting on each sub-segment inclined at an angle θ can be computed from the stress state at the centre of the sub-segment, defined by σ_x, σ_y, and τ_{xy}:

$$\sigma_n = \sigma_x \sin^2\theta + \sigma_y \cos^2\theta - \tau_{xy} \sin 2\theta \tag{3.25}$$

$$\tau = [(\sigma_x - \sigma_y)/2] \sin 2\theta - \tau_{xy} \cos 2\theta \tag{3.26}$$

The shear strength, τ_f, is computed using the saturated/unsaturated shear strength parameters and the values of σ_n and u_w at the centre of each sub-segment. The shear strength increase with respect to soil suction can be based on a prediction technique dependent upon the SWCC, as will be presented in the following sections. The resisting forces at the centre of each sub-segment, R_c and S_c, are determined by multiplying τ and τ_f by the corresponding sub-segment length. The values at each entire segment, R_i, and S_i, are equal to the sum of R_c and S_c at each sub-segment forming the slip surface segment.

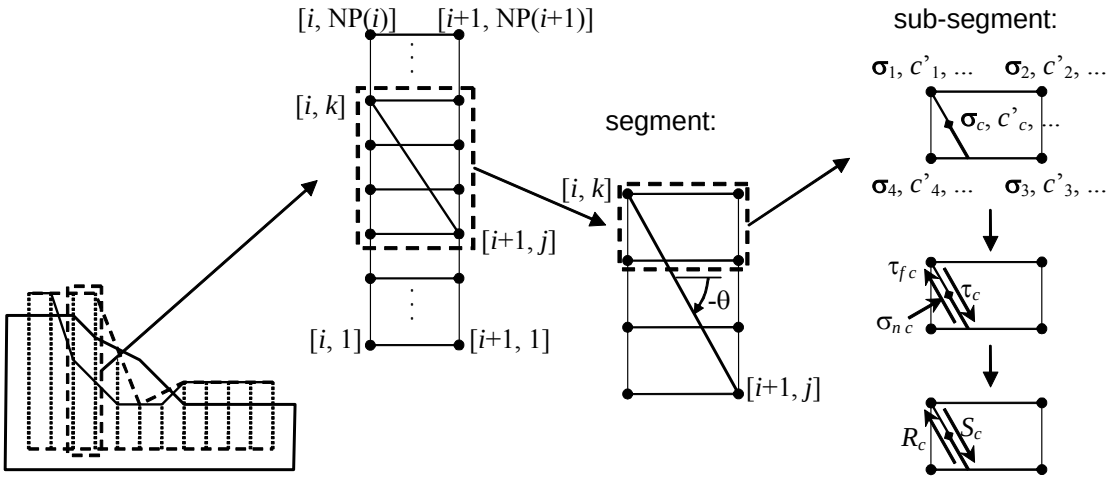

Figure 3.13 Optimum Variables on a segment connecting two state points.

A Dynamic Programming algorithm called Safe-DP (Stability Analysis using Finite Element stress fields and Dynamic Programming) has been developed herein, following the theory presented in this chapter. Details about the algorithm implementation and verification will the presented in Chapter 4. The stresses and pore-water pressures utilised in the stability analyses by Safe-DP are calculated by solving the partial differential equations (PDEs) governing equilibrium, moisture, and heat flow. In order to solve the system of PDEs a general purposed solver called FlexPDE (PDE Solutions Inc., 2003) is used. Details about the development, implementation and verification of scripts for the numerical models using FlexPDE are also presented in Chapter 4.

3.3.5 *Summary of the system of PDEs governing the thermo-hydro-mechanical behaviour of saturated/unsaturated soils*

The system formed by the PDEs 3.9, 3.13, 3.15, and 3.16 represents a thermal-hydro-mechanical model appropriate for the application at hand. This system of PDEs forms, along with appropriate boundary conditions and the Dynamic Programming embankment stability solution, the deterministic core of the weather-related geo-hazard assessment model (W-GHA model). Figure 3.14 presents the deterministic core of the W-GHA model, identifying the role of each of the PDEs and the equation representing the weather-related boundary condition. The PDEs governing flow of moisture and heat and the soil-atmospheric boundary conditions correspond to a transient process that must be solved for a period of time of interest. Values of the pore-water pressure and degree of saturation throughout the embankment must be sampled at various pre-determined times, and used in the computation of the *factor of safety* of the railway embankment.

In order to solve the PDEs governing soil behaviour, the W-GHA model uses a multi-purpose partial differential equation solver, FlexPDE (PDE Solutions, 2003). FlexPDE uses the Finite Element (FE) and the Finite Difference (FD) methods combined with Newton-type methods of solution of non-linear coupled systems. The friendly input and output features combined with automatic mesh generation, time-step control, and choice of non-linear approaches makes FlexPDE a complete *problem solving environment* (PSE). Aspects related to PSE development are discussed by Gallopoulos et al. (1994) and Carter et al. (2000).

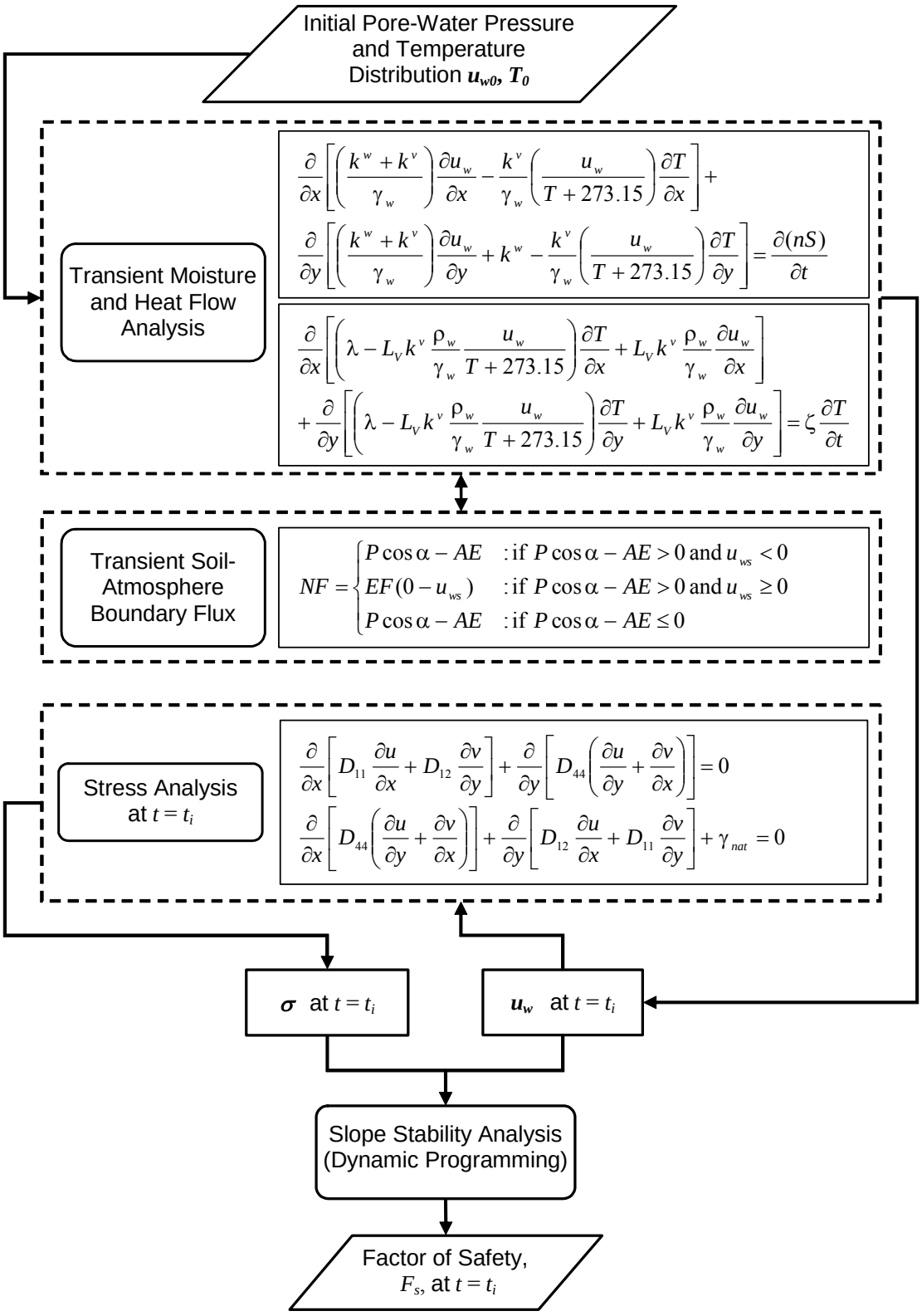

Figure 3.14 Flowchart for the deterministic core of the W-GHA model.

3.4 ASSESSMENT OF UNSATURATED SOIL PROPERTY FUNCTIONS

The term "*unsaturated soil property functions*" is used herein to refer to mathematical representations of nonlinear soil properties that embrace both saturated and unsaturated conditions. Unsaturated soil properties change continuously according to the soil suction and are generally considered constant for saturated conditions (i.e., for pore-water pressures higher than the air-entry value). The use of continuous soil property functions is of paramount importance for the stability and efficiency of numerical solutions of the PDEs governing the behaviour of saturated/unsaturated soils (Fredlund et al., 2000 and Gitirana Jr. et al., 2001).

A large number of soil property functions and related soil parameters are required in order to solve the system of PDEs presented in Fig. 3.14. The properties associated with unsaturated soil behaviour are particularly difficult to determine. Figure 3.15 presents some approaches that can be taken for the determination of unsaturated soil properties. Direct (laboratory and field) and indirect (prediction) methods can be used. The different laboratory and field approaches have diverse advantages and limitations, but all have as a common characteristic the complexity, high cost, and to be time consuming. The W-GHA model would not be feasible using demanding field and laboratory procedures for the assessment of unsaturated soil properties.

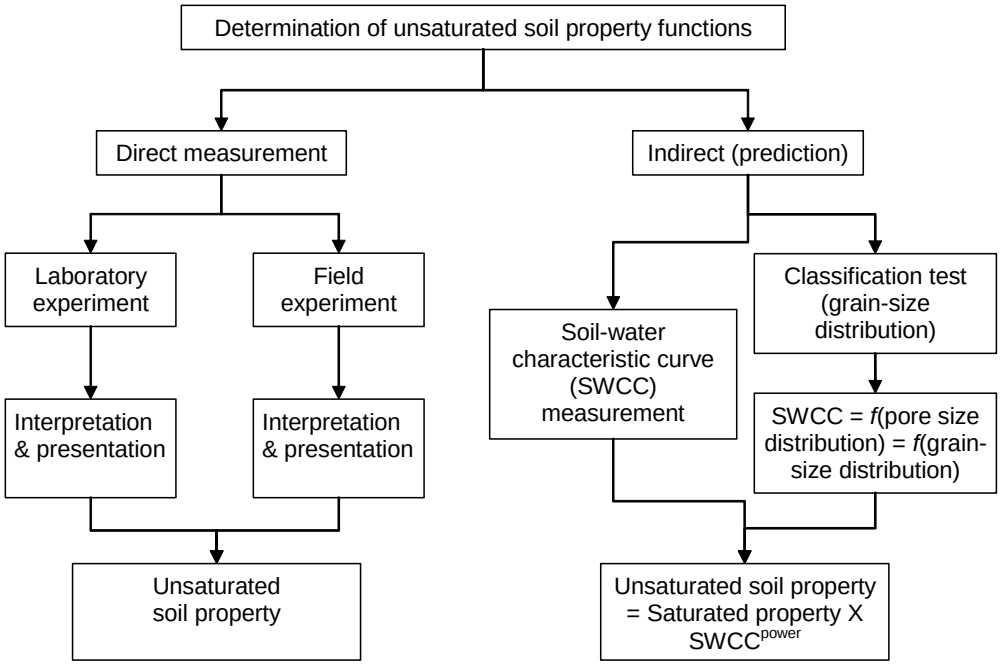

Figure 3.15 Approaches to determine unsaturated soil property functions.

The second branch of the diagram from Fig. 3.15 presents two indirect prediction approaches. The prediction methods rely on simpler and easier to obtain soil data, including the relationship between the amount of water in the soil pores and the soil suction; namely, the soil-water characteristic curve, SWCC. The SWCC has a central role in the prediction of unsaturated soil properties and therefore in the implementation of unsaturated soils theories into geotechnical engineering practice (Barbour, 1998, Fredlund, 2002). Unsaturated soil property functions such as the hydraulic conductivity (Brooks and Corey 1964, Mualen 1976, Fredlund et al. 1994) and the shear strength (Fredlund et al. 1996, Vanapalli et al. 1996) can be predicted based on the soil-water characteristic curve and based on the saturated soil properties.

Table 3.1 presents a summary of the soil property functions and related soil parameters required by the W-GHA model. Several of these properties are found in the PDEs governing the hydro-thermo-mechanical behaviour of the soil comprising a railway embankment (Eqs. 3.9, 3.13, 3.15, and 3.16). The shear strength properties required by the *Dynamic Programming* optimization scheme are also listed. Columns 3 and 4 of Table 3.1 present the saturated and unsaturated soil parameters that are required in order to obtain the soil property functions presented in Column 2. Most unsaturated property functions can be predicted by some combination of the saturated soil parameters and the SWCC parameters, ψ_b, λ_d, λ_{res}.

Table 3.1 Soil property functions and related soil parameters required by the W-GHA model.

Type of analysis (1)	Soil property function (2)	Related soil parameters (3)	Related unsaturated soil parameters (4)	(*) (5)
Moisture flow analysis	$\theta = nS$	n, m_v	ψ_b, λ_d, λ_{res}	2
	k^w	k^w_{sat}	ψ_b, λ_d, λ_{res}, η	2
	D^{v*}	n, D^v	ψ_b, λ_d, λ_{res}	1
Heat flow analysis	L_V	L_V	---	1
	λ	λ_s, λ_w, λ_{a1}, λ_{a2}	ψ_b, λ_d, λ_{res}	4
	ζ	n, ζ_s, ζ_w	ψ_b, λ_d, λ_{res}	2
Stress and stability analysis	D_{ij}	E, μ	---	2
	b_y	n, G_s	ψ_b, λ_d, λ_{res}	1
	τ_f	c', ϕ'	ψ_b, λ_d, λ_{res}, κ	3

(*) – Number of exclusive parameters, excluding the soil-water characteristic curve parameters.

3.4.1 *Soil-water characteristic curve and hysteresis modelling*

The second main branch in Fig. 3.15 indicates two approaches for determining the SWCC; namely, direct measurement methods and prediction methods based on the grain-size distribution. A review of methods of prediction of the SWCC based on the grain size distribution can be found in Fredlund (1999). Regardless of the laboratory or predictive approach taken, two issues must be addressed regarding the use of the SWCC in the W-GHA model. First, appropriate fitting equations must be selected, in order to represent the soil-water characteristic curve. Secondly, appropriate approaches must be taken in order to include the SWCC hysteresis into the W-GHA model since the W-GHA model is directed towards the prediction of hazards considering conditions that may include cycles of dry and wet weather.

Numerous equations have been proposed to represent the soil-water characteristic curve. Unfortunately, most available continuous equations are not based on mathematically independent parameters. As a result, difficulties arise in the statistical assessment of SWCC's due to the non-uniqueness of the sets of fitting parameters (Gitirana and Fredlund, 2004). In order to overcome such difficulties, Gitirana Jr. and Fredlund (2004) developed a set of SWCC equations based on the parameters ψ_b, ψ_{res}, and S_{res} (or ψ_b, λ_d, λ_{res}, as indicated in Table 3.1). The proposed equations are presented in detail in Appendix B. The parameter ψ_b is the air-entry value, ψ_{res} is the residual suction, and S_{res} is the residual degree of saturation. The parameters λ_d and λ_{res} are the primary and residual drainage slopes. The parameter that controls the sharpness of the transitions at the bending points was defined as a. A fixed value can be assumed for a. SWCC's with one bending point can be described by two parameters, ψ_b and a. The parameters ψ_b, ψ_{res}, S_{res}, and a are mathematically independent and have physical significance.

Pham (2002) presents a detailed review of SWCC hysteresis models. The modelling of SWCC hysteresis involves the definition of the main drying, main wetting, and scanning curves. The implementation of hysteresis models in moisture flow analysis models results in intensive computational work and can be considered unfeasible at the present time (Pham, 2002). Nevertheless, simplifications can be made in order to take into account hysteresis while keeping the moisture flow model computationally efficient. Pham (2002) observed that the main drying and main wetting curves can be assumed approximately parallel. It was also observed that the distance between the main drying and wetting curves, δ_{dw}, varies between 0.15 and 0.35 log cycle for sands, and varies between 0.35 and 0.60 log cycle for loams. These distances were found to be roughly constant for individual textural types of soil (Pham, 2002). Therefore,

typical values of δ_{dw} can be established based on previously observed data.

A simplified approach is proposed herein in order to include the SWCC hysteresis into the W-GHA model while minimising the computational work demanded. The proposed approach is presented in Figs. 3.16 and 3.17. According to the simplified approach adopted, the SWCC hysteresis can be incorporated into the W-GHA model by using the *average* curve (in logarithm of suction scale) between the main drying and main wetting SWCC's. The *average* SWCC can be determined based on the drying SWCC and based on the knowledge of the distance between the main drying and wetting curves. The position of the *average* SWCC is dictated by the air-entry value, and can be calculated according to the following equation:

$$\psi_{b\,ave} = 10^{\left[\log_{10}(\psi_{b\,drying}) - \frac{\delta_{dw}}{2}\right]} \tag{3.27}$$

where:

$\psi_{b\,ave}$ = air-entry value of the *average* SWCC;

$\psi_{b\,drying}$ = air-entry value of the drying SWCC;

δ_{dw} = logarithmic distance between the main drying and wetting SWCC's.

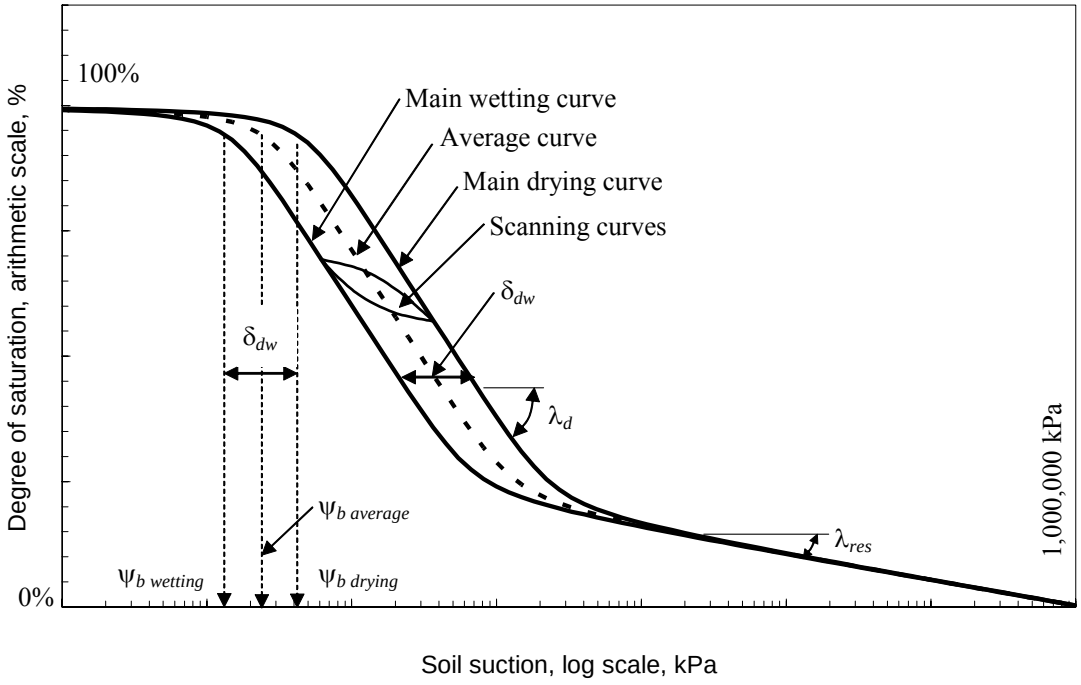

Figure 3.16 Hysteresis of soil-water characteristic curves with two bending points.

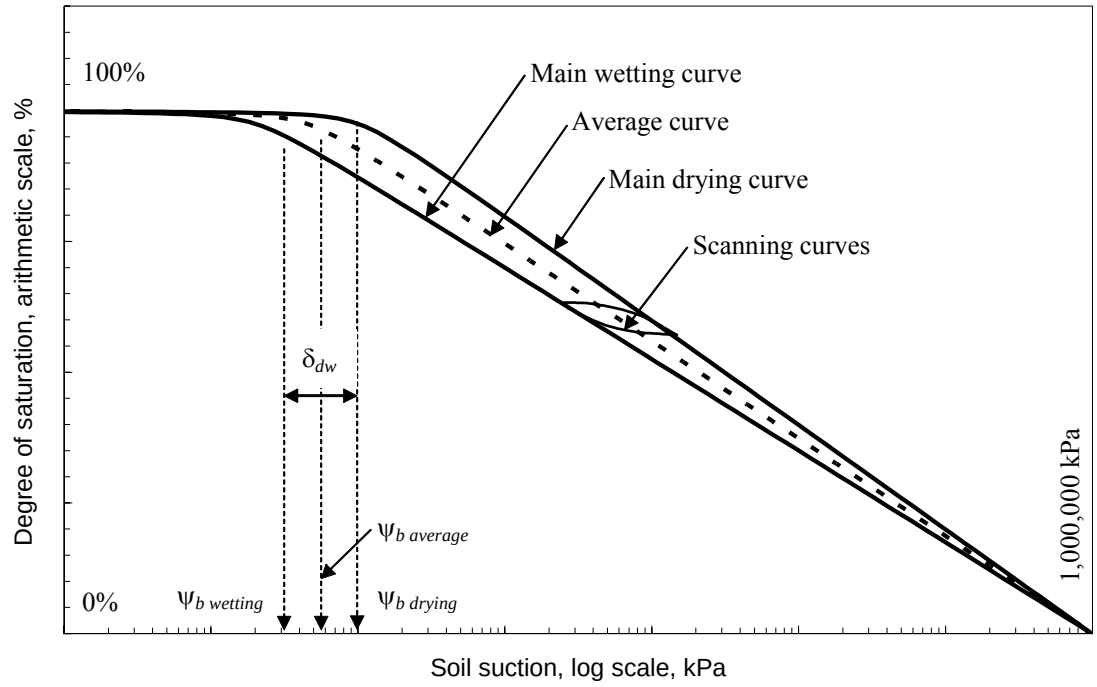

Figure 3.17 Hysteresis of soil-water characteristic curves with one bending point.

The values of the remaining SWCC parameters, λ_d and λ_{res}, are constant and correspond to the values obtained for the main drying curve. In other words, the main drying, main wetting, and average SWCC's have the same shape in terms of λ_d and λ_{res} and the difference lies exclusively on the position of the SWCC's, dictated by the air-entry value. The *average* SWCC's with <u>one</u> bending point (Fig. 3.17) were also defined based on the difference between the air-entry values, but the drainage slope varies. Again, the difference between the air-entry values of the main drying curve and main wetting curve can be estimated based on previously observed data.

3.4.2 *Properties associated with moisture flow*

The properties associated with the flow of moisture are the hydraulic conductivity, k^w, and the coefficient of vapour diffusion through soil, D^{v*}. These soil property functions can be calculated/predicted based on the SWCC. Figure 3.18 shows plots of a typical soil-water characteristic curve and the predicted properties associated with moisture flow. The equations available for the prediction of k^w are based on empirical observations or on statistical and mechanistic approaches. Features of the property functions, such as the location and steepness of the k^w and D^{v*} function are illustrated in Fig. 3.18. These features depend on the air-entry value and on the steepness of the soil-water characteristic curve, as will be shown next.

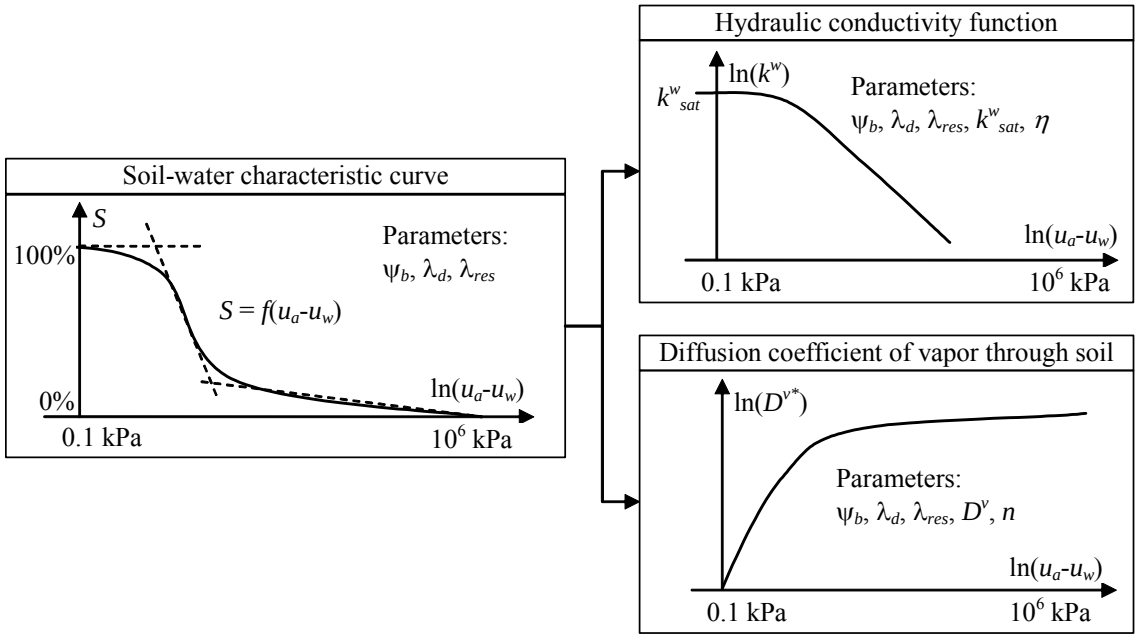

Figure 3.18 Prediction of moisture flow properties based on the soil-water characteristic curve.

3.4.2.1 *Hydraulic conductivity*

The methods of prediction of the hydraulic conductivity function can be classified as (i) *empirical models*; (ii) *mechanistic models*; and (iii) *statistical models*. Huang et al. (1998) presents a detailed review of the available methods. Empirical predictive equations are based on fitting equations and comparisons against experimental observations. Empirical equations have as their main advantage their simplicity. *Mechanistic models* are based on the application of the capillary theory to the soil pores. The soil-water characteristic curve is used by the *mechanistic models* in order to determine the size of the water-filled pores for any given soil suction. Brooks and Corey (1964) developed the following equation using the mechanistic approach:

$$k^w = k^w_{sat} \text{ for } (u_a - u_w) < \psi_b$$
$$k^w = k^w_{sat}\left[\psi_b/(u_a - u_w)\right]^{\eta} \text{ for } (u_a - u_w) \geq \psi_b \qquad (3.28)$$

where:

k^w_{sat} = saturated hydraulic conductivity;

η = $2 + 3\lambda$;

λ = $\Delta[\log(S_e)]/\Delta[\log(u_a - u_w)]$;

S_e = $[(S - S_{res})/(1 - S_{res})]$.

The equation proposed by Brooks and Corey (1964) is based on the assumptions that the portion of the SWCC past the air entry value follows a straight line when plotted in terms of the logarithm of S_e and $(u_a - u_w)$. The parameter η is completely defined by the SWCC. Another similar mechanistic model was proposed by Mualem (1976). The mechanistic equations have a strong theoretical basis and have been thoroughly verified against experimental data, with good results (Huang et al., 1998). Another advantage of the use of mechanistic equations is the simplicity of most equations. Most hydraulic conductivity functions obtained using *mechanistic models* are represented by closed-form equations readily available for numerical modelling.

The third type of prediction models for the hydraulic conductivity involves the so-called *statistical models*. *Statistical models* are based on the assumption that the pore-sizes are randomly distributed. The SWCC is used to determine the size of the pores for any soil suction. Childs and Collis-George (1950) proposed one of the most used *statistical models*. Later, Fredlund et at. (1994) proposed an equation that uses a similar approach, but using the Fredlund and Xing (1994) SWCC equation. Statistical equations provide some theoretical improvement over the mechanistic equations. Unfortunately, closed-form equations are not available.

Some limitations associated mainly with clayey soils are observed for all predictive approaches of the hydraulic conductivity function. Nevertheless, the predictive approaches represent an attractive alternative, given the difficulties associated with the direct measurement of the hydraulic conductivity function. The equation proposed by Brooks and Corey (1964) was adopted herein, due to its simplicity, wide acceptance, and relatively sound theoretical basis.

3.4.2.2 *Diffusion coefficient of vapour through soil*

Equation 3.3 shows how the coefficient of vapour diffusion through soils, D^{v*}, can be predicted/calculated. The definition of D^{v*} is based on the fundamental definition of Fick's law (Eq. 3.3). Yet, an important factor has not been taken into account in Eq. 3.3; namely, the tortuosity factor for the diffusion of vapour through the soil pores (Lai et al., 1976). Tortuosity can be taken into account by adding a "tortuosity factor" to the equation for D^{v*}, as follows:

$$D^{v*} = \alpha\beta D^{v} W_{v} / RT \tag{3.29}$$

where:

D^{v*} = coefficient of vapour diffusion through soil, (kg.m)/(kN.s);

α = tortuosity factor of the soil, $\alpha = \beta^{2/3}$ (Lai et al., 1976);

β = cross sectional area of soil available for vapour flow per total area;

β = $(1\text{-}S)n$;

D^v = molecular diffusivity of water vapour in air;

D^v = $0.229\times10^{-4}[1 + (T + 273.15)/273.15)^{1.75}$, m^2/s (Kimball et al., 1976);

W_v = molecular weight of water, 18.016 kg/kmol;

R = universal gas constant, 8.314 J/(mol.K);

T = temperature, ^oC.

Equation 3.29 shows that D^{v*} is a function of S and n, which are obtained from the SWCC as a function of soil suction. As Fig. 3.18 suggests, D^{v*} (and consequently k^v) is equal to zero when the soil is saturated and begins to increase as the air starts occupying part of the soil pores. On the other hand, the hydraulic conductivity, k^w, is at its highest value when the soil is saturated and starts declining as the air starts entering the soil pores. As the soil dries, $[k^v/\gamma_w][\partial u_w/\partial x - (u_w/T)(\partial T/\partial x)]$ and $[k^v/\gamma_w][\partial u_w/\partial y - (u_w/T)(\partial T/\partial y)]$ tend to become larger than $(k^w/\gamma_w)(\partial u_w/\partial x)$ and $(k^w/\gamma_w)(\partial u_w/\partial y) + k^w$, respectively, (see Eq. 3.9). At this point, vapour flow begins to dominate over liquid water flow.

3.4.3 *Properties associated with heat flow*

The volumetric heat capacity, ζ, and the thermal conductivity, λ, of a soil can be calculated using theoretical equations proposed by de Vries (1963). The equations proposed by de Vries (1963) are based on the fact that the thermal properties of the soil are a function of the thermal property of each of the soil phases and their relative proportions, given by the degree of saturation. The measurement of the amount of water within the soil pores is obtained using the soil-water characteristic curve. Figure 3.19 illustrates the relationship between the SWCC and the soil thermal properties. The thermal conductivity and volumetric heat capacity of the soil decrease as the soil desaturates, because values of ζ and λ of the water phase are higher than those of the air phase. The equation for the heat capacity of the soil proposed by de Vries (1963) neglects the heat capacity of the air phase. The equation can be written as follows:

$$\zeta = \zeta_s \frac{V_s}{V} + \zeta_w \frac{V_w}{V} = \zeta_s (1-n) + \zeta_w nS \tag{3.30}$$

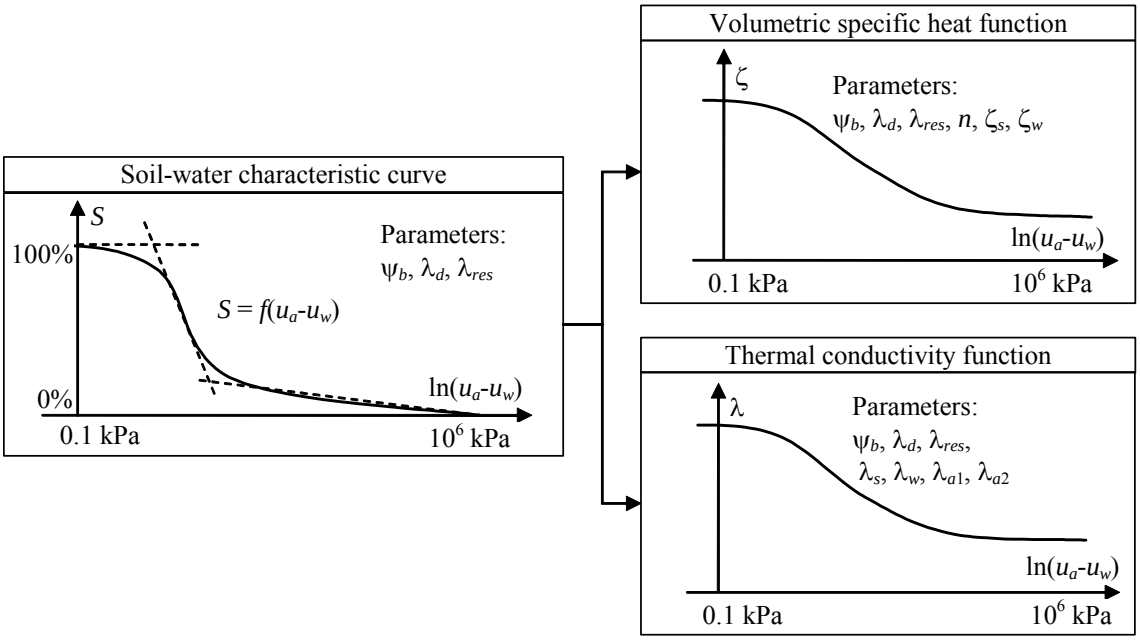

Figure 3.19 Prediction of soil thermal properties based on the soil-water characteristic curve.

where:

ζ_s = volumetric specific heat of solids, 2.235×10^6, J/(m^3 ^{o}C);

ζ_w = volumetric specific heat of water, 4.154×10^6 at 25^{o}C, J/(m^3 ^{o}C).

The thermal conductivity of the soil depends on the proportion of the soil phases and also on the arrangement and shape of the soil particles. The equation for the soil thermal conductivity proposed by de Vries (1963) is as follows:

$$\lambda = \frac{F_s\lambda_s\frac{V_s}{V} + F_w\lambda_w\frac{V_w}{V} + F_a\lambda_a\frac{V_a}{V}}{F_s\frac{V_s}{V} + F_w\frac{V_w}{V} + F_a\frac{V_a}{V}} = \frac{F_s\lambda_s(1-n) + F_w\lambda_w nS + F_a\lambda_a n(1-S)}{F_s(1-n) + F_w nS + F_a n(1-S)} \tag{3.31}$$

where:

λ_s = thermal conductivity of solids; typical value: λ_s = 6.0, W/(m ^{o}C);

λ_w = thermal conductivity of water; typical value: λ_w = 0.57, W/(m ^{o}C);

λ_a = $\lambda_{da} + \lambda_{va}$;

λ_{da} = thermal conductivity of dry air; typical value: λ_{da} = 0.025, W/(m ^{o}C);

λ_{va} = thermal conductivity of water vapour, $\lambda_{va} = (0.0736)S$, W/(m ^{o}C);

$$F_{s,a} = \frac{1}{3}\sum_{i=1}^{3}\left[1+\left(\frac{\lambda_{s,a}}{\lambda_w}-1\right)g_i^{s,a}\right]^{-1};$$

F_w = 1.0 (water assumed as the continuum medium) ;

g_i^a = 1/3;

$g_1^s = 0.015 + (0.333 - 0.015)S$ (Jame and Norum, 1980) ;

$g_2^s = g_1$;

$g_3^s = 1 - g_1 - g_2$.

The theoretical equations proposed by de Vries (1963) for the prediction of the volumetric heat capacity and thermal conductivity of soils were compared with experimental results by Jame and Norum (1980). Close agreement was found for a variety of soil types. The prediction of thermal properties can be considered more "certain" than the prediction of other unsaturated soil properties, such as the hydraulic conductivity function. This relatively little variability is due to the fact that the thermal properties of each soil fraction can be considered as a fixed, well-established value.

3.4.4 *Properties associated with stress and stability analyses*

The properties associated with stress and stability analyses are the stress-strain parameters, E and μ, the unit weight of the soil, γ_{nat}, and the shear strength, τ_f. The Young Modulus, E, can be obtained from compression tests (triaxial or oedometric) or estimated based on simpler soil data, such as Atterberg limits and void ratio (Herrero, 1980 and Carrier, 1985). Scoular (1997) has shown that for problems involving homogeneous soils (no contacts between materials with different values of E) the stress field results are not significantly influenced by the values of E. Therefore, the use of approximate values for the Young modulus can be considered as appropriate for the W-GHA model.

The Poisson ratio, μ, can be obtained from more sophisticated compression test with measurement of horizontal stresses (oedometer test) or horizontal strains (triaxial test). The Poisson ratio can also be estimated based on the friction angle for normally consolidated soils or based on the friction angle and on the overconsolidation ratio (OCR) for overconsolidated soils (Jaky, 1944 and Mayne and Kulhawy, 1982). Scoular (1997), Pham (2002) and Gitirana Jr. and Fredlund (2003a) have shown that the value of the Poisson ratio has a strong influence on the stress analysis results and its values must be carefully determined.

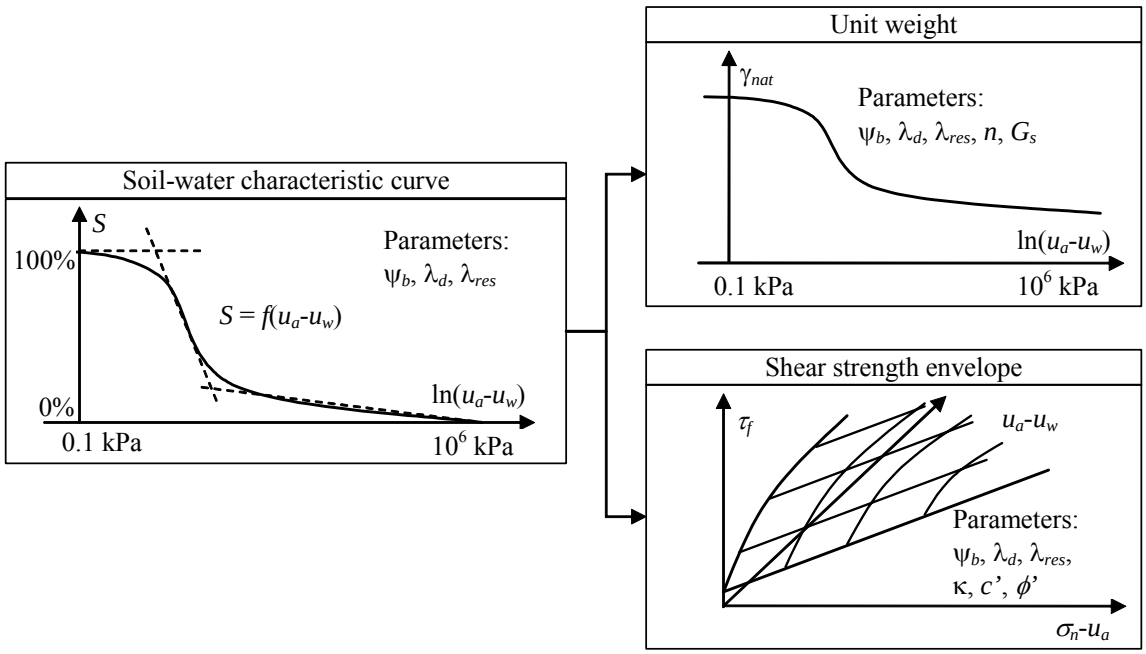

Figure 3.20 Prediction of unit weight and shear strength envelope based on the soil-water characteristic curve.

The shear strength and the unit weight of the soil are functions of the degree of saturation and matric suction of the soil, as illustrated on Fig. 3.20. The change in unit weight and shear strength with soil suction can be calculated/predicted based on the soil-water characteristic curve. The unit weight can be calculated using a volume-mass relationship (see Eqs. 3.15 and 3.16). The shear strength envelope for an unsaturated soil, τ_f, can be predicted using the soil-water characteristic curve and the saturated shear strength parameters, c' and ϕ'. Theoretical models supported by experimental evidence show that the slope of the plot of shear strength versus soil suction begins to deviate from the effective angle of internal friction as the soil desaturates. This reduced slope is associated with the increasingly reduction in the wetted area of contact past the air-entry value. Fredlund et al. (1996) proposed the following equation:

$$\tau_f = c' + (\sigma_n - u_a)\tan\phi' + (u_a - u_w)\Theta^{\kappa}\tan\phi' \qquad (3.32)$$

where:

c' = cohesion, kPa;

ϕ' = friction angle, radians;

Θ dimensionless parameter to account for the wetter area of contact, assumed to be equal to the degree of saturation, S;

κ = fitting parameter to account for any non-linearity between the volume and the amount of water contributing to the shear strength.

Vanapalli et al. (1996) presents a slightly modified procedure, defining $\Theta = \Theta_n = (S - S_{res})/(1 - S_{res})$ and not requiring κ. This second procedure, based on normalised (or effective) water content, renders the envelope potentially less flexible because the fitting parameter κ is not used. However, the use of Θ_n may be interpreted as a direct method for accounting for the same non-linearity that κ accounts for. Yet, the use of $\Theta = S$ seems appropriate for the W-GHA model, because a definition of τ_f along the entire soil suction range is provided in this way.

3.5 PROBABILISTIC MODEL AND SENSITIVITY ANALYSIS FRAMEWORK

Probabilistic and sensitivity analysis correspond to steps 4 and 5, respectively, on the *Decision Analysis* cycle (see Fig. 3.1). According to the decision analysis framework presented in this chapter, weather-related geo-hazards must be assessed probabilistically. The identification of the sensitivity of the *factor of safety* to the various input parameters is also of paramount importance. The advantages of a probabilistic hazard assessment over purely deterministic predictions were presented in Chapter 2. In addition, probabilistic measures of hazard are required for the subsequent assessment of risks associated with geo-hazards.

The probabilistic assessment of geo-hazards can be performed based on the first few moments of the probability distribution of the *factor of safety*, F_s. A summary of probabilistic measures of stability has been presented in Chapter 2. Among the numerous probabilistic measures presented previously, the *reliability index*, β, and the *probability of failure*, P_f, seem to be the most widely accepted and have been adopted herein.

The reliability index corresponds to the number of standard deviation of F_s, $\sigma[F_s]$, separating the computed mean value of F_s, $E[F_s]$, and the value of F_s that represents imminent failure (i.e., F_s equals 1). The reliability index can be determined according to the following equation:

$$\beta = \frac{E[F_s] - 1}{\sigma[F_s]} \tag{3.33}$$

where:

$E[F_s]$ = expected value of the factor of safety;

$\sigma[F_s]$ = standard deviation of the factor of safety.

The *probability of failure*, P_f, is a more complete measure, based on the first few statistical moments of F_s (or on the entire probability density function of F_s when available) and corresponds to the probability of the event "$F_s < 1$":

$$P_f = P(F_s < 1) \tag{3.34}$$

The reliability index requires the computation of the expected value and standard deviation of F_s. When using an approximate method, the probability of failure requires these two measures and an assumption regarding the shape of the probability density function of F_s. The lognormal distribution has been adopted herein as the p.d.f. of F_s, based on the recommendation of Becker (1996a), among others. Once a probability density function is assumed, the *probability of failure* can be obtained from tabulated integrals of the assumed p.d.f. or using built-in functions available in spreadsheets, such as Microsoft® Excel 2002 (Microsoft Corporation, 2001).

The next sections present the theoretical background of the *alternative point estimate method* used in order to compute the expected value and standard deviation of the factor of safety. The method presented is based on the combination of the Taylor series approach and the univariated point estimate method proposed by Rosenblueth (1975, 1981). The *alternative PEM* presented herein can accommodate multivariate functions of correlated non-symmetric random input variables, such as F_s. Later, a formal framework for sensitivity analysis will be presented.

3.5.1 *Theoretical development of the alternative point estimate method*

Exact closed-form solutions for the first few statistical moments of F_s are rarely available. Therefore, approximate solutions are often used. Chapter 2 presented a comprehensive review of probabilistic approaches available. All probabilistic models are based on the analyses of the deterministic *factor of safety* for a number of case scenarios. The first approach presented in Chapter 2 was the Monte Carlo method. Monte Carlo approaches were not recommended

because of the excessive deterministic computations required. A number of approximate approaches were also described, and the relative accuracy and computational requirements were discussed. The Taylor series methods were considered inappropriate, because they require partial derivatives that are not readily available. A number of point estimate approaches and the decision tree method were also presented. The point estimate methods available and the decision tree method require a smaller number of computations and provided relatively accurate results. However, the number of computations required by conventional point estimate methods and by the decision tree method increases sharply as the number of input random variables increases. The number of input variables in the W-GHA model makes these methods unadvised.

A probabilistic method for the factor of safety needs to be able to accommodate a multivariate function of numerous correlated non-symmetric random variables. The method presented herein has these capabilities and is based on the combination of the Taylor series approach and the univariated point estimate method proposed by Rosenblueth (1975, 1981).

In order to combine the Taylor series approximation and the two-point estimation method, the factor of safety, F_s, must first be expanded using a Taylor series about the mean values of the input random variables. The following equation uses terms up to the second order:

$$F_s(X) = F_s(E[X]) + \sum_{i=1}^{n} \left.\frac{\partial F_s}{\partial x_i}\right|_{E[X]} (x_i - E[x_i]) + \frac{1}{2}\sum_{i=1}^{n} \left.\frac{\partial^2 F_s}{\partial x_i^2}\right|_{E[X]} (x_i - E[x_i])^2 + \sum_{\substack{i \\ j>i}} \sum_{j} \left.\frac{\partial^2 F_s}{\partial x_i \partial x_j}\right|_{E[X]} (x_i - E[x_i])(x_j - E[x_j]) \tag{3.35}$$

where:

F_s	=	factor of safety;
X	=	set of n input random variables, $x_1, x_2, \ldots, x_n$;
$E[\ ]$	=	expected value;
$F_s(E[X])$	=	$F_s(E[x_1], E[x_2], ..., E[x_n])$.

The derivatives appearing in Eq. 3.35 must be obtained at the mean values, $E[X]$, as indicated. The expected value of F_s, $E[F_s(X)]$, can be obtained by taking the expected value of both sides of Eq. 3.35, as follows:

$$E[F_s(X)] = F_s(E[X]) + \frac{1}{2}\sum_{i=1}^{n} \left.\frac{\partial^2 F_s}{\partial x_i^2}\right|_{E[X]} Var[x_i] + \sum_{\substack{i \\ i<j}} \sum_{j} \left.\frac{\partial^2 F_s}{\partial x_i \partial x_j}\right|_{E[X]} Cov[x_i, x_j] \tag{3.36}$$

where:

$Var[x_i]$ = $E[(x_i - E[x_i])^2]$, is the variance of x_i;

$Cov[x_i, x_j]$ = $E[(x_i - E[x_i])(x_j - E[x_j])]$, is the covariance between x_i and x_j.

Equation 3.36 corresponds to the Taylor series method for calculating the mean value of a function of several random variables, as presented in Chapter 2. Moments of F_s of order m, $\mu_m[F_s]$, can be obtained based on the definition: $\mu_m[F_s] = E[(F_s - E[F_s])^m]$. For instance, the variance of F_s can be calculated using the equation $Var[F_s] = E[(F_s - E[F_s])^2]$. Any other higher order statistical moment of F_s can be obtained using Eq. 3.36 and replacing F_s by $(F_s - E[F_s])^m$.

The derivatives required by Eq. 3.36 are not readily available, leaving the equation of little use. The univariated two-point estimation method proposed by Rosenblueth (1975, 1981) can be employed in order to obtain the terms from Eq. 3.36. In order to do so, let us first define $F_s(x_i) = F_s(E[x_1],...,E[x_{i-1}], x_i, E[x_{i+1}],...,E[x_n])$. According to the method proposed by Rosenblueth (1981), the following univariated two-point estimate of $E[F_s(x_i)]$ can be written:

$$E[F_s(x_i)] = p_i^+ F_s(x_i^+) + p_i^- F_s(x_i^-) \tag{3.37}$$

where:

$F_s(x_i)$ = $F_s(E[x_1],...,E[x_{i-1}], x_i, E[x_{i+1}],...,E[x_n])$;

$F_s(x_i^\pm)$ = $F_s(E[x_1],...,E[x_{i-1}], x_i^\pm, E[x_{i+1}],...,E[x_n])$;

$x_i^\pm$ = $E[x_i] + \xi^\pm[x_i]\sigma[x_i]$;

$\xi^\pm[x_i]$ = $\gamma_1[x_i]/2 \pm \sqrt{1 + (\gamma_1[x_i]/2)^2}$;

$\gamma_1[x_i]$ = $\mu_3[x_i]/\{\sigma[x_i]\}^3$, is the skewness of x_i;

$\mu_3[x_i]$ = the third statistical moment of x_i;

$\sigma[x_i]$ = $\sqrt{Var[x_i]}$, is the standard deviation of x_i;

$p_i^\pm$ = $\frac{1}{2}\left[1 \mp \sqrt{1 - \frac{1}{1 + [\gamma_1[x_i]/2]^2}}\right]$.

The univariated two-point estimate presented in Eq. 3.37 is based on the moment-matching equations up to the third statistical moment. Note that $x_i^{\pm} = E[x_i] \pm \sigma[x_i]$ and $p_i^{\pm} = 1/2$ when x_i is assumed as symmetrically distributed (i.e., $\gamma_1[x_i] = 0$).

An alternative equation for $E[F_s(x_i)]$ can be obtained using a univariated Taylor series expansion of $F_s(x_i)$ about the mean values of the input variables. The following equation is obtained by keeping the terms up to the second order and applying the expectancy operator:

$$E[F_s(x_i)] = F_s(E[X]) + \frac{1}{2}\frac{\partial^2 F_s}{\partial x_i^2}\bigg|_{E[X]} Var[x_i] \tag{3.38}$$

The following equation can be obtained after equalising Eqs. 3.37 and 3.38, summing the equation obtained for all n input variables, and rearranging:

$$F_s(E[X]) + \frac{1}{2}\sum_{i=1}^{n}\frac{\partial^2 F_s}{\partial x_i^2}\bigg|_{E[X]} Var[x_i] = F_s(E[X]) + \sum_{i=1}^{n}\left[p_i^+ F_s(x_i^+) + p_i^- F_s(x_i^-) - F_s(E[X])\right] \tag{3.39}$$

All terms from Eq. 3.39 have been previously defined. Equation 3.39 provides the two first terms of the right-hand side of Eq. 3.36. The last term of the right-hand side of Eq. 3.36 can be determined if the second order derivative $\partial^2 F_s / \partial x_i \partial x_j$ is obtained. In order to do so, let us define $F_s(x_i^+, x_j^+) = F_s(E[x_1],...,E[x_{i-1}], x_i^+, E[x_{i+1}],...,E[x_{j-1}], x_j^+, E[x_{j+1}],...,E[x_n])$. One manner for obtaining $\partial^2 F_s / \partial x_i \partial x_j$ is to use the Taylor series expansion of $F_s(x_i^+, x_j^+)$ about the mean values of the input variables. Such Taylor series expansion can be written as follows:

$$\begin{aligned} F_s(x_i^+, x_j^+) = {} & F_s(E[X]) + \frac{\partial F_s}{\partial x_i}\bigg|_{E[X]}(x_i^+ - E[x_i]) + \frac{\partial F_s}{\partial x_j}\bigg|_{E[X]}(x_j^+ - E[x_j]) \\ & + \frac{1}{2}\frac{\partial^2 F_s}{\partial x_i^2}\bigg|_{E[X]}(x_i^+ - E[x_i])^2 + \frac{1}{2}\frac{\partial^2 F_s}{\partial x_j^2}\bigg|_{E[X]}(x_j^+ - E[x_j])^2 \\ & + \frac{\partial^2 F_s}{\partial x_i \partial x_j}\bigg|_{E[X]}(x_i^+ - E[x_i])(x_j^+ - E[x_j]) \end{aligned} \tag{3.40}$$

where:

$$F_s(x_i^+, x_j^+) \quad = \quad F_s(E[x_1],...,E[x_{i-1}], x_i^+, E[x_{i+1}],...,E[x_{j-1}], x_j^+, E[x_{j+1}],...,E[x_n]).$$

Noting that $\partial F_s/\partial x_i\big|_{E[X]}(x_i^+ - E[x_i]) + (1/2)(\partial^2 F_s/\partial x_i^2\big|_{E[X]})(x_i^+ - E[x_i])^2 = F_s(x_i^+) - F_s(E[X])$, Eq. 3.40 can be rearranged as follows:

$$\left.\frac{\partial^2 F_s}{\partial x_i \partial x_j}\right|_{E[X]} = \frac{F_s(x_i^+, x_j^+) - F_s(x_i^+) - F_s(x_j^+) + F_s(E[X])}{\xi^+[x_i]\sigma[x_i]\xi^+[x_j]\sigma[x_j]} \tag{3.41}$$

Equation 3.41 provides the last term required in order to define all terms from Eq. 3.36. The following equation is obtained after combining Eqs. 3.36, 3.39, and 3.41:

$$\begin{aligned} E[F_s(X)] = F_s(E[X]) &+ \sum_{i=1}^{n}\left[p_i^+ F_s(x_i^+) + p_i^- F_s(x_i^-) - F_s(E[X])\right] \\ &+ \sum_{\substack{i \\ i<j}} \sum_{j} \left[F_s(x_i^+, x_j^+) - F_s(x_i^+) - F_s(x_j^+) + F_s(E[X])\right] \frac{\rho[x_i, x_j]}{\xi^+[x_i]\xi^+[x_j]} \end{aligned} \tag{3.42}$$

where:

$F_s(E[X]) \quad = \quad F_s(E[x_1], E[x_2],..., E[x_n])$;

$F_s(x_i^{\pm}) \quad = \quad F_s(E[x_1], E[x_2],...E[x_{i-1}], x_i^{\pm}, E[x_{i+1}],..., E[x_n])$;

$x_i^{\pm} \quad = \quad E[x_i] + \xi^{\pm}[x_i]\sigma[x_i]$;

$\xi^{\pm}[x_i] \quad = \quad \gamma_1[x_i]/2 \pm \sqrt{1 + (\gamma_1[x_i]/2)^2}$;

$p_i^{\pm} \quad = \quad \frac{1}{2}\left[1 \mp \sqrt{1 - \frac{1}{1 + [\gamma_1[x_i]/2]^2}}\right]$;

$F_s(x_i^+, x_j^+) \quad = \quad F_s(E[x_1],..., E[x_{i-1}], x_i^+, E[x_{i+1}],..., E[x_{j-1}], x_j^+, E[x_{j+1}],..., E[x_n])$;

$\rho[x_i, x_j] \quad = \quad$ the correlation coefficient between x_i and x_j;

$\rho[x_i, x_j] \quad = \quad \frac{Cov[x_i, x_j]}{\sigma[x_i]\sigma[x_j]}$.

Equation 3.42 is the final equation for the computation of the expected value of F_s. Any moment of F_s of order m can be obtained based on the definition, $\mu_m[F_s]=E[\{F_s - E[F_s]\}^m]$, as mentioned previously. In other words, the higher order statistical moments of F_s can be obtained using Eq.

3.42 and replacing F_s by $\{F_s(X) - E[F_s]\}^m$:

$$\begin{aligned}\mu_m[F_s(X)] &= E[\{F_s(X) - E[F_s(X)]\}^m] \\ &= \{F_s(E[X]) - E[F_s(X)]\}^m \\ &+ \sum_{i=1}^{n}\begin{bmatrix} p_i^+\{F_s(x_i^+) - E[F_s(X)]\}^m + p_i^-\{F_s(x_i^-) - E[F_s(X)]\}^m \\ -\{F_s(E[X]) - E[F_s(X)]\}^m \end{bmatrix} \\ &+ \sum_{\substack{i \\ i<j}} \sum_{j}\begin{bmatrix} \{F_s(x_i^+, x_j^+) - E[F_s(X)]\}^m - \{F_s(x_i^+) - E[F_s(X)]\}^m \\ -\{F_s(x_j^+) - E[F_s(X)]\}^m + \{F_s(E[X]) - E[F_s(X)]\}^m \end{bmatrix} \frac{\rho[x_i, x_j]}{\xi^+[x_i]\xi^+[x_j]}\end{aligned} \tag{3.43}$$

where:

$\mu_m[F_s(X)]$ = statistical moment of F_s of order m;

$E[F_s(X)]$ = is computed using Eq. 3.42.

Equations 3.42 and 3.43 can be used in the computation of the first few statistical moments of F_s. The moments of F_s can be used in the computation of the *reliability index* and the *probability of failure*. The input requirements of Eqs. 3.42 and 3.43 are the mean, standard deviation (or coefficient of variation), skewness, and correlation matrix of the input random variables. The required number of evaluations of F_s is $(n^2 + 3n + 2)/2$, n being the number of input variables. It will be shown latter that the efficiency of the equations presented herein is far superior to that of conventional *point estimate methods* and the *decision tree method*. In addition, the accuracy of the equations presented herein is the same as that of the Rosenblueth (1975, 1981) method, since the same moment-matching estimate points were adopted.

The next sections will present a concise presentation of the relative efficiency of the probabilistic analysis equation presented herein and a formal framework for the sensitivity analysis of F_s. The sensitivity analysis framework presented makes use of tools traditionally employed in Decision Analysis models. A concise description of two probability density functions required for the statistical representation of the input variables of the W-GHA model (i.e., the normal and lognormal distributions) can be found in Appendix A.

3.5.2 *Efficiency of the alternative point estimate method*

The combination of the univariated two-point estimation equation proposed by Rosenblueth (1975, 1981) and the univariated and multivariated Taylor series expansions of F_s produces a

theoretically sound equation with a significantly higher efficiency when compared with conventional point estimate methods. Figure 3.21 presents a comparison of the number of evaluations required by different probabilistic approaches. Equations 3.42 and 3.43 require $(n^2 + 3n + 2)/2$ evaluations of F_s if all variables are correlated and $2n + 1$ evaluations of F_s if all variables are independent. The PEM proposed by Rosenblueth (1975) requires 2^n evaluations of F_s for the 2-point approximation and 3^n evaluations of F_s for the 3-point approximation. The Decision Tree approach requires the same number of evaluations of F_s as the Rosenblueth (1975) equations. It becomes apparent that the Rosenblueth (1975) and Decision Tree approaches are unfeasible because of the demanding numerical computations required by the W-GHA model. The Taylor series approximation requires $n + 1$ evaluations of F_s if the approximate numerical procedure proposed by Sandroni and Sayão (1993) is followed.

Figure 3.21 shows that for $n \geq 5$ the equations presented herein require significantly less evaluations than the 2- and 3-point approximations using the equations proposed by Rosenblueth (1975) and the decision tree approach. For $n \leq 4$ the number of evaluations required by the equations presented herein for correlated variables and by the 2-point approximation proposed by Rosenblueth (1975) is not significantly different. Figure 3.21 shows also that the number of evaluations required by the 2-point approximation proposed by Rosenblueth (1975) is significantly lower than the number of evaluations required by the 3-point approximation. The same observation applies to the decision tree approach using two and three branches.

It can be observed from Fig. 3.21 that the Taylor series approximation based on the numerical procedure proposed by Sandroni and Sayão (1993) is the most efficient method. However, it is important to point out that the numerical procedure proposed by Sandroni and Sayão (1993) is not based on a sound theoretical basis and there is no well established criteria for the size for the increment used in the evaluation of the derivatives of $F_s(X)$.

Figure 3.21 shows also that the equations presented herein require a number of evaluations relatively close to the number of evaluations required by the Taylor series *FOSM* approximation when the variables are considered independent. For a case where only part of the input variables are correlated, the number of evaluation lays between the "all correlated" and the "all independent" curves. Nevertheless, the rate of increase of the number of evaluations is fairly constant and significantly lower than that of the other point estimate methods and that of the decision tree method.

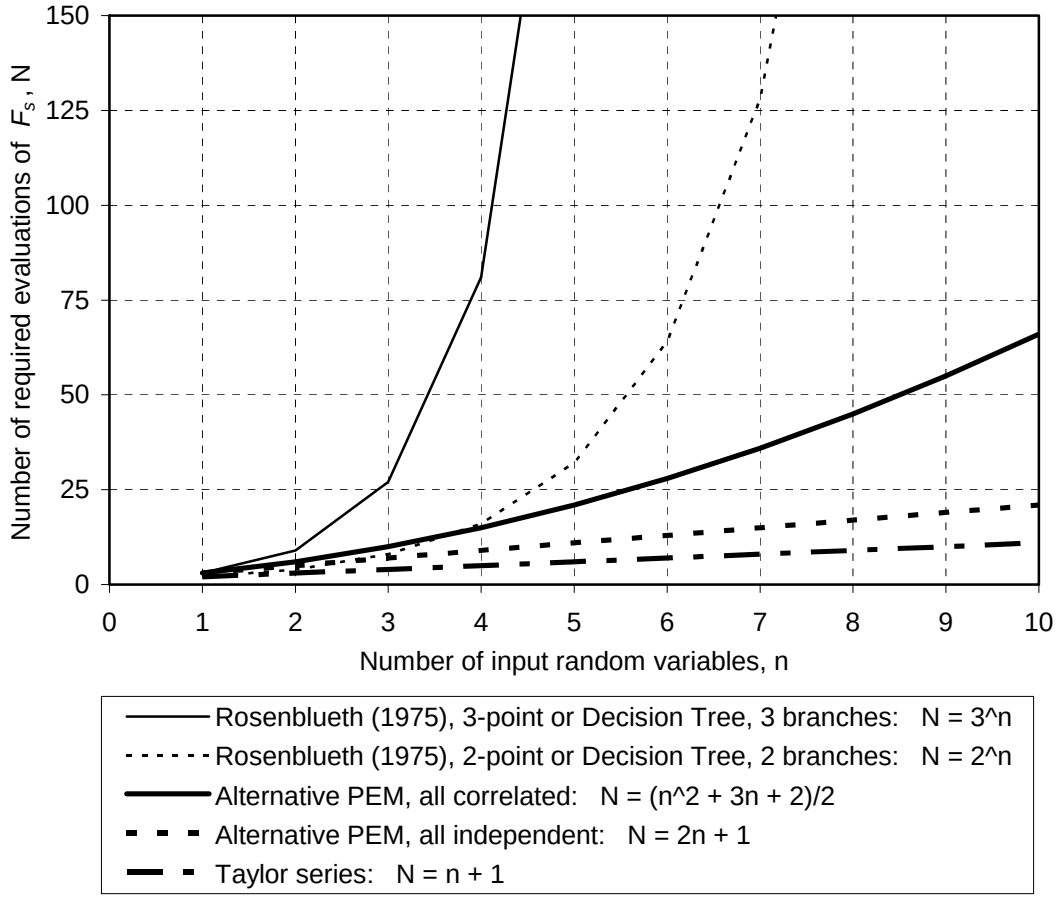

Figure 3.21 Number of evaluations of F_s required by several probabilistic methods.

3.5.3 *Sensitivity analysis framework*

This section presents a formal framework for sensitivity analysis, based on fundamental *Decision Analysis* concepts. The most fundamental objective of sensitivity analysis is to aid in the decision and to determine what input variables have significant influence in the decision at hand (Clemen, 1996). In the railway embankment stability problem context, the main objective of sensitivity analyses is to aid in the decision of *taking action* or *not taking action*. In addition, simplifications and/or refinements to the W-GHA model may be considered, depending on the importance of each input variable to the stability of a railway embankment.

One- and two-way sensitivity analysis, *tornado diagrams*, and *spiderplots* are some of the most straightforward approaches for studying the sensitivity of the input variables in a decision problem (Eschenbach, 1992, Clemen, 1996, Applied Decision Analysis LLC., 1998). *One and two-way sensitivity analyses* are performed for one and two input variables at a time,

respectively. The input variables are varied along a range of possible values, and the remaining input variables must be kept at the *base value*. *One-way sensitivity analyses* of several input variable can be compared using *spiderplots* or *tornado diagrams*. These diagrams indicate which variables require close consideration and which variables can be considered as certain values. The terms *spiderplot* and *tornado diagram* refer to the typical appearance of these plots.

Tornado diagrams were selected to be used in the probabilistic component of the W-GHA model to show and compare how much each input variable's uncertainty is transformed into uncertainty in the *factor of safety*. Two types of *tornado diagrams* can be used for the same purpose; namely, *base case tornado diagram* and *event tornado diagram* (Applied Decision Analysis LLC., 1998). *Base case tornado diagrams* are a simple way of studying the sensitivity of input variables since they are not based on strict construction rules. For instance, the range of variations adopted can be defined as "reasonable expected ranges". *Base case tornado diagrams* can be recommended when detailed statistical information is not available.

Deterministic and probabilistic event tornado diagrams are based on more rigorous construction rules and can benefit from detailed statistical information about the input random variables. In a *deterministic event tornado diagram*, all but one source of uncertainty in the model are removed at a time. Therefore, correlations are not considered. In a *probabilistic event tornado diagram*, one source of uncertainty in the model is removed at a time and all the remaining probabilistic information is kept, including any existing correlations. The procedure for constructing *probabilistic tornado diagrams* is presented next. The procedure for constructing *deterministic tornado diagrams* will be described in a concise manner.

Probabilistic Event Tornado Diagram for the W-GHA model

The variable targeted in sensitivity analysis using the W-GHA model is the *factor of safety*, F_s. As explained earlier in this chapter, according to the W-GHA model, the *factor of safety* can be assumed irrelevant in the case where action is taken. In other words, it can be assumed that the railway managers are able to take appropriate actions when they are deemed necessary. As a result, the stability problem becomes similar to a reliability-based analysis problem and only one policy is considered in the sensitivity analysis and *tornado diagrams*.

Figure 3.22 presents an illustrative, hypothetical *probabilistic event tornado diagram*. The values used for the construction of this illustrative tornado diagram are also presented in Fig.

3.22. The *tornado diagram* shows how much each input variable's uncertainty contributes to the uncertainty in the *factor of safety*. *Probabilistic event tornado diagrams* receive this name because this is the type of tornado diagram that is capable of retaining the most uncertainty in a model (Applied Decision Analysis LLC., 1998). The following steps are followed in this thesis for the construction of *probabilistic event tornado diagrams*:

i) The uncertainty of one input variable is removed and the first and second moments of the *factor of safety* are calculated using equations based on the *alternative point estimate method* presented in the previous sections. In order to remove the uncertainty of one variable (the k^{th} variable), Eqs. 3.42 and 3.43 must be modified as follows:

$$E[F_s(X)]_k = F_s(E[X]) + \sum_{\substack{i=1 \\ i\neq k}}^{n}\left[p_i^+ F_s(x_i^+) + p_i^- F_s(x_i^-) - F_s(E[X])\right] + \sum_{\substack{i \\ i<j \text{ and } i\neq k}}\sum_{j}\left[F_s(x_i^+, x_j^+) - F_s(x_i^+) - F_s(x_j^+) + F_s(E[X])\right]\frac{\rho[x_i, x_j]}{\xi^+[x_i]\xi^+[x_j]} \tag{3.44}$$

$$\begin{aligned} Var[F_s(X)]_k &= \left\{F_s(E[X]) - E[F_s(X)]_k\right\}^2 \\ &+ \sum_{\substack{i=1 \\ i\neq k}}^{n}\left[\begin{array}{l} p_i^+\left\{F_s(x_i^+) - E[F_s(X)]_k\right\}^2 + p_i^-\left\{F_s(x_i^-) - E[F_s(X)]_k\right\}^2 \\ -\left\{F_s(E[X]) - E[F_s(X)]_k\right\}^2 \end{array}\right] \\ &+ \sum_{\substack{i \\ i<j \text{ and } i\neq k}}\sum_{j}\left[\begin{array}{l} \left\{F_s(x_i^+, x_j^+) - E[F_s(X)]_k\right\}^2 - \left\{F_s(x_i^+) - E[F_s(X)]_k\right\}^2 \\ -\left\{F_s(x_j^+) - E[F_s(X)]_k\right\}^2 + \left\{F_s(E[X]) - E[F_s(X)]_k\right\}^2 \end{array}\right]\frac{\rho[x_i, x_j]}{\xi^+[x_i]\xi^+[x_j]} \end{aligned} \tag{3.45}$$

where:

$E[F_s(X)]_k$ = the first statistical moment of F_s calculated when the uncertainty of the input variable k is removed;

$Var[F_s(X)]_k$ = the second statistical moment of F_s calculated when the uncertainty of the input variable k is removed.

ii) The first and second statistical moments obtained for the *factor of safety* (Eqs. 3.44 and 3.45) are used in order to compute the 10th, 50th, and 90th percentiles. A lognormal distribution is assumed for the *factor of safety* in order to compute the percentiles;

iii) The procedure depicted in steps "i" and "ii" is repeated for all random input variables;

iv) A bar is created on the tornado diagram for each run performed following steps "i" to "iii". Each bar corresponds to the input random variable whose uncertainty was removed

from the model. The ends of the bars correspond to the 10th and 90th percentiles of the F_s and a line located near or at the middle of the bar indicates the 50th percentile;

v) The procedure described in steps "i" to "iv" is repeated for the "full model" (i.e., without removing any input variable uncertainty) and a "full model" bar is created;

vi) Finally, the bars are sorted from widest to narrowest, resulting in the tornado-shaped appearance. Sorting the bars helps identifying the input variables with greatest impacts.

The size of each bar shown in Fig. 3.22 is directly proportional to how spread the factor of safety p.d.f. is. Therefore, the size of each bar can be related to the uncertainty that was carried from the input variables into the *factor of safety*. The closer the size of a bar is to that of the "full model" bar, the less sensitive is F_s to the corresponding input variable. For instance, Fig. 3.22 shows that Variables 4, 5, and 6 have impacts considerably higher than Variables 1 and 2. Variables 1 and 2 could be considered certain variables, and this simplification would not affect the analysis results considerably. Variable 3 appears to have an intermediate impact in F_s.

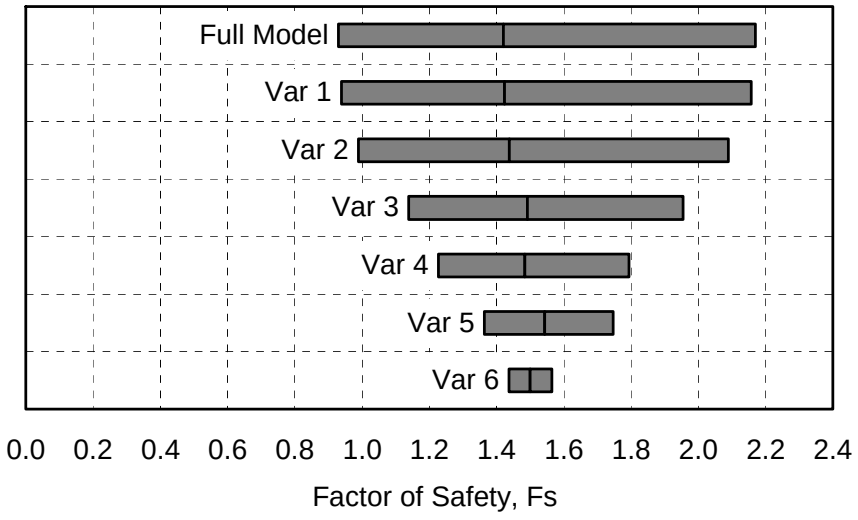

Summary of data

Variable	$E[F_s]_k$	$Var[F_s]_k$	10th percentile	50th percentile	90th percentile
Full Model	1.500	0.260	0.930	1.420	2.170
Var 1	1.500	0.250	0.939	1.423	2.157
Var 2	1.500	0.200	0.989	1.437	2.089
Var 3	1.525	0.106	1.138	1.492	1.954
Var 4	1.500	0.050	1.227	1.484	1.794
Var 5	1.550	0.023	1.363	1.543	1.746
Var 6	1.500	0.003	1.436	1.499	1.565

Figure 3.22 Probabilistic Event Tornado diagram for the W-GHA model.

It becomes apparent from examining Eqs. 3.44 and 3.45 that any existing correlations between input variables are fully considered. It is also important to point out that the computations of *factor of safety* required by the "full model" bar are sufficient in order to construct the other bars of a *probabilistic event tornado diagram*. Therefore, a *probabilistic event tornado diagram* can always be constructed whenever the full W-GHA model is used and no additional computations of *factor of safety* are required. The efficiency and capabilities of the probabilistic framework proposed herein represents a significant improvement over conventional decision tree methods usually employed by Decision Analysis software, such as DLP (Applied Decision Analysis LLC., 1998) and @Risk 4.5 (Palisade Corporation, 2004).

3.6 CHAPTER SUMMARY

A model for the assessment of weather-related geo-hazards (W-GHA model) using a *Decision Analysis* framework has been presented. The deterministic core of the W-GHA model consists of a two-dimensional embankment stability model combined with the analysis of the effects of weather conditions on the pore-water pressures. A series of partial differential equations governing the thermo-hydro-mechanical behaviour of saturated/unsaturated soils was presented, along with appropriate soil-atmosphere coupling equations. A slope stability optimization algorithm using *Dynamic Programming* (Safe-DP) has been developed and incorporated into the W-GHA model. Ultimately, the stability conditions can be deterministically quantified using Safe-DP, the stress distribution, and the pore-water pressure distribution that reflect the weather conditions. Unsaturated soil property assessment techniques based on the soil-water characteristic curve were presented, allowing the implementation of the W-GHA model.

The probabilistic core of the W-GHA model was based on a combination of the *point estimate* and *Taylor series methods*. The *alternative point estimate method* presented herein provides the first few statistical moments of the *factor of safety*, F_s, based on the analysis of a reduced number of "case scenarios" (i.e., estimate points). The equations presented herein can accommodate multivariate functions of skewed and correlated variables. The accuracy of the equations was theoretically shown to be similar or greater than other point estimated methods that require a considerably higher number of evaluations of F_s. Finally, a formal framework for sensitivity analysis was presented, using *deterministic and probabilistic event tornado diagrams* based on the *alternative point estimate method*.

Chapter 4

Implementation and Verification of Numerical and Analytical Models

4.1 GENERAL

This chapter presents the implementation and verification of the numerical and analytical core of the W-GHA model. The W-GHA model has three main components; namely, (i) the model for heat and moisture flow; (ii) the model for stability analysis; (iii) and the model for probabilistic and sensitivity analysis. Section 4.2 presents the implementation of numerical and analytical models for the solution of each of the three main components of the W-GHA model. Details about the solution approach taken and the computational tools employed for each model component are given. Section 4.3 presents the verification of the numerical and analytical models. Simple problems were designed in order to verify the results obtained using the models implemented herein. The results were compared against solutions obtained using well-established numerical models. Finally, Section 4.4 presents a summary of the chapter.

4.2 IMPLEMENTATION OF THE NUMERICAL AND ANALYTICAL CORE OF THE W-GHA MODEL

The implementation of numerical and analytical models for the solution of the W-GHA model was divided in three parts, corresponding to the three main model components. First, a

numerical model was developed for the solution of the partial differential equations (PDEs) governing the coupled flow of heat and moisture within the saturated/unsaturated soil comprising a railway embankment. The numerical model for heat and moisture flow takes into account the complex soil-atmosphere boundary conditions required in order to bring the effect of the weather conditions into the assessment of geo-hazards. Secondly, a numerical and analytical model was developed for the deterministic quantification of weather-related geo-hazards. The model for quantification of geo-hazards is comprised of an optimization model for the analysis of stability of embankments and a numerical model for the analysis of total stresses acting within an embankment. The stability model makes use of the pore-water pressure distributions obtained from the coupled heat and moisture flow model. Lastly, an analytical model was developed for the probabilistic assessment of geo-hazards.

4.2.1 *Implementation of the numerical model for coupled heat and moisture flow*

The heat and moisture flow model presented in Chapter 3 consists of two coupled, two-dimensional, nonlinear, and transient partial differential equations. Analytical solutions of these types of PDEs are known only for simple geometries, simple boundary conditions, and constant soil properties. Therefore, approximate numerical solutions are required. Numerical solutions of several PDEs governing the behaviour of saturated/unsaturated soils have been presented elsewhere. Fredlund and Rahardjo (1993) presented Finite Difference and Finite Element equations for the solution of a PDE governing flow of liquid water. Pereira (1996) and Gitirana Jr. (1999) presented in great detail the development and implementation of variational Finite Element and Finite Difference models for the PDEs governing coupled liquid water flow and static equilibrium, for saturated/unsaturated soils. The general mathematical approach typically undertaken for the solution of such PDEs can be applied for the solution of the PDEs governing coupled moisture (i.e., water vapour and liquid water) and heat flow.

A more general treatment about variational numerical techniques for the solution of partial differential equations can be found in Reddy (1993). The variational *spatial solution* of PDEs governing the behaviour of saturated/unsaturated soils involves the integration by parts of the PDEs, along with the weighting of residuals (i.e., the use of the so-called Galerkin weak formulation). The derivation by parts results in two types of boundary conditions; namely, natural boundary conditions (fluxes and/or forces), and essential boundary conditions (nodal values for the primary variables). Polynomials (i.e., shape functions) that are function of nodal values are used in order to represent in a discrete manner the distributions of the primary

variables along a unit *Finite Element*. The type of polynomial used corresponds to the type of *Finite Element* adopted. Linear and quadratic polynomials are often used. Next, the discretised equations are extended from local coordinates to global coordinates by the use of coupling Jacobian matrices. Compatibility conditions are then applied to the Finite Elements boundaries. The *time discretisation* of the finite element equation is typically done using the Finite Difference method or unconditionally stable *Green* approaches.

The finite element programs presented by Pereira (1996), Gitirana Jr. (1999), and also Geo-Slope International Ltd. (2002a, 2002b, 2002c, and 2002d) are all based on the general approach described in the previous paragraphs and described by Reddy (1993). Unfortunately, the modification and extension of such programs for additional physical processes, new soil constitutive models, and new boundary conditions involves laborious adaptations.

A new philosophy for the solution of PDEs has been introduced during the end of the 1990's, when general purpose partial differential equations solvers emerged. The philosophy behind these PDE solvers is based on the striking fact that a general approach could be implemented in order to handle in a single program most types of PDEs, either one- two- or three-dimensional, linear or non-linear, steady state or transient. Reddy (1993) had already envisaged that such general treatment was possible, but the Finite Element program presented by Reddy (1993) did not include a large number of features. PDE Solutions Inc. (http://www.pdesolutions.com/) has introduced in 2000 a powerful general purposed finite element solver with a degree of generality greater than that of any previous PDE software.

4.2.1.1 *Implementation of a numerical model using FlexPDE*

A solution for the model for moisture and heat flow has been formulated using the scripted general purpose partial differential equations solver, FlexPDE Version 3 (PDE Solutions, 2003). FlexPDE can be considered a *problem solving environment*, as it performs the entire range of functions necessary to solve partial differential equation (PDE) systems. From a script written by the user, FlexPDE builds a finite element model, solves the system, and presents graphical outputs of the results. Figures 4.1a and 4.1b show the script editing environment and an example of customised graphical outputs. In order to use FlexPDE, the equations governing the physical problem need to be laid out in the form of a scripted model. The script completely describes the equation system and problem domain. As a result, there is no uncertainty about what equations are being solved, as might be the case with a fixed-application program. A

Finite Element model cannot be implemented in FlexPDE without the complete knowledge of the physical processes and equations governing them.

FlexPDE can solve systems of first- or second-order partial differential equations in Cartesian or axis-symmetric two-dimensional geometry or in three-dimensional Cartesian geometry. The system may be steady-state or time-dependent and multiple equations can be mixed in a single problem. Any number of simultaneous equations can be solved, subject to the processing limitations of the computer on which FlexPDE is run. The PDEs can be linear or nonlinear. Nonlinear systems are solved by applying a modified Newton-Raphson iteration process. Any number of regions of different material properties may be defined.

The set of steps taken by FlexPDE for the solution of PDEs corresponds to the conventional Finite Element approach described previously. The fundamental difference in the FlexPDE approach lies in its generality and in the additional modules created in order to make the choice of the solutions approach automatic. A symbolic equation analyzer expands parameters and relationships defined in the script model, performs spatial differentiation, and symbolically applies integration by parts to reduce second order terms to create symbolic Galerkin equations (i.e., the weak formulation). Next, the solver differentiates the Galerkin equations to form the Jacobian coupling matrix. A mesh generation module constructs a triangular finite element mesh over a two-dimensional problem domain. A Finite Element numerical analysis module selects an appropriate solution scheme for steady-state or time-dependent problems, with separate procedures for linear and nonlinear systems. The finite element polynomials may be linear, quadratic or cubic. An adaptive mesh refinement procedure measures the adequacy of the mesh and refines the mesh wherever the error is large. The system iterates the mesh refinement and solution until a user-defined error tolerance is achieved.

FlexPDE has been thoroughly verified for liquid water flux, uncoupled heat flux, and uncoupled stress analysis (Nguyen, 1999, Pentland et al., 2001, Vu, 2003). Script models have been implemented herein, to solve the coupled heat and moisture flow equations along with soil-atmospheric boundary conditions. Uncoupled versions were also implemented, for the verification of the models. Appendix B presents the FlexPDE script programs corresponding to the model for coupled heat and moisture flow, isothermal moisture flow, and uncoupled heat flow. An example of a script model for the stress analysis is also presented.

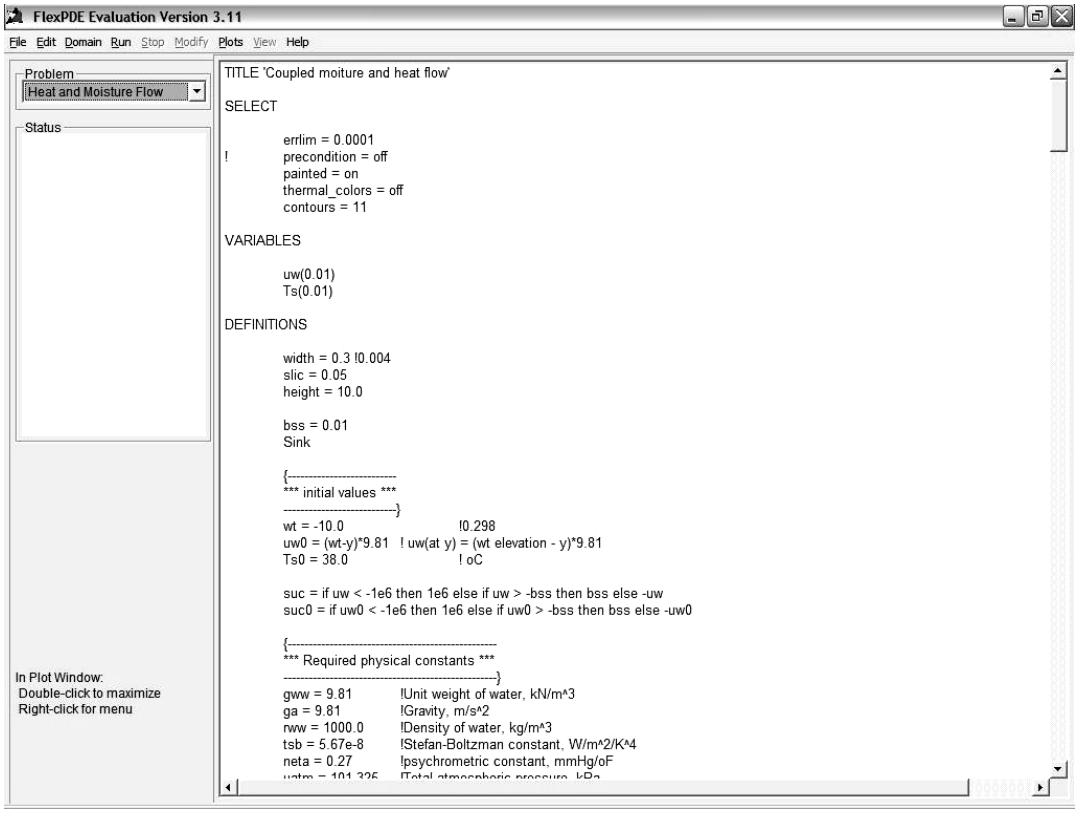

(a)

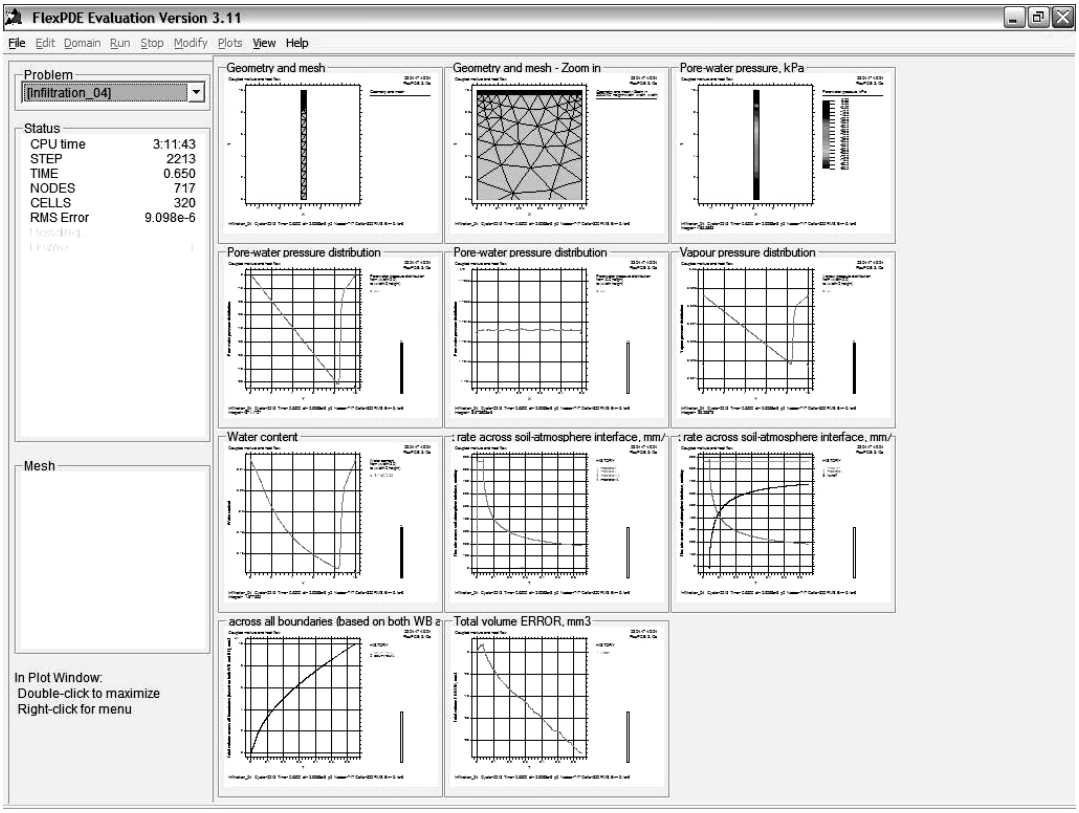

(b)

Figure 4.1 FlexPDE: (a) script editing environment, and (b) example of customised graphical outputs.

4.2.2 *Implementation of a model for stability analysis using dynamic programming*

A computer model for stability analysis named Safe-DP was developed based on the *dynamic programming* method presented in Chapter 3. The program was written in FORTRAN language and compiled using Compaq Visual Fortran 6.0 (Digital Equipment Corporation, 1999). The stress distributions used by Safe-DP are calculated using FlexPDE in order to solve the PDEs governing static equilibrium. Safe-DP is able to handle the complex geometries and heterogeneous soil conditions of the research program presented in the next chapters. The computer program Safe-DP was developed for the purpose of research, but further testing and thorough verification may permit its use in routine engineering design.

Safe-DP is based on the same theory used by the program Dynprog, presented by Pham et al. (2001). Both Safe-DP and Dynprog are based on the theory proposed by Baker (1980) and Yamagami and Ueta (1988b). Pham (2002) compared the Dynamic Programming method against conventional limit equilibrium methods of slices and finite element stress methods, using the program Dynprog. The results of the comparisons presented by Pham (2002) have been summarised in Chapter 2. Safe-DP was implemented in order to handle more general conditions that could not be handled by Dynprog. Safe-DP can analyse failure mechanisms oriented in any direction, any surface geometry, and general stratigraphy conditions. These improvements were essential, given the characteristics of the stability computations required by the research program presented in this Thesis.

4.2.2.1 *Safe-DP flowchart and subroutines*

Figure 4.2 presents a flowchart for the program Safe-DP. The program Safe-DP is comprised of a main program and six subroutines. The main program manages the subroutines and calls each subroutine required for the analysis. The subroutine READIN reads and stores the input data. The definition of the direction of the failure movement, surface geometry, search-boundary coordinates, initial factor of safety guess, and error tolerances are the required input. Figure 4.3 presents how the search boundary is defined. A total of seven points are required in order to define the search grid boundary. This number of points provides a flexible search grid that is able to handle sloped surfaces. In addition to the input data already mentioned, Safe-DP requires the input of grids of stresses, pore-water pressures, and shear strength parameters, which are all imported from FlexPDE. The data is imported from FlexPDE in regular data-grid format by means of a “table” output. The format of such outputs is documented in the FlexPDE User’s Manual (PDE Solutions, 2003). Subsurface conditions and stratigraphy are considered in the

stress analysis and are imported directly from FlexPDE in the regular data-grid format. The data-grid density is also defined in FlexPDE.

Next, the main program calls COVERIF. The subroutine COVERIF performs two main tasks. First, the search grid boundary coordinates originally provided in the input file are "snapped" to the FlexPDE data-grid. A search grid that coincides with the FlexPDE data grid greatly simplifies the computations required. The automatic "snapping" preserves the approximate initial coordinates of the search grid boundary, and makes the snapping process automatic. The second task performed by COVERIF is to verify the input data and check for errors, such as coordinates in wrong sequence, search grid boundaries out of the data grid, etc.

The subroutine SEARCHGRID performs two main tasks. First, SEARCHGRID defines the stages and state point coordinates, based on the snapped search grid boundary and on the FlexPDE data-grid. The state points are defined as the data grid points that are positioned within the search grid boundaries. The state points are numbered in sequence, and the corresponding coordinates are stored. The second task performed by SEARCHGRID is to determine the relative position of the state points with respect to the ground surface (i.e., above, below, or at the ground surface), and store this information.

The optimization process starts with the assignment of an initial factor of safety. The *dynamic programming* optimization is performed by the subroutine DP. The staged computations that are performed by DP are based on the *principle of optimality* and were described in Chapter 3. The results of the optimization process provide the coordinates of the critical slip surface. The critical slip surface obtained corresponds to the minimum value of the auxiliary additive functional G. The factor of safety of the critical slip surface obtained by DP is computed by the subroutine FS. Next, the factor of safety computed by FS is compared against the initial guess. If the difference is higher than a pre-established tolerance, *tol*, a new value for the factor of safety is assigned, and the subroutines DP and FS are called once again, in a new loop. A value of θ equal to 1 results in faster convergence in most cases, but lower values (2/3 or 1/2) may be required in some cases, for a more stable convergence. If the difference is lower than *tol* the loop is stopped, and the pos-processing subroutine READOUT is called. READOUT writes the output files describing the results of the analysis. More details about the optimization procedure will be given in the next section.

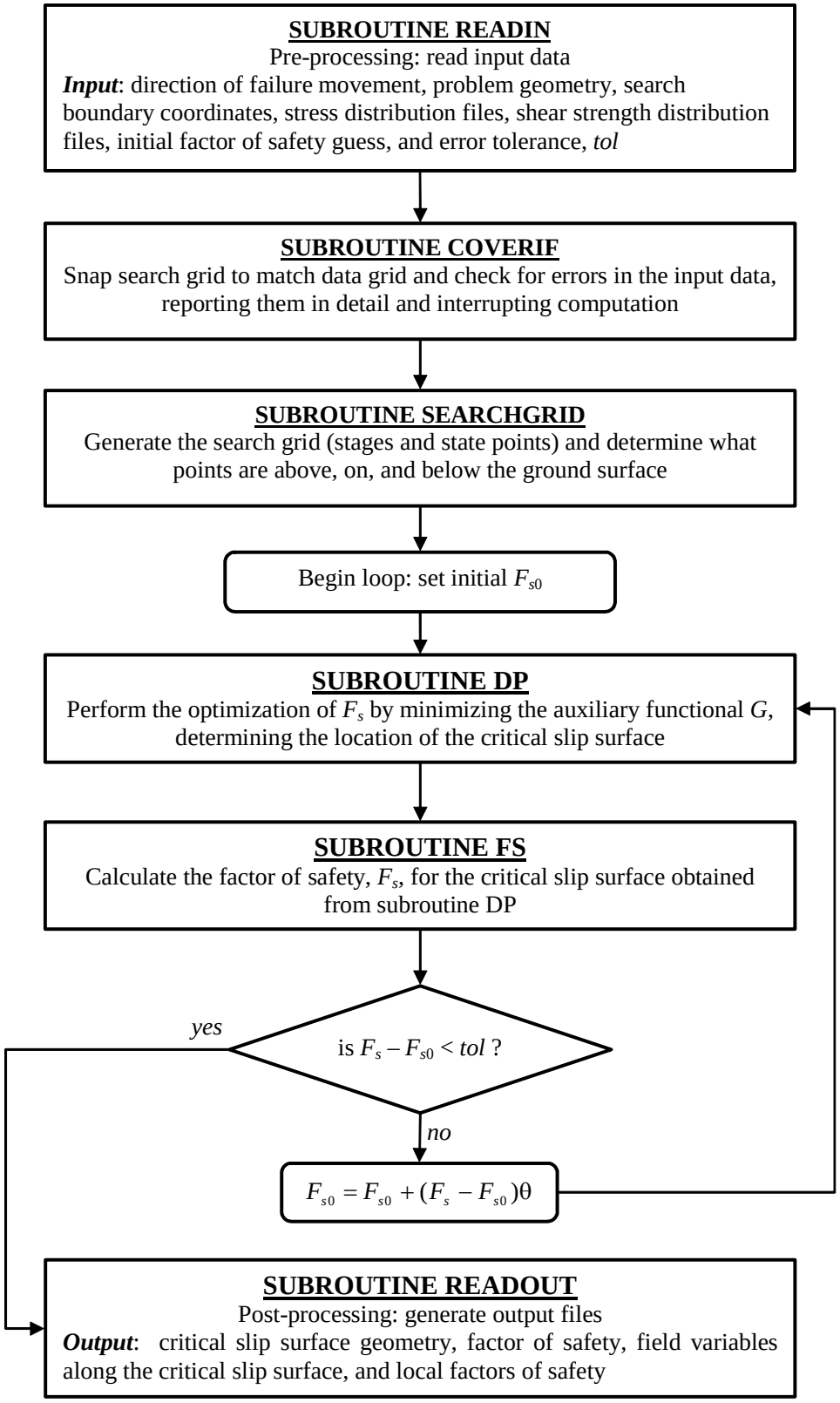

Figure 4.2 Flowchart for the Safe-DP program.

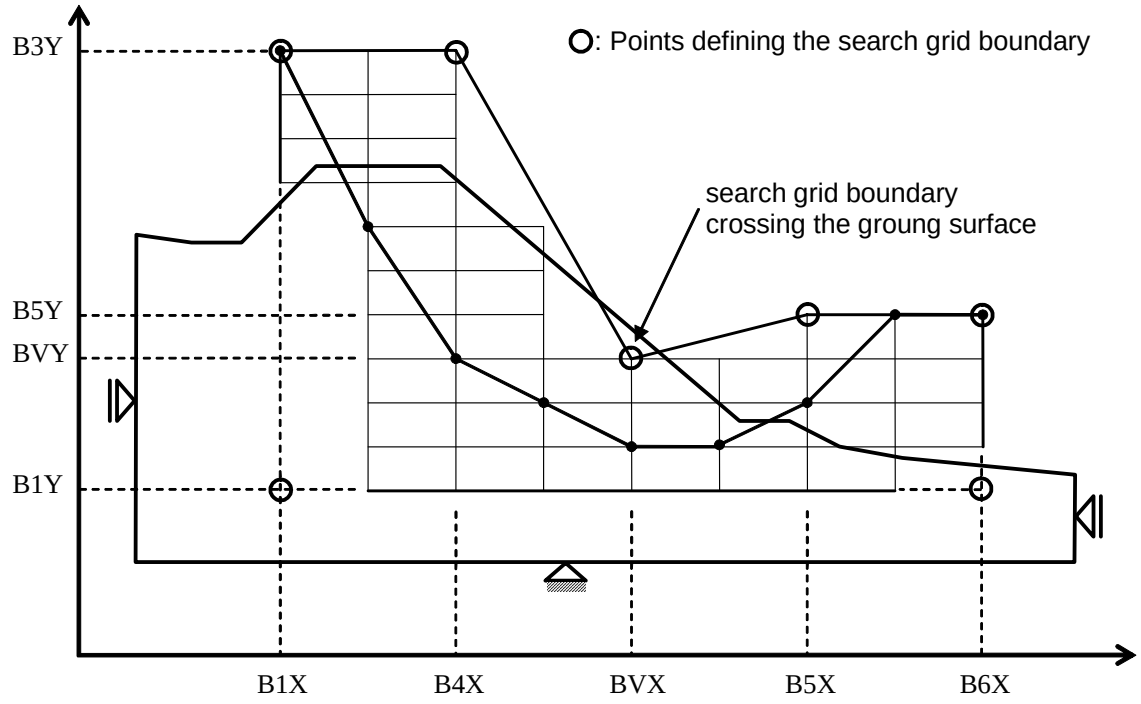

Figure 4.3 Definition of the search grid boundary for the stability analysis using Safe-DP.

4.2.2.2 *Optimization procedure*

The optimization procedure implemented in the subroutine DP is based on the *Dynamic Programming* theory presented in Chapter 3. The sequence of computational loops and the logic behind the *Dynamic Programming* theory can be understood by a careful examination of the equations presented in Chapter 3. Nevertheless, further details will be provided herein. Such details are merely a translation of Eq. 3.23 and of the analytical scheme for stability analysis presented in Figs. 3.10 to 3.12. The sequence of computations is as follows:

(i) Set the optimal functions $H_1(k)$ as equal to zero. $H_1(k)$ are the NP(1) optimal functions at the NP(1) state points located at the first state;

(ii) Compute and store the values of the NP(2) optimal functions $H_2(j)$ using Eq. 3.32. $H_2(j)$ are the optimal functions at the NP(2) state points located in the second stage. The optimal functions $H_2(j)$ are computed by determining the minimum value of the sum of the return function *DG* for each state point and the optimal function at the trial state point located at the previous stage, which is zero for the first stage. Each trial return function depends on the shear strength and acting shear stress along the trial slip surface segment and the initial factor of safety, F_{s0}. The total number of trials will be equal to

NP(1)·NP(2);

(iii) Store the location of the state point at the previous stage that gives the optimum function for each state point in the second stage;

(iv) Repeat the computations described in the two previous steps, for each of the next stages, until the final stage is reached;

(v) Compare the values of the optimal functions at the last stage, $H_{n+1}(j)$. The minimum value corresponds to the set of segments that gives the minimum value of G. Store the coordinate of the state point corresponding to the minimum optimal function at the last stage;

(vi) Determine the coordinate of the points defining the critical slip surface by tracing back to the previous stages. This can be accomplished by using the location of the state points that give the optimum function at each state point of each stage. These locations were determined and stored in step (iii);

The sequence of computations presented in these six steps is done considering a given initial factor of safety, used in Eq. 3.23. The factor of safety corresponding to the critical slip surface must be computed and compared to the initial factor of safety, as presented in Fig. 4.2. If the difference is higher than a pre-established tolerance, *tol*, a new value for the factor of safety is assigned, and the optimization procedure must be repeated. This loop must continue until a sufficiently small error is achieved.

4.2.3 *Implementation of the alternative point estimate solution routine*

The *alternative point estimate* theory presented in Chapter 3 was implemented in a spreadsheet routine using Microsoft® Excel 2002 (Microsoft Corporation, 2001). The spreadsheet routine implemented can accommodate a large number of input variables. Figure 4.4 presents a simplified spreadsheet, for three variables and with two variables defined. The greyed fields are computed values. The required input data are as follows:

(i) the expected value of each input variable, $E[X]$;

(ii) the coefficient of variation of each input variable, $CV[X]$;

(iii) the probability density function assumed for each variable; and

(iv) the correlation matrix, if any of the input variables are correlated.

The input fields are identified in Fig. 4.4. Two probability density functions presented in Appendix A were implemented; namely, the normal distribution and the lognormal distribution.

Based on the expected value, the coefficient of variation, and on the probability density function chosen, the spreadsheet routine automatically selects the appropriate equations to calculate the skewness and kurtosis of the probability density function of each input variable. The variance and standard deviation of each input variable are calculated based on the expected values and coefficients of variations. The equations of the skewness and kurtosis of the probability distributions used herein were presented in Chapter 3.

Next, the spreadsheet routine calculated the estimate points, x^+ and x^-, and the discrete probabilities or "weights", p^+ and p^-. The equations used for the computation of the estimation points and weights were presented by Eq. 3.37. Figure 4.4 presents estimation points for a variable defined by a normal distribution and for a variable defined by a lognormal distribution. The estimation points for the normally distributed variable are symmetrical with respect to the expected value. Non-symmetric estimation points are presented for the log normally distributed variable.

Once the univariated estimate points and concentrated discrete probabilities are determined, the spreadsheet routine lays out the sets of variable values required for the multivariate analysis. The sets of values are organised in four groups. The first set corresponds to the expected values. The second group corresponds to the sets using upper estimate points, x^+. The third group corresponds to the sets using lower estimate points, x^-. The fourth group corresponds to the estimate points required by correlated variables. The total number of sets required is a function of the number of input variables, as presented in Chapter 3. Five evaluation sets are required for two uncorrelated variables, and six evaluation sets are required for two correlated variables. The sets of variables are them exported, in order to be used in external applications, for the quantification of F_s.

Five analyses rendering five values of F_s are required by the simple example presented in Fig. 4.4. The values of F_s are then imported into the spreadsheet routine. These values are used for the computation of the expected value of F_s, variance, and higher order moments. The equations used for the computation of $E[F_s]$ and $Var[F_s]$ were presented in Chapter 3. Given the computed expected value and variance of F_s, the reliability index, β, and the probability of failure, P_f, can be computed by assuming a probability density function of F_s. Figure 4.4 shows the values of P_f for a normal and for a lognormal distribution.

Multivariate Point Estimate Analysis

Number of variables		2	
Counter	**1**	**2**	**3**
Variables	**ϕ**	**k^{w}_{sat}**	**X3**
E[x]	**25.0**	**1.0E-05**	**0.0**
CV, %	**10.0**	**50.0**	**0.0**
Distribution	**Normal**	**Log Normal**	**Normal**
Control	OK	OK	VOID
Var[x]	6.25	2.5E-11	VOID
σ[x]	2.50	5.0E-06	VOID
γ_1(X) skewness	0.0000	1.6250	VOID
γ_2(X) kurtosis	3.0000	8.0352	VOID

Output fields, calculated from the values of E[F(X)] and Var[F(X)] (see spreadsheet botton)

Results	
E[F_s(X)]	1.612
Var[F_s(X)]	0.052
σ[F_s(X)]	0.228
β_{Fs}	2.685
P_f (N)	0.363
P_f (LN)	0.045

Input fields

Correlations	*1*	*2*	*3*
1	1	**0**	**0**
2	0	1	**0**
3	0	0	0

alfa (-)	-1.7321	-1.6481	VOID
alfa (+)	1.7321	3.2731	VOID
x (-)	20.670	1.8E-06	VOID
x (0)	25.000	1.0E-05	VOID
x (+)	29.330	2.6E-05	VOID
p (-)	0.167	0.123	VOID
p (0)	0.667	0.815	VOID
p (+)	0.167	0.062	VOID
δ_{ij}	***1***	***2***	***3***
1	1	0	VOID
2	0	1	VOID
3	VOID	VOID	VOID
δ_i	1.000	1.000	0.000
δ	2.000	**Σp_0**	1.481

Sets of values to be exported for the computation of F_s

Values of F_s computed (imported from the SAFE-DP program)

Set of variables for the evaluations

6 evaluations		5 (if all uncorrelated)	
Counter	**1**	**2**	**3**
Variables	**ϕ**	**k^{w}_{sat}**	**X3**
F(E[x])	25.0	1.0E-05	VOID
F[x1(+)]	29.3	1.0E-05	VOID
F[x2(+)]	25.0	2.6E-05	VOID
F[x3(+)]	VOID	VOID	VOID
F[x1(-)]	20.7	1.0E-05	VOID
F[x2(-)]	25.0	1.8E-06	VOID
F[x3(-)]	VOID	VOID	VOID
F[x1(+),x2(+)]	29.3	2.6E-05	VOID
F[x1(+),x3(+)]	VOID	VOID	VOID
F[x2(+),x3(+)]	VOID	VOID	VOID

f(x)	p	f(x)*p	{f(x)-E[f(x)]}^2	p*{f(x)-E[f(x)]}^2
1.600	0.481	0.770		
1.952	0.167	0.325	0.116	0.019
1.401	0.062	0.087	0.045	0.003
0.000	VOID	VOID	VOID	VOID
1.229	0.167	0.205	0.147	0.024
1.823	0.123	0.225	0.045	0.005
0.000	VOID	VOID	VOID	VOID
0.000	0.000	0.000	2.598	0.000
0.000	VOID	VOID	VOID	VOID
0.000	VOID	VOID	VOID	VOID
	E[F_s(X)]	1.612	**Var[F_s(X)]**	0.052

Figure 4.4 Spreadsheet routine for the point estimation probabilistic analysis.

4.3 VERIFICATION OF THE NUMERICAL AND ANALYTICAL MODELS

This section presents the verification of the numerical and analytical models described in the previous section. Relatively simple problems with known solutions were selected for the verification of the numerical models. The verification is accomplished by means of comparisons against solutions obtained using other well-established numerical models available that are capable of solving the simple problems presented in this chapter. The full capabilities of the analysis core of the W-GHA model will be demonstrated by the analysis presented in the following chapters.

4.3.1 *Verification of the transient moisture and heat flow numerical model*

The verification of the two-dimensional transient moisture and heat flow model was done considering three different problems. The first problem was designed to verify the simulation of an isothermal infiltration/runoff problem. The second problem was designed to verify the simulation of a heat flow problem with constant pore-water pressures. Finally, the numerical model for fully coupled moisture and heat flow was verified using an evaporation problem.

4.3.1.1 *Verification for an isothermal infiltration/runoff problem*

The analysis of a soil column subjected to precipitation under isothermal conditions (Fig. 4.5) is presented herein. The results obtained using the numerical moisture flow model for liquid water and water vapour were compared against the results obtained using Seep/W (Geo-Slope International Ltd., 2002a). Seep/W is a finite element program specifically designed for solving isothermal steady state and transient seepage problems for saturated/unsaturated soils in two-dimensional and axis-symmetric conditions. Vapour flow is not accounted for by Seep/W. Nevertheless, the infiltration-runoff conditions analysed in this section are expected to produce negligible amounts of vapour flow, as will be shown later. Seep/W has been thoroughly verified and its results can be adopted as reliable benchmarks (Nguyen, 1999).

Figure 4.5 presents the problem geometry adopted and finite element meshes. The isothermal moisture flow problem consists of a soil column 10 m high. The horizontal dimension of the soil column is irrelevant as the flow pattern will be one-dimensional. The mesh manually constructed in Seep/W consists of 100 eight-node isoparametric elements. The mesh automatically generated by FlexPDE has a number of elements that varies according to the

degree of nonlinearity of the problem at a given time step. As many as 500 elements were required for an error tolerance of 0.1%. The initial pore-water pressure distribution corresponds to a hydrostatic pore-water pressure distribution (Fig. 4.5e), with the water table located at the bottom of the column (elevation = 0 m).

A "no flow" natural boundary condition was applied at the lateral and lower boundaries of both FlexPDE and Seep/W meshes. The boundary condition applied to the upper boundary of the FlexPDE mesh corresponds to the conditional soil-atmosphere natural boundary equation presented in Chapter 3. The amount of infiltration and runoff is automatically computed according to the amount of precipitation (and/or evaporation) and according to the pore-water pressure at the soil surface. The boundary condition available in Seep/W that best represents the precipitation/runoff conditions analysed herein corresponds to a unit flux boundary condition with a "potential seepage face review". Different amounts of precipitation were selected in order to produce different amounts of infiltration and runoff. The precipitation rates applied at the upper boundary were equal to $1\times k^{w}_{sat}$, $1.5\times k^{w}_{sat}$, $2\times k^{w}_{sat}$, $4\times k^{w}_{sat}$, and $10\times k^{w}_{sat}$. These amounts of precipitation were applied during a period of time of 7 days.

Figure 4.6 presents the soil properties assumed. The saturated hydraulic conductivity of 1×10^{-6} m/s corresponds to a moderate permeability, typical of silts and certain loams. Figure 4.6 shows that the vapour conductivity, k^{v}, of this soil is negligible for soil suctions lower than 7000 kPa. Therefore, though the vapour flow is included in the moisture flow model, it should not affect the results because the soil suction is expected to be lower than 100 kPa at all time steps. This combination of initial and boundary conditions and hydraulic properties is expected to produce sharp wetting fronts and considerable runoff for the higher precipitation rates.

Figures 4.7 and 4.8 present the computed infiltration rates and infiltration over precipitation rates, respectively. These values were computed for precipitation rates of $1\times k^{w}_{sat}$, $1.5\times k^{w}_{sat}$, $2\times k^{w}_{sat}$, $4\times k^{w}_{sat}$, and $10\times k^{w}_{sat}$, corresponding to 86.4, 129.4, 172.8, 345.6, and 864 mm/day, respectively. It can be observed in Fig. 4.7 that the results obtained using the moisture flow model implemented in FlexPDE agree qualitatively with the experimental limiting curve proposed by Horton (1933) and presented in Chapter 2. The higher the precipitation rate, the sooner runoff started. Runoff occurred for all precipitation rates, with exception of the precipitation rate corresponding to $1\times k^{w}_{sat}$, as expected. The amount of runoff can be calculated by taking the difference between the amounts of precipitation and computed infiltration.

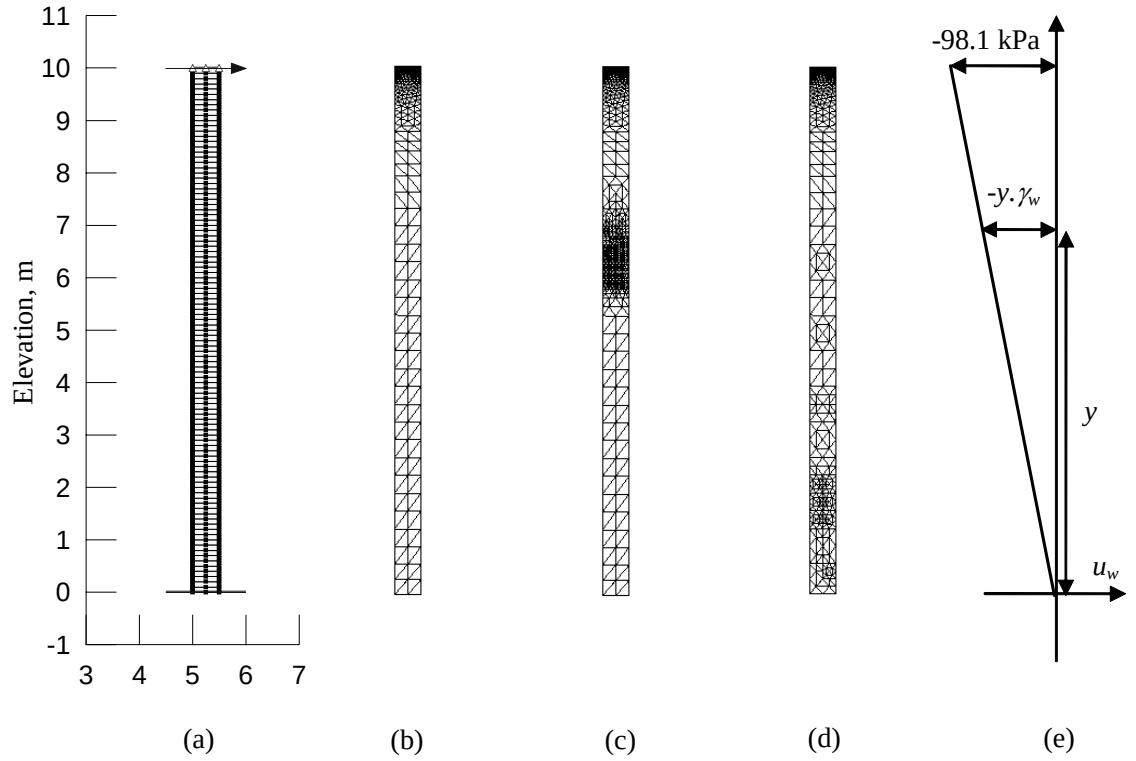

Figure 4.5 Verification of the moisture flow model for infiltration/runoff conditions: geometry, mesh, and boundary conditions. (a) Seep/W mesh; (b) FlexPDE mesh for t = 0 day; (c) FlexPDE mesh for t = 3 days; (d) FlexPDE mesh for t = 7 days; and (e) initial pore-water pressure distribution.

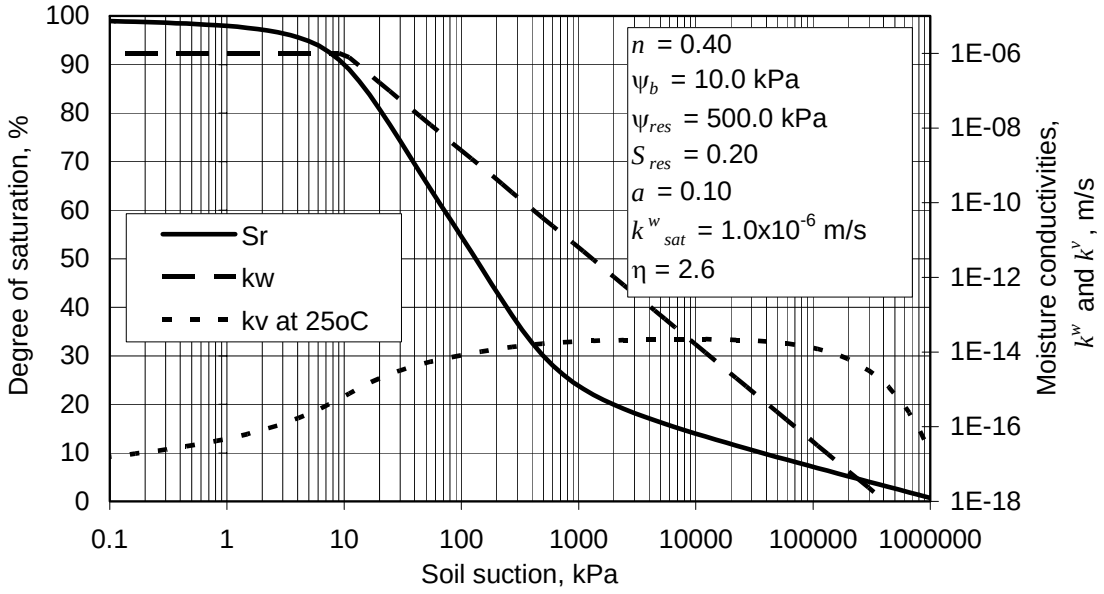

Figure 4.6 Hydraulic properties used in the verification of the moisture flow model for infiltration/runoff conditions.

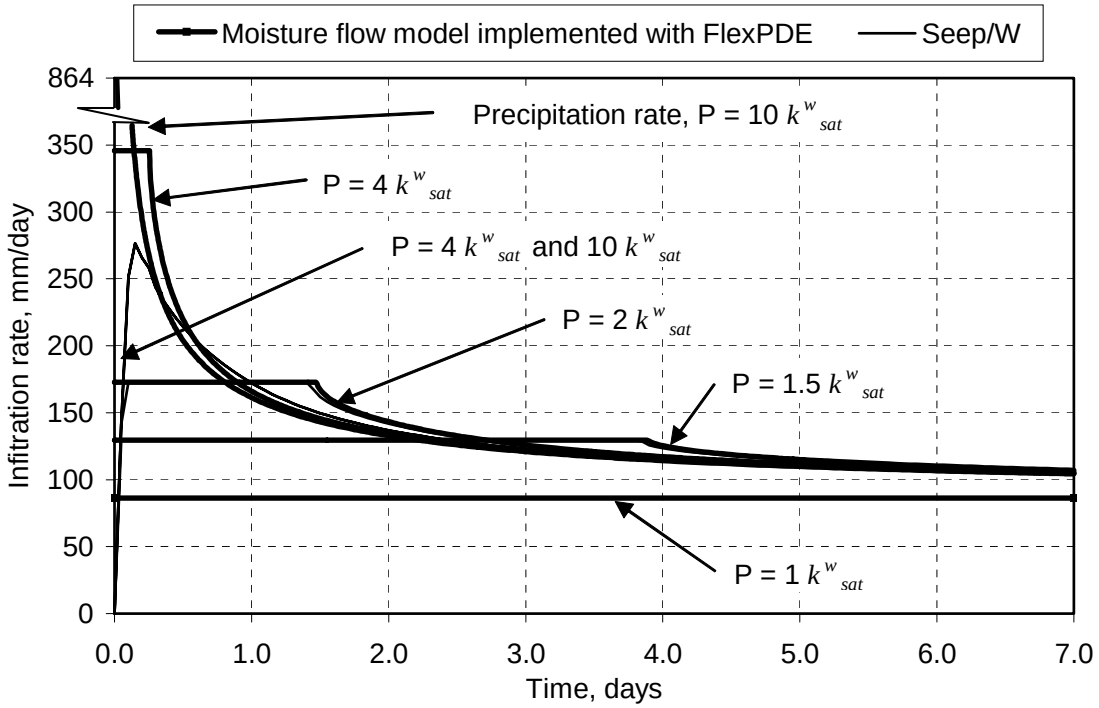

Figure 4.7 Verification of the moisture flow model for infiltration/runoff conditions: comparison of the infiltration rates for different precipitation rates.

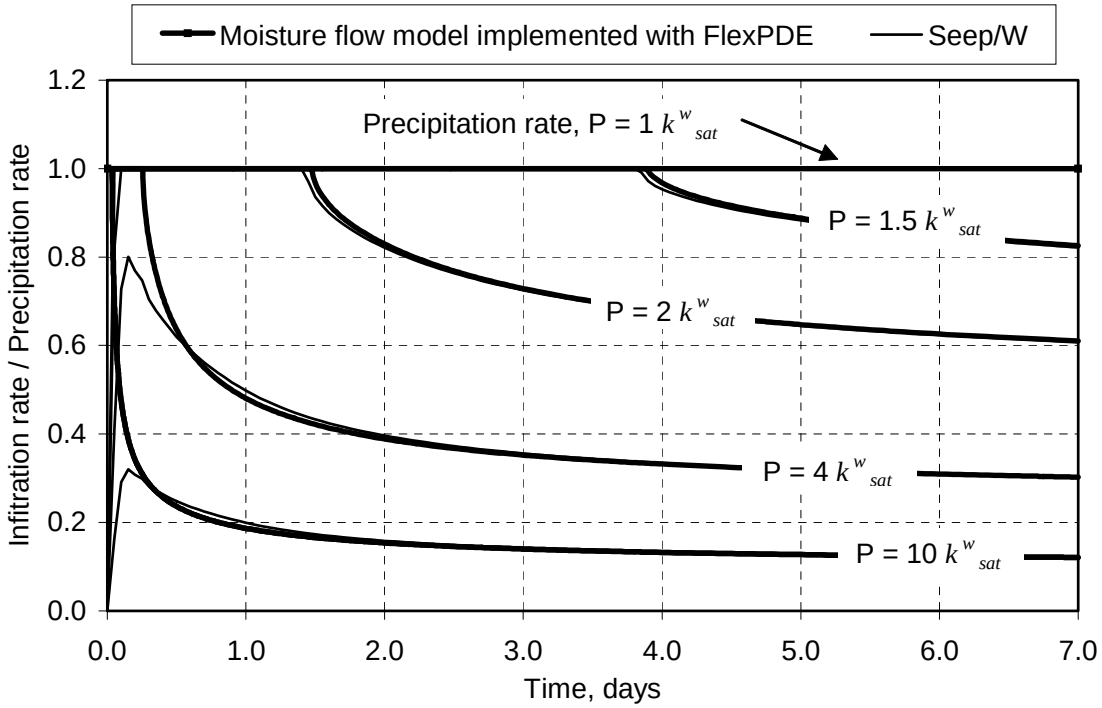

Figure 4.8 Verification of the moisture flow model for infiltration/runoff conditions: comparison of the infiltration rates / precipitation for different precipitation rates.

The infiltration rates computed using FlexPDE and Seep/W were in close agreement for precipitation rates up to $2\times k^w_{sat}$. Somewhat different results were obtained for higher precipitation rates, during the first few hours. Seep/W was not capable of reproducing the high pore-water pressure gradients that occur during the beginning of the wetting process. The moisture flow model implemented in FlexPDE was able to track down high pressure gradients through the use of an adaptive mesh. Therefore, lower infiltration rates were computed by Seep/W and the shape of the limiting infiltration curve presented by Horton (1933) could not be completely obtained. The results are in closer agreement after t = 1 day. A relatively dense mesh was used in Seep/W. Further mesh refinement was tried, with relatively little improvement. It is interesting to note that such manual refinement and mesh sensitivity studies are not required when using FlexPDE, due to the automatic mesh refinement.

Figures 4.9, 4.10, and 4.11 present the pore-water pressure profiles at several time steps for precipitation rates of $1\times k^w_{sat}$, $1.5\times k^w_{sat}$, and $4\times k^w_{sat}$, respectively. Sharp infiltration fronts were obtained for all three cases, as expected. The higher the precipitation rate the deeper the wetting front, at any given time step. For a precipitation rate equal to the saturated hydraulic conductivity the matric suction at the soil surface remained equal to the matric suction at the break point of the k^w function (i.e., 10 kPa). Higher precipitation rates produced larger pore-water pressures at the soil surface, eventually reaching zero and resulting in runoff. For instance, Fig. 4.10 shows that pore-water pressures at the soil surface reaches zero at approximately 4 days, as indirectly observed in Figs. 4.7 and 4.8. The water table at the bottom of the soil column was unaffected by precipitation rates of $1\times k^w_{sat}$, $1.5\times k^w_{sat}$, but moved upwards for higher precipitation rates (see Fig. 4.11, t = 7 days).

Good agreement was observed between the pore-water pressure profiles obtained using the moisture flow model implemented in FlexPDE and Seep/W, for precipitation rates lower or equal than $1.5\times k^w_{sat}$. Due to the poor infiltration profile obtained by Seep/W for high precipitation rates, the wetting front lagged behind the front obtained using the moisture flow model implemented in FlexPDE, as can be seen in Fig. 4.11. The lag in the position of the wetting front calculated using Seep/W was proportional to the error in the amount of infiltration for the first few hours for precipitation rates higher or equal than $4\times k^w_{sat}$, as shown in Figs. 4.7 and 4.8.

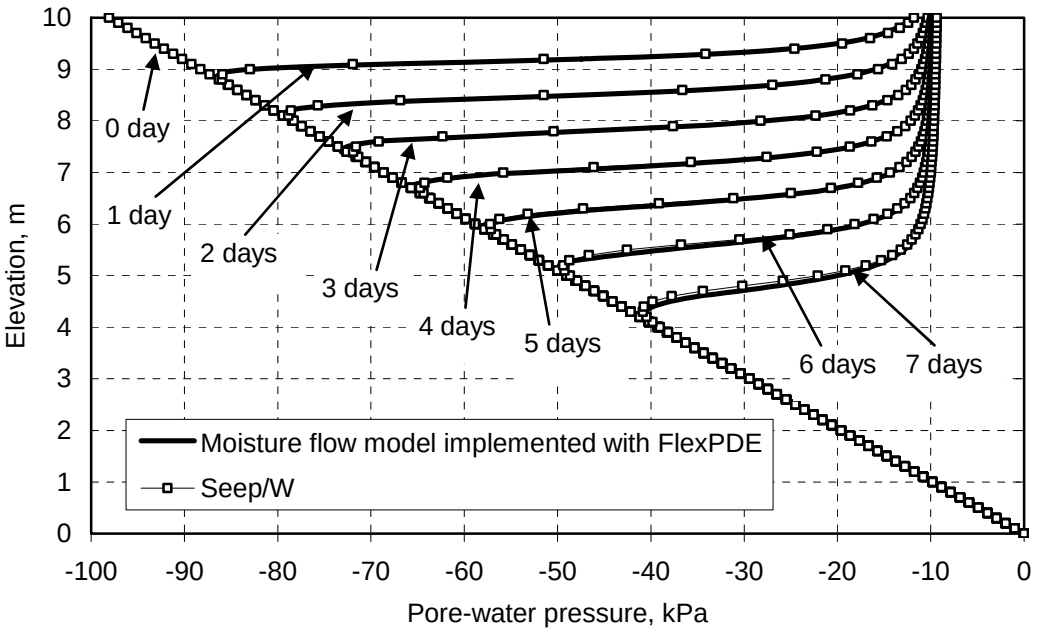

Figure 4.9 Verification of the moisture flow model for infiltration/runoff conditions: comparison of the infiltration profiles for Precipitation = k^w_{sat}.

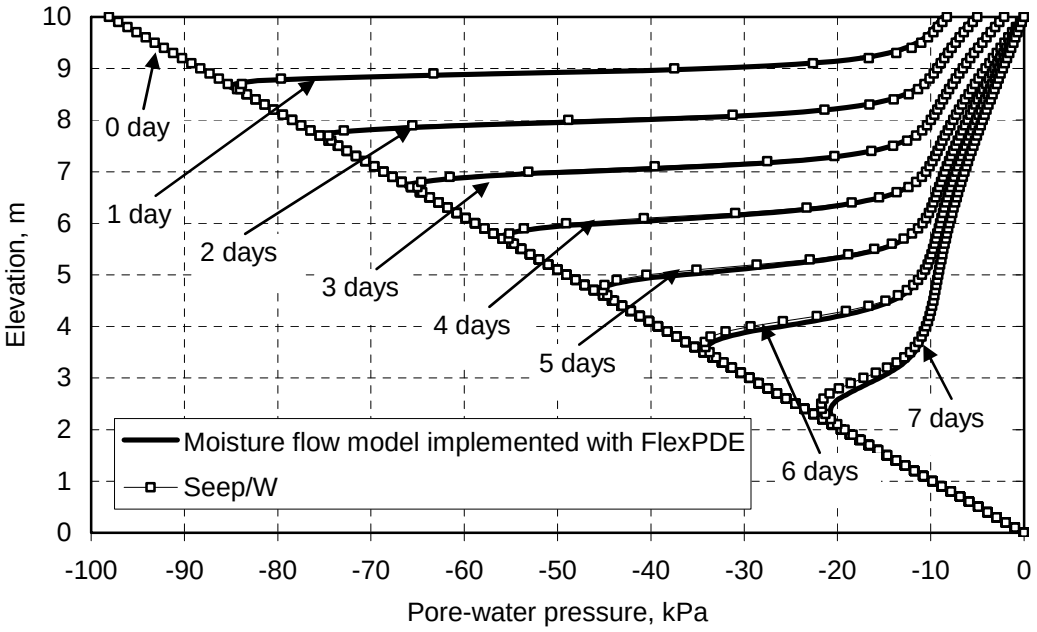

Figure 4.10 Verification of the moisture flow model for infiltration/runoff conditions: comparison of the infiltration profiles for Precipitation = 1.5 k^w_{sat}.

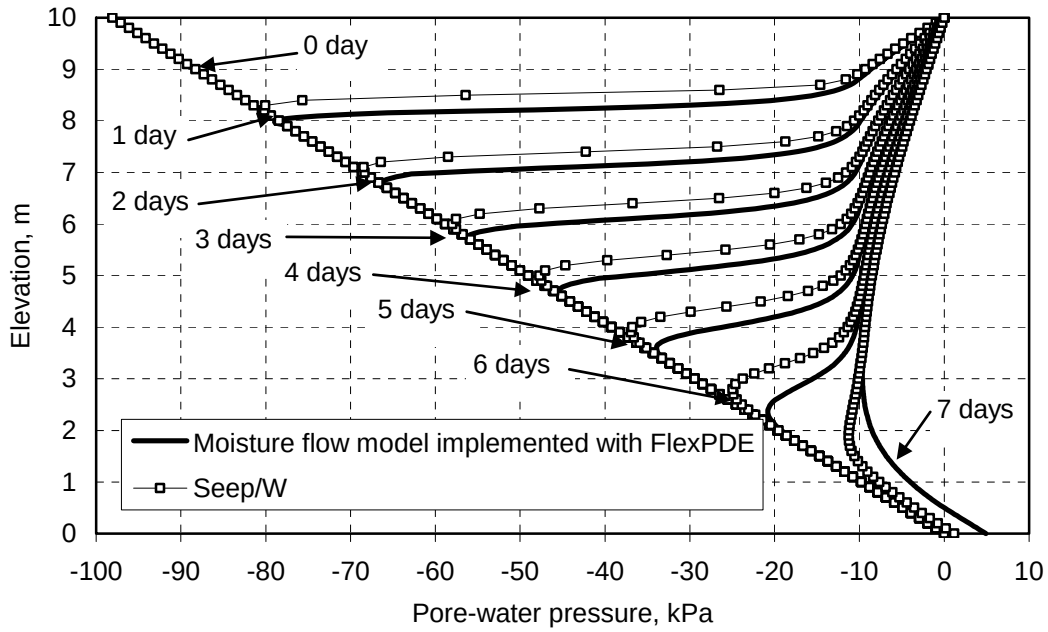

Figure 4.11 Verification of the moisture flow model for infiltration/runoff conditions: comparison of the infiltration profiles for Precipitation = 4 k^w_{sat}.

4.3.1.2 *Verification for a heat transfer problem*

A soil column subjected to a negative heat flux at the soil-atmosphere boundary was analysed in order to verify the numerical model for heat flow. The results obtained using the numerical model presented herein were compared against the results obtained using Temp/W (Geo-Slope International Ltd., 2002d). Temp/W is a finite element program specifically designed for solving steady state and transient conductive heat flow problems for temperatures above and below the water freezing point in two-dimensional and axis-symmetric conditions. Temp/W is not intended for the analysis of coupled heat and moisture flow. Latent heat of vaporization is not accounted for by Temp/W. Therefore, the verification examples presented in this section will not consider the more general aspects of the proposed heat flow model. Temp/W has been thoroughly verified and its results can be adopted as reliable benchmarks (Pentland et al., 2001).

The verification problem consists of a soil column with the same dimensions as those of the soil column presented in Fig. 4.5 (i.e, 10 m high) and subjected to one-dimensional heat flow conditions. The mesh manually constructed in Temp/W consists of 100 eight-noded isoparametric elements. The mesh automatically generated by FlexPDE has a number of elements that varies according to the degree of nonlinearity of the problem at a given time step.

The initial temperature distribution was assumed constant throughout the soil column and equal to 25°C. The boundary condition applied to the upper boundary corresponds to a negative heat flux (heat flow out) of 4.8×10^6 J/(m^2 day). This negative heat flux, which is qualitatively similar to the latent heat consumption during evaporation, was applied during a period of 7 days. A "no flow" natural boundary condition was applied at the lateral and lower boundaries of the soil column. The heat conductivity and volumetric heat capacity, assumed as equal to 1.728×10^5 J/(m day °C) and 2.99×10^6 J/(m^3 °C) respectively, correspond to the heat conductivity of a saturated silt.

Figures 4.12 and 4.13 present the computed temperature changes at several time steps and points along the soil column. The temperature profiles show an increasingly deep cooling front, as expected. Close agreement was observed between the temperature profiles obtained using the heat flow model implemented with FlexPDE and the results obtained using Temp/W. The results of the verification analysis presented in this section show that accurate results were obtained using the heat flow model implemented using FlexPDE. Another verification problem will be presented in the next section, considering coupled heat and moisture flow. The coupled heat and moisture problem presented in the next section includes nonlinear thermal properties and latent heat flow.

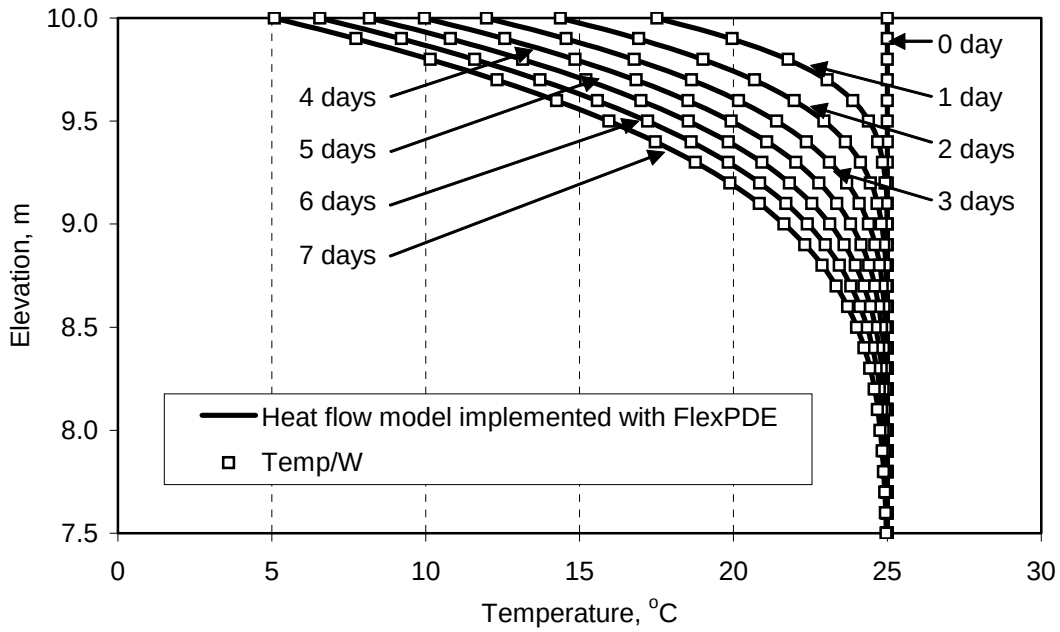

Figure 4.12 Verification of the heat flow model: comparison of the temperature profiles at several time steps.

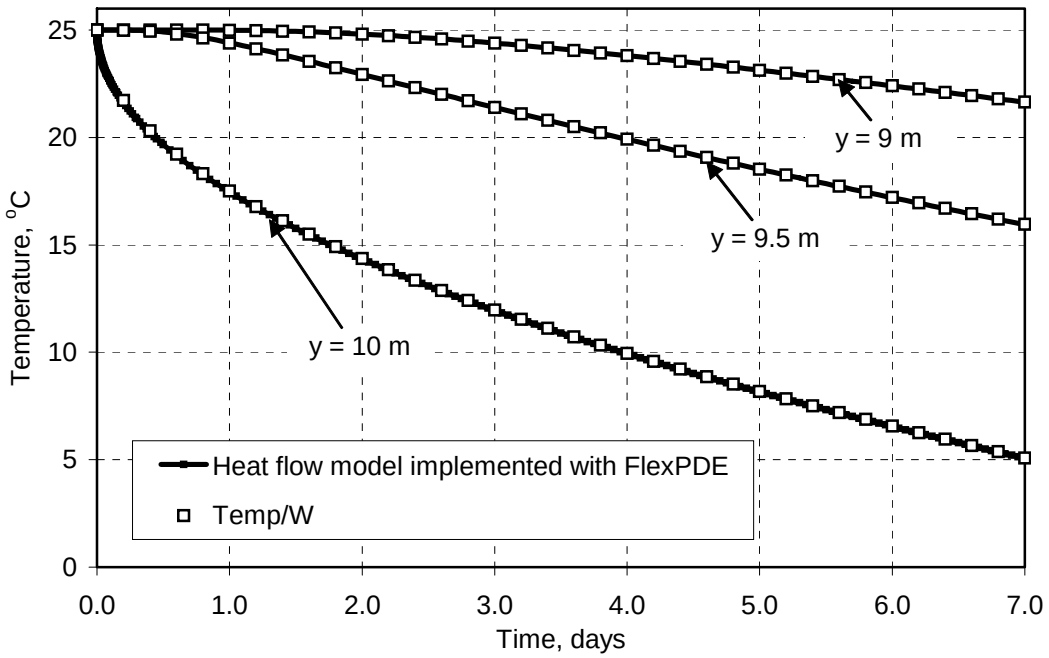

Figure 4.13 Verification of the heat flow model: comparison of the temperature changes with time at different elevations along a soil column.

4.3.1.3 *Verification of the fully coupled heat and moisture flow numerical model for an evaporation problem*

This verification example demonstrates the coupling between moisture and heat and the importance of the water vapour flow component during evaporation. The heat and moisture flow model was verified by means of a coupled analysis of evaporation of a column of sand. The results of a sand column drying experiment performed by Wilson (1990) were selected. Both experimental and simulation results are available for comparison. The drying test was performed in the laboratory, under controlled temperature and relative humidity conditions. Measurements of actual evaporation and the distributions of temperature along the column depth were obtained, providing several measures that can be used for the verification of the numerical model. Wilson (1990) presented also a one-dimensional finite difference numerical model called "Flux" for the simulation of the drying test. Reasonable results were obtained from the comparison of measured data and results computed using the Flux program. Both the measured and computed results from Wilson (1990) are compared against the result obtained using the numerical model presented herein.

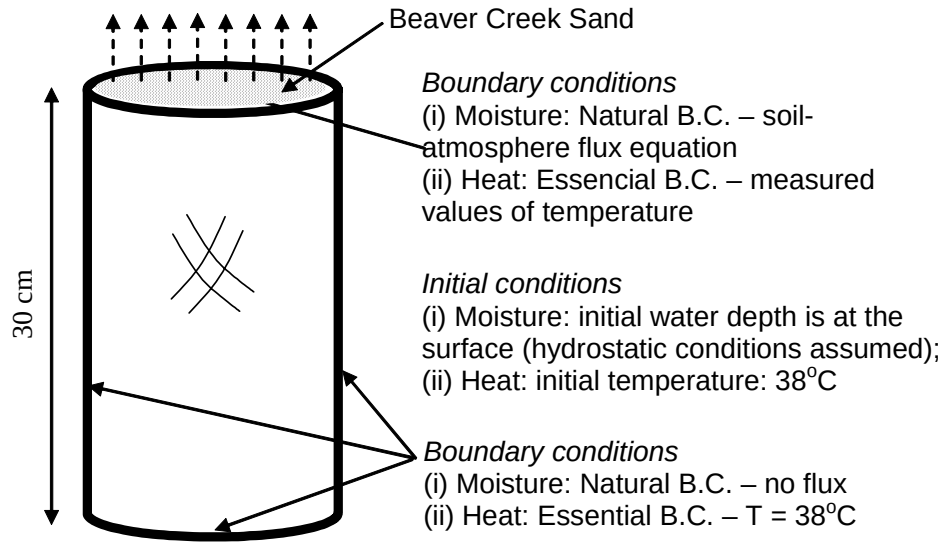

Figure 4.14 Numerical simulation of the drying column test – initial and boundary conditions (Wilson, 1990).

Figure 4.14 presents the geometry of the drying column experiment and the initial and boundary conditions. Due to the problem geometry and boundary conditions, the flow is essentially one-dimensional. Therefore, the three-dimensional axisymmetric geometry was reduced to a one-dimensional problem. Because the numerical model presented herein uses two-dimensional plane elements, a two-dimensional mesh was used. The width of the problem has no influence on the solution, though large widths result in an unnecessary number of elements, reducing the solution efficiency. Boundary conditions forcing zero moisture and heat flow were applied at the bottom and lateral boundaries of the column.

More complex boundary conditions were applied to the upper boundary, which is in contact with the atmosphere. The temperature boundary condition applied to the upper end of the column was the experimentally measured surface temperatures (see Table 4.1). The moisture flow boundary condition applied was the soil-atmosphere coupling evaporation equation proposed by Wilson et al. (1997). The values of potential evaporation required by the equation proposed by Wilson et al. (1997) were obtained during the drying column test; from measured values of evaporation from a water pan (see Table 4.1). Table 4.1 presents additional variables required by the soil-atmosphere coupling boundary condition; namely, the relative humidity and the air temperature. Only the data from "column B" (see Table 4.1) was used in the analyses presented herein and presented by Wilson (1990).

Table 4.1 Summary of daily values for the column drying test (Wilson, 1990).

Day	Air Temp °C	Relative Humidity %	PE mm/day	Water Temp °C	Surface AE Col. A mm/day	Temp Col. A °C	Surface AE Col. B mm/day	Temp Col. B °C
0	38.6	23.0	7.37	29.0	6.96	37.4	7.55	37.8
1	38.2	22.0	7.38	31.3	6.65	30.2	6.84	31.3
2	38.1	20.0	7.60	31.0	6.78	30.1	6.94	29.8
3	38.0	18.0	7.74	30.5	7.18	29.7	6.08	30.0
4	38.4	15.5	7.53	30.7	6.52	29.6	5.29	31.2
5	38.7	15.0	7.82	30.5	4.88	31.6	4.47	32.4
6	38.1	15.0	8.01	30.8	3.97	32.7	3.80	33.2
7	39.0	16.0	7.53	30.7	3.35	33.8	3.31	34.2
8	37.7	18.0	7.59	30.6	3.04	34.4	2.87	34.5
9	37.8	17.0	7.76	30.9	2.76	34.8	2.65	35.1
10	38.8	16.5	7.74	30.7	2.47	35.2	2.46	35.6
11	37.7	16.5	7.76	30.8	2.04	35.4	2.17	35.6
12	38.7	16.0	7.86	30.4	2.06	35.7	2.02	35.8
13	38.2	17.0	7.96	30.9	2.05	35.9	1.98	36.2
14	39.1	13.0	8.08	30.7	2.02	36.3	1.98	36.6
15	38.7	16.0	7.87	30.7	1.81	36.4	1.81	36.6
16	38.2	14.0	8.21	30.6	1.85	36.4	1.65	36.6
17	38.2	13.0	8.05	30.4	1.59	36.8	1.59	36.6
18	38.4	13.5	8.04	30.7	1.56	36.7	1.44	36.6
19	37.6	12.5	8.25	30.3	1.52	36.8	1.40	36.6
20	38.6	12.5	8.05	30.4	1.36	36.8	1.32	36.8
21	38.0	16.5	7.72	30.9	1.36	37.1	1.32	36.9
22	38.5	15.0	8.03	30.6	1.31	37.2	1.22	36.9
23	38.3	14.5	7.92	30.4	1.15	37.2	1.19	37.0
24	38.3	16.5	7.83	30.7	1.22	37.0	1.18	37.0
25	38.0	14.0	7.57	30.8	1.19	37.2	1.12	37.1
26	38.0	12.5	8.24	30.4	1.23	37.4	1.10	37.2
27	37.6	12.5	8.13	30.4	1.08	37.5	0.98	37.3
28	38.6	12.5	8.12	30.4	0.94	37.7	0.91	37.5
29	37.5	12.0	8.23	30.4	0.93	37.6	0.90	37.4
30	38.0	12.5	8.24	30.3	0.91	37.8	0.83	37.6
31	38.0	12.5	8.12	30.7	0.87	37.4	0.81	37.5
32	38.2	14.0	7.74	30.7	0.78	38.0	0.75	37.7
33	38.9	12.5	7.86	30.6	0.81	37.7	0.73	37.9
34	38.8	14.0	8.11	30.4	0.82	37.8	0.66	37.7
35	37.5	12.5	8.27	30.2	0.69	38.0	0.66	37.7
36	38.0	11.5	8.29	30.3	0.70	38.0	0.66	37.9
37	38.9	12.5	8.09	30.4	0.67	38.2	0.52	38.1
38	37.7	13.0	7.68	30.6	0.61	38.0	0.57	37.8
39	38.5	13.0	7.79	30.7	0.58	37.9	0.56	38.1
40	38.5	14.5	8.24	30.3	0.53	38.3	0.50	38.1
41	37.7	12.5	8.32	30.4	0.46	38.1	0.44	38.1
42	38.3	14.0	7.26	30.2	0.36	38.1	0.44	38.0

The soil selected by Wilson (1990) for the analyses was the Beaver Creek sand. Figure 4.15 presents the hydraulic soil properties of the soil used. The soil-water characteristic curve was obtained by Wilson (1990) using Tempe cell tests and desiccators. The hydraulic conductivity function was obtained from the saturated hydraulic conductivity obtained in the laboratory and using the Brooks and Corey equation. The moisture conductivity corresponding to the vapour diffusion coefficient is also presented in Fig. 4.15. A comparison of the functions k^w and k^v provides an estimation of the range of soil suction and water content for which liquid water flow or water vapour flow dominate. For the Beaver Creek sand, vapour diffusion takes over for values of soil suction higher than approximately 20 kPa and degree of saturation lower than approximately 20%. The highly steep hydraulic conductivity function shown in Fig. 4.15 poses a considerable challenge for the numerical model.

Figure 4.16 presents the thermal property functions of the Beaver Creek sand. These functions were obtained using the formulations presented in Chapter 3 and based on the equations proposed by de Vries (1963, 1987). According to the prediction equations, the thermal conductivity and the volumetric specific heat are function of the characteristics of the individual phases and are functions of the amount of water stored in the soil. The effect of the amount of water stored in the soil pores is shown by the decrease in thermal conductivity and volumetric specific heat, as soil suction increases.

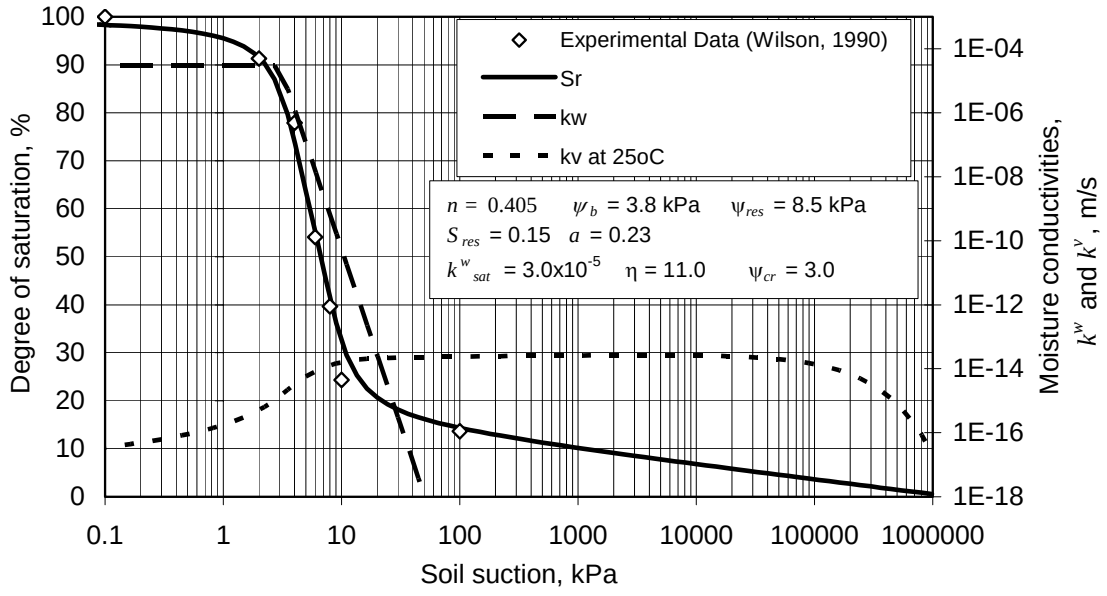

Figure 4.15 Hydraulic properties for the Beaver Creek sand.

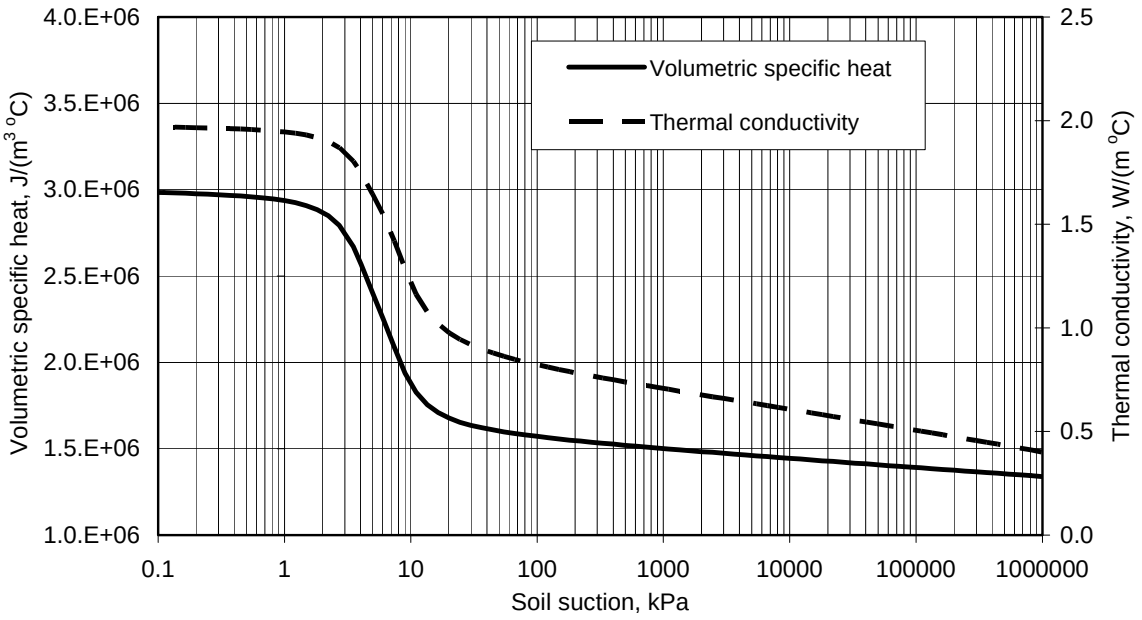

Figure 4.16 Thermal properties for the Beaver Creek sand.

The experiment and the numerical analyses were carried out for a period of 40 days. Figure 4.17 presents the actual evaporation values obtained using the numerical model presented herein along with experimental results from Wilson (1990) and numerical analysis results obtained by Wilson (1990) using the finite difference program "Flux". Close agreement was observed between the all the results. The hydraulic property functions of the sand are extremely steep, and pose a numerical challenge. The automatic mesh and time refinement procedures were able to track the nonlinearities and ameliorate the numerical difficulties in solving the nonlinear system. The computing time required was approximately 20 hours on a Pentium 3 600MHz.

Figure 4.18 presents the pore-water pressure profiles for t = 29 days. Close agreement is observed between the experimental measurements, the results obtained using the Flux program, and the results using the model presented herein. A sharp drying front is observed. The differences between the simulation results and the measured values of soil suction were discussed by Wilson (1990). The pore-water pressure near the ground surface corresponds to a considerably dry condition, and approaches 1,000,000 kPa as time advances. The difficulty in computing extremely low hydraulic conductivities at the drying front were considered the cause of the small differences between computed and measured values.

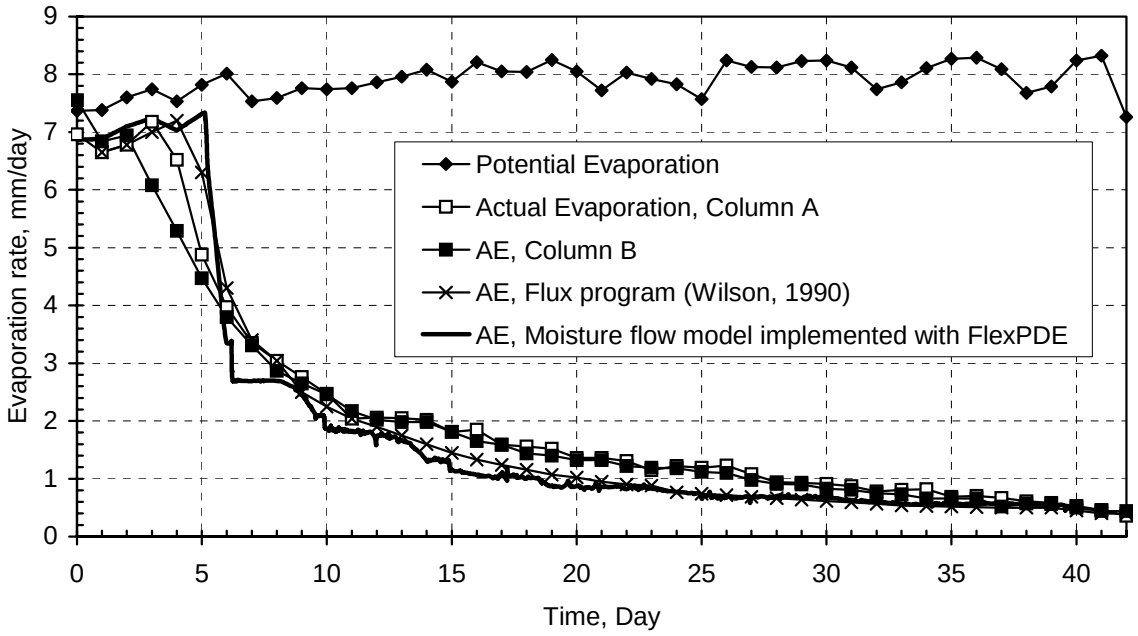

Figure 4.17 Verification of the coupled heat and moisture flow model: evaporation rates.

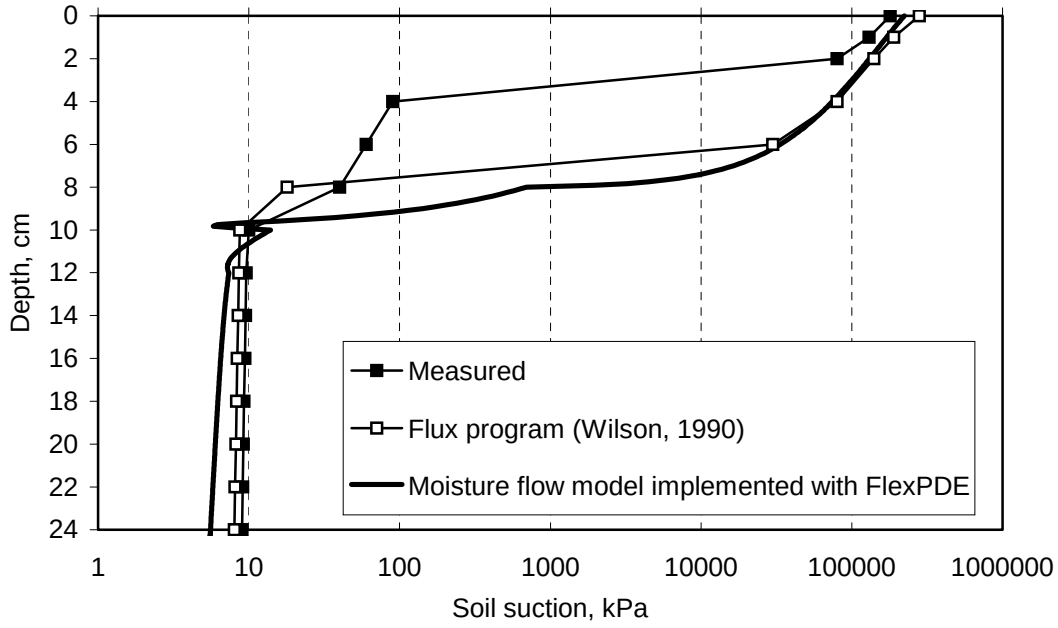

Figure 4.18 Verification of the coupled heat and moisture flow model: pore-water pressure distributions for t = 29 days.

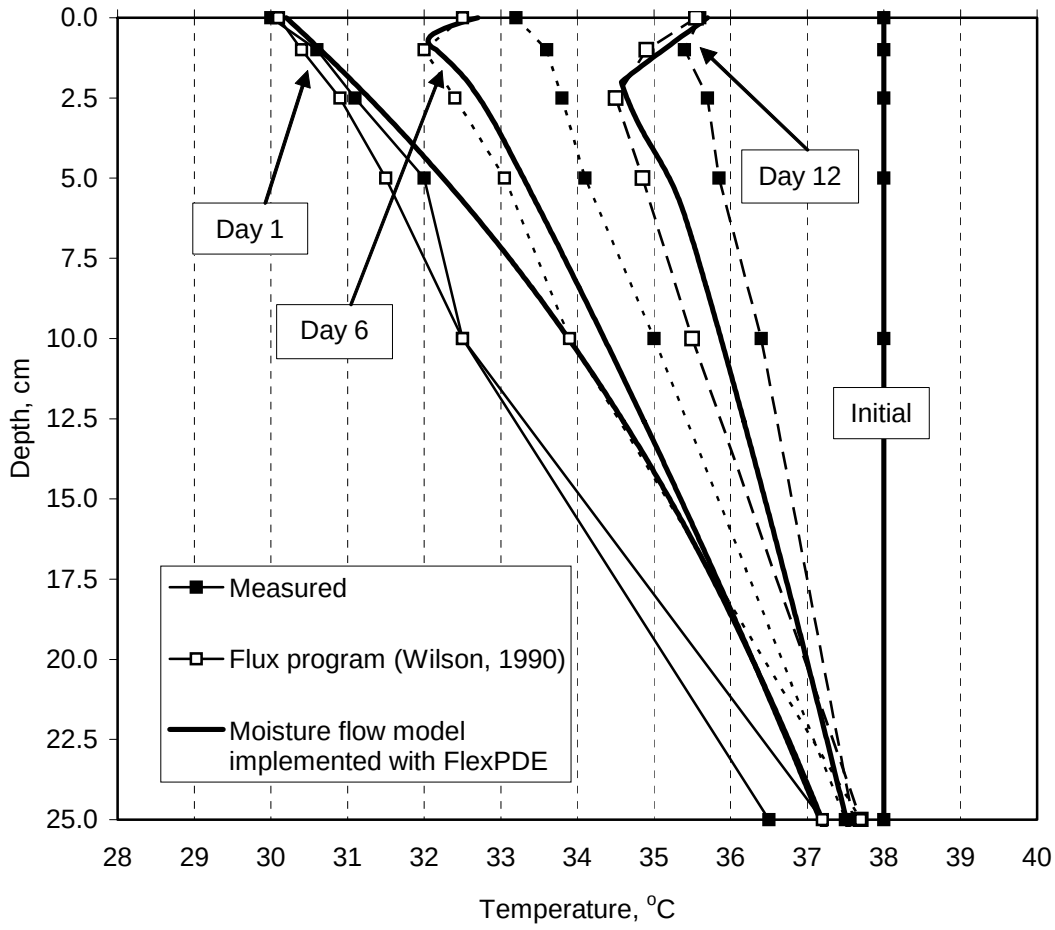

Figure 4.19 Verification of the coupled heat and moisture flow model: temperature distributions for several time steps.

Figure 4.19 presents the temperature profiles for t = 1 day, 6 days, and 12 days. Close agreement is once again observed between the experimental measurements, the results obtained using the Flux program, and the results using the model presented herein. The results obtained using the model presented herein are intermediate, located between the experimental values and the results using the Flux program. The differences between the simulation results and the measured values of temperature were discussed by Wilson (1990). As the soil begins drying, the surface starts to cool, because of the latent heat of vaporization (see profile for day 1 in Fig. 4.19). The profiles for day 6 and 12 show that the cooling front follows the drying front, as expected. In summary, the results of the verification analysis presented in this section show that accurate results were obtained using the moisture flow model implemented using FlexPDE.

4.3.2 *Verification of the slope stability model*

This section presents a series of relatively simple embankment stability analyses designed in order to verify the slope stability model Safe-DP (Stability Analysis based on Finite Element Analysis and using Dynamic Programming). An exact method of slope stability analysis that could be used as comparison does not exist. However, the conventional limit equilibrium method of slices can be considered as an appropriate benchmark. The method of slices has been widely used in geotechnical engineering practice and its results have compared well with field observations (Fredlund and Krahn, 1977).

The Safe-DP results have been compared against the results obtained using Slope/W (Geo-Slope International Ltd., 2002c), a commercially available limit equilibrium slope stability software. The Morgenstern and Price (1965) method of slices and a half-sine interslice shear force function were selected for the analyses using Slope/W. Slope/W uses circular and composite slip surfaces and a "brute force" search procedure to determine the position of the critical circular slip surface. Slope/W has been thoroughly verified by numerous research papers and its results can be adopted as reliable benchmarks (Scoular, 1997).

Slope/W cannot handle nonlinear shear strength envelopes for unsaturated soils. Therefore, a linear envelope defined by c', ϕ', and ϕ^b was used. Safe-DP was simplified in order to accommodate the linear shear strength envelope. The shear strength envelope was defined by the following equation (Fredlund et al., 1978):

$$\tau_f = c' + (\sigma_n - u_a)\tan\phi' + (u_a - u_w)\tan\phi^b \qquad (2.1)$$

where:

ϕ^b = the angle of internal friction with respect to matric suction.

Two soils were used for the verification of Safe-DP; namely, a silty soil and a clayey soil. The properties adopted are presented in Table 4.2. The silty soil has a very low cohesion and a relatively high friction angle while most of the shear strength of the clayey soil is due to cohesion and only a small fraction is related to the friction angle. These two distinct shear strength characteristics are expected to provide different failure mechanisms, particularly when the soil is saturated (i.e., when the shear strength is not influenced by the matric suction).

Table 4.2 Soil properties used in the Safe-DP verification problems.

Soil	Silty soil	Clayey soil
(1)	(2)	(3)
Unit weight, γ_{nat}	20 kN/m^3	20 kN/m^3
Cohesion, c'	2 kPa	20 kPa
Friction angle, ϕ'	30^o	15^o
Friction angle w.r.t. $(u_a - u_w)$, ϕ^b	20^o	10^o
Poisson Ratio, μ	0.40	0.40
Young modulus, E	15,000 kPa	15,000 kPa

The stress distributions required by Safe-DP where obtained by solving the partial differential equations (PDEs) governing static equilibrium for the vertical and horizontal directions and considering plane-strain conditions. The generalised linear Hooke's stress-strain law was assumed, as presented in Chapter 3. The values assumed for the soil parameters associated with Hooke's law (i.e., Young modulus, E, and Poisson ratio, μ) are presented in Table 4.2. The solution of the static equilibrium PDEs using FlexPDE has been thoroughly verified by Vu (2003), with excellent results. Vu (2003) found that the stress fields obtained using FlexPDE are in agreement with analytical solutions for simple cases and are in agreement with the results obtained from other software based on the finite element method, such as Sigma/W (Geo-slope International Ltd., 2002c).

The embankment geometry and boundary conditions used in the finite element stress analysis are presented in Fig. 4.20. An external load of 70 kN/m distributed along 2.5 m (the typical length of railway ties) was used to represent a reasonably high train load being transmitted to the ground through the railway ties. The resulting distributed load is 28 kN/m^2. Three geometries and three pore-water pressure conditions were considered herein, resulting in 9 verification problems for each of the two soil types. A summary of the verification cases is presented in Table 4.3. The selected cases provide a wide range of pore-water pressure conditions. The "wet" slopes, G(1,2,3)-wet, correspond to a pore-water pressure of 0 kPa throughout the embankment. The cases G(1,2,3)-S correspond to a "shallow" water table (W = 2 m) and the cases G(1,2,3)-D correspond to a "deep" water table (W = 8 m). The pore-water pressure distributions defined by water table depths were assumed hydrostatic.

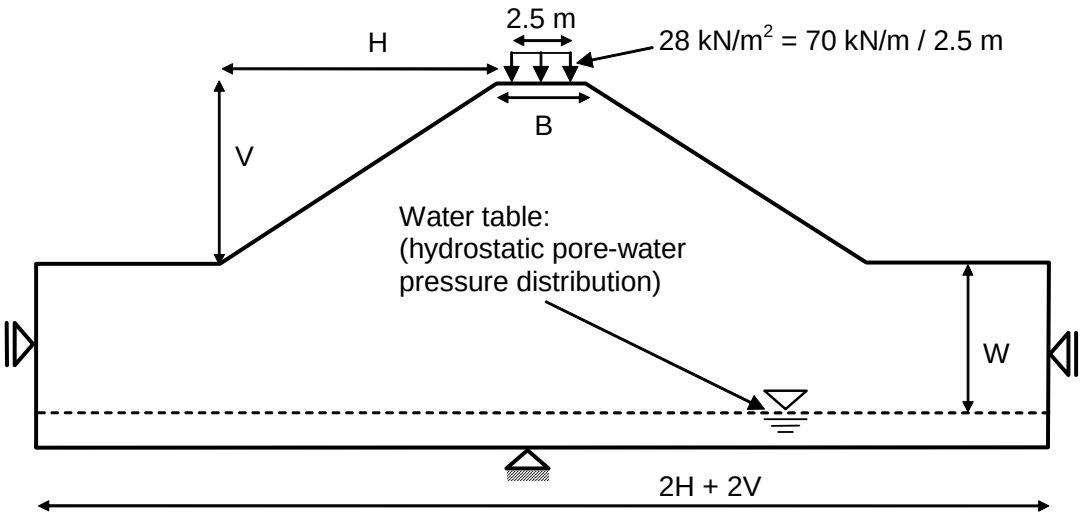

Figure 4.20 Embankment geometry used in the Safe-DP verification problems.

Table 4.3 Embankment geometry and pore-water pressures used in the Safe-DP verification problems: case scenarios.

Case number (1)	B (m) (2)	V (m) (3)	H (m) (4)	H:V (5)	u_w (kPa) (6)
G1-wet	5	5	7.5	1.5H : 1.0V	u_w = 0 kPa
G1-S	5	5	7.5	1.5H : 1.0V	W = 2 m
G1-D	5	5	7.5	1.5H : 1.0V	W = 8 m
G2-wet	5	10	15	1.5H : 1.0V	u_w = 0 kPa
G2-S	5	10	15	1.5H : 1.0V	W = 2 m
G2-D	5	10	15	1.5H : 1.0V	W = 8 m
G3-wet	5	15	22.5	1.5H : 1.0V	u_w = 0 kPa
G3-S	5	15	22.5	1.5H : 1.0V	W = 2 m
G3-D	5	15	22.5	1.5H : 1.0V	W = 8 m

4.3.2.1 *Results for the silty soil embankment*

Table 4.4 presents a summary of the factors of safety obtained for the silty soil embankments. The values of F_s for different embankment heights and pore-water pressure distributions appear consistent with the expected results. The values of F_s decreased as the embankment height was increased and as the pore-water pressure was increased. The maximum difference between the factor of safety obtained using Slope/W (Morgenstern-Price method) and Safe-DP (*Dynamic Programming*) was of 6.19% and can be considered small. The factor of safety obtained using Safe-DP was larger than the factor of safety obtained using Slope/W in all cases, with exception

of case G3-D. Pham (2002) also observed small differences between the results obtained using *Dynamic Programming* and conventional methods of slices. Pham (2002) observed that the factor of safety obtained using *Dynamic Programming* combined with finite element stress fields was larger than the factor of safety from conventional limit equilibrium methods when Poisson's ratio is 0.48 and is smaller when Poisson's ratio is 0.33. The intermediate value of Poisson ratio used herein ($\mu = 0.40$) was expected to produce intermediate values of F_s that could be either larger or smaller then those obtained using Slope/W.

Figures 4.21, 4.22, and 4.23 present the critical slip surfaces obtained using Safe-DP and Slope/W. The slip surfaces obtained using Safe-DP are smooth (without kinks) and show failure mechanisms that can be considered admissible. The larger the soil suction the deeper the critical slip surfaces found, as expected. The position of the slip surfaces obtained using Safe-DP and Slope/W agree well in most cases, even though both methods are based on distinct search procedures. However, the position of the entry and exit points is considerably different in some cases. The differences on the position of the entry and exit points are due to the stress concentrations near the train load and at the toe of the slope, respectively. The shape of the slip surfaces obtained using Safe-DP did not deviate from circular shapes considerably. Nevertheless, the slip surface shape may deviate from a circular shape for certain soil properties, stratigraphy, and stress concentrations (Gitirana Jr. and Fredlund, 2003a).

Table 4.4 Verification examples for the silty soil: factors of safety obtained using Safe-DP (Dynamic Programming method) and Slope/W (Morgenstern-Price method).

Case number	F_s (M - P) (Slope/W)	F_s (DP) (Safe-DP)	$\Delta F_s = F_s(DP) - F_s(M - P)$	$\frac{\Delta F_s}{F_s(M - P)}$, %
(1)	(2)	(3)	(4)	(5)
G1-wet	1.227	1.303	0.076	6.19
G1-S	2.026	2.060	0.034	1.68
G1-D	3.172	3.194	0.022	0.69
G2-wet	1.091	1.127	0.036	3.30
G2-S	1.803	1.845	0.042	2.33
G2-D	2.531	2.539	0.008	0.32
G3-wet	1.037	1.062	0.025	2.41
G3-S	1.718	1.755	0.037	2.15
G3-D	2.249	2.240	-0.009	-0.40

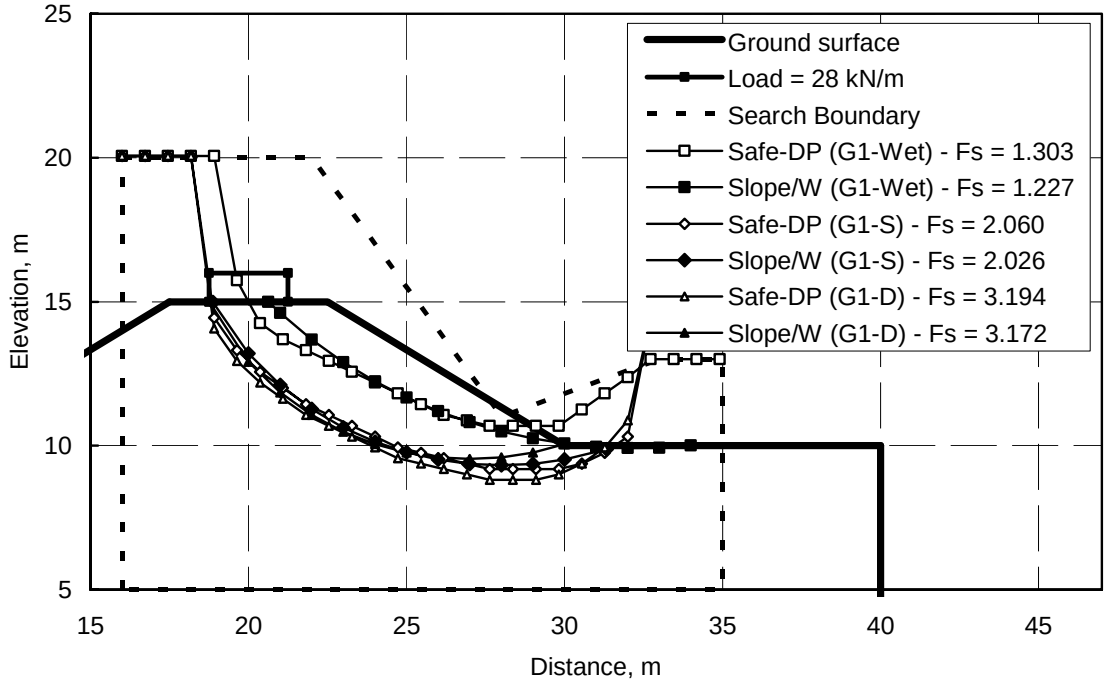

Figure 4.21 Verification examples for the silty soil, using the geometry G1: slip surfaces obtained using Safe-DP (Dynamic Programming method) and Slope/W (Morgenstern-Price method).

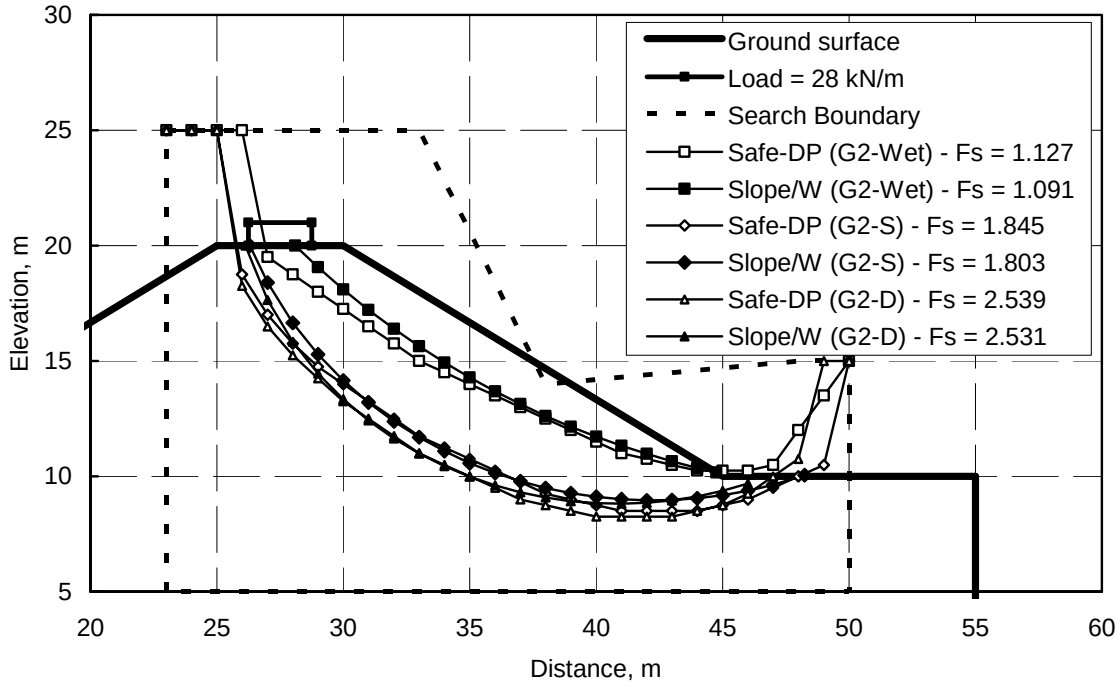

Figure 4.22 Verification examples for the silty soil, using the geometry G2: slip surfaces obtained using Safe-DP (Dynamic Programming method) and Slope/W (Morgenstern-Price method).

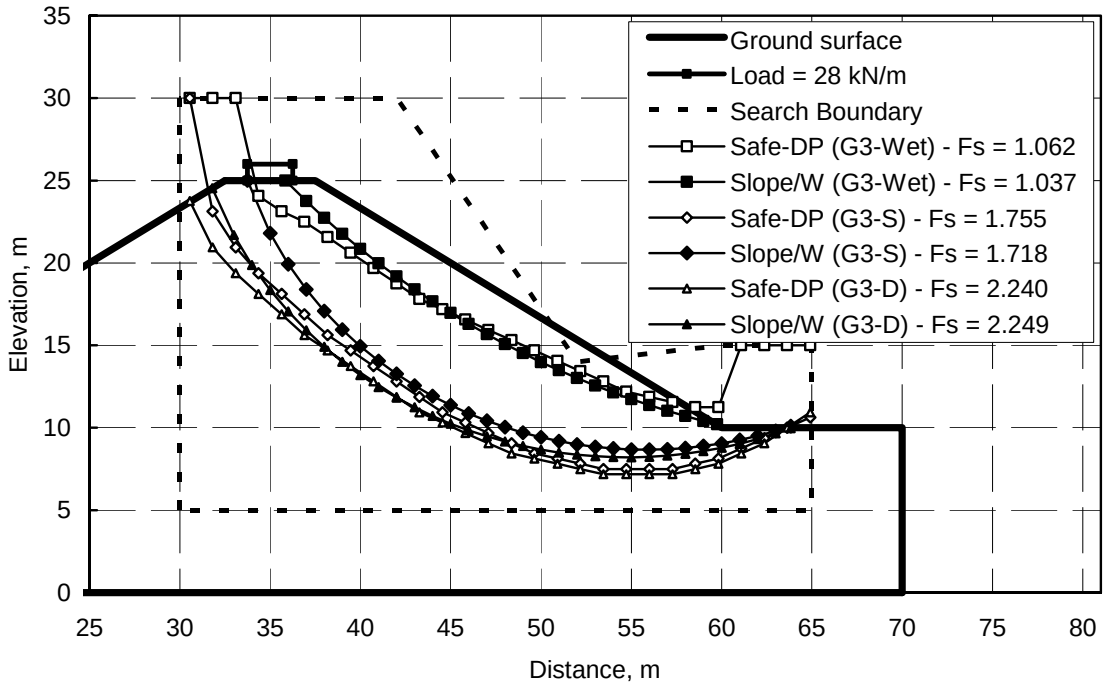

Figure 4.23 Verification examples for the silty soil, using the geometry G3: slip surfaces obtained using Safe-DP (Dynamic Programming method) and Slope/W (Morgenstern-Price method).

4.3.2.2 *Results for the clayey soil embankment*

Table 4.5 presents a summary of the factors of safety obtained for the clayey soil embankments. As for the silty soil embankment, the relative values of F_s for different embankment height and pore-water pressure distributions appear consistent with the expected results. The values of F_s decreased as the embankment height was increased and as the pore-water pressure was increased. The maximum difference between the factor of safety obtained using Slope/W and Safe-DP for the clayey embankment was of 1.99%. The difference was one third of the difference observed for the silty embankment. The factor of safety obtained using Safe-DP was slightly smaller than the factor of safety obtained using Slope/W for half of the cases.

Figures 4.24, 4.25, and 4.26 present the critical slip surfaces obtained using Safe-DP and Slope/W. The slip surfaces obtained using Safe-DP are again smooth (without kinks) and show failure mechanisms that can be considered admissible. The larger the soil suction the deeper the critical slip surface, as expected. The shape and position of the slip surfaces obtained using Safe-DP and Slope/W did not agree well in some cases. The differences in the shape and position of the critical slip surfaces are due to the stress concentrations near the train load and at the toe of the slope and the difference in the stresses used in the analyses.

Table 4.5 Verification examples for the clayey soil: factors of safety obtained using Safe-DP (Dynamic Programming method) and Slope/W (Morgenstern-Price method).

Case number	F_s (M - P) (Slope/W)	F_s (DP) (Safe-DP)	$\Delta F_s = F_s(DP) - F_s(M\text{ - }P)$	$\frac{\Delta F_s}{F_s(M\text{ - }P)}$, %
(1)	(2)	(3)	(4)	(5)
G1-wet	1.703	1.717	0.014	0.82
G1-S	1.954	1.963	0.009	0.46
G1-D	2.489	2.495	0.006	0.24
G2-wet	1.246	1.254	0.008	0.64
G2-S	1.478	1.457	-0.021	-1.42
G2-D	1.804	1.773	-0.031	-1.72
G3-wet	1.046	1.047	0.001	0.10
G3-S	1.256	1.231	-0.025	-1.99
G3-D	1.484	1.461	-0.023	-1.55

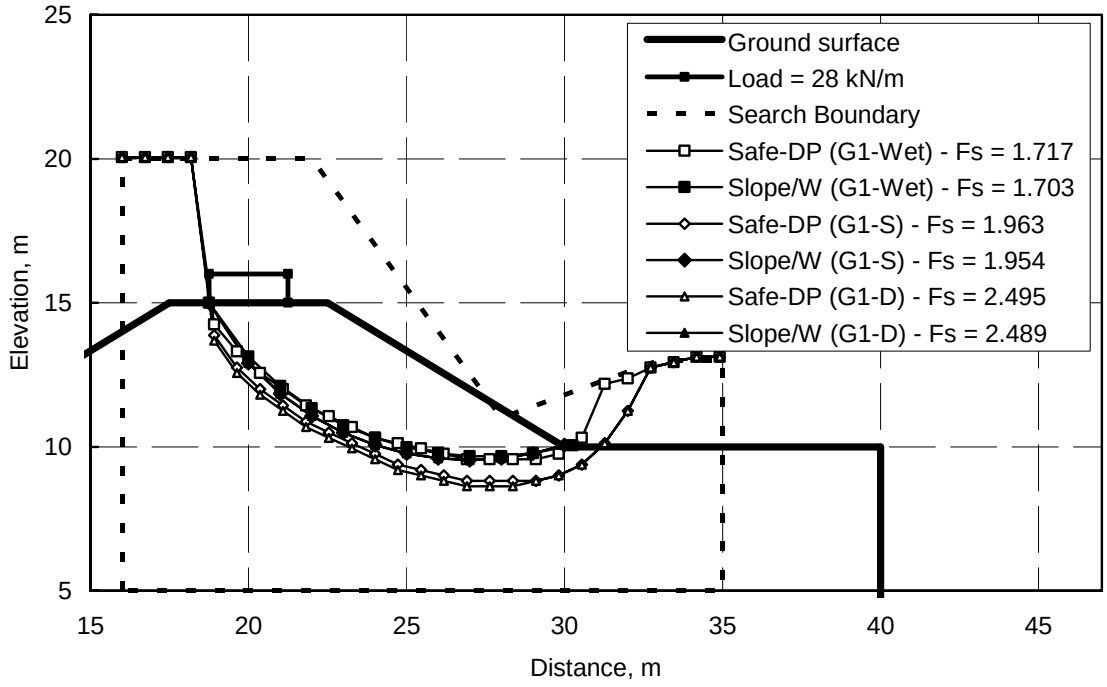

Figure 4.24 Verification examples for the clayey soil, using the geometry G1: slip surfaces obtained using Safe-DP (Dynamic Programming method) and Slope/W (Morgenstern-Price method).

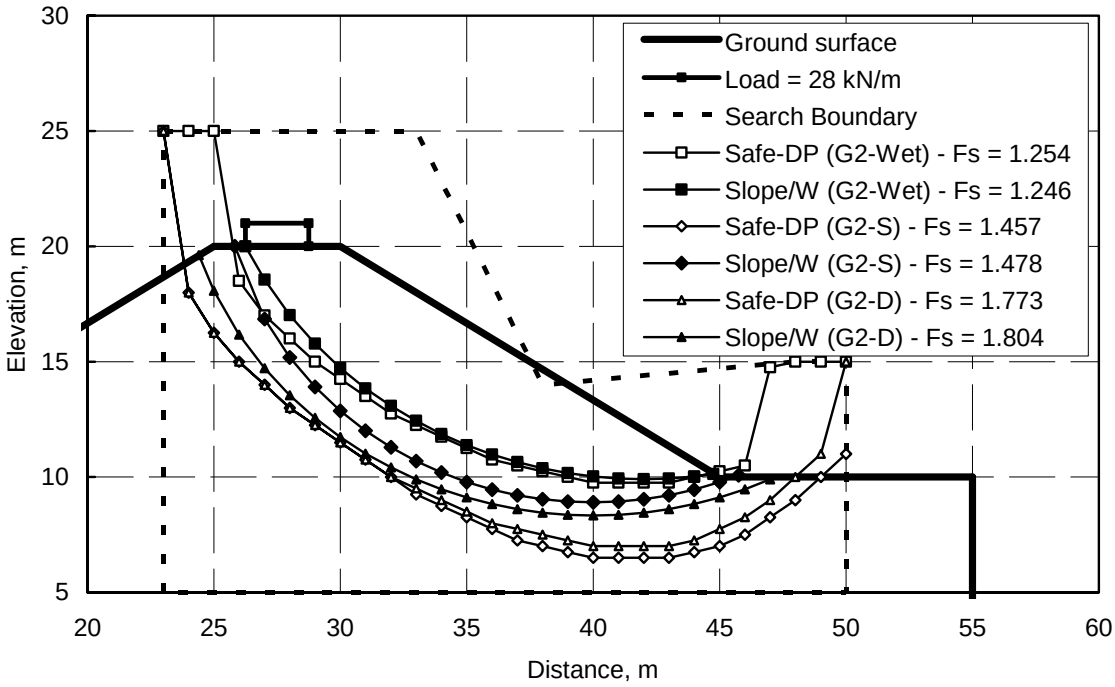

Figure 4.25 Verification examples for the clayey soil, using the geometry G2: slip surfaces obtained using Safe-DP (Dynamic Programming method) and Slope/W (Morgenstern-Price method).

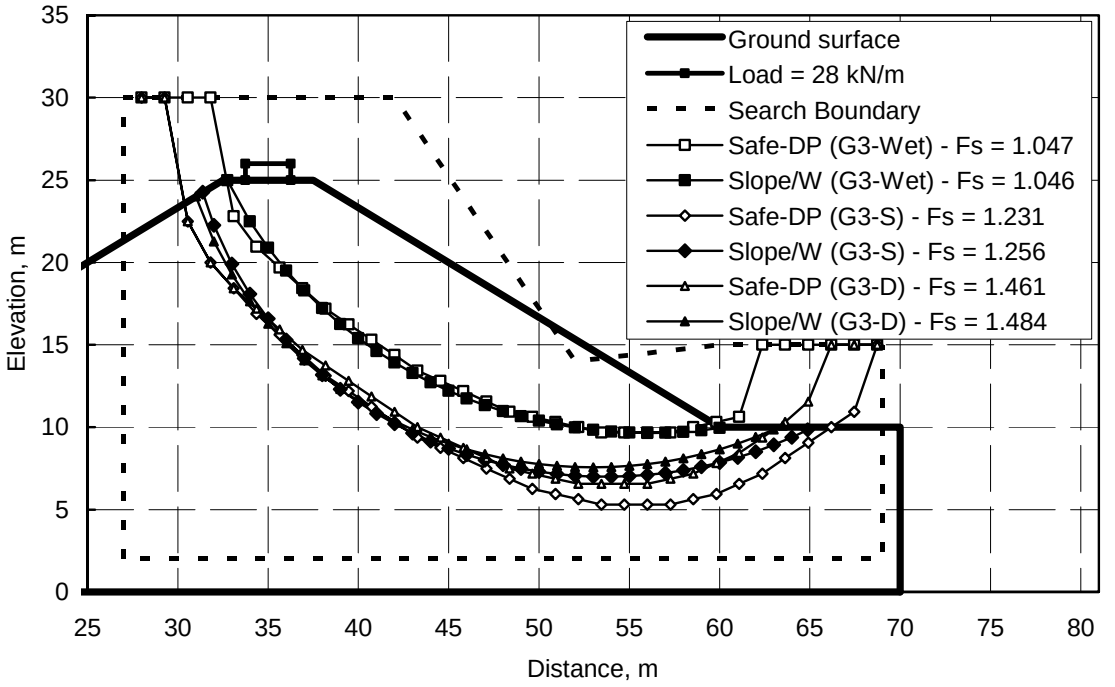

Figure 4.26 Verification examples for the clayey soil, using the geometry G3: slip surfaces obtained using Safe-DP (Dynamic Programming method) and Slope/W (Morgenstern-Price method).

4.4 CHAPTER SUMMARY

This chapter presented the implementation and verification of numerical and analytical models for the solution of the W-GHA model. Section 4.2 presented details about the implementation of the numerical and analytical core for the solution of the W-GHA model. The three main components of the W-GHA model where implemented using different computational tools, appropriate for each case. A general purpose partial differential equation solver named FlexPDE was used for the implementation of a model for coupled heat and moisture flow. The model for stability analysis using Dynamic Programming was implemented in a program written in FORTRAN, named Safe-DP. The partial differential equations governing static equilibrium were implemented using FlexPDE. The total stress distributions are required for the stability analysis using Safe-DP. A spreadsheet routine was implemented for the probabilistic analyses using the point estimate method presented in Chapter 3.

Section 4.3 presented the verification of the numerical and analytical models presented in Section 4.2. Simple problems were designed in order to verify the solutions of the models implemented herein. The results were compared against known solutions and solutions obtained using well-established analytical and numerical models. Close agreement was observed between the results obtained using the numerical and analytical core of the W-GHA model and results obtained using other software, capable of solving the simple problem used for the verification. The analyses presented later in this thesis will make use of the full capabilities of the analytical core of the W-GHA model.

Chapter 5

Statistical Assessment of Unsaturated Soil Properties

5.1 GENERAL

A large number of soil properties are required by the W-GHA model. The probabilistic assessment of weather-related geo-hazards requires the quantification of central tendency values and the knowledge of the variability of the variables involved. It is generally accepted that approximate typical values of parameter variability can be established for each geotechnical parameter. Numerous studies can be found in the literature, suggesting values for the typical variability of saturated soils parameters, usually in terms of the coefficient of variation. Conversely, a limited number of studies are available involving unsaturated soil parameters.

The primary objective of this chapter is to present approximate variability values that can be used in the implementation of the W-GHA model. First, Section 5.2 presents a concise overview of sources of geotechnical uncertainty and a description of some of the most used approaches for the assessment of geotechnical uncertainty. Section 5.3 presents values of saturated soil parameter variability collected from the literature. Section 5.4 presents the core of this chapter, which is the statistical assessment of unsaturated soil properties. The study was based on a large database of soils (SoilVision Systems, 2003) and was performed considering soil groups established based on the USDA classification system and based on the soil texture. Typical central tendency measures, variability measures, and correlation coefficients are established for each soil group. Finally, Section 5.5 presents a summary of the chapter.

5.2 SOURCES OF GEOTECHNICAL VARIABILITY AND VARIABILITY ASSESSMENT APPROACHES

Geotechnical property variability results from several factors. Whitman (1984) identifies four sources of parameter uncertainty; namely, (i) inherent spatial variability; (ii) measurement noise resulting from random testing errors; (iii) "statistical" error in evaluation of mean values because of finite number of samples; and (iv) measurement bias, from sampling disturbance or errors associated with in situ testing. *Spatial variability* and *random testing errors* are characterised as *scatter* in the data. Data *scatter* averages over large soil volumes and its contribution to parameter uncertainty decrease as the volume of the problem increases. The other two sources of variability are *systematic errors* that do not average out over the soil volume and have great influence on the overall uncertainty. Later, Phoon and Kulhawy (1999a) presented a more detailed conceptual model, dividing the sources of parameter uncertainty as soil inherent variability, measurement variability, and estimation model uncertainty (Fig. 5.1). The next section contains some approaches used in the assessment of geotechnical property variability, considering the several existing sources of variability.

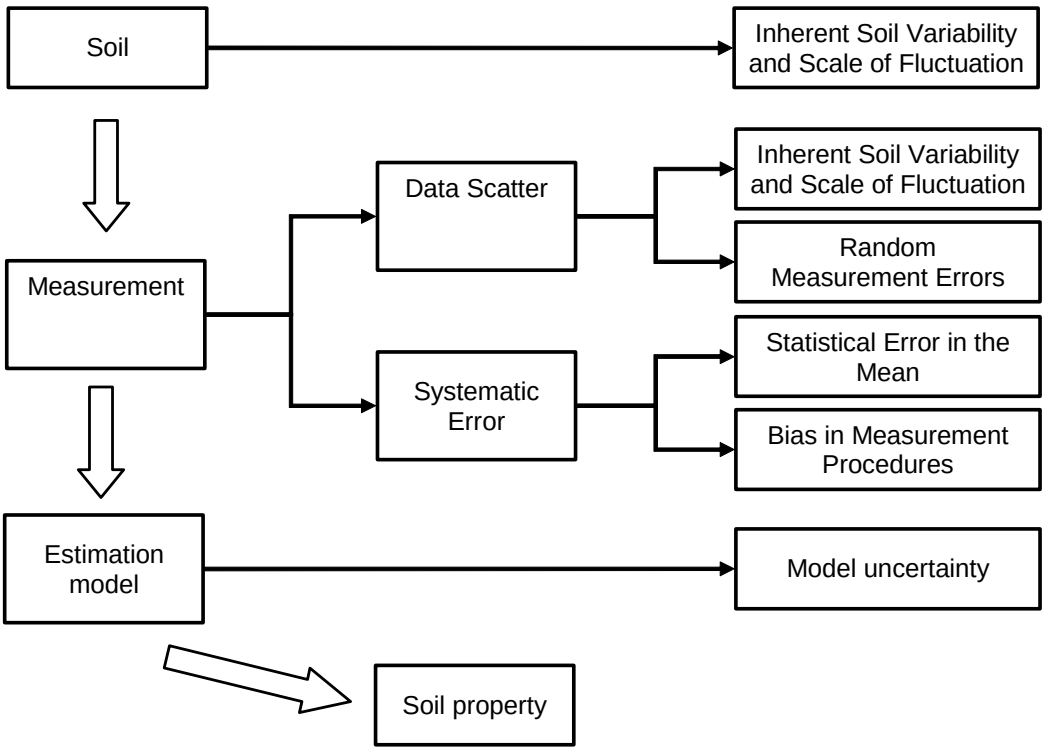

Figure 5.1 Sources of geotechnical uncertainty (modified from Phoon and Kulhawy, 1999a).

5.2.1 *Evaluation of geotechnical uncertainty using descriptive statistics*

A review of descriptive statistics applied in geotechnical engineering problems is presented by Ladd (1983). Basic descriptive statistics is the most fundamental way of assessing geotechnical property variability. Some of the unbiased estimators mostly used in descriptive statistics are presented in the following equations. Equation 5.1 presents the estimator used for the mean of a property x, $E[x]$, also known as the *expected value* or *first moment* of the probability distribution function:

$$E[x] = (1/n)\sum x_i \tag{5.1}$$

where:

x = a random variable;

x_i = samples of x;

n = number of samples.

Equation 5.2 is used for estimating the *variance* or *second moment* of the probability distribution function of x. The measure $Var[x]$ is the mostly used measure of dispersion. The parameter $\sigma[x]$ is defined as the standard deviation, SD, of x.

$$Var[x] = \sigma[x]^2 = [1/(n-1)]\sum (x_i - E[x])^2 \tag{5.2}$$

Estimators for the *covariance*, $Cov[x, y]$, and the *correlation coefficient*, $\rho_{x,y}$, which are measures of the degree of dependency between two different variables, are presented in Eqs. 5.3 and 5.4:

$$Cov[x, y] = [1/(n-1)]\sum (x_i - E[x])(y_i - E[y]) \tag{5.3}$$

$$\rho_{x,y} = Cov[x, y]/(\sigma[x]\sigma[y]) \tag{5.4}$$

where:

y = a random variable;

y_i = samples of y.

Finally, estimators for the *autocovariance*, $C_x(h)$, and the *autocorrelation coefficient*, $R_x(h)$,

which are measures of how well the value of the parameter x at a given point can predict the value at another point separated from the first point by a distance h, are presented in Eqs. 5.5 and 5.6:

$$C_x(h) = [1/(n-1)]\sum (x_i - E[x])(x_{i+h} - E[x]) \tag{5.5}$$

$$R_x(h) = C_x(h)/Var[x] \tag{5.6}$$

where:

h = separation between two points.

The *standard deviation* and *variance* are measures of dispersion that are strongly affected by the first moment (mean) and the scale of the variable x. As a result, standard deviations of different parameters cannot be directly compared. For this reason, the *coefficient of variation*, $CV[x]$, is commonly used as a measure of dispersion:

$$CV[x] = \frac{\sqrt{Var[x]}}{ABS\,|\,E[x]\,|} \tag{5.7}$$

where:

$ABS|\ |$ = absolute value.

The coefficient of variation provides an appropriate measure of parameter variability and is reasonably independent of the mean value. One shortcoming that must be mentioned is that the equation defining $CV[x]$ breaks down if the mean of the variable approaches zero.

Christian et al. (1992) presents a detailed example where field vane test data was used in order to characterise the variability of the undrained shear strength for dikes of the James Bay hydroelectric project. The individual components of uncertainty, as described by Whitman (1984), where carefully estimated. The *scatter* component of variability was divided into *spatial variability* and *measurement noise* by means of an autocovariance function obtained from a large amount of spatially distributed vane tests data from the site being studied (Fig. 5.2). A review of the procedures for calculating the autocovariance functions and basic concepts on geostatistics can be found in Isaaks and Srivastava (1989) and Gitirana Jr. (2000).

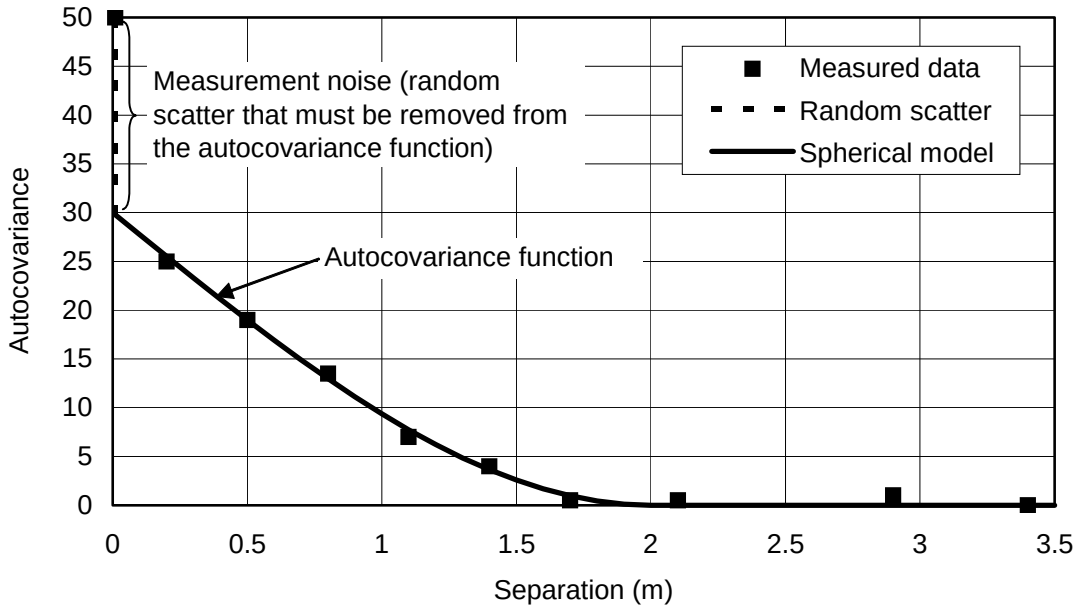

Figure 5.2 Composition of an autocovariance function (modified from Christian et al., 1992).

Unfortunately, a large quantity of data is required in order to obtain an autocorrelation function. Moreover, various issues must be analysed using a considerable amount of subjective judgement in order to define the direction for which the autocorrelation function must be obtained and how many different elevations along the strata should be analysed.

Christian et al. (1992) pointed out that measurement noise should not be included in the slope stability analysis as it is a local phenomenon related mostly to operation and instrument error and does not affect the soil behaviour in the field. However, the removal of measurement noise is controversial. Several authors, such as Phoon and Kulhawy (1999a) suggest that measurement noise must not be removed from the property uncertainty. These authors state that the uncertainty due to measurement noise contributes to the uncertainty in design, even though it may not represent the real soil behaviour in the field.

5.2.2 *Evaluation of geotechnical uncertainty using subjective information*

Dai and Wang (1992) and Duncan (2000) indicate that the *three-sigma rule* is a useful approximation for the evaluation of coefficients of variation of geotechnical properties. Since 99.73% of all values of a normally distributed parameter fall within three standard deviations of

the mean value, the following equation can be used to estimate the coefficient of variation of a parameter:

$$CV[x] = \frac{1}{ABS\,|\,E[x]\,|}\,\frac{HCV - LCV}{6} \tag{5.8}$$

where:

HCV	=	the highest conceivable value of the parameter *x*;
LCV	=	the lowest conceivable value of the parameter *x*.

Studies have shown that there is a tendency to subjectively estimate ranges of conceivable values that are smaller than the real ranges. Duncan (2000) observes that with practice and experience, the subjective estimation exercise should become more accurate. Duncan (2000) also suggests that "an effort should be made to make the range of conceivable values as wide as seemingly possible or even wider, to overcome the natural tendency to make the range too small." According to Harr (1987) and Duncan (2000), since the *three-sigma rule* is applicable to other distributions, Eq. 5.8 can be used if the parameter follows other probability density functions.

5.3 TYPICAL VARIABILITY OF SATURATED SOIL PROPERTIES

The components of soil property uncertainty can be evaluated using conventional descriptive statistics, as shown in the previous section. Unfortunately, conventional descriptive statistics are rarely employed in geotechnical engineering practice, as it requires large quantities of data. The assessment of scales of fluctuation requires an even larger number of measurements. The number of samples and tests required in order to obtain values of statistical significance is prohibitive for most projects, both in terms of costs and available time. The hazard assessment for a large railway system is even more critical because of the size of the system. As a result, property uncertainty is often estimated based on published values of typical variability and the separation of the distinct sources of uncertainty is rarely done.

The statistical characterization of saturated geotechnical properties has been studied by several researchers. The definition of a probability density function, expected value, and the coefficient

of variation usually suffice in order to characterize a geotechnical property. The expected value may vary considerably for each soil, even within a soil classification group. However, the probability density function shape and the coefficient of variation of each soil property vary considerably less. As a result, it has been advocated by several authors that probabilistic approaches in geotechnical engineering can be successfully performed based on fixed typical values of coefficient of variation and probability density function shapes, established based on experience (Harr, 1987).

Table 5.1 presents a compilation of values of coefficient of variation from published data. The ranges presented cover all the values provided by the several sources cited. The parameters of greatest interest are the shear strength parameters and the saturated hydraulic conductivity. Whitman (1984) observes that the coefficient of variation of effective shear strength as a whole varies from 10% to 15%, but points out that larger coefficients of variation are observed when cohesion is significant. The shear strength parameters of natural soils are usually considered normally distributed (Lumb, 1966) or beta distributed (Lumb, 1976, Alfaro and Harr, 1981). Lumb (1966) observed that the coefficient of internal friction, tan(ϕ'), is generally better described by a normal distribution than is the angle of internal friction, ϕ'. However, several other authors have advocated the use of ϕ' instead of tan(ϕ') (Harr, 1987).

The hydraulic conductivity is typically assumed to follow a lognormal probability density function. Nielsen et al. (1973), Freeze (1975), Hoeksema and Kitadinis (1985), and Gui (2000), among others, have used lognormal distributions for the hydraulic conductivity. Nielsen et al. (1973) observed that even seemingly uniform land areas manifest large variations in hydraulic conductivity values. Variations in texture, unit weight, and water content are much less variable.

Phoon and Kulhawy (1999a) presented a detailed study about the characterisation and evaluation of geotechnical property variability. An extensive literature review was conducted to collect information required to determine inherent soil variability, scales of spatial fluctuation, measurement error variability, and transformation uncertainty. Typical scales of fluctuation, required to compute variance reduction by spatial averaging, can be found in Phoon and Kulhawy (1999a).

Table 5.1 Compilation of values of coefficient of variation of saturated soil properties obtained from the literature.

Property (1)	Coefficient of variation, *CV* (2)	Source (3)
Porosity, n	10%	Schulze (1971)
Void ratio, e	10 – 20%	Krahn and Fredlund (1983)
Unit weight, γ_{nat}	3 – 7%	Hammitt (1966), Kulhawy (1992), Tan et al. (1993)
Friction angle, ϕ'	7 – 12%	Schulze (1971), Lacasse and Nadim (1997), Duncan (2000), Phoon and Kulhawy (1999a)
Friction angle, $tan(\phi')$	5 – 25%	Lumb (1966), Tan et al. (1993)
Cohesion, c'	10 – 50%	Fredlund and Dahlman (1971), Harr (1987), Kulwahy (1992), Tan et al. (1993), Lacasse and Nadim (1997), Phoon and Kulhawy (1999a), Duncan (2000)
Undrained strength, S_u	50 – 80%	Krahn and Fredlund (1983), Phoon and Kulhawy (1999a)
Saturated water coefficient of permeability, k^w_{sat}	68 – 90%	Nielsen et al. (1973), Duncan (2000)
Unsaturated water coefficient of permeability, k^w	130 – 240%	Nielsen et al. (1973), Benson et al. (1999)
Preconsolidation pressure, σ'_p	10 – 35%	Padilla and Vanmarcke (1974), Lacasse and Nadim (1997), Duncan (2000)
Compression index, C_c	10 – 37%	Lumb (1966), Padilla and Vanmarcke (1974), Krahn and Fredlund (1983), Kulwahy (1992), Duncan (2000)

5.4 STATISTICAL ASSESSMENT OF UNSATURATED SOIL PROPERTIES USING A SOILS DATABASE

Saturated and unsaturated soil property variability must be determined in order to implement the W-GHA model into practice. The previous section has presented a collection of typical coefficients of variation for several geotechnical properties related to the behaviour of saturated soils. Unfortunately, only few reports of statistical assessments of unsaturated soil properties can be found in the literature, with limited practical applicability.

Confidence bands are often used in the statistical characterization of functions (Bates and Watts, 1988). A relatively rigorous statistical characterisation of the curve variability is obtained by means of confidence bands. Such an approach was applied to the statistical characterisation of the SWCC by Mishra et al. (1989) and Zapata et al. (2000). Confidence bands were obtained for the SWCC, based on regression analyses. The variability of the curve was obtained according to the position along the curve. Unfortunately, such approach is not practical in terms of reliability analysis. Reliability analysis can only be applied in practice if property variability is characterised in terms of the variability of a finite and relatively small number of curve parameters.

This section presents a statistical study of the unsaturated soil properties required by the W-GHA model. Appropriate soil property functions with a relatively small number of soil parameters were adopted. The main objectives of the study undertaken were: (i) to perform normality tests on the unsaturated soil parameters; (ii) to establish typical central tendency values for the unsaturated soil parameters; (iii) to establish the typical variability of the unsaturated soil parameters; and (iv) to study the correlation between the unsaturated soil parameters. The measures of variability presented herein are aimed at giving a general indication of the typical variability of unsaturated soil properties, given that crude information about soil texture is available.

In order to achieve these objectives, a relatively large number of soil records were randomly mined from a soils database called SoilVision (SoilVision, 2003). A total of 186 soil record samples were selected. These soil records pertain to diverse soil formations, with distinct characteristics. The sampled records were grouped according to their textural characteristics, in order to establish distinct "populations". Ideally, the statistical assessment of individual "soil types" would be preferable (Fredlund and Dahlman, 1971), even though the definition of the

term “soil type” is not totally precise. The separation of individual soil types is aimed at grouping soils with similar engineering behaviour. Nevertheless, soil behaviour depends also on the soil genesis, mineralogy, plasticity, micro- and macro-structure, and stress history.

The typical central tendency values and variability obtained for each soil group will be used as an aid in the design of the sensitivity analyses cases presented in the next chapter. The soil variability will be characterised in terms of coefficients of variation and standard deviations. The coefficients of variation and standard deviations presented herein include diverse sources of uncertainty. Individual sources of parameter variability could not be assessed. Nevertheless, the presented standard deviations and coefficients of variations serve as a general indication and as a first approximation. The information presented herein can be refined in future studies, as more information is collected and organised using an appropriate database of soils. The results presented serve also as a starting point that can be combined with a Bayesian update approach for statistical assessment of geotechnical properties.

The next section will present the statistical assessment methodology adopted. Later, a detailed presentation and analysis of the statistical assessment of unsaturated soils properties will be given. Normality tests will be used to define whether the normal of lognormal distributions can be used to represent each unsaturated soil property. Typical central tendency values for each soil group will be presented. Finally, coefficients of variation and correlation matrices will be presented, for the parameters studied. The last section presents and overview of the results obtained and a concise description of the suggested typical mean values and variability of unsaturated soil parameters.

5.4.1 *Methodology for the statistical assessment of unsaturated soil properties*

This section presents the statistical assessment methodology adopted herein. First, the properties studied will be listed, along with the criteria for selection of data records. Then, a detailed description of the fitting equations and soil parameters adopted will be presented, along with the soil grouping criteria.

5.4.1.1 *Soil properties studied and criteria for selection of data records*

Chapter 3 presented a summary of the soil properties required by the W-GHA model. The unsaturated soil properties presented in Table 3.1 can be determined following three main approaches, illustrated in Fig. 3.14:

(i) direct measurement of all unsaturated soil properties (laboratory or field testing);
(ii) direct measurement of the soil-water characteristic curve and estimation of the remaining unsaturated soil properties based on the soil-water characteristic curve;
(iii) estimation of all unsaturated soil properties based the grain-size distribution and on the estimated soil-water characteristic curve.

The properties studied herein are the soil-water characteristic curve, SWCC, and the hydraulic conductivity function. Though some studies have been undertaken (Mishra et al., 1989, Zapata et al., 2000), the uncertainty associated with the prediction methods mentioned in items (ii) and (iii) above is not fully understood yet. Therefore, only directly measured data were used for the statistical assessment of unsaturated soil properties.

The majority of the SWCC and hydraulic conductivity data available in the SoilVision database correspond to drying tests. Chapter 3 presents the theory and simplifications required in order to embrace wetting and drying cycles in the assessment of weather-related geo-hazards. The theory presented in Chapter 3 is based on drying curves. Therefore, it was decided to select only drying curves from the SoilVision database, in order to have consistent data for the statistical analyses.

The vapour conductivity, thermal properties, and shear strength were not analysed in the same fashion as the SWCC and hydraulic conductivity function for two reasons. First, very limited data for these properties are available in the SoilVision database, making a meaningful statistical study unfeasible. Secondly, these unsaturated soil properties can be treated as variables dependent on the soil-water characteristic curve. Relatively satisfactory prediction equations are available, based on the soil-water characteristic curve. These predictive equations were presented in Chapter 3. As a result, the statistical assessment of the soil-water characteristic curve becomes of primary importance for the application of the W-GHA model.

The hydraulic conductivity function could also be treated as a variable dependent on the SWCC. Chapter 3 presented a concise review of hydraulic conductivity prediction methods and described in detail the equation proposed by Brooks and Corey (1964). There are a considerable number of prediction methods available in the literature. Nevertheless, a large amount of directly measured hydraulic conductivity data is available in the SoilVision database, justifying an independent analysis.

The number of records sampled from the SoilVision database was limited by the number of available "complete" soil records. To be considered "complete", a soil record was required to present the grain-size distribution, the soil porosity, n, the drying soil-water characteristic curve, the saturated hydraulic conductivity, and the hydraulic conductivity function. The porosity was required in order to obtain the total water storage. The grain-size distribution was required in order to classify each soil record and form groups of similar soils. A total of 186 soil records were sampled from a total of 520 "complete" records.

5.4.1.2 *Fitting equations and corresponding soil parameters*

The properties analysed herein (i.e., the soil-water characteristic curve and the hydraulic conductivity function) are nonlinear soil property functions (see Figs. 5.3, 5.4 and 5.5) and are function of the soil suction. These soil property functions can be described using various equations with different soil parameters (Fredlund and Xing, 1994). The soil parameters can be treated as fitting parameter and a nonlinear fitting algorithm can be employed in order to obtain the best-fit parameters for a given data set. This section presents the fitting equations and parameters used to define the SWCC and the hydraulic conductivity function.

Soil-water characteristic curve

The soil-water characteristic curves were fitted using the unimodal equations proposed by Gitirana Jr. and Fredlund (2004). Appendix D presents a description of these equations, along with parametric analyses showing the role of each SWCC parameter and the fitting capabilities. Two equations were used herein; namely, unimodal equation with two bending points and unimodal equation with one bending point. The number of fitting parameters corresponds to the number of features of the shape of typical SWCC's. Figure 5.3 shows that four shape features define a SWCC with two bending points. The primary shape features are the following:

ψ_b air-entry value;

ψ_{res} residual suction;

S_{res} residual degree of saturation;

a parameter defining the sharpness of the transition at the two bending points.

The physical meaning of the parameters ψ_b, ψ_{res}, S_{res}, and a is discussed in greater detail in Appendix D. In addition to the four parameters above, other SWCC parameters can be defined. For instance, Fig. 5.3 indicates the two following additional parameters: λ_d, the primary drainage slope; and λ_{res}, the residual drainage slope.

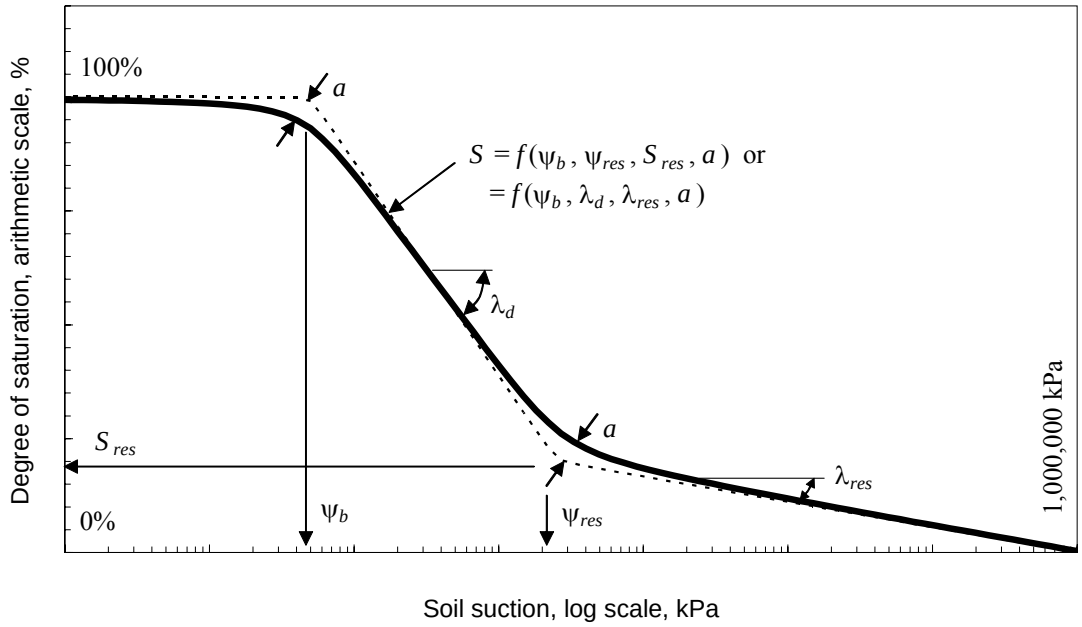

Figure 5.3 Idealization of a unimodal soil-water characteristic curve with two bending points.

The primary and residual drainage slopes can be obtained as function of the parameters ψ_b, ψ_{res}, S_{res}, using the following equations:

$$\lambda_d = \frac{1 - S_{res}}{\log_{10}(\psi_{res}/\psi_b)} \tag{5.9}$$

$$\lambda_{res} = \frac{S_{res}}{\log_{10}(1{,}000{,}000/\psi_{res})} \tag{5.10}$$

Conversely, the soil-water characteristic curve parameters S_{res} and ψ_{res} can be calculated based on ψ_b, λ_d, and λ_{res}, using the following equations:

$$S_{res} = \frac{\lambda_{res}}{\lambda_d - \lambda_{res}}\left[\lambda_d \log_{10}\left(\frac{1{,}000{,}000}{\psi_b}\right) - 1\right] \tag{5.11}$$

$$\psi_{res} = \psi_b 10^{\frac{1-S_{res}}{\lambda_d}} \tag{5.12}$$

The primary drainage slope, λ_d, indicates how spread the pore-size distribution is. The more uniform the pore-size distribution is (i.e., the less spread the pore-size distribution is) the steeper

the primary drainage slope is. The residual drainage slope, λ_{res}, bears not as much physical meaning as λ_d does. Nevertheless, the residual drainage slope indicates to a certain extent the amount of water held by the soil particles by forces other than capillary forces.

Regardless of the parameters chosen to describe the SWCC, four parameters must be used because there are four distinct shape features. The use of a number of parameters lower than four would impose restrictions to the SWCC shape and the use of a number of parameters larger than four would involve redundant parameters. It was decided to define the SWCC's using the set of parameters ψ_b, λ_d, λ_{res}, and a.

Several sets of parameter (i.e., multivariate estimate points) are used in probabilistic analyses using the approach presented in Chapter 3. Difficulties could arise in probabilistic analyses using estimate points of ψ_b and ψ_{res} simultaneously. Depending on the variability of ψ_b and ψ_{res} and on the difference between ψ_b and ψ_{res}, some sets of estimate points could involve values of ψ_b and ψ_{res} for which $\psi_b > \psi_{res}$. The use of constraints to prevent $\psi_b > \psi_{res}$ would be mathematically cumbersome. On the other hand, simple constraint could be used for λ_d if necessary. Therefore, the set of parameters ψ_b, λ_d, λ_{res}, and a was deemed the most appropriate. As will be shown later, the parameter a can be considered as a fixed value. Appropriate values of a will be selected for each soil type.

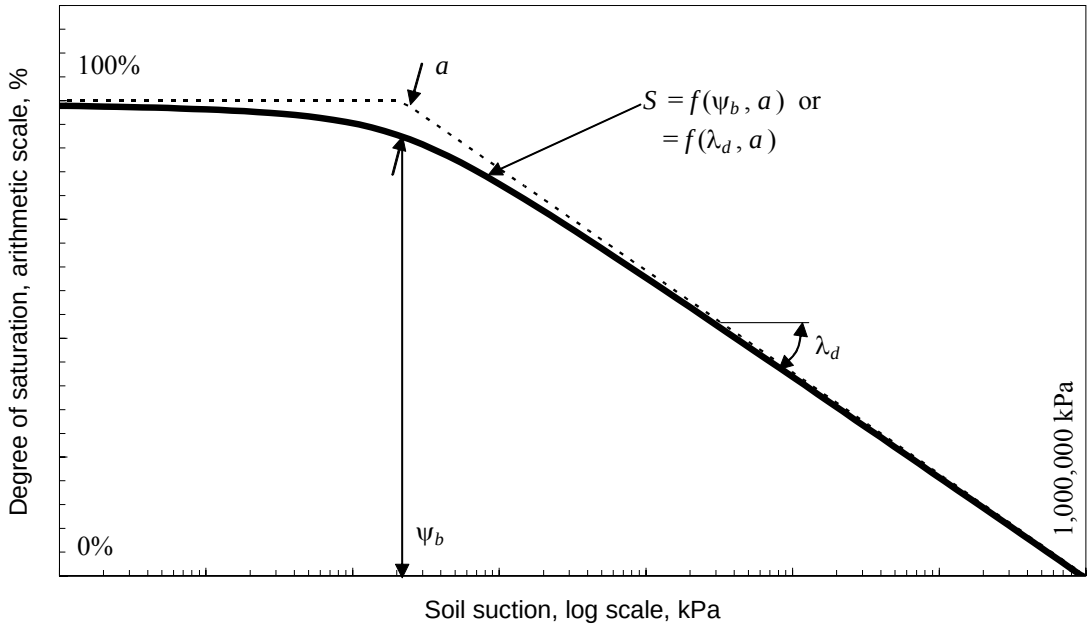

Figure 5.4 Idealization of a unimodal soil-water characteristic curve with one bending point.

Most soil types generally have soil-water characteristic curves with two bending points, as shown in Fig. 5.3. A preliminary examination of the sampled record data confirmed this observation. It was observed, however, that most soils classified as clays have soil-water characteristic curves with only one bending point and do not present a distinguishable residual point. Most clay soils have soil-water characteristic curves that can be defined by two parameters, ψ_b and a or λ_d and a, as shown in Fig. 5.4. Therefore, the clay sampled records were fitted using the unimodal equation with one bending point (see Appendix D). It was decided to define the unimodal SWCC's with one bending point using the parameters ψ_b and a.

Hydraulic conductivity function

The hydraulic conductivity functions were fitted using a bi-linear function on a log versus log plot (Fig. 5.5). The bi-linear shape was found to fit reasonably well most experimental curves. The first portion of the curve is defined by a constant value, equal to the saturated hydraulic conductivity, k^w_{sat}. The value of k^w_{sat} was not treated as a fitting parameter in most analysis steps, but as an independent fixed measurement present in each "complete" sampled record. The second portion of the curve was assumed to be a straight line on a log of soil suction versus log of hydraulic conductivity plot and defined by a constant slope, η. The bi-linear equation used is as follows:

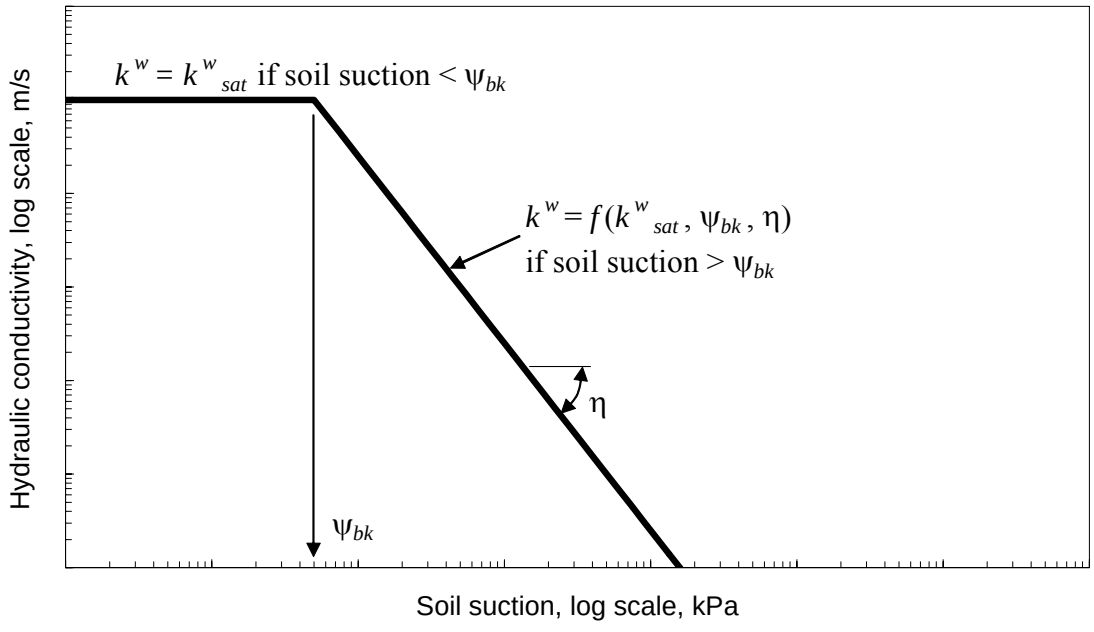

Figure 5.5 Idealization of a hydraulic conductivity function.

$$k^w = k^w_{sat} \quad \text{for } (u_a - u_w) \le \psi_{bk}$$
$$k^w = k^w_{sat} \left[\psi_{bk} / (u_a - u_w)\right]^{\eta} \quad \text{for } (u_a - u_w) > \psi_{bk} \tag{5.13}$$

where:

k^w	=	hydraulic conductivity;
k^w_{sat}	=	saturated hydraulic conductivity;
$(u_a - u_w)$	=	matric suction;
ψ_{bk}	=	break point in the hydraulic conductivity function;
η	=	slope of the hydraulic conductivity function.

Equation 5.13 resembles the equation proposed by Brooks and Corey (1964), where η is defined by the pore-size distribution index obtained from the soil-water characteristic curve. In theory, the break point, ψ_{bk}, corresponds to the air-entry value, ψ_b. However, the air-entry value obtained from the SWCC fitting does not match the break point observed in the hydraulic conductivity function in numerous sampled records as will be shown later. The use of $\psi_{bk} = \psi_b$ would compromise the fitting capability of Eq. 5.13 and an accurate measure of η would not be obtained for those soil records for which ψ_{bk} is significantly different than ψ_b. As a result, it was decided to perform the fitting of the hydraulic conductivity function independently of the soil-water characteristic curve fit (i.e., not using the same air-entry value).

In summary, the following soil parameters will be statistically assessed: n, ψ_b, λ_d, λ_{res}, k^w_{sat}, ψ_{bk}, and η. As mentioned previously, the parameter "a" will be assumed as a fixed value, chosen for each soil type. The data records sampled from the SoilVision database were imported into MS Excel 97^{tm}. The fitting of the soil-water characteristic curves and hydraulic conductivity functions was performed by minimizing the sum of the squared residuals (SSR) between the experimental data and the fitting curve. The nonlinear minimization solver available in MS Excel 97^{tm} was utilized. The nonlinear fitting application appeared to perform well provided that the initial guesses were sufficiently close to the fitting parameters. Other minimization techniques are available and some of them are described in detail by Fredlund and Xing (1994).

5.4.1.3 *Soil grouping using the USDA textural classification system*

Important information can be obtained from statistical analyses of sampled records organised according to "soil types". Several criteria and soil characteristics can be used to establish such

soil types. The two main soil characteristics used in geotechnical engineering practice for soil classification are the textural characteristics and Atterberg limits. Significant correlation exists between the hydraulic properties and the textural percentages of sand, silt, and clay. In fact, the textural characteristics are generally considered the main factor governing the hydraulic behaviour of soils. Other important but more difficult to quantify characteristics that can be taken into account in soil characterization and classification are soil genesis, mineralogy, micro- and macro-structure, and stress history.

Two of the most used soil classification systems are the USDA system (Soil Survey Staff, 1975) and the Unified Soil Classification System, USCS, (ASTM, 1993). The USDA system is based solely on textural fractions, while the USCS is based on both textural fractions and the Atterberg limits. The USCS system is generally preferred by geotechnical engineers but other systems are often used and deemed acceptable (such as the USDA system). The number of "complete" records in the SoilVision database presenting the Atterberg limits is small, making the use of the USCS system unfeasible in this study. As a result, the USDA system has been adopted herein.

Figure 5.6 presents the textural diagram which is used by the USDA system for the classification of soils (Soil Survey Staff, 1975) along with the soil data records sampled from the SoilVision database. The percentages of sand, silt and clay plotted in Fig. 5.6 were defined by the following grain-size intervals:

Clay	< 0.002 mm
Silt	$0.002 \leq x < 0.05$ mm
Sand	$0.05 \leq x < 2$ mm
Coarse	$2 \leq x < 300$ mm

Three main groups are identified in the diagram showed in Fig. 5.6; namely, sands (Sa), loams (L), and clays (C). The silt and silty fractions (Si) are placed within the loam fraction. The number of sampled records pertaining to each main soil group is 62, making a total of 186 sampled records. Several soil samples have the same grain-size distribution making the number of sampled records shown in Fig. 5.6 appear to be less than 186. Each of the three main soil groups is subdivided into a number of subgroups. Statistical analyses to each soil subgroup can be also performed, though an insufficient number of sampled records is found in certain subgroups, notably the silts group (Si), Silt Clay Loam group (Si-C-L), Clay Loam group (C-L), and the Sand Clay group (Sa-C).

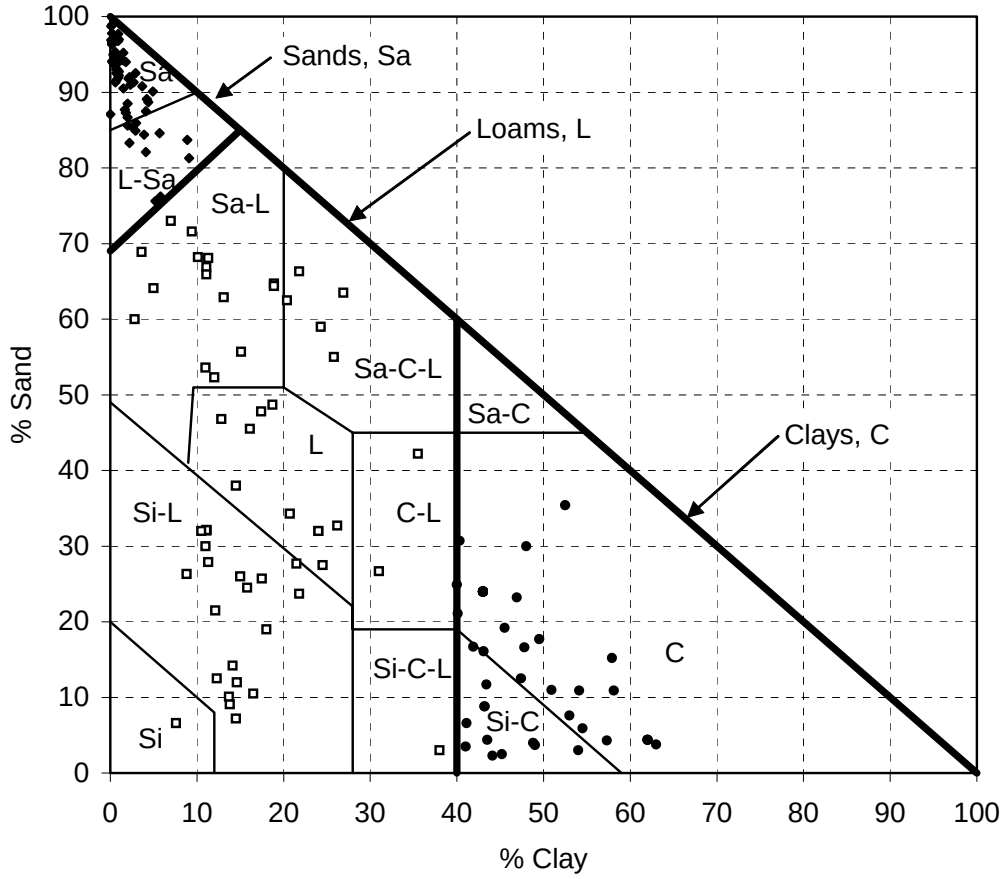

Figure 5.6 Sampled soil records classified according to the USDA classification system.

5.4.2 *Results and analysis of the statistical assessment of unsaturated soil parameters*

The statistical assessment of unsaturated soil properties was performed according to the methodology presented in the previous section. Figures 5.7 and 5.8 present how the soil-water characteristic curve and the hydraulic conductivity function can be statistically characterised based on the statistical characterisation of the soil parameters ψ_b, λ_d, λ_{res}, k^w_{sat}, ψ_{bk}, and η. Each curve parameter can be considered as a random variable with a certain frequency distribution, as indicated in Figs. 5.7 and 5.8. The frequency distributions can be statistically characterized based on statistical descriptive measures. Such an approach is similar to what has traditionally been done for other soil property functions, such as the shear strength envelope (Lumb, 1966, 1970, Whitman, 1984, Christian et al. 1994, Phoon and Kulhawy, 1999b, to name only a few).

The statistical characterization of the parameters defining the SWCC and hydraulic conductivity function involved several steps, briefly mentioned earlier in this chapter. First, the soil

parameters n, ψ_b, λ_d, λ_{res}, k^w_{sat}, ψ_{bk}, and η were collected/determined for all sampled records. Fitting analyses of the SWCC's and hydraulic conductivity functions were performed to each sampled records. The 186 data sets used in the analyses are presented in Figs. 5.11 to 5.16. The following soil parameters were obtained through the fitting analyses of each soil record: ψ_b, ψ_{res}, S_{res}, ψ_{bk}, and η. The parameters λ_d and λ_{res} were calculated based on Eqs. 5.9 and 5.10. The parameters n and k^w_{sat} were not treated as fitting parameters and were obtained directly from the SoilVision database. The parameters obtained are presented in Table D.1 of Appendix D. The value of the parameter "a" was fixed. A value a equal to 0.075 was selected for Sands, a equal to 0.050 for Loams, and a equal to 0.025 for Clays. The 186 sets of parameters were grouped according to the USDA system and the three main soil groups presented in Section 5.4.1 (i.e., Sa, L, and C). The statistical analyses were performed considering these soil groups.

Next, normality tests were performed for the soil parameters and to the natural logarithm of most soil parameters to determine whether normal or lognormal density functions can be used to represent each unsaturated soil parameter. Measures of central tendency were evaluated for each soil property so that typical values could be established. The typical variability of the soil parameters were evaluated in terms of variability measures, such as the standard deviation and coefficient of variations. Lastly, the correlation between the unsaturated soil parameters was evaluated. The next sections will present the results and discussion of the statistical analyses.

5.4.2.1 *Normality tests of unsaturated soil parameters*

Normality tests were performed with the aid of Minitab 13 (Minitab Inc., 2000). Minitab has three hypothesis tests for testing normality available; namely, Anderson-Darling test; Ryan-Joiner test; and Kolmogorov-Smirnov test. D'Augostino and Stevens (1986) present detailed descriptions and comparisons of these tests for normality. The Anderson-Darling test has relatively superior power for detecting non-normality and was selected. The null hypothesis for the Anderson-Darling test is H0: data follow a normal distribution. The results of the normality tests are presented in terms of P-values and A^2 values. P-values represent the probability of making a *type* 1 *error*, which is "rejecting the null hypothesis when it is true." The smaller the P-value, the smaller is the probability that a mistake would be made by rejecting the null hypothesis. A cut-off value often used is 5%, which means "reject the null hypothesis when the P-value is less than 5%" (D'Augostino and Stevens, 1986). The quantity "A^2" is a measure of the "goodness of fit". The closer A^2 is to zero, the closer the parameter's distribution is to a normal distribution.

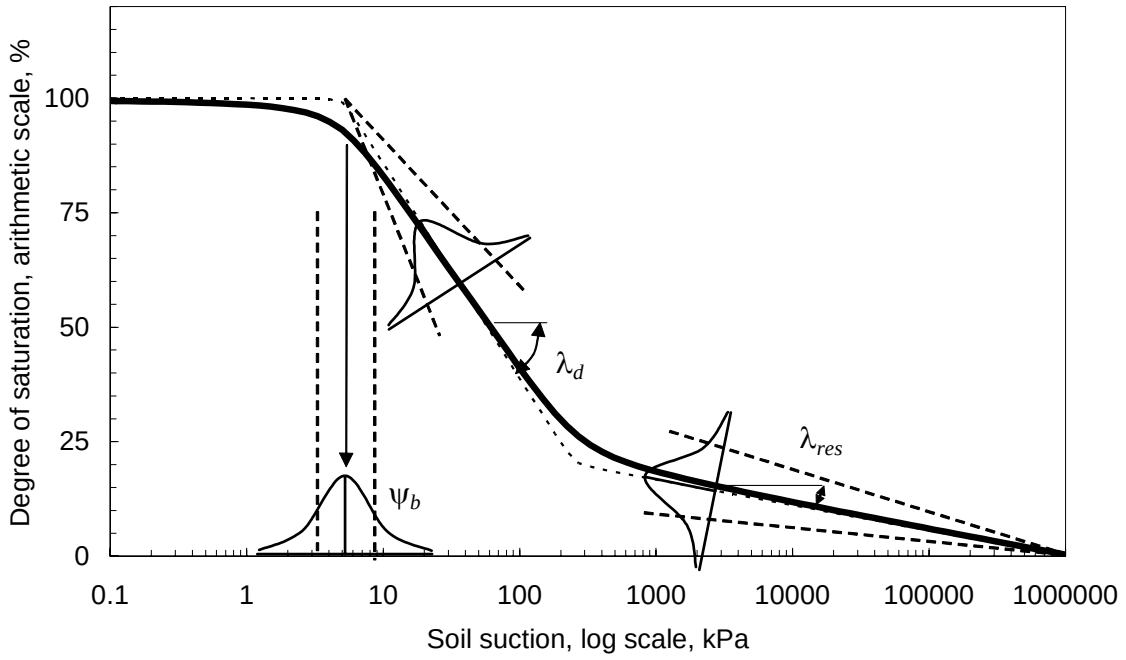

Figure 5.7 Statistical description of the soil-water characteristic curve.

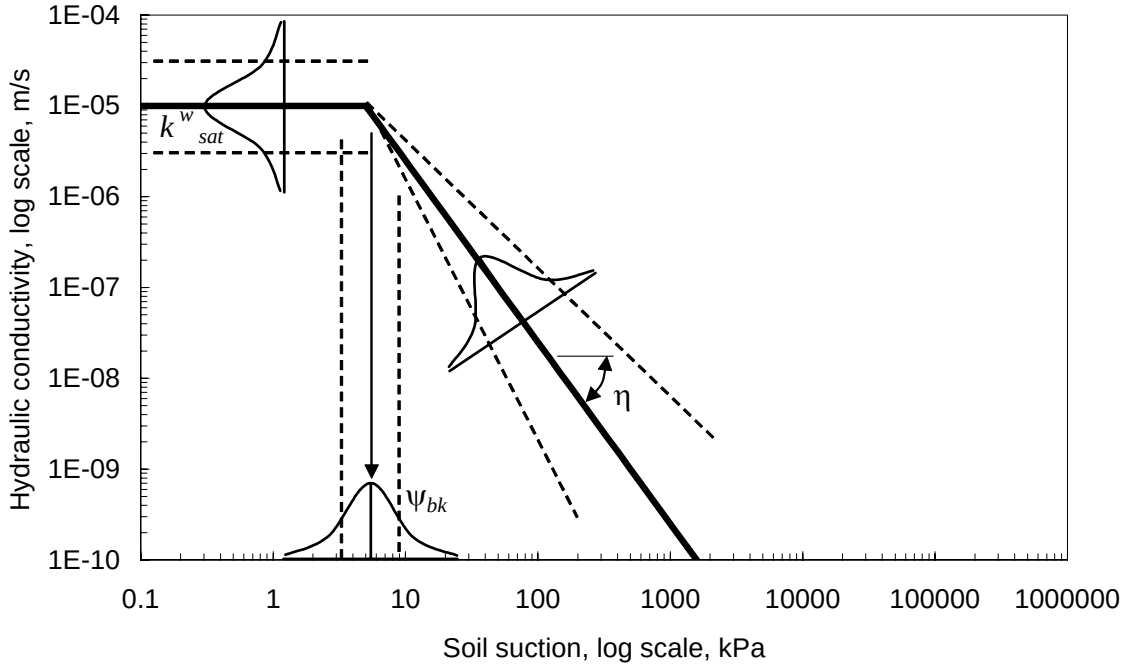

Figure 5.8 Statistical description of the hydraulic conductivity function.

The following soil parameters were tested for normality: n, ψ_b, $\ln(\psi_b)$, λ_d, $\ln(\lambda_d)$, λ_{res}, $\ln(\lambda_{res})$, k^w_{sat}, $\ln(k^w_{sat})$, ψ_{bk}, $\ln(\psi_{bk})$, η, and $\ln(\eta)$. The parameters found to vary by more than one order of magnitude or to have frequency distributions positively skewed (i.e., skewed to the left) were tested considering the natural logarithms. If the natural logarithm of a parameter is found to be normally distributed, then the parameter is log normally distributed.

Sampled records were grouped according to the USDA classification system, presented in Fig. 5.6. The tests were performed using all the sampled records as one single group, using the three main groups of soils (i.e., Sa, L, and C), and using the soils subgroups indicated in Fig. 5.6. The soil subgroups Si, C-L, Si-C-L, and Sa-C could not be analysed because of the small number of sampled records pertaining to those subgroups.

Figures 5.9 and 5.10 present the results of the normality tests in terms of P-values. The dotted lines presented in Figs. 5.9 and 5.10 indicate the threshold of 5%, below which the null hypothesis was rejected. Figure 5.9 shows that most parameters and soil groups deviate to some extent from a normal distribution. This is particularly true for ψ_b, λ_d, λ_{res}, k^w_{sat}, ψ_{bk}, and η. When the logarithm of ψ_b, λ_d, λ_{res}, k^w_{sat}, ψ_{bk}, and η were tested, significantly closer agreement was found for most parameters (i.e., larger P-values). Based on the results presented in Fig. 5.9, it was concluded that the parameters ψ_b, λ_d, λ_{res}, k^w_{sat}, ψ_{bk}, and η can be considered log normally distributed.

The effect to the normality tests of more detailed grouping of soils can be observed to some extent in Fig. 5.9. When all sampled records were analysed as a single group, none of the parameters were found to be normally or log normally distributed. Figure 5.10 shows the effect of testing the sampled records when organised as even smaller subgroups. Table 5.2 summarises the results of the normality tests presented in Fig. 5.10 for the soil subgroups. The results are presented in terms of both A^2 and P-values. The results presented in Fig. 5.10 are similar to those observed in Fig. 5.9. All parameters presented in Fig. 5.10 were found to be better described using the normal and/or lognormal distributions when compared to the larger groups presented in Fig. 5.9. Therefore, a more detailed soil textural classification appears to produce parameter distributions that can be better described by the normal and lognormal distributions.

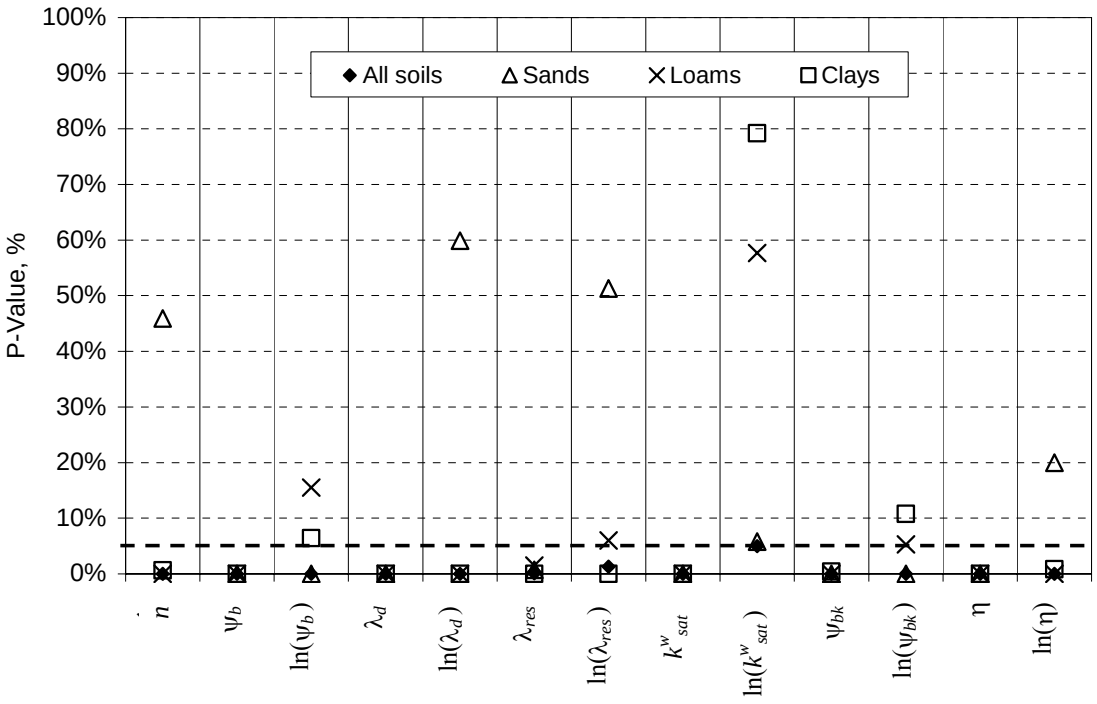

Figure 5.9 Normality tests: P-values for all soil parameters considering the three main soil groups.

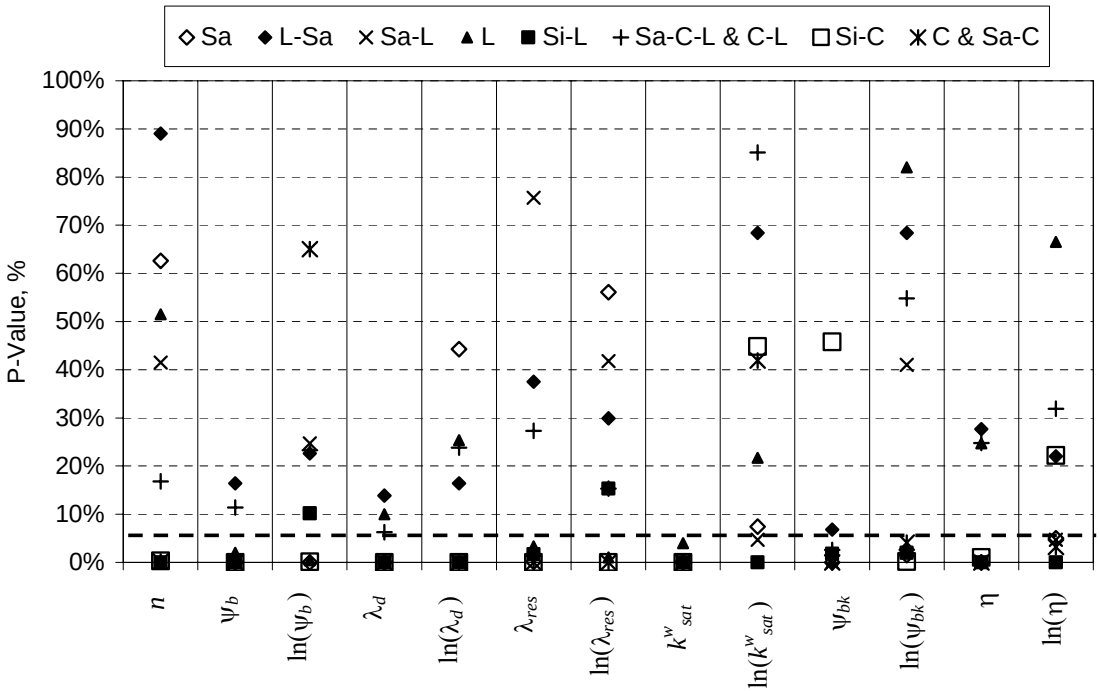

Figure 5.10 Normality tests: P-values for all soil parameters considering all soil subgroups.

Table 5.2 Anderson-Darling normality test for unsaturated soil parameters (normality is represented by A^2 approaching 0 and P > 5%).

Parameter	Sands		Loams				Clays	
(1)	Sa (2)	L-Sa (3)	Sa-L (4)	Si-L (5)	L (6)	Sa-C-L & C-L (7)	Si-C (8)	C & Sa-C (9)
n	$A^2 = 0.281$ P = 62.6 %	$A^2 = 0.176$ P = 89.0 %	$A^2 = 0.354$ P = 41.5 %	$A^2 = 2.117$ P = 0.0 %	$A^2 = 0.306$ P = 51.5 %	$A^2 = 0.476$ P = 16.8 %	$A^2 = 1.232$ P = 0.3 %	$A^2 = 1.307$ P = 0.2 %
ψ_b, kPa	$A^2 = 3.966$ P = 0.0 %	$A^2 = 0.488$ P = 16.4 %	$A^2 = 2.178$ P = 0.0 %	$A^2 = 3.887$ P = 0.0 %	$A^2 = 0.844$ P = 2.0 %	$A^2 = 0.539$ P = 11.4 %	$A^2 = 7.862$ P = 0.0 %	$A^2 = 9.887$ P = 0.0 %
$\ln(\psi_b)$	$A^2 = 2.141$ P = 0.0 %	$A^2 = 0.437$ P = 22.6 %	$A^2 = 0.443$ P = 24.7 %	$A^2 = 0.608$ P = 10.2 %	$A^2 = 1.125$ P = 0.4 %	$A^2 = 0.426$ P = 23.3 %	$A^2 = 1.387$ P = 0.1 %	$A^2 = 0.273$ P = 65.0 %
λ_d	$A^2 = 1.932$ P = 0.0 %	$A^2 = 0.514$ P = 13.9 %	$A^2 = 3.384$ P = 0.0 %	$A^2 = 3.541$ P = 0.0 %	$A^2 = 0.585$ P = 10.0 %	$A^2 = 0.630$ P = 6.3 %	--	--
$\ln(\lambda_d)$	$A^2 = 0.357$ P = 44.3 %	$A^2 = 0.488$ P = 16.4 %	$A^2 = 2.388$ P = 0.0 %	$A^2 = 2.374$ P = 0.0 %	$A^2 = 0.431$ P = 25.4 %	$A^2 = 0.422$ P = 23.8 %	--	--
λ_{res}	$A^2 = 1.438$ P = 0.1 %	$A^2 = 0.354$ P = 37.5 %	$A^2 = 0.232$ P = 75.7 %	$A^2 = 0.913$ P = 1.7 %	$A^2 = 0.764$ P = 3.3 %	$A^2 = 0.400$ P = 27.3 %	--	--
$\ln(\lambda_{res})$	$A^2 = 0.303$ P = 56.1 %	$A^2 = 0.392$ P = 29.9 %	$A^2 = 0.352$ P = 41.8 %	$A^2 = 0.538$ P = 15.3 %	$A^2 = 0.966$ P = 1.0 %	$A^2 = 0.491$ P = 15.3 %	--	--
k^w_{sat}, m/s	$A^2 = 6.196$ P = 0.0 %	$A^2 = 1.835$ P = 0.0 %	$A^2 = 3.825$ P = 0.0 %	$A^2 = 3.897$ P = 0.0 %	$A^2 = 0.734$ P = 4.0 %	$A^2 = 1.192$ P = 0.2 %	$A^2 = 4.623$ P = 0.0 %	$A^2 = 6.552$ P = 0.0 %
$\ln(k^w_{sat})$	$A^2 = 0.674$ P = 7.4 %	$A^2 = 0.241$ P = 68.4 %	$A^2 = 0.721$ P = 4.7 %	$A^2 = 2.117$ P = 0.0 %	$A^2 = 0.457$ P = 21.7 %	$A^2 = 0.190$ P = 85.1 %	$A^2 = 0.347$ P = 44.8 %	$A^2 = 0.365$ P = 41.9 %
ψ_{bk}, kPa	$A^2 = 1.983$ P = 0.0 %	$A^2 = 0.629$ P = 6.8 %	$A^2 = 1.570$ P = 0.0 %	$A^2 = 0.908$ P = 1.8 %	$A^2 = 1.184$ P = 0.3 %	$A^2 = 0.769$ P = 2.6 %	$A^2 = 0.343$ P = 45.8 %	$A^2 = 1.531$ P = 0.0 %
$\ln(\psi_{bk})$	$A^2 = 0.946$ P = 1.5 %	$A^2 = 0.241$ P = 68.4 %	$A^2 = 0.356$ P = 41.0 %	$A^2 = 0.885$ P = 2.0 %	$A^2 = 0.209$ P = 82.0 %	$A^2 = 0.278$ P = 54.8 %	$A^2 = 1.239$ P = 0.2 %	$A^2 = 0.773$ P = 4.1 %
η	$A^2 = 2.038$ P = 0.0 %	$A^2 = 0.404$ P = 27.7 %	$A^2 = 1.470$ P = 0.1 %	$A^2 = 3.480$ P = 0.0 %	$A^2 = 0.436$ P = 24.7 %	$A^2 = 0.416$ P = 24.8 %	$A^2 = 0.996$ P = 1.0 %	$A^2 = 1.942$ P = 0.0 %
$\ln(\eta)$	$A^2 = 0.743$ P = 5.0 %	$A^2 = 0.441$ P = 22.0 %	$A^2 = 0.721$ P = 4.7 %	$A^2 = 2.497$ P = 0.0 %	$A^2 = 0.254$ P = 66.5 %	$A^2 = 0.375$ P = 31.9 %	$A^2 = 0.471$ P = 22.2 %	$A^2 = 0.818$ P = 3.2 %

5.4.2.2 *Basic descriptive statistics and measures of central tendency of unsaturated soil parameters*

Table 5.3 presents descriptive statistical parameters obtained for the three distinct soil types; namely, sands (Sa), loams (L), and clays (C). Tables D.2 to D.12 from Appendix D presents more detailed descriptive statistical parameters, considering also the numerous textural subgroups. The minimum and maximum values are presented, along with measures of central tendency and a measure of data variability, the standard deviation. Three measures of central tendency were calculated; namely, the median, the mean, and the fitting parameters obtained by using all data sets together. The data sets and the fitting results obtained by considering all data sets together for each soil group are presented in Figs. 5.11 to 5.16.

Porosity

The mean value of porosity is 0.410 for sands, 0.501 for loams, and 0.534 for clays. The median values obtained do not differ considerably from the mean. Both the mean and median values appear reasonable measures of central tendency for the porosity. The minimum, maximum, median, and mean porosities increased for finer grained soils, as expected. The standard deviations also increased for finer grained soils, indicating a possibly higher variability. However, the standard deviation values are not totally reliable measures of variability as they are influenced by the first statistical moment. The coefficients of variation presented in the next sections give another representation of parameter variability.

Air-entry value

The mean air-entry value is 2.9 kPa for sands, 4.4 kPa for loams, and 91.4 kPa for clays. The median values of ψ_b are considerably lower than the mean values (notably the ψ_b of clays), indicating some positive skewness in the frequency distribution. The strongly positive skewness of ψ_b is confirmed by the results presented in Tables D.2 to D.12 from Appendix D. Alternatively, the mean and median values of $\ln(\psi_b)$ are in reasonable agreement. This observation corroborates with the previous observations indicating the log normality of ψ_b. The modest skewness of $\ln(\psi_b)$ presented in Tables D.2 to D.12 from Appendix D is in agreement with such observations. In addition, the values of ψ_b obtained by fitting the SWCC to all data sets together (see Figs. 5.11, 5.13, and 5.15) appear to be in poor agreement with the mean values of ψ_b and in relatively better agreement with the median values of ψ_b and with the values of ψ_b obtained from the mean values of $\ln(\psi_b)$. As a result, the mean values of $\ln(\psi_b)$ appear to be best measurements of central tendency associated with ψ_b.

Table 5.3 Descriptive statistics for the hydraulic properties of unsaturated soils (a = 0.075 for sands, 0.050 for loams, and 0.025 for clays).

Group	Measure	n	ψ_b kPa	$\ln(\psi_b)$	λ_d	$\ln(\lambda_d)$	λ_{res}	$\ln(\lambda_{res})$	k^w_{sat} m/s	$\ln(k^w_{sat})$	ψ_{bk} kPa	$\ln(\psi_{bk})$	η	$\ln(\eta)$
(1)	(2)	(3)	(4)	(5)	(6)	(7)	(8)	(9)	(10)	(11)	(12)	(13)	(14)	(15)
Sands	Min	0.297	0.183	-1.701	0.405	-0.904	0.019	-3.968	3.81×10^{-7}	-14.78	0.100	-2.303	1.288	0.253
	Max	0.570	12.00	2.485	4.228	1.442	0.126	-2.068	3.50×10^{-4}	-7.96	7.239	1.979	10.500	2.351
	Median	0.409	2.438	0.891	1.178	0.163	0.044	-3.119	1.82×10^{-5}	-10.91	1.585	0.461	3.484	1.248
	Mean	0.410	2.937	0.856	1.446	0.198	0.047	-3.141	3.88×10^{-5}	-11.34	1.874	0.119	4.037	1.268
	Sands fit	--	1.64	--	0.844	--	0.049	--	7.06×10^{-6}	--	1.550	--	3.107	--
	Std. Dev.	0.055	2.050	0.733	0.880	0.592	0.021	0.430	6.34×10^{-5}	1.736	1.582	1.180	2.141	0.506
Loams	Min	0.378	0.054	-2.914	0.177	-1.734	0.038	-3.270	3.49×10^{-8}	-17.17	0.040	-3.219	1.027	0.027
	Max	0.715	40.00	3.689	2.471	0.905	0.144	-1.940	1.33×10^{-4}	-8.92	10.00	2.303	7.657	2.036
	Median	0.471	2.697	0.992	0.371	-0.991	0.087	-2.446	3.23×10^{-6}	-12.64	1.00	0.000	2.057	0.721
	Mean	0.501	4.398	0.927	0.633	-0.737	0.090	-2.445	1.42×10^{-5}	-12.58	2.032	-0.047	2.792	0.895
	Loams fit	--	1.351	--	0.334	--	0.103	--	3.14×10^{-6}	--	0.830	--	1.954	--
	Std. Dev.	0.085	6.190	1.090	0.571	0.689	0.025	0.291	2.50×10^{-5}	1.870	2.261	1.391	1.624	0.492
Clays	Min	0.351	0.035	-3.347	--	--	--	--	5.42×10^{-10}	-21.34	0.030	-3.507	1.094	0.089
	Max	0.790	4932.4	8.504	--	--	--	--	5.88×10^{-6}	-12.04	6.000	1.792	4.933	1.596
	Median	0.544	2.11	0.743	--	--	--	--	1.17×10^{-7}	-15.96	2.078	0.731	2.000	0.693
	Mean	0.534	91.4	0.999	--	--	--	--	5.51×10^{-7}	-16.03	2.363	0.527	2.095	0.682
	Clays fit	--	2.505	--	--	--	--	--	1.39×10^{-6}	--	0.179	--	1.571	--
	Std. Dev.	0.100	626.1	2.064	--	--	--	--	1.16×10^{-6}	2.053	1.614	0.992	0.791	0.331

The maximum and mean values of air-entry value increased for finer grained soils, as expected. The relatively small pores found in fine grained soils can hold relatively large capillary forces. The minimum and median values do not present the increasing trend. Some factors other than the relationship between pore-size distribution and texture interfere with the SWCC and the air-entry value. Soil structure, for instance, has a particularly important effect in the air-entry value of clay soils. Therefore, the values of ψ_b of clay soils can vary along relatively large ranges and are not necessarily always higher than those of sand and loam soils.

Primary drainage slope

The mean values of the primary drainage slope, λ_d, were 1.446 for sands and 0.633 for loams. Clay soils do not present an identifiable residual degree of saturation, as discussed previously and are described only by ψ_b and a. The mean values of λ_d obtained disagreed with the median values indicating non symmetric frequency distributions. Alternatively, the mean and median values of $\ln(\lambda_d)$ are in relatively better agreement. This observation corroborates with the previous observations indicating the log normality of λ_d. The values of λ_d obtained by fitting the SWCC to all data sets together (see Figs. 5.11, 5.13, and 5.15) appear to be in good agreement with the values of λ_d obtained from the mean of $\ln(\lambda_d)$. As a result, the mean values of $\ln(\lambda_d)$ appear to be best measurements of central tendency associated with λ_d. The values of λ_d for sands are higher than those of loams, as expected. Loam soils tend to have relatively broad pore-size distributions that reflect well-graded grain-size distributions.

Residual drainage slope

The mean values of the residual drainage slope, λ_{res}, are 0.047 for sands and 0.090 for loams. The mean values of λ_{res} agreed reasonably well with the median values. Nevertheless, the mean and median values of $\ln(\lambda_{res})$ are in even better agreement. This observation corroborates with the previous observations indicating the log normality of λ_{res} (see Figs. 5.9 and 5.10). The values of λ_{res} obtained by fitting the SWCC to all data sets together (see Figs. 5.11, 5.13, and 5.15) appear to be in good agreement with the values of λ_{res} obtained from the mean of both λ_{res} and $\ln(\lambda_{res})$. Therefore, mean values of $\ln(\lambda_{res})$ appear to be good measurements of central tendency associated with λ_{res}. The values of λ_{res} for sands were significantly lower than those of loams, as expected. The smaller pores found in loam soils are capable of holding water at higher soil suctions due to relatively larger capillary forces. Fractions of clay found in the loam soils also contribute to increase the values of λ_{res}.

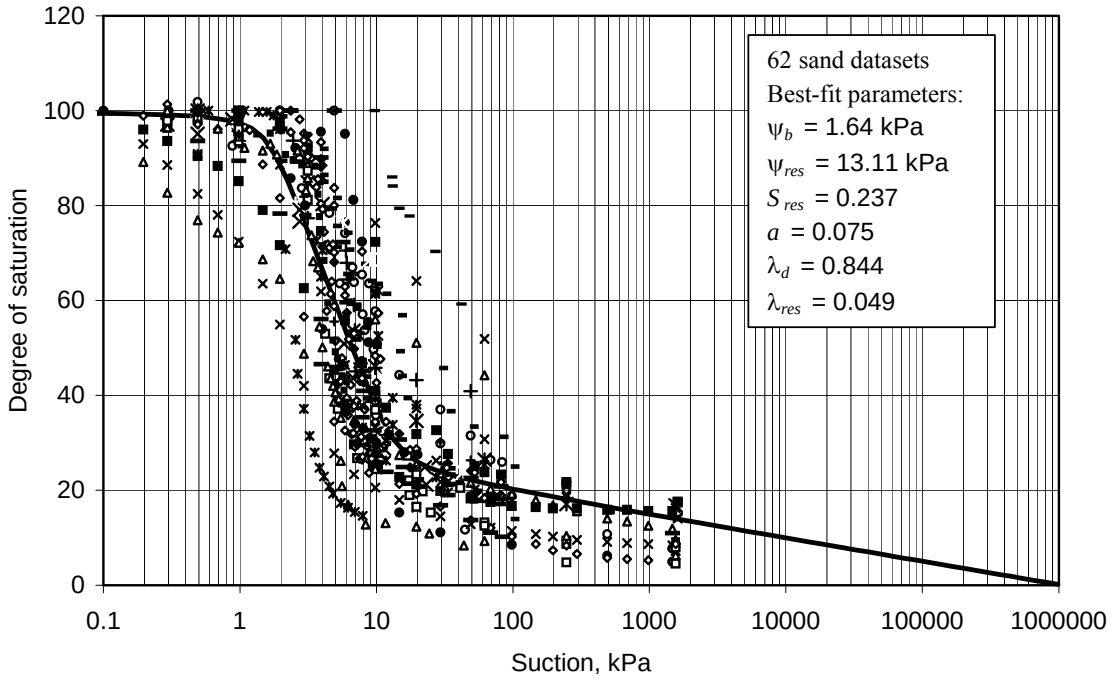

Figure 5.11 Soil-water characteristic curve for the sampled records of sand soils: experimental data and best-fit curve.

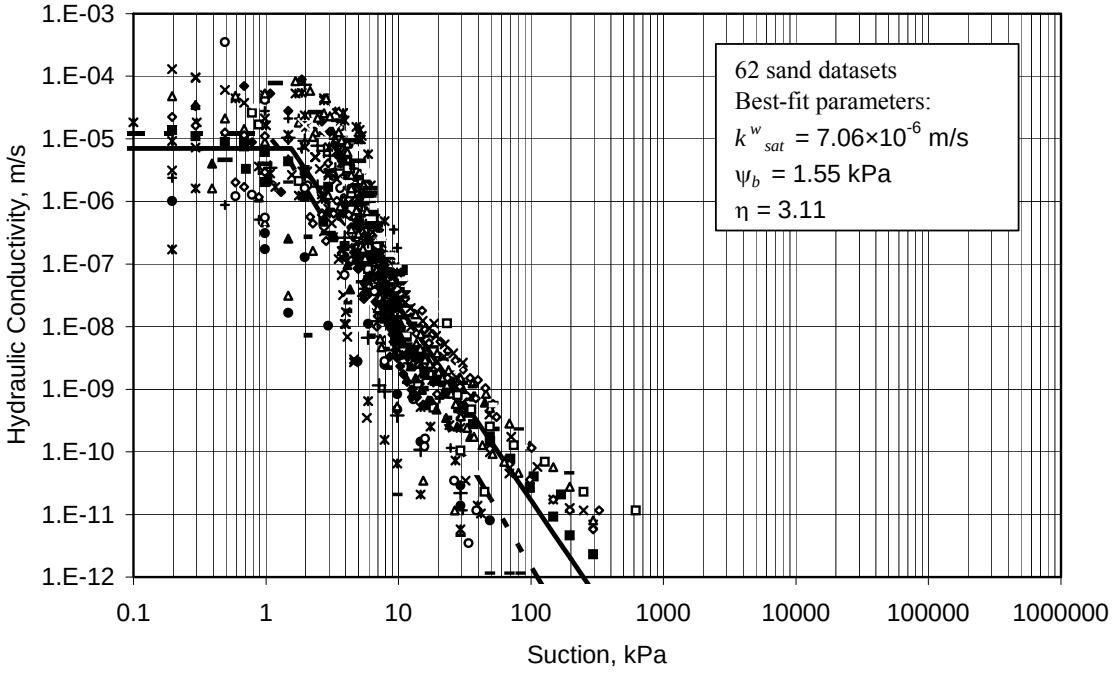

Figure 5.12 Hydraulic conductivity function for the sampled records of sand soils: experimental data and best-fit curve.

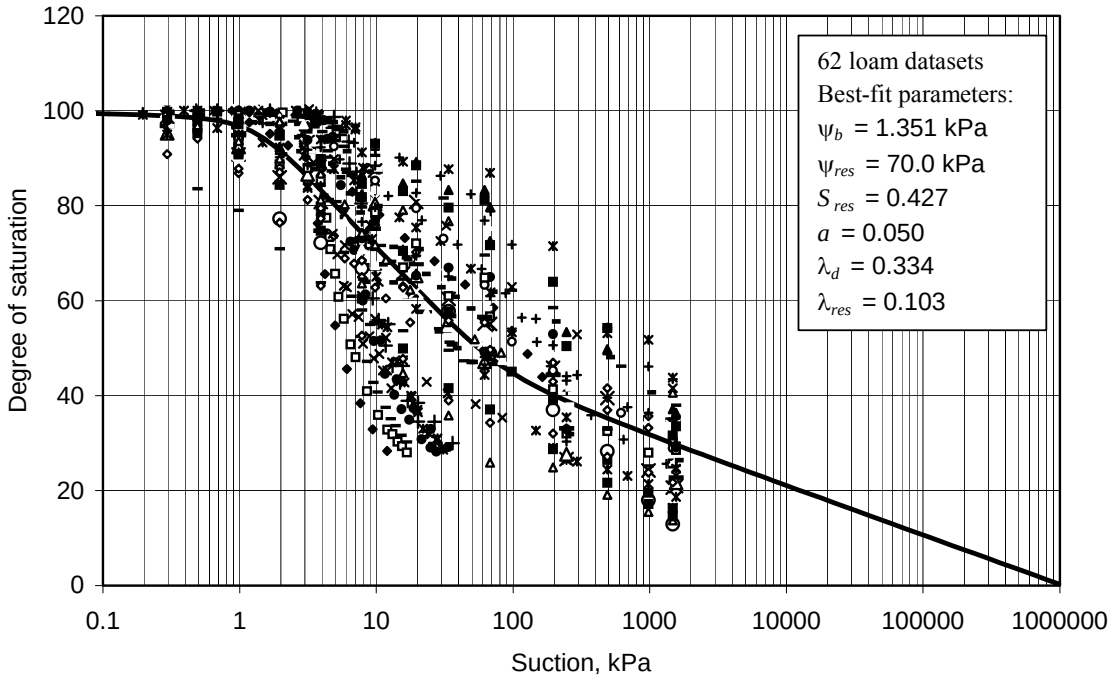

Figure 5.13 Soil-water characteristic curve for the sampled records of loam soils: experimental data and best-fit curve.

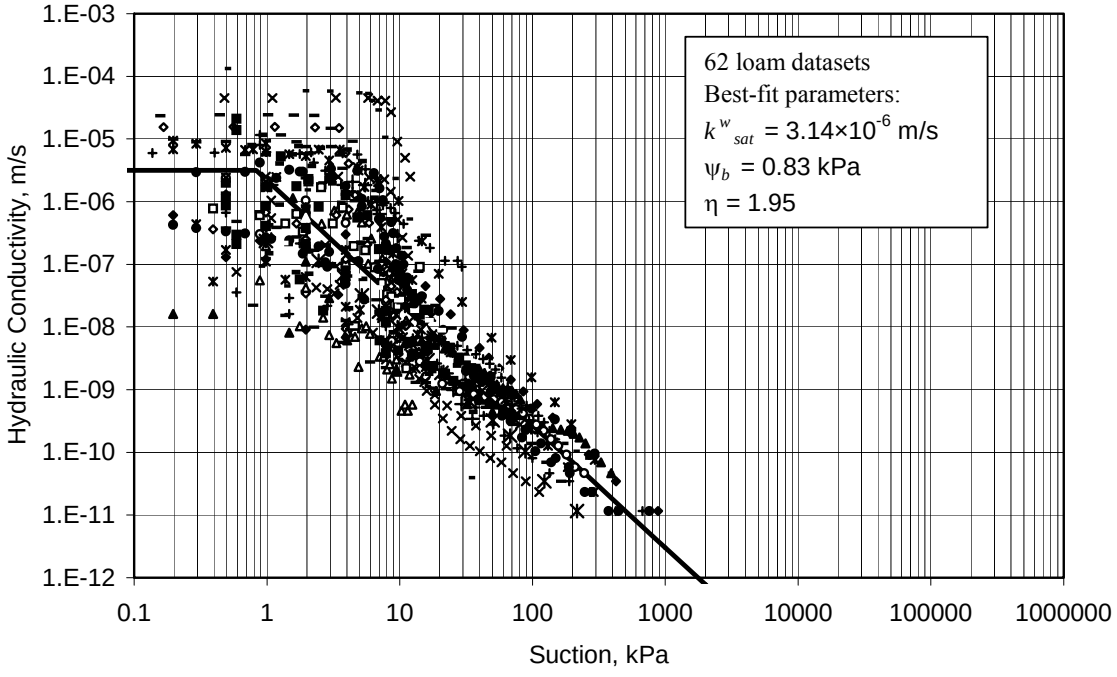

Figure 5.14 Hydraulic conductivity function for the sampled records of loam soils: experimental data and best-fit curve.

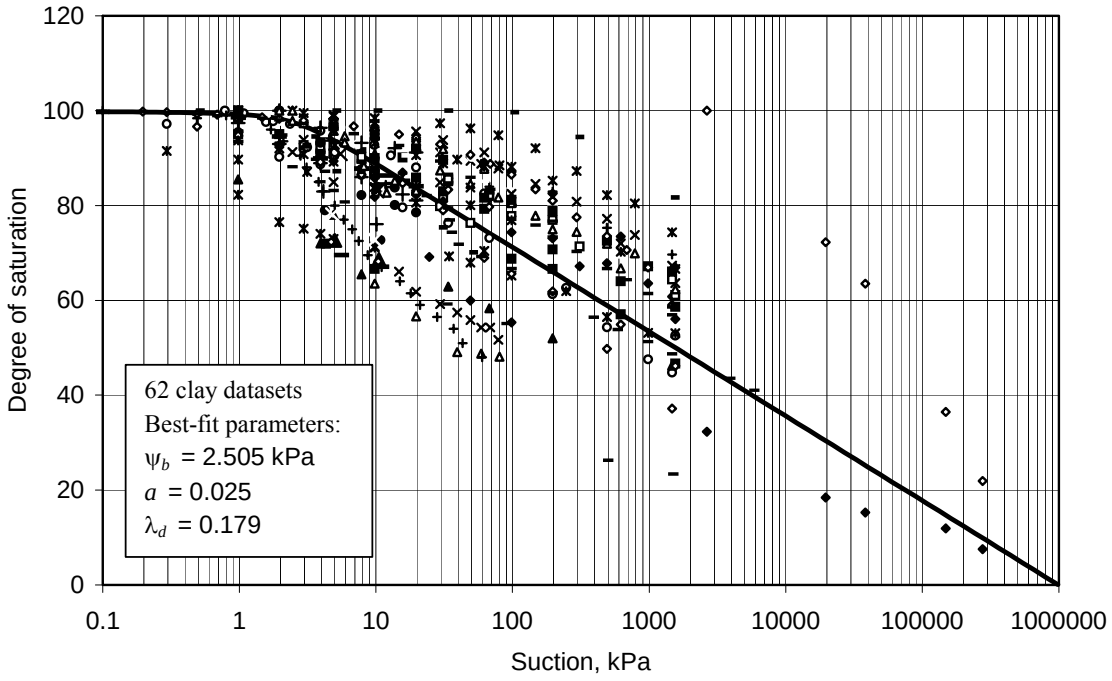

Figure 5.15 Soil-water characteristic curve for the sampled records of clay soils: experimental data and best-fit curve.

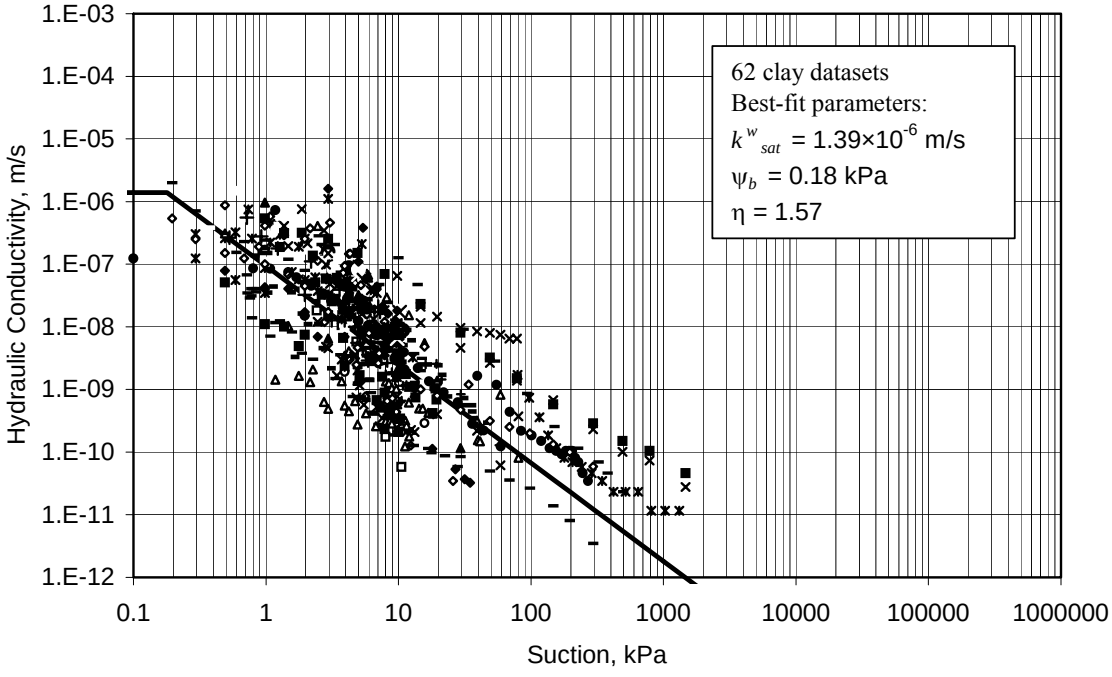

Figure 5.16 Hydraulic conductivity function for the sampled records of clay soils: experimental data and best-fit curve.

Saturated hydraulic conductivity

Central tendency measures of the saturated hydraulic conductivity, k^w_{sat}, can be misleading. The frequency distribution of k^w_{sat} is positively skewed and the values of k^w_{sat} may vary over several orders of magnitude. Relatively large sample values of k^w_{sat} have a strong influence in the mean value of k^w_{sat}. The mean values of k^w_{sat} found were 3.88×10^{-5} m/s for sands, 1.42×10^{-5} m/s for loams, and 5.51×10^{-7} m/s for clays. The median values of k^w_{sat} found were 1.82×10^{-5} m/s for sands, 3.23×10^{-6} m/s for loams, and 1.17×10^{-7} m/s for clays. As can be seen, the median values obtained were considerably lower than the mean values and appear to represent a better measure of central tendency when compared to the minimum and maximum values. Alternatively, the mean and median values of $\ln(k^w_{sat})$ are in close agreement. This observation corroborates with the previous observations indicating the log normality of k^w_{sat}. Therefore, the mean values of $\ln(k^w_{sat})$ can be considered better measurements of central tendency.

The range of variation of $\ln(k^w_{sat})$ increased for finer grained soils. The relative variability of $\ln(k^w_{sat})$ needs to be verified by better measures of variability, such as the coefficient of variation. The values of k^w_{sat} and $\ln(k^w_{sat})$ decreased for finer grained soils, as expected. The mean values of $\ln(k^w_{sat})$ are -11.3 for sands, -12.6 for loams, and -16.0 for clays, which is equivalent to $k^w_{sat} = 1.23\times10^{-5}$ m/s for sands, $k^w_{sat} = 3.37\times10^{-6}$ m/s for loams, and $k^w_{sat} = 1.09\times10^{-7}$ m/s for clays.

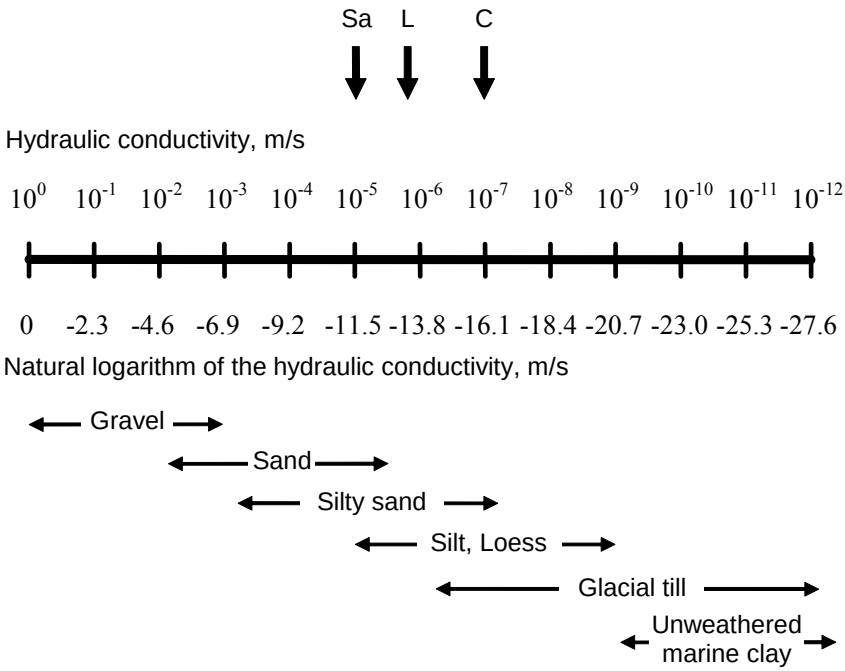

Figure 5.17 Saturated hydraulic conductivity for each main soil group.

The central tendency values based on the mean of $\ln(k^w_{sat})$ are indicated in Fig. 5.17 along with typical intervals for several soil textures (Freeze and Cherry, 1979). The value obtained for the sand soils is close to the maximum value for sands suggested by Freeze and Cherry (1979). The value of k^w_{sat} for loam soils is within the interval for silts, as expected. The value of k^w_{sat} for clays is well below the range suggested for marine clay, but is within the range of tills. It must be observed, however, that the values of k^w_{sat} for clays suggested by Freeze and Cherry (1979) are typical of intact clays and may vary considerably, based on the type of testing procedure. While the values obtained for clays appear high, the values suggested for intact clays do not represent field conditions in most cases.

Air-entry value obtained from the hydraulic conductivity function

The mean values of the air-entry value obtained from the hydraulic conductivity function, ψ_{bk}, are 1.87 kPa for sands, 2.03 kPa for loams, and 2.36 kPa for clays. The median values of ψ_{bk} obtained were slightly lower than the mean values, indicating some positive skewness in the frequency distribution. The positive skewness of ψ_{bk} is confirmed by most results presented in Tables D.2 to D.12 from Appendix D. The mean and median values of $\ln(\psi_{bk})$ are in slightly better agreement. In addition, the values of ψ_{bk} obtained by fitting the hydraulic conductivity function to all data sets together (see Figs. 5.11, 5.13, and 5.15) appear to be in poor agreement with the mean values of ψ_{bk} and in relatively better agreement with the median values of ψ_{bk}, with exception of the results obtained for the clay soils. The global best-fit results are also in agreement with the values of ψ_{bk} obtained from the mean values of $\ln(\psi_{bk})$ with exception of the value obtained for the clay soils. In summary, the mean values of $\ln(\psi_{bk})$ appear to be best measurements of central tendency associated with ψ_{bk}.

The overall trends regarding the value of ψ_{bk} and the soil texture was the same as that observed previously for ψ_b, as expected. Figure 5.18 presents a comparison of ψ_{bk} and ψ_b. In theory, the values of ψ_{bk} should be similar to the values of ψ_b. This tendency is in part confirmed by Fig. 5.18, with numerous data points near the 1:1 line. However, some dispersion is observed and the values of ψ_{bk} tend to be lower than the values of ψ_b. This is particularly true for fine grained soils. Clay soils often suffer significant volume changes, even at soil suctions lower than the air-entry value, ψ_b. Such volume changes may cause a decrease in the hydraulic conductivity (Huang et al., 1998). As a result, the break point in the hydraulic conductivity function may be located at a value of soil suction slightly below the value of ψ_b obtained from the SWCC.

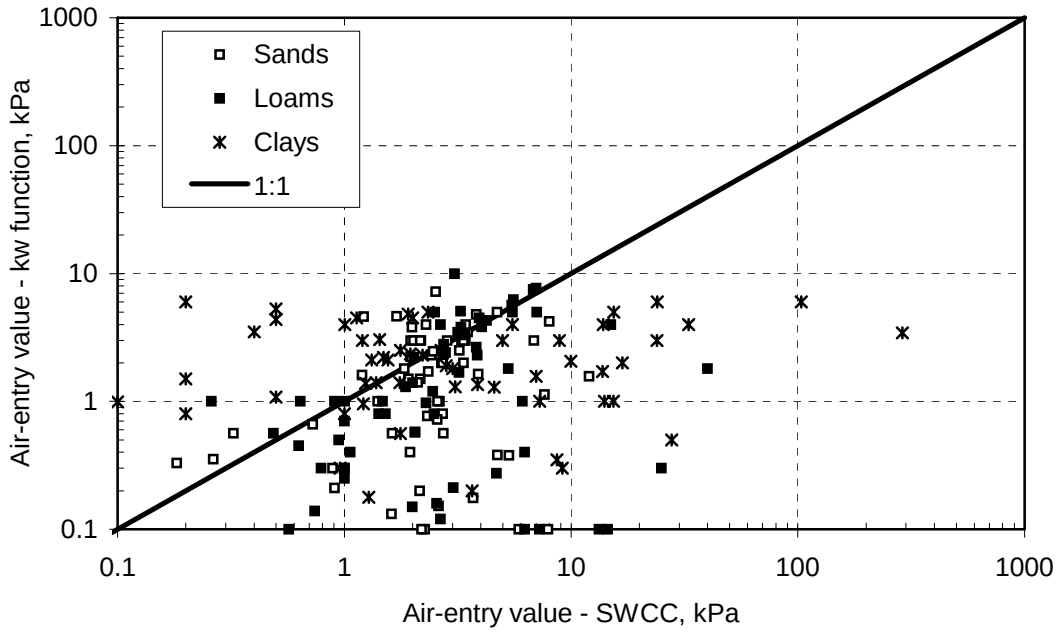

Figure 5.18 Air-entry values obtained by best-fit of the soil-water characteristic curve and the hydraulic conductivity function.

Hydraulic conductivity function slope

The mean values of the hydraulic conductivity function slope, η, were 4.037 for sands, 2.792 for loams, and 2.095 for clays. The mean values of η disagreed with the median values, indicating non symmetric frequency distributions. The hydraulic conductivity function slope was also analysed in terms of natural logarithm. The mean and median values of ln(η) are in relatively better agreement. This observation corroborates with the previous observations indicating the log normality of η. The values of η obtained by fitting the SWCC to all data sets together (see Figs. 5.11, 5.13, and 5.15) appear to be in reasonable agreement with the values of η obtained from the mean of ln(η). In summary, the mean values of ln(η) appear to be best measurements of central tendency associated with η.

The expected relative changes of η according with the soil texture were observed. The values of η for sands are higher than those of loams and clays. This trend was observed for the minimum, maximum, median, and mean values. The value obtained by the best-fit analysis using all data sets shows the same trend. While the pores of sand soils are usually drained by small increments of soil suction, loam soils tend to have well-graded grain-size distributions, producing relatively smooth hydraulic conductivity changes.

5.4.2.3 *Variability of unsaturated soil parameters*

The variability of the unsaturated soil parameters was analysed for each soil group, as defined in previous sections. It is important to emphasize part of the objectives of the study presented in this chapter. The measures of variability presented herein are aimed at giving an indication of the typical variability of unsaturated soil properties, given that crude information about soil texture is available. These values will provide useful information even in situations where site specific measures of the soil-water characteristic curve and/or of the hydraulic permeability curve are available. Typical measures of variability can be used as a base for comparison and to identify unusual data. The values provided herein can also be used in connection with a Bayesian update approach, where the typical values presented can be combined with site specific data to provide a better estimation of parameter uncertainty.

Two main measures are usually considered in the quantification of variability; namely, the standard deviation, SD, and the coefficient of variation, CV. These measures where previously defined. The standard deviation of a random variable is strongly influenced by the mean values and depends on the variable's unit. The coefficient of variation, on the other hand, offers a way of normalising the value of standard variation with respect to the mean value and is unitless. Sections 5.2 and 5.3 showed that the coefficient of variation has been traditionally used in the characterisation of geotechnical parameter variability. Therefore, closer attention will be given to the values of CV for the parameters under study.

Table 5.4 presents a summary of the coefficients of variation, CV, obtained from the statistical analyses. It was shown in the previous section that the parameters ψ_b, λ_d, λ_{res}, k^w_{sat}, ψ_{bk}, and η should be analysed in terms of natural logarithm, since the use of a natural logarithmic transformation results in simpler and more meaningful results. Therefore, values of CV are presented for the natural logarithms of most soil parameters, with exception of porosity, which was not considered log normally distributed. The coefficients of variations for n, $\ln(\psi_b)$, $\ln(\lambda_d)$, $\ln(\lambda_{res})$, $\ln(k^w_{sat})$, $\ln(\psi_{bk})$, and $\ln(\eta)$ are presented, for each soil group. The USDA soil groups presented previously were adopted in the analyses. The number of records pertaining to each soil group is also presented in Table 5.4. Some neighbouring groups with a reduced number of records where joined, as indicated.

The results presented in Table 5.4 indicate that the values of CV tend to increase when soil records pertaining to distinct soil types are treated as a single group. This result was somehow

expected, as the sampled soil records appear to form distinct populations when analysed in terms of textural groups. The values of CV for loams is generally higher then the values of CV for sands and clays. Sands presented the lower values of CV, for most parameters. The soil group "size" may be one of the reasons for the generally higher variability of loams and clays. The sand group includes relatively small textural percentage ranges, while the loam and clay groups involve considerably larger ranges. Yet, this observation is not consistently observed for all soil parameters. For instance, the CV of $\ln(\lambda_{res})$ and of $\ln(k^{w}_{sat})$ of sands was higher than that of loams; clays presented the lowest vales of CV of $\ln(k^{w}_{sat})$. Other factors must be responsible for the lower CV of $\ln(k^{w}_{sat})$ for loams and sands and the relative "size" of each soil group should not be the only factor under scrutiny. The following paragraphs will provide a more detailed analysis in qualitative and quantitative terms of the values of CV obtained for each soil parameter.

Table 5.4 Coefficients of variation for the hydraulic properties of unsaturated soil based on a sample of typical results.

Group	Sub-group	Records	n	$\ln(\psi_b)$	$\ln(\lambda_d)$	$\ln(\lambda_{res})$	$\ln(k^{w}_{sat})$	$\ln(\psi_{bk})$	$\ln(\eta)$
(1)	(2)	(3)	(4)	(5)	(6)	(7)	(8)	(9)	(10)
All	---	186	20.2	151.6	294.4	18.1	20.6	608.8	53.7
Sands	All	62	13.5	85.6	299.3	13.7	15.3	988.7	39.9
	Sa	53	12.7	92.1	279.9	13.9	15.4	5439.9	43.0
	L-Sa	9	13.7	53.2	655.6	8.5	15.3	111.3	14.4
Loams	All	62	17.1	117.6	93.5	11.9	14.9	2962.5	55.0
	Sa-L	15	11.3	105.5	74.5	10.2	13.6	539.3	60.3
	Si-L	27	13.5	74.3	133.2	11.4	15.7	365.4	57.7
	L	12	18.0	684.0	49.6	8.9	13.5	177.2	33.3
	Sa-C-L & C-L	8	16.3	149.2	101.0	12.2	14.3	937.3	55.3
Clays	All	62	18.7	206.6	--	--	12.8	188.2	48.6
	Si-C	22	26.3	125.5	--	--	10.4	76.5	52.2
	Sa-C & C	40	13.4	295.2	--	--	13.3	369.2	44.7

Porosity

The coefficients of variation of porosity obtained are 13.5% for sands, 17.1% for loams, and 18.7% for clays. The CV of porosity increased for fine grained soils and all of the values appear to be realistic. The values previously reported in the literature for porosity and void ratio vary from 10% to 20%. In most cases, the reports available do not indicate the soil type studied. The results obtained herein suggest that the variability of the soil records studied may be somewhat higher than that of soil records obtained from a single location or soil formation, as are those used in previous studies. Nevertheless, the small difference indicates that the results presented herein are acceptable.

Figure 5.19 presents a plot of mean values of porosity versus the computed coefficients of variation. Each data point corresponds to a distinct soil group gathered from the sampled soil records. Two lines surrounding the data points were computed and plotted. These lines correspond to constant values of standard deviation of 0.05 and 0.10. One outlier was ignored. The data points plotted in Fig. 5.19 indicate that the measures of CV of porosity appear to show little variation with the mean value. The results obtained herein suggest that a value of CV between 13 and 19% should be adopted.

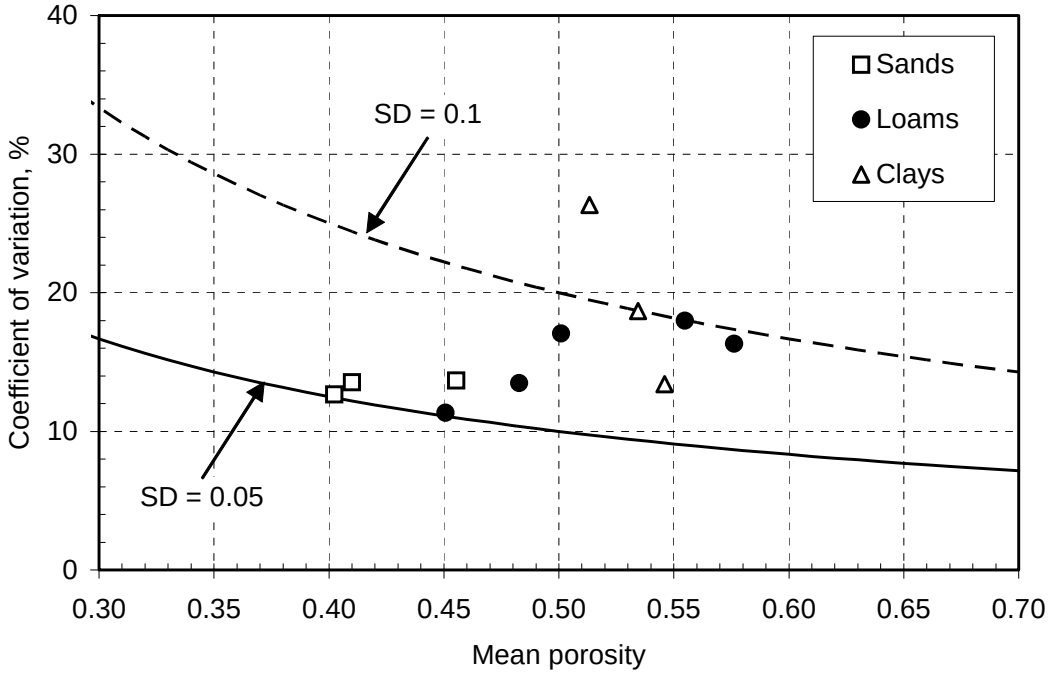

Figure 5.19 Mean versus the coefficient of variation of the soil porosity, *n*.

Air-entry value obtained from the SWCC and from the hydraulic conductivity curve

The coefficient of variation of $\ln(\psi_b)$ is 85.6% for sands, 117.6% for loams, and 206.6% for clays. The coefficients of variation of $\ln(\psi_{bk})$ seem unreasonably high. The CV of $\ln(\psi_{bk})$ found is 989% for sands, 2962% for loams, and 188.2% for clays. The high values of CV of $\ln(\psi_b)$ and remarkably high values of CV of $\ln(\psi_{bk})$ are due to the fact that some of the mean values of $\ln(\psi_b)$ and $\ln(\psi_{bk})$ are between -1 and 1 ln(kPa) making them close to 0 ln(kPa). The values of CV are exceptionally sensitive to small changes in the mean value when the mean value is between -1 and 1 ln(kPa) and close to 0 ln(kPa). The sensitivity of CV can be realized by examining its definition, which is based on Eq. 5.7.

Figure 5.20 presents a plot of absolute values of the mean $\ln(\psi_b)$ and $\ln(\psi_{bk})$ versus the computed CV's. Each data point corresponds to a distinct soil group gathered from the sampled soil records. The two lines surrounding the data points correspond to constant values of SD equal to 0.8 ln(kPa) and 2.1 ln(kPa). Figure 5.20 shows that most data points are located between CV = 75 and 125%. However, when the mean values of $\ln(\psi_b)$ and $\ln(\psi_{bk})$ fall between -0.5 and 0.5 ln(kPa) and approach 0 ln(kPa), significantly higher values of CV are obtained.

The coefficients of variation for $\ln(\psi_b)$ and $\ln(\psi_{bk})$ show a clear trend with soil texture. The values of CV of $\ln(\psi_b)$ and $\ln(\psi_{bk})$ increase for fine grained soils. This result is expected, since it is generally known that sands have air entry values varying along a small range of soil suctions and loams and clays present widely varying values of air-entry value. In terms of comparison between the variability of $\ln(\psi_b)$ and $\ln(\psi_{bk})$, the results show that similar results are obtained in terms of standard deviation. Most data points are within a range of variation of standard deviation between 0.8 and 2.1 ln(kPa). However, the mean values of $\ln(\psi_{bk})$ are generally smaller then the mean values of $\ln(\psi_b)$. As a result, the values of coefficient of variation of $\ln(\psi_b)$ are significantly affected because the mean values were between -1 and 1 ln(kPa) and close to 0 ln(kPa).

The results obtained herein suggest that a value of CV between 75 and 125% should be adopted in cases where the mean values of $\ln(\psi_b)$ or $\ln(\psi_{bk})$ are not within the -0.5 to 0.5 ln(kPa) range. In cases where the mean values of $\ln(\psi_b)$ or $\ln(\psi_{bk})$ are within the -0.5 to 0.5 ln(kPa) range, the values of CV suggested above should be abandoned and the parameter variability should be defined respecting a range of standard deviations between 0.8 and 2.1 ln(kPa).

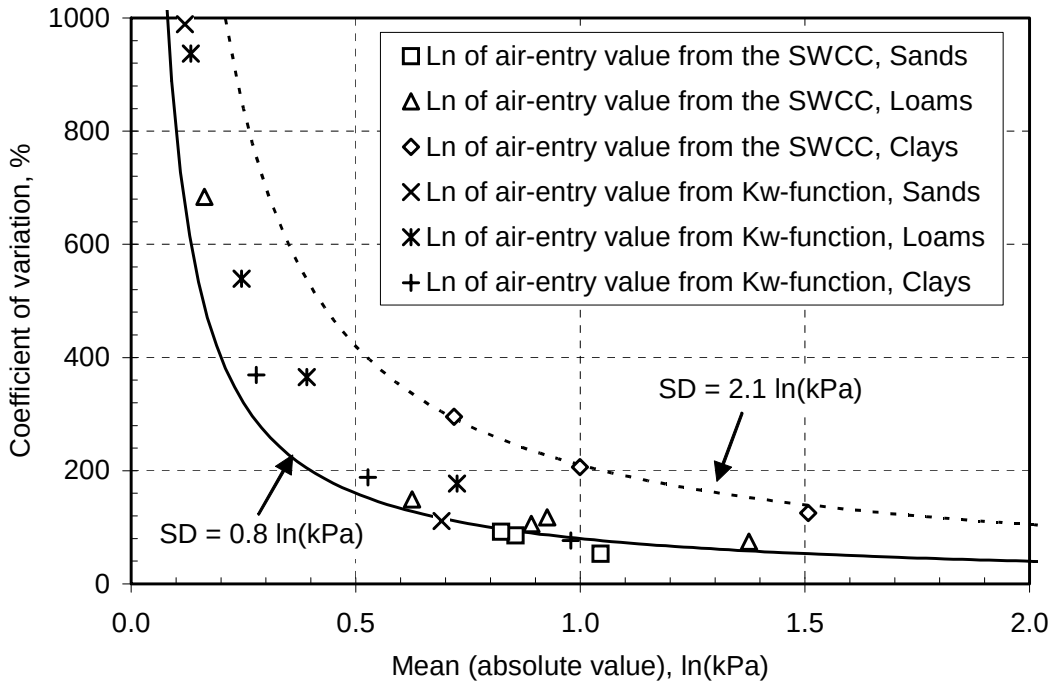

Figure 5.20 Mean versus the coefficient of variation of the natural logarithm of air-entry value obtained from the SWCC and from the k^w function, ln(ψ_b) and ln(ψ_{bk}), ln(kPa).

Natural logarithm of the primary drainage slope

The variability of the primary drainage slope was analysed in the same fashion as the previous parameters. The coefficient of variation of ln(λ_d) found is 299.3% for sands and 93.5% for loams. The CV values for clay soils are not considered herein, as the parameters ψ_b and "*a*" were chosen previously as the only parameters defining the shape of the SWCC's of clays. The simultaneous analysis of ψ_b and λ_d of clays would be redundant.

The CV of ln(λ_d) of loams is significantly lower than that of sands. This result does not reflect the widely varying grain size distribution of the loams group and the knowingly narrower variation of grain size distribution of the sands group. This apparently "abnormal" result was due to the mean values of ln(λ_d), that had a significant effect on the values of CV. Figure 5.21 presents a plot of mean values of ln(λ_d) versus the computed CV's. The two lines plotted correspond to constant values of SD equal to 0.45 and 0.80. The loam data points are closer to the SD = 0.80 line. Figure 5.21 shows that most data points are located between CV = 75 and 100%. However, the mean values of ln(λ_d) of sands fell within the -0.5 and 0.5 range and approached 0, resulting in higher values of CV.

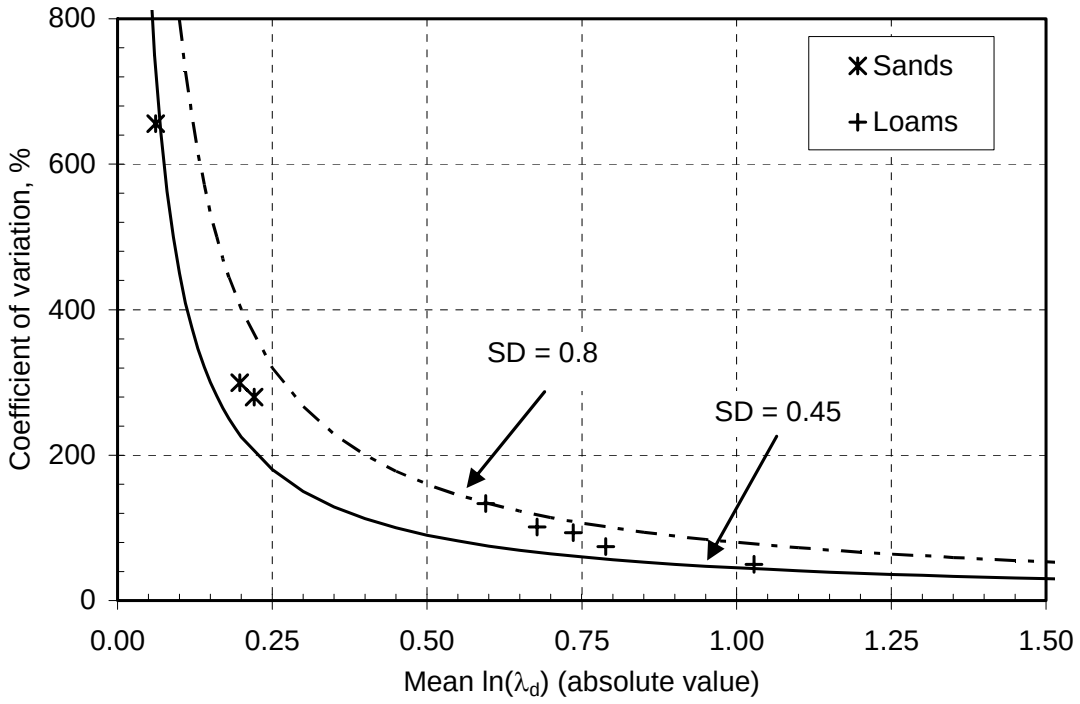

Figure 5.21 Mean versus the coefficient of variation of the natural logarithm of the primary drainage slope, $\ln(\lambda_d)$.

The results obtained herein suggest that a value of CV between 75 and 100% should be adopted in cases where the mean values of $\ln(\lambda_d)$ are not within the -0.5 – 0.5 range. In cases where the mean values of $\ln(\lambda_d)$ are within the -0.5 – 0.5 range, the values of CV suggested above should be abandoned and the parameter variability should be established respecting a range of standard deviations between 0.45 and 0.80.

Natural logarithm of the residual drainage slope

The coefficient of variation of $\ln(\lambda_{res})$ is 13.7% for sands and 11.9% for loams. Again, the CV values for clay soils were not considered, since the parameters ψ_b and "*a*" were chosen previously as the only parameters defining the shape of the SWCC's of clays. The CV of $\ln(\lambda_{res})$ of loams is slightly lower than that of sands. The mean values of $\ln(\lambda_{res})$ did not have a significant effect on the values of CV as they did not fall within the -0.5 and 0.5 range. Figure 5.22 presents a plot of mean values of $\ln(\lambda_{res})$ versus the computed CV's. The two lines plotted correspond to constant values of SD equal to 0.2 and 0.45. The sand data points are closer to the SD = 0.45 line but have higher mean values. Figure 5.22 shows that most data points are located between CV = 8 and 12%.

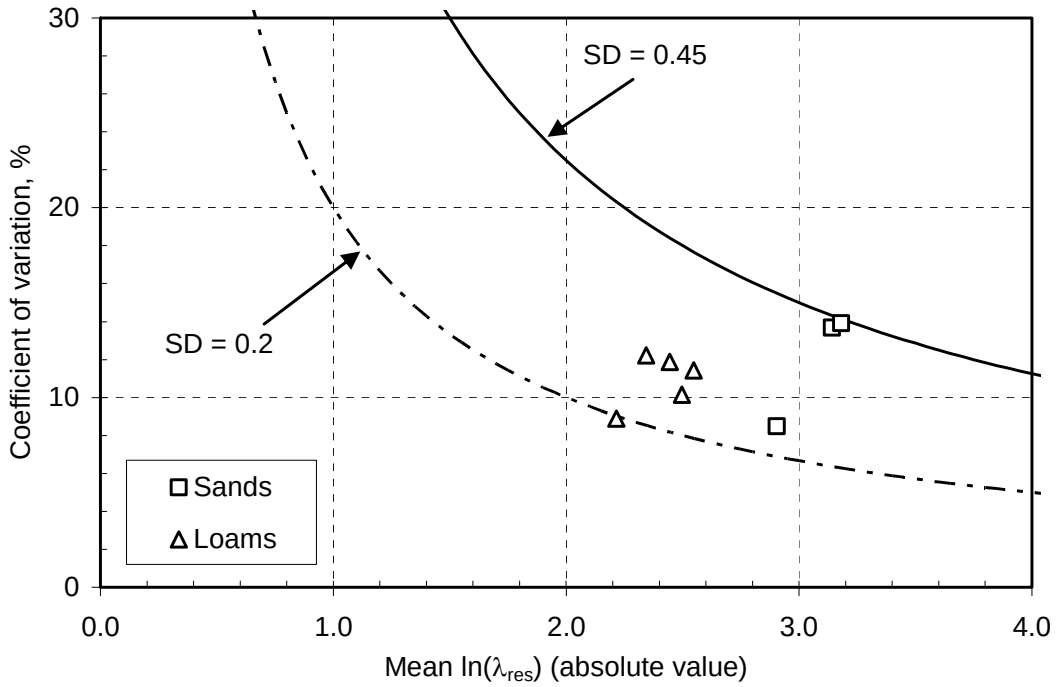

Figure 5.22 Mean versus the coefficient of variation of the natural logarithm of the residual drainage slope, $\ln(\lambda_{res})$.

The results obtained herein suggest that a value of CV between 8 and 12% should be adopted. Nevertheless, the mean values of $\ln(\lambda_{res})$ should always be verified. In case the mean values of $\ln(\lambda_{res})$ are within the -0.5 – 0.5 range, the values of CV suggested above should be abandoned and the parameter variability should be established respecting a range of standard deviations between 0.2 and 0.45.

Natural logarithm of the saturated hydraulic conductivity

The variability of the saturated hydraulic conductivity was analysed using the natural logarithm transformation. The coefficients of variation of $\ln(k^{w}_{sat})$ found were 15.3% for sands, 14.9% for loams, and 12.8% for clays. The CV of $\ln(k^{w}_{sat})$ appears to slightly decrease for fine grained soils. Figure 5.23 presents a plot of mean values of $\ln(k^{w}_{sat})$ versus the computed CV's. The two lines plotted correspond to constant values of SD equal to 1.6 ln(m/s) and 2.1 ln(m/s). The sand data points are closer to the SD = 2.1 ln(m/s) line than the other data points. The data points plotted in Fig. 5.23 indicate that the measures of CV of $\ln(k^{w}_{sat})$ appear to show little variation with the mean values. The results obtained herein suggest that a value of CV of $\ln(k^{w}_{sat})$ between 13 and 16% should be adopted.

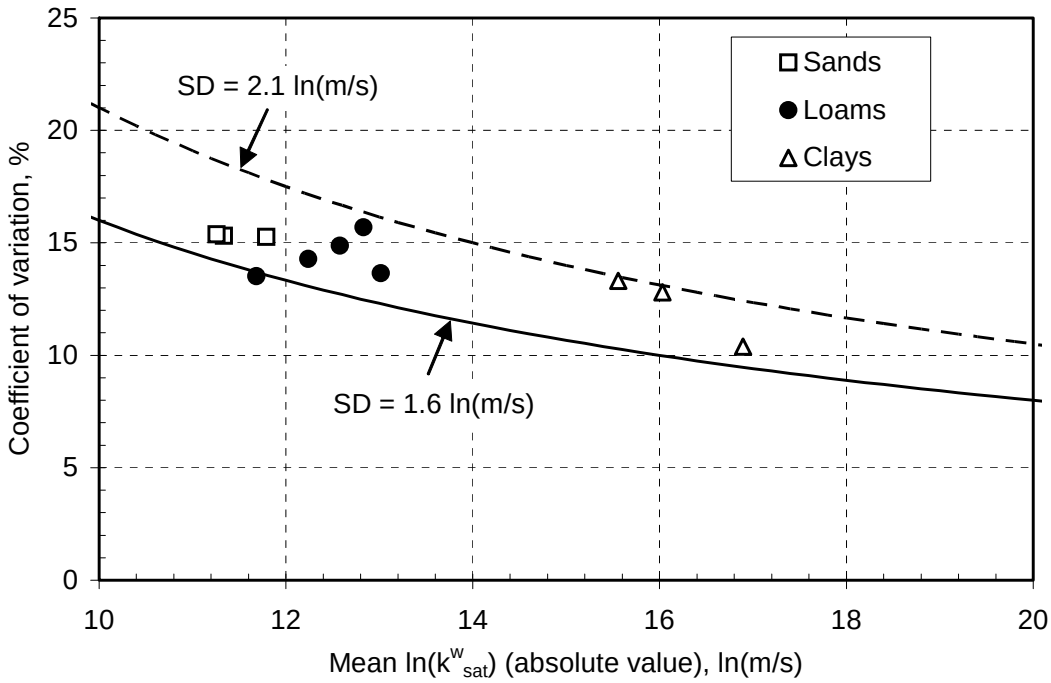

Figure 5.23 Mean versus the coefficient of variation of the natural logarithm of the saturated hydraulic conductivity, ln(k^w_{sat}), m/s.

Natural logarithm of the hydraulic conductivity function slope

It was shown in the previous sections that η is log normally distributed. Therefore, the variability of the hydraulic conductivity function slope was also analysed using the natural logarithm transformation. The coefficients of variation of ln(η) found are 39.9% for sands, 55.0% for loams, and 48.6% for clays. The CV of ln(η) does not show any clear relationship with soil texture, though it appeared to slightly increase for fine grained soils.

Figure 5.24 presents a plot of mean values of ln(η) versus the computed CV's. The two lines plotted correspond to constant values of SD equal to 0.28 and 0.58. One outliner was ignored. Most data points are within a range of CV between 40 and 55%. The data points plotted in Fig. 5.24 do not indicate any clear relationship between the measures of CV of ln(η) and the mean values. The results obtained herein suggest that values of CV of ln(η) between 40 and 55% should be adopted.

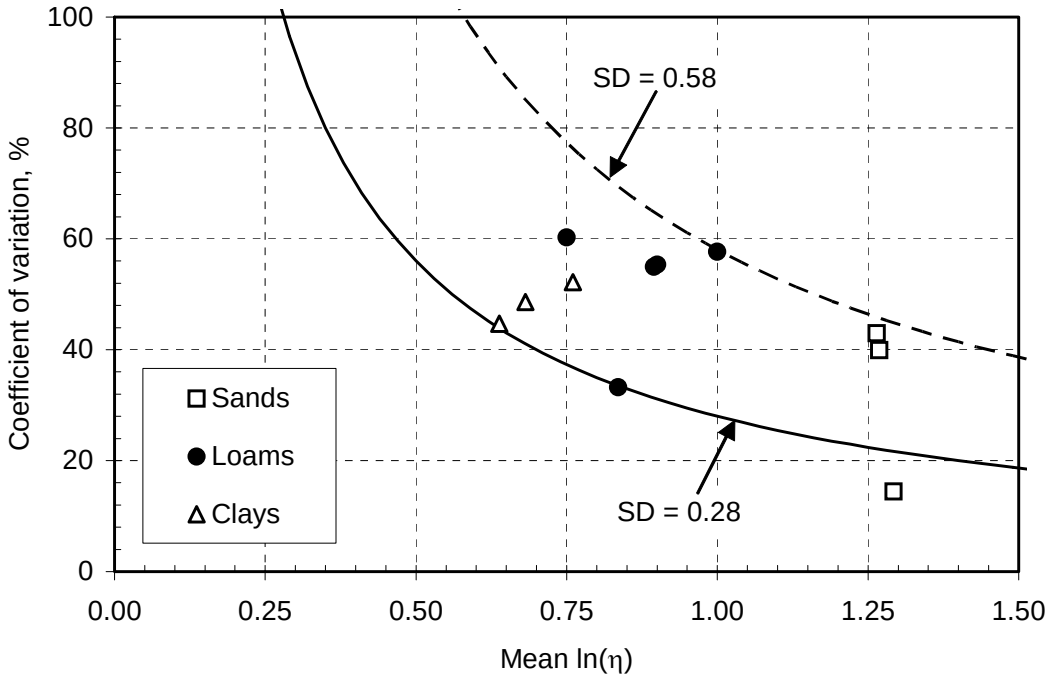

Figure 5.24 Mean versus the coefficient of variation of the natural logarithm of the hydraulic conductivity function slope, ln(η).

5.4.2.4 *Correlation coefficients between unsaturated soil parameters*

The correlation coefficient, ρ, between each pair of unsaturated soil parameters was determined with the aid of Minitab 13 (Minitab Inc., 2000). The parameters studied were n, $\ln(\psi_b)$, $\ln(\lambda_d)$, $\ln(\lambda_{res})$, $\ln(k^w_{sat})$, $\ln(\psi_{bk})$, and $\ln(\eta)$. The correlation coefficient, defined earlier in this chapter, is a measure of the degree of linear relationship between two variables. The correlation coefficient assumes a value between -1 and +1. If one variable tends to increase as the other decreases, the correlation coefficient is negative. Conversely, if the two variables tend to increase together the correlation coefficient is positive. A two-tailed correlation test was applied. The null hypothesis of the test performed was H0: coefficient of correlation is zero. P-values were computed, representing the probability of making a *type* 1 *error*, which is "rejecting the null hypothesis when it is true." The smaller the P-value, the smaller is the probability that a mistake would be made by rejecting the null hypothesis. The cut-off value used was 5%, that is, the null hypothesis was rejected when the P-value was less than 5%.

Table 5.5 presents the results of the correlation analyses. The coefficients of correlation are

presented for all pairs of variables, along with the symbol (*), indicating those tests for which the P-value obtained is less than 5% (i.e., the probability of rejecting the hypothesis that $\rho = 0$ when it is true is less than 5%). Figures D.1 to D.28 from Appendix D present a series of scatter plots for all possible pairs of variables, considering the parameters n, $\ln(\psi_b)$, $\ln(\lambda_d)$, $\ln(\lambda_{res})$, $\ln(k^w_{sat})$, $\ln(\psi_{bk})$, and $\ln(\eta)$. These scatter plots were used in the analysis of the data and as a qualitative verification of the analysis results.

The correlation coefficients presented in Table 5.5 were calculated considering all data records as a single group and also considering the three soil groups (Sa, L, and C) individually. Some correlation coefficients decreased when the data records where considered as a single group and others increased. Therefore, no clear trend was observed. Nevertheless, the P-values tended to decrease when the data records where considered as a single group. This is expected since an increase in the data points number results in a decrease in the uncertainty associated with a type 1 error. Table D.13 from Appendix D shows similar results, considering the numerous soil subgroups. The next paragraphs present a concise discussion focused on those correlation coefficients that presented P-values lower than 5% for all soil groups.

Porosity did not present substantial correlation with any parameter, with exception of the parameter $\ln(\lambda_{res})$. Still, the coefficient of correlation between n and $\ln(\lambda_{res})$ does not have a P-value lower than 5% for all soil groups. Similarly, the variable $\ln(\lambda_{res})$ does not present substantial correlation with any other parameter, with exception of the aforementioned correlation with porosity and some mild correlation with $\ln(\psi_b)$.

Noteworthy correlations involving the air-entry value were found considering both $\ln(\psi_b)$ and $\ln(\psi_{bk})$. While $\ln(\psi_b)$ presented considerable correlations with the SWCC-related parameters, $\ln(\psi_{bk})$ showed significant correlations with the parameters related to the k^w function. The parameters $\ln(\psi_b)$ and $\ln(\lambda_d)$ presented correlation coefficients that varied from +0.374 to +0.587. This significant positive correlation indicates that soils with larger air-entry value tend to be the same soils that have “poorly graded” grain and pore-size distributions. The parameters $\ln(\psi_b)$ and $\ln(\lambda_{res})$ presented correlation coefficients that varied from +0.211 to +0.281. This correlation was not expected, since in principle there is little physical meaning for the relationship between the air-entry value and the residual drainage slope.

Table 5.5 Correlation matrix for the hydraulic property parameters of unsaturated soil.

Param. (1)	Group (2)	n (3)	$\ln(\psi_b)$ (4)	$\ln(\lambda_d)$ (5)	$\ln(\lambda_{res})$ (6)	$\ln(k^w_{sat})$ (8)	$\ln(\psi_{bk})$ (9)	$\ln(\eta)$ (10)
n	All soils	1						
	Sands	1						
	Loams	1						
	Clays	1						
$\ln(\psi_b)$	All soils	-0.147*	1					
	Sands	-0.079	1					
	Loams	-0.096	1					
	Clays	-0.282*	1					
$\ln(\lambda_d)$	All soils	-0.311*	0.374*	1				
	Sands	0.084	0.587*	1				
	Loams	-0.032	0.443*	1				
	Clays	--	--	--				
$\ln(\lambda_{res})$	All soils	0.534*	0.211*	-0.399*	1			
	Sands	0.354*	0.270*	0.096	1			
	Loams	0.227	0.281*	-0.080	1			
	Clays	--	--	--	--			
$\ln(k^w_{sat})$	All soils	-0.210*	-0.216*	0.354*	-0.233*	1		
	Sands	0.193	-0.276*	0.234	-0.086	1		
	Loams	0.249	-0.174	0.192	0.095	1		
	Clays	0.228	-0.347*	--	--	1		
$\ln(\psi_{bk})$	All soils	0.078	0.140	0.373*	-0.041	-0.408*	1	
	Sands	0.073	0.187	0.127	0.141	-0.427*	1	
	Loams	0.012	0.320*	0.626*	-0.167	-0.275*	1	
	Clays	0.032	0.023	--	--	-0.630*	1	
$\ln(\eta)$	All soils	-0.151*	0.025	0.675*	-0.227*	0.393*	0.500*	1
	Sands	0.092	0.083	0.365*	0.105	0.057	0.755*	1
	Loams	0.079	0.228	0.847*	-0.095	0.280*	0.700*	1
	Clays	0.300*	-0.084	--	--	0.023	0.338*	1

symmetric

(*) indicates the correlation coefficients for which the P-value < 5%.

The parameters $\ln(\psi_{bk})$ and $\ln(k^w_{sat})$ presented moderate to high correlation coefficients that varied from -0.275 to -0.630. The negative correlation between $\ln(\psi_b)$ and $\ln(k^w_{sat})$ was also expected since the same factors that cause higher air-entry values are responsible for lower values of k^w_{sat}, such as larger fractions of fines. The parameters $\ln(\psi_{bk})$ and $\ln(\eta)$ presented correlation coefficients that varied from +0.338 to +0.755. This significant degree of correlation indicates that soils with larger air-entry value tend to be the same soils that have "poorly graded" grain and pore-size distributions.

Finally, the parameters $\ln(\eta)$ and $\ln(\lambda_d)$ presented high degrees of correlation that varied from +0.365 to +0.847. This high degree of positive correlation was also expected. Several mechanistic models of prediction of the hydraulic conductivity function indicate that the slope of the k^w function increases with increasing values of λ_d (e.g., Brooks and Corey, 1964).

5.4.3 *Summary of the results of the statistical study of unsaturated soil parameters*

Table 5.6 presents a summary of the mean values for the unsaturated soil parameters n, $\ln(\psi_b)$, $\ln(\lambda_d)$, $\ln(\lambda_{res})$, $\ln(k^w_{sat})$, and $\ln(\eta)$ along with the exponential value of all variables, except for porosity. The values of $\ln(\psi_{bk})$ presented in the previous sections cannot be ignored since they differ significantly from the mean values of $\ln(\psi_b)$. Therefore, independent best estimate of mean value of the air-entry value are suggested for $\ln(\psi_b)$ and $\ln(\psi_{bk})$. The values presented in Table 5.6 are suggested as the best measures of central tendency for each main soil group. All parameters presented in Table 5.6 can be assumed as normally distributed.

Table 5.7 presents a summary of the coefficients of variation for the unsaturated soil parameters n, $\ln(\psi_b)$, $\ln(\lambda_d)$, $\ln(\lambda_{res})$, $\ln(k^w_{sat})$, and $\ln(\eta)$. The values of $\ln(\psi_b)$ were established by combining the results obtained for $\ln(\psi_b)$ and $\ln(\psi_{bk})$. General ranges considering all soil types are presented, along with specific information for each main soil group, Sa, L, and C. The general ranges were defined based on the range of all soil groups. Some ranges of coefficient of variation suggested in column 2 are not applicable when the mean value of the parameter is within the range -0.5 and 0.5. In that case, the values of standard deviation provided in column 2 of Table 5.7 must be adopted. The same criteria regarding the mean values between -0.5 and 0.5 must be extended for the variability of each soil group. Therefore, the values provided in columns 3, 4, and 5 of Table 5.7 must also be replaced by the standard values provided in column 2, when the mean value of the variable is within the range -0.5 and 0.5.

Table 5.6 Mean values for unsaturated soil properties by soil group.

Group (1)	Sands (2)	Loams (3)	Clays (4)
n	0.410	0.500	0.534
$\ln(\psi_b)$, ln(kPa)	0.856	0.927	0.999
exponential	2.35	2.53	2.71
$\ln(\lambda_d)$	0.198	-0.737	--
exponential	1.219	0.478	--
$\ln(\lambda_{res})$	-3.141	-2.445	--
exponential	0.043	0.087	--
$\ln(k^w_{sat})$, ln(m/s)	-11.34	-12.58	-16.03
exponential	1.19×10^{-5}	3.44×10^{-6}	1.09×10^{-7}
$\ln(\psi_{bk})$, ln(kPa)	0.119	-0.047	0.527
exponential	1.13	0.95	1.69
$\ln(\eta)$	1.268	0.895	0.682
exponential	3.554	2.447	1.978

Table 5.7 Variability of unsaturated soil properties.

Soil parameter (1)	General ranges for all soils of the Coefficient of Variation (CV) and Standard Deviation (SD) (2)	Coefficient of Variation		
		Sands (3)	Loams (4)	Clays (5)
n	CV = 13 – 19%	13%	17%	19%
$\ln(\psi_b)$	CV = 75 – 205% for -0.5 > E[$\ln(\psi_b)$] > 0.5 ln(kPa) otherwise, SD = 0.8 – 2.1 ln(kPa)	85%	115%	205%
$\ln(\lambda_d)$	CV = 75 – 100% for -0.5 > E[$\ln(\lambda_d)$] > 0.5 otherwise, SD = 0.45 – 0.80	100%	90%	--
$\ln(\lambda_{res})$	CV = 8 – 14% for -0.5 > E[$\ln(\lambda_{res})$] > 0.5 otherwise, SD = 0.20 – 0.45	14%	12%	--
$\ln(k^w_{sat})$	CV = 13 – 16%	16%	15%	13%
$\ln(\eta)$	CV = 40 – 55%	40%	55%	50%

Table 5.8 Correlation matrix for the hydraulic property parameters of unsaturated soil.

Parameter (1)	n (2)	$\ln(\psi_b)$ (3)	$\ln(\lambda_d)$ (4)	$\ln(\lambda_{res})$ (5)	$\ln(k^w_{sat})$ (6)	$\ln(\eta)$ (7)
n	1					
$\ln(\psi_b)$	0	1			*symmetric*	
$\ln(\lambda_d)$	0	0.450	1			
$\ln(\lambda_{res})$	0	0.250	0	1		
$\ln(k^w_{sat})$	0	-0.400	0	0	1	
$\ln(\eta)$	0	0	0.600	0	0.600	1

Table 5.8 presents a summary of the correlation coefficients for pairs of unsaturated soil parameters, considering the parameters n, $\ln(\psi_b)$, $\ln(\lambda_d)$, $\ln(\lambda_{res})$, $\ln(k^w_{sat})$, and $\ln(\eta)$. The correlation coefficients associated with the air-entry value were established by combining the results obtained for $\ln(\psi_b)$ and $\ln(\psi_{bk})$. Average values applicable to all soil types were established in order to simplify the results. The values presented in Table 5.8 are suggested as general approximate values applicable to any soil type.

5.4.4 *Soil-water characteristic curve and hydraulic conductivity function scenarios considering estimate points of the soil parameters*

The alternative point estimate method and sensitivity analysis framework presented in Chapter 3 are based on the computation of the *factor of safety* for a number of input variable case scenarios. The central tendency and variability measures presented in the previous section must be used in order to establish case scenarios required. The several input parameter case scenarios produce the series of unsaturated soil property function scenarios shown herein.

Assuming that n is the number of input random variables, a total of $2n+1$ case scenarios (i.e., estimate points) are required for uncorrelated input variables. According to the alternative point estimate method, the first scenario is composed of the mean values of each input random variable. The remaining $2n$ scenarios are obtained by shifting one input variable at a time and

taking the mean values for the remaining input variables. Normally distributed variables must be shifted around the mean value by plus and minus one standard deviation.

It has been shown in the previous sections that the soil-water characteristic curve and hydraulic conductivity function parameters are log normally distributed. The log normally distributed parameters can be analysed as normally distributed parameters if the natural logarithm transformation is taken. Therefore, each case scenario (or estimate point) can be established based on the natural logarithm values. In order to perform the transient coupled heat and moisture flow analyses, transformed variables must be converted back, taking the exponential.

Figures 5.25, 5.26, and 5.27 present the case scenarios for the soil-water characteristic curve of sand, loam, and clay soils, based on the data provided in the previous sections. The mean values used are those presented in Table 5.6. The case scenarios were established taking standard deviation values based on the coefficients of variations presented in Table 5.7. The only exception was the variation of variable $\ln(\lambda_d)$, which was taken as SD = 0.592. It can be seen in Figs. 5.25, 5.26, and 5.27 that the 7 ($2n$+1 with n = 3) case scenarios form envelopes that surround the region with greater concentration of data points.

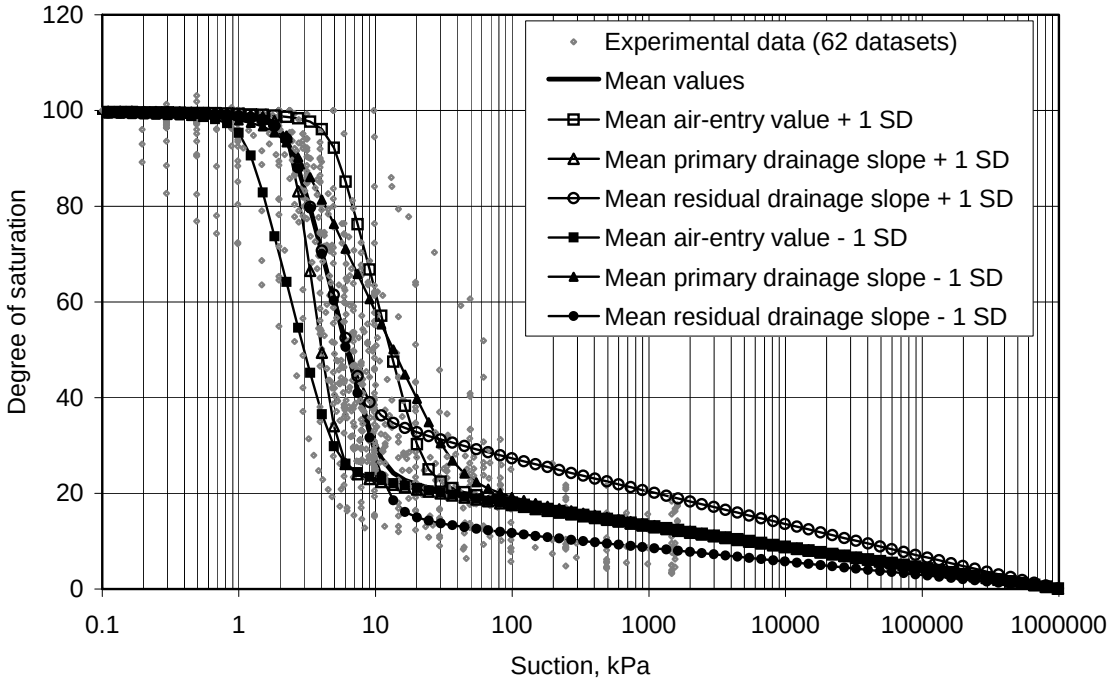

Figure 5.25 Sand soil-water characteristic curves for various scenarios considering the computed mean and standard deviation values of the SWCC parameters.

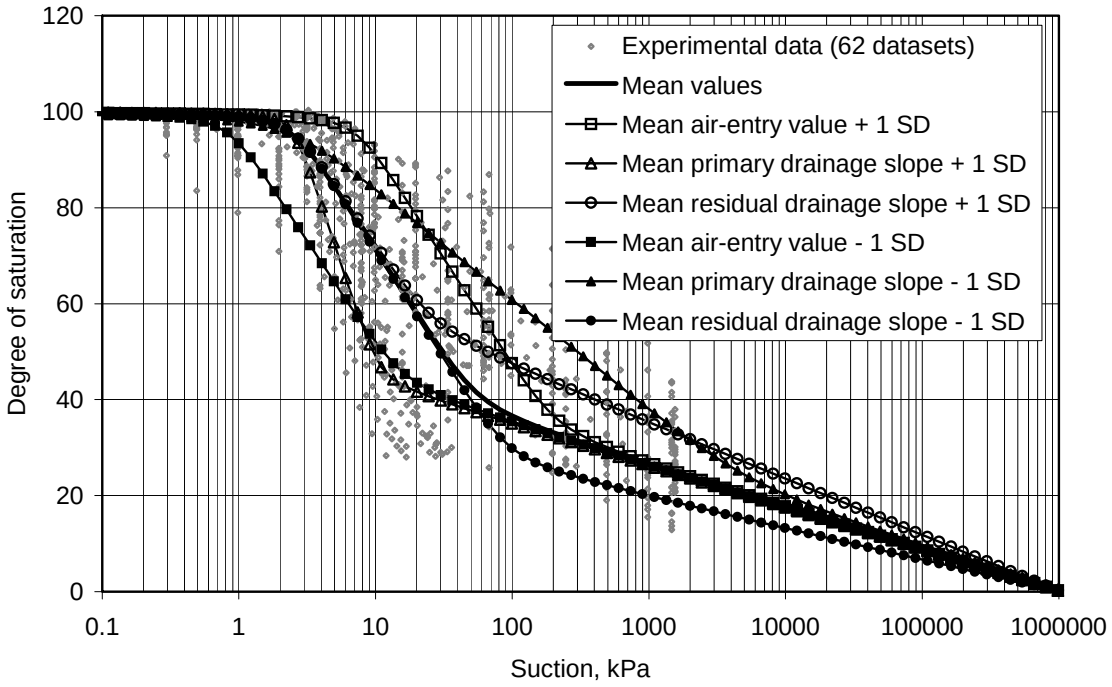

Figure 5.26 Loam soil-water characteristic curves for various scenarios considering the computed mean and standard deviation values of the SWCC parameters.

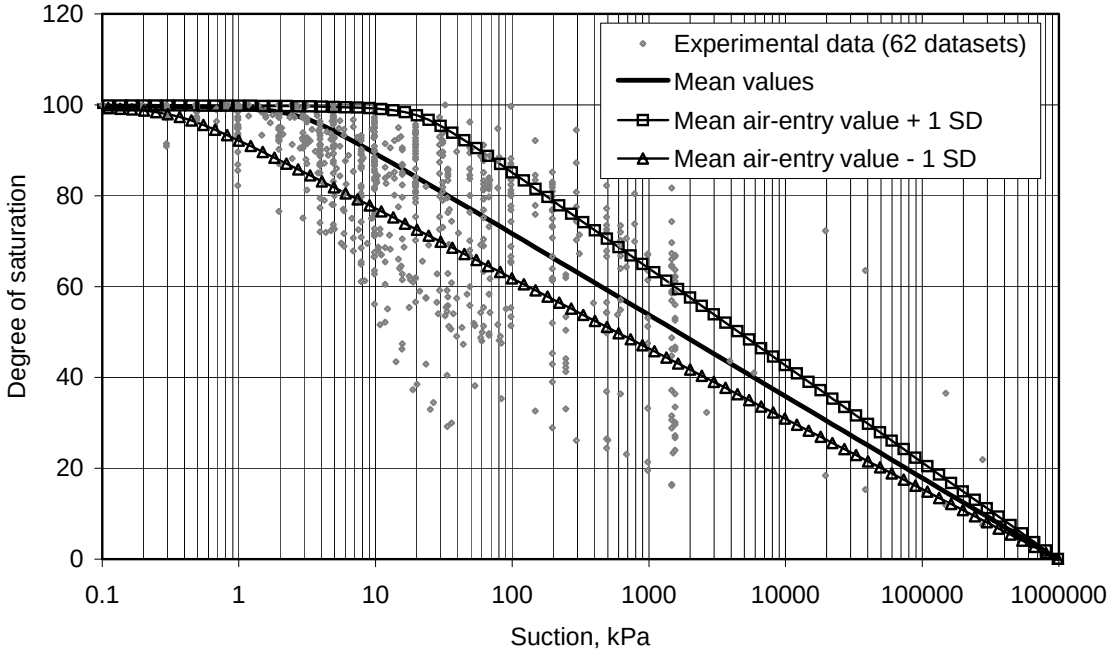

Figure 5.27 Clay soil-water characteristic curves for various scenarios considering the computed mean and standard deviation values of the SWCC parameters.

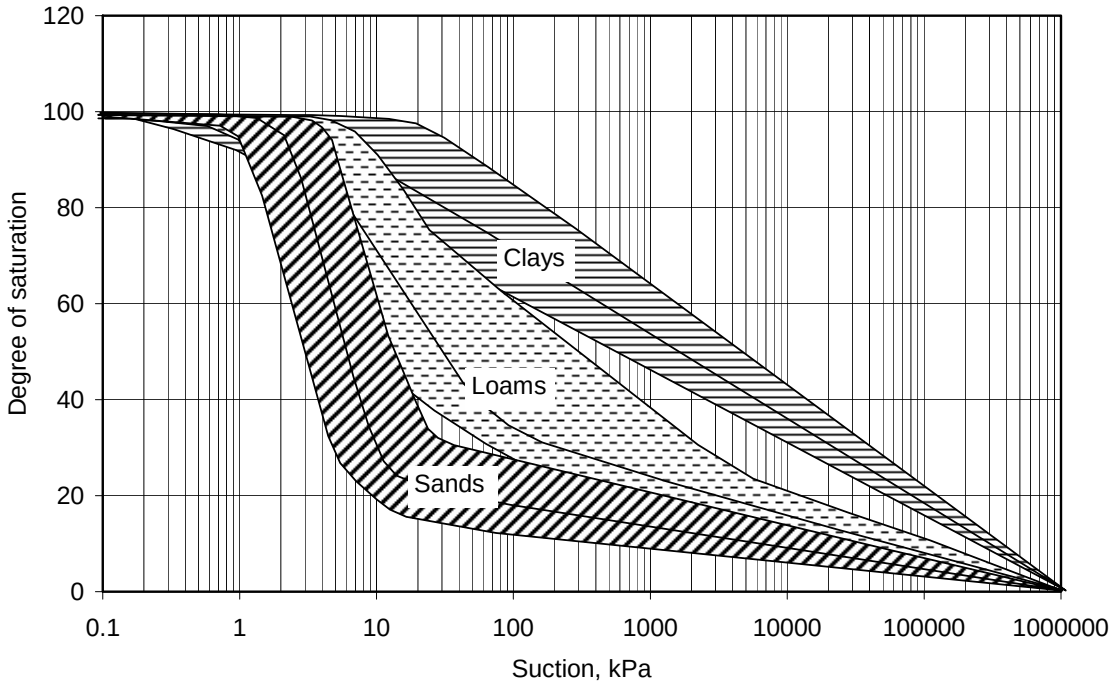

Figure 5.28 Regions indicating typical soil-water characteristic curves for the three main soil groups.

Envelopes for the three soil types were drawn and plotted in Fig. 5.28. A clear distinction between the envelopes of each soil type is observed. The mean values of $\ln(\psi_b)$ are not significantly different, but the coefficients of variation of $\ln(\psi_b)$ increase considerably for fine grained soils. The most striking difference between the SWCC's of each soil type is in terms of the primary and residual drainage slopes.

Figures 5.29, 5.30, and 5.31 present the case scenarios for the hydraulic conductivity function of sand, loam, and clay soils. The mean values adopted are those presented in Table 5.6. The one-standard deviation variations used for the establishment of the case scenarios were based on the coefficients of variations presented in Table 5.7. The only exception was the variation of the variable $\ln(\psi_{bk})$, which was taken as SD = 1.18 ln(kPa) for sands and SD = 1.39 ln(kPa) for loams. Once again, the 7 case scenarios presented in Figs. 5.29, 5.30, and 5.31 form envelopes surrounding the regions with greater concentration of data points. Such envelopes were drawn and plotted together in Fig. 5.32. A clear distinction between the envelopes of each soil type is observed, both in terms of k^w_{sat} and η. It is interesting to note that the break point (ψ_{bk}) decreases for soils with more fines.

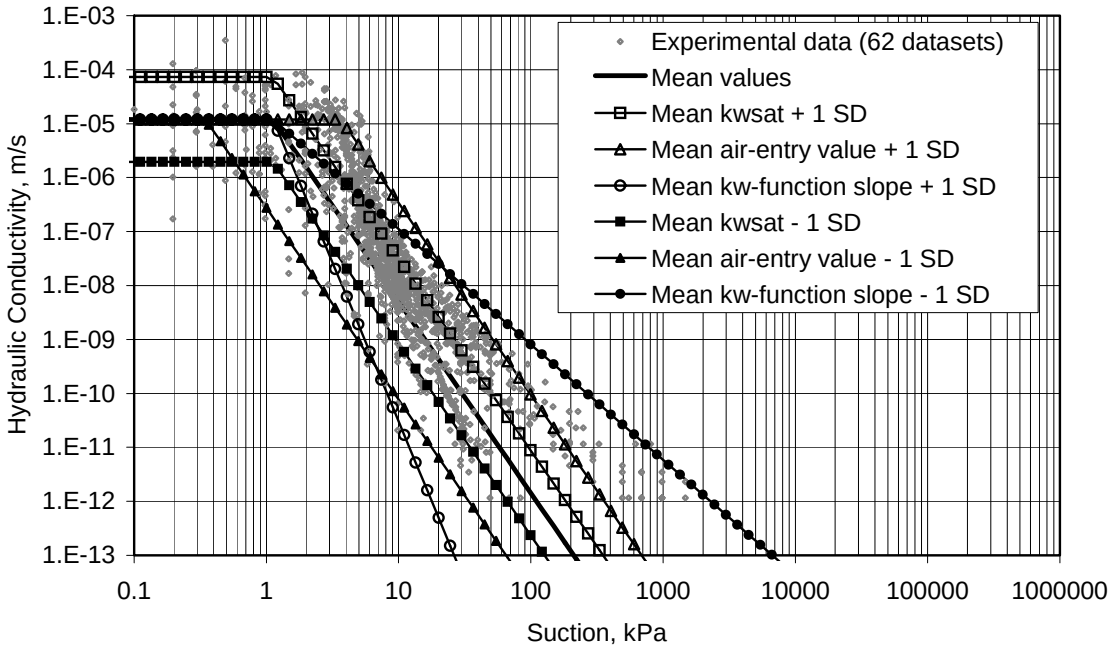

Figure 5.29 Sand hydraulic conductivity functions for various scenarios considering the computed mean and standard deviation values of the k^w function parameters.

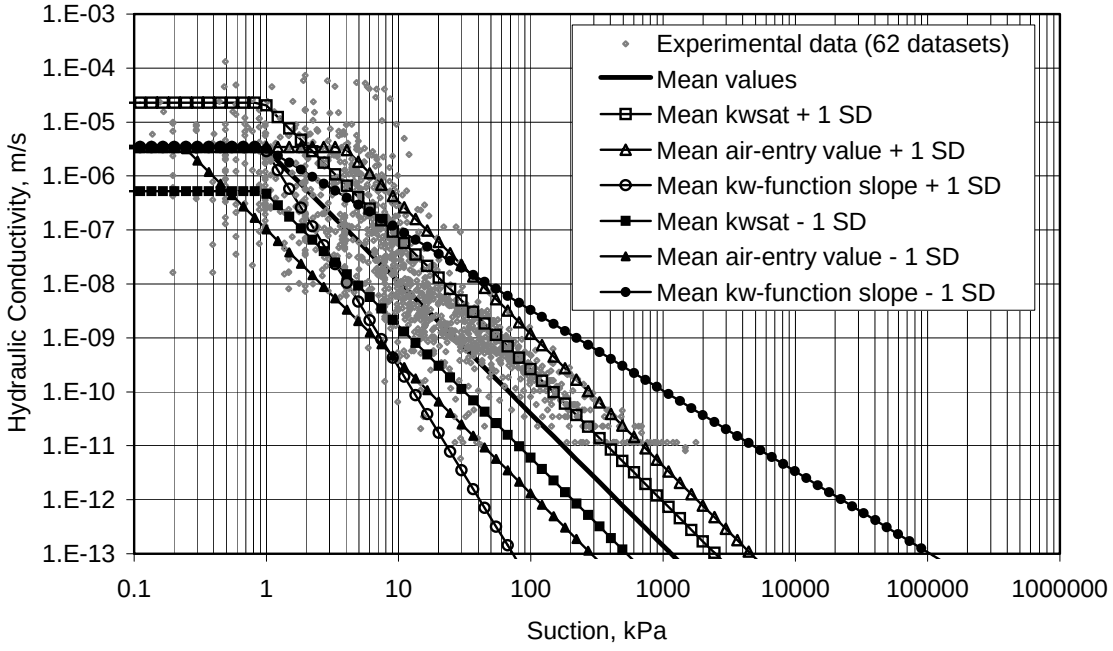

Figure 5.30 Loam hydraulic conductivity functions for various scenarios considering the computed mean and standard deviation values of the k^w function parameters.

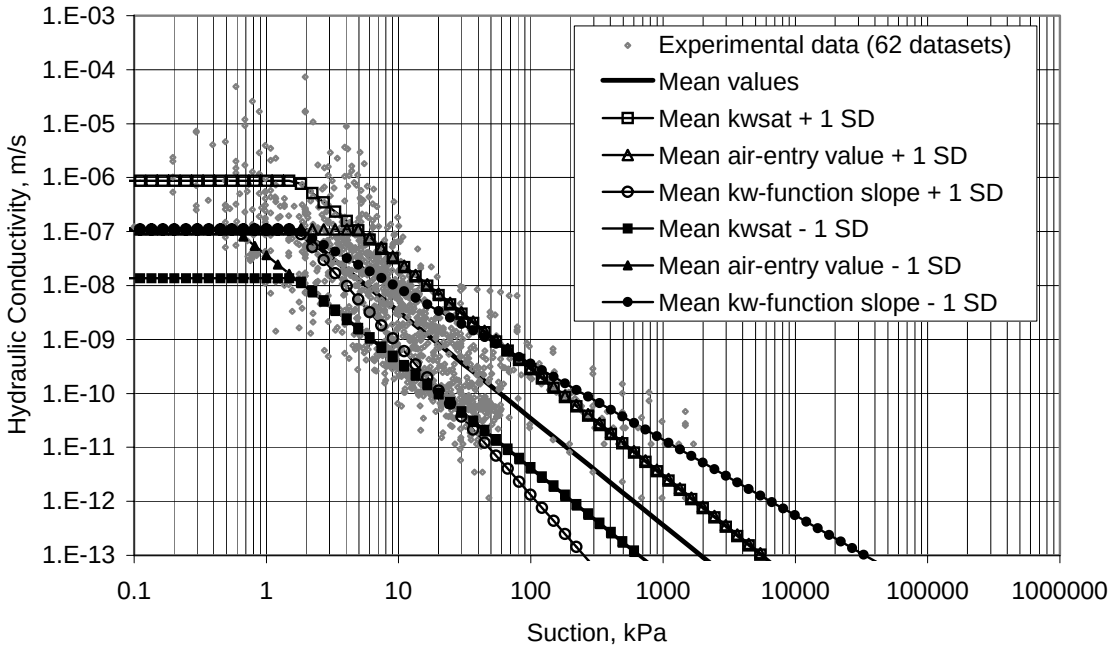

Figure 5.31 Clay hydraulic conductivity functions for various scenarios considering the computed mean and standard deviation values of the k^w function parameters.

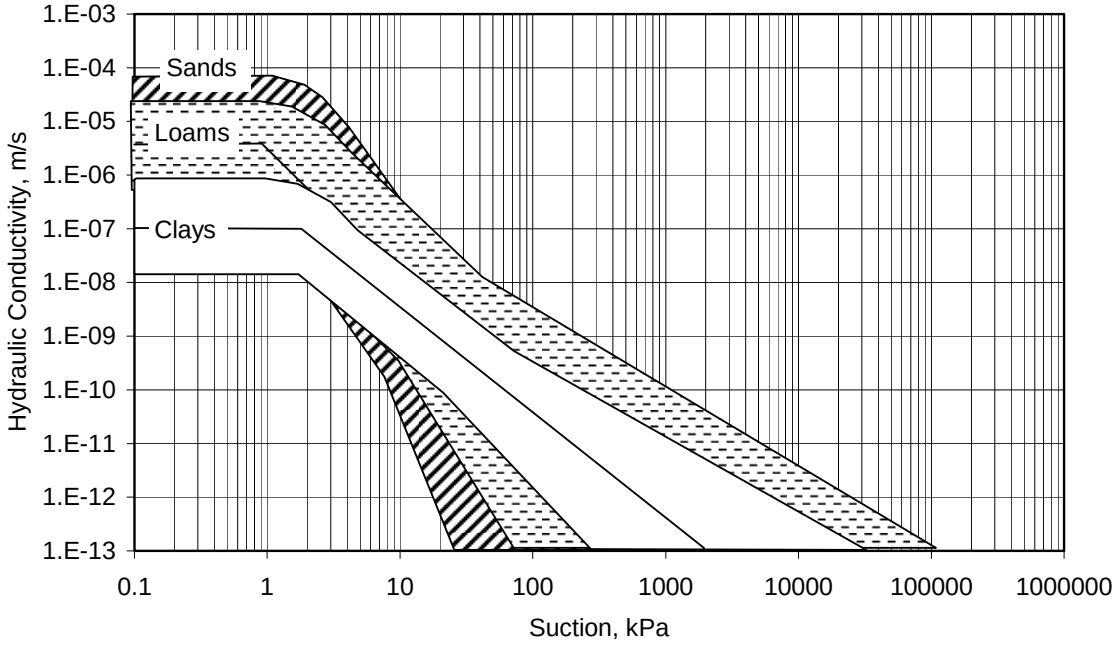

Figure 5.32 Regions indicating typical hydraulic conductivity function for the three main soil groups.

5.5 CHAPTER SUMMARY

This chapter presented a comprehensive statistical study of unsaturated soil property variability. The primary objective was to present approximate variability values that could be used in the implementation of the W-GHA model. The approximate values presented herein can also be combined with site or region-specific statistical data, through a Bayesian update approach.

A concise overview of the variability of saturated soil properties was presented first. Section 5.2 presented the sources of geotechnical uncertainty and a description of some of the most used approaches for the assessment of geotechnical variability. It was shown that most probabilistic analyses can be performed based on typical variability data, rather than relying on laborious measurement repetitions. Section 5.3 presented a summary of typical values of saturated soils parameter variability collected from the literature. Variability data was presented for various soil parameters, including the shear strength parameters and the saturated hydraulic conductivity. It was shown that most soil properties can be considered normally or log normally distributed.

Section 5.4 presented the statistical assessment of unsaturated soil properties. The property functions studied were the soil-water characteristic curve and the hydraulic conductivity function. The statistical study was based on a large database of soils (SoilVision Systems, 2003). A total of 186 data sets were sampled from the SoilVision database. The study was undertaken considering soil groups established based on the USDA textural classification system. Three soil groups were established; namely, sands, loams, and clays.

A methodology was developed for the statistical assessment of unsaturated soil property functions. According to the methodology developed herein, appropriate nonlinear unsaturated soil property equations and fitting parameters must be employed. All equation parameters must be related to a clearly defined curve feature and the equation parameters must be mathematically independent. A new soil-water characteristic curve equation was developed to this end (see Appendix C) and a bilinear equation was adopted for the hydraulic conductivity. The following soil parameters were defined: n, ψ_b, λ_d, λ_{res}, k^w_{sat}, ψ_{bk}, and η. The data sets sampled from the SoilVision database were fitted using the equations proposed herein and a minimum squared residuals algorithm implemented in Microsoft® Excel 2002. The statistical analyses were carried out on the collection of best-fit parameters thereby obtained.

The following statistical analyses and measures were undertaken: normality tests; basic

descriptive statistics; variability measures; and correlation matrices. The normality tests showed that unsaturated soil parameters can be considered log normally distributed. It was suggested that such parameters should be handled using the natural logarithm values. A normal distribution can be employed to represent the natural logarithm of the unsaturated soil parameters. Various central tendency measures were contemplated. The mean values of the natural logarithm of the soil parameters provided the best central tendency measure. The best measures of central tendency values for each soil group (i.e., sands, loams, and clays) were summarised in Section 3.4.3.

Variability measures were presented in terms of standard deviations and coefficients of variation. Fairly constant coefficients of variations were determined for various soil properties and soil groups. However, some unsaturated soil parameters have mean values that may fall within a -0.5 – 0.5 range. It was found that the coefficient of variations may provide a poor measure of variability for such soil parameters. A combination of standard deviation and coefficient of variation values were proposed for these parameters. Variability measures for each soil group were summarised in Section 3.4.3.

The correlation matrices were determined considering the three soil groups individually and all data sets together. Some correlation coefficients decreased when the data records where considered as a single group and others increased. Therefore, no clear trend was observed. Noteworthy correlations involving the air-entry value were found considering both $\ln(\psi_b)$ and $\ln(\psi_{bk})$. While $\ln(\psi_b)$ presented considerable correlations with the SWCC-related parameters, $\ln(\psi_{bk})$ showed significant correlations with the parameters related to the k^w function. A significant positive correlation between $\ln(\psi_b)$ and $\ln(\lambda_d)$ indicated that soils with larger air-entry value tend to be the same soils that have "poorly graded" grain and pore-size distributions. The parameters $\ln(\psi_{bk})$ and $\ln(k^w_{sat})$ presented moderate to high negative correlations, as expected. The pair $\ln(\psi_{bk}) - \ln(\eta)$, $\ln(\eta) - \ln(\lambda_d)$, and $\ln(\eta) - \ln(k^w_{sat})$ presented moderate to strong positive correlation, as expected. The correlation coefficients obtained were summarised in Section 3.4.3.

Finally, the central tendency and variability measures presented herein were used in order to establish case scenarios required by the alternative point estimate method and sensitivity analysis framework presented in Chapter 3. The several input parameter case scenarios produced a series of unsaturated soil property function scenarios surrounding the regions with greater concentration of data points, as expected.

Chapter 6

Analysis of Hypothetical Railway Embankments and Sensitivity Analysis

6.1 GENERAL

This chapter presents analyses of hypothetical embankments designed to demonstrate the application of the W-GHA model to typical railway conditions and a sensitivity analysis study. The analyses presented herein have the following objectives:

i) Demonstrate the application of the W-GHA model to hypothetical railway embankment conditions and evaluate the performance of the W-GHA model;
ii) Determine the sensitivity of the stability of hypothetical embankments to the inherent variability of the input parameters, indicating what parameters require more detailed assessment and what parameters can be treated as fixed, certain variables;
iii) Indicate whether any simplifications can be made to the W-GHA model.

Sensitivity analysis corresponds to the final analytical step towards the completion of the decision analysis process cycle (Figure 3.1) and is an essential component of the hazard assessment procedure. The simplified term "sensitivity" is used throughout this chapter to refer to how much the uncertainty of the *factor of safety* is sensitive to the inherent uncertainty of a given input parameter. The sensitivity of the *factor of safety* to a given input parameters can be

assessed using a number of different approaches. The sensitivity of the *factor of safety* to each input parameter will be assessed herein using *Tornado Diagrams* and following the sensitivity analysis framework presented in Chapter 3.

Section 6.2 presents the description of the hypothetical embankment case scenarios. The case scenarios were established in order to cover a wide range of possible embankment configurations. Varying geometry, soil types, and initial conditions are considered herein. Two distinct weather conditions were analysed; namely, a precipitation event and an evaporation event. The soil-atmosphere boundary conditions were separated in this manner in order to identify the sensitivity of the parameters and demonstrate the performance of the W-GHA model for the two opposite atmospheric forcing conditions. Section 6.3 describes the selection of soil properties and the statistical modelling of soil properties required for establishing soil property case scenarios. Section 6.4 presents a concise description of the analysis procedure.

Section 6.5 presents the results and discussions corresponding to the analyses using the W-GHA model and hypothetical embankment configurations. Section 6.6 presents the sensitivity analysis results and discussions. The sensitivity analysis study was carried out using the same embankment configurations presented in Section 6.5. Section 6.7 presents a summary of the findings. Section 6.8 presents a concise description of how the proposed framework for quantification of embankment hazards can be applied in the practice under various conditions. Finally, Section 6.9 presents a summary of the chapter.

6.2 DESIGN OF HYPOTHETICAL EMBANKMENT CONFIGURATIONS

A summary of derailment occurrences during the 1990' that were investigated by the Transportation Safety Board (TSB) was presented in Chapter 2. The occurrences presented in Chapter 2 are examples of typical derailments caused by embankment failures. It was shown that diverse conditions can be found along the Canadian railway networks. The failed railway embankments presented in Chapter 2 were used as a reference for establishing hypothetical railway embankment configurations.

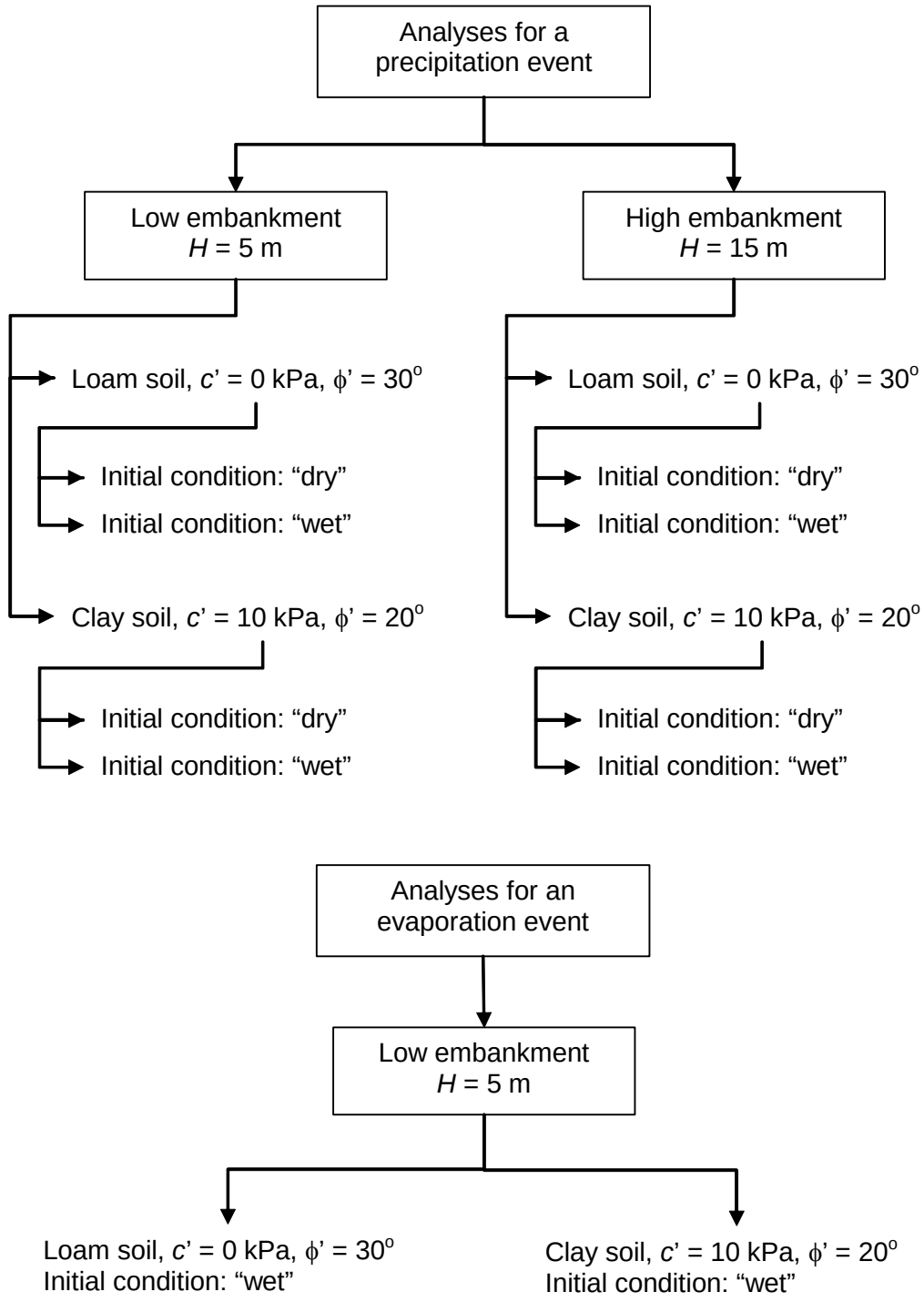

"dry" condition: hydrostatic pore-water pressure diagram with minimun u_w = -100 kPa
"wet" condition: hydrostatic pore-water pressure diagram with minimun u_w = -20 kPa

Figure 6.1 Embankment configurations analysed.

This section presents a detailed description of the hypothetical embankment configurations selected for the analyses using the W-GHA model and sensitivity analyses. The embankment configurations were defined by a combination of typical geometries ranges, soil properties, initial conditions, and weather conditions. The embankment configurations presented herein result in a range of conditions that cover a large number of embankments found along the Canadian Pacific Railway network.

Figure 6.1 presents a summary of the embankment configurations analyses herein. Two typical embankment heights were selected; namely, "*High*" and "*Low*" embankment. Two distinct soil types were analysed for each embankment size; namely, "*Loam*" and "*Clay*" embankment. The "Loam" embankment corresponds to a silty soil. The effect of antecedent weather conditions was considered through two different initial pore-water pressure distributions; namely, "*Dry*" and "*Wet*" embankment conditions. All analyses were performed for a precipitation period of 14 days or an evaporation period of 42 days. Constant precipitation and potential evaporation rates were applied, in order to simplify the analyses. However, it is suggested herein that weather conditions can be more accurately represented by using sinusoidal functions. The next sections will describe in detail the case scenarios selected.

6.2.1 *General embankment description: geometry, boundary, and initial conditions*

Figures 6.2 and 6.3 present the embankment geometries selected for the sensitivity analyses. Derailments caused by embankment failures have been observed in both relatively low and relatively high embankments. Failed embankments as low as 6 meters and as high as 15 meters have been observed (see Table 2.1). In order to reflect these conditions, two embankment sizes were selected for the sensitivity analyses, 5 and 15 m high. The side slopes selected, at 1.5H:1.0V (33.7^o), can be considered representative of a large number of embankments found along the Canadian railways network. An embankment crest width of 5 meters was selected, corresponding to a single lane. The lateral and bottom boundaries were extended away from the base of the embankment, as shown in Figs. 6.2 and 6.3, in order to avoid artificial boundary effects that could interfere with the analyses.

6.2.1.1 *Boundary conditions for the PDEs governing force equilibrium*

External loads and fixed displacement boundary conditions can be used for the PDE governing force equilibrium. An external load of 28 kN/m^2 distributed along 2.5 meters was selected to represent the train load, as shown in Figs. 6.2 and 6.3. Displacement restrictions in the *x*- and *y*-

directions were placed at the bottom boundary and displacement restrictions in the *x*-direction were placed in the lateral boundaries. These displacement conditions were selected in order to reproduce the "switch-on" gravity conditions with no restrictions for vertical settlement.

6.2.1.2 *Boundary conditions for the PDE governing water flow*

Two distinct soil-atmosphere boundary conditions were analysed, corresponding to a *precipitation event* and an *evaporation event*. A constant precipitation of 40 mm/day was selected for the precipitation analyses. The precipitation rate of 40 mm/day is comparable to the antecedent precipitation rates and melting rates measured for the Conrad, Creston, and Keewatin derailments (see Chapter 2). The use of constant potential evaporation and precipitation rates is compatible with the data available through conventional weather forecast. More detailed weather data (e.g., hourly data) could only be obtained based on measured data, after a weather event took place.

A potential evaporation rate of 8 mm/day was selected for the evaporation analyses. This value was applied as a constant rate throughout the analysis period (i.e., 42 days for the evaporation analyses). A constant potential evaporation rate is deemed as an appropriate approximation given the objectives of the analyses presented herein. Nevertheless, relative humidity, air temperature, and net radiation would be better described by using a cyclic function, such as a sinusoid. This could be done by establishing the maximum and minimum daily values and establishing the function phase. Further refinements could be done, by taking an exact measure of the daylight length for the period of the year of concern. Daylight lengths can be considered fixed throughout the year for regions at relatively low latitudes, close to or between the Tropics of Cancer and Capricorn.

Figures 6.2 and 6.3 present also the internal water flow boundary conditions selected. A no-flow condition was selected above the initial water table and a constant head was selected bellow the initial water table. These boundary conditions reflect a condition were the groundwater regimes have negligible interaction with the soil-atmosphere water flow. This simplification is adequate on the short-term analyses (Freeze and Cherry, 1979), such as the analyses for the assessment of near ground surface railway embankment stability.

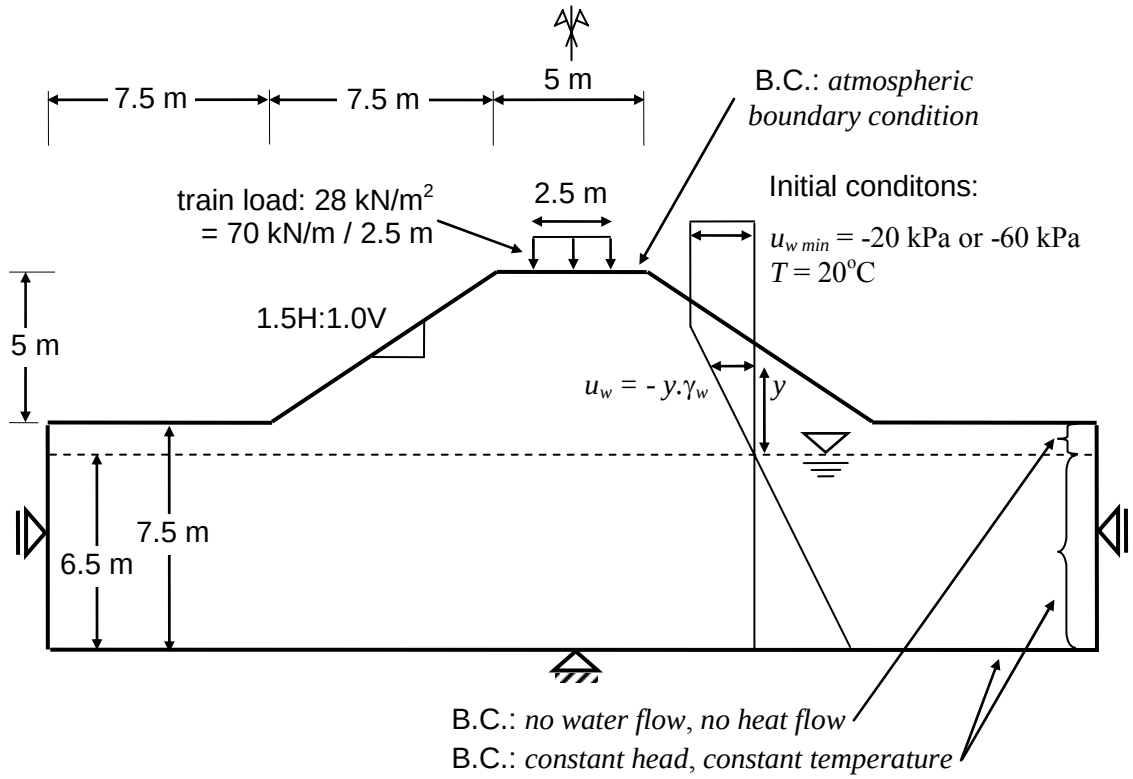

Figure 6.2 Low embankment: geometry, boundary conditions, and initial conditions.

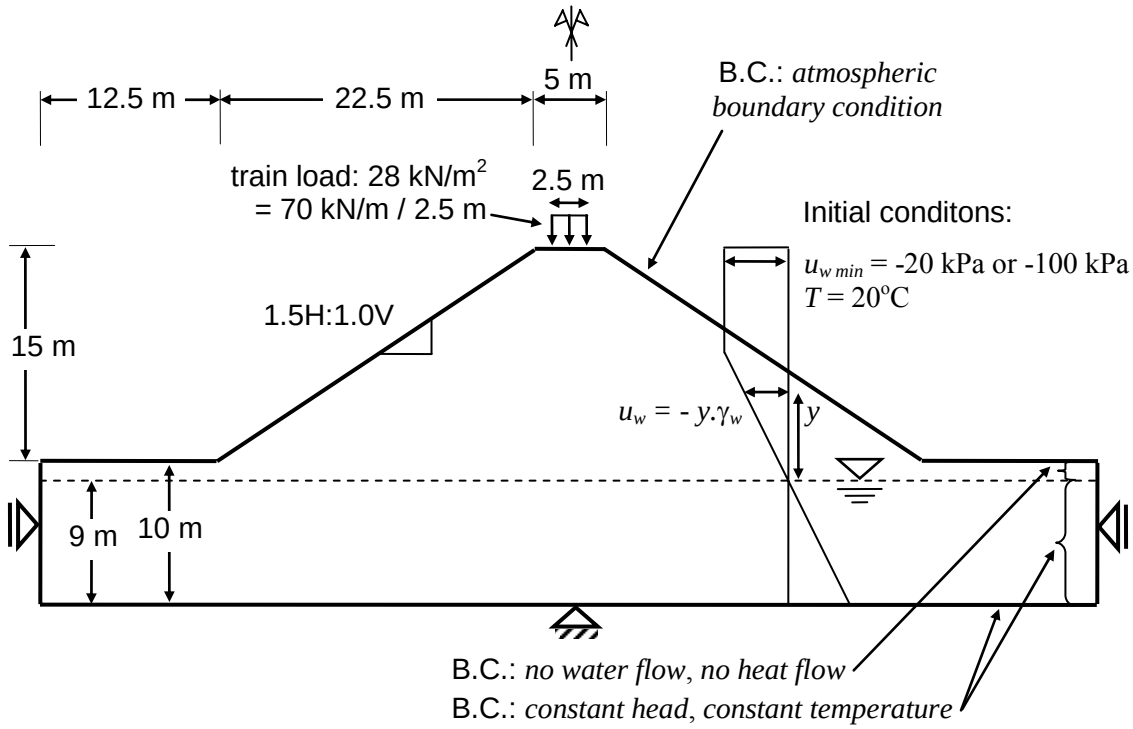

Figure 6.3 High embankment: geometry, boundary conditions, and initial conditions.

6.2.1.3 *Boundary conditions for the PDE governing heat flow*

A constant net radiation rate of 15 mm/day was selected for the evaporation analyses. A sinusoid similar to that described for the potential evaporation conditions could be applied to the net radiation conditions. Figures 6.2 and 6.3 present the internal heat flow boundary conditions selected. A no-flow heat condition was selected above the initial water table and a constant temperature was selected below the initial water table, equal to 20°C. These boundary conditions correspond to negligible geothermal gradients. This simplification is adequate for short-term analyses such as the analyses for the assessment of railway embankment stability.

6.2.1.4 *Initial conditions for temperature and pore-water pressure*

Initial pore-water pressures and initial temperature distributions must be established for the assessment of weather-related geo-hazards. Initial pore-water pressure distributions where established based on a combination of hydrostatic distributions and minimum pore-water pressure values. Two scenarios were considered herein, as shown in Figs. 6.2 and 6.3; namely, a relatively "*dry*" condition, with a minimum pore-water pressure of -100 kPa (-60 kPa for the low embankment) and a relatively "*wet*" condition, with a minimum pore-water pressure of -20 kPa. Both initial conditions were based on a water table located one meter below the embankment foot (i.e., at $y = 6.5$ and 9 m for the low and high embankments, respectively). A homogeneous temperature distribution was assumed, the temperature being 20°C. Table 6.1 presents a summary of the embankments geometry, boundary conditions, and initial conditions adopted.

6.3 SELECTION AND STATISTICAL ASSESSMENT OF SOIL PROPERTIES

This section presents the selection and statistical modelling of soil properties. The soil properties were statistically modelled based on case scenarios established according to the *alternative point estimate method*. The case scenarios for the soil properties are established based on appropriate soil parameters and soil parameter variability. The use of predictive approaches for unsaturated soil property functions was accommodated through the updating of predicted soil properties for each SWCC parameter case scenarios.

6.3.1 *Soil properties for the loam soil*

Two distinct soil types; namely *loam soil* and *clay soil* where chosen for the analyses,

representing typical conditions described in the TSB investigation reports presented in Chapter 2. The soil properties selected represent distinct conditions in terms of hydraulic properties and shear strength characteristics. The loam soil corresponds to a cohesionless soil with moderate hydraulic conductivity. The clay soil corresponds to a soil with a relatively low friction angle, higher cohesion, and relatively low hydraulic conductivity.

Tables 6.2 presents a summary of the soil properties and coefficients of variation selected for the loam soil. The parameters whose values are indicated in the bottom of Tables 6.2 are well defined and can be assumed as constants (i.e., not modelled as random variables). A total of 12 random variables are listed in Table 6.2. According to the *alternative point estimate method*, 12 random input variables result in 25 evaluations of the *factor of safety*, F_s. The selected soil-water characteristic curve parameters and saturated hydraulic conductivity correspond to the mean values presented in Chapter 5 for the loam soil type. The remaining unsaturated soil property functions where obtained using predictive equations based on the soil-water characteristic curve and selected saturated soil properties, as presented in Chapter 3. Correlations between soil parameters were neglected in order to narrow the scope of the analyses. The next sections will present in detail the mean values and coefficients of variation selected for the soil properties.

Table 6.1 Summary of embankment geometry, boundary, and initial conditions.

Variables (1)	Condition (2)
Height, *V*	5 and 15 m
Side slope	1.5H:1.0V
Train load	28 kN/m^2 distributed along 2.5 m
Precipitation rate for precipitation analyses	40 mm/day, constant, during 7 days
Evaporation rate for evaporation analyses	8 mm/day, constant, during 42 days
Soil-atmosphere heat flux for evaporation analyses	15 mm/day
Initial pore-water pressure distribution	Hydrostatic: water table at 1 m and a minimum pore-water pressure of -100 kPa for the dry condition (-60 kPa for the low embankment) and -20 kPa for the wet condition.
Initial temperature	20^{o}C

Table 6.2 Soil properties and coefficients of variation for the loam soil.

Analysis (1)	Soil property (2)	Related parameters (3)	Expected value (*) (4)	CV (**) (5)
Moisture flow analysis	$\theta = nS$	n	0.500	17%
		$\ln(\psi_b)$, ln(kPa)	0.927 (2.50)	115%
		$\ln(\lambda_d)$	-0.737 (0.50)	90%
		$\ln(\lambda_{res})$	-2.445 (0.090)	12%
	k^w	$\ln(k^w_{sat})$, ln(m/s)	-12.58 (3.5×10^{-6})	15%
	k^v	$\ln(D^v_{25^oC})$, ln(m^2/s)	-9.4 (8.33×10^{-5})	15%
Heat flow	λ	λ_s, W/(m ^oC)	6.0	25%
Stress and stability analysis	D_{ij}	E, kPa	15,000	30%
		μ	0.35	22%
	τ_f	c', kPa	0.0	30%
		ϕ'	30^o	10%
		$\ln(\kappa)$	0 (1)	SD = 0.5

Fixed parameters: $a = 0.050$; $G_s = 2.65$; $L_V = 2.501\times10^6 - 2.361\times10^3 T$ J/kg;
$\zeta_s = 2.23\times10^6$ W/(m^3 ^oC); $\zeta_w = 4.15\times10^6$ W/(m^3 ^oC);
(*) values between brackets are the exponential value;
(**) values for which the mean is close to zero may have the variability indicated in terms of standard deviation, SD.

6.3.1.1 *Soil-water characteristic curve for the loam soil*

Figure 6.4 presents the mean soil-water characteristic curve selected and the case scenarios defined based on the mean values and coefficients of variation presented in Table 6.2. The mean values and coefficients of variation adopted for the parameters $\ln(\psi_b)$, $\ln(\lambda_d)$, and $\ln(\lambda_{res})$ correspond to the typical values presented in Chapter 5 for loam soils. The three input variables, ψ_b, λ_d, and λ_{res}, are log normally distributed, as shown in Chapter 5. Mean values and coefficients of variation are presented for the natural logarithm of the parameters in order to provide more meaningful and adequate statistical measures. A total of 7 case scenarios are presented in Fig. 6.4, corresponding to the 3 input random variables. The 3 input parameters were varied by one standard deviation, in accordance with the *alternative point estimate method* procedure.

The variability of the SWCC parameters, $\ln(\psi_b)$, $\ln(\lambda_d)$, and $\ln(\lambda_{res})$, results in variability of the

unsaturated soil properties that were predicted using the SWCC; namely, the hydraulic conductivity function, water vapour conductivity function, the thermal conductivity function, and the shear strength envelope. The variability of predicted properties due to SWCC variability is considered herein by updating all the predicted properties for each of the 7 soil-water characteristic curve scenarios. Therefore, the sensitivity of the factor of safety to the SWCC parameters obtained during the sensitivity analyses incorporates the corresponding impacts due to several predicted properties.

6.3.1.2 *Hydraulic conductivity function for the loam soil*

The hydraulic conductivity function used herein has been predicted based on the soil-water characteristic curve, using the equation proposed by Brooks and Corey (1964):

$$k^w = k^w_{sat} \text{ for } (u_a - u_w) < \psi_b$$
$$k^w = f(k^w_{sat}, \psi_{b,}, \lambda_d, \lambda_{res}) = k^w_{sat}\left[\psi_b/(u_a - u_w)\right]^{\eta} \text{ for } (u_a - u_w) \geq \psi_b \quad (6.1)$$

where:

k^w_{sat} = saturated hydraulic conductivity;

η = $2 + 3\lambda$;

λ = $\Delta[\log(S_e)]/\Delta[\log(u_a - u_w)] \cong \dfrac{-\log[(1 + S_{res})/2]}{\log(\psi_b \psi_{res})/2 - \log\psi_b}$;

S_e = $[(S - S_{res})/(1 - S_{res})]$.

It is assumed that the variability of the predicted hydraulic conductivity function results from the variability in the input SWCC's parameters, ψ_b, λ_d, and λ_{res}, and results from to the variability in the saturated hydraulic conductivity, k^w_{sat}. The variability of the predicted k^w function must be considered by updating the k^w function for each soil-water characteristic curve scenario presented in Fig. 6.4. The variability of the saturated hydraulic conductivity, k^w_{sat}, is considered through additional case scenarios based on the coefficient of variation of $\ln(k^w_{sat})$ for loam soils presented in Chapter 5 and reproduced in Table 6.2. The hydraulic conductivity, k^w_{sat}, is log normally distributed. For this reason, the mean value and coefficient of variation are described for the natural logarithm of k^w_{sat}. The value of $\ln(k^w_{sat})$ was varied by one standard deviation. Figure 6.5 presents the resulting hydraulic conductivity function case scenarios, taking the variations of k^w_{sat} and the mean values for the SWCC parameters.

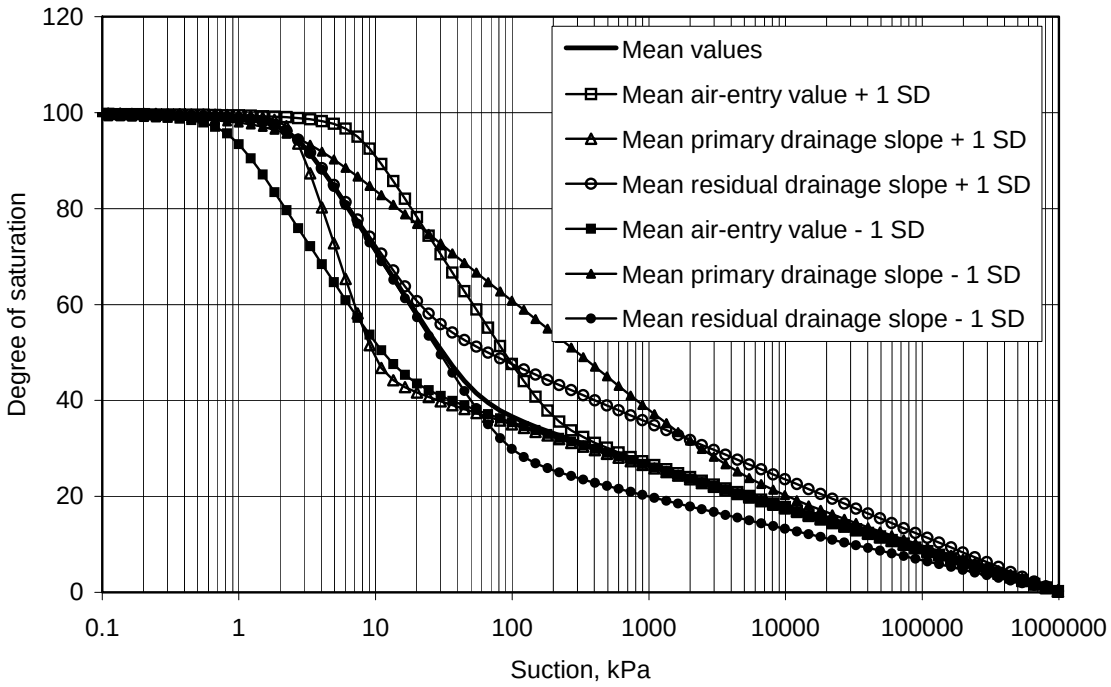

Figure 6.4 Case scenarios for the soil-water characteristic curve of the loam soil.

A large quantity of unsaturated hydraulic conductivity data has been collected and analysed in Chapter 5. This allowed an independent assessment of the variability of η. The coefficients of variation of ln(η) presented in Chapter 5 are not used within the W-GHA model framework and the hydraulic conductivity function is predicted based on the SWCC. Nevertheless, the information provided in Chapter 5 about the mean values and the variability of η serves as a base of comparison and verification of the predicted values using the Brooks and Corey (1964) equation. A value of η = 2.75 was predicted using the mean SWCC presented in Fig. 6.4. The mean value for Loam soils presented in Chapter 5 was η = 2.45. The value predicted can be considered representative of a typical value for a loam soil.

6.3.1.3 *Water vapour conductivity function for the loam soil*

The conductivity of water vapour through soil, k^v, must be predicted using the formulation presented in Chapter 3, based on the soil-water characteristic curve:

$$k^v = f(D^v, \psi_{b,} \lambda_d, \lambda_{res}) = \frac{\overline{u}_a + p_v}{\overline{u}_a} \frac{gW_v p_v}{R(T + 273.15)} \frac{D^{v*}}{\rho_w} \qquad (6.2)$$

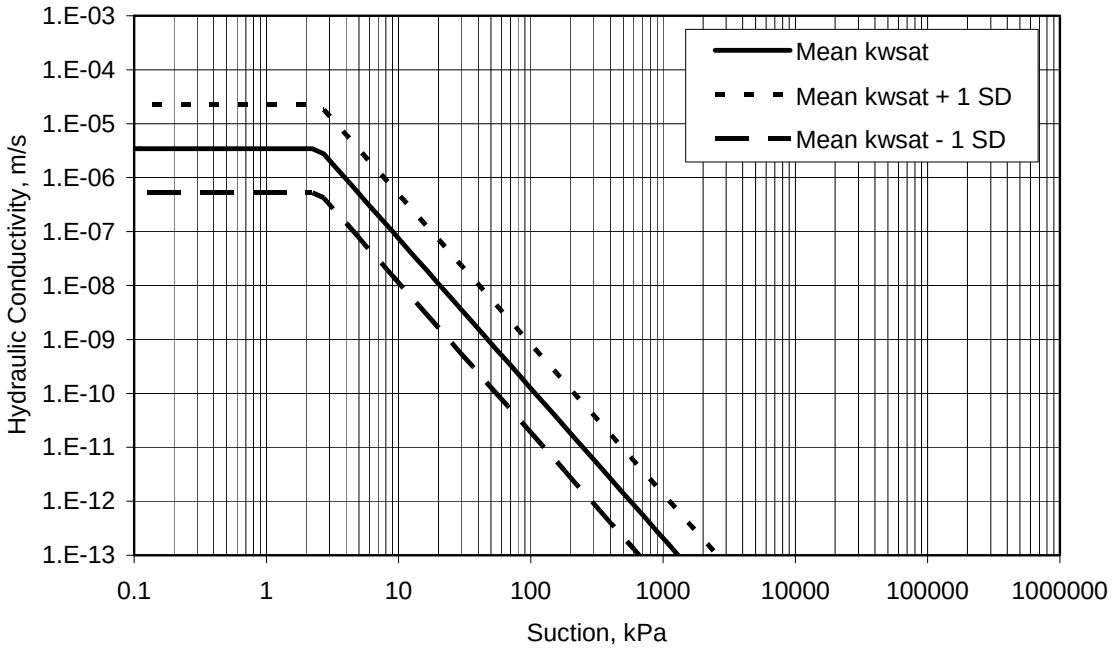

Figure 6.5 Case scenarios for the hydraulic conductivity function of the loam soil considering the variability of k^w_{sat}; E[ln(k^w_{sat})] = -12.58 ln(m^2/s) and CV[ln(k^w_{sat})] = 15%.

where:

D^{v*} = $[(1-S)n]^{5/3} D^v W_v / RT$;

D^v = molecular diffusivity of water vapour in air;

D^v = $0.229\times10^{-4}[1 + (T + 273.15)/273.15)^{1.75}$, m^2/s, (Kimball et al., 1976).

The predicted water vapour conductivity function presents variability due to the variability in the input SWCC's parameters, ψ_b, λ_d, and λ_{res}, and due to the variability in the molecular diffusivity of water vapour in air, D^v. The variability of the predicted water vapour conductivity function must be considered by updating the water vapour conductivity function for each soil-water characteristic curve scenario presented in Fig. 6.4.

Limited data can be found in the literature about the variability of D^v. An alternative procedure was followed herein, in order to establish the case scenarios for D^v. The equation proposed by Kimball et al. (1976) was re-written in terms of the value of D^v at 25°C, $D^v_{25°C}$, making $D^v_{25°C}$ the primary parameter defining D_v. An alternative equation provided by Philip and de Vries (1957) was also used for the computation of D^v. The equations used herein are as follows:

$$D^v_{Kimball} = D^v_{25^oC}(0.003073T + 0.9235) \quad (6.3)$$

$$D^v_{Philip} = 5.82 \times 10^{11}(T + 273.15)^{2.3} \quad (6.4)$$

where:

D^v = molecular diffusivity of water vapour in air;

$D^v_{25^oC}$ = D^v at 25°C; $D^v_{25^oC} = 8.33 \times 10^{-5}$ m^2/s.

$D^v_{25^oC}$ was assumed log normally distributed. The best estimate of $D^v_{25^oC}$ was assumed as given by Eq. 6.3 (i.e., $D^v_{25^oC} = 8.33 \times 10^{-5}$ m^2/s). The two other case scenarios were defined by the pair of curves obtained using Eq. 6.3 and roughly enveloping the curve provided by Philip and de Vries (1957), as shown in Fig. 6.6. The coefficient of variation of $\ln(D^v_{25^oC})$ that produced such pair of curves was equal to 15%. Figure 6.7 presents the case scenarios for k^v, based on the variation selected for $D^v_{25^oC}$ and taking the mean values for the SWCC parameters.

6.3.1.4 *Thermal conductivity function for the loam soil*

The thermal conductivity function, λ, must be predicted based on the SWCC, using the formulations presented in Chapter 3. The equation proposed by de Vries (1963) has been selected herein:

$$\lambda = f(\lambda_s, n, \psi_b, \lambda_d, \lambda_{res}) = \frac{F_s\lambda_s(1-n) + F_w\lambda_w nS + F_a\lambda_a n(1-S)}{F_s(1-n) + F_w nS + F_a n(1-S)} \quad (6.5)$$

where:

λ_s = thermal conductivity of solids; λ_s = 6.0, W/(m °C);

λ_w = thermal conductivity of water; λ_w = 0.57, W/(m °C);

λ_a = $\lambda_{da} + \lambda_{va}$;

λ_{da} = thermal conductivity of dry air; λ_{da} = 0.025, W/(m °C);

λ_{va} = thermal conductivity of water vapour, $\lambda_{va} = (0.0736)S$, W/(m °C);

$F_{s,a\,w}$ and g_i^s = constants defined in detail in Chapter 3.

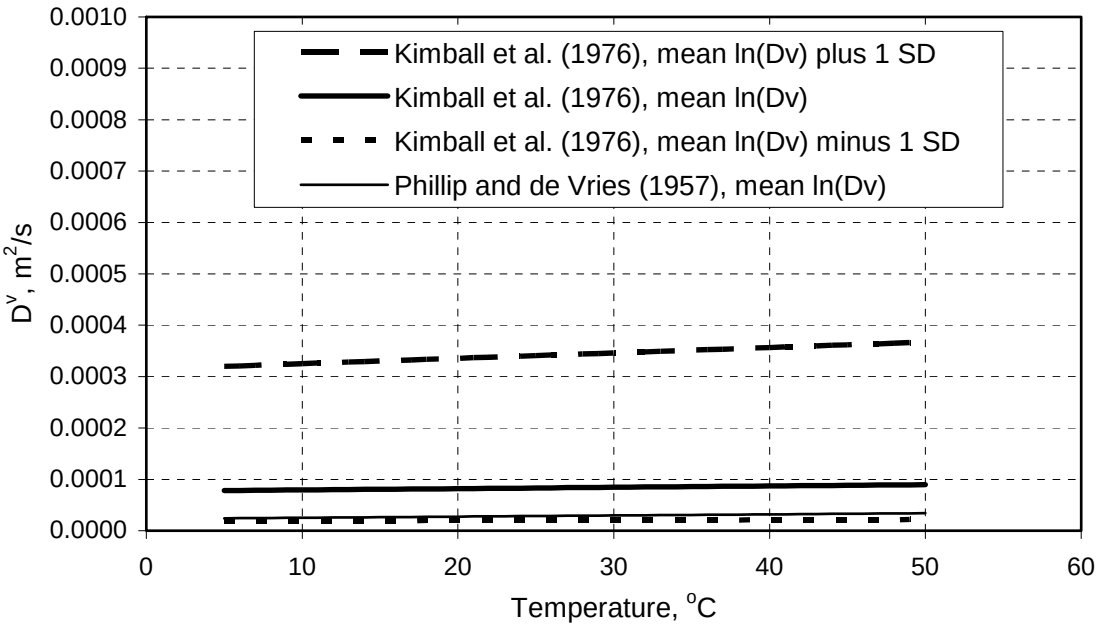

Figure 6.6 Case scenarios for the diffusivity of water vapour in air.

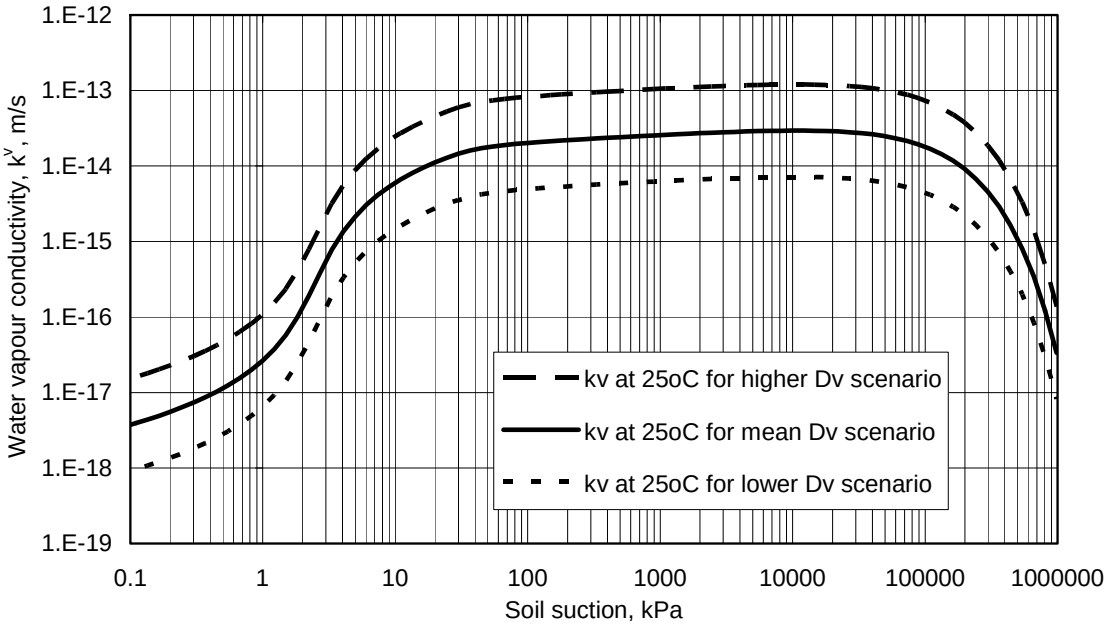

Figure 6.7 Case scenarios for the water vapour conductivity through the loam soil considering the variability of $D^v_{25^oC}$; E[ln($D^v_{25^oC}$)] = -9.4 ln(m^2/s) and CV[ln($D^v_{25^oC}$)] = 15%.

The predicted thermal conductivity function presents variability due to the input SWCC's parameters, ψ_b, λ_d, and λ_{res}, due to the soil porosity, n, and due to the variability in the thermal conductivity of the individual soil phases. The variability due to SWCC and porosity variability must be considered by updating the thermal conductivity function for each soil-water characteristic curve and porosity scenario. The variability of λ_a and λ_w can be neglected since these parameters are well defined. The variability of the thermal conductivity of the solids, λ_s, is considerably higher (Johansen, 1975). Case scenarios were established by varying the thermal conductivity of the solids, λ_s. A normal distribution was used to represent λ_s. Based on Wilson (1990), the mean value of λ_s was assumed as equal to 6.0 W/(m ^oC).

The standard deviation of λ_s was defined based on the *three-sigma* rule, described in Chapter 5 (Duncan, 2000). Based on data collected from the literature (de Vries, 1963 and Johansen, 1975), the highest and lowest conceivable values (HCV and LCV) of λ_s were defined as 1.5 and 10.5 W/(m ^oC). These values resulted in a coefficient of variation of λ_s of 25%. Figure 6.8 presents the λ functions corresponding to the HCL and LCV of λ_s and the three case scenarios of λ based on variations of λ_s.

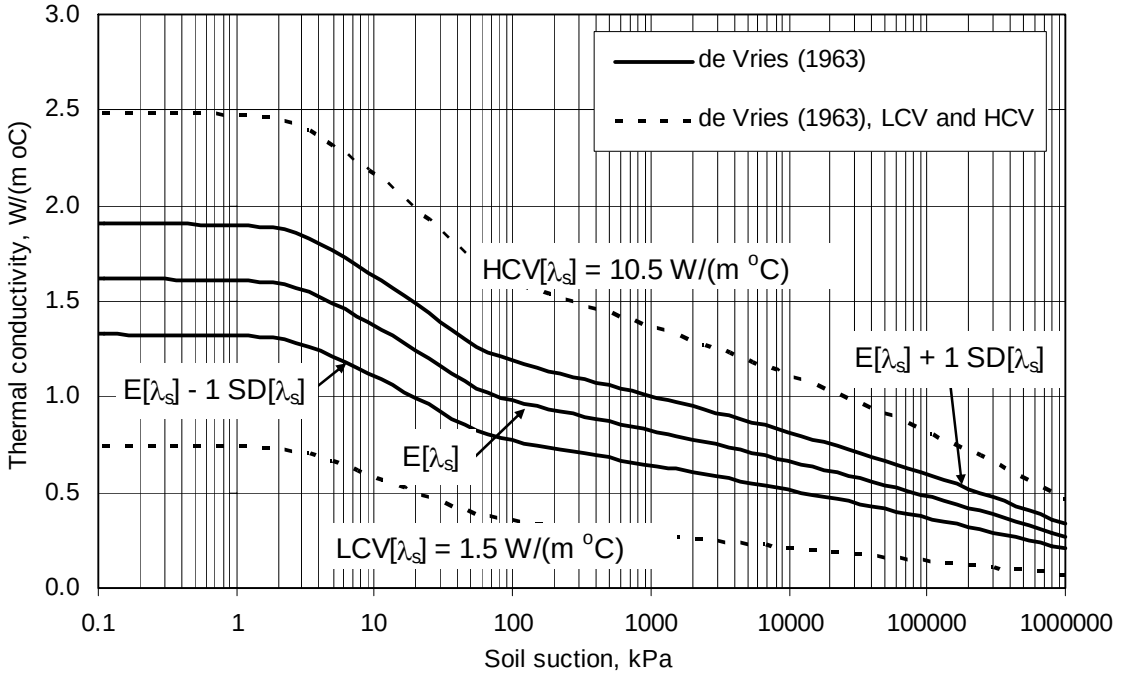

Figure 6.8 Case scenarios for the thermal conductivity of the loam soil considering the variability of λ_s; E[λ_s] = 6 W/(m ^oC) and CV[λ_s] = 25%.

6.3.1.5 *Elastic parameters for the loam soil*

Table 6.2 presents the mean values and coefficients of variation selected for the Young modulus, *E*, and Poisson's ratio, μ, for the loam soil. The mean values were selected based on typical values obtained from the literature (Bowles, 1996). The coefficient of variation of *E* (CV = 30%) was selected based on the variability of the compression index (Table 5.1). A coefficient of variation of μ (CV = 22%) was selected based on the *three-sigma* rule, taking the mean value as 0.35, and taking the LCV and HCV of μ as equal to 0.05 and 0.5, respectively.

6.3.1.6 *Shear strength envelope for the loam soil*

The shear strength envelope for an unsaturated soil, τ_f, can be predicted using the soil-water characteristic curve and the saturated shear strength parameters, *c*' and ϕ'. Fredlund et al. (1996) and Vanapalli et al. (1996) provide two similar predictive equations, as follows:

$$\begin{aligned}\tau_f &= f(c', \phi', \kappa, \psi_{b,} \lambda_d, \lambda_{res}) \\ &= c' + (\sigma_n - u_a)\tan\phi' + (u_a - u_w)\Theta^{\kappa}\tan\phi'\end{aligned} \qquad (6.6)$$

where:

c' = cohesion, kPa;

ϕ' = friction angle, radians;

Θ = *S* according to Fredlund et al. (1996); or

Θ = $\Theta_n = (S - S_{res})/(1 - S_{res})$ according to Vanapalli et al. (1996);

κ = fitting parameter.

Equation 6.6 produces an unlimited increase in shear strength. As a result, unreasonably high shear strength values can be obtained during evaporation events, when the near surface soil reaches soil suctions higher than 100,000 kPa. Limited information is available regarding upper limits for unsaturated shear strength. In order to limit the value of τ_f at high suction values the shear strength values were assumed constant for soil suctions higher than 1500 kPa. This approximation does not interfere with the precipitation analysis results.

Table 6.2 presents the mean values and the coefficients of variation selected (see Table 5.1 for typical CV's). The *c*' and ϕ' values selected correspond to a typical loam soil (i.e., silt), with low or no cohesion and relatively high friction angle. The selection of κ was less

straightforward. Vanapalli et al. (1996) defined κ as equal to 1, while Fredlund et al. (1996) suggest that despite the typical κ value being 1, it may vary. The uncertainty of the parameter κ can be regarded as an uncertainty on the predictive model. Due to the difficulty in assessing the value of κ, the "model uncertainty" must be incorporated by considering κ an uncertain variable.

The predicted unsaturated shear strength presents variability due to the input SWCC's parameters, ψ_b, λ_d, and λ_{res}, due to the parameters c', ϕ', and due to the parameter κ. The variability of the predicted unsaturated shear strength due to the SWCC variability must be considered by updating the unsaturated shear strength envelope for each SWCC scenario presented in Fig. 6.4. The variability in the shear strength due to c' and ϕ' must be addressed by establishing additional case scenarios, using the mean values and CV's presented in Table 6.2.

Additional case scenarios were established in order to accommodate the variability in the shear strength due to the parameter κ. The envelope proposed by Fredlund et al. (1996) was adopted. In order to reproduce the existence of the lower bound, κ = 0, the parameter κ was assumed log normally distributed. A mean value E[ln(κ)] = 0 was defined based on the recommendations by Fredlund et al. (1996) and Vanapalli et al. (1996). The standard deviation of ln(κ), SD[ln(κ)] = 0.5, was determined based on the *three-sigma* rule (Duncan, 2000). Figure 6.9 shows how the HCV and LCV were estimated, taking as reference the κ = 0 envelope (i.e., the minimum theoretical value) and the Vanapalli et al. (1996) envelope.

6.3.2 *Soil properties for the clay soil*

Table 6.3 presents a summary of the soil properties and coefficients of variation selected for the clay soil. The parameters whose values are indicated in the bottom of the table are well defined and can be assumed as constants (i.e., not modelled as random variables). A total of 10 random variables are listed in Table 6.3. According to the *alternative point estimate method*, 10 random input variables results in 21 evaluations of the *factor of safety*, F_s.

The soil-water characteristic curve and the saturated hydraulic conductivity selected correspond to the mean values presented in Chapter 5 for clay soils. The remaining unsaturated soil property functions where obtained using the same procedure presented in the previous section, for the loam soil. Correlations between soil parameters were neglected in order to narrow the scope of the analyses. The next sections will present in detail the procedure for establishing the

mean values and coefficients of variation selected for the soil properties.

6.3.2.1 *Soil-water characteristic curve for the clay soil*

Figure 6.10 presents the soil-water characteristic curve selected and the case scenarios defined based on the mean value and coefficient of variation presented in Table 6.3. The mean value and coefficient of variation adopted for $\ln(\psi_b)$ correspond to the values presented in Chapter 5 for the clay soils. The variables λ_d and λ_{res} are not listed because clay soils can usually be represented by a SWCC equation with one bending point, as shown in Chapter 5. A total of 3 case scenarios are presented in Fig. 6.10, for to the variations in ψ_b. The value of $\ln(\psi_b)$ was varied by one standard deviation, in accordance with the *alternative point estimate method*.

The variability of $\ln(\psi_b)$ results in variability of the remaining unsaturated soil properties, predicted using the SWCC. The variability of predicted properties due to SWCC variability is considered herein by updating the predicted properties for each of the 3 soil-water characteristic curve scenarios. Therefore, the sensitivity of the factor of safety to the SWCC parameters obtained during the sensitivity analyses incorporates the corresponding variations of the predicted properties.

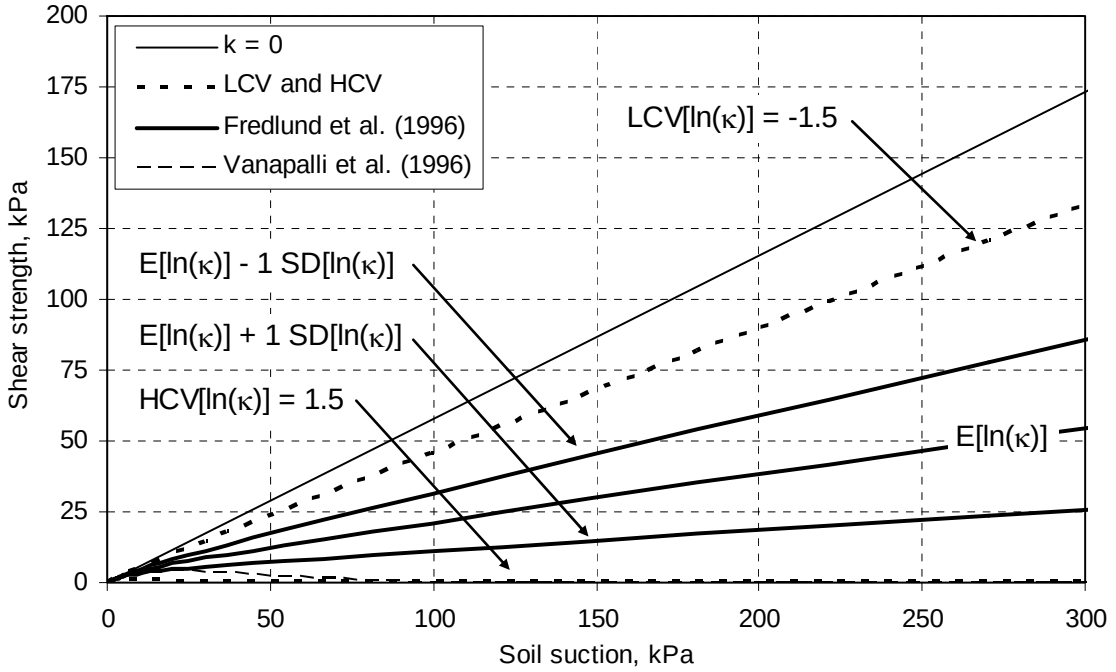

Figure 6.9 Case scenarios for the unsaturated shear strength of the loam soil considering the variability of κ; E[ln(κ)] = 0 and SD[ln(κ)] = 0.5.

Table 6.3 Soil properties and coefficients of variation for the clay soil.

Analysis (1)	Soil property (2)	Related parameters (3)	Expected value (*) (4)	CV (**) (5)
Moisture flow analysis	$\theta = nS$	n	0.534	19%
		$\ln(\psi_b)$, ln(kPa)	0.999 (2.71)	205%
	k^w	$\ln(k^w_{sat})$, ln(m/s)	-16.03 (1.1×10^{-7})	13%
	k^v	$\ln(D^v_{25^oC})$, ln(m^2/s)	-9.4 (8.33×10^{-5})	15%
Heat flow	λ	λ_s, W/(m ^oC)	6.0	25%
Stress and stability analysis	D_{ij}	E, kPa	7,000	30%
		μ	0.40	17%
	τ_f	c', kPa	10.0	30%
		ϕ'	20^o	10%
		$\ln(\kappa)$	0 (1)	SD = 0.5

Fixed parameters: $a = 0.025$; $G_s = 2.65$; $L_V = 2.501\times10^6 - 2.361\times10^3 T$ J/kg;
$\zeta_s = 2.23\times10^6$ W/(m^3 ^{o}C); $\zeta_w = 4.15\times10^6$ W/(m^3 ^{o}C);
(*) values between brackets are the exponential value;
(**) values for which the mean is close to zero may have the variability indicated in terms of standard deviation, SD.

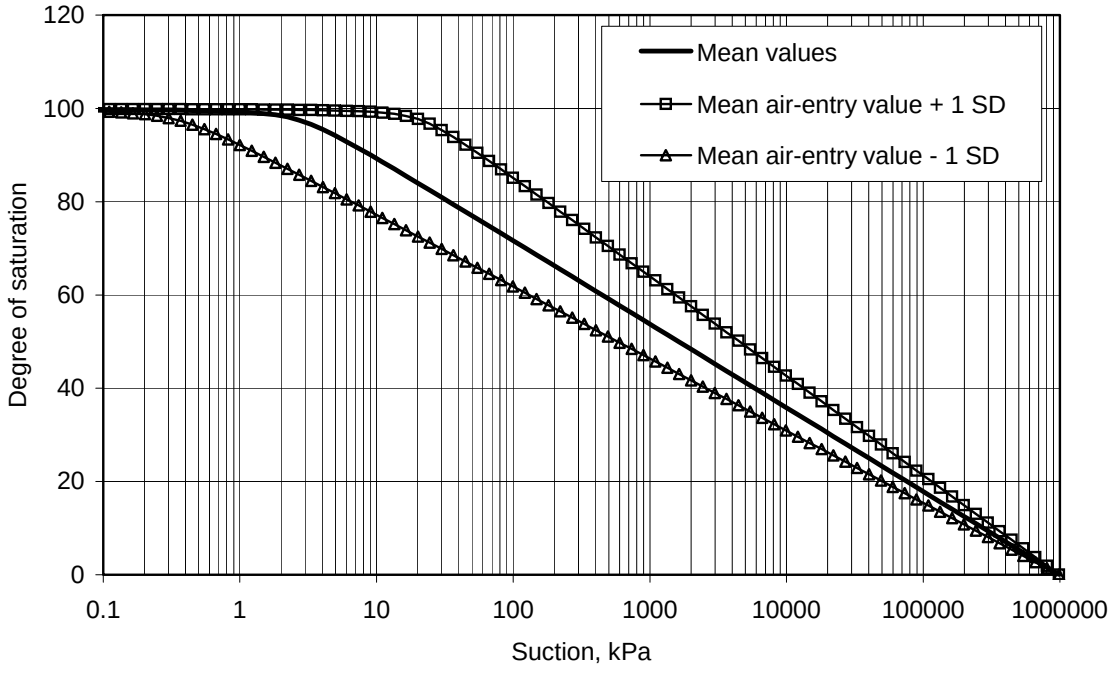

Figure 6.10 Case scenarios for the soil-water characteristic curve of the clay soil.

6.3.2.2 *Hydraulic conductivity function for the clay soil*

The hydraulic conductivity function presented herein has been predicted based on the soil-water characteristic curve, using the equation proposed by Brooks and Corey (1964). The predicted hydraulic conductivity function variability results from the variability in the input SWCC's parameter, ψ_b, and from to the variability in the saturated hydraulic conductivity, k^w_{sat}. The variability of the predicted k^w function must be considered by updating the k^w function for each soil-water characteristic curve scenario presented in Fig. 6.10.

The variability of the saturated hydraulic conductivity, k^w_{sat}, is considered through additional case scenarios based on the coefficient of variation of $\ln(k^w_{sat})$ for clay soils presented in Chapter 5 and indicated in Table 6.3. Figure 6.11 presents the resulting hydraulic conductivity function case scenarios, taking the variations of k^w_{sat} and the mean values for the SWCC parameters. A value of $\eta = 2.27$ was predicted using the mean SWCC presented in Fig. 6.10. The mean value presented in Chapter 5 for clay soils was similar, $\eta = 1.98$. Therefore, the value predicted can be considered representative of a typical value for a clay soil.

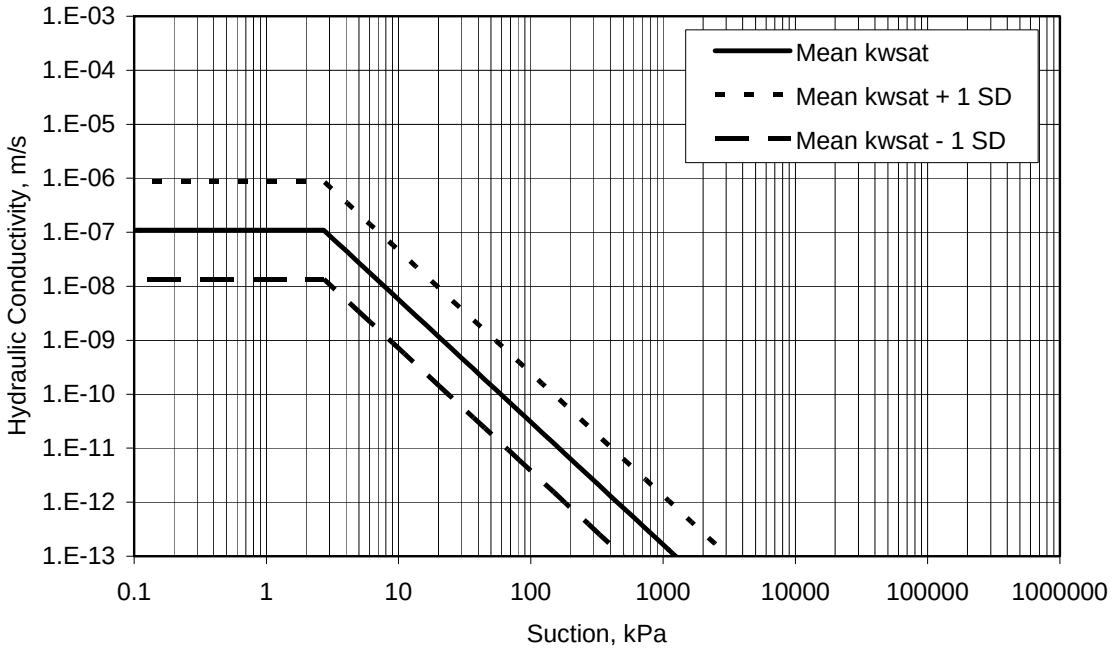

Figure 6.11 Case scenarios for the hydraulic conductivity function of the clay soil considering the variability of k^w_{sat}; $E[\ln(k^w_{sat})] = -16.03$ ln(m^2/s) and $CV[\ln(k^w_{sat})] = 13\%$.

6.3.2.3 *Water vapour conductivity function for the clay soil*

The conductivity of water vapour through soil, k^v, must be predicted based on the formulations presented in Chapter 3, using the soil-water characteristic curve. The predicted water vapour conductivity function presents variability due to the variability in the input SWCC's parameter, ψ_b, and due to the variability in the molecular diffusivity of water vapour in air, D^v. The variability of the predicted water vapour conductivity function must be considered by updating the water vapour conductivity function for each SWCC scenario presented in Fig. 6.4. The variability of D^v was represented in terms of the coefficient of variation of $\ln(D^v_{25^oC}) = 15\%$, as shown in the previous section. Figure 6.12 presents the case scenarios for k^v, based on the variations of $D^v_{25^oC}$ and taking the mean value of $\ln(\psi_b)$.

6.3.2.4 *Thermal conductivity function for the clay soil*

The thermal conductivity function, λ, has been predicted based on the equation proposed by de Vries (1963). The predicted thermal conductivity function presents variability due to the input SWCC's parameter, ψ_b, due to the soil porosity, n, and due to the variability in the thermal conductivity of the individual soil phases. The variability due to SWCC and porosity variability must be considered by updating the thermal conductivity function for each soil-water characteristic curve and porosity scenario.

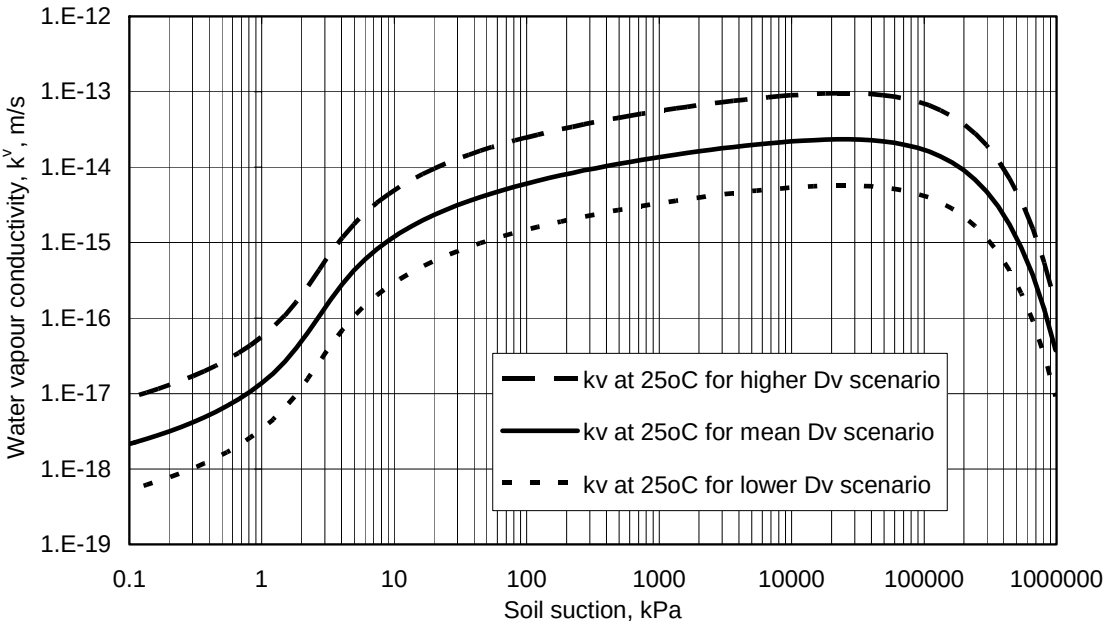

Figure 6.12 Case scenarios for the water vapour conductivity through the clay soil considering the variability of $D^v_{25^oC}$; $E[\ln(D^v_{25^oC})] = -9.4$ $\ln(m^2/s)$ and $CV[\ln(D^v_{25^oC})] = 15\%$.

As explained for the loam soil, case scenarios were established by varying the thermal conductivity of the solids, λ_s. A normal distribution was used to represent λ_s. Based on Wilson (1990), the mean value of λ_s was assumed as equal to 6.0 W/(m ^oC). The standard deviation of λ_s was defined based on the *three-sigma* rule described in Chapter 5 (Duncan, 2000). Based on data collected from the literature (de Vries, 1963 and Johansen, 1975), the highest and lowest conceivable values of λ_s (HCV and LCV) were defined as 1.5 and 10.5 W/(m ^oC). These values resulted in a coefficient of variation of λ_s of 25%. Figure 6.13 presents the predicted λ functions for the HCL and LCV of λ_s and the three case scenarios of λ based on variations of λ_s.

6.3.2.5 *Elastic parameters for the clay soil*

Table 6.3 presents the mean values and coefficients of variation selected for the Young modulus, *E*, and Poisson's ratio, μ of the clay soil. The mean values were selected based on typical values obtained from the literature (Bowles, 1996). The coefficient of variation of *E* (CV = 30%) was selected based on the variability of the compression index (Table 5.1). A coefficient of variation of μ (CV = 17%) was selected based on the *three-sigma* rule, taking the mean value as 0.40, and taking the LCV and HCV as 0.1 and 0.5, respectively.

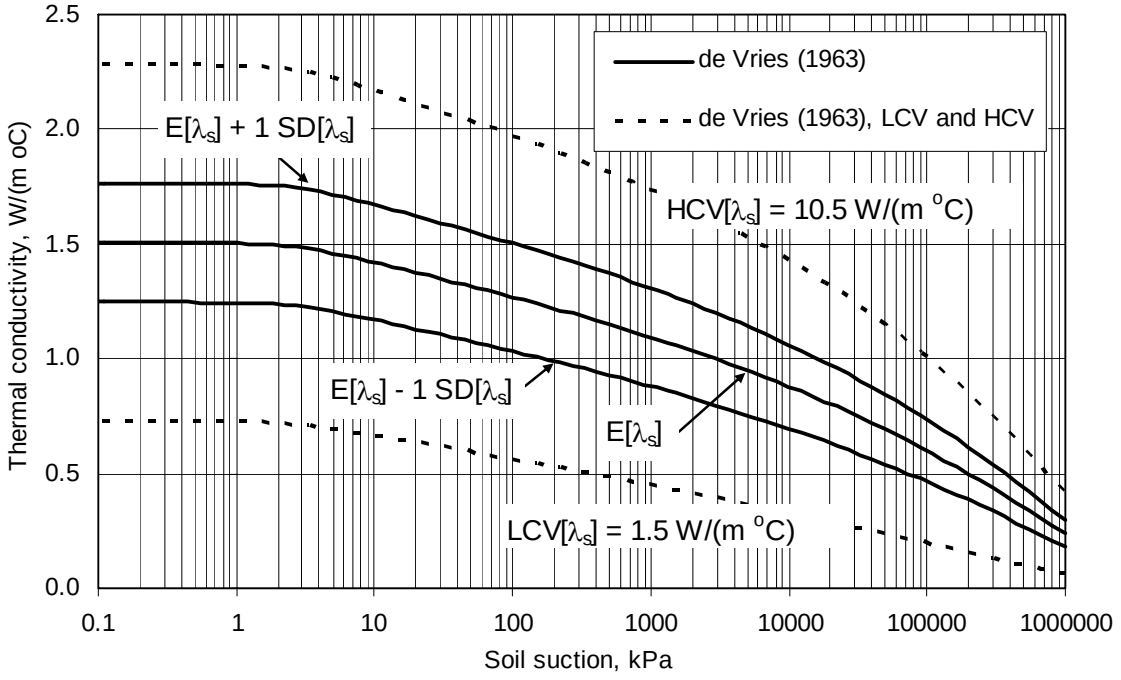

Figure 6.13 Case scenarios for the thermal conductivity of the clay soil considering the variability of λ_s; E[λ_s] = 6 W/(m ^oC) and CV[λ_s] = 25%.

6.3.2.6 *Shear strength envelope for the clay soil*

Table 6.3 presents the mean values and coefficients of variation selected for the shear strength parameters. The *c*' and ϕ' values selected correspond to a typical clay soil with a low friction angle and relatively high cohesion (see Table 5.1 for typical CV's). The parameter κ was selected using the same approach taken for the loam soil. The predicted unsaturated shear strength presents variability due to the input SWCC's parameter, ψ_b, due to the parameters *c*', ϕ', and due to the parameter κ. The variability of the predicted unsaturated shear strength due to the SWCC variability must be considered by updating the unsaturated shear strength envelope for each SWCC scenario presented in Fig. 6.10. The variability due to *c*' and ϕ' must be addressed using case scenarios based on mean values and coefficients of variation presented in Table 6.3.

Additional case scenarios were established for the parameter κ. Again, the envelope proposed by Fredlund et al. (1996) was adopted. The parameter κ was assumed log normally distributed and a mean value E[ln(κ)] = 0 was defined based on Fredlund et al. (1996). The standard deviation of κ, SD[ln(κ)] = 0.5, was determined based on the *three-sigma* rule (Duncan, 2000). Figure 6.14 shows the selected HCV and LCV values along with the case scenarios for κ.

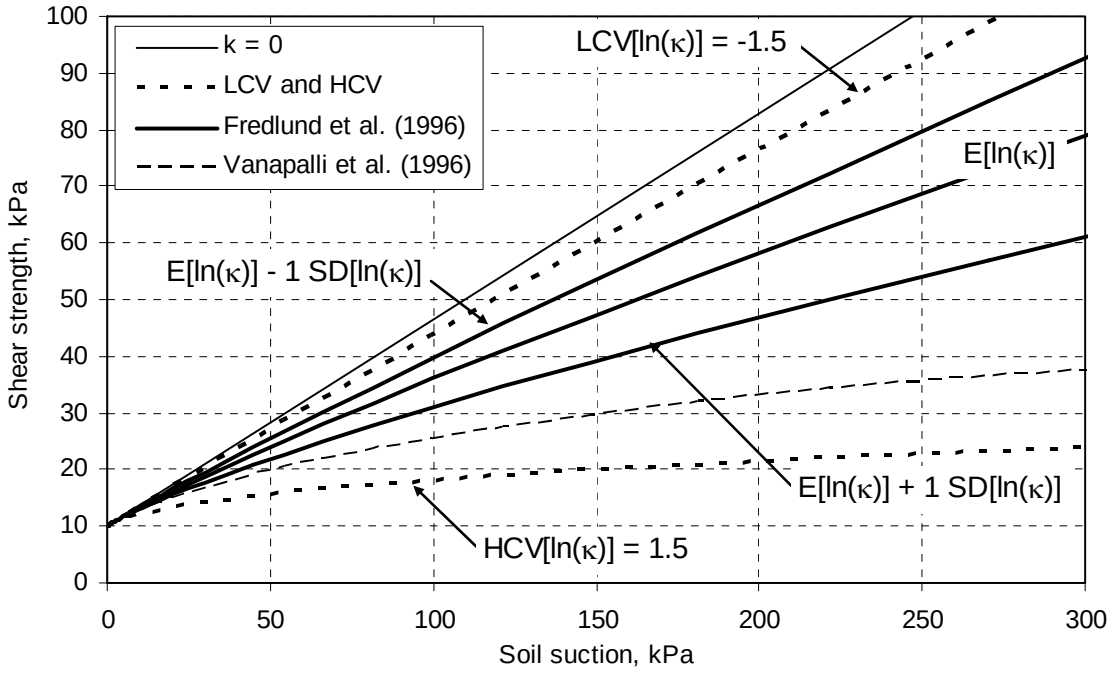

Figure 6.14 Case scenarios for the unsaturated shear strength of the clay soil considering the variability of κ; E[ln(κ)] = 0 and SD[ln(κ)] = 0.5.

6.4 ANALYSIS PROCEDURE

Tables 6.4 and 6.5 present the property case scenarios required by the W-GHA model and established based on the mean values and coefficients of variations presented in Tables 6.2 and 6.3. The analytical procedure established by the W-GHA model was described in detail in Chapter 3 and summarised in Fig. 3.14. Each embankment configuration requires $2n + 1$ runs of the deterministic core of the W-GHA model if the n input variables are assumed uncorrelated. The property case scenarios are required in order to compute the statistical moments of the factor of safety and are required for the sensitivity analyses. The property case scenarios can be used to identify the effect of each soil property on the behaviour of the railway embankments.

The property case scenarios presented in Tables 6.4 and 6.5 result in different scenarios for the pore-water pressure, temperature, and stress distributions. Chapter 4 presented details about the numerical models implemented using FlexPDE (PDE Solutions Inc., 2003). The finite element model for heat flow, water flow, and stress analyses uses automatically generated and dynamically refined meshes. Figure 6.15 presents illustrative meshes for the analysis of coupled water and heat flow, considering the low and high embankments. The total number of nodes varied for each case scenario, but was generally between 500 and 2000 nodes. Densely refined mesh regions are located at regions with higher pore-water pressure gradients (e.g., at the wetting and drying fronts). Dense spatial discretisation is found also at regions with high temperature gradients and at regions with high stress concentrations (e.g., near the train load boundary).

The numerical models for water and heat flow and for stress analysis were applied considering the entire embankment, even though the problem is symmetric with respect to the mid section (i.e., $x = 17.5$ m for the low embankment and $x = 37.5$ m for the high embankment). Pore-water pressure and stress distributions for the entire embankment were required by the dynamic programming analysis, since critical slip surfaces may be located across the whole embankment crest. The computing time required for the precipitation analyses varied for each case scenario, but was generally between 20 and 40 minutes on a Pentium 4-M running at 1.8GHz and with 512 of RAM. The computing time for the evaporation analyses was considerably longer, generally around 1 hour but up to 3 hours when more severe gradients occurred. The longer computation times required by the evaporation analyses are due to the significantly higher pore-water pressure gradients located at the drying fronts.

Table 6.4 Sets of soil parameters for each case scenario for the Loam soil.

Case scenarios	n	ψ_b kPa	λ_d ln(kPa^{-1})	λ_{res} ln(kPa^{-1})	k^w_{sat} m/s	$D^v_{25^oC}$ m^2/s	λ_s W/(m ^{o}C)	E kPa	μ	c' kPa	ϕ'	κ
(1)	(2)	(3)	(4)	(5)	(6)	(7)	(8)	(9)	(10)	(11)	(12)	(13)
E[ ]	0.500	2.53	0.478	0.087	3.4×10^{-6}	8.3×10^{-5}	6.0	15,000	0.35	0.0	30.0	1.0
n (+)	**0.585**	2.53	0.478	0.087	3.4×10^{-6}	8.3×10^{-5}	6.0	15,000	0.35	0.0	30.0	1.0
ln(ψ_b) (+)	0.500	**7.33**	0.478	0.087	3.4×10^{-6}	8.3×10^{-5}	6.0	15,000	0.35	0.0	30.0	1.0
ln(λ_d) (+)	0.500	2.53	**0.929**	0.087	3.4×10^{-6}	8.3×10^{-5}	6.0	15,000	0.35	0.0	30.0	1.0
ln(λ_{res}) (+)	0.500	2.53	0.478	**0.116**	3.4×10^{-6}	8.3×10^{-5}	6.0	15,000	0.35	0.0	30.0	1.0
ln(k^w_{sat}) (+)	0.500	2.53	0.478	0.087	$\mathbf{2.3\times10^{-5}}$	8.3×10^{-5}	6.0	15,000	0.35	0.0	30.0	1.0
ln($D^v_{25^oC}$) (+)	0.500	2.53	0.478	0.087	3.4×10^{-6}	$\mathbf{3.3\times10^{-4}}$	6.0	15,000	0.35	0.0	30.0	1.0
λ_s (+)	0.500	2.53	0.478	0.087	3.4×10^{-6}	8.3×10^{-5}	**7.5**	15,000	0.35	0.0	30.0	1.0
E (+)	0.500	2.53	0.478	0.087	3.4×10^{-6}	8.3×10^{-5}	6.0	**19,500**	0.35	0.0	30.0	1.0
μ (+)	0.500	2.53	0.478	0.087	3.4×10^{-6}	8.3×10^{-5}	6.0	15,000	**0.427**	0.0	30.0	1.0
c' (+)	0.500	2.53	0.478	0.087	3.4×10^{-6}	8.3×10^{-5}	6.0	15,000	0.35	**3.0**	30.0	1.0
ϕ' (+)	0.500	2.53	0.478	0.087	3.4×10^{-6}	8.3×10^{-5}	6.0	15,000	0.35	0.0	**33.3**	1.0
ln(κ) (+)	0.500	2.53	0.478	0.087	3.4×10^{-6}	8.3×10^{-5}	6.0	15,000	0.35	0.0	30.0	**1.649**
n (–)	**0.415**	2.53	0.478	0.087	3.4×10^{-6}	8.3×10^{-5}	6.0	15,000	0.35	0.0	30.0	1.0
ln(ψ_b) (–)	0.500	**0.87**	0.478	0.087	3.4×10^{-6}	8.3×10^{-5}	6.0	15,000	0.35	0.0	30.0	1.0
ln(λ_d) (–)	0.500	2.53	**0.246**	0.087	3.4×10^{-6}	8.3×10^{-5}	6.0	15,000	0.35	0.0	30.0	1.0
ln(λ_{res}) (–)	0.500	2.53	0.478	**0.064**	3.4×10^{-6}	8.3×10^{-5}	6.0	15,000	0.35	0.0	30.0	1.0
ln(k^w_{sat}) (–)	0.500	2.53	0.478	0.087	$\mathbf{5.2\times10^{-7}}$	8.3×10^{-5}	6.0	15,000	0.35	0.0	30.0	1.0
ln($D^v_{25^oC}$) (–)	0.500	2.53	0.478	0.087	3.4×10^{-6}	$\mathbf{2.0\times10^{-5}}$	6.0	15,000	0.35	0.0	30.0	1.0
λ_s (–)	0.500	2.53	0.478	0.087	3.4×10^{-6}	8.3×10^{-5}	**4.5**	15,000	0.35	0.0	30.0	1.0
E (–)	0.500	2.53	0.478	0.087	3.4×10^{-6}	8.3×10^{-5}	6.0	**10,500**	0.35	0.0	30.0	1.0
μ (–)	0.500	2.53	0.478	0.087	3.4×10^{-6}	8.3×10^{-5}	6.0	15,000	**0.273**	0.0	30.0	1.0
c' (–)	0.500	2.53	0.478	0.087	3.4×10^{-6}	8.3×10^{-5}	6.0	15,000	0.35	**0.0**	30.0	1.0
ϕ' (–)	0.500	2.53	0.478	0.087	3.4×10^{-6}	8.3×10^{-5}	6.0	15,000	0.35	0.0	**27.0**	1.0
ln(κ) (–)	0.500	2.53	0.478	0.087	3.4×10^{-6}	8.3×10^{-5}	6.0	15,000	0.35	0.0	30.0	**0.606**

Table 6.5 Sets of soil parameters for each case scenario for the Clay soil.

Case scenarios	n	ψ_b kPa	k^w_{sat} m/s	$D^v_{25^oC}$ m^2/s	λ_s W/(m ^oC)	E kPa	μ	c' kPa	ϕ'	κ
(1)	(2)	(3)	(4)	(5)	(6)	(7)	(8)	(9)	(10)	(11)
E[ ]	0.534	2.71	1.1×10^{-7}	8.3×10^{-5}	6.0	7,000	0.40	10.0	20.0	1.0
n (+)	**0.635**	2.71	1.1×10^{-7}	8.3×10^{-5}	6.0	7,000	0.40	10.0	20.0	1.0
$\ln(\psi_b)$ (+)	0.534	**21.05**	1.1×10^{-7}	8.3×10^{-5}	6.0	7,000	0.40	10.0	20.0	1.0
$\ln(k^w_{sat})$ (+)	0.534	2.71	$\mathbf{8.8\times10^{-7}}$	8.3×10^{-5}	6.0	7,000	0.40	10.0	20.0	1.0
$\ln(D^v_{25^oC})$ (+)	0.534	2.71	1.1×10^{-7}	$\mathbf{3.3\times10^{-4}}$	6.0	7,000	0.40	10.0	20.0	1.0
λ_s (+)	0.534	2.71	1.1×10^{-7}	8.3×10^{-5}	**7.5**	7,000	0.40	10.0	20.0	1.0
E (+)	0.534	2.71	1.1×10^{-7}	8.3×10^{-5}	6.0	**9,100**	0.40	10.0	20.0	1.0
μ (+)	0.534	2.71	1.1×10^{-7}	8.3×10^{-5}	6.0	7,000	**0.468**	10.0	20.0	1.0
c' (+)	0.534	2.71	1.1×10^{-7}	8.3×10^{-5}	6.0	7,000	0.40	**13.0**	20.0	1.0
ϕ' (+)	0.534	2.71	1.1×10^{-7}	8.3×10^{-5}	6.0	7,000	0.40	10.0	**22.0**	1.0
$\ln(\kappa)$ (+)	0.534	2.71	1.1×10^{-7}	8.3×10^{-5}	6.0	7,000	0.40	10.0	20.0	**1.649**
n (–)	**0.432**	2.71	1.1×10^{-7}	8.3×10^{-5}	6.0	7,000	0.40	10.0	20.0	1.0
$\ln(\psi_b)$ (–)	0.534	**0.35**	1.1×10^{-7}	8.3×10^{-5}	6.0	7,000	0.40	10.0	20.0	1.0
$\ln(k^w_{sat})$ (–)	0.534	2.71	$\mathbf{1.4\times10^{-8}}$	8.3×10^{-5}	6.0	7,000	0.40	10.0	20.0	1.0
$\ln(D^v_{25^oC})$ (–)	0.534	2.71	1.1×10^{-7}	$\mathbf{2.0\times10^{-5}}$	6.0	7,000	0.40	10.0	20.0	1.0
λ_s (–)	0.534	2.71	1.1×10^{-7}	8.3×10^{-5}	**4.5**	7,000	0.40	10.0	20.0	1.0
E (–)	0.534	2.71	1.1×10^{-7}	8.3×10^{-5}	6.0	**4,900**	0.40	10.0	20.0	1.0
μ (–)	0.534	2.71	1.1×10^{-7}	8.3×10^{-5}	6.0	7,000	**0.332**	10.0	20.0	1.0
c' (–)	0.534	2.71	1.1×10^{-7}	8.3×10^{-5}	6.0	7,000	0.40	**7.0**	20.0	1.0
ϕ' (–)	0.534	2.71	1.1×10^{-7}	8.3×10^{-5}	6.0	7,000	0.40	10.0	**18.0**	1.0
$\ln(\kappa)$ (–)	0.534	2.71	1.1×10^{-7}	8.3×10^{-5}	6.0	7,000	0.40	10.0	20.0	**0.606**

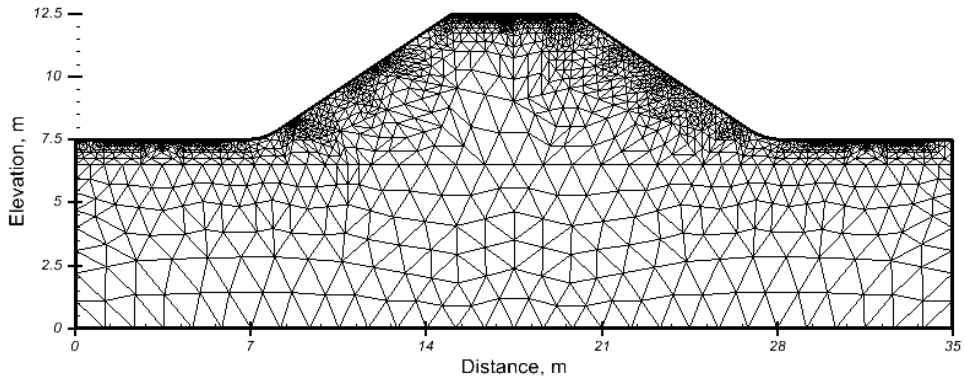

(a)

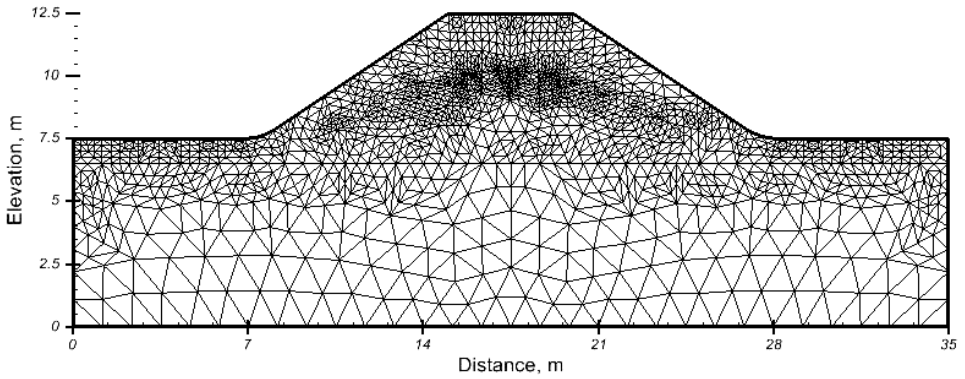

(b)

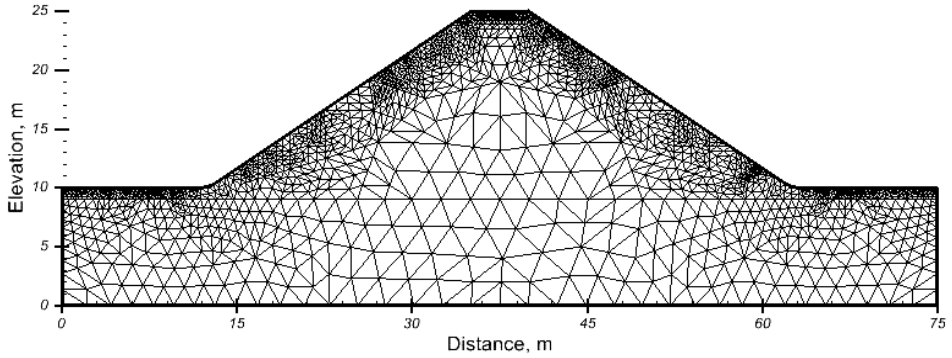

(c)

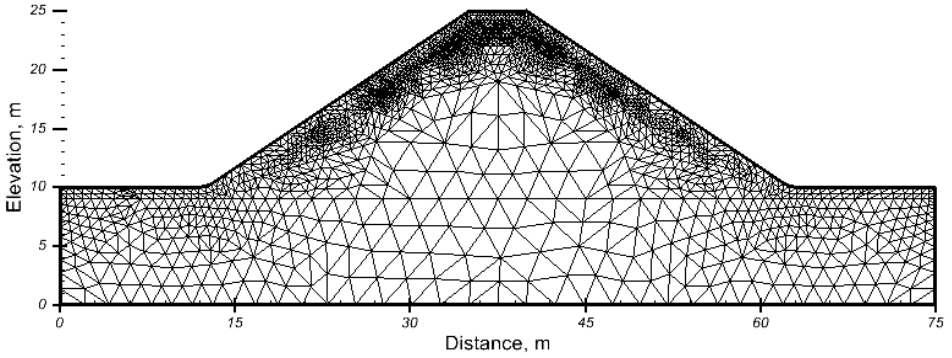

(d)

Figure 6.15 Automatically generated and dynamically refined mesh for water and heat flow precipitation analyses: (a) low embankment, t = 0.5 days; (b) low embankment, t = 14 days; (c) high embankment, t = 0.5 days; and (d) high embankment, t = 14 days.

Details about the implementation of the dynamic programming solution scheme were presented in Chapter 4. Reasonably refined search grids were selected for the dynamic programming optimization analyses using the program Safe-DP. The search grid for the low embankments consisted of intervals of 0.5 meters between stages (i.e., *x*-direction) and 0.125 meters between state points (i.e., *y*-direction). The search grid for the high embankments consisted of intervals of 1 meter between stages (i.e., *x*-direction) and 0.250 meters between state points (i.e., *y*-direction). Horizontal over vertical search grid densities of 1/4 or lower appear to result in greater flexibility to the slip surface shape. The computing time required by Safe-DP varied from approximately 30 seconds to slightly over one minute. The guidelines presented by Gitirana Jr. and Fredlund (2003a) were followed for establishing the search grid boundary.

6.5 ANALYSIS OF TYPICAL RAILWAY EMBANKMENTS

This section presents the application of the W-GHA model for the assessment of embankment hazard considering the embankment configurations described in the previous sections. A total of eight embankment configurations are analysed for the precipitation conditions and two embankments are analysed for the evaporation conditions, as shown in Fig. 6.1. The embankment geometries, boundary conditions, initial conditions, and soil properties selected were described in detail in the previous section.

6.5.1 *Analysis of precipitation conditions*

The precipitation event considered herein corresponds to a severe rainfall event, with average precipitation of 40 mm/day during 14 days. The results of the analyses were grouped according to the embankment height. The analysis of the low embankments is presented first, followed by the analysis of the high embankments. The hazard assessment is presented and discussed considering both final and transient stability conditions.

6.5.1.1 *Low embankments*

Final stability conditions for the Low Loam embankment

The results presented in this section correspond to the case scenario using the mean parameters for the loam soil. Figure 6.16 presents the final pore-water pressure distributions (t = 14 days), considering "dry" and "wet" initial conditions (i.e., minimum u_w equal to -60 kPa and -20 kPa, respectively). The soil suctions observed at the end of the precipitation event are higher for the

initially dry embankment, as expected. Pore-water pressure distributions have similar patterns. The core of both embankments presents suctions higher than what is found near the ground surface. This pattern has been observed by Krahn et al. (1989) by field measurement on similar railway embankments. The pore-water pressure at the ground surface did not reach a completely saturated state. The slightly negative pore-water pressures at the embankment surface are the result of a rainfall rate (40 mm/day) lower than the saturated hydraulic conductivity (297 mm/day) and the result of the availability of water storage at the embankment core.

Local factors of safety were computed considering the pore-water pressures, stress distributions, and shear strength characteristics of the soil. The following equation was employed:

$$F_{sL} = \frac{\tau_f}{(\sigma_1 - \sigma_3)/2} = \frac{c' + [(\sigma_1 + \sigma_3)/2 - u_a] \tan \phi' + (u_a - u_w)\Theta^{\kappa} \tan \phi}{(\sigma_1 - \sigma_3)/2} \qquad (6.7)$$

where:

F_{sL} = local factor of safety;
σ_1 = major principal stress;
σ_3 = minor principal stress.

Figure 6.17 presents the distribution of local factors of safety for the low, loam embankments. Lower final factors of safety were observed for the initially wet embankment, as expected. The near ground surface regions on the face of the embankment slope present the lowest local factors of safety. Local factors of safety lower than 1 were observed in both cases and indicate shallow failure surfaces. Local factors of safety provide valuable information regarding the local stability conditions of the embankment. However, the local factor of safety does not take into account the complete stress state and disregards the direction of principal stresses. Different local factors of safety may result, depending on the stress plane considered.

Figures 6.18 and 6.19 present the critical slip surfaces for the initially dry and wet embankments, respectively, obtained using dynamic programming. Slip surfaces and factors of safety are presented for the initial conditions and for t = 4, 8, and 14 days. The initial factors of safety (i.e., F_s equal to 1.697 and 1.601) show that both embankment conditions are relatively stable. As the precipitation event progressed, factors of safety decreased, reaching 1.334 and 1.330 for the initially dry and initially wet embankments, respectively.

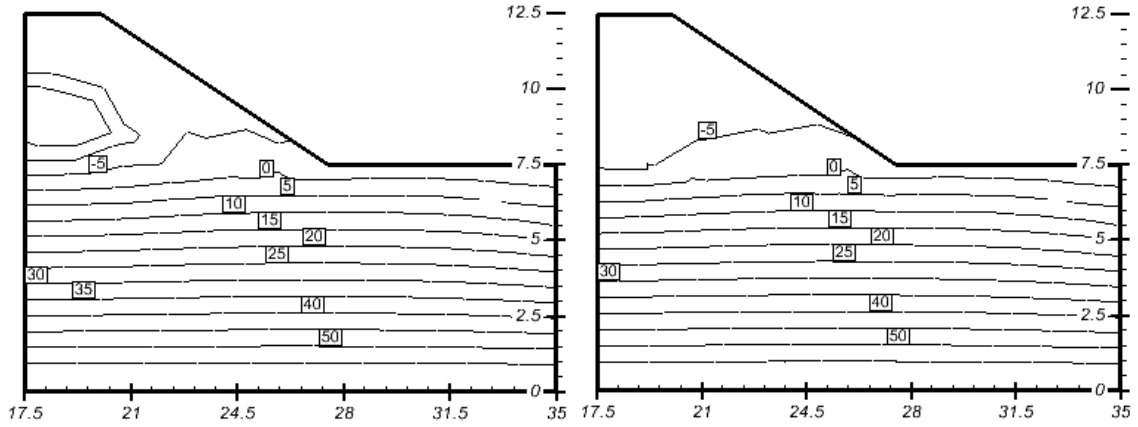

(a) (b)

Figure 6.16 Final pore-water pressure distribution for the low, loam embankment. Initial conditions: (a) $u_{w\,min}$ = -60 kPa and (b) $u_{w\,min}$ = -20 kPa.

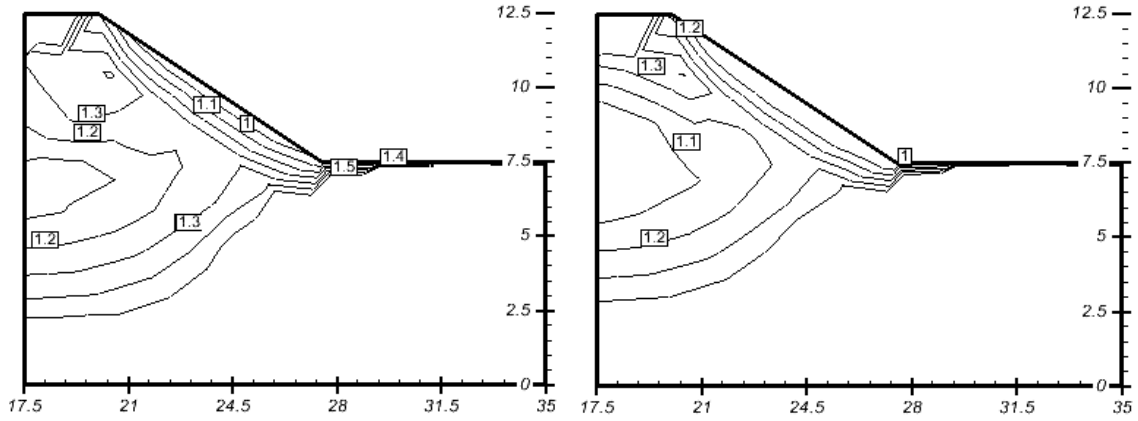

(a) (b)

Figure 6.17 Final local factors of safety for the low, loam embankment. Initial conditions: (a) $u_{w\,min}$ = -60 kPa and (b) $u_{w\,min}$ = -20 kPa.

The final overall factors of safety presented in Figs. 6.18 and 6.19 indicate fairly stable conditions. The overall factors of safety obtained using dynamic programming and the local factors of safety (Fig. 6.17) appear to be disagreement. However, it must be pointed out that the local factors of safety do not indicate overall stability conditions along a single slip surface. Local factors of safety correspond to lower bound conditions while the overall factors of safety are closely related to an upper bound measurement of stability conditions (Chen, 1975).

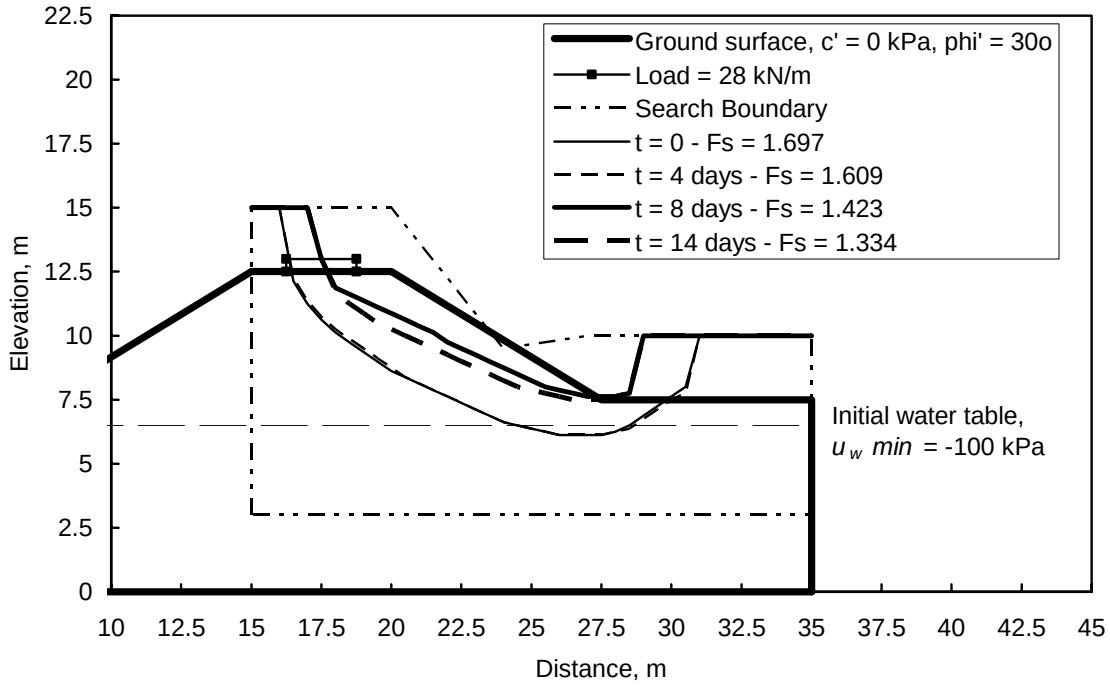

Figure 6.18 Slip surfaces for the low, loam embankment. Initial conditions: $u_{w\,min}$ = -60 kPa.

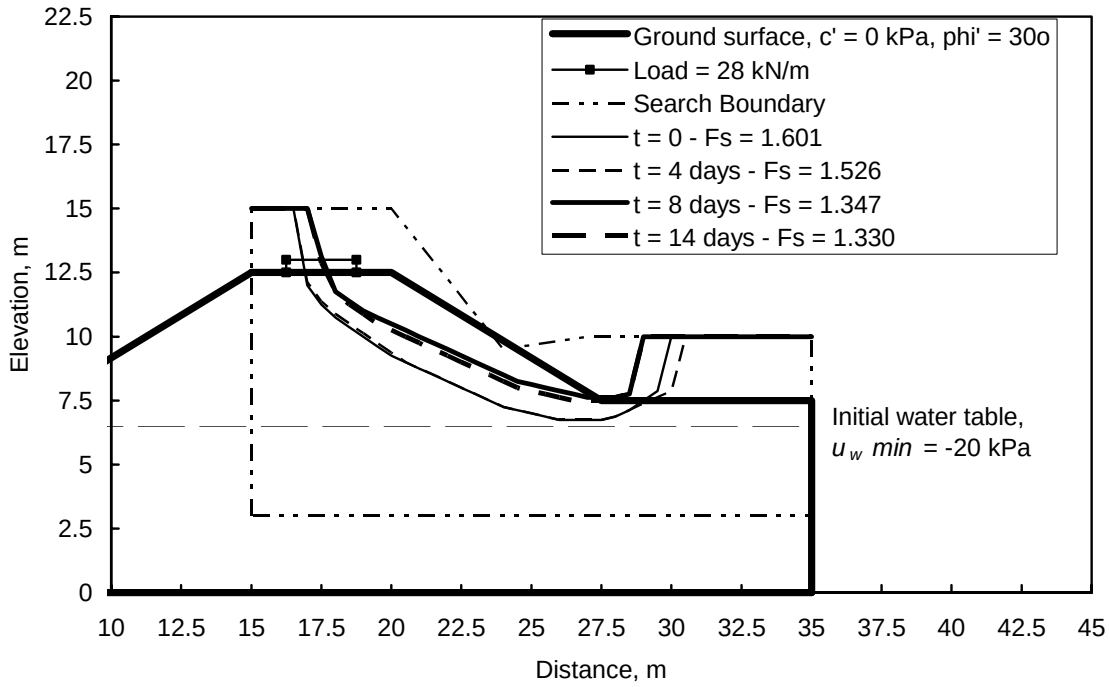

Figure 6.19 Slip surfaces for the low, loam embankment. Initial conditions: $u_{w\,min}$ = -20 kPa.

The final stability conditions of the "dry" and "wet" embankments are similar, indicating that the difference in initial conditions did not influence the stability of the embankment at the end of the precipitation event. The higher suction values observed for the initially dry embankment are located in the core of the embankment. However, near surface conditions at the embankment slope are essentially the same for both the initially dry and initially wet embankment, explaining the similar overall factors of safety at the end of the precipitation event.

Figures 6.18 and 6.19 indicate deep critical slip surfaces for the initial conditions. The deep critical slip surfaces are in agreement with the high cohesion effect that results from the shear strength due to soil suction. As the near ground surface soil saturates, the critical slip surfaces moves towards the ground surface. The near ground surface soil presents reduced shear strength due to soil suction and is held primarily by the internal friction angle. The shallow failure mechanism predicted is similar to that observed in the field by Krahn et al. (1989), for similar embankments constructed using lacustrine silt.

Final stability conditions for the Low Clay embankment

The results presented in this section correspond to the case scenario using the mean parameters of the clay soil. Figure 6.20 presents the final pore-water pressure distributions (t = 14 days) for the low, clay embankment, considering the "dry" and "wet" initial conditions. Slightly higher suctions are observed for the initially dry embankment at the end of the precipitation event. Nevertheless, the pore-water pressure distributions present similar patterns. The core of both embankments presents higher suction than the near surface soil, as observed for the loam embankment. The surface of the embankments reached completely saturated conditions. The rainfall rate (40 mm/day) is higher than the saturated hydraulic conductivity (9.4 mm/day). Consequently, the water delivered to the near ground surface produced the high pore-water pressures conditions computed.

Figure 6.21 presents the distribution of local factors of safety for the low, clay embankments. The core of the embankments presents the lowest local factors of safety. The soil near the ground surface at the embankment slope presents relatively high local factors of safety (higher than 1.5), due to the soil cohesion. Slightly lower local factors of safety were observed for the initially wet embankment, as expected. Local factors of safety considerably higher than 1 were observed in both cases, indicating stable conditions. Nevertheless, overall factors of safety may provide a more precise measure of the overall stability of the embankment.

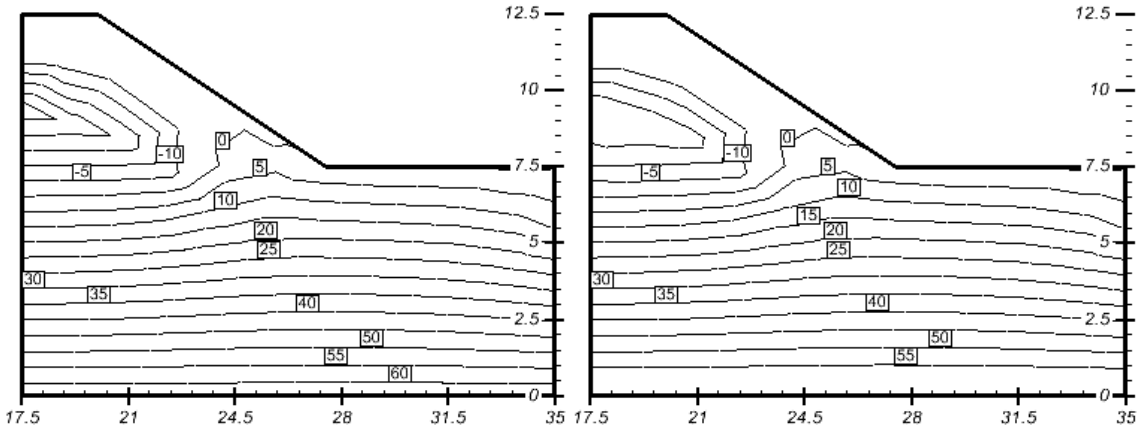

(a) (b)

Figure 6.20 Final pore-water pressure distribution for the low, clay embankment. Initial conditions: (a) $u_{w\,min}$ = -60 kPa and (b) $u_{w\,min}$ = -20 kPa.

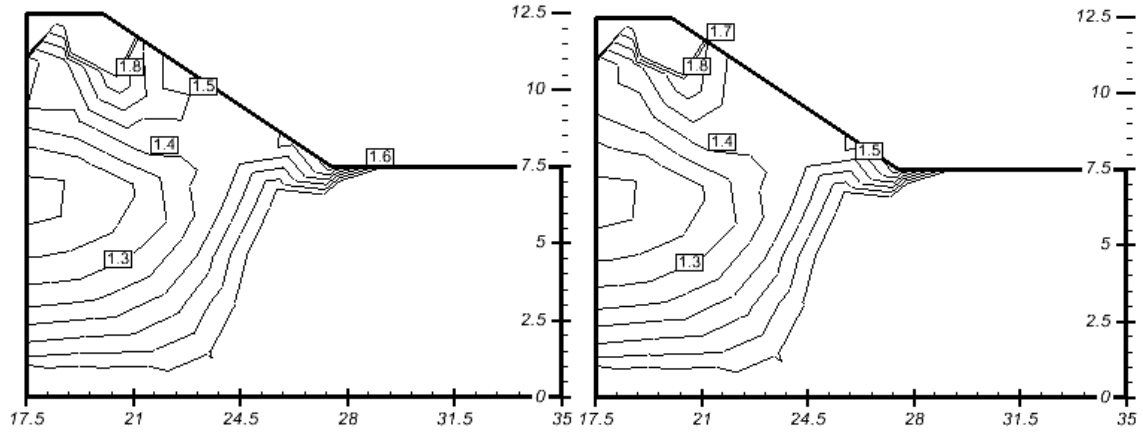

(a) (b)

Figure 6.21 Final local factors of safety for the low, clay embankment. Initial conditions: (a) $u_{w\,min}$ = -60 kPa and (b) $u_{w\,min}$ = -20 kPa.

Figures 6.22 and 6.23 present the critical slip surfaces obtained using dynamic programming for the initially dry and wet embankments, respectively. Slip surfaces and factors of safety are presented for the initial conditions and for t = 4, 8, and 14 days. The initial factors of safety (i.e., F_s equal to 1.788 and 1.691) show that both embankment conditions are relatively stable prior to the precipitation event. As the precipitation event progressed, factors of safety decreased, reaching 1.597 and 1.524 for the initially dry and initially wet embankments, respectively.

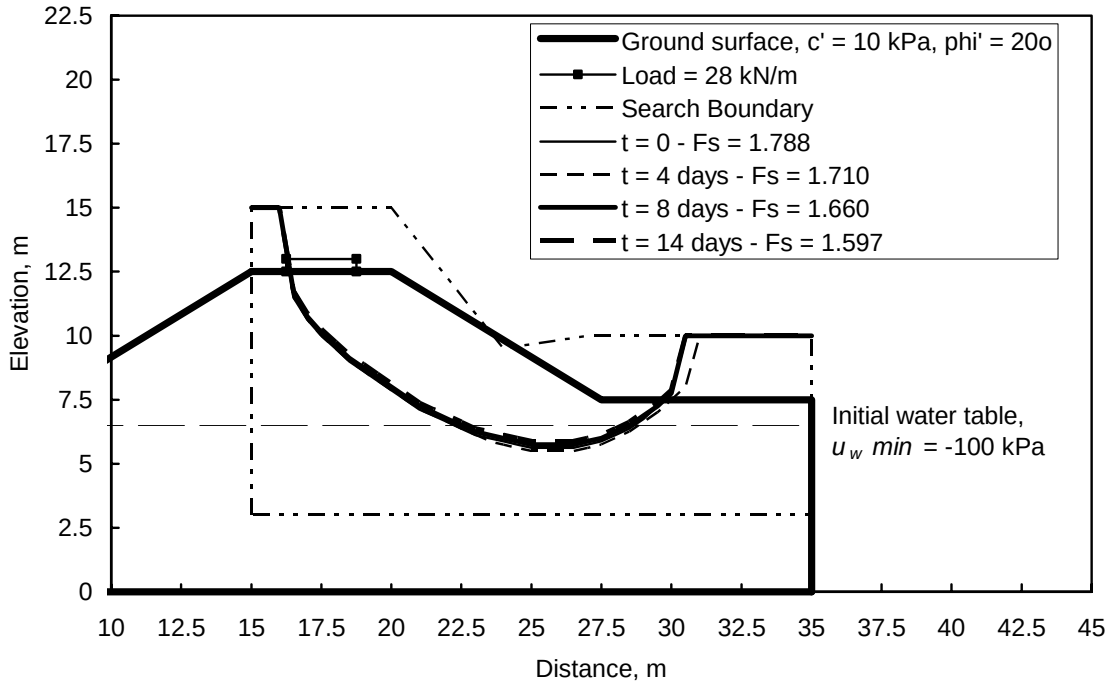

Figure 6.22 Slip surfaces for the low, clay embankment. Initial conditions: $u_{w\,min}$ = -60 kPa.

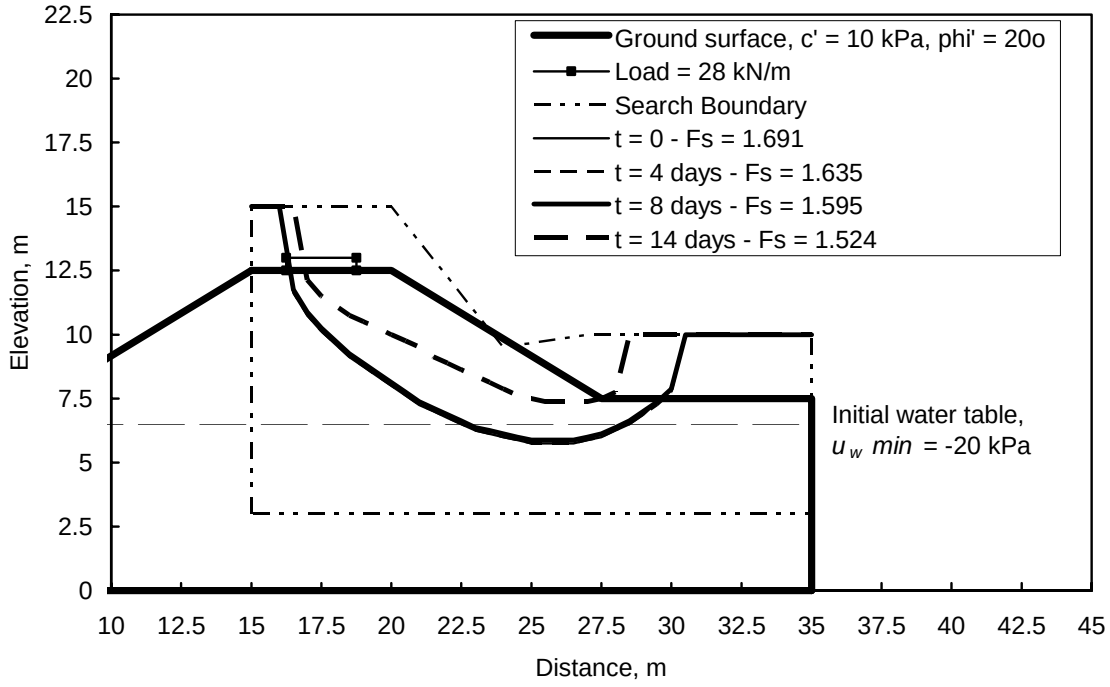

Figure 6.23 Slip surfaces for the low, clay embankment. Initial conditions: $u_{w\,min}$ = -20 kPa.

The final overall factors of safety presented in Figs. 6.22 and 6.23 indicate stable conditions. The overall factors of safety obtained using dynamic programming and the local factors of safety presented in Fig. 6.21 are in reasonable agreement. The final stability conditions of the initially dry and initially wet embankments are somewhat different, indicating that the initial pore-water pressures played a significant role. The higher soil suction values observed for the initially dry embankment are located in a small region at the centre of the embankment core. However, the final pore-water pressure distributions indicate a deeper wetting front for the initially "wet" embankment.

The critical slip surfaces presented in Figs. 6.22 and 6.23 indicate relatively deep critical slip surfaces throughout the precipitation event. The deep critical slip surfaces are in agreement with the relatively high cohesion of the clay soil. The location of the critical slip surface does not vary considerably during the precipitation event, since the cohesion components of the soil shear strength is independent of the soil suction.

Transient stability conditions for the Low Loam embankment

According to the framework proposed herein, transient stability conditions can be quantified in terms of overall factors of safety and probability of rupture. Appendix E presents the factors of safety computed for all case scenarios described in Tables 6.4 and 6.5. The results of these case scenarios were used, along with the probabilistic framework presented in Chapter 3, in order to compute the mean factors of safety, the standard deviation of the factor of safety, and the probability of failure. Factors of safety were computed within intervals of two days. Therefore, a total of 8 computations of factors of safety were performed, for each property case scenario.

Figures 6.24 and 6.25 present the changes in the mean factor of safety and probability of failure during the precipitation event, considering the initially dry and initially wet conditions, respectively. The computed values of the mean factor of safety plus and minus one standard deviation are also presented. The initial probability of failure was approximately 0.01% (i.e., 1/10,000) for the "dry" embankment and 0.3% (i.e., 3/1,000) for the "wet" embankment, as shown in Figs. 6.24 and 6.25. According to Whitman (1984) and Becker (1992a), among others, the typical range of acceptable probabilities of failure adopted in slope and foundation engineering projects varies from 0.1 to 1%. Therefore, the initial probability of failure for the low loam embankments appears within acceptable limits.

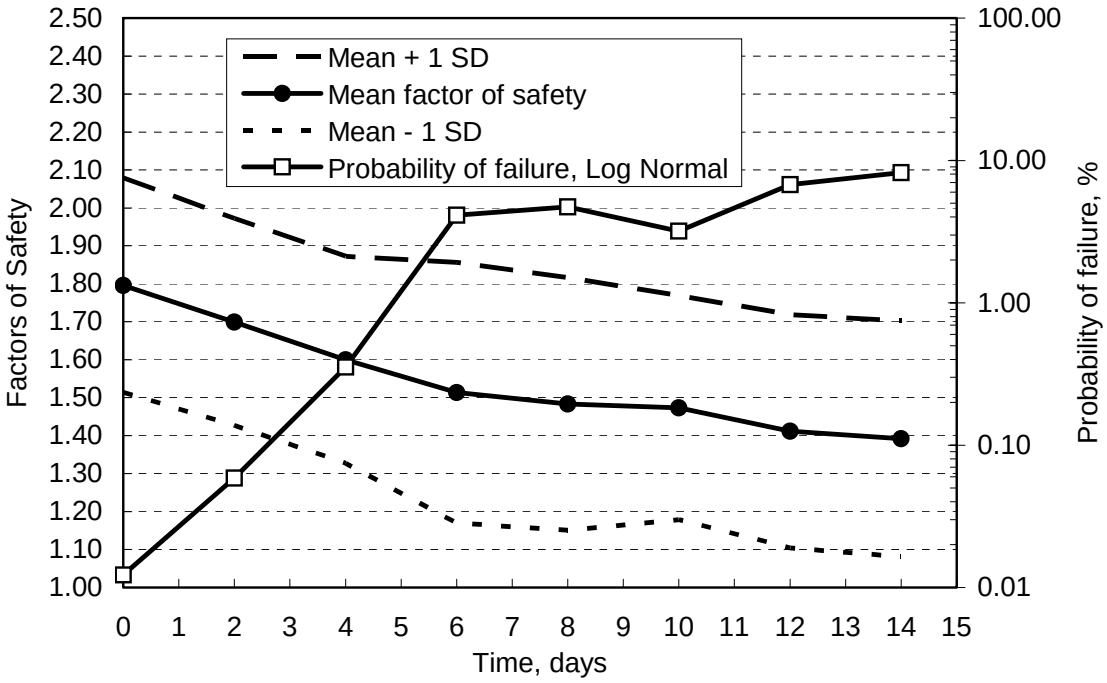

Figure 6.24 Evolution of the mean factor of safety and probability of failure for the low, loam embankment. Initial conditions: $u_{w\,min}$ = -60 kPa.

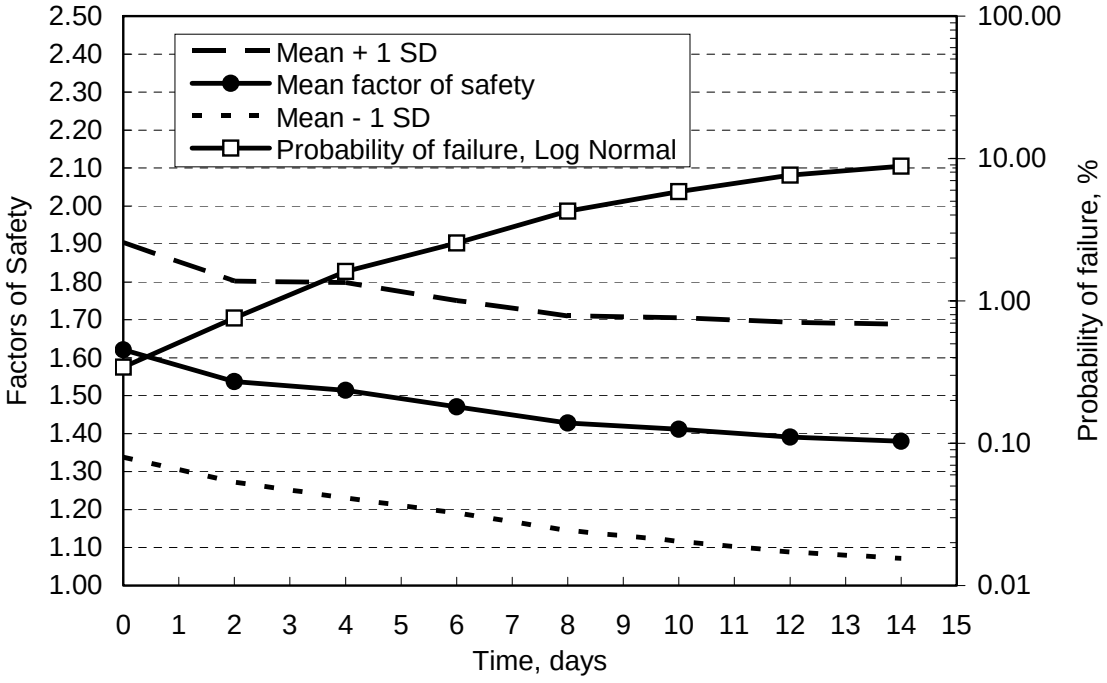

Figure 6.25 Evolution of the mean factor of safety and probability of failure for the low, loam embankment. Initial conditions: $u_{w\,min}$ = -20 kPa.

A relatively high rate of increase in the probability of failure was observed during the first 6 days of the precipitation event. The initial rate of increase of the probability of failure was considerably higher for the dry embankment. The probability of failure of the dry embankment increased from 0.01% for the initial conditions to 4% on the sixth day. The probability of failure of the wet embankment increased from 0.3% for the initial conditions to approximately 3% on the sixth day. The probability of failure of both embankments appears to have reached a plateau past the sixth day. In summary, the initial conditions played a significant role during early stages, up to the 6^{th} day, but did not play a significant role for the hazard level past the 6^{th} day.

Figures 6.24 and 6.25 show that the increase in the probability of failure is a result of the decrease in the mean factor of safety. The change in the standard deviation of the factor of safety appears negligible, as shown by the mean values plus and minus one standard deviation. The same pattern was observed for the initially dry and initially wet embankments.

Figures 6.24 and 6.25 show also that the uncertainty associated with the input soil properties may be of paramount importance. The factors of safety obtained shown in the previous section for the mean parameters and the mean factors of safety presented in Figs. 6.24 and 6.25 indicate stable embankment conditions throughout the precipitation event (i.e., $F_s > 1.40$). However, the railway embankment hazard level depends on highly uncertain variables. The values obtained for the standard deviation of the factor of safety result in fairly high probabilities of failure at the end of the precipitation event. A final probability of failure of approximately 8% (8/100) was obtained for both the initially dry and initially wet embankments.

Transient stability conditions for the Low Clay embankment

Figures 6.26 and 6.27 present the changes in the mean factor of safety and probability of failure during the precipitation event, considering the initially dry and initially wet conditions, respectively. The computed values of the mean factor of safety plus and minus one standard deviation are also presented. The initial probability of failure is approximately 0.001% (i.e., 1/100,000) for the "dry" embankment and 0.008% (i.e., 8/100,000) for the "wet" embankment, as shown by Figs. 6.26 and 6.27. Therefore, the initial probability of failure for the low clay embankments appears well within acceptable limits (Whitman, 1984, Becker, 1992a).

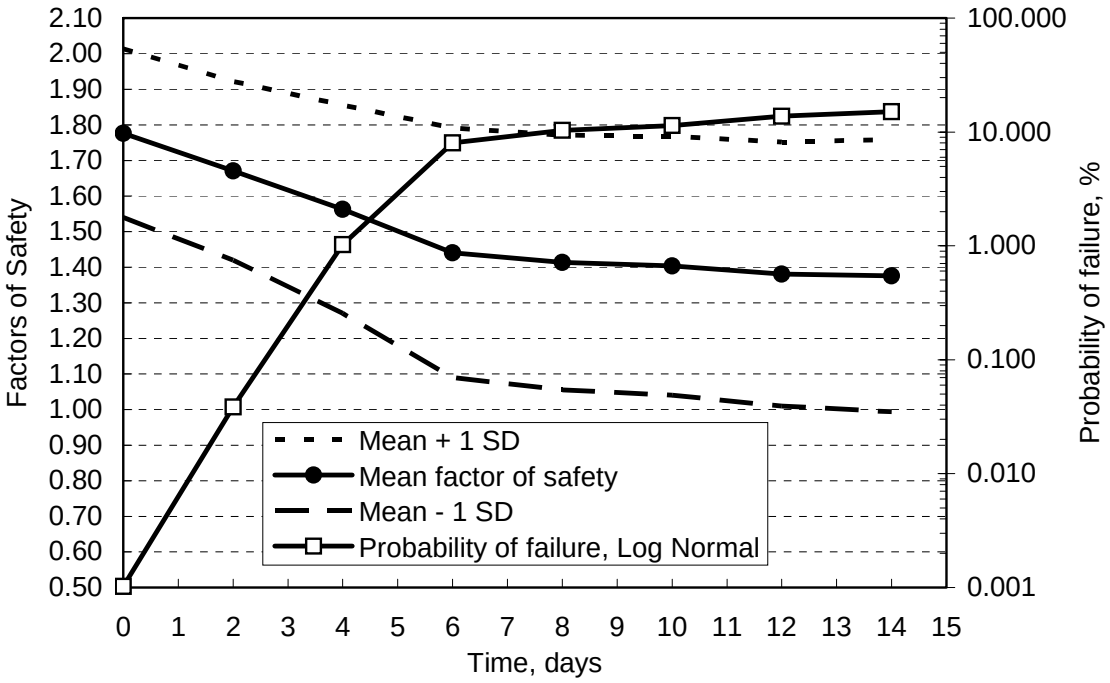

Figure 6.26 Evolution of the mean factor of safety and probability of failure for the low, clay embankment. Initial conditions: $u_{w\,min}$ = -60 kPa.

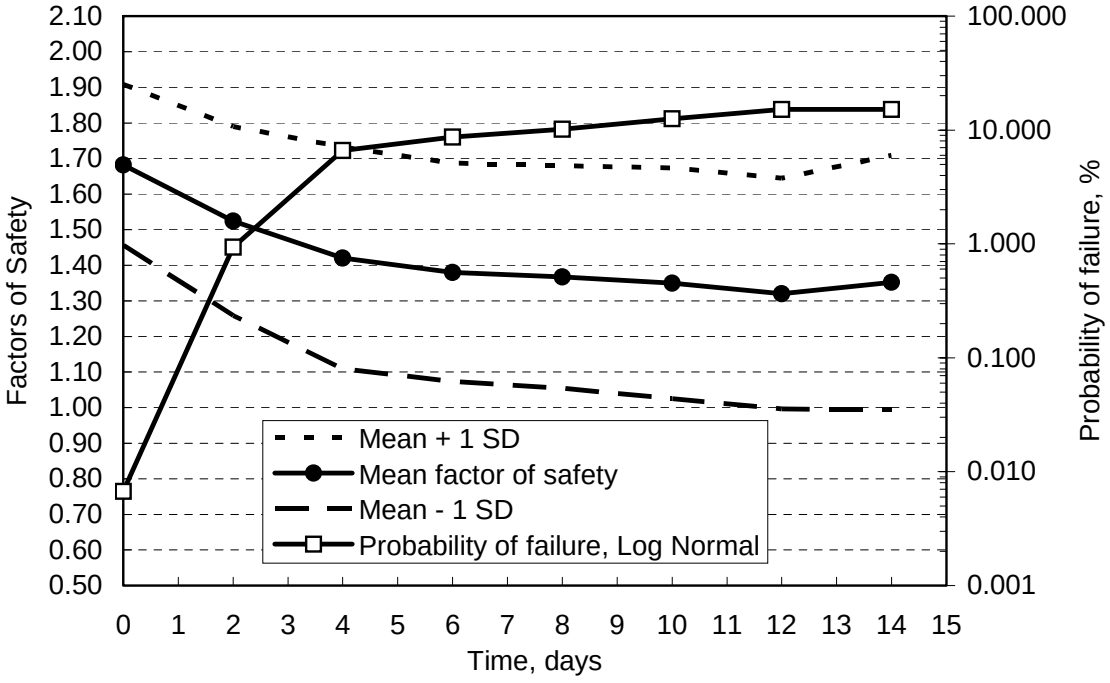

Figure 6.27 Evolution of the mean factor of safety and probability of failure for the low, clay embankment. Initial conditions: $u_{w\,min}$ = -20 kPa.

A high rate of increase in the probability of failure was observed during the first few days of the precipitation event, similar to what was observed for the loam embankments. The period of high rate of increase of probability of failure was longer for the dry embankment. The probability of failure of the dry embankment increased from 0.001% for the initial conditions to 8% on the sixth day. The probability of failure of the wet embankment increased from 0.008% for the initial conditions to approximately 8% on the fourth day. The probability of failure of both embankments appears to have reached a plateau past the initial period of 6 and 4 days. Therefore, the initial pore-water pressure conditions played a significant role during early stages, up to the 6th day but did not play an important role regarding the final hazard level.

Figures 6.26 and 6.27 show that the increase in the probability of failure of the clay embankment is a result of the decrease in the mean factor of safety and a result of the increase on the standard deviation. The change in the standard deviation of the factor of safety appears considerably larger than that observed for the loam embankment. The standard deviation increased from approximately 0.23 for the initial conditions to 0.37 on the 14th day. The same pattern was observed for both the initially dry and initially wet embankments.

Figures 6.26 and 6.27 show again that the uncertainty associated with the input soil properties may be of paramount importance. The factors of safety obtained for the mean parameters and the mean factors of safety presented in Figs. 6.26 and 6.27 indicate stable embankment conditions throughout the precipitation event. However, the values obtained for the standard deviation of the factor of safety result in high probabilities of failure at the end of the precipitation event (>10%).

6.5.1.2 *High embankments*

Final stability conditions for the High Loam embankment

The results presented in this section correspond to the case scenario using the mean parameters for the loam soil. Figure 6.28 presents the final pore-water pressure distributions (t = 14 days), considering "dry" and "wet" initial conditions (i.e., minimum u_w equal to -100 kPa and -20 kPa, respectively). The soil suctions observed at the end of the precipitation event are considerably higher for the initially dry embankment. However, the pore-water pressure distributions have similar patterns. The core of both embankments presents suctions higher than that found near the ground surface. As mentioned before, this pattern has been observed by Krahn et al. (1989)

by field measurement on similar railway embankments. The ground surface reached a nearly saturated state. The slightly negative pore-water pressures at the embankment surface are the result of the availability of water storage at the embankment core.

Local factors of safety were computed, considering the pore-water pressures, stress distributions, and shear strength characteristics of the loam soil, and using Eq. 6.7. Figure 6.29 presents the distribution of local factors of safety for the high, loam embankments. Lower final factors of safety were observed for the initially wet embankment, as expected. The near ground surface regions on the face of the embankment slope present the lowest local factors of safety. Local factors of safety lower than 1 were observed in both cases and indicate extremely shallow failure surfaces. Local factors of safety provide valuable information regarding the local stability conditions of the embankment, but different factors of safety may be obtained, depending on the stress plane considered.

Figures 6.30 and 6.31 present the critical slip surfaces for the initially dry and wet embankments, respectively, obtained using dynamic programming, for the initial conditions and for t = 4, 8, and 14 days. The initial factors of safety (i.e., F_s equal to 1.504 and 1.267) show that both embankment conditions are relatively stable. As the precipitation event progressed, factors of safety decreased, reaching 1.163 and 1.085 for the "dry" and "wet" embankments, respectively. The final overall factors of safety presented in Figs. 6.30 and 6.31 indicate marginally stable conditions. The overall factors of safety obtained using dynamic programming and the local factors of safety appear to be in fair agreement. The final stability conditions of the "dry" and "wet" embankments are considerably apart, indicating that the difference in initial conditions did have influence the stability of the embankment at the end of the precipitation event. The higher suction values observed for the initially dry embankment are located in the core of the embankment. However, near surface conditions at the embankment slope are also affected, explaining the different overall factors of safety at the end of the precipitation event.

Figures 6.30 and 6.31 show relatively deep critical slip surfaces for the initial conditions. The deep critical slip surfaces are in agreement with the high cohesion effect that results from the shear strength due to soil suction. As the near ground surface soil saturates, the critical slip surfaces moves towards the ground surface. The near ground surface soil presents reduced shear strength due to soil suction and is held primarily by the internal friction angle.

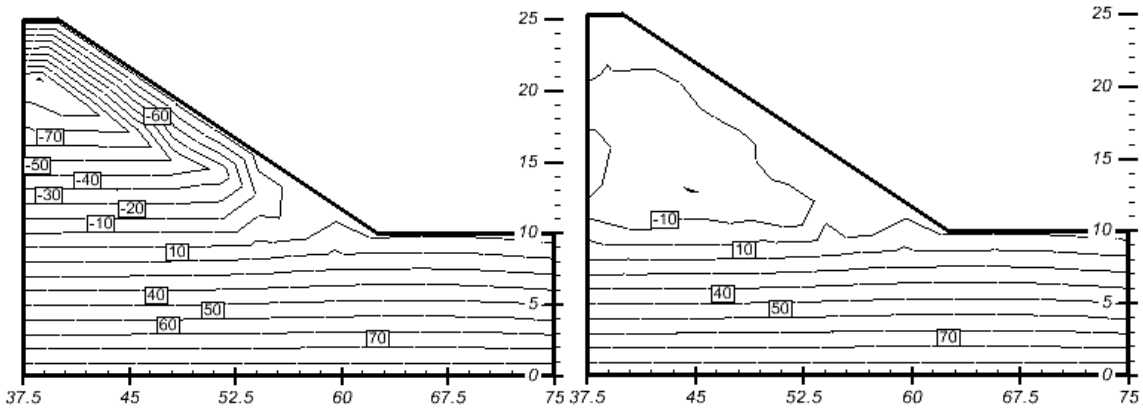

(a) (b)

Figure 6.28 Final pore-water pressure distribution for the high, loam embankment. Initial conditions: (a) $u_{w\,min}$ = -100 kPa and (b) $u_{w\,min}$ = -20 kPa.

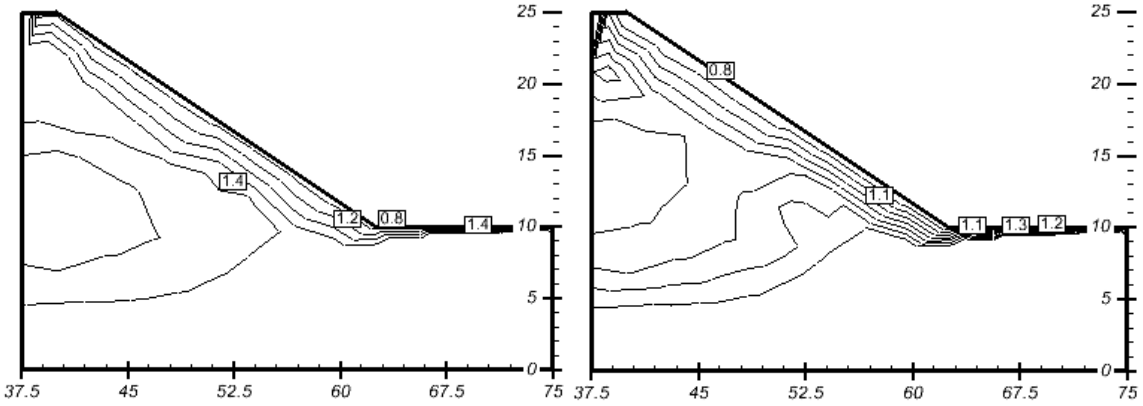

(a) (b)

Figure 6.29 Final local factors of safety for the high, loam embankment. Initial conditions: (a) $u_{w\,min}$ = -100 kPa and (b) $u_{w\,min}$ = -20 kPa.

The extremely shallow failure mechanism predicted in Figs. 6.30 and 6.31 is somewhat similar to that observed in the field by Krahn et al. (1989), for similar embankments constructed using lacustrine silt. It is important to point out that the peel-shaped critical slip surfaces could not be predicted by conventional limit equilibrium methods, based on circular slip surfaces. The failure mechanisms shown in Fig. 6.30 and 6.31 are a remarkable illustration of the flexibility of the dynamic programming approach for embankment stability.

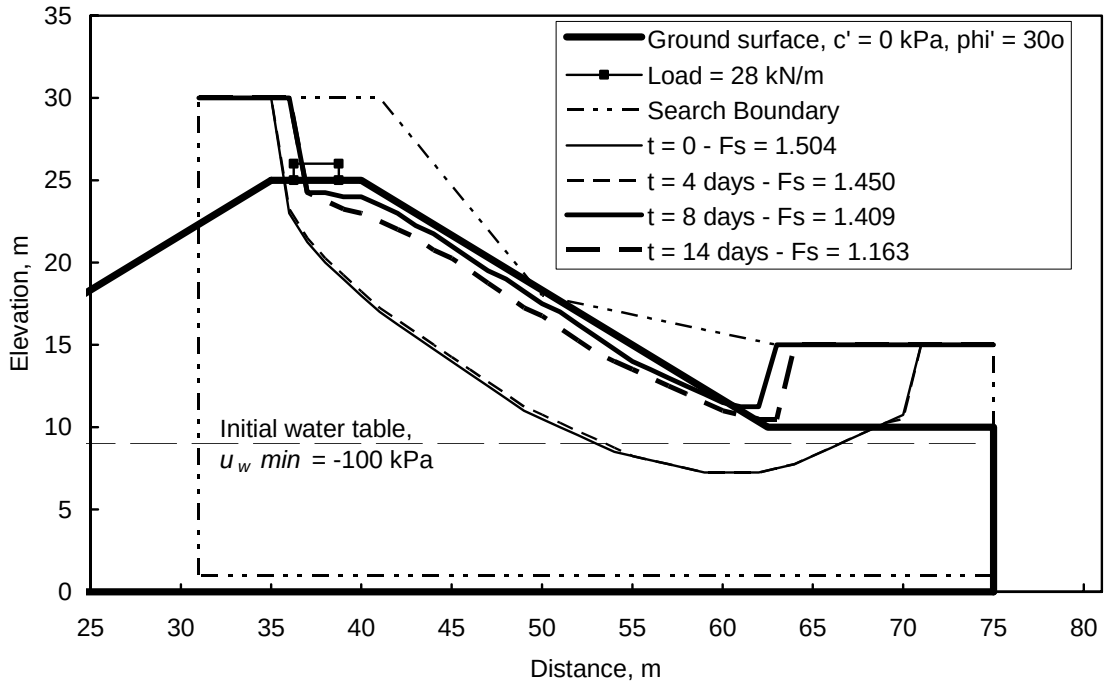

Figure 6.30 Slip surfaces for the high, loam embankment. Initial conditions: $u_{w\,min}$ = -100 kPa.

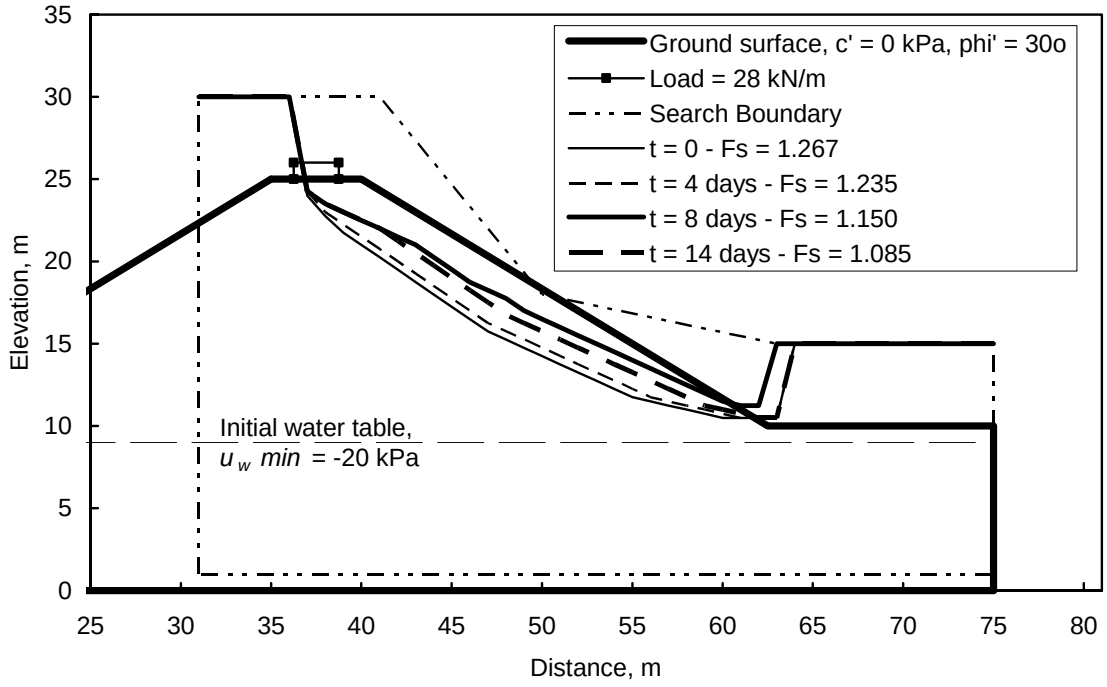

Figure 6.31 Slip surfaces for the high, loam embankment. Initial conditions: $u_{w\,min}$ = -20 kPa.

Final stability conditions for the High Clay embankment

The results presented in this section correspond to the case scenario using the mean parameters for the clay soil. Figure 6.32 presents the final pore-water pressure distributions (t = 14 days), considering "dry" and "wet" initial conditions (i.e., minimum u_w equal to -100 kPa and -20 kPa, respectively). Again, the soil suctions observed at the end of the precipitation event are considerably higher for the initially dry embankment. The pore-water pressure distributions have similar patterns, with the core of both embankments presenting suctions higher than those found near the ground surface. The ground surface reached a completely saturated state. The saturated state at the embankment surface is the result of the precipitation rate (40 mm/day) higher than the saturated hydraulic conductivity (9.4 mm/day).

Local factors of safety were computed, considering the pore-water pressures, stress distributions, and shear strength characteristics of the clay soil, and using Eq. 6.7. Figure 6.33 presents the distribution of local factors of safety for the high, clay embankments. Somewhat mixed results were obtained. Lower final factors of safety were observed for the initially wet embankment, as indicated by the larger region with F_s = 1.3, below the "dry" embankment slope surface. However, ground surface regions on the face of both embankment slope present similar local factors of safety. Local factors of safety lower than 1 were observed in small regions, for both cases, and indicate small and extremely shallow failure surfaces.

Figures 6.34 and 6.35 present the critical slip surfaces for the initially dry and wet embankments, for the initial conditions and for t = 4, 8, and 14 days, obtained using dynamic programming. The initial factors of safety (i.e., F_s equal to 1.329 and 1.167) show that both embankments are relatively stable, but closer than the loam embankment to unstable conditions. As the precipitation event progressed, factors of safety slightly decreased, reaching 1.291 and 1.128 for the "dry" and "wet" embankments, respectively. The final overall factors of safety presented in Figs. 6.34 and 6.35 indicate relatively stable conditions. The overall factors of safety obtained using dynamic programming and the local factors of safety appear to be in fair agreement. The final stability conditions of the "dry" and "wet" embankments indicate that different initial conditions influenced the stability of the embankment at the end of the precipitation event.

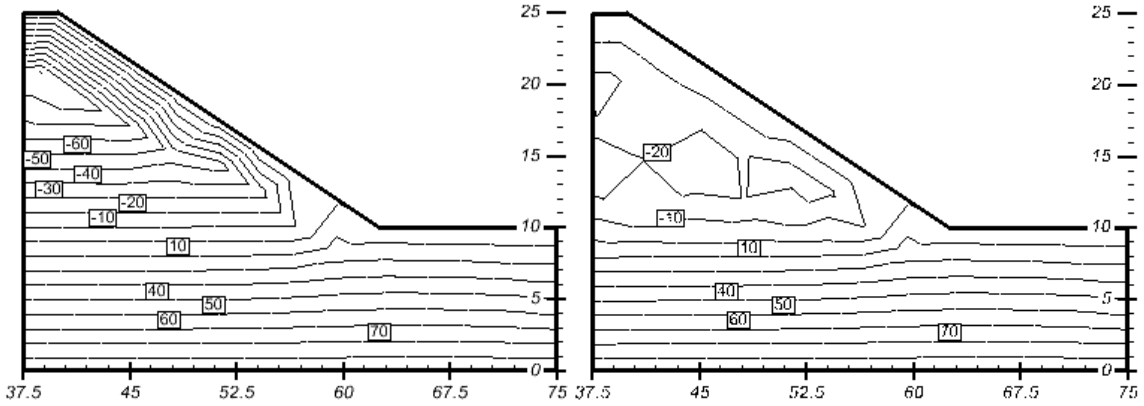

(a) (b)

Figure 6.32 Final pore-water pressure distribution for the high, clay embankment. Initial conditions: (a) $u_{w\,min}$ = -100 kPa and (b) $u_{w\,min}$ = -20 kPa.

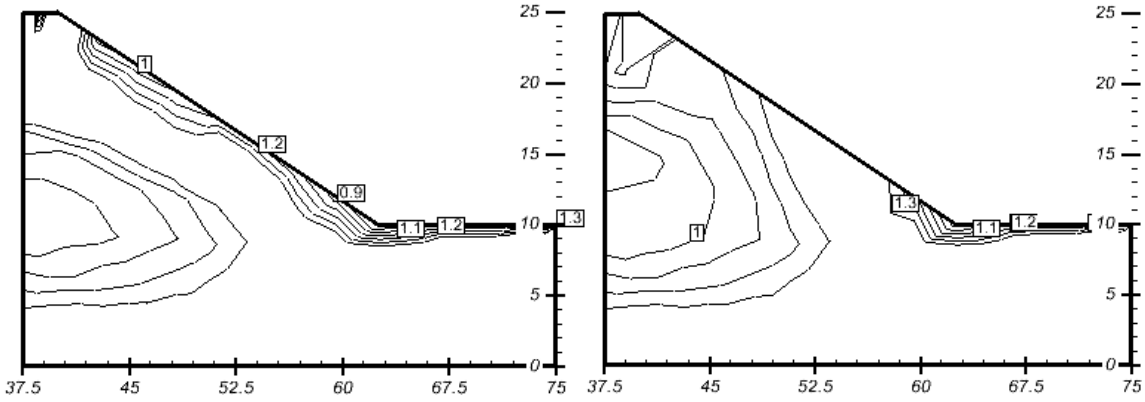

(a) (b)

Figure 6.33 Final local factors of safety for the high, clay embankment. Initial conditions: (a) $u_{w\,min}$ = -100 kPa and (b) $u_{w\,min}$ = -20 kPa.

Figures 6.34 and 6.35 show deep critical slip surfaces for all time steps. The deep critical slip surfaces are in agreement with the high cohesion of the clay soil. The small change in factor of safety and in the position of the critical slip surfaces during the precipitation event appears to be the result of the low hydraulic conductivity of the clay embankments. Water has less opportunity of infiltrate and percolated through the embankment, during the 14 days long precipitation event.

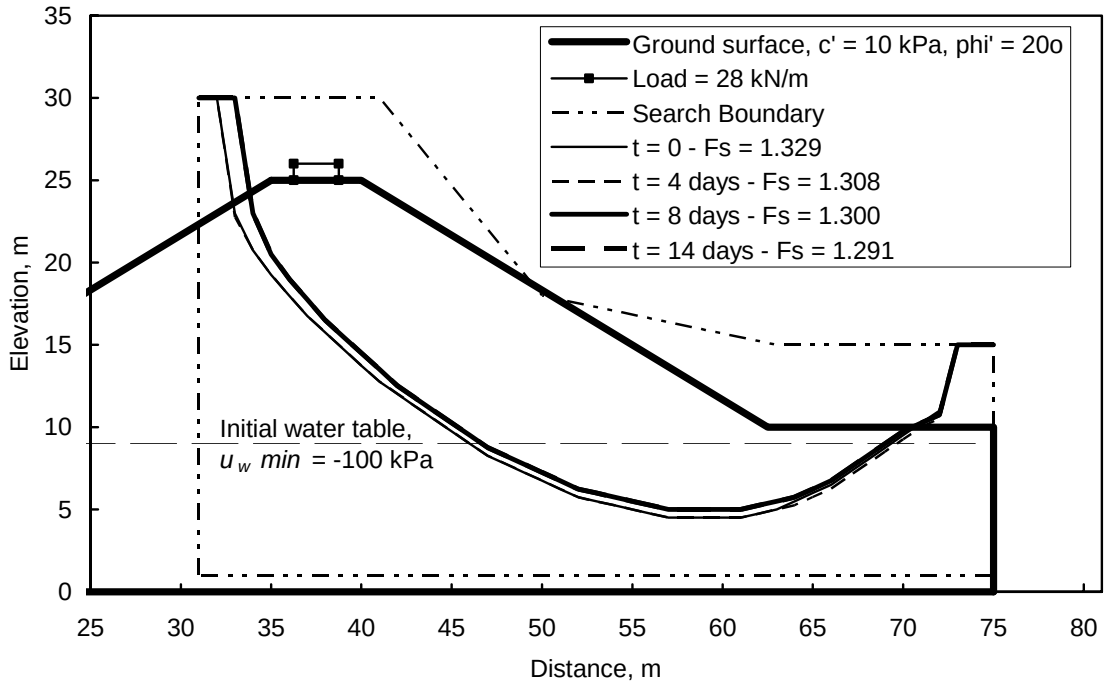

Figure 6.34 Slip surfaces for the high, clay embankment. Initial conditions: $u_{w\,min}$ = -100 kPa.

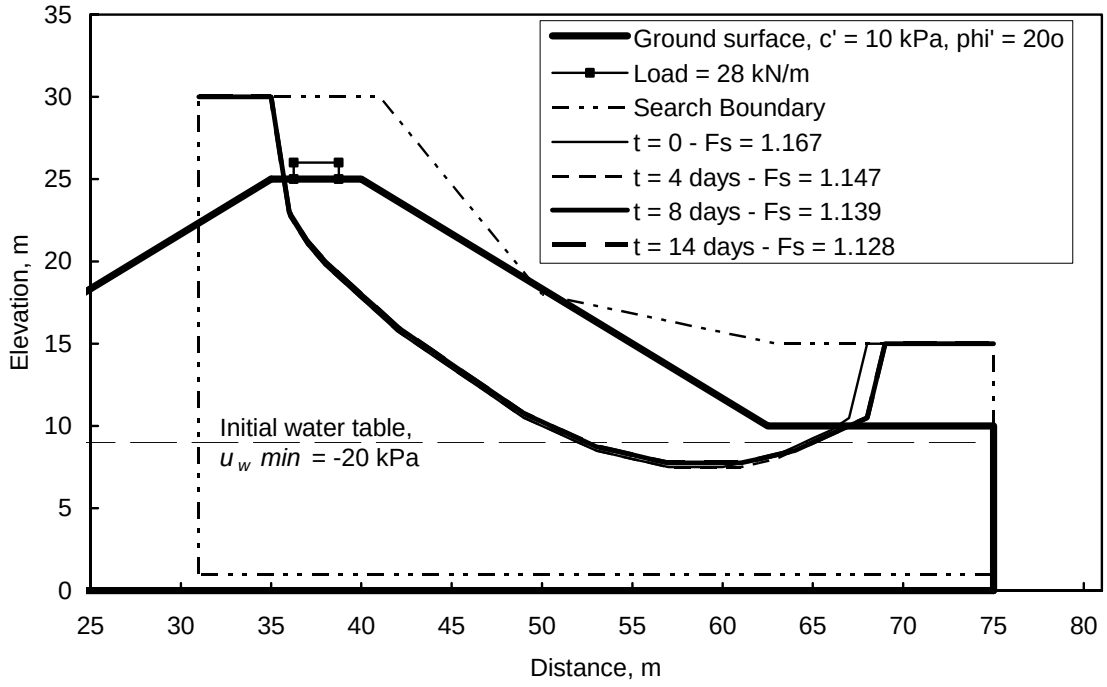

Figure 6.35 Slip surfaces for the high, clay embankment. Initial conditions: $u_{w\,min}$ = -20 kPa.

Transient stability conditions for the High Loam embankment

According to the framework proposed herein, transient stability conditions can be quantified in terms of overall factors of safety and probability of rupture. The results of the case scenarios presented in Tables 6.4 and 6.5 and in Appendix E were used, along with the probabilistic framework presented in Chapter 3, in order to compute the mean factors of safety, the standard deviation of the factor of safety, and the probability of failure. The factors of safety were computed within intervals of two days in the same fashion done for the low embankments,. Therefore, a total of 8 computations of factors of safety were performed, for each property case scenario.

Figures 6.36 and 6.37 present the changes in the mean factor of safety and probability of failure during the precipitation event, considering the initially dry and initially wet conditions, respectively. The computed values of the mean factor of safety plus and minus one standard deviation are also presented. The initial probability of failure was approximately 0.2% (i.e., 2/1,000) for the "dry" embankment and 4.0% (i.e., 4/100) for the "wet" embankment, as shown in Figs. 6.36 and 6.37. According to Whitman (1984) and Becker (1992a), among others, the typical range of acceptable probabilities of failure adopted in slope and foundation engineering projects varies from 0.1 to 1%. Therefore, the initial probability of failure for the high loam embankments appears to be near the acceptable limits.

The probability of failure of the "dry" loam embankment suffered a slight decrease during the first 4 days, due to a small decrease in the standard deviation. The change is not significant though and can be attributed to (i) the small changes in mean factor of safety and (ii) the high sensitivity of the standard deviation. A relatively high rate of increase in the probability of failure was observed during the first 6 or 8 days of the precipitation event. The initial rate of increase of the probability of failure was considerably higher for the dry embankment. The probability of failure of the dry embankment increased from 0.2% for the initial conditions to 9% on the eight day. The probability of failure of the wet embankment increased from 4.0% for the initial conditions to approximately 12% on the sixth day. The probability of failure of both embankments appears to have reached a plateau past the eighth and sixth day. In summary, the initial conditions played a significant role during early stages, up to the 8^{th} and 6^{th} day, but did not play a significant role in the final hazard level past the initial period.

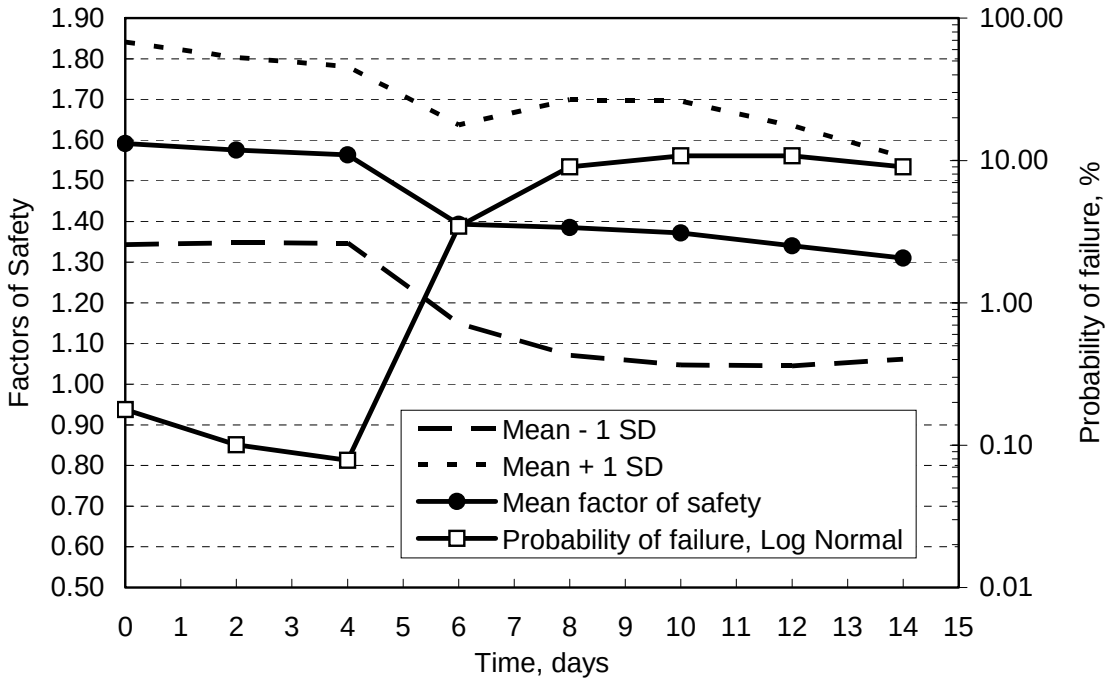

Figure 6.36 Evolution of the mean factor of safety and probability of failure for the high, loam embankment. Initial conditions: $u_{w\,min}$ = -100 kPa.

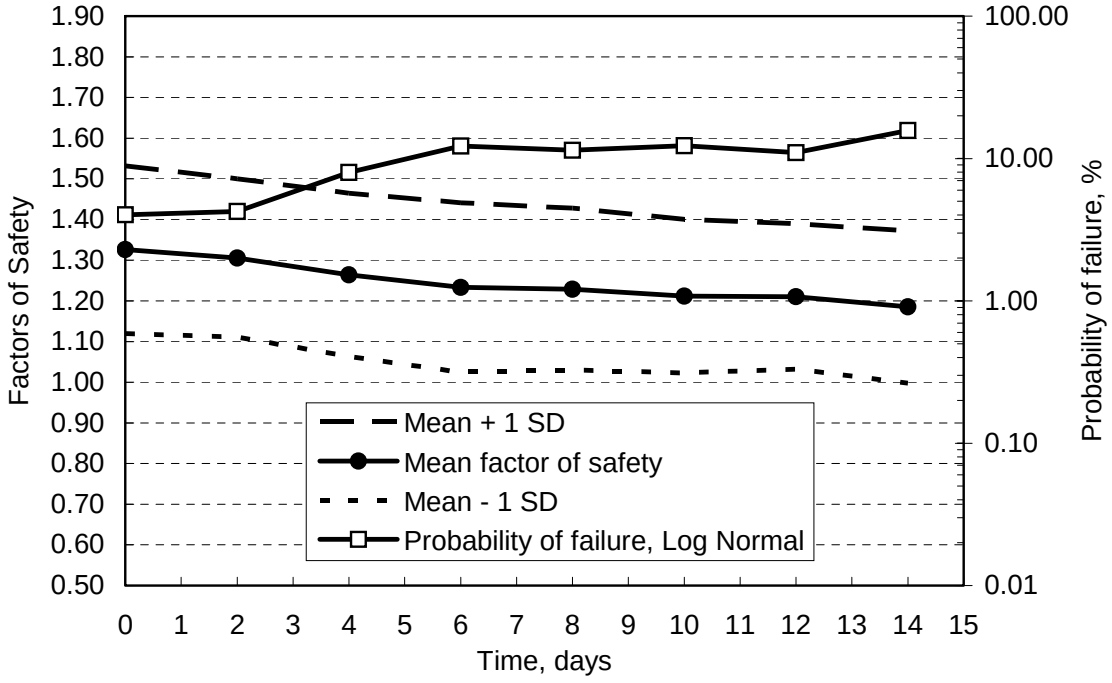

Figure 6.37 Evolution of the mean factor of safety and probability of failure for the high, loam embankment. Initial conditions: $u_{w\,min}$ = -20 kPa.

Figures 6.36 and 6.37 show that the increase in the probability of failure is primarily a result of the decrease in the mean factor of safety. The change in the standard deviation of the factor of safety appears negligible, as shown by the mean values plus and minus one standard deviation, with exception of some fluctuations that occurred between the 4th and 8th days for the "dry" embankment. The same general pattern was observed for the initially dry and initially wet embankments.

Figures 6.36 and 6.37 show that the uncertainty associated with the input soil properties may be of paramount importance for the assessment of railway embankment hazards. The factors of safety shown in the previous section for the mean parameters and the mean factors of safety presented in Figs. 6.36 and 6.37 indicate misleadingly stable embankment conditions throughout the precipitation event. The values obtained for the standard deviation of the factor of safety result in fairly high probabilities of failure at the end of the precipitation event. A final probability of failure higher than 10% (10/100) was obtained for both the initially dry and initially wet loam embankments.

Transient stability conditions for the High Clay embankment

Figures 6.38 and 6.39 present the changes in the mean factor of safety and probability of failure during the precipitation event for the clay embankments. The initial probability of failure was approximately 0.7% (i.e., 7/1,000) for the "dry" embankment and 11.0% (i.e., 11/100) for the "wet" embankment, as shown in Figs. 6.38 and 6.39. The initial probabilities of failure for the high clay embankments appear beyond acceptable limits (Whitman, 1984 and Becker, 1992a). A relatively constant rate of increase in the probability of failure was observed throughout the precipitation event. The probability of failure of the "dry" and "wet" embankments reached 25% and 65%, respectively, on the fourteenth day. Therefore, the initial conditions played a significant role during both the early and later stages of the precipitation event.

Figure 6.38 shows that the increase in the probability of failure of the "dry" embankment is a result of the decrease in the mean factor of safety. The change in the standard deviation of the factor of safety appears negligible for the "dry" embankment, as shown by the mean values plus and minus one standard deviation. Figures 6.39 shows that the increase in the probability of failure of the "wet" embankment is a combined result of the decrease in the mean factor of safety and the increase in the standard deviation of the factor of safety. The standard deviation of the factor of safety for the "wet" embankment increased from 0.135 to 0.187.

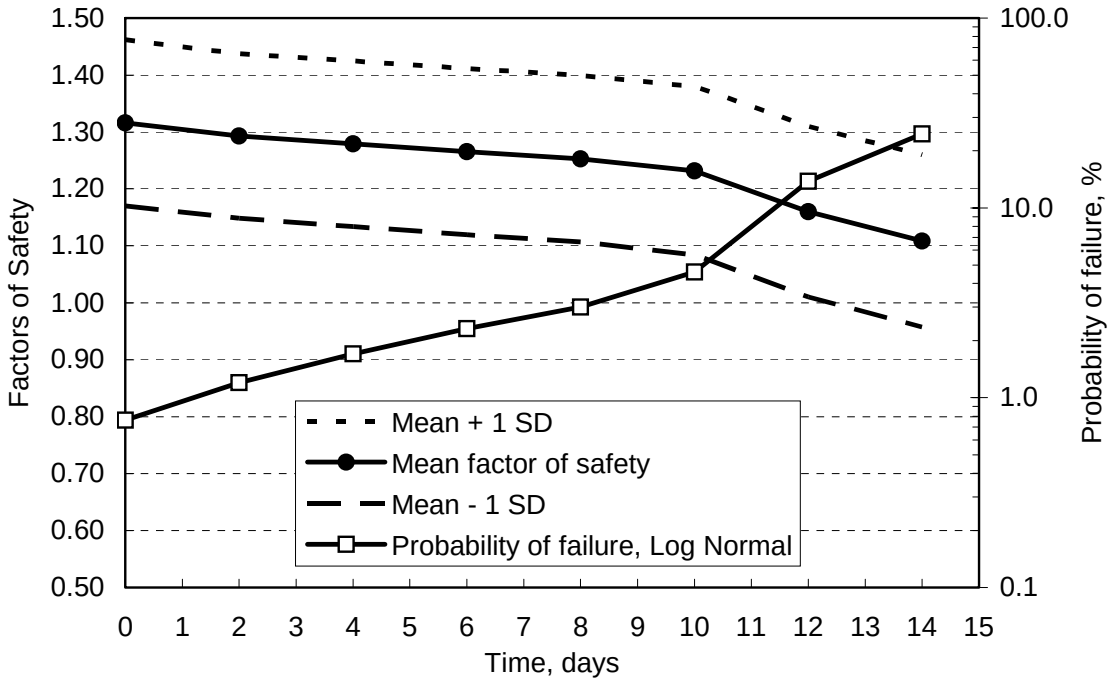

Figure 6.38 Evolution of the mean factor of safety and probability of failure for the high, clay embankment. Initial conditions: $u_{w\,min}$ = -100 kPa.

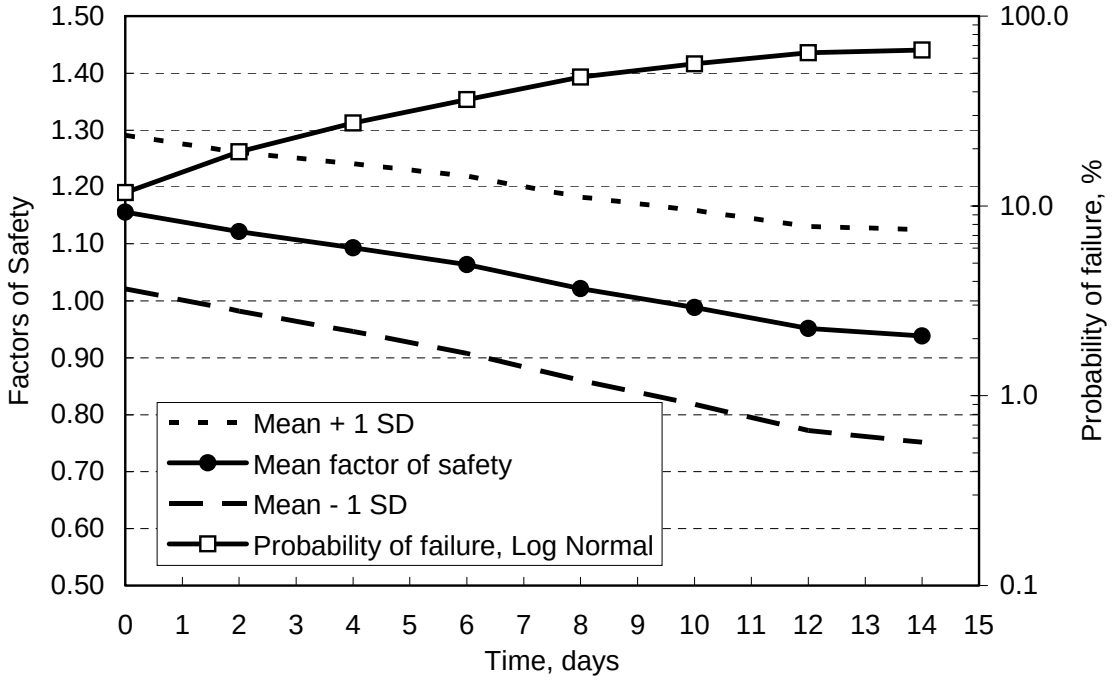

Figure 6.39 Evolution of the mean factor of safety and probability of failure for the high, clay embankment. Initial conditions: $u_{w\,min}$ = -20 kPa.

6.5.2 *Analysis of evaporation conditions*

This section presents the assessment of embankment hazard considering the evaporation event described in Sections 6.2 and 6.3. Two embankment configurations are analysed herein, as shown in Fig. 6.1. The embankment geometries, boundary conditions, initial conditions, and soil properties selected were described in detail in the Section 6.2. The evaporation event corresponds to a period of 42 days.

Final stability conditions

Figure 6.40 presents contours for the degree of saturation (t = 42 days), considering the mean parameters for the loam and clay soils. Figure 6.40 shows that the degree of saturation at the end of the evaporation event decreased considerably near the ground surface. Sharp drying fronts are observed for both soil types, as anticipated. The upper contour, closest to the ground surface indicates a minimum degree of saturation of 0.2. The degree of saturation changes from 0.2 near the ground surface to values close to the initial conditions (S = 0.7) over a short active zone less than 2 meters deep. The results using both soil types indicate that pore-water pressures vary from positive values to negative values as low as -500,000 kPa near the ground surface. Because of the wide variations over small distances, meaningful contours for pore-water pressures are difficult to establish.

Local factors of safety were computed, considering the pore-water pressures, stress distributions, and shear strength characteristics of the loam and clay soils, and using Eq. 6.7. Figure 6.41 presents the distribution of local factors of safety for the loam and clay embankments. The observed local factors of safety near the ground surface reflect the computed pore-water pressures, degrees of saturation, and the position of the active zone. The near ground surface regions on the face of the embankment slope present relatively high local factors of safety. The local factors of safety indicate stable condition throughout the embankment and suggest that critical slip surfaces must be deep seated.

Figures 6.42 and 6.43 present the critical slip surfaces for the loam and clay embankments, respectively, obtained using dynamic programming. Slip surfaces are presented for the initial conditions and for t = 20 and 42 days. The initial factors of safety (i.e., F_s equal to 1.601 and 1.691) show that both embankment conditions are relatively stable. As the evaporation event progressed, the factors of safety increased, reaching 1.734 and 2.001 for loam and clay embankments, respectively.

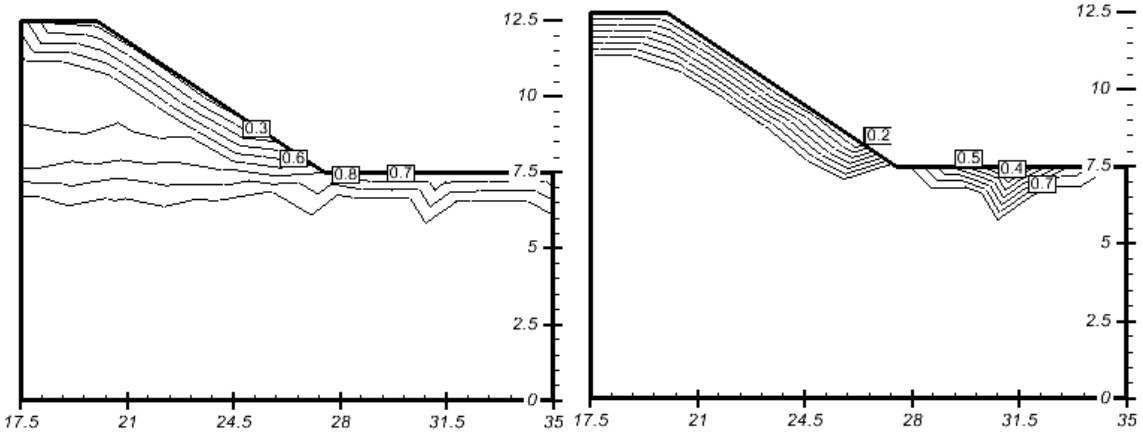

(a) (b)

Figure 6.40 Final degree of saturation distribution for the railway embankment past the evaporation event. Soil type: (a) loam soil and (b) clay soil.

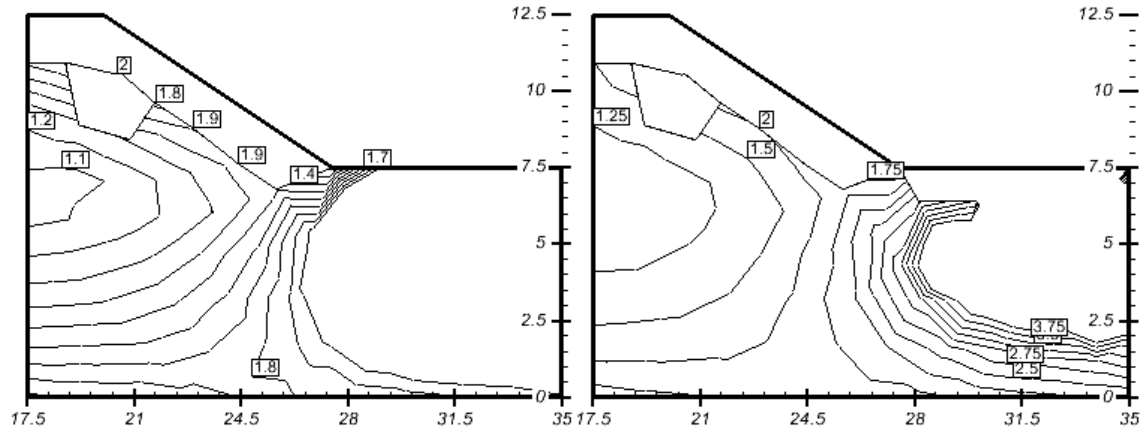

(a) (b)

Figure 6.41 Final local factors of safety for the railway embankment past the evaporation event.. Soil type: (a) loam soil and (b) clay soil.

The final overall factors of safety presented in Figs. 6.42 and 6.43 indicate stable conditions. The overall factors of safety obtained using dynamic programming and the local factors of safety appear to be in fair agreement. Figures 6.42 and 6.43 show relatively deep critical slip surfaces throughout the evaporation event. As the near ground surface soil dries, most critical slip surfaces become deeper, as anticipated. The deep critical slip surfaces are in agreement with the high cohesion effect that results from the shear strength due to soil suction near the embankment surface.

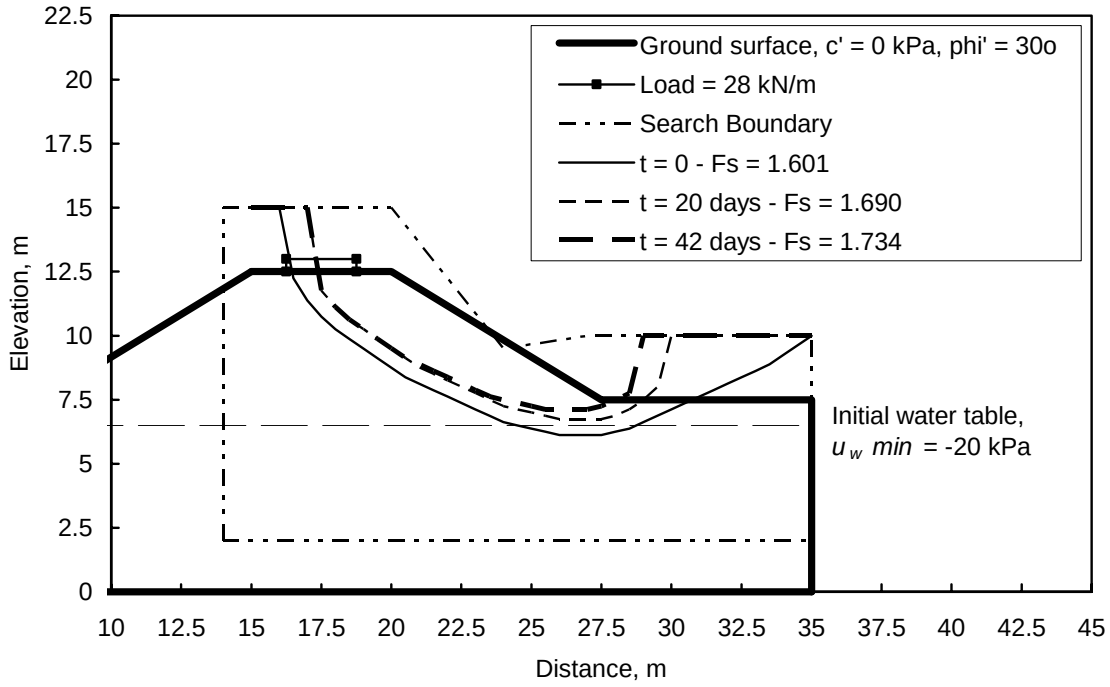

Figure 6.42 Slip surfaces for the loam embankment during the evaporation event.

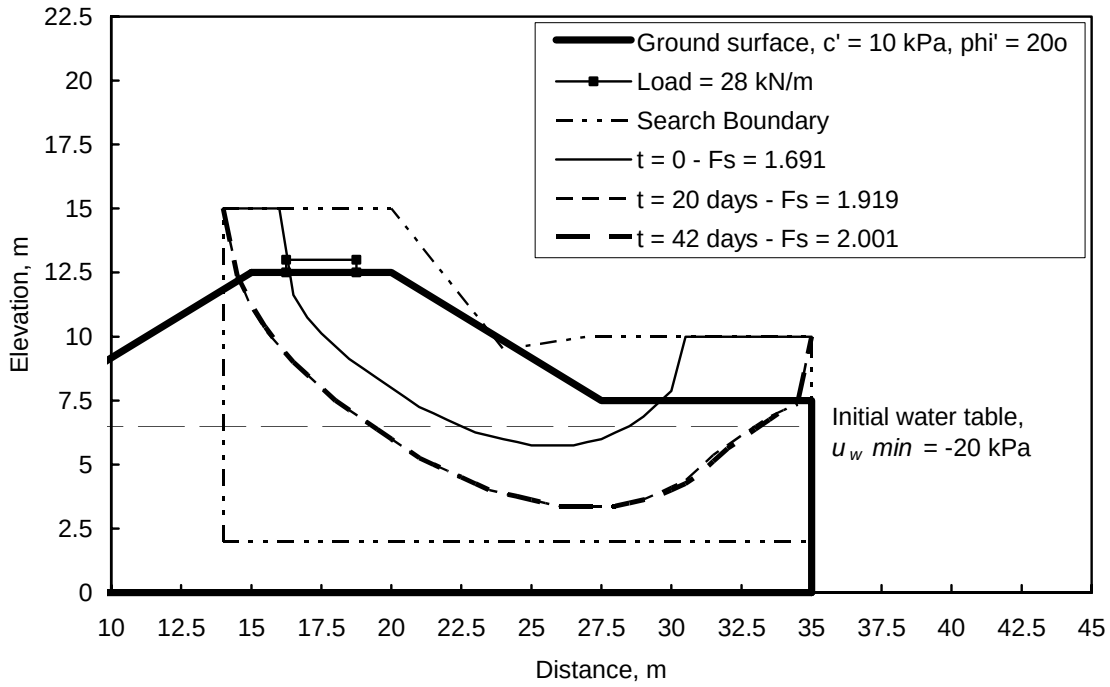

Figure 6.43 Slip surfaces for the clay embankment during the evaporation event.

Transient stability conditions

Figures 6.44 and 6.45 present the changes in the mean factor of safety and probability of failure during the evaporation event, considering the loam and clay embankments, respectively. The computed values of the mean factor of safety, plus and minus one standard deviation are also presented. The evolution of the mean factor appears in agreement with the anticipated results. The factor of safety increases steady, as the evaporation event progressed. Similar patterns where observed for both embankments.

The decrease in the probability of failure was anticipated. The probability of failure of the loam embankment decreased by more than one order of magnitude, from 0.3% for the initial conditions to approximately 0.01% on the 42nd day. The probability of failure of the clay embankment decreased by approximately two orders of magnitude, from 0.007% for the initial conditions to 0.0002% on the 42nd day. The probability of failure of both embankments appears to steadily decrease past the 20th day.

A relatively low rate of decrease in the probability of failure was observed during the first 20 days of the evaporation event for the clay embankment. Figures 6.44 and 6.45 show that the decrease in the probability of failure is primarily a result of the increase in the mean factor of safety. The standard deviation of the factor of safety increased for both embankments as the evaporation event advances. However, the increase in the mean factor of safety shifts the probability density distribution of the factor of safety to considerably higher values. The same general pattern was observed for the loam and clay embankments.

6.6 SENSITIVITY ANALYSIS

This section presents the sensitivity analysis study carried out considering the same embankment configurations presented in the previous section. The sensitivity analysis study presented herein indicates the contribution of the inherent variability of the input variables to the variability of the *factor of safety*. As explained previously, the simplified term "sensitivity" is used throughout this chapter to refer to how much the uncertainty of the factor of safety is affected by the inherent uncertainty of a given input parameter.

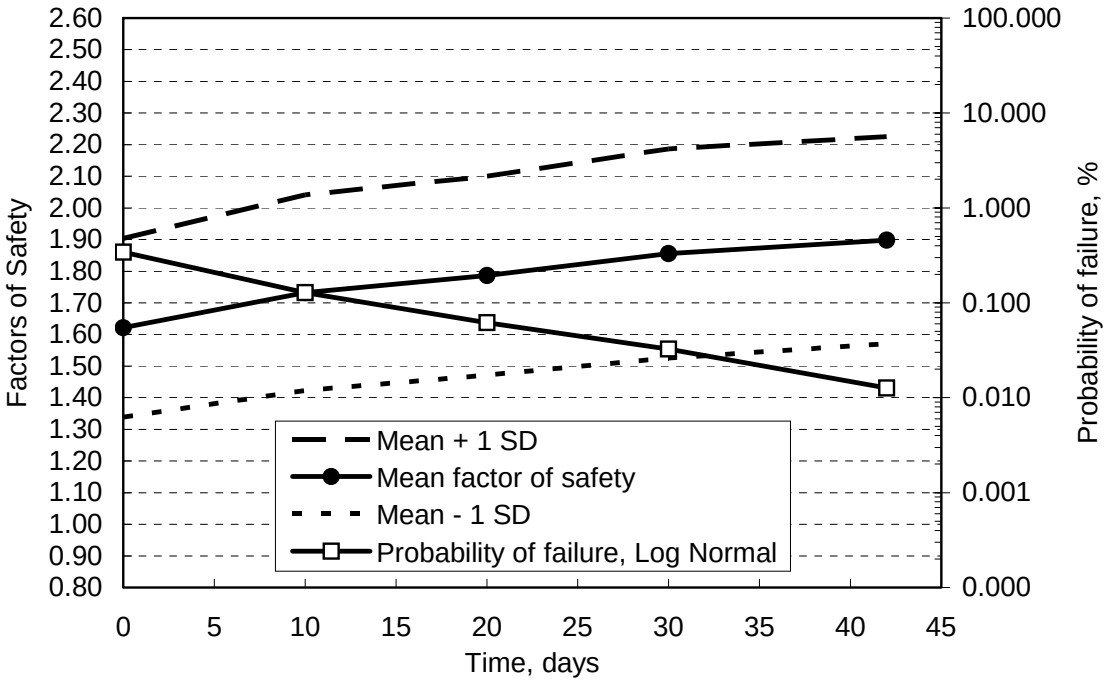

Figure 6.44 Evolution of the mean factor of safety and probability of failure for the loam embankment during the evaporation event.

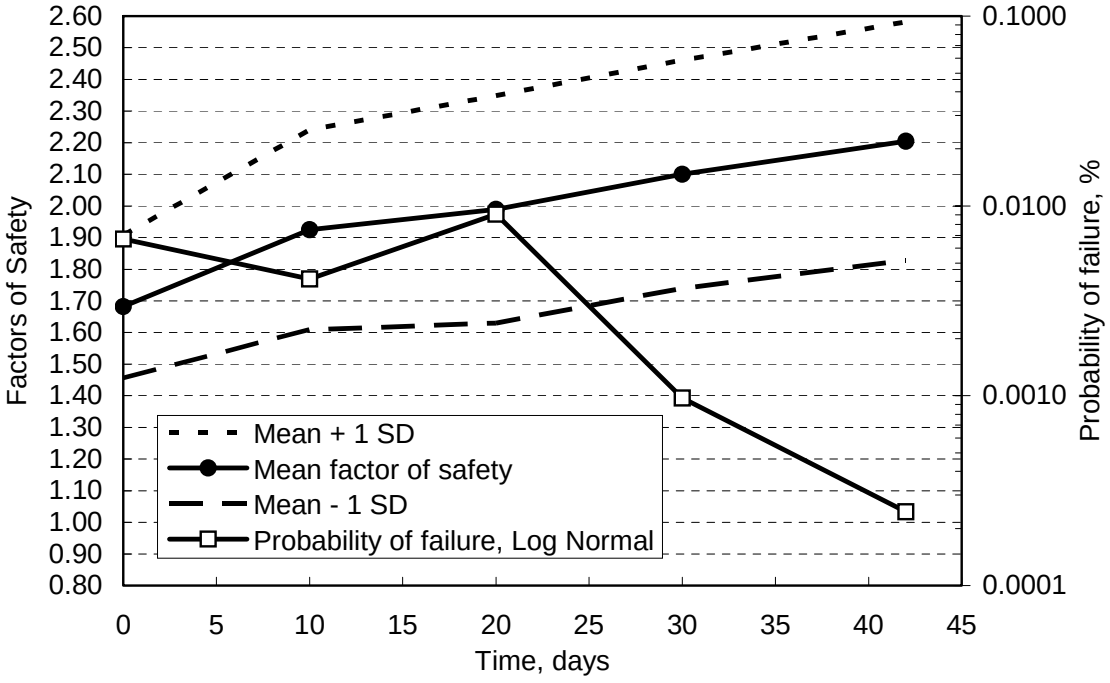

Figure 6.45 Evolution of the mean factor of safety and probability of failure for the clay embankment during the evaporation event.

Tornado diagrams are used herein to evaluate the sensitivity of the factor of safety to the input parameters. The factors of safety computed for the case scenarios described in Tables 6.4 and 6.5 were utilised for the construction of deterministic and probabilistic event tornado diagrams. The procedure adopted for the construction of tornado diagrams was described in detail in Chapter 3. Tornado diagrams are adequate to evaluate snapshots of the transient hazard, at any given time step. Additional plots derived from the tornado diagrams are presented herein in order to show the evolution with time of the sensitivity of the factor of safety.

6.6.1 *Analysis for precipitation conditions*

The precipitation event considered herein corresponds to the same severe rainfall event presented previously, with average precipitation of 40 mm/day during 14 days. The results of the analyses were again grouped according to the embankment height. The analysis of the low embankments is presented first, followed by the analysis of the high embankments.

6.6.1.1 *Low embankments*

Low Loam embankments

Input variables such as the shear strength parameters and the elastic parameters have a direct influence in the factor of safety. However, soil parameters related to the flow of water and heat affect the factor of safety in an indirect manner, through changes in the pore-water pressure distribution with time. The sensitivity analyses presented herein were performed in terms of factor of safety. However, it is also important to examine the effect of hydraulic properties on the pore-water pressure distributions.

Figure 6.46 presents the final pore-water pressure profiles (t = 14 days) for the mid-section of the low railway embankment considering two initial conditions (i.e., “dry” and “wet”). It can be observed that the wetting fronts are considerably deeper for the “wet” embankment, as expected. Figure 6.46 presents also the profiles obtained using the estimate points for the saturated hydraulic conductivity and the air-entry value. The pore-water pressure profiles show that an increase in the air-entry value results in higher pore-water pressures at greater depths and results in a smooth or non-existent wetting front. This effect was expected, since an increase in the air-entry value results in higher degrees of saturation and in a higher hydraulic conductivity for a larger range of soil suctions. A smaller air-entry value resulted in a sharper wetting front and lower pore-water pressures at greater depths.

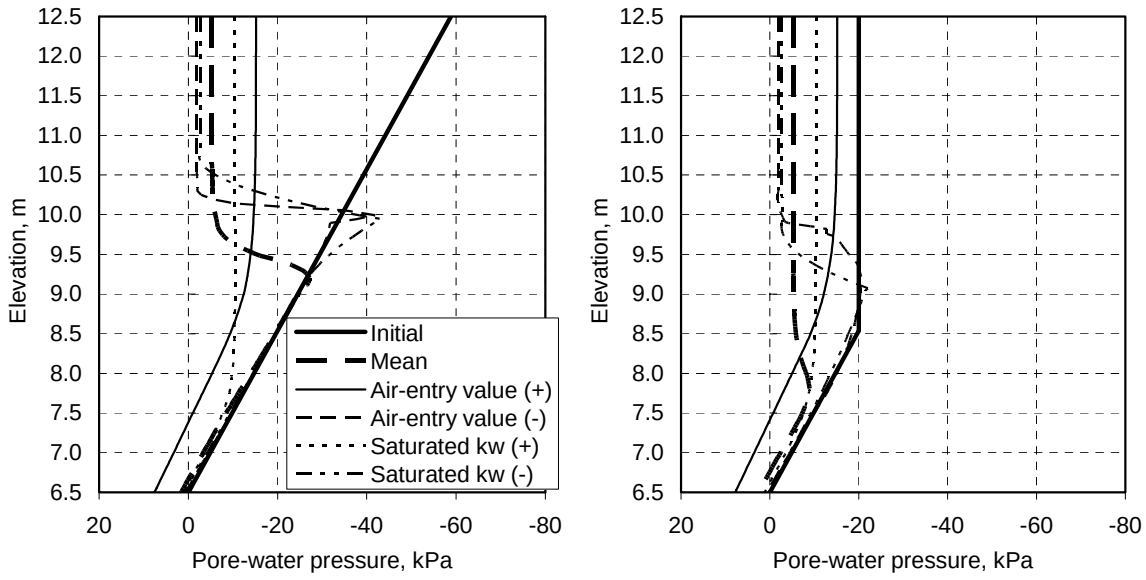

Figure 6.46 Pore-water pressure profile at the mid-section of the low, loam embankment. Initial conditions: (a) $u_{w\,min}$ = -60 kPa and (b) $u_{w\,min}$ = -20 kPa.

The effects of changes in the saturated hydraulic conductivity are also shown in Fig. 6.46. An increase in the saturated hydraulic conductivity resulted in the absence of a wetting front. The entire negative pore-water pressure profile presents a constant value that increases as the soil saturates. The absence of a sharp wetting front resulted in higher soil suctions at the soil surface. Therefore, higher saturated hydraulic conductivities are expected to decrease the hazard levels. The opposite effect was observed when the saturated hydraulic conductivity was reduced.

Figure 6.47 presents deterministic event tornado diagrams for the low, loam embankment, considering initially "dry" and initially "wet" conditions. The tornado diagrams presented in Fig. 6.47 correspond to the final embankment condition, at t = 14 days. The deterministic event tornado diagrams are obtained by adding the uncertainty of one variable at a time and computing the resulting variability of the factor of safety. The left and right coordinates of the bars presented in Fig. 6.47 correspond to the 10^{th} and 90^{th} percentiles of the factor of safety p.d.f.. The line on the middle of each bar corresponds to the 50^{th} percentile. A lognormal distribution was assumed for the factor of safety, as explained previously. The larger the size of a bar, the more sensitive is the factor of safety to the input variable corresponding to that bar.

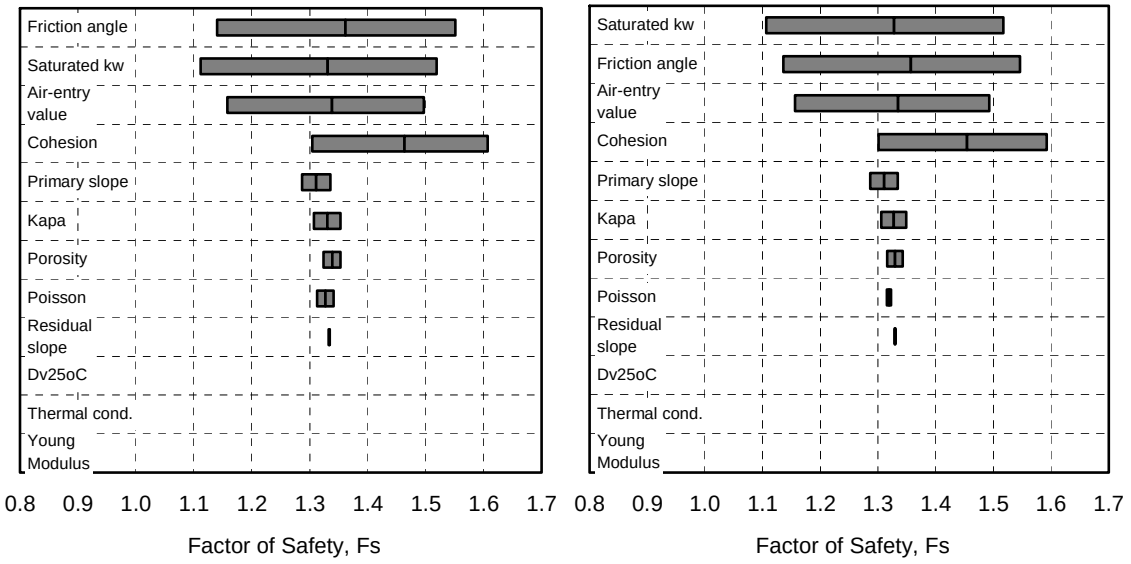

Figure 6.47 Deterministic event tornado diagrams at t = 14 days for the low, loam embankment. Initial conditions: (a) $u_{w\,min}$ = -60 kPa; (b) $u_{w\,min}$ = -20 kPa.

Figure 6.47 shows that the friction angle, the saturated hydraulic conductivity, the air-entry value, and the effective cohesion have important impacts to the factor of safety. The primary SWCC slope, the unsaturated shear strength parameter, κ, the soil porosity, Poisson's ratio, and the residual SWCC slope have minor effects and appear to be adequately modeled if considered as certain, fixed parameters. The parameters associated with vapour flow, $D^{v}_{25^{o}C}$ and heat flow, λ_s, had no influence whatsoever on the factor of safety. The flow of water during a precipitation event takes place primarily as liquid flow, and the flow of vapour is negligible. Young modulus had no effect in the factor of safety. The case scenarios for E produced identical factors of safety. This confirms the observations by Scoular (1997).

Figure 6.48 presents probabilistic event tornado diagrams for the low, loam embankments, considering initially "dry" and initially "wet" conditions. The tornado diagrams presented in Fig. 6.48 correspond to the final embankment condition, at t = 14 days. The probabilistic event tornado diagrams are obtained by removing the uncertainty of one variable at a time and computing the resulting variability in the factor of safety. The left and right coordinates of the bars presented in Fig. 6.48 correspond to the 10^{th} and 90^{th} percentile of the factor of safety p.d.f.. The line on the middle of each bar corresponds to the 50^{th} percentile. A lognormal distribution was assumed for the factor of safety, as explained previously. The smaller the size of the bar, the more sensitive is the factor of safety to the input variable corresponding to that bar.

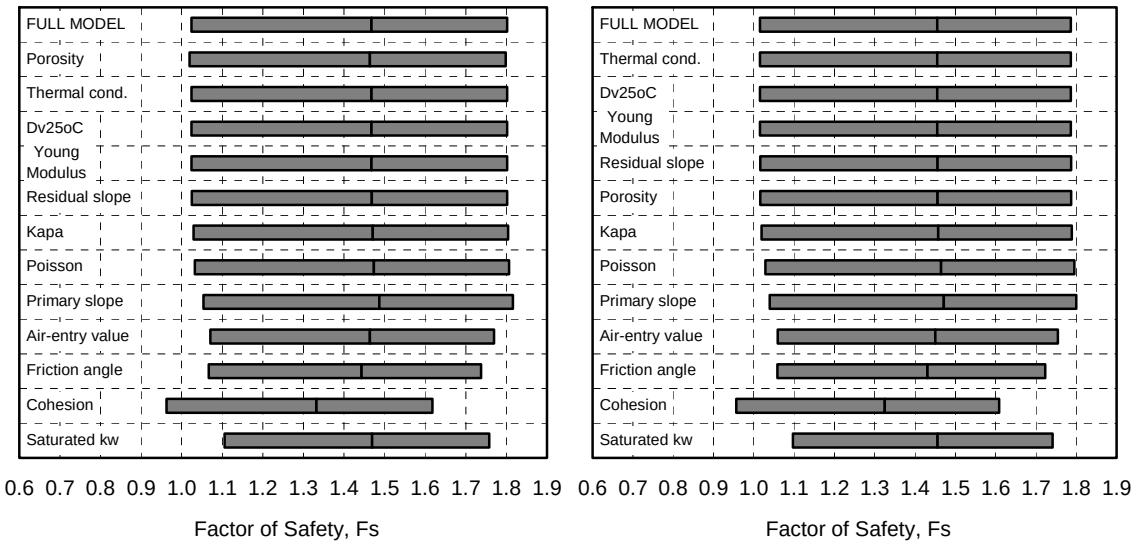

(a) (b)

Figure 6.48 Probabilistic event tornado diagrams at t = 14 days for the low, loam embankment. Initial conditions: (a) $u_{w\,min}$ = -60 kPa; (b) $u_{w\,min}$ = -20 kPa.

Probabilistic event tornado diagrams tend to have a less appealing appearance but are more realistic than deterministic diagrams, since they preserve most of the uncertainty of the model (Clemen, 1996). Deterministic event tornado diagrams show how much uncertainty would exist in the model if the uncertainty of a given input parameter was the only uncertainty of the model. This scenario provides useful information, but does no correspond to realistic conditions. On the other hand, a probabilistic event tornado diagram shows how much uncertainty remains in the model if the uncertainty of a single given parameter was eliminated.

Figure 6.48 confirms that the parameters with the greatest impacts on the factor of safety are the saturated hydraulic conductivity, the effective cohesion, the friction angle, and the air-entry value. The relative sensitivity of the factor of safety to the input parameters does not vary considerably when comparing the initially "dry" and "wet" conditions. The low-impact parameters are the same parameters identified by the deterministic event tornado diagrams. The primary SWCC slope, the unsaturated shear strength parameter, κ, the soil porosity, the Poisson's ratio, and the residual SWCC slope have minor effects and could be simplified, being considered as fixed parameters. Again, the parameters associated with vapour flow, $D^{v}_{25^{o}C}$, heat flow, and the Young modulus have no influence in the factor of safety.

The difference between the 10th percentile and F_s = 1 provides insight into the embankment hazard level. Figure 6.48 shows that the 10th percentile is close to the unity for the full model and for a large number of variables. This results in a probability of failure of almost 10%, as shown by Figs. 6.24 and 6.25. The 10th percentile increases considerably when the variability of some "high-impact" variables is removed, such as the variability of the saturated hydraulic conductivity and friction angle.

Figures 6.49 and 6.50 present the transient sensitivity of the factor of safety to the input variables based on deterministic event tornado diagrams for the low, loam embankment. The transient sensitivity of F_s to the input parameters is summarised in terms of the size of the bars, computed by subtracting the 90th and 10th factor of safety percentiles. According to Figs. 6.49 and 6.50, the friction angle was the variable with the greatest impact throughout the precipitation event. However, the sensitivity of the factor of safety to the friction angle was slightly decreased as the precipitation event advanced. The effective cohesion was the second most important parameter overall, with exception of the last three to four days of the precipitation event. The impact of effective cohesion increased slightly with time.

Several input variables have an impact to the factor of safety that changes considerably with time. The primary SWCC slope and the unsaturated shear strength parameter, κ, appear to have a significant role in the beginning of the precipitation event. However, as time advanced, the sensitivity of the factor of safety to the primary SWCC slope and κ reduced, being considered minor past the 4th day and 8th day, respectively.

The sensitivity of the factor of safety to the air-entry value and to the saturated hydraulic conductivity increased with time. The impact of the hydraulic properties accumulates as the precipitation event advances. It appears that the longer the precipitation event, the higher the sensitivity of the factor of safety to the inherent uncertainty of the saturated hydraulic conductivity. However, the impact of the air-entry value reached a plateau on the 12nd day. The remaining input parameters appear to have relatively small or no influence on the factors of safety throughout the precipitation event.

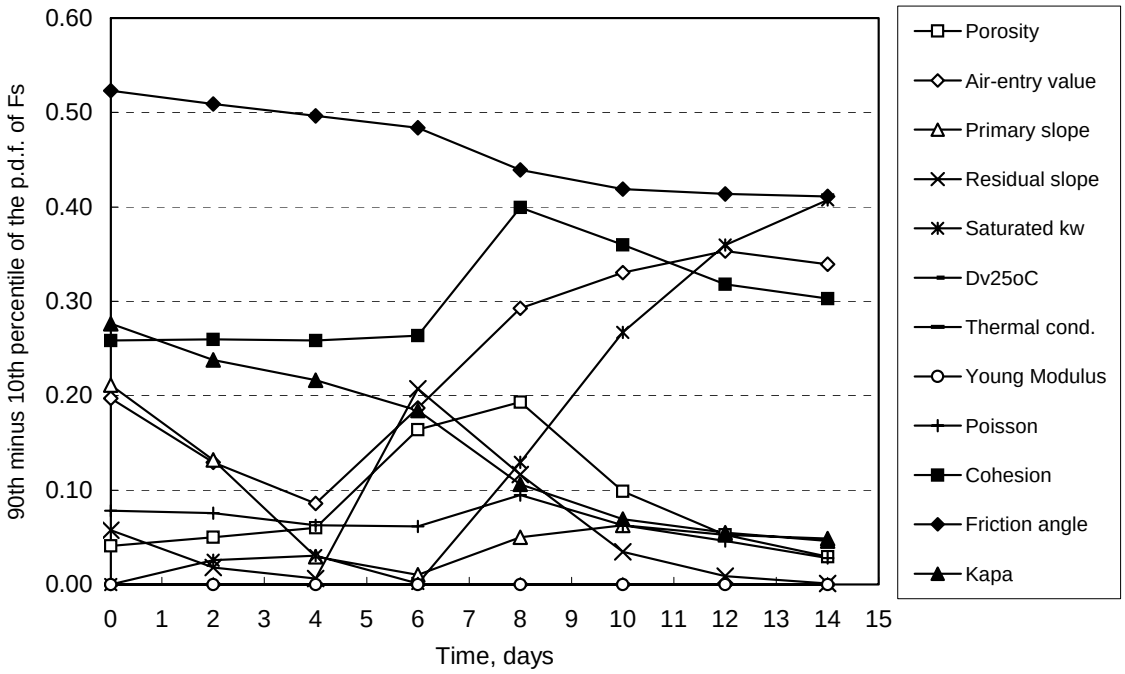

Figure 6.49 Transient sensitivity based on deterministic event tornado diagrams for the low, loam embankment. Initial conditions: $u_{w\,min}$ = -60 kPa.

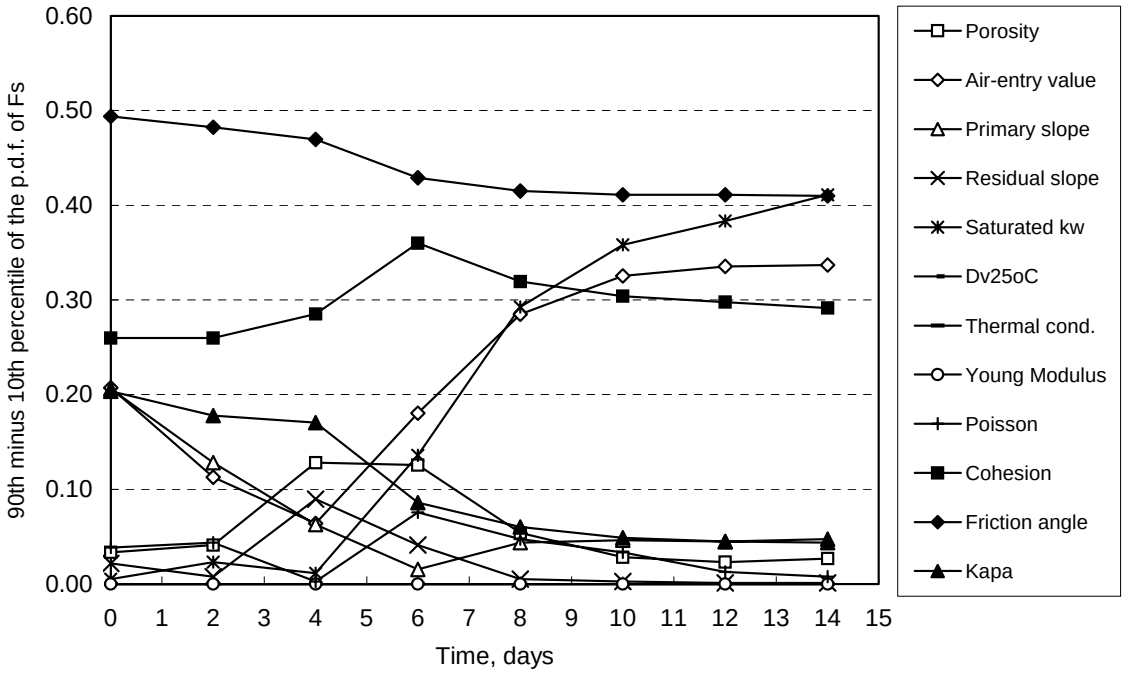

Figure 6.50 Transient sensitivity based on deterministic event tornado diagrams for the low, loam embankment. Initial conditions: $u_{w\,min}$ = -20 kPa.

Figures 6.51 and 6.52 present the transient sensitivity of the factor of safety to the input variables based on probabilistic event tornado diagrams. The results for both the initially wet and initially dry embankments are presented. The transient impact of the input parameters is summarised in terms of the probability of failure computed after removing the uncertainty of one input variable at a time. Figures 6.51 and 6.52 show that the friction angle and the unsaturated shear strength parameter, κ, have the highest impacts to the factor of safety at the beginning of the precipitation event. The sensitivity of the factor of safety to both variables decreased considerably as the precipitation event advanced. On the other hand, the uncertainty in the effective cohesion appeared to have a positive influence in the probability of failure. In other words, higher probabilities of failure were obtained when the effective cohesion uncertainty was removed.

The primary SWCC slope appears to have a significant role in the beginning of the precipitation event, up to the 10^{th} day. The significance of the primary SWCC slope appears to be greater than that shown by the deterministic sensitivity analyses. Figures 6.51 and 6.52 show that the sensitivity of the factor of safety to the primary SWCC slope reaches a peak near the 6^{th} day and the 4^{th} day for the "dry" and "wet" embankments, respectively. This peak appears to be associated with the period of time when the degree of saturation of the near surface soil is along the primary drainage curve and approaching the air-entry value.

The sensitivity of the factor of safety to the air-entry value and to the saturated hydraulic conductivity appear to change with time too. It can be seen that the influence of the saturated hydraulic conductivity accumulates as the precipitation event advanced. The longer the precipitation event the higher the sensitivity of the saturated hydraulic conductivity. On the other hand, the impact of the air-entry value appears not to vary considerably throughout the precipitation event. The remaining input parameters appear to have minor or no influence on the factors of safety throughout the precipitation event.

Based on the above observations, two distinct stages can be established, regarding the sensitivity of the factor of safety to the input parameters for the low, loam embankment. During the first stage, which extends up to approximately the 7^{th} day, the dominating parameters are (i) the friction angle, (ii) the unsaturated shear strength parameter κ, (iii) the primary SWCC slope, and (iv) the air-entry value. During the second stage, which starts at approximately the 7^{th} day, the input parameters with the greatest impacts are the (i) saturated hydraulic conductivity, (ii) the friction angle, and (iii) the air-entry value.

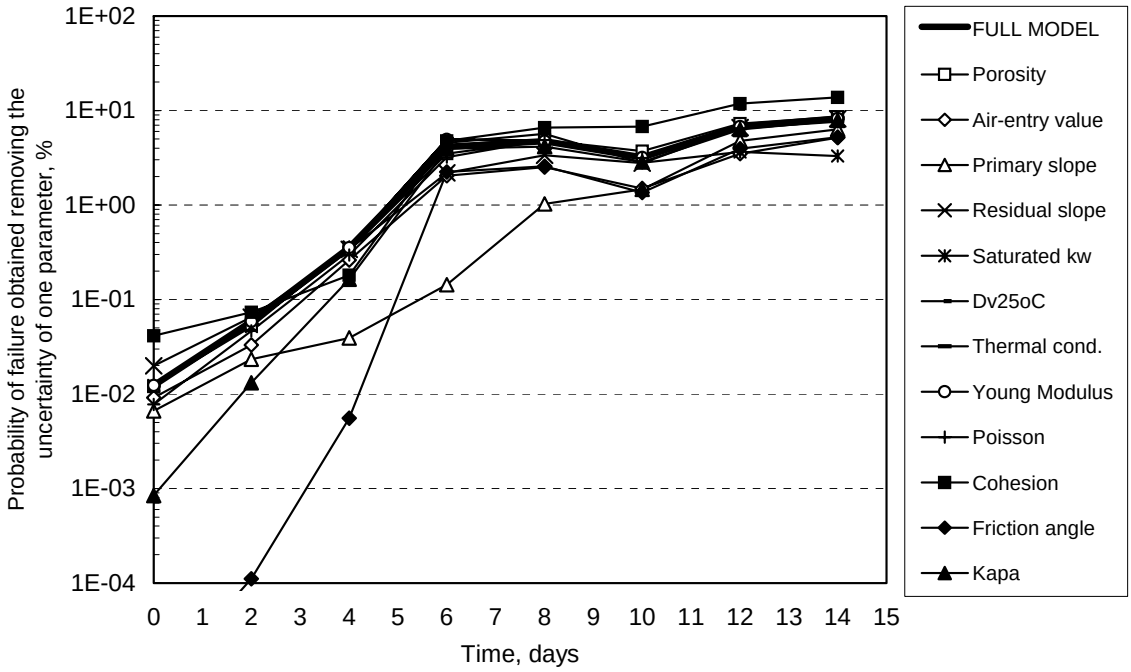

Figure 6.51 Transient sensitivity based on probabilistic event tornado diagrams for the low, loam embankment. Initial conditions: $u_{w\,min}$ = -60 kPa.

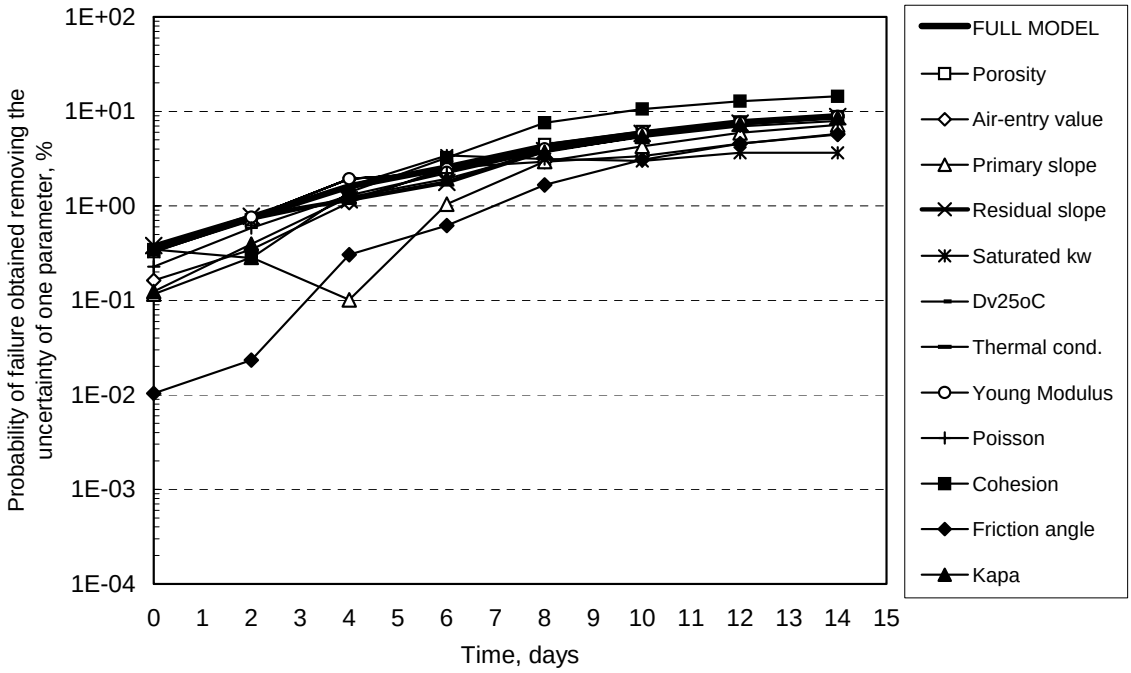

Figure 6.52 Transient sensitivity based on probabilistic event tornado diagrams for the low, loam embankment. Initial conditions: $u_{w\,min}$ = -20 kPa.

Low Clay embankments

Figure 6.53 presents the final pore-water pressure profiles (t = 14 days) for the mid-section of the low railway embankment considering two initial conditions (i.e., "dry" and "wet"). Similar to the loam embankment, the wetting fronts are considerably deeper for the "wet" initial conditions. Figure 6.53 presents also the profiles obtained using the estimate points for the saturated hydraulic conductivity and the air-entry value. The pore-water pressure profiles show that an increase in the air-entry value or an increase in the saturated hydraulic conductivity result in higher pore-water pressures at greater depths and results in a smooth or non-existent wetting front.

The high value of saturated hydraulic conductivity resulted also in higher pore-water pressures overall, but slightly negative pore-water pressures at the ground surface. The slightly negative values at the ground surface are due to the high percolation resulting from the higher hydraulic conductivity. The decrease in the air-entry value and the saturated hydraulic conductivity had opposite effects. A smaller air-entry value and smaller saturated hydraulic conductivity resulted in a sharper wetting front and lower pore-water pressures at greater depths.

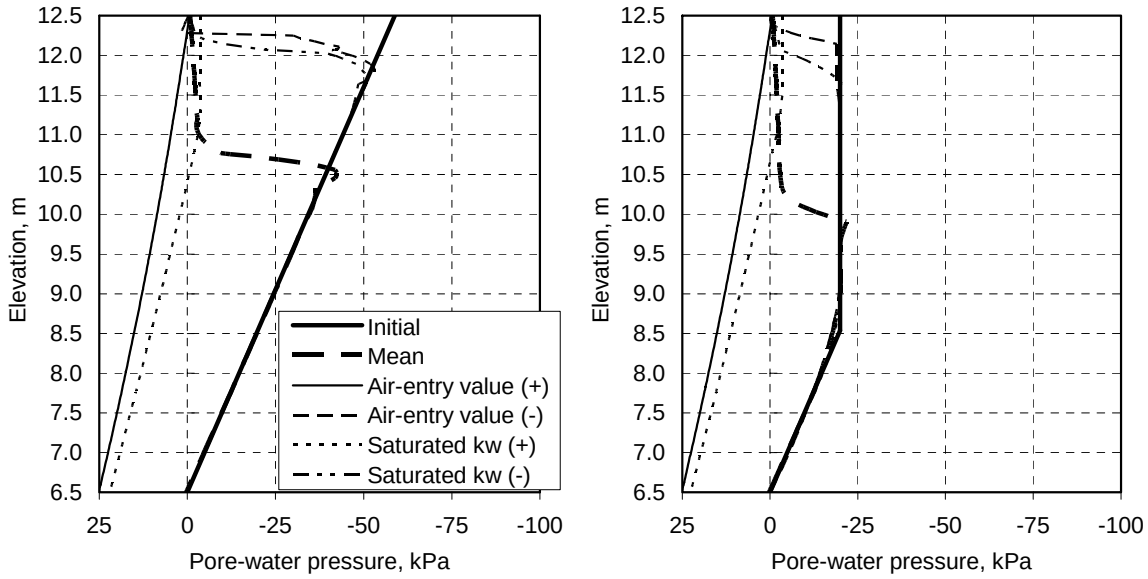

Figure 6.53 Pore-water pressure profile at the mid-section of the low, clay embankment. Initial conditions: (a) $u_{w\,min}$ = -60 kPa and (b) $u_{w\,min}$ = -20 kPa.

Figure 6.54 presents deterministic event tornado diagrams for the low, clay embankment, considering initially "dry" and initially "wet" conditions, for the final embankment condition (i.e., t = 14 days). Figure 6.54 shows that the air-entry value, the saturated hydraulic conductivity, and the effective cohesion have significant impacts to the factor of safety. The friction angle and soil porosity present intermediate impacts. The unsaturated shear strength parameter, κ, and Poisson's ratio have minor effects. The parameters associated with vapour flow, $D^{v}_{25^{o}C}$, heat flow, λ_s, and the Young modulus have no influence on the factor of safety, as expected. The high impact of the air-entry value and saturated hydraulic conductivity are consistent with the pore-water pressure changes shown in Fig. 6.53.

Figure 6.55 presents probabilistic event tornado diagrams for the low, clay embankments, considering initially "dry" and initially "wet" conditions, at t = 14 days. Figure 6.55 confirms that the air-entry value, the effective cohesion, and the saturated hydraulic conductivity have high inpacts. The sensitivity of the input parameters does not vary considerably when comparing the initially "dry" and "wet" conditions. The non-sensitive parameters are the same parameters identified by the deterministic event tornado diagrams. The unsaturated shear strength parameter, κ, and Poisson's ratio have minor effect and could be considered fixed parameters. Again, the parameters associated with vapour flow, $D^{v}_{25^{o}C}$, heat flow, and the Young modulus have no influence in the factor of safety.

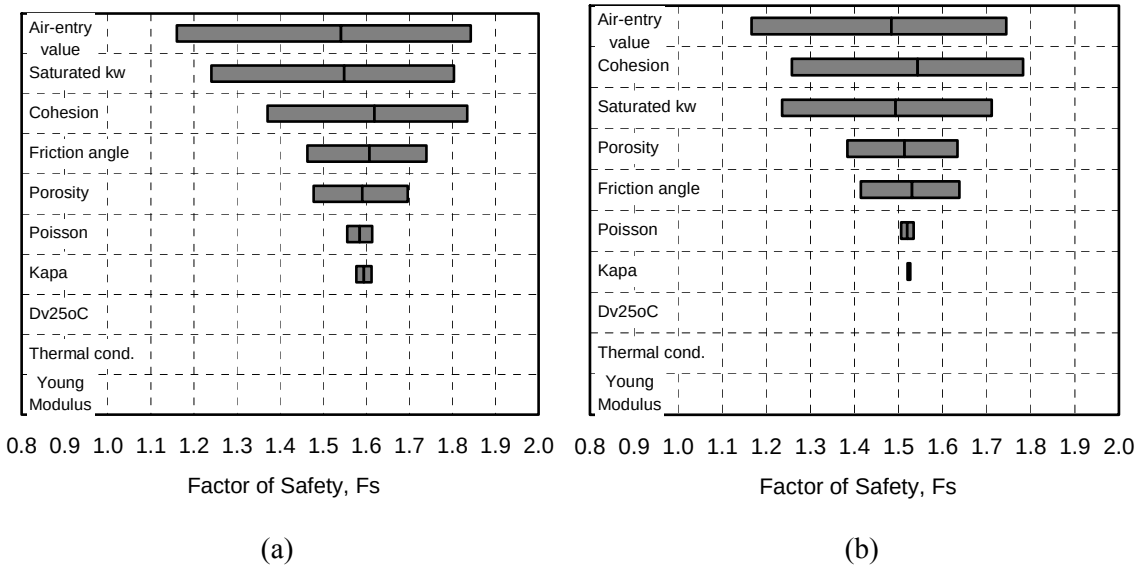

(a) (b)

Figure 6.54 Deterministic event tornado diagrams at t = 14 days for the low, clay embankment. Initial conditions: (a) $u_{w\,min}$ = -60 kPa; (b) $u_{w\,min}$ = -20 kPa.

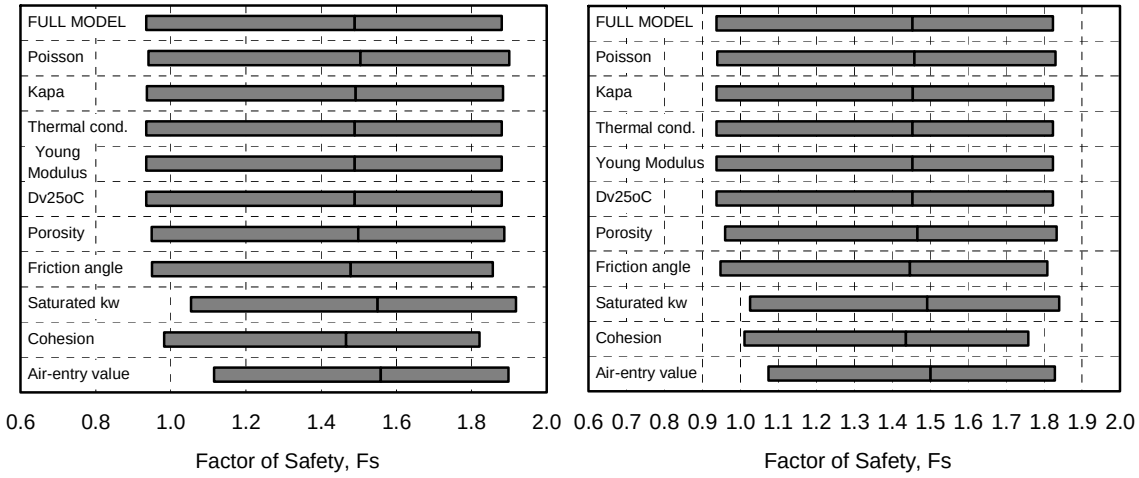

Figure 6.55 Probabilistic event tornado diagrams at t = 14 days for the low, clay embankment. Initial conditions: (a) $u_{w\,min}$ = -60 kPa; (b) $u_{w\,min}$ = -20 kPa.

Figures 6.56 and 6.57 present the transient sensitivity of the factor of safety to the input variables based on deterministic event tornado diagrams for the low, clay embankment. According to Figs. 6.56 and 6.57, the effective cohesion has the greatest impact to the factor of safety up to the fourth day. The saturated hydraulic conductivity became the most important parameter past the fourth day. The soil cohesion, friction angle, soil porosity, Poisson's ratio, and unsaturated shear strength parameter, κ, present roughly constant impacts throughout the precipitation event. However, the sensitivity of the factor of safety to κ slightly decreased as the precipitation event advanced.

The saturated hydraulic conductivity and the air-entry values have time-dependent impacts, as shown for the loam soils. The sensitivity of the factor of safety to the saturated hydraulic conductivity and the air-entry value increased with time. The influence of the hydraulic properties accumulates as the precipitation event advanced. It appears that the longer the precipitation event, the higher the impact of the saturated hydraulic conductivity, until a plateau was reached on the sixth day. This plateau appears to indicate that the pore-water pressure distribution has reached near steady state conditions past the fourth and sixth days. The relatively short time required for reaching steady state conditions is due to the low percolation rate.

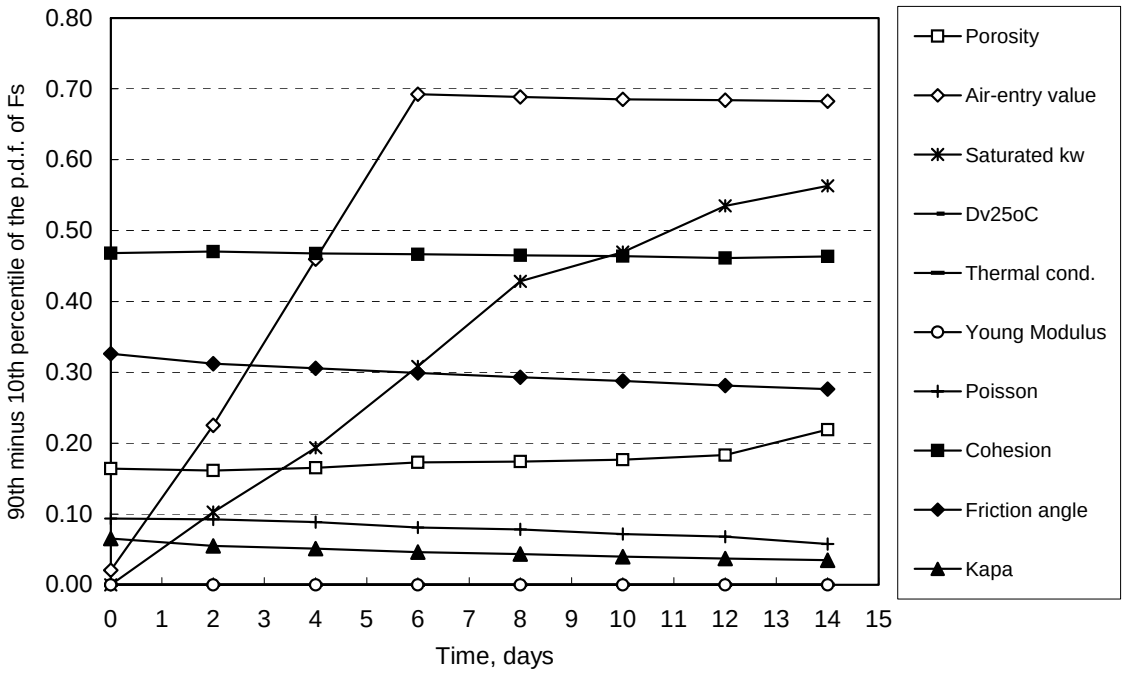

Figure 6.56 Transient sensitivity based on deterministic event tornado diagrams for the low, clay embankment. Initial conditions: $u_{w\,min}$ = -60 kPa.

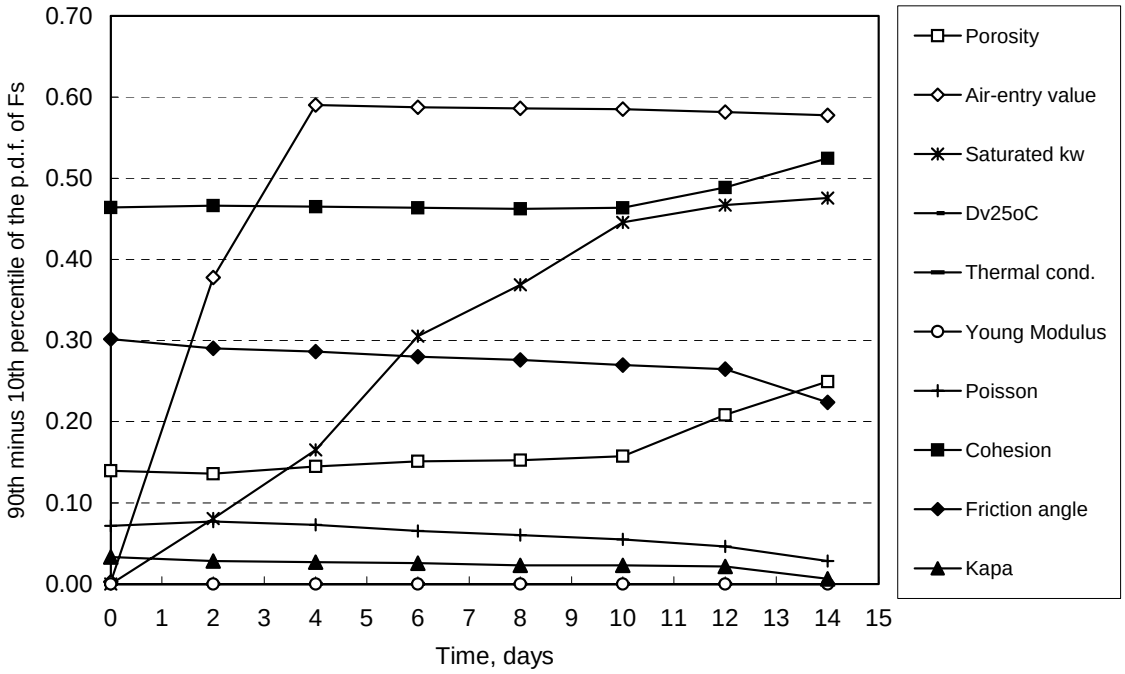

Figure 6.57 Transient sensitivity based on deterministic event tornado diagrams for the low, clay embankment. Initial conditions: $u_{w\,min}$ = -20 kPa.

Figures 6.58 and 6.59 present the transient sensitivity of the factor of safety to the input variables based on probabilistic event tornado diagrams. The results for both the initially wet and initially dry embankments are presented. Figures 6.58 and 6.59 show that the effective cohesion and the friction angle have the greatest impacts among all parameters at the beginning of the precipitation event. The sensitivity of both variables decreased considerably as the precipitation event advanced.

The unsaturated shear strength parameter, κ, has a negligible effect. The air-entry value has a significant role throughout the precipitation event. The relative significance of the air-entry value increases with time, confirming what has been shown by the deterministic sensitivity analyses. Figures 6.58 and 6.59 confirms that the sensitivity of the factor of safety to the saturated hydraulic conductivity is negligible in the beginning of the precipitation event and becomes increasingly important as time advances. Again, the parameters associated with vapour flow, $D^{v}_{25^{o}C}$, heat flow, λ_s, and the Young modulus have no influence on the factor of safety whatsoever, as expected.

Based on the above observations, two distinct stages can be established, regarding the sensitivity of the factor of safety to the input parameters for the low, clay embankment. During the first stage, which extends up to approximately the 5th day, the dominating parameters are (i) the effective cohesion and (ii) the friction angle. During the second stage, which starts at approximately the 5th day, the input parameters with the greatest impacts are the (i) the air-entry value, (ii) the saturated hydraulic conductivity, and (ii) the effective cohesion. The friction angle and the soil porosity have intermediate and constant impacts throughout the precipitation event.

6.6.1.2 *High embankments*

This section presents the sensitivity analyses for the high, loam and clay embankments. The factors of safety computed for the case scenarios described in Tables 6.4 and 6.5 were utilised for the construction of deterministic and probabilistic event tornado diagrams. Similar to what was done for the low embankments, additional plots derived from the tornado diagrams are presented herein in order to show the evolution of the sensitivity of the input parameters during the precipitation event.

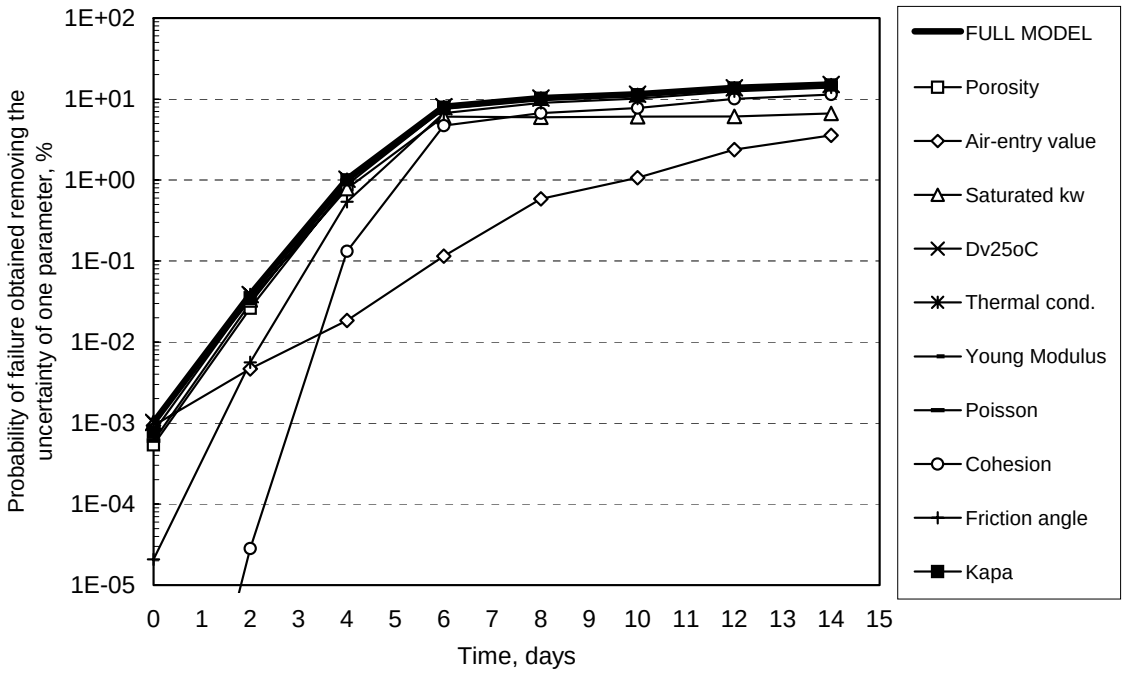

Figure 6.58 Transient sensitivity based on probabilistic event tornado diagrams for the low, clay embankment. Initial conditions: $u_{w\,min}$ = -60 kPa.

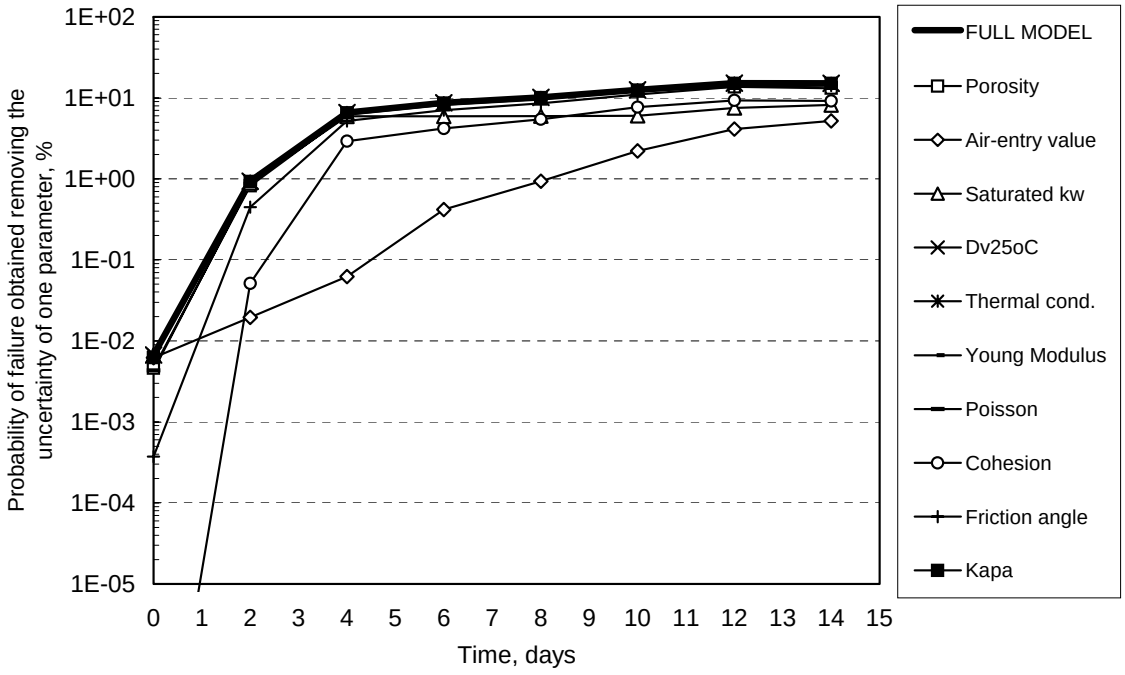

Figure 6.59 Transient sensitivity based on probabilistic event tornado diagrams for the low, clay embankment. Initial conditions: $u_{w\,min}$ = -20 kPa.

High Loam embankments

Figure 6.60 presents the final pore-water pressure profiles (t = 14 days) for the mid-section of the high railway embankment considering the two initial conditions (i.e., "dry" and "wet"). The wetting fronts are considerably deeper for the "wet" embankment, as expected. The wetting front for the "dry" embankment was approximately 2.5 m deep. On the other hand, the wetting front for the "wet" embankment was smoother, and approximately 5.0 m deep. The pore-water pressure at the ground surface is slightly negative in both cases. The relatively high hydraulic conductivity of the loam soil and the availability of water storage within the embankment resulted in the negative pore-water pressure at the ground surface, as discussed previously.

Figure 6.60 presents also the profiles for varying saturated hydraulic conductivity and the air-entry value. The increase in the air-entry value resulted in higher pore-water pressures at greater depths, smoother wetting fronts, and higher suction at the surface. The smaller air-entry value resulted in a sharper and shallower wetting front. The sharper wetting front resulted in somewhat longer computation times, associated with the more refined spatial discretisation required. The effects of changes in the saturated hydraulic conductivity are also shown in Fig. 6.60. The increase in the saturated hydraulic conductivity resulted in a deeper wetting front. The decrease in the saturated hydraulic conductivity had the opposite effect.

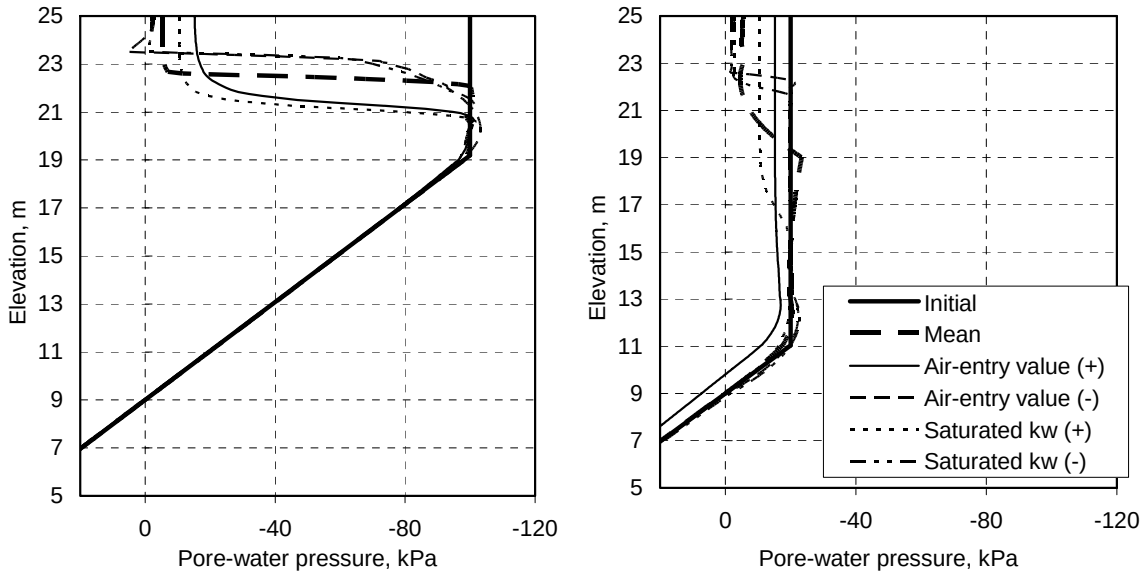

(a) (b)

Figure 6.60 Pore-water pressure profile at the mid-section of the high, loam embankment. Initial conditions: (a) $u_{w\,min}$ = -100 kPa and (b) $u_{w\,min}$ = -20 kPa.

Figure 6.61 presents deterministic event tornado diagrams for the loam embankment at t = 14 days, considering the "dry" and "wet" conditions. Figure 6.61 shows that the factor of safety is highly sensitive to the friction angle, air-entry value, and effective cohesion. The saturated hydraulic conductivity presented a low impact for the "dry" embankment and an intermediate impact for the "wet" embankment. The porosity, the primary SWCC slope, the residual SWCC slope, the unsaturated shear strength parameter, κ, and Poisson's ratio presented intermediate to minor effects and appear to be adequately modeled if considered as certain, fixed parameters. The parameters associated with vapour flow, $D^{v}_{25^{o}C}$, and heat flow, λ_s, had no influence whatsoever on the factor of safety, as expected. The case scenarios for E produced identical factors of safety, once again confirming the observations by Scoular (1997).

Figure 6.62 presents probabilistic event tornado diagrams for the loam embankments at t = 14 days. The results presented in Fig. 6.62 are not in complete agreement with the deterministic tornado diagrams presented in Fig. 6.61. Figure 6.62 confirms that the friction angle and the air-entry value high impact on the factor of safety. However, Fig. 6.62 shows that cohesion has a relatively minor effect and that the primary SWCC slope may have a significant role. The relative sensitivity of the input parameters does vary considerably when comparing the initially "dry" and "wet" conditions. The parameters with low impacts are those same parameters identified by the deterministic event tornado diagrams; namely, the unsaturated shear strength parameter, κ, soil porosity, Poisson's ratio, and the residual SWCC. The parameters controlling vapour flow, $D^{v}_{25^{o}C}$, heat flow, λ_s, and the Young modulus are non-sensitive.

Figures 6.63 and 6.64 present the transient sensitivity of the input variables based on deterministic event tornado diagrams. According to Figs. 6.63 and 6.64, the friction angle was the parameter with the highest impact on the factor of safety throughout the precipitation event. The impact of the friction angle was slightly decreased as the precipitation event advanced, but remained the highest. The unsaturated shear strength parameter, κ, was the second most important parameter overall. However, the importance of κ was considerably lower for the "wet" embankment, in comparison with the "dry" embankment. The high impact of the friction angle is associated with the relatively larger size of the embankment and the relatively high confining stresses. The significance of κ can be explained by the relatively high friction angle. The effective cohesion had an intermediate impact on the factor of safety. This result indicates that the shear strength of the high loam embankment originates primarily from frictional forces.

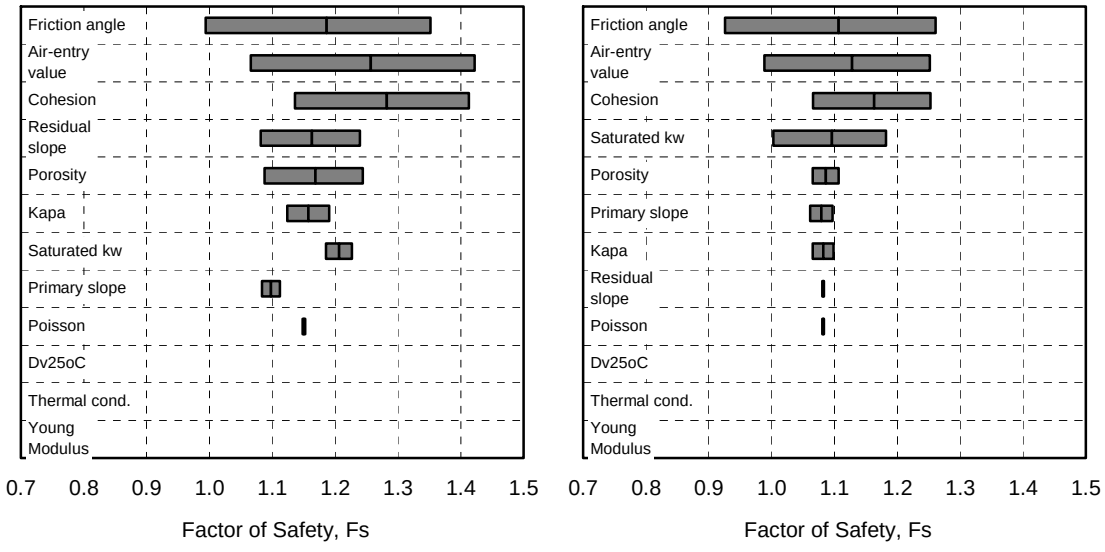

(a) (b)

Figure 6.61 Deterministic event tornado diagrams at t = 14 days for the high, loam embankment. Initial conditions: (a) $u_{w\,min}$ = -100 kPa; (b) $u_{w\,min}$ = -20 kPa.

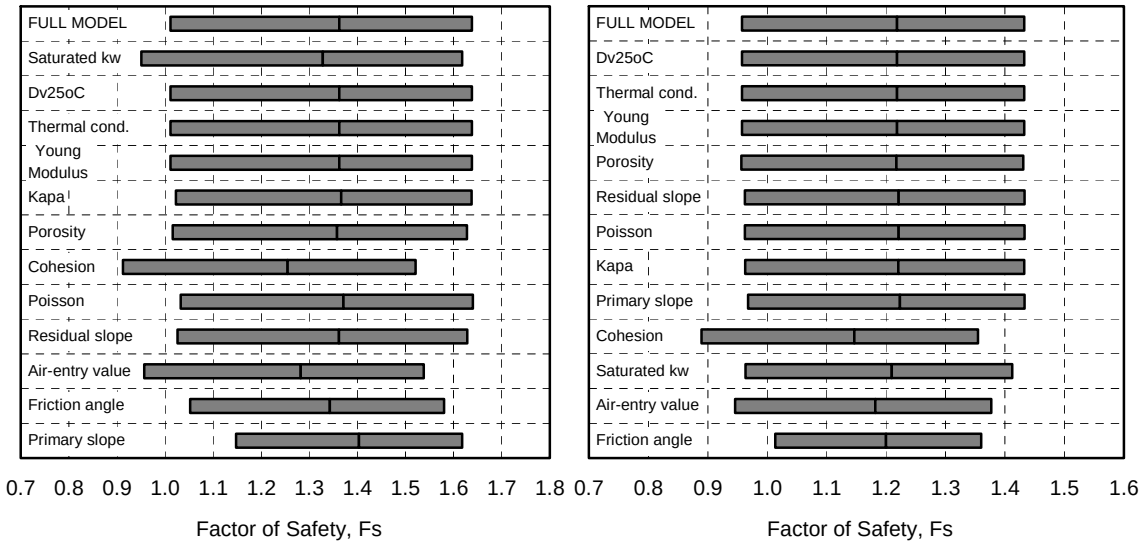

(a) (b)

Figure 6.62 Probabilistic event tornado diagrams at t = 14 days for the high, loam embankment. Initial conditions: (a) $u_{w\,min}$ = -100 kPa; (b) $u_{w\,min}$ = -20 kPa.

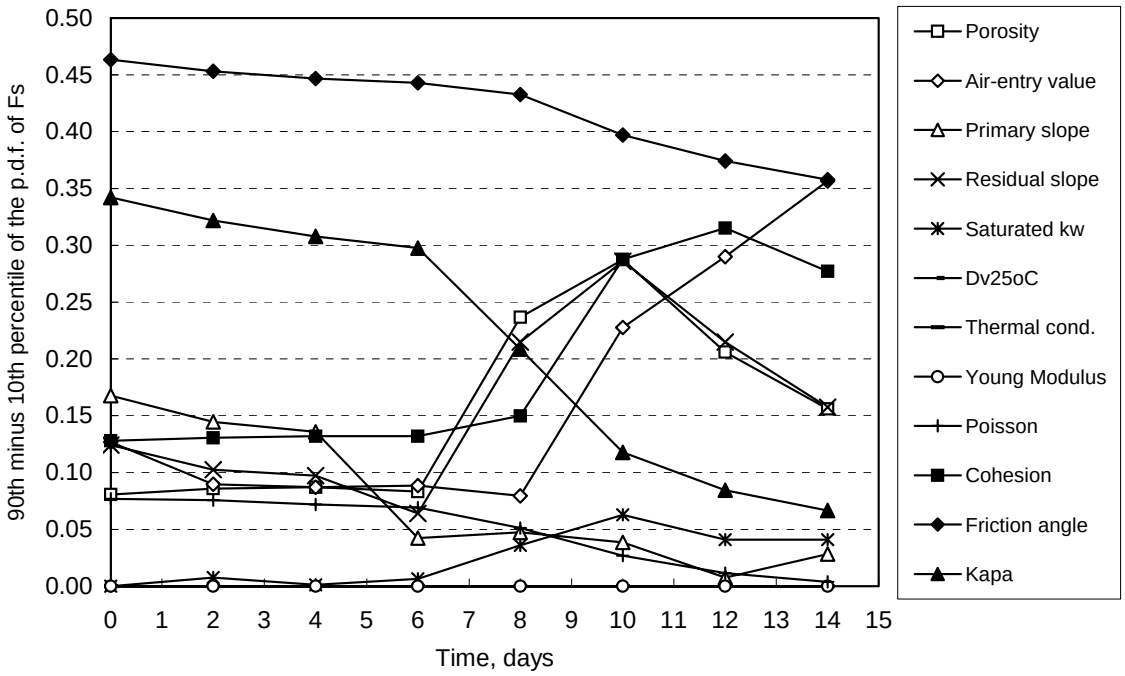

Figure 6.63 Transient sensitivity based on deterministic event tornado diagrams for the high, loam embankment. Initial conditions: $u_{w\,min}$ = -100 kPa.

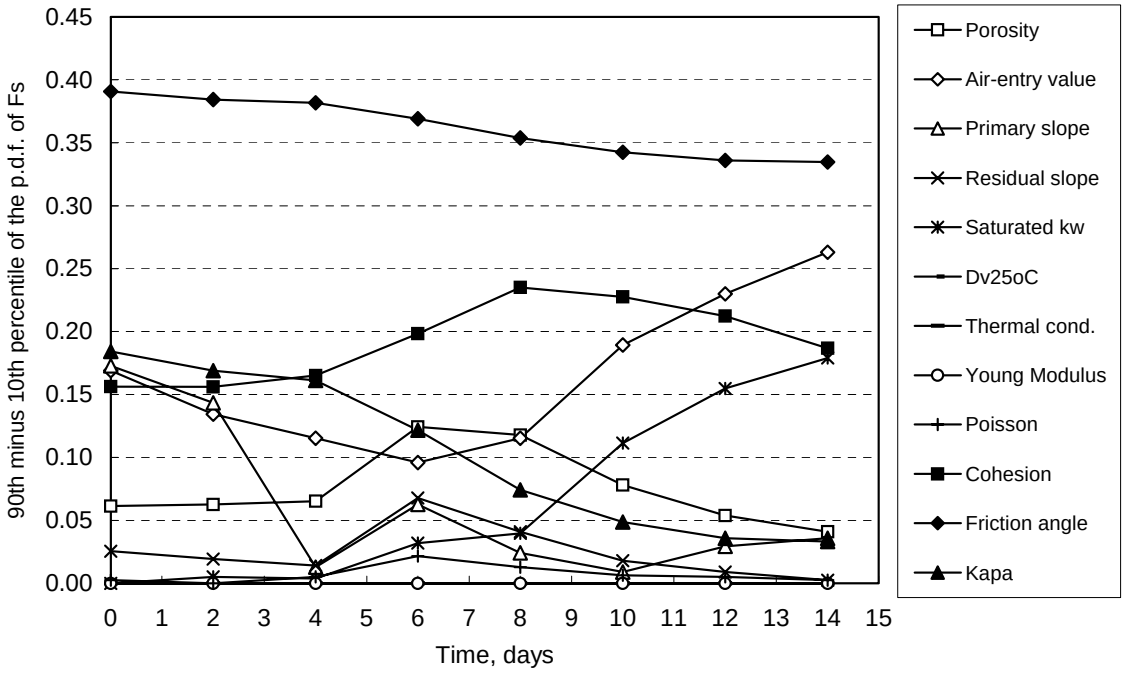

Figure 6.64 Transient sensitivity based on deterministic event tornado diagrams for the high, loam embankment. Initial conditions: $u_{w\,min}$ = -20 kPa.

Several input variables have time-dependent impacts, as observed for the previous embankment configurations. The sensitivity of the factor of safety to the air-entry value and to the saturated hydraulic conductivity increased with time. The impact of the air-entry value is intermediate to low during the beginning of the precipitation event and becomes high by the end of the 14th day. The saturated hydraulic conductivity has a small, but increasing impact. The time-dependent sensitivity of the factor of safety is a product of the accumulation of the influence of the hydraulic properties as the precipitation event advanced. The longer the precipitation event the higher the impact of the air-entry value and the higher the impact of the saturated hydraulic conductivity. Soil porosity presented an intermediate to low impact. The remaining input parameters shown in Figs. 6.63 and 6.64 appear to have relatively small or no influence on the factors of safety throughout the precipitation event.

Figures 6.65 and 6.66 present the transient sensitivity of the factor of safety to the input variables based on probabilistic event tornado diagrams. Figures 6.65 and 6.66 confirm that the friction angle and the unsaturated shear strength parameter, κ, are the greatest impacts at the beginning of the precipitation event. The removal of the uncertainty of either the friction angle or κ results in a decrease in the probability of failure by more than one order of magnitude. However, the sensitivity of the factor of safety to the friction angle and κ decreased considerably as the precipitation event advanced. The uncertainty in the effective cohesion appeared to have a positive influence in the probability of failure. In other words, higher probabilities of failure were obtained when the effective cohesion uncertainty was removed.

The significance of the primary SWCC slope shown by the probabilistic sensitivity analyses was greater than that shown by the deterministic sensitivity analyses. Figures 6.65 and 6.66 show that the impact of the primary SWCC slope increases steadily with time for the "dry" embankment and reaches a peak near the 6th day for the "wet" embankment. In fact, the primary SWCC slope is the most important parameter at the end of the precipitation event for the "dry" embankment. The probability of failure of the "dry" embankment on the 14th day decreases by one order of magnitude when the uncertainty of the primary SWCC slope is removed. Case scenarios for the SWCC parameters affect several other predicted properties, such as the hydraulic conductivity function and the unsaturated shear strength. Therefore, it is difficult to isolate the most important factor associated with the high sensitivity of the primary SWCC slope. The sensitivity of all the remaining variables is low or negligible.

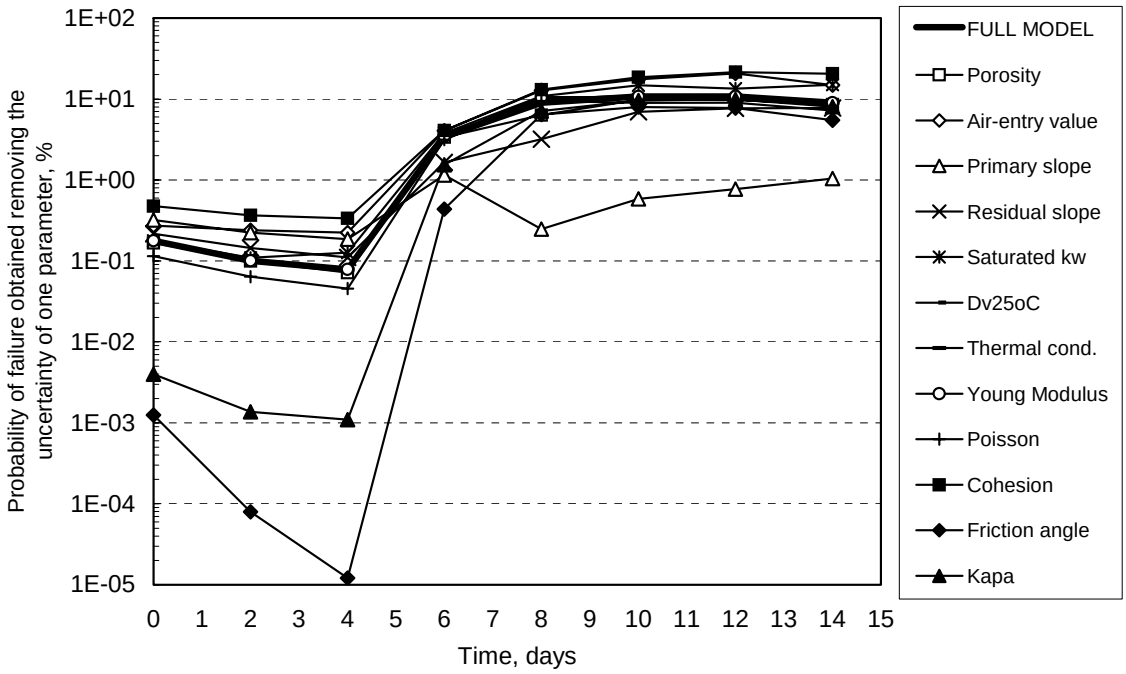

Figure 6.65 Transient sensitivity based on probabilistic event tornado diagrams for the high, loam embankment. Initial conditions: $u_{w\,min}$ = -100 kPa.

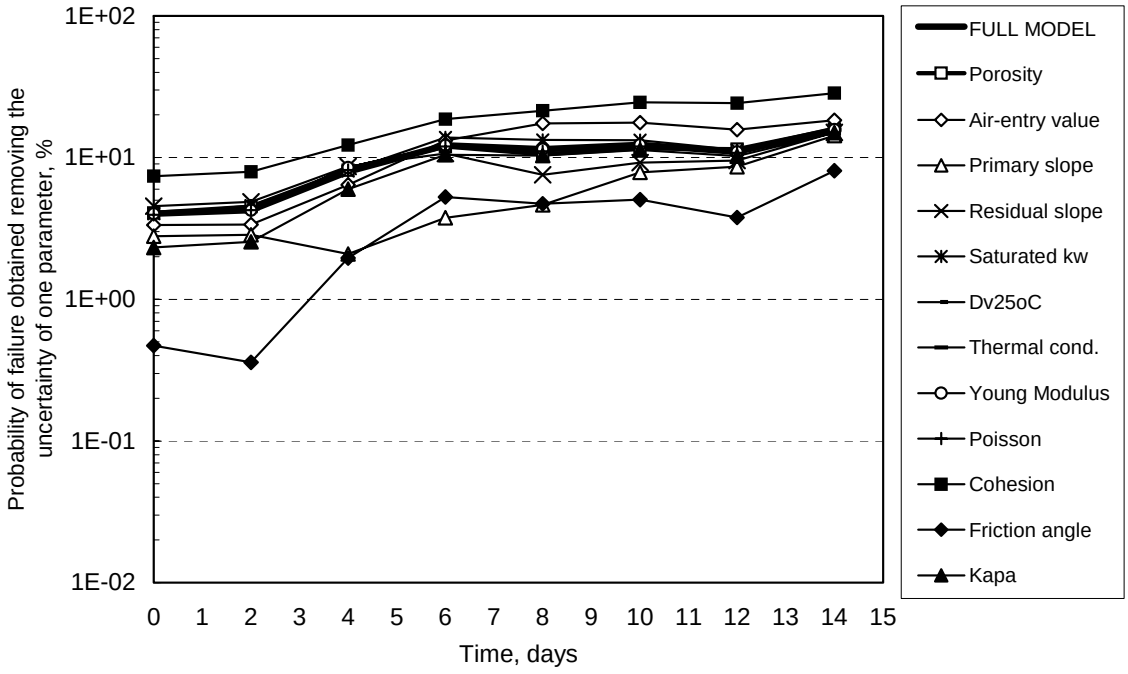

Figure 6.66 Transient sensitivity based on probabilistic event tornado diagrams for the high, loam embankment. Initial conditions: $u_{w\,min}$ = -20 kPa.

Based on the above observations, two distinct stages can be established, regarding the sensitivity of the input parameters for the high, loam embankment. During the first stage, which extends up to approximately the 6th day, the most important parameters are (i) the friction angle and (ii) the unsaturated shear strength parameter κ. During the second stage, which starts on the 7th day, the input parameters with the greatest impacts are the (i) primary SWCC slope and (ii) the friction angle.

High Clay embankments

Figure 6.67 presents the final pore-water pressure profiles (t = 14 days) for the mid-section of the high clay railway embankment considering the two initial conditions (i.e., "dry" and "wet"). The wetting fronts are considerably deeper for the "wet" embankment, as observed previously. The wetting front for the "dry" embankment was approximately 1.5 m deep. The wetting front for the "wet" embankment was approximately 2.5 m deep. The ground surface is completely saturated and has a pore-water pressure equal to 0 on both cases. The relatively low hydraulic conductivity of the clay soil and the low water storage available within the embankment resulted in the completely saturated conditions at the ground surface.

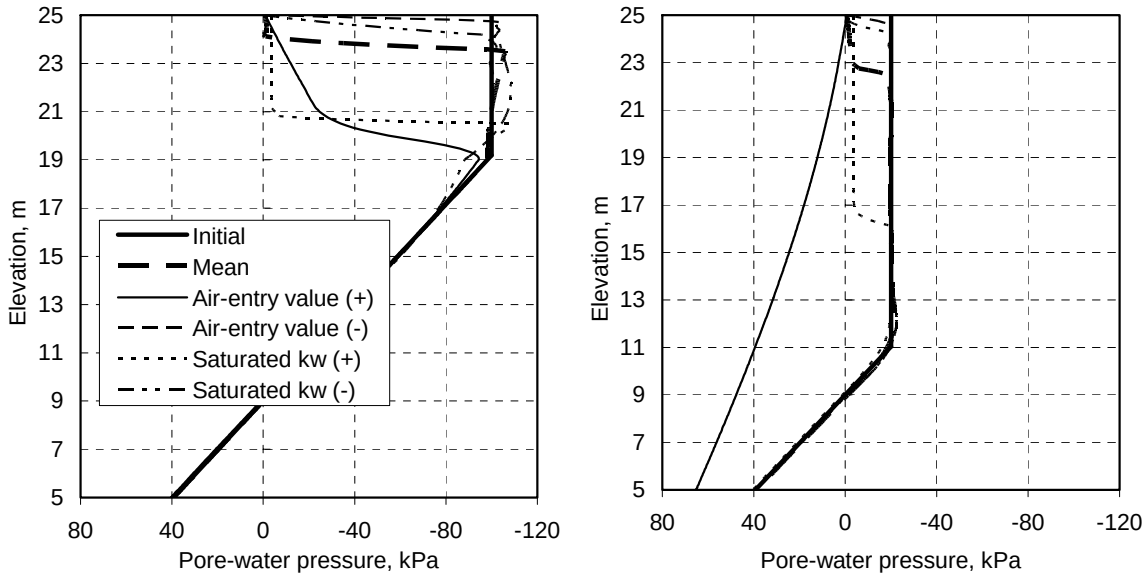

Figure 6.67 Pore-water pressure profile at the mid-section of the high, clay embankment. Initial conditions: (a) $u_{w\,min}$ = -100 kPa and (b) $u_{w\,min}$ = -20 kPa.

Figure 6.67 shows that the increase in the air-entry value resulted in higher pore-water pressures at greater depths and resulted in a smoother or non-existent wetting front. The decrease in the air-entry value had the opposite effect. The smaller air-entry value resulted in a sharper and shallower wetting front. The effects of changes in the saturated hydraulic conductivity are also shown in Fig. 6.67. The increase in the saturated hydraulic conductivity resulted in a deeper wetting front. The decrease in the saturated hydraulic conductivity had the opposite effect.

Figure 6.68 presents deterministic event tornado diagrams for the clay embankment at t = 14 days, considering the "dry" and "wet" conditions. Figure 6.68 suggests that the air-entry value, saturated hydraulic conductivity, friction angle, and effective cohesion have high impact on the factor of safety. Poisson's ratio, porosity, the unsaturated shear strength parameter, κ, presented intermediate to minor effects and appear to be adequately modeled if considered as fixed parameters. Once again, the parameters associated with vapour flow, $D^{v}_{25^{o}C}$, heat flow, λ_s, and the Young modulus had no influence on the factor of safety, as expected.

Figure 6.69 presents probabilistic event tornado diagrams for the loam embankments at t = 14 days. Figure 6.69 confirms that the friction angle and the effective cohesion have high impacts. Figure 6.69 shows also that the factor of safety is highly sensitive to the air-entry value and the saturated hydraulic conductivity. However, the effect of the air-entry value and the saturated hydraulic conductivity is masked by the skewed effect on the factor of safety, which produced a considerably higher mean factor of safety. The high impact of the air-entry value and the saturated hydraulic conductivity is shown by the higher 10^{th} percentiles. This observation contradicts the general rule that says that wider bars indicate lower sensitivity. Probabilistic event tornado diagrams must be interpreted with care when skewed effect takes place.

The relative sensitivity of the factor of safety to the inherent uncertainty of the input parameters did not vary considerably when comparing the initially "dry" and "wet" conditions. The air-entry value and the saturated hydraulic conductivity remained important parameters for both cases. The non-sensitive parameters are the same parameters identified by the deterministic event tornado diagrams; namely, Poisson's ratio, porosity, and the unsaturated shear strength parameter, κ. The parameters controlling vapour flow, $D^{v}_{25^{o}C}$, heat flow, λ_s, and the Young modulus have negligible effect on the factor of safety.

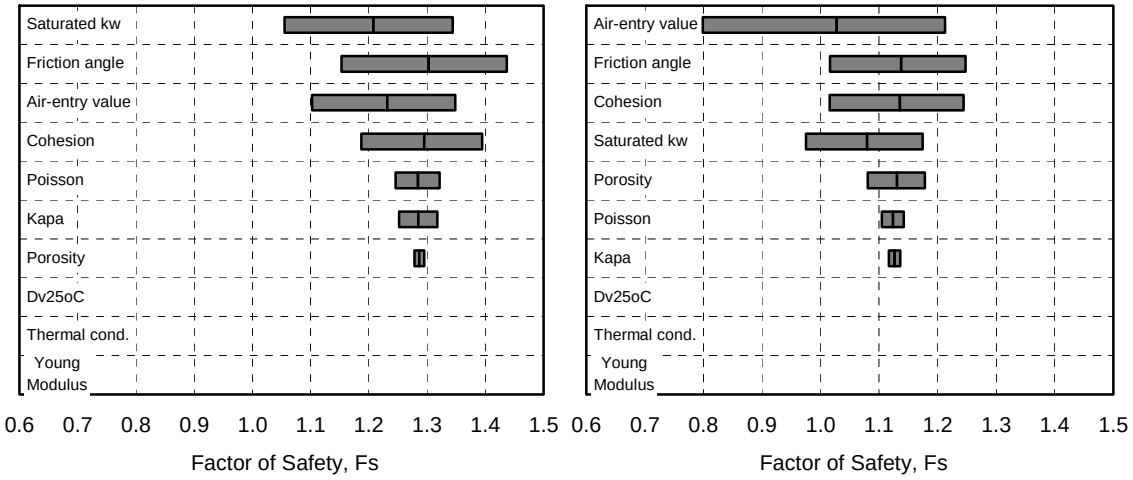

Figure 6.68 Deterministic event tornado diagrams at t = 14 days for the high, clay embankment. Initial conditions: (a) $u_{w\,min}$ = -100 kPa; (b) $u_{w\,min}$ = -20 kPa.

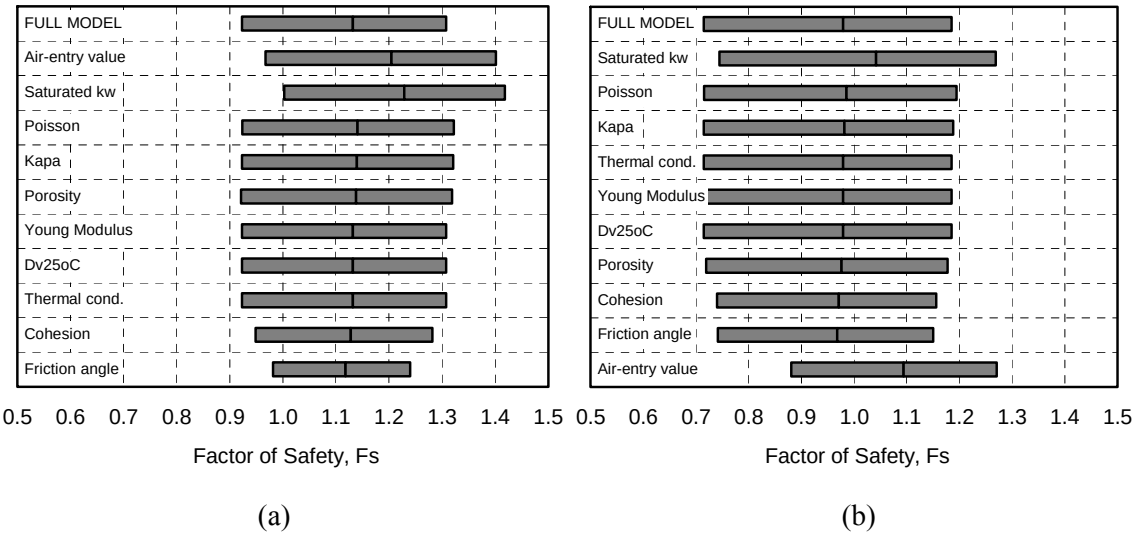

Figure 6.69 Probabilistic event tornado diagrams at t = 14 days for the high, clay embankment. Initial conditions: (a) $u_{w\,min}$ = -100 kPa; (b) $u_{w\,min}$ = -20 kPa.

Figures 6.70 and 6.71 present the transient sensitivity of the factor of safety to the input variables based on deterministic event tornado diagrams. According to Figs. 6.70 and 6.71, the friction angle was the variable with the highest impact throughout the precipitation event. However, the impact of the friction angle decreased considerably for the "wet" embankment, due to the considerable decrease in the effective confining stresses. Poisson's ratio, unsaturated shear

strength parameter, κ, and porosity presented intermediate to low impacts.

All properties have constant impacts throughout the precipitation event, with exception of the air-entry value and the saturated hydraulic conductivity. The sensitivity of the factor of safety to the air-entry value and the saturated hydraulic conductivity increased with time, as observed in the previous embankment configurations. The air-entry value and the saturated hydraulic conductivity have a small but increasing impact during the first 6 days. The sensitivity of factor of safety to both variables increased sharply past the 10^{th} day. In other words, the longer the precipitation event the higher the importance of the air-entry value and the higher the importance of the saturated hydraulic conductivity. The sensitivity of the factor of safety to the air-entry value was particularly high on the 14^{th} day. An increase in the air-entry value may result in near completely saturated initial conditions, explaining the high impact. The remaining input parameters shown in Figs. 6.70 and 6.71 appear to have relatively small or no influence on the factors of safety throughout the precipitation event.

Figures 6.72 and 6.73 present the transient sensitivity of the factor of safety to the input variables based on probabilistic event tornado diagrams. Figures 6.72 and 6.73 confirm that the friction angle and the effective cohesion are the most important variables, particularly at the beginning of the precipitation event. The removal of the uncertainty of either the friction angle or the effective cohesion results in a decrease in the initial probability of failure by one or two orders of magnitude. Figures 6.72 and 6.73 confirm also that the air-entry value and the saturated hydraulic conductivity have time-dependent impacts. However, the significance of the sensitivity of the air-entry value and the saturated hydraulic conductivity becomes irrelevant due to the high probabilities of failure on the 14^{th} day.

Based on the above observations, two distinct stages can be established, regarding the sensitivity of the factor of safety to the input parameters for the high, clay embankment. During the first stage, which extends up to approximately the 6^{th} day, the dominating parameters are (i) the friction angle and (ii) the effective cohesion. During the second stage, which starts at approximately the 7^{th} day, the most important input parameters are the (i) air-entry value and (ii) the saturated hydraulic conductivity.

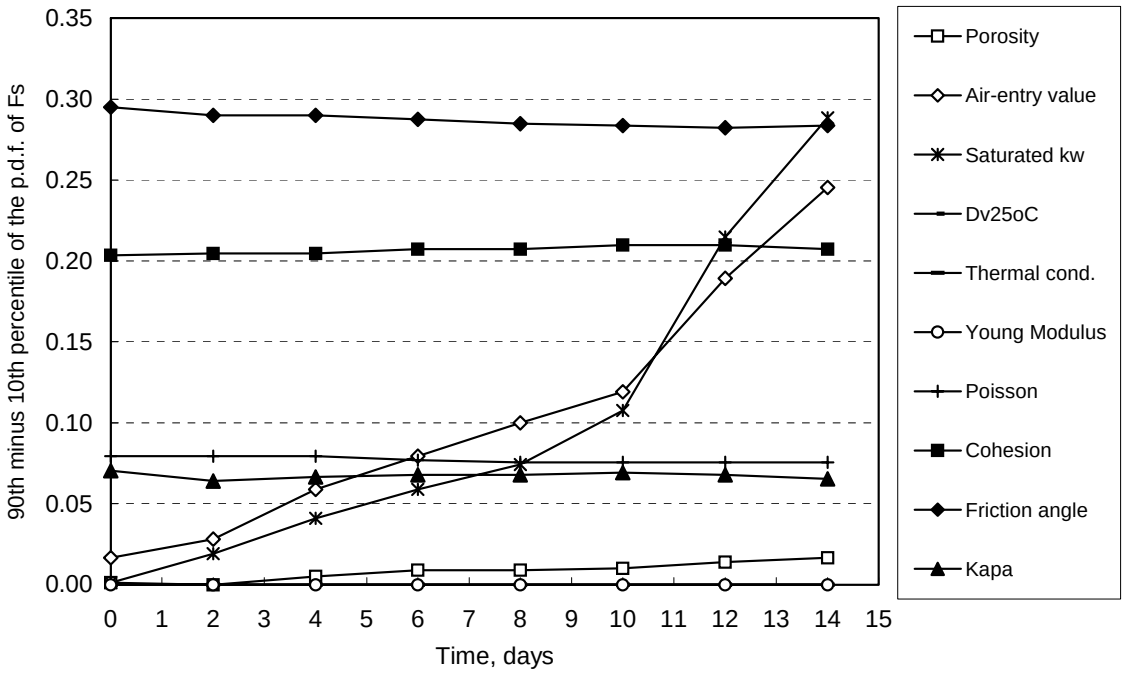

Figure 6.70 Transient sensitivity based on deterministic event tornado diagrams for the high, clay embankment. Initial conditions: $u_{w\,min}$ = -100 kPa.

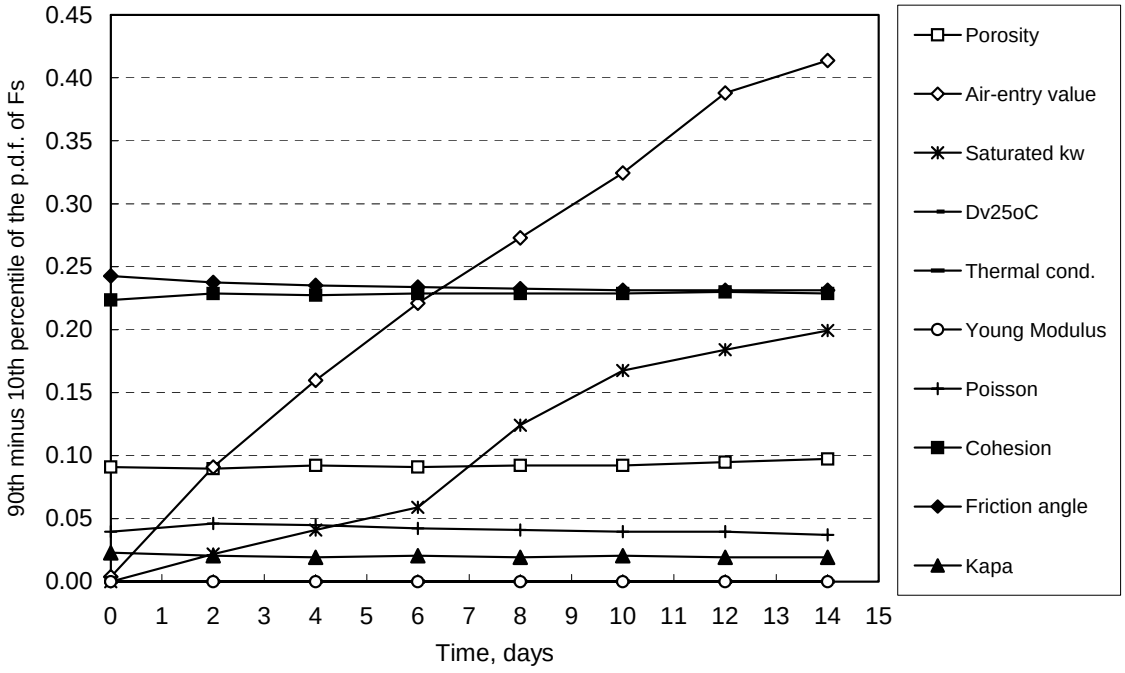

Figure 6.71 Transient sensitivity based on deterministic event tornado diagrams for the high, clay embankment. Initial conditions: $u_{w\,min}$ = -20 kPa.

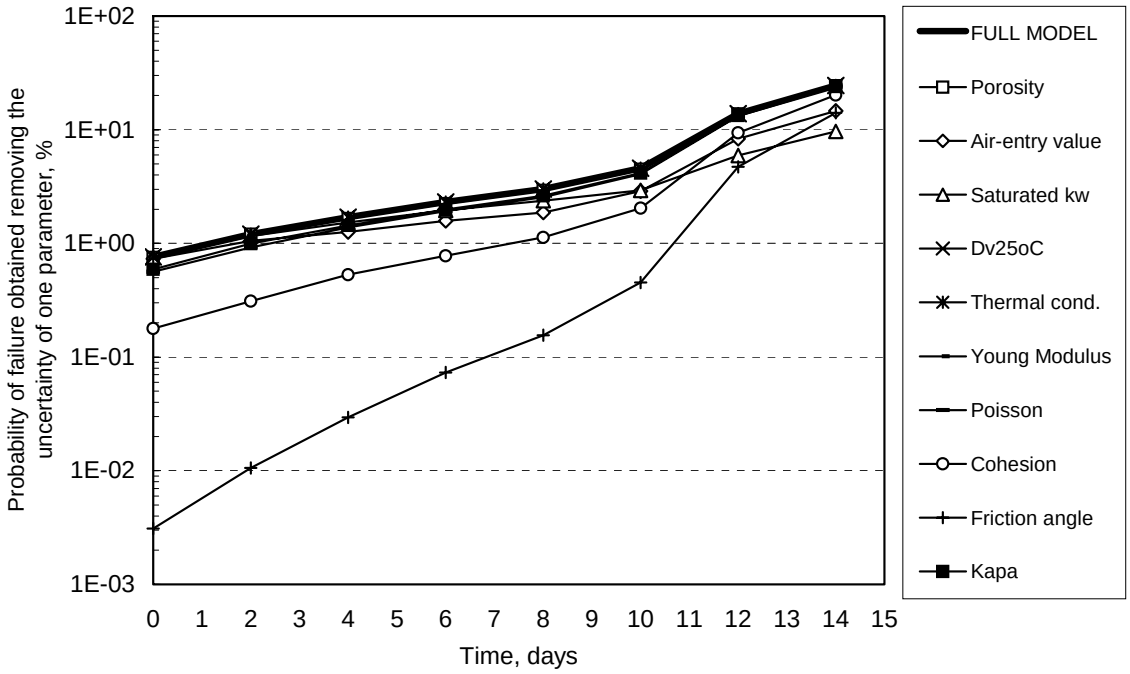

Figure 6.72 Transient sensitivity based on probabilistic event tornado diagrams for the high, clay embankment. Initial conditions: $u_{w\,min}$ = -100 kPa.

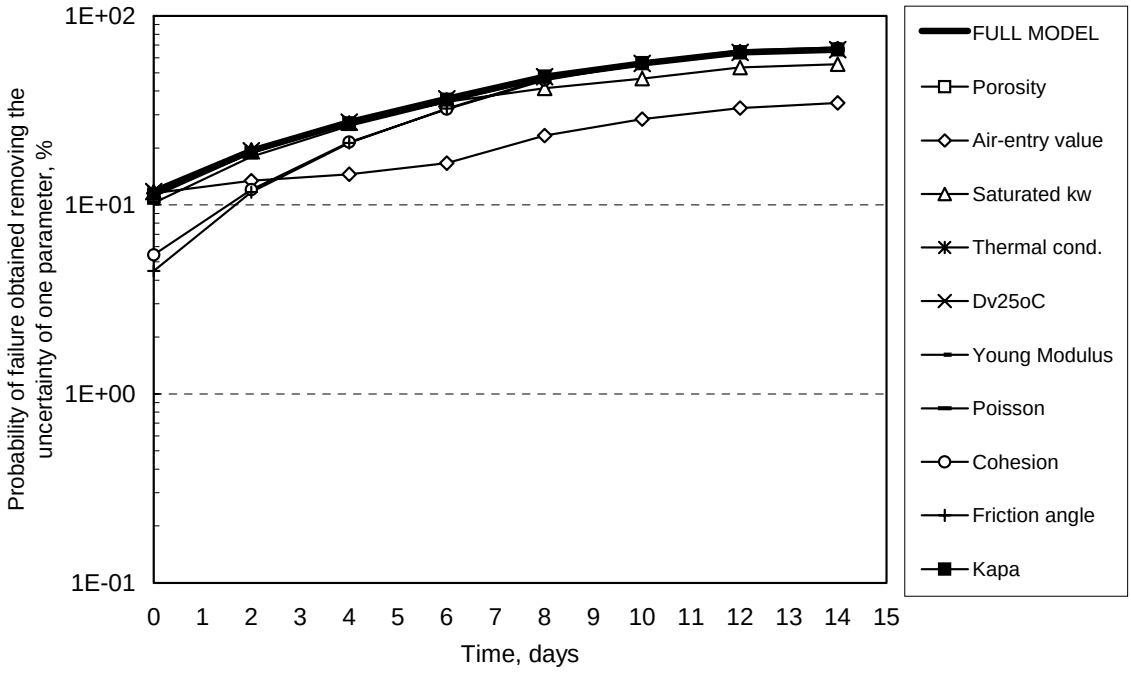

Figure 6.73 Transient sensitivity based on probabilistic event tornado diagrams for the high, clay embankment. Initial conditions: $u_{w\,min}$ = -20 kPa.

6.6.2 *Analysis of evaporation conditions*

This section presents the sensitivity analyses for the evaporation event, considering the loam and clay embankments. The factors of safety computed for the case scenarios described in Tables 6.4 and 6.5 were utilised for the construction of deterministic and probabilistic event tornado diagrams. Figure 6.74 presents deterministic event tornado diagrams for the loam and clay embankments at t = 42 days. Figure 6.74 shows that the effective cohesion, the air-entry value, and the friction angle have high impacts on the factor of safety. Porosity, vapour diffusivity, and the unsaturated shear strength parameter, κ, appear to have intermediate impacts for both embankment configurations. The remaining soil properties presented relatively minor effects and appear to be adequately modeled if considered as certain, fixed parameters.

Figure 6.75 presents probabilistic event tornado diagrams for the evaporation event at t = 42 days. The results presented in Fig. 6.75 are not in complete agreement with the deterministic tornado diagrams presented in Fig. 6.74. Figure 6.75 confirms that the factor of safety is highly sensitive to the air-entry value. Different from Fig. 6.74, Fig. 6.75 shows that vapour diffusivity has an important effect on the factors of safety during the evaporation event. Figure 6.75 confirms that hydraulic conductivity, thermal conductivity, Young modulus, and Poisson's ratio presented relatively low impacts on the factor of safety.

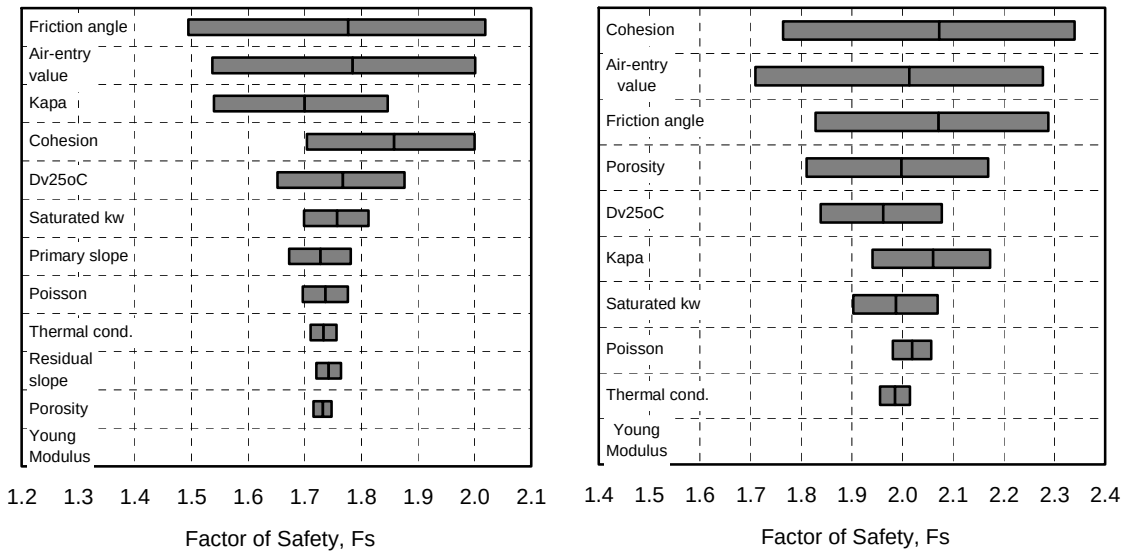

(a) (b)

Figure 6.74 Deterministic event tornado diagrams at t = 42 days. Soil types: (a) loam soil; (b) clay soil.

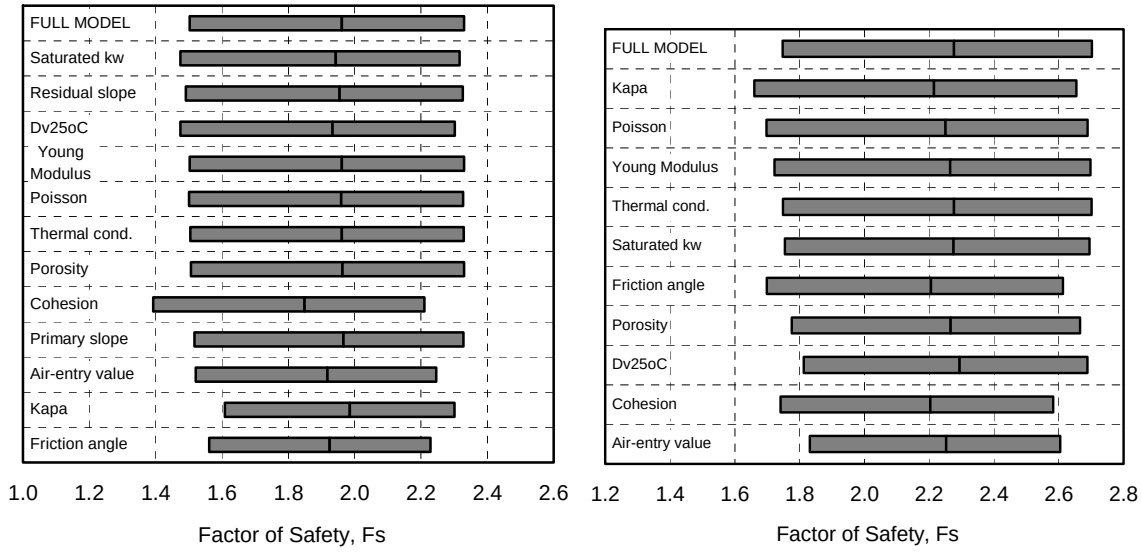

(a) (b)

Figure 6.75 Probabilistic event tornado diagrams at t = 42 days. Soil types: (a) loam soil; (b) clay soil.

Figure 6.75 indicated that the friction angle and the unsaturated shear strength parameter, κ, have important impacts on the factor of safety of the loam embankment and cohesion has an intermediate impact. Figure 6.75 shows also that the effective cohesion is an important parameters for the clay embankment and that the friction angle and the unsaturated shear strength parameter, κ, have intermediate to low impacts. These results were anticipated, based on the shear strength characteristics of each soil type.

Figures 6.76 and 6.77 present the transient sensitivity of the factor of safety to the input variables based on deterministic event tornado diagrams. According to Figs. 6.76 and 6.77, the air-entry value, the effective cohesion, and the friction angle were the most important variables throughout the evaporation event. Soil porosity and the unsaturated shear strength parameter, κ, presented intermediate impacts. The sensitivity of the factor of safety to the soil porosity and κ appear to increase as the soil desaturates. The sensitivity of the factor of safety to the inherent uncertainty of κ was slightly higher for the loam embankment, due to the relatively high friction angle.

Several input variables have time-dependent impacts on the factor of safety, as observed for the previous embankment configurations. The sensitivity of the factor of safety to the air-entry

value, saturated hydraulic conductivity, and vapour diffusivity increased with time. However, while the impact of the air-entry value increased sharply during early stages of the evaporation event, the impact of the hydraulic conductivity and the vapour diffusivity increased at a lower rate and remained intermediate. As explained previously, the time-dependent sensitivity is a product of the accumulation of the influence of the hydraulic properties as the precipitation event advanced. The longer the evaporation event the higher the impact of the air-entry value and the higher the sensitivity of the saturated hydraulic conductivity. The remaining input parameters shown in Figs. 6.76 and 6.77 appear to have relatively small or no influence on the factors of safety throughout the precipitation event.

Figures 6.78 and 6.79 present the transient sensitivity of the factor of safety to the input variables based on probabilistic event tornado diagrams. Figures 6.78 and 6.79 confirm that the air-entry value, effective cohesion, and friction angle have high or intermediate impacts on the factor of safety, depending on the soil type. Cohesion and friction angle are the most important variables at the beginning of the evaporation event for the clay embankment. For instance, the removal of the uncertainty of the effective cohesion results in a decrease in the probability of failure by five orders of magnitude for the clay embankment.

The sensitivity of the factor of safety to the shear strength parameters decreased considerably as the evaporation event advanced. The uncertainty in the unsaturated shear strength parameter, κ, appeared to have a positive influence in the probability of failure of the clay embankment. In other words, higher probabilities of failure were obtained when the uncertainty of κ was removed. This result can be attributed to an skewed effect of the parameter k for this embankment configuration.

The sensitivity of the factor of safety to the inherent uncertainty of the vapour diffusivity increased during the evaporation event and reached an intermediate value by the 42^{nd} day. The relatively high sensitivity of the factor of safety to the vapour diffusivity was expected. The results presented in Figs. 6.78 and 6.79 indicate that the relevance of the vapour diffusivity increases with time. Long term analyses of evaporation events require the consideration of vapour diffusivity variability.

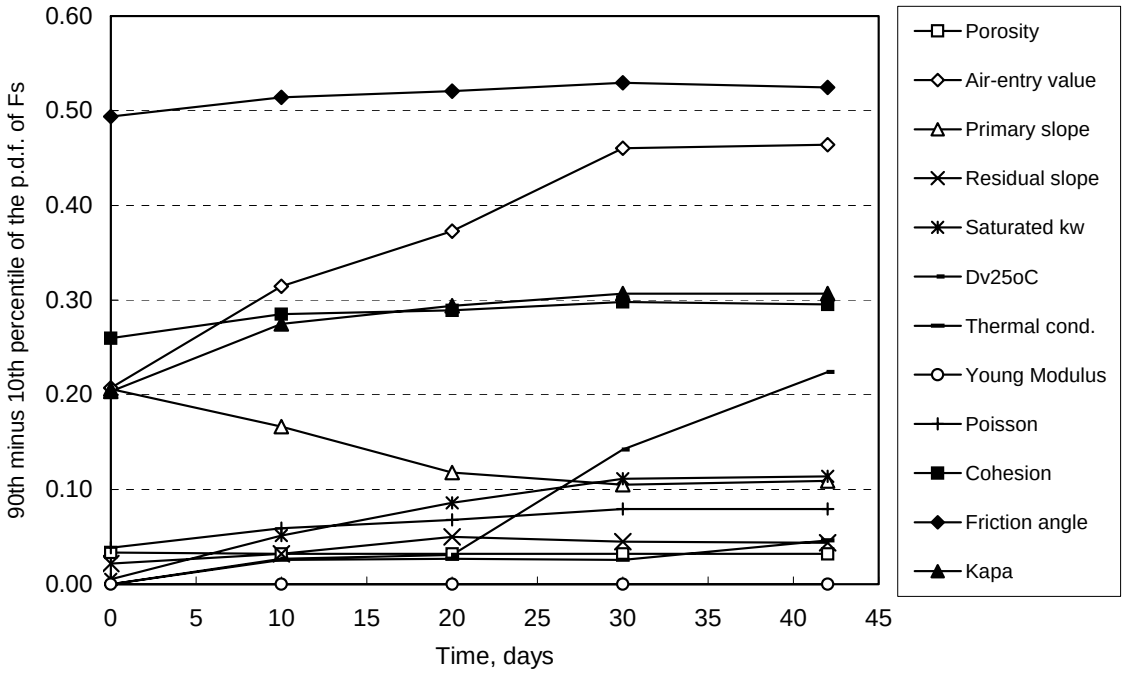

Figure 6.76 Transient sensitivity during the evaporation event based on deterministic event tornado diagrams for loam embankment.

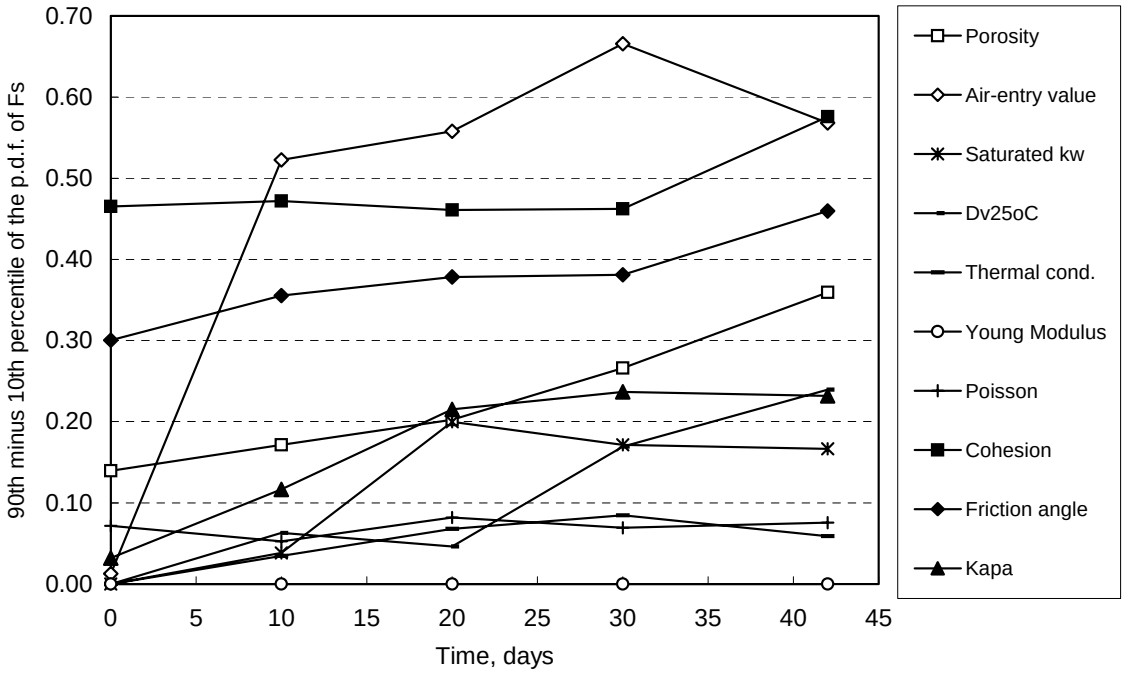

Figure 6.77 Transient sensitivity during the evaporation event based on deterministic event tornado diagrams for clay embankment.

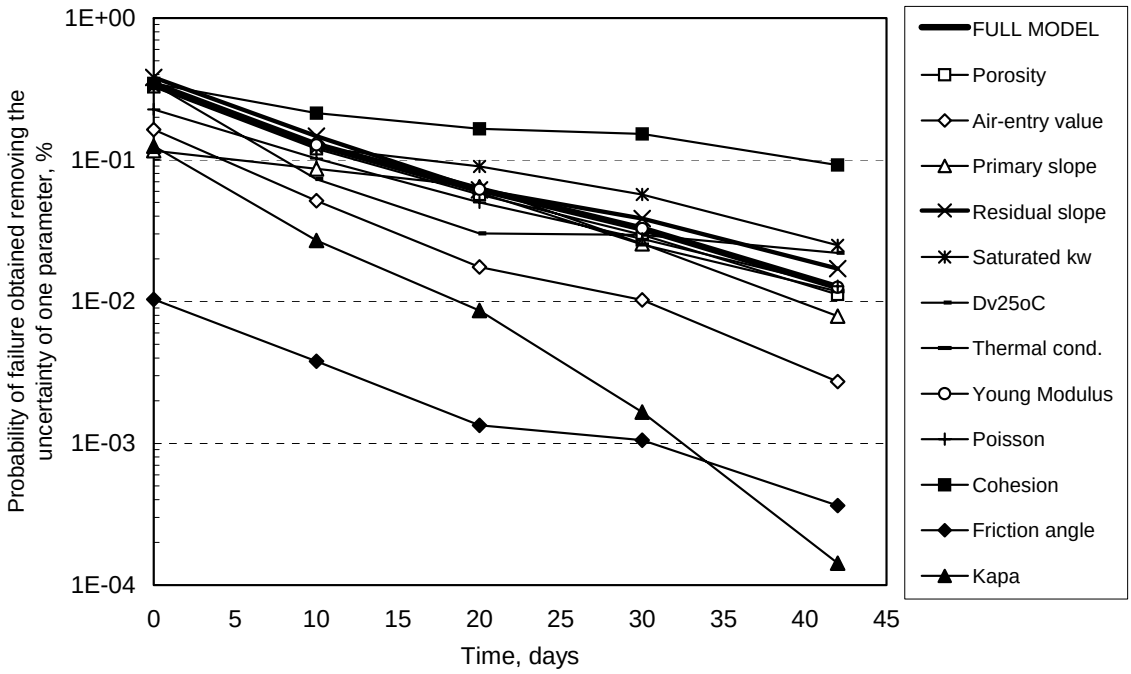

Figure 6.78 Transient sensitivity during the evaporation event based on probabilistic event tornado diagrams for loam embankment.

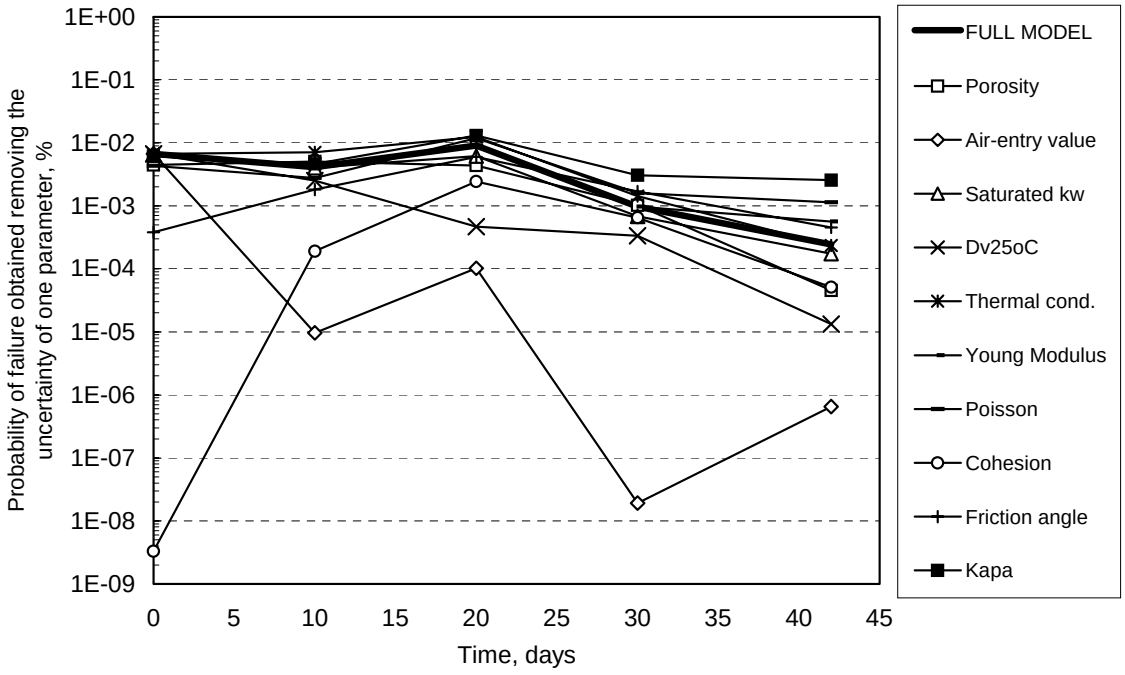

Figure 6.79 Transient sensitivity during the evaporation event based on probabilistic event tornado diagrams for clay embankment.

6.7 SUMMARY OF THE SENSITIVITY ANALYSIS STUDY FINDINGS AND PERFORMANCE OF THE W-GHA MODEL

This section presents a discussion and summary of the findings for the hazard assessment analyses and sensitivity analyses, considering the precipitation and evaporation event. A summary of the findings from the sensitivity analysis study is discussed first, followed by a discussion of the overall performance of the W-GHA in the later part of this section.

6.7.1 *Sensitivity during precipitation conditions*

Table 6.6 presents a summary of the sensitivity of the factor of safety to the inherent uncertainty of the input random variables, considering all embankment configurations and the precipitation conditions. Three qualitative levels were chosen to describe the impacts of the input variables. The "High" level corresponds to the variables with highest impacts on the factor of safety. The variability of these parameters must be considered for the assessment of railway embankment hazards. The "Intermediate" level corresponds to those variables that have intermediate impacts and that may or may not be considered as uncertain variables, depending on the level of refinement required. The "Low" level corresponds to those variables that have markedly low impacts, and that can be considered fixed variables within the W-GHA model framework.

Table 6.6 shows that the uncertainty in porosity has a low impact on the factor of safety for loam embankments and intermediate impacts for the clay embankments. The slightly higher sensitivity of the factor of safety to the soil porosity for clay embankments appears to be mostly associated with the changes in the unit weight of the soil for different degrees of saturation. The higher the soil porosity, the higher the change in the unit weight of the soil for different degrees of saturation. Changes in the unit weight of the soil produce changes in the acting stresses within the embankment and changes in the shear strength due to the friction angle. Nevertheless, the results suggest that porosity must be treated as a fixed, certain parameter.

The analyses results have shown that the variability of the air-entry value has a time-dependent impact on the variability of the factor of safety. The changes in the air-entry result in changes in several predicted properties; namely, the hydraulic conductivity function, the vapour conductivity function, the thermal properties, and the unsaturated shear strength envelope. However, the time dependent characteristics of the air-entry value sensitivity suggests that the change in the predicted hydraulic conductivity function is responsible for the high sensitivity of air-entry value.

Table 6.6 Summary of the sensitivity analysis results for a precipitation event.

Parameter	Low embankment				High embankment			
	Loam		Clay		Loam		Clay	
	Initial	Final	Initial	Final	Initial	Final	Initial	Final
(1)	(2)	(3)	(4)	(5)	(6)	(7)	(8)	(9)
n	L	L	I	I	L	L	I	I
ψ_b	I	**H**	L	**H**	I	**H**	L	**H**
λ_d	I	L	--	--	I	L	--	--
λ_{res}	L	L	--	--	I	L	--	--
k^w_{sat}	L	**H**	L	**H**	L	L	L	**H**
$D^v_{25^oC}$	L	L	L	L	L	L	L	L
λ_s	L	L	L	L	L	L	L	L
E	L	L	L	L	L	L	L	L
μ	L	L	L	L	L	L	L	L
c'	**H**	**H**	**H**	**H**	I	I	**H**	**H**
ϕ'	**H**	**H**	**H**	**H**	**H**	**H**	**H**	**H**
$\ln(\kappa)$	**H**	L	L	L	**H**	I	L	L

Legend:
L – low sensitivity, I – intermediate sensitivity, H – high sensitivity

Two distinct stages were identified regarding the sensitivity of the factor of safety to the uncertainty in the air-entry value. During the first stage, the sensitivity of the factor of safety to the uncertainty in the air-entry value is low or intermediate. The second stage is characterised by the high impact of the air-entry value. This suggests that the uncertainty of the air-entry value may be neglected if the duration of the precipitation event is short enough. The duration of the first stage varied for the several embankment scenarios. The loam embankments presented low impact of the air-entry value during the first 6 to 8 days for the low embankment and 10 to 12 days for the high embankment. Longer periods were observed for the initially "wet" loam embankments. The clay embankments presented low impacts of the air-entry value during the first 2 to 4 days for the low embankment and 6 to 12 days for the high embankment. However, longer periods were observed for the initially "dry" loam embankments. A clear threshold cannot be established, but it appears that most case scenarios could be appropriately modelled without considering the variability of the air-entry value, given that the precipitation

event is shorter than 6 days, with exception of the low clay embankment. However, the air-entry value uncertainty is of paramount importance for analyses of longer periods and must be considered as an uncertain, random variable.

The variability of the primary and residual SWCC slopes presented intermediate to low impacts on the factor of safety. Lower initial degrees of saturation resulted in higher impacts for both parameters. The sensitivity of the factor of safety to the uncertainty in the primary and residual SWCC slopes decreased as the precipitation event progressed. The case scenarios presented herein corresponded to relatively "dry" and relatively "wet" initial conditions. Figure 6.4 shows that the initial condition for the loam embankment corresponds to a degree of saturation slightly lower than the residual point for the "dry" case and about half way along the primary drainage slope for the "wet" case. Figure 6.10 shows that the initial condition for the clay embankment is at about S = 70% for the "dry" case and about S = 85% for the "wet" case. The analysis results have shown that the impact of the SWCC shape is particularly low when a relatively wet soil experiences wetting. In summary, the results presented herein suggest that the primary and residual SWCC slopes have relatively low impacts on the factor of safety and may be modelled as certain, fixed values.

According to the sensitivity analysis presented herein, the uncertainty on the saturated hydraulic conductivity has a time-dependent impact on the uncertainty of the factor of safety. Two distinct stages were identified regarding the sensitivity of the factor of safety to the uncertainty saturated hydraulic conductivity. During the first stage, the impact of the uncertainty in the saturated hydraulic conductivity is low, but increasingly higher. The second stage is characterised by the high impact of the uncertainty in the saturated hydraulic conductivity. The duration of the first stage varied for the several embankment scenarios. The loam embankments presented low sensitivity of the factor of safety to the uncertainty in the saturated hydraulic conductivity during the first 8 days for the low embankment and throughout the precipitation event for the high embankment. The clay embankments presented low sensitivity of the factor of safety to the uncertainty in the saturated hydraulic conductivity during the first 4 to 6 days for the low embankment and 8 to 10 days for the high embankment. The initial conditions did not play a significant role on the duration of the stages. The uncertainty of the saturated hydraulic conductivity may be neglected if the duration of the precipitation event is short enough. Again, a clear threshold cannot be established, but it appears that most case scenarios could be appropriately modelled without considering the variability of the saturated hydraulic

conductivity, given that the precipitation event is shorter than 4 days.

The inherent uncertainties of the vapour diffusivity, thermal conductivity, and Young modulus have negligible impacts on the uncertainty in the factor of safety throughout the precipitation event, for all embankment configurations. As discussed previously, water flow takes place primarily as liquid flow during precipitation events. The amount of vapour flow is negligible when compared to the amount of vapour flow. The flow of heat may have some influence on the flow of water vapour, but does not play a role on the flow of liquid water. Therefore, the flow of heat is irrelevant and the thermal conductivity of the soil does not have a significant impact.

The variability of the Young modulus proved to have a negligible impact to the variability in the factor of safety. However, this conclusion cannot be extended to problems were layers of different soils, with contacts of different moduli (Gitirana Jr. and Fredlund, 2003a). The Young modulus does not play a role on the conservation of momentum within a soil mass, but has a fundamental role on the strain distributions. Therefore, the Young modulus is likely to be an important parameter for serviceability problems (i.e., problems associated with soil settlement).

Several researchers have shown the role of Poisson ratio on the stability of slopes (Scoular, 1997, Pham, 2002, Gitirana Jr. and Fredlund, 2003a). The sensitivity analysis study presented herein demonstrated that indeed, Poisson's ratio variability affects the variability in the factor of safety. However, is has also been shown that the sensitivity of the factor of safety to Poisson's ratio is small when compared to the sensitivity to other soil properties, such as effective cohesion, friction angle, unsaturated shear strength parameter, κ, air-entry values, and saturated hydraulic conductivity. It is suggested herein that Poisson's ratio must be treated as a fixed, certain variable, for most practical applications.

Effective cohesion and friction angle have proven to have high impacts on the factor of safety. The impacts of effective cohesion and friction angle are significantly higher than the impacts of the remaining properties. The sensitivity of the factor of safety to uncertainty in effective cohesion and friction angle appear to be generally constant throughout a precipitation event. Only the air-entry value and the saturated hydraulic conductivity have comparable of higher impacts, given that the duration of the precipitation event is long enough. The sensitivity of the factor of safety to uncertainty in soil cohesion appears to decrease somewhat for higher embankments with relatively low cohesion. Higher railway embankments have more significant

friction components and the less important cohesive component of the shear strength. In summary, the inherent uncertainties of the effective cohesion and friction angle have important impacts on the uncertainty of the factor of safety and must be treated as uncertain variables.

Finally, the uncertainty in the unsaturated shear strength parameter, κ, has a high impact on the uncertainty in the factor of safety during early stages of the precipitation event for the loam embankments. However, the impact of κ decreases as the precipitation event advances and the soil suctions decrease. The impact of κ is high or intermediate up to the sixth day, with exception of the high, clay embankment, which presented a low sensitivity of the factor of safety to the uncertainty in κ throughout the precipitation event. The importance of the uncertainty in κ is relatively low for the clay embankments, due to the low friction angle. In theory, lower friction angles result in relatively low unsaturated shear strength. This conclusion is based on the assumptions regarding the shape of the unsaturated shear strength envelope. A review of the pertinent literature indicates that further research is required for a better characterisation and modelling of the unsaturated shear strength of cohesive soils. Nevertheless, the uncertainty modelling approach proposed herein for the unsaturated shear strength envelope provides an alternative framework for addressing the uncertainties associated with the shear strength of unsaturated soils.

6.7.2 *Sensitivity during evaporation conditions*

Table 6.7 presents a summary of the impact of the uncertainty in the input random variables on the uncertainty in the factor of safety, considering the loam and clay embankments and the evaporation conditions. The three qualitative levels of sensitivity described in the previous sections were used herein. Table 6.7 shows that the sensitivity of the factor of safety to the uncertainty of most soil properties is similar to that found for the precipitation event, with the main exceptions being the saturated hydraulic conductivity and the vapour diffusivity. The uncertainty in soil porosity presented an intermediate impact for both the loam and clay embankments. The higher impact of the uncertainty in soil porosity when compared to that found for the precipitation event appears to be mostly associated with the changes in the vapour conductivity function, which is dependent on the amount of voids available for vapour flow. Nevertheless, the importance of the uncertainty in soil porosity can be considered relatively low when compared against other soil parameters. As a result, soil porosity can be considered a fixed, certain input parameter.

Table 6.7 Summary of the sensitivity analysis results for an evaporation event.

Parameter	Loam		Clay	
	Initial	Final	Initial	Final
(1)	(2)	(3)	(4)	(5)
n	I	I	I	I
ψ_b	L	**H**	L	**H**
λ_d	I	L	--	--
λ_{res}	L	L	--	--
k^w_{sat}	L	I	L	I
$D^v_{25^oC}$	L	**H**	L	**H**
λ_s	L	L	L	L
E	L	L	L	L
μ	L	L	L	L
c'	**H**	**H**	**H**	**H**
ϕ'	**H**	**H**	**H**	**H**
$\ln(\kappa)$	**H**	I	L	I

Legend:
L – low sensitivity, I – intermediate sensitivity, H – high sensitivity

The analysis results have shown that the air-entry value has a time-dependent impact similar to that observed for the precipitation event. Two distinct stages were identified regarding the importance of the air-entry value. During the first stage, the impact of the air-entry value is low. The second stage is characterised by the high sensitivity of the factor of safety to the air-entry value. The duration of the first stage appear to be rather short when compared to the period of time considered for the evaporation event. Therefore, it is suggested herein that the air-entry values must be considered an uncertainty variable and should not be simplified.

The primary and residual SWCC slopes presented intermediate to low impacts on the factor of safety. The sensitivity of the factor of safety to the primary SWCC slope tends to be higher during early stages of the evaporation event, when the soil was closer to saturation. The analyses results have shown that the impact of the SWCC shape is generally low when compared to other variables. In summary, the results presented herein suggest that the primary and residual SWCC slopes have relatively low impacts and may be modelled as certain, fixed values. A time-dependent impact was again observed for the saturated hydraulic conductivity. The two

distinct stages described in the previous section were identified for the sensitivity of the factor of safety to the saturated hydraulic conductivity. However, the importance of the saturated hydraulic conductivity was considerably lower than that of other parameters, such as the shear strength parameters, and it may be considered a fixed parameter for periods not much longer than 42 days. It appears that the importance of the saturated hydraulic conductivity may be high for long term moisture flow analyses and should not be neglected in those cases.

The sensitivity of the factor of safety to the vapour diffusivity during the evaporation event is considerably high. During evaporation events a layer of relatively dry soil forms near the ground surface. The layer of relatively dry soil prevents liquid flow and allows flow of moisture primarily as water vapour. Therefore, the vapour diffusivity becomes the primary variable controlling the rate of moisture movement at the near surface soil. The results presented herein suggest that the uncertainty associated with the vapour diffusivity should not be neglected when periods of prolonged evaporation occur. However, short term analyses of less than approximately four weeks could be analysed without considering the uncertainty associate with the vapour diffusivity.

The inherent uncertainty of thermal conductivity, Young modulus, and Poisson's ratio have negligible impacts on the uncertainty in the factor of safety throughout the evaporation event for both the loam and clay embankments. The flow of heat appears to affect the flow of water, but does not play a significant role for the embankment conditions presented herein. Therefore, the flow of heat is irrelevant and the uncertainty in the thermal conductivity of the soil does not have a significant impact in the uncertainty in the factor of safety. This indicates that the equation of conservation of heat may be disregarded. However, heat flow appears to be time dependent and may be considerably higher for long term analyses.

The uncertainty in effective cohesion and friction angle were shown to have high impacts on the uncertainty in the factor of safety during the evaporation event. The sensitivity of the factor of safety to the effective cohesion and friction angle appear to be fairly constant throughout an evaporation event. Only the uncertainty of vapour diffusivity has comparable impact, given that the duration of the precipitation event is long enough. Therefore, the effective cohesion and friction angle are highly important parameters that must be treated as uncertain variables. Finally, the inherent uncertainty of the unsaturated shear strength parameter, κ, has a high impact on the uncertainty in the factor of safety during the evaporation event for the loam soil

and intermediate sensitivity for the clay soil. It appears that the uncertainty associated with κ must not be neglected.

6.7.3 *Performance of the W-GHA model and model components*

The results of the analyses for the several embankment configurations presented in this chapter show that the W-GHA model is capable of quantifying embankment stability during precipitation and evaporation events successfully. The approach proposed for addressing uncertainties associated with the soil properties proved to be efficient. The uncertainty of the factor of safety was successfully computed for all embankment configurations.

The factors of safety and probabilities of failure presented herein provide two complementary hazard quantification measures. A comparison of the factors of safety and probabilities of failure presented in Figs. 6.24 to 6.27, 6.36 to 6.39, 6.44, and 6.45 indicates that the factor of safety may provide a misleading measure of embankment stability for certain cases. The uncertainty of the factor of safety provides useful information and provides a rational way of addressing the uncertainty associated with the soil properties.

The dynamic programming code presented in this thesis, Safe-DP, was able to locate critical slip surfaces for all case scenarios. No convergence issues were observed. The computation times required by the dynamic programming solution did not exceed 2 minutes for each analysis. Fairly dense search grids were adopted, with vertical distances that varied from 0.25 m to 0.5 m. The dynamic programming solution required minimum human interference for the solution. A sufficiently large search boundary was selected for each embankment size and performed satisfactorily for all analyses.

The dynamic programming solution proved to be a superior method of slope stability compared to conventional limit equilibrium methods, for the cases analysed herein. The failure mechanisms predicted were in accordance with the expected results. Deeper slip surfaces where obtained when cohesive forces were dominant. Shallow slip surfaces were obtained when cohesive forces were absent. Most slip surfaces presented non-circular shapes, indicating that the circular failure mechanism adopted by conventional limit equilibrium method may not be accurate. Extremely shallow and peel-shaped slip surfaces were obtained for a number of case scenarios. Shallow slip surfaces were observed for cohesionless conditions combined with sharp wetting fronts. This failure mechanism has been previously observed bt Krahn et al., (1989).

Transient analyses of coupled moisture and heat flow were successfully performed using the finite element model implemented using FlexPDE. The computation times varied depending on the soil properties and severity of the pore-water pressure gradients. The highly non-linear soil properties were successfully accommodated, through dynamically refined meshes and time steps. The results obtained herein show that FlexPDE can be used for the solution of highly complex phenomena, such as the solution of fully coupled thermo-hydro-mechanical phenomena on unsaturated soils.

Initial conditions proved to be of paramount importance. Considerably higher hazard levels were obtained for lower initial soil suctions. The initial pore-water pressure and water content conditions are function of the antecedent weather conditions. In situ measurements of initial conditions appear to be an option for the establishment of initial condition. Alternatively, the probabilistic framework proposed herein could potentially be extended to accommodate in a formal manner the uncertainty associated with the initial conditions.

The results of the sensitivity analyses presented in this section provide important information that can be used towards the simplification of the W-GHA model. According to the findings presented herein, a maximum number of 6 soil properties require probabilistic modelling; namely, the air-entry value, the saturated hydraulic conductivity, the vapour diffusivity, the effective cohesion, the friction angle, and the unsaturated shear strength parameter, κ. Considerable saves in computation time are obtained. Only three parameters associated with moisture-heat flow finite element simulations require probabilistic case scenarios (i.e., the air-entry value and the saturated hydraulic conductivity). As a result, only 7 moisture-heat flow finite element analyses are required.

The threshold found herein for the first and second "sensitivity stages" for the air-entry value, saturated hydraulic conductivity, and vapour diffusivity appears to vary considerably depending on the initial conditions, embankment size, and soil type. The uncertainty associated with the size of the "sensitivity stages" indicates that both properties should be maintained as uncertain variables. On the other hand, the relatively high coefficients of variation used herein suggest that the sensitivity of the air-entry value and the saturated hydraulic conductivity may have sensitivities somewhat lower when more specific soil data is available. Ultimately, the decision regarding whether or not to perform the probabilistic modelling considering the air-entry value and the saturated hydraulic conductivity will depend on the level of detail and accuracy required.

6.8 IMPLEMENTATION OF THE W-GHA MODEL IN PRACTICE

This thesis laid out a theoretical framework for the quantification of embankment hazards at a local scale (i.e., considering specific embankments). The proposed framework utilises unsaturated soil mechanics and hydrology concepts in order to model the mechanical behaviour of the near ground surface soil comprising railway embankments. Practical hurdles associated with the difficulty in obtaining unsaturated soil properties were overcome using approximate predictive techniques and by addressing the uncertainty associated with soil properties through a probabilistic and sensitivity analysis framework. Ultimately, the embankment hazard is assessed based on the factor of safety and probability of failure.

While the theoretical framework is comprehensive and was established based on feasible data, additional research and development is required in order to implement the proposed framework into practice. A number of issues must be addressed, mostly regarding protocols for data collection and the definition of the level of detail required for data collection. These issues are briefly outlined in the following paragraphs:

Selection of embankments that require monitoring: The choice of railway embankments to be monitored may consider several criteria. The criteria for selection of embankments that require closer monitoring may involve: (i) field observations of embankment instability, (ii) the recognition of soil types that result in embankments that are prone to failure, and (iii) the recognition of embankment geometries that are not in accordance with typical standards.

Input data for soil properties: soil properties may be accessed through various levels of detail. A rough estimate of soil properties may be obtained based on the predictive approaches presented herein and additional prediction method for saturated shear strength parameters. Regardless of the level of data collection detail, the theoretical framework presented in this thesis offers a rational method of addressing the uncertainty associated with soil properties.

Input data for initial conditions: the analysis of hypothetical embankments presented in this chapter has shown that the initial pore-water pressure conditions play an important role on the stability of railway embankments. A number of approaches are available for determining initial conditions in the field. A range of suction measurement devices is available and can be used for the long term monitoring of pore-water pressure conditions. The pore-water pressure conditions

measured at any point in time can be used for the analysis of embankment stability, given a set of forecast weather data. An alternative approach could be based on rough estimates of initial conditions along with the assessment of the sensitivity of the factor of safety to the initial conditions. Such approach would require the extension of the probabilistic framework.

Input data for weather conditions: weather forecast is available at several levels of detail. The stability of a railway embankment can be predicted based on weather data forecast and using the proposed methodology. However, there's a need of further studies for the establishment of minimum acceptable detail levels. The proposed methodology would benefit from the extension of the model in order to address weather forecast uncertainty.

Assessment of vulnerability and risk levels: there are several approaches available for the assessment of vulnerability. Vulnerability depends on the travel distance of a failing embankment, the presence of neighbouring structures and facilities, and most importantly, the nature of the freight. Hazardous goods, such as certain chemical products, result in a sharp increase of the vulnerability of neighbouring communities that can be harmed by toxic gases. A vulnerability ranking system must be established, considering the above mentioned factors. Risk levels must be computed by combining the probability of failure computed using the W-GHA model and the vulnerability rank for the site at hand.

Acceptable risk levels: the framework proposed and applied herein must be combined with clearly defined levels of acceptable risks. According to Whitman (1984) and Becker (1992a), among others, the typical range of acceptable probabilities of failure adopted in slope and foundation engineering projects varies from 0.1 to slightly lower than 1%. These acceptable probabilities of failure are rough estimates and do not take into account vulnerability levels in a rigorous manner. Acceptable risk levels can be established following a number of approaches. One such approach is to compile observed frequencies and consequences of natural and man-made events and use these values as a comparative basis. Figure 6.80 presents a compilation involving the annual rate of single events causing various numbers of fatalities (Whitman, 1984). The frequency of failures of structures and other civil engineering projects is shown in Fig. 6.80.

Meyerhof (1970, 1993, 1995) cited by Becker (1992a) presented another useful compilation, involving typical values of overall factors of safety and reliability indexes (Fig. 6.81). Figure 6.81 is based on a compilation of failures of foundations, earthworks, retaining walls, and uses

semi-probabilistic methods and judgement based on experience. According to Fig. 6.81, the lifetime probability of failure of earthworks is about 0.1%.

Besides being applied to the quantification of embankment hazards at a local scale, the framework proposed herein can also be used towards the development of methods of assessment of hazards in a regional scale. The assessment of embankment hazards in a local scale requires the establishment of simple functions that provides a measure of hazard based on embankment and weather conditions. Such a function must have a simple form so that they can be used in association with a *Geographic Information System* (GIS) environment. At the same time, a functional for embankment hazard level must be founded on the mechanisms associate with local scale embankment failures. The W-GHA can be employed in the analysis of hypothetical case scenarios and the results can be used toward the development of a semi-empirical functional appropriate for GIS applications.

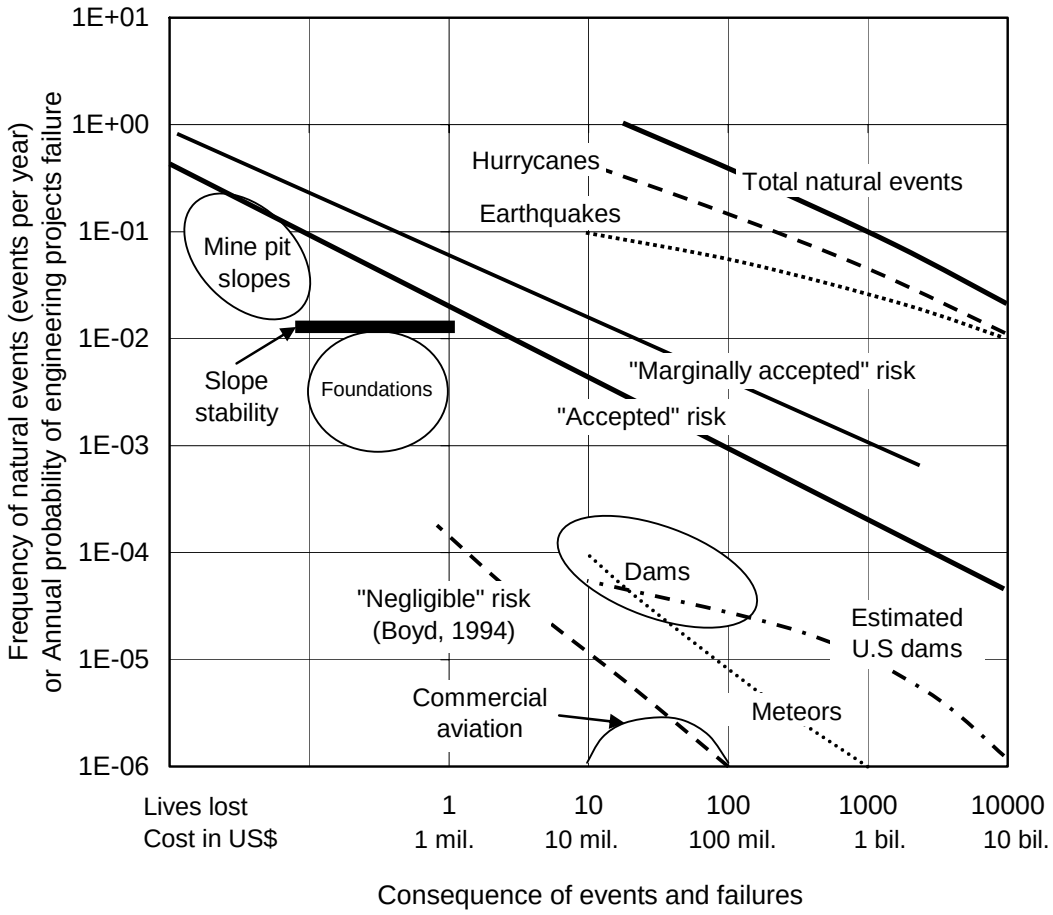

Figure 6.80 Risks for natural events and engineering projects designed according to current practice (modified from Whitman, 1984).

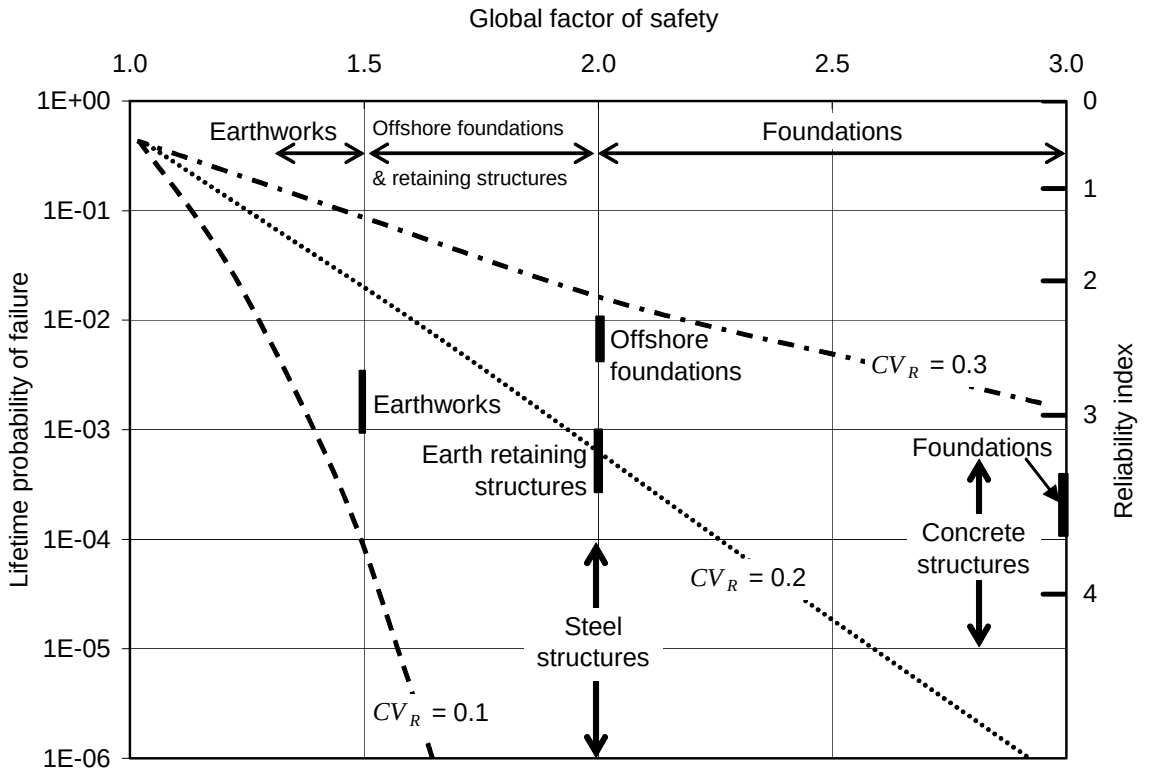

Figure 6.81 Comparison between global factor of safety and probability of failure (modified from Becker, 1992a); CV_R is the coefficient of variation of resistance; the curves of CV_R vs. Global factor of safety where determined considering lognormal distributions.

6.9 CHAPTER SUMMARY

This chapter presented the analysis of hypothetical embankment configurations designed to demonstrate the application W-GHA model to the assessment of railway embankment hazards. The hypothetical embankment configurations were designed also in order to determine the sensitivity of the uncertainty of the factor of safety to the uncertainty of input parameters, indicating what parameters require more detailed assessment and what parameters can be treated as fixed, certain variables.

Section 6.2 presented the description of the hypothetical embankment case scenarios. The case scenarios were selected in order to cover a wide range of possible embankment configurations. Varying geometry, soil types, and initial conditions are considered herein. Two distinct weather conditions were analysed; namely, a precipitation event and an evaporation event. Section 6.3 described the statistical modelling of soil properties required for establishing soil property case

scenarios. Two types of soils were selected; namely, a loam soil and a clay soil. Mean values and coefficients of variation presented in Chapter 5 were selected for the soils analysed herein. Soil property case scenarios were established based on the *alternative point estimate method*. Section 6.4 presented a concise description of the analysis procedure.

Section 6.5 presented the results and discussion of the analysis of the embankment configurations described in the previous sections. The results of the analyses for the several embankment configurations showed that the W-GHA model is capable of quantifying embankment stability during precipitation and evaporation events. The approach proposed for addressing uncertainties associated with the soil properties proved to be efficient. A comparison of the factors of safety and probabilities of failure presented indicates that the factor of safety may provide a misleading measure of embankment stability for certain cases.

The dynamic programming code presented in this thesis, Safe-DP, was able to locate critical slip surfaces for all case scenarios. The dynamic programming solution proved to be a superior method of slope stability compared to conventional limit equilibrium methods, for the cases analysed herein. The failure mechanisms predicted were in accordance with the expected results. Transient analyses of coupled moisture and heat flow were successfully performed using the finite element model implemented using FlexPDE. The results obtained herein show that FlexPDE can be used for the solution of highly complex phenomena, such as the solution of fully coupled thermo-hydro-mechanical phenomena on unsaturated soils.

Sections 6.6 present the sensitivity analysis results and discussions. The sensitivity of the factor of safety to the inherent uncertainty of the input parameters was analysed in terms of the final embankment conditions and in terms of the transient evolution of the factors of safety and probabilities of failure. According to the findings presented herein, 6 soil properties have high impact on the factor of safety; namely, the air-entry value, the saturated hydraulic conductivity, the vapour diffusivity, the effective cohesion, the friction angle, and the unsaturated shear strength parameter, κ. Air-entry value, saturated hydraulic conductivity, and vapour diffusivity have transient impacts that increase with time. The remaining input parameters have low impacts and can be modelled as fixed, certain variables.

Section 6.7 presented a summary of the findings and Section 6.8 presented a brief discussion of how the proposed methodology can be applied in practice and the required future developments.

Chapter 7

Conclusions and Recommendations

7.1 THESIS SUMMARY

The primary objective of this thesis is to develop a model for the local scale quantification of weather-related railway embankment hazards. The model for quantification of embankment hazards constitutes an essential component of a *decision support system* that is required for the management of railway embankment hazards. The research focus of this thesis is on the application of unsaturated soil mechanics concepts for the quantification of railway embankment hazards.

A number of methodological steps were established and are prerequisite for the fulfillment of the primary objective. As stated in Chapter 1, the methodological steps consisted of:

(i) the identification and modelling of the physical processes and soil variables that control the behaviour of the near ground surface soil comprising a railway embankment;
(ii) the identification and modelling of the physical processes and variables associated with soil-atmosphere interaction;
(iii) the establishment of a probabilistic framework for the assessment of embankment hazards that is capable of addressing the inherent uncertainty of unsaturated soil properties;
(iv) the development and verification of numerical and analytical models based on the deterministic and probabilistic hazard assessment theory developed herein;

(v) the establishment of a methodology for the statistical assessment of unsaturated soil property uncertainty and the statistical assessment of unsaturated soil parameter uncertainty using the proposed methodology and a database of soils; and

(vi) The analysis of hypothetical railway embankments and the analysis of the sensitivity of the factor of safety to the parameters controlling the stability of railway embankments. The hypothetical case scenarios analysed should be designed to demonstrate the application of the hazard quantification model to typical railway conditions.

The methodological steps described above were fulfilled in a progressive manner. Chapter 2 presented a literature review intended to characterise derailments caused by railway embankment failures and a review of theories available for assessment of weather-related geo-hazards. Chapter 3 presented the theoretical development of a deterministic and probabilistic model for the assessment of weather-related geo-hazards (W-GHA model) based on unsaturated soil mechanics concepts. Chapter 4 presented the implementation and verification of numerical and analytical models for the solution of the W-GHA model. Chapter 5 presented a framework for characterisation and assessment of unsaturated soil property variability and statistical studies using the proposed framework and a database of soils. Finally, Chapter 6 presented the analysis of typical railway embankment scenarios designed in order to demonstrate the application of the W-GHA model to a range of typical railway embankment conditions and designed in order to evaluate the sensitivity of the factor of safety to the input parameters. The research results provide a comprehensive model for assessment of weather-related geo-hazards and a framework for the application of unsaturated soil mechanics to geotechnical engineering practice.

7.2 CONCLUSIONS

The results of the research carried out indicate that the study objective has been met. A comprehensive model has been proposed for the quantification of railway embankment hazards. A methodology for the application of the proposed model was laid out and put into practice considering hypothetical embankment scenarios. The proposed model consists of a framework for deterministic and probabilistic analyses based on predicted unsaturated soil properties, a framework for the assessment and modelling of unsaturated soil property variability, and a framework for sensitivity analyses. The sensitivity of the factor of safety to the various input parameters was determined based on the hypothetical embankment configurations analysed.

The following conclusions can be drawn from the present study:

1. Unsaturated soil mechanics can be successfully employed towards the assessment of weather-related geo-hazards. The proposed model for the quantification of embankment hazards is comprehensive, sufficiently versatile, and employs soil data that is relatively easy to obtain. The model is capable of quantifying in deterministic and probabilistic terms the stability of railway embankments subjected to various atmospheric conditions.

2. A framework for the statistical characterisation and assessment of unsaturated soil properties was developed. The framework was applied to soil data that was sampled from a large database of soils and grouped according to the USDA classification system. The following conclusions can be drawn from the statistical study of unsaturated soil properties:

    2.1. The proposed framework for characterisation and assessment of unsaturated soil property variability can be successfully employed to provide the data required by probabilistic analyses of geotechnical problem involving unsaturated soils;

    2.2. The nonlinear unsaturated soil property equations and the fitting parameters proposed in this thesis provide an appropriate description of unsaturated soil property functions. The fitting functions proposed herein have good fitting capabilities, considering the sampled data used in this study. The use of mathematically independent soil parameters that are individually related to distinct features of the soil property functions resulted in meaningful measures of unsaturated soil property variability.

    2.3. The air-entry value, primary SWCC slope, residual SWCC slope, saturated hydraulic conductivity, and hydraulic conductivity function slope can be accurately described using a lognormal probability density function. Therefore, the natural logarithm of the above mentioned properties can be represented by a normal distribution. Soil porosity can be considered normally distributed.

    2.4. Typical central tendency measures, variability measures, and correlation coefficients were successfully established for the parameters of each soil group. Tables 5.6, 5.7, and 5.8 presented a summary of the central tendency measures, variability measures, and correlation coefficients obtained.

3. The analysis of a large number of hypothetical embankment configurations showed that factor of safety and probability of failure provide two complementary hazard quantification measures. A comparison of the factors of safety and probabilities of failure presented indicates that the factor of safety may provide a misleading measure of embankment stability for certain cases. The information provided by the alternative point estimate case scenarios allows a rational assessment of embankment hazards, considering the inherent uncertainty of the soil properties. The framework proposed and applied herein can be combined with clearly defined levels of acceptable hazard (i.e., acceptable factors of safety, probabilities of failure, combined with consequence estimates), toward the management of weather-related geo-hazards for railway embankments.

4. The study of the sensitivity of the factor of safety to the input parameters was successfully undertaken. The effect of the inherent uncertainty of the input parameters on the uncertainty of the factor of safety was determined for a large number of embankment configurations. The proposed sensitivity analysis framework proved to be efficient and comprehensive. The deterministic and probabilistic event tornado diagrams provided important and complementary information about the sensitivity of the input variables. The following conclusions can be drawn from the results of the sensitivity analysis study:

    4.1. The friction angle, effective cohesion, and unsaturated shear strength parameter, κ, are generally the parameters with the greatest impact on the factor of safety, regardless of the atmospheric forcing conditions. The sensitivity of the factor of safety to the shear strength parameters is roughly constant throughout the precipitation and evaporation events, with exception of κ. The sensitivity of the factor of safety to κ decreases as the near ground surface soil saturates. The results of the sensitivity study suggest that the uncertainty associated with the shear strength parameters cannot be neglected and must be addressed using the probabilistic framework provided herein.

    4.2. The sensitivity of the factor of safety to the air-entry value and the saturated hydraulic conductivity increases during the precipitation and evaporation events. The longer the analysis period, the greatest the impact of the air-entry value and the saturated hydraulic conductivity. Two distinct stages were identified. During the first stage, the impact of the air-entry value and saturated hydraulic conductivity are low and may be neglected. The sensitivity of the factor of safety to both parameters

increases steadily with time. During the second stage, the impact of the air-entry value and saturated hydraulic conductivity is high and may become higher than the impact of the shear strength parameters. Therefore, the uncertainty associated with the air-entry value and saturated hydraulic conductivity variability should not be neglected during the second stage.

4.3. The threshold separating the first and second sensitivity stages described above is a function of the initial conditions, embankment height, and soil type. In view of the difficulty in predicting the duration of the first stage, it is suggested that the uncertainty of the air-entry value and saturated hydraulic conductivity should not be neglected and should be addressed using the probabilistic framework provided herein.

4.4. The sensitivity of the factor of safety to the soil porosity, primary SWCC slope, and residual SWCC slope is low to intermediate and appears to be time-dependent. Nevertheless, the results of the sensitivity study suggest that the uncertainty of all three parameters may be neglected. In other words, the soil porosity, primary and residual SWCC slopes may be considered as certain, fixed parameters.

4.5. The sensitivity of factor of safety to the Young modulus is negligible for all embankment configurations studied herein. However, this conclusion does not apply to serviceability analyses, where volume change is the main factor under study. In addition, the Young modulus may have a more important role when contacts between soils with different Young Moduli exist.

4.6. Poisson's ratio affects the factor of safety. However, the results of the sensitivity analyses have shown that the impact of Poisson's ratio is small when compared to the sensitivity of other soil properties, such as effective cohesion, friction angle, unsaturated shear strength parameter, κ, air-entry values, and saturated hydraulic conductivity. The results of the sensitivity analysis study suggest that Poisson's ratio may be treated as a fixed, certain variable, for most practical applications.

4.7. The sensitivity of the factor of safety to the thermal conductivity is negligible during both evaporation and precipitation events. Therefore, the thermal conductivity may be considered as a certain, fixed parameter.

4.8. The sensitivity of the factor of safety to the vapour diffusivity is negligible during precipitation events. However, the impact of the vapour diffusivity is considerably higher for evaporation events. During evaporation events, a layer of relatively dry soil forms near the ground surface. The layer of relatively dry soil prevents liquid flow and allows flow of moisture primarily as water vapour. Therefore, the vapour diffusivity becomes the primary variable controlling the rate of moisture movement at the near surface soil. The results presented herein suggest that the uncertainty associated with the vapour diffusivity should not be neglected when periods of prolonged evaporation occur. However, short term analyses for less than approximately four weeks could be analysed without considering the uncertainty associate with the vapour diffusivity.

5. The conclusions drawn from the sensitivity analysis study result in important simplifications of the W-GHA model. According to the findings presented herein, a maximum number of 6 soil properties require probabilistic modelling; namely, the air-entry value, the saturated hydraulic conductivity, the vapour diffusivity, the effective cohesion, the friction angle, and the unsaturated shear strength parameter, κ. As a result, only 7 moisture-heat flow finite element analyses are required. Considerable savings in terms of computation time are obtained through these simplifications.

6. Initial pore-water pressure conditions proved to be of paramount importance. Considerably higher hazard levels were obtained for lower initial soil suctions. The initial pore-water pressure and water content conditions are function of the antecedent weather conditions.

7. The general purpose partial differential equation solver, FlexPDE, can be successfully used for the numerical solution of the system of partial differential equation governing the thermo-hydro-mechanical behaviour of saturated/unsaturated soils. Verification problems were compared against known solutions and solutions obtained using well-established analytical and numerical models. Close agreement was observed between the results obtained using the numerical model using FlexPDE and results obtained using other software, capable of solving the simple problem used for verification purposes.

8. Dynamic Programming can be successfully applied for the computation of factors of safety for railway embankments. Dynamic programming provides a superior method for the analysis of embankment stability when compared to conventional limit equilibrium

methods. Restrictions related to the slip surface shape are significantly relaxed. Non-circular slip surface were frequently observed for the analysis presented in this thesis.

9. The approach proposed in this thesis forms a protocol for application of unsaturated soil mechanics to geotechnical engineering practice. This protocol is based on predicted unsaturated soil properties and based on case scenarios for addressing soil property uncertainty. Other classes of unsaturated soil problems will benefit from the protocol presented in this thesis.

7.3 RECOMMENDATIONS FOR FUTURE RESEARCH

The following recommendations for future research arise from this study:

1. Soil suction sensors based on heat dissipation can be successfully used in the long term monitoring of embankments (Marjerison, 2001). Theoretical predictions using the W-GHA model could be verified against soil suction data obtained from instrumented embankments.

2. Initial pore-water pressure conditions are of paramount importance. Alternatives for establishing initial conditions must be studied. A methodology for assessment of railway embankment stability hazards requires a reliable measure of initial conditions. Water content measurements or soil suction measurement using soils suction sensors based on heat dissipation are among the option for long term in situ measurement of initial conditions (Marjerison, 2001, Tan et al., 2004). Alternatively, the framework proposed herein could potentially be extended to accommodate in a formal manner the uncertainty associated with the initial conditions. Rough estimates of typical pore-water pressure conditions could be established for different soil and climate conditions and reasonable fluctuation measures for the active zone could be used for the establishment of case scenarios for the initial conditions.

3. Soil-water characteristic curve hysteresis may have an important role in the soil-atmosphere fluxes. There is a need to verify the effect of SWCC hysteresis during cycles of evaporation and precipitation events.

4. Evidences of the influence of cyclic loading in the increase of saturation and in the

decrease of shear strength of railway subgrades can be found in the literature (Miller et al., 2000). Subgrade degradation due to cyclic loading can be included in the proposed framework if a reliable characterisation of the relationship between cyclic load and shear strength is made available.

5. A study of the effect of the track ballast on the moisture changes during alternated dry and wet periods is required. The ballast has little effect in the overall moisture change during infiltration events and the area affected by the ballast cover can be considered small when compared to the whole embankment surface. Therefore, overall embankment stability is not likely to be affected by the presence of the relatively small ballast cover. However, the bearing capacity of the ballast/subgrade system depends on the soil near the ballast and may be affected by the different water regimes that result from the ballast characteristics. It is expected that different evaporation rates should be obtained, since the ballast works as a soil cover system, preventing high rates of evaporation.

6. Plant transpiration should be incorporated into the heat-moisture model. Embankments covered by vegetation may experience considerably larger evaporation rates, directly affecting the stability of the embankments. The incorporation of a transpiration component can be undertaken by considering a sink term in the water mass conservation equations. Tratch et al. (1995) presents in detail how transpiration can be incorporated in the analysis of one-dimensional moisture flow in unsaturated soils.

7. Typical correlation coefficients for unsaturated soil properties were presented in this study. However, the scope of the hazard assessment analyses for hypothetical embankments did not include the consideration of correlation coefficients. A study of the relevance of such correlations is required.

8. The statistical assessment of unsaturated soil properties did not include the characterisation of spatial variability. Spatial averaging may reduce the probability of failure. General guidelines for incorporating spatial variability are described by Phoon and Kulhawy (1999b) and Gitirana Jr. (2000). The available procedures could be readily included in the W-GHA model framework.

9. Unsaturated shear strength conditions at residual saturation conditions are poorly understood. The shear strength at residual saturation conditions is not of great practical significance for most engineering problems. However, a number of noteworthy

engineering problems may benefit from a more detailed understanding of strength conditions at residual saturation conditions. Experimental and theoretical research on the shear strength of unsaturated soils at residual conditions is recommended.

10. FlexPDE has been applied successfully in the solution of a wide range of saturated/unsaturated geotechnical problems. Most models presented to this date using FlexPDE involved uncoupled solution procedures (Pentland et al., 2001, Pham, 2002, Vu, 2003). The results of this study have shown that FlexPDE can be used for the solution of fully coupled unsaturated soil systems. Further studies are recommended, towards the implementation of additional couplings, such as volume change-water flow coupling, air-flow coupling, etc.

References

Adikari, G.S.N. and Cummins, P.J. (1985). "An effective stress slope stability analysis method for dams". *In Proceedings of the 11th International Conference on Soil Mechanics and Foundation Engineering*, San Francisco, 713-718.

Aitchison, G.D., Russam, K., and Richards, B.G. (19658). "Engineering concepts of moisture equilibria and moisture changes in soils, moisture equilibria and moisture changes in soils beneath covered areas". *Review Panel Presentation*, Butterworth, Sydney, Australia, 7-21.

Alfaro, L.D. and Harr, M.E. (1981). "Reliability of soil slopes." *Transp. Res. Rec.*, No. 809.

Ang, A.H-S. and Tang, W.H. (1975). "*Probability Concepts in Engineering Planning and Design*". John Wiley and Sons. New York. 562p.

Applied Decision Analysis LLC. (1998). "*DPL 4.0 – Professional Decision Analysis Software – Academic Edition.*" Price Water House Coopers. Pacific Grove, USA.. 682p.

Arai, K., and Tagyo, K. (1985). "Determination of noncircular slip surface giving the minimum factor of safety in slope stability analysis". *Soils and Foundations*, 25(1): 43-51.

ASTM D 2487-93 (1993). "*Standard Classification of Soils for Engineering Purposes (Unified Soil Classification System)*".

Baker, R. (1980). "Determination of the critical slip surface in slope stability computations". *International Journal for Numerical and Analytical Methods in Geomechanics*, 4, 333-359.

Baker, R. and Garber, M. (1978). "Theoretical analysis of the stability of slopes". *Geotechnique*, 28(4): 395-411.

Barbour, S.L. (1998). "19th Canadian Geotechnical Colloquium: The soil-water characteristic curve: a historical perspective." *Canadian Geotechnical Journal*, Ottawa, 35: 873-894.

Barry, R.G. (1969). "Evaporation and transpiration", in Chorley, R.J. (Ed.), *Water, Earth and Man*, Methuen, London, 169-184.

Bates, D. and Watts, D. (1988). "*Nonlinear Regression Analysis and its Applications.*" John Wiley & Sons, New York, United States of America.

Baver, L.D., Gardner, W.H., and Gardner, W.R. (1972). "*Soil Physics.*" John Wiley & Sons,

Inc., New York, USA, 497p.

Bear, J. (1972). "*Dynamic of Fluids in Porous Media.*" Dover Science, New York, USA, 714p.

Becker, D.E. (1996a). "Eighteenth Canadian Geotechnical Colloquium: Limit states design for foundations. Part I. An overview of the foundation design process." *Canadian Geotechnical Journal*, 33: 956-983.

Becker, D.E. (1996b). "Eighteenth Canadian Geotechnical Colloquium: Limit states design for foundations. Part II. Development for the national building code of Canada." *Canadian Geotechnical Journal*, 33: 984-1007.

Bellman, R. (1957). "*Dynamic programming.*" Princeton University press, Princeton, New Jersey, USA.

Benson, C.H., Daniel, D.E., and Boutwell, G.P. (1999). "Field performance of compacted clay liners." *Journal of Geotechnical and Geoenvironmental Engineering, ASCE*, 125(5): 390-403.

Bishop, A.W. (1952). "*The stability of earth dams*". Ph.D. thesis, University of London, London, UK.

Bishop, A.W. (1955). "The use of the slip circle in the stability analysis of slopes". *Geotechnique*, 5: 7-17.

Blaney, H.F. and Criddle, W.D. (1950). "Determining water requirements in irrigated areas from climatological and irrigation data". *Soil Conservation Service Technical Paper 96*, Soil Conservation Service, U.S. Dept. of Agriculture: Washington, D.C..

Blondeau, F., Mieussens, C., Queyroi, D. D., Levillain, J. P., Peignand, M., and Vogien, M. (1977). "Intrumentation du remblai experimental 'A' de Cubzac-Les-Ponts". *In Proceedings of the International Symposium on Soft Clay*, Bangkok, 119-136.

Boutrup, E. and Lovell, C.W. (1980). "Search technique in slope stability analysis". *Engineering Geology*, 16(1): 51-61.

Bouyoucos, G.J. (1915). "Effect of temperature on the movement of water vapour and capillary moisture in soils." *Journal of Agricultural R.*, 5: 141-172.

Bowles, J.E. (1996). "*Foundations Analysis and Design*." McGraw Hill, New York, NY, 5e., 1175p.

Brito, C.C., Pereira, J.H.F., Gitirana Jr., G.F.N. and Fredlund, D.G. (2004). "Transient stability analysis of a collapsible dam using dynamic programming combined with finite element stress state fields." *In IX International Symposium on Landslides*, Rio de Janeiro, Brazil. 2: 1079-1084.

Brooks, R.H. and Corey, A.T. (1964). "Hydraulic properties of porous media." *Hydrology. Paper No. 3*, Colorado State University, Fort Collins, Colorado, 27.

Bruch, P. (1993). "*A Laboratory Study of Evaporative Fluxes in Homogenous and Layered Soils*." M.Sc. thesis, Dep. of Civil Engrg., University of Saskatchewan, Saskatoon, SK,

Canada.

Buckingham, E. (1907). "*Studies of the movement of soil moisture*." U.S.D.A. Bur. Soils Bull. No. 38.

Bunn, D. (1984). "*Decision Analysis with Multiple Conflicting Objectives*." John Wiley and Sons, New York.

Burger, C.A. and Shackelford, C.D. (2001). "Evaluating dual porosity of pelletized diatomaceous earth using bimodal soil-water characteristic curve functions." *Canadian Geotechnical Journal*, Ottawa, 38: 53-66.

Camapum de Carvalho, J., Guimarães, R.C., and Pereira, J.H.F. (2002). "Courbes de retention d'eau d'un profil d'alteration." *Proc., 3rd Int. Conf. on Unsaturated Soils*, Recife, Brazil, 289-294. (in French)

Carrier, W.D. (1985). "Consolidation parameters derived from index tests." *Géotechnique*, 35(2): 211-213.

Carter, R.K. (1971). "Computer oriented slope stability analysis by method of slices". *Ph.D. thesis*, Purdue University, Indiana, USA.

Carter, J.P., Desai, C.S., Potts, D.M., Schweiger, H.F. and Sloan, S.W. (2000). "Computing and computer modeling in geotechnical engineering". *Proceedings, GeoEng 2000*, Melbourne, Australia, Vol. 1, 1157-1252.

Casagrande, A. (1937). "Seepage through dams." *J. New England Water Works*, 51(2): 295-336.

Cassel, D.K., Nielsen, D.R., and Biggar, J.W. (1969). "Soil-water movement in response to imposed temperature gradients" *Soil Science Society American Procedures*, 33: 493-500.

Cedergren, H.R. (1977). "*Seepage Drainage and Flow Nets*." John Wiley & Sons, New York, 465p.

Celestino, T.B. and Duncan, J.M. (1981). "Simplified search for non-circular slip surfaces". *In Proceedings of the 10th International Conference on Soil Mechanics and Foundation Engineering*, Stockholm, 3, 391-394.

Chang, C., Tung, Y., and Yang, J. (1995). "Evaluation of probability point estimate methods." *Applied Mathematical Modelling*, 19(2): 95-105.

Chen, W.F. (1975). "Limit Analysis and Soil Plasticity". *Developments in Geotechnical Engineering #7*. Elsevier. 638p.

Childs, E.C. and Collins-George, N. (1950). "The permeability of porous materials." *Proceedings Royal Society.* vol. 201A, 392-405.

Chou, P.C. and Pagano, N.J. (1992). "*Elasticity*." Toronto: Van Nostrand, 290p.

Chowdhury, R.N. (1978). "*Slope analysis*". Elsevier Scientific Publishing Company.

Christian, J.T., Ladd, C.C., and Baecher, G.B. (1992). Reliability and probability in stability analysis. ASCE. *Geotechnical Special Publication No 31*. 1071-1111.

Christian, J.T., Ladd, C.C., and Baecher, G.B. (1994). "Reliability Applied to Slope Stability Analysis." *Journal of Geotechnical Engineering*, 120(12): 2180-2207.

Clemen, R.T. (1996). "*Making Hard Decisions*." Duxbury Press, U.S.. 664p.

Dai, S.-H. and Wang, M.-O. (1992). "*Reliability analysis in engineering applications*." Van Nostrand Reinhold, New York.

Dai, Y., Fredlund, D.G., and Stolte, W.J. (1993). "Probabilistic slope stability analysis using deterministic computer software." *Proceeding of the Conference on Probabilistic Methods in Geotechnical Engineering*, 267-275.

Dakshanamurthy, V. and Fredlund, D.G. (1980). "Moisture and air flow in an unsaturated soil." *Proceedings, 4th International Conference on Expansive Soils*, American Society of Civil Engineers, Denver, CO, USA, 1, 514-532.

Dakshanamurthy, V. and Fredlund, D.G. (1981a). "A mathematical model for predicting moisture flow in an unsaturated soil under hydraulics and temperature gradients." *Water Resources Research*, 17(3): 714-722.

Dakshanamurthy, V. and Fredlund, D.G. (1981b). "Predicting of moisture flow and related heaving and shrinking in unsaturated soil continua." *Proceedings of the Eight Canadian Congress of Applied Mechanics*, Monoton, 2, 281-282.

D'Augostino, R.B. and Stevens, M.A. (1986). "*Goodness-of-Fit Techniques*." Marcel Dekker.

de Josselin de Jong, G. (1981). "A variational fallacy". *Geotechniqué*, 31(2), 289-290.

de Natale, J.S. (1991). "Rapid identification of critical slip surface: structure". *Journal of Geotechnical Engineering*, ASCE, 117(10): 1568-1589.

de Vries, D.A. (1963). "Thermal properties of soils." *Physics of Plant Environment*. W.R. van Wijk (ed.), Amsterdam, New Holland, 382p.

de Vries, D.A. (1987). "The theory of heat and moisture transfer in porous media revisited." *International Journal of Heat and Mass Transfer*, 30(7): 1343-1350.

Dempsey, B.J. (1978). "A mathematical model for predicting coupled heat and water movement in unsaturated soil." *International Journal for Numerical and Analytical Methods in Geomechanics*, 2: 19-36.

Digital Equipment Corporation (1999). "*Compaq Visual Fortran, Version 6.1.0*." Copyright 1997-1999. Digital Equipment Corporation.

Ditlevsen, O. (1981). "*Uncertainty Modeling*." McGraw Hill, New York.

Duncan, M. (2000). "Factors of safety and reliability in geotechnical engineering." *Journal of Geotechnical and Geoenvironmental Engineering, ASCE*, 126(4): 307-316.

Durner, W. (1994). "Hydraulic conductivity estimation for soils with heterogeneous pore structure." *Water Resources Research*, 30(2): 211-223.

Eagleson, P.S. (1970). "*Dynamic Hydrology*." McGraw-Hill, Inc., New York, USA, 462p.

Edlefsen, N.E. and Anderson, A.B.C. (1943). "Thermodynamics of Soil Moisture." *Hilgardia*, 15(2): 31-298.

Eschanbach, T.G. (1992). "Spiderplots versus Tornado diagrams for sensitivity analysis." *Interfaces*, 22(6): 40-46.

Evans, D.H. (1967). "An application of numerical techniques to statistical tolerancing." *Technometrics*, vol. 9.

Evans, D.H. (1972). "An application of numerical integration techniques to statistical tolerancing, general distributions." *Technometrics*, vol. 14.

Farias, M.M. and Assis, A.P. (1998). "Uma comparação entre métodos probabilísticos aplicados à estabilidade de taludes." *XI Brazilian Congress on Soil Mechanics and Geotechnical Engineering*. ABMS, Brasília, DF, Brazil. 2: 1305-1313.

Farias, M.M. and Naylor, D.J. (1996). "Safety analysis using finite elements". *Infogeo 96*, São Paulo, Brazil.

Fletcher, R. and Revees, C.M. (1964). "Function minimization by conjugate gradient". *Computer Journal*, 7: 149-154.

Fredlund, D.G. (1964). "*Comparison of soil suction and one-dimensional consolidation characteristics of a highly plastic clay*." M.Sc. thesis, Dept. of Civil Engrg., University of Alberta, Edmonton, AB, Canada.

Fredlund, D.G. (1981). "*SLOPE-II Computer Program*". User's Manual S-10, Geo-Slope Programming Ltd., Calgary, Canada.

Fredlund, D.G. (1984). "Analytical method of slope stability analysis". *In Proceedings of the 4th International Symposium on Landslides*, Toronto, Canada, 1: 229-250.

Fredlund, D.G. (2002). "Use of soil-water characteristic curves in the implementation of unsaturated soil mechanics, keynote address". *Proc., 3rd Int. Conf. on Unsaturated Soils*, March 10-13, Recife, Brazil, Volume 3, 1-23.

Fredlund, D.G. and Dahlman, A.E. (1971). "Statistical geotechnical properties of glacial lake Edmonton sediments." *Proceedings of the 1st International Conference on Applications of Statistics and Probability to Soil and Structural Engineering*, Hong Kong, September 13-16, 1971, 204-228.

Fredlund, D.G. and Hasan, J.U. (1979). "One-dimensional consolidation theory: unsaturated soils." *Canadian Geotechnical Journal*, 16: 521-531.

Fredlund, D.G. and Krahn, J. (1977). "Comparison of slope stability methods of analysis." *Canadian Geotechnical Journal*, 14: 429-439.

Fredlund, D.G. and Morgenstern, N.R. (1977). "Stress state variables for unsaturated soils." *Journal of Geotechnical Engineering Division*, Proceedings, American Society of Civil Engineers, GT5, 103: 447-466.

Fredlund, D.G. and Rahardjo, H. (1993). "*Soil Mechanics for Unsaturated Soil*." John Wiley & Sons, New York, United States of America, 517p.

Fredlund, D. G. and Scoular, R. E. G. (1999). "Using limit equilibrium in finite element slope stability analysis". *Slope Stability Engineering*, Rotterdam, 31-47.

Fredlund, D.G. and Xing, A. (1994). "Equations for the soil-water characteristic curve." *Canadian Geotechnical Journal*, 31(4): 533-546.

Fredlund, D.G., Krahn, J., and Pufahl, D.E. (1981). "The relationship between limit equilibrium slope stability methods." *In Proceedings of the 10th International Conference on Soil Mechanics and Foundation Engineering*, Stockholm, 3: 409-416.

Fredlund, D.G., Morgenstern, N.R., and Widger, R.A. (1978). "The shear strength of unsaturated soils." *Canadian Geotechnical Journal*, 15(3): 313-321.

Fredlund, D.G., Xing, A., and Fredlund, M.D. (1996). "The relationship of the unsaturated shear strength to the soil-water characteristic curve." *Canadian Geotechnical Journal*, 33(3): 440-448.

Fredlund, D.G., Xing, A., and Huang, S. (1994). "Predicting the permeability function for unsaturated soil using the soil-water characteristic curve." *Canadian Geotechnical Journal*, 31(4): 533-546.

Fredlund, M.D. (1999). "*The Role of Unsaturated Soil Property Functions in the Practice of Unsaturated Soil Mechanics.*" Ph.D. Thesis. University of Saskatchewan, Saskatoon, Canada. 292p.

Fredlund, M.D., Fredlund, D.G., and Wilson, G.W. (2000). "An equation to represent grain-size distribution." *Canadian Geotechnical Journal*, Ottawa, 31: 817-827.

Freeze, R.A. (1975). "A stochastic-conceptual analysis of one-dimensional groundwater flow in nonuniform homogeneous media." *Water Resources Research*, 11(5): 725-741.

Freeze, R.A. and Cherry, J.A. (1979). "*Groundwater*." Prentice Hall, Inc., New Jersey, USA, 604p.

Gallopoulos, E., Houstis, E., and Rice, J.R. (1994). "Computer as thinker/doer: problem-solving environments for computational science." *IEEE Computational Science & Engineering*, 1(2): 11-23

Gardner, W.R. (1958). "Laboratory studies of evaporation from soil columns in the presence of a water table." *Soil Science Amer.*, 85: 244.

Geo-Slope International Ltd. (2002a). "*Seep/W User's Manual, Version 5.12*." Copyright 1991-2002. Geo-Slope Ltd., Calgary, Alberta, Canada.

Geo-Slope International Ltd. (2002b). "*Sigma/W User's Manual, Version 5.12*." Copyright 1991-2002. Geo-Slope Ltd., Calgary, Alberta, Canada.

Geo-Slope International Ltd. (2002c). "*Slope/W User's Manual, Version 5.12*." Copyright 1991-2002. Geo-Slope Ltd., Calgary, Alberta, Canada.

Geo-Slope International Ltd. (2002d). "*Temp/W User's Manual, Version 5.12*." Copyright 1991-2002. Geo-Slope Ltd., Calgary, Alberta, Canada.

Giam, P.S.K., (1989). "*Improved methods and computational approaches to geotechnical stability analysis*". Ph.D. thesis, Monash University, Melbourne, Australia.

Gitirana Jr., G.F.N. (1999). "*Numerical Modelling for the Coupled Hydro-Mechanical Behaviour of Unsaturated Soils Considering Elastic and Critical State Models.*" Pub. G.DM 063A/99, Dept. de Eng. Civil, UnB, Brasília, DF, 126p. (in Portuguese)

Gitirana Jr., G.F.N. (2000). "*Special Topics in Geostatistics: Methods of Description of Data and Estimation*." University of Saskatchewan, Saskatoon, Canada, 63p.

Gitirana Jr., G.F.N. and Fredlund, D.G. (2003a). "Transient embankment stability analysis using dynamic programming." *Proceedings of the 56th Canadian Geotechnical Conference*, Winnipeg, MB, Canada. 1: 808-814.

Gitirana Jr., G.F.N. and Fredlund, D.G. (2003b). "Keynote address: From experimental evidences towards the assessment of weather-related railway embankment hazards." *In From Experimental Evidences Towards Unsaturated Soil Practice*, Weimar, Germany. 21-52.

Gitirana Jr., G.F.N. and Fredlund, D.G. (2004). "Soil-water characteristic curve equation with independent properties." *Journal of Geotechnical and Geoenvironmental Engineering, ASCE*, 130(2): 209-212.

Gitirana Jr., G.F.N., Peixoto, R.J., Pereira, J.H.F., and Bezerra, L.M. (2001). "Mechanical behaviour model for the collapsible clay of Brasilia." *Proc., 4th Brazilian Symp. on Unsat. Soils*, Mar. 22-23, P. Alegre, Brazil, 11-28.

Greco, V.R. (1988). "Numerical methods for locating the critical slip surface in slope-stability analysis." *In Proceedings of the 6th International Conference on Numerical Methods in Geomechanics*, Innsbruck, 1219-1223.

Greco, V.R. (1996). "Efficient Monte-Carlo technique for locating critical slip surface." *Journal of Geotechnical Engineering*, ASCE, 122(7): 517-525.

Green, W.H. and Ampt, G.A. (1911). "Studies on soil physics. Part 1. The flow of air and water through soils." *Journal of Agricultural Science*, 4(1): 1-24.

Gui, S., Zhang, R., Turner, J.P., and Xue, X. (2000). "Probabilistic slope stability analysis with stochastic soil hydraulic conductivity." *Journal of Geotechnical and Geoenvironmental Engineering, ASCE*, 126(1): 1-9.

Gurr, C.G., Marshall, T.J., and Hutton, J.T. (1952). "Movement of water in soil due to a temperature gradient." *Soil Science*, 74(5): 335-345.

Hahn, G.J. and Shapiro, S.S. (1967). "*Statistical Models in Engineering*." John Wiley & Sons, New York.

Hammersley, J.M. and Handscomb, D.C. (1964). "*Monte Carlo Method*." John Wiley & Sons, New York.

Hammitt, G.M. (1966). "Statistical analysis of data from a comparative laboratory test program sponsored by ACIL." Miscellaneous Paper 4-785, U.S. Army Engineering Waterways Experiment Station, Corps of Engineers.

Hargreaves, G.H. and Samani, Z.A. (1985). "Reference crop evapotranspiration from temperature" *Applied Engineering Agriculture*, 1: 96-99.

Harr, M.E. (1987). "*Reliability-Based Design in Civil Engineering*." John Wiley and Sons. New York. 291p.

Harr, M.E. (1989). "Probabilistic estimates for multivariate analyses." *Applied Mathematical Modelling*, 13: 313-318.

Herrero, O.R. (1980). "Universal compression index equation." *Journal of Geotechnical and Geoenvironmental Engineering, ASCE*, GT11, 106: 1179-1200.

Hillel, D. (1971). "*Soil and Water, Physical Principles and Processes*." Academic Press, New York, USA, 288p.

Hillel, D. (1982). "*Introduction to soil physics*." Academic Press, Inc., San Diego, USA, 365p.

Hoeksema, R.J. and Kitanidis, P.K. (1985). "Analysis of the spatial structure of properties of selected aquifers." *Water Resources Research*, 21(4): 563-572.

Holmes, R.M. (1961). "Estimation of soil moisture content using evaporation data." *Proc. of Hydrology Symposium, No. 2 Evaporation*, Queen's Printer, Ottawa, 184-196.

Horton, R.E. (1933). "The role of infiltration in the hydrological cycle." *Trans. American Geophys. Union*, 14: 446-460.

Huang, S., Barbour, S.L., and Fredlund, D.G. (1998). "Development and verification of a coefficient of permeability function for a deformable unsaturated soil." *Canadian Geotechnical Journal*, 35: 411-425.

Isaaks, E.H. and Srivastava, R.M. (1989). "*An Introduction to Applied Geostatistics*." Oxford University Press, 561p.

IUGS Working Group on Landslides, Committee on Risk Assessment (1997). "Quantitative risk assessment for slopes and landslides". *Landslide Risk Assessment*, Cruden and Fell (eds), Balkema, Rotterdam, Netherlands, 3-14.

Jackson, R.D., Kimball, B.A., Reginato, R.J., Idso, S.B., and Nakayama, F.S. (1975). "Heat and water transfer in a natural soil environment. Heat and mass transfer in the biosphere, 1." *Transfer process in plant environment*, Scripta Book Company, Washington, D.C. 67-76.

Jaky, J. (1944). "The coefficient of earth pressure at rest." *Journal of the Society of Hungarian Architects and Engineers*. Budapest, Hungary. 355-358.

Jame, Y. and Norum, D.I. (1980). "Heat and mass transfer in a freezing unsaturated porous medium." *Water Resources Research*, 16(4): 811-819.

Janbu, N. (1954). "Stability analysis of slopes with dimensionless parameters". *Harvard Soil*

Mechanics Series, 46, 811.

Jensen, M.E and Haise, H.R. (1963). "Estimating evapotranspiration from solar radiation." *Proceeding of the American Society of Civil Engineers, Journal of Irrigation and Drainage*, IR4, 89: 15-41.

Johansen, O. (1975). "*Thermal Conductivity of Soils*." Ph.D. Thesis, University of Throndeim, Norway.

Joshi, B. (1993). "*A finite element model for the coupled flow of moisture and heat in soils under atmospheric forcing*." M.Sc. Thesis, University of Saskatchewan, Saskatoon, Saskatchewan, Canada.

Jury, W.A. and Miller, E.E. (1974). "Measurement of the transport coefficients for coupled flow of heat and moisture in a medium sand." *Soil Science Society American Proceedings*, 38: 551-557.

Kaye, G.W.C. and Laby, T.H. (1973). "*Tables of Physical and Chemical Constants*." 14th Ed., Longman, 386p.

Kimball, B.A., Jackson, R.D., Reginato, R.J., Nakayama, F.S., and Idso, S.B. (1976). "Comparison of field-measures and calculated soil-heat fluxes." *Soil Science Society of America Proceedings*, 40(1): 18-25.

Koorevar, P., Menelik, G., and Dirksen, C. (1983). "*Elements of Soil Physics*." Elsevier, Amsterdam, The Netherlands, 230p.

Kopacsy, J. (1957). "Three-dimensional stress distribution and slip surfaces in earth works at rupture". *In Proceedings of the 4th International Conference on Soil Mechanics and Foundation Engineering*, London, 1: 339-342.

Kostiakov, A.N. (1932). "On the dynamics of the coefficient of water percolation in soils and the necessity of studying it from dynamic point of view for purposes of amelioration." *Trans. 6th Comm. Int. Soc. Soil Sci. Russian Pt.* A15-21.

Krahn, J. (2003). "The 2001 R.M. Hardy Lecture: The limits of limit equilibrium analysis." *Canadian Geotechnical Journal*, 40: 643-660.

Krahn, J. and Fredlund, D.G. (1983). "Variability in the engineering properties of natural soil deposits". *In Proceedings of the 4th International Conference on Applications of Statistics and Probability in Soil and Structural Engineering*, University of Firenze, Italy.

Krahn, J., Fredlund, D.G., and Klassen, M.J. (1989). "Effect of soil suction on slope stability at Notch Hill." *Canadian Geotechnical Journal*, 26: 269-278.

Kulhawy, F.H. (1969). "*Finite element analysis of the behavior of embankments*". Ph.D. thesis, University of California, Berkley, California, USA.

Kulhawy, F.H. (1992). "On the evaluation of soil properties." *ASCE Geotech. Spetial Publication*, No. 31, 95-115.

La Rochelle, P. (1960). "*The short term stability of slopes in London clay*". Ph.D. thesis,

University of London, London, UK.

La Rochelle, P., Trak, B., Tavenas, F., and Roy, M. (1974). "Failure of test embankments on a sensitive champlain clay deposit". *Canadian Geotechnical Journal*, 11, 142-164.

Lacasse, S. and Nadim, F. (1997). "Uncertainties in characterizing soil properties." *Publication No. 201*, Norwegian Geotechnical Institute, Olso, Norway, 49-75.

Ladd, C.C. (1983). "Geotechnical exploration in clay deposits with emphasis on recent advances in laboratory and in situ testing and analysis of data scatter." *Journal of Civil and Hydraulic Engineering*, Taiwan, 10(3): 3-35.

Lai, S., Tiedje, J.M., and Erickson, A.E. (1976). "In situ measurement of gas diffusion coefficient in soils." *Soil Science Society of America Proceedings*, 40(l): 3-6.

Lam, L., Fredlund, D.G., and Barbour, S.L., (1987). "Transient seepage model for saturated-unsaturated soil systems: a geotechnical engineering approach." *Canadian Geotechnical Journal*, 24: 565-280

Leong, E.C. and Rahardjo, H. (1997). "Review of soil-water characteristic curve equations." *Journal of Geotechnical and Geo-environmental Engineering*, ASCE, New York, 123(12): 1106-1117.

Leshchinsky, D. (1990). "Slope stability analysis: Generalized approach". *Journal of Geotechnical Engineering*, ASCE, 116(5): 851-867.

Leshchinsky, D. and Huang, C. C. (1992a). "Generalized slope stability analysis: Interpretation, modification and comparison". *Journal of Geotechnical Engineering*, ASCE, 118(10): 1559-1567.

Leshchinsky, D. and Huang, C. C. (1992b). "Generalized three-dimensional slope stability analysis". *Journal of Geotechnical Engineering*, ASCE, 118(11): 1748-1764.

Li, K.S. and White, W. (1987). "Rapid evaluation of the critical slip surface in slope stability problems". *International Journal for Numerical and Analytical Methods in Geomechanics*, 11: 449-473.

Li, K.S. (1991). "Point estimate methods in geotechnics." *Computational Mechanics*, Cheung, Lee, and Leung (eds), 827-832.

Li, K.S. (1992). "Point estimate method for calculating statistical moments." *Journal of Engineering Mechanics*, 118(7): 1506-1511.

Lind, N.C. (1983). "Modelling of uncertainty in discrete dynamical systems." *Applied Mathematical Modelling*, 7: 146-152.

Linsley, R.K., Kohler, M.A., and Pulhus, J.L.H. (1949). "*Applied Hydrology*." McGraw-Hill, New York, 689p.

Linsley Jr, R.K., Kohler, M.A., and Paulhus, J.L.H. (1958). "*Hydrology for Engineers*." McGraw-Hill, New York, USA. 340p.

Lumb, P. (1966). “The variability if natural soils.” *Canadian Geotechnical Journal*. 3(2): 74-97.

Lumb, P. (1970). “Safety Factors and the Probability Distribution of Soil Strength.” *Canadian Geotechnical Journal*, 7(3): 225-242.

Mackay, C.H. and Bunce, C. (2001). “Personal communication.” Canadian Pacific Railway. Engineering Div.

Marjerison, B. (2001). “Measurement of matric suction in thin membrane surface Highways using thermal conductivity sensors.” M.Sc. Thesis. University of Saskatchewan, Saskatoon, SK, Canada.

Mayne, P.W. and Kulhawy, F.H. (1982). “K_0-OCR relationship in soil.” *Journal of Geotechnical and Geoenvironmental Engineering, ASCE*, GT6, 108: 851-872.

Microsoft Corporation (2001). “Microsoft® Excel 2002” Copyright 1985-2001. Copyright© Microsoft Corporation.

Miller, G.A., The, S.Y., Li, D., and Zaman, M.M. (2000). “Cyclic shear strength of soft railroad subgrade.” *Journal of Geotechnical and Geoenvironmental Engineering, ASCE*, 126(2): 139-147.

Milly, P.C.D. (1984). “A linear analysis of thermal effects on evaporation from soil.” *Water Resources Research*, 20(8): 1075-1085.

Minitab Inc. (2000). “*Minitab User's Manual, Version 13*.” Copyright 2000. Minicab Inc. State College, PA, USA.

Mishra, S., Parker, L.C., and Singhal, N. (1989). “Estimation of soil hydraulic properties and their uncertainty from particle size distribution data.” *Journal of Hydrology*, 108: 1-18.

Mitchell, J.K. (1976). “*Fundamentals of Soil Behavior*.” John-Wiley & Sons, Inc., New York.

Monteith, J.L. (1965). “Evaporation and the environment.” *In the movement of water in living organisms*, XIX Symposium Soc. Exp. Biol., Swansea, Cambridge, University Press. 19: 205-234

Morgenstern, N.R. and Price, V.E. (1965). “The analysis of the stability of generalised slip surfaces.” *Géotechnique*, 15: 79-93.

Mualen, Y. (1976). “A new model for predicting the hydraulic conductivity of unsaturated porous media.” *Water Resources Research*, 12: 513-522.

Nelder, J.A. and Mead, R. (1965). “A simplex method for function minimization”. *Computer Journal*, 7: 308-313.

Nguyen, T.M.T. (1999). “Solution of saturated/unsaturated seepage problems using a general partial differential equation solver.” *M.Sc. thesis*, University of Saskatchewan, Saskatoon, Canada.

Nguyen, V.U. (1985). “Determination of critical slope failure surfaces.” *Journal of Geotechnical Engineering*, ASCE, 111(2): 238-250.

Nielsen, D.R., Biggar, J.W., and Erh, K.T. (1973). "Spatial variability of field-measured soil-water properties." *Hilgardia*, 42(7): 215-260.

Office of Critical Infrastructure Protection and Emergency Preparedness. (2001). "*Natural Hazards of Canada: Landslides and Snow Avalanches Map*." Government of Canada.

Oke, T.R. (1970). "Turbulent transport near the ground in stable conditions." *J. Applied Meteorology*, 8: 778-786.

Padilla, J.D. and Vanmarcke, E.H. (1974). "Settlement of structures on shallow foundations: a probabilistic analysis." *Res. Pes. R74-9*, MIT, Cambridge, Mass, USA.

Palisade Corporation (2004). "*@Risk 4.5 – Risk Analysis Software*." Palisade Corporation. Newfield, NY, USA.

Panchalingam, G. and Harr, M.E. (1994). "Modelling of many correlated and skewed random variables." *Applied Mathematical Modelling*, 18: 635-640.

PDE Solutions Inc. (2003). "*FlexPDE 3.10 - Reference Manual*." Antioch, CA, USA.

Pegg, R.K. and Ward, R.C. (1972). "Evapotranspiration from a small clay catchment." *Journal of Hydrology*, 15: 149-165.

Penman, H.L. (1948). "Natural evapotranspiration from open water, bare soil and grass." *Proc. R. Soc. London Ser. A*. 193: 120-145.

Pentland, J.S., Gitirana Jr., G.F.N., and Fredlund, D.G. (2001). "Use of a general partial differential equation solver for solution of mass and heat transfer problems in geotechnical engineering." *4th Brazilian Symposium on Unsaturated Soils*, *NSAT 2001*, Porto Alegre, RS, Brazil, 29-45.

Pereira, J.H.F. (1996). "*Numerical analysis of the mechanical behavior of collapsing earth dams during first reservoir filling*." Ph.D. thesis, Department of Civil Engineering, University of Saskatchewan, Saskatoon, Canada, 449p.

Petrov, I.P. (1968). "*Variational methods in optimum control theory*". New York: Academic Press.

Pham, Q.H. (2002). "*An engineering model of hysteresis for soil-water characteristic curves.*" M.Sc. Thesis. University of Saskatchewan, Saskatoon, SK, Canada, 190p.

Pham, H.T.V. (2002). "*Slope stability analysis using dynamic programming combined with finite element stress analysis.*" M.Sc. Thesis. University of Saskatchewan, Saskatoon, SK, Canada, 200p.

Pham, H.T.V., Fredlund, D.G., and Gitirana Jr., G.F.N. (2001). "Slope stability analysis using dynamic programming combined with finite element stress analysis." *In International Conference on Management of the Land and Water Resources – MLWR*. Hanoi, Vietnam. 1: 107-114.

Philip, J.R. (1957). "The theory of infiltration: the infiltration equation and its solution." *Soil Science*, 83: 345-357.

Philip, J.R. and de Vries, D.A. (1957). "Moisture movement in porous materials under temperature gradients." *Transactions, American Geophysical Union*, 38(2): 222-232.

Phoon, K.-K. and Kulhawy, F.H. (1999a). "Characterization of geotechnical variability." *Canadian Geotechnical Journal*, 36: 612-624.

Phoon, K.-K. and Kulhawy, F.H. (1999b). "Evaluation of geotechnical property variability." *Canadian Geotechnical Journal*, 36: 625-639.

Priestley, C.H.B. and Taylor, R.J. (1972). "On the assessment of surface heat flux and evaporation using large-scale parameters." *Monthly Weather Review*, 100: 81-92.

Ramamurthy, T., Narayan, C.G.P., and Bhatkar, V.P. (1977). "Variational method for slope stability analysis". *In Proceedings of the 9th International Conference on Soil Mechanics and Foundation Engineering*, Tokyo, 2: 139-142.

Reddy, J.N. (1993). "*An Introduction to the Finite Element Method*." McGraw-Hill, New York, United States of America, 2e, 684p.

Resendiz, D. (1974). "Accuracy of equilibrium slope stability analysis". *Journal of the Soil Mechanics and Foundations Division*, ASCE, 967-970.

Revilla, J., and Castillo, E. (1977). "The calculus of variations applied to stability of slopes". *In Proceedings of the Earth and Earth-Supported Structure*, ASCE, New York, 1: 817-836.

Richards, L.A. (1928). "The usefulness of capillary potential to soil moisture and plant investigators." *J. Agriculture Res.*, 37: 719-742.

Richards, L.A. (1931). "Capillary conduction of liquids through porous mediums." *Physics*, 1: 318-333.

Ritchie, J.T. (1972). "Model for predicting evapotranspiration from a row crop with incomplete cover." *Water Resources Research*, 8: 1204-1213.

Rohwer, C. (1931). "Evaporation from free water surfaces." *Technical Bulletin no. 271*. U.S. Dept. of Agriculture, Washington, D.C.

Rollins, R.L., Spangler, and M.G., Kirkham, H. (1954). "Movement of soil moisture under a thermal gradient.." *Highway Res. Board Proc.*, 33: 492-508.

Rosenblueth, E. (1975). "Point estimates for probability moments." *Proc. National Academy of Sciences*, 72(10): 3812-3814.

Rosenblueth, E. (1981). "Two-point estimates in probabilities." *Applied Mathematical Modelling*, 5: 329-335.

Rubinstein, A. (1981). "Simulation and the Monte Carlo Method." John Wiley and Sons, New York.

Sandroni, S.S. and Sayão, A.S.F. (1993). "The use of relative probability of failure in the design of open pit mine slopes." *Innovative Mine Design for the 21st Century*. Balkema, Rotterdam, The Netherlands. 21-24.

Scoular, R.E.G. (1997). "Limit equilibrium slope stability analysis using a stress analysis". *M.Sc. thesis*, University of Saskatchewan, Saskatoon, Canada.

Schultze, E. (1971). "Frequency distributions and correlations of soil properties." *Proceedings of the First International Conference on Applications of Statistics and Probabilistic in Soil and Structure Engineering*, Hong Kong. 371-387.

Sillers, W.S. (1997). "*The mathematical representation of the soil-water characteristic curve*." M.Sc. thesis, Dept. of Civil Engrg., University of Saskatchewan, Saskatoon, SK, Canada.

Sillers, W.S., Fredlund, D.G., and Zakerzadeh, N. (2001). "Mathematical attributes of some soil-water characteristic models." *Geotech. and Geol. Eng*., 19: 243-283.

Smith, J.E. (1993). "Moment methods for decision analysis." *Management Science*, The Institute of Management Science, 39(3): 340-358.

Smith, W.O. (1943). "Thermal transfer of moisture in soils." *Trans. Amer. Geophys. Union*, 24: 511-523.

Soil Survey Staff (1975). "Soil taxonomy: A basic system of soil classification for making and interpreting surveys." *USDA-SCS Agriculture Handbook*, U.S. Gov. Print. Office, Washington, D.C..

SoilVision Systems Ltd. (2003). "*SoilVision User's Guide – a Knowledge-based System for Geotechnical Engineers. Version 1.0*." Saskatoon, SK, Canada.

Sophocleous, M.A. (1979). "Analysis of water and heat flow in unsaturated-saturated porous media." *Water Resources Research*, 15(5): 1195-1206.

Spencer, E. (1967). "A method for analysis of the stability of embankments assuming parallel interslice forces". *Geotechnique*, 17(1): 11-26.

Spendley, N., Hext, G.R., and Himsworth, F.R. (1962). "Sequential application of simplex design in operations and evolutionary operations". *Technometrics*, 14(4): 441-459.

Spraghe, R.H. and Carlson, E.D. (1982). "*Building Effective Decision Support Systems*." Prentice-Hall, New Jersey, 329p.

Talesnik, M. and Baker, R. (1984). "Comparison of observed and calculated slip surface in slope stability calculation". *Canadian Geotechnical Journal*, 21: 713-719.

Tan, C.P., Donald, I.B., and Melchers, R.E. (1993). "Probabilistic slip circle analysis of earth and rockfill dams." *Proceedings of the Conference on Probabilistic Methods in Geotechnical Engineering*, Camberra, Australia. 281-288.

Tan, E., Fredlund, D.G., and Gitirana Jr., G.F.N. (2004). "Comparison of correction method for factors influencing thermal conductivity suction sensors." *In Proceedings of the 5th Brazilian Symposium on Unsaturated Soils*, São Carlos, SP, Brazil, 1: 127-132.

Terzaghi, K. (1943). "*Theoretical Soil Mechanics*." 14th printing, John Wiley & Sons, Inc., New York, USA, 510p.

Thornthwaite, C.W. (1948). "An approach toward a rational classification of climate." *The*

Geographical Review, 38: 55-94.

Thornthwaite, C.W. and Holzman, B. (1942). "Measurement of evaporation from land and water surface." *USDA Technical Bulleting*, 817: 1-75.

Transportation Safety Board. (1994). "A Special Study of Main Track Derailments." *Transportation Safety Board Press*, Gatineau, Quebec, Canada.

Transportation Safety Board. (1995). "Derailment CN North America Train No. 336-KP-24 Mile 89.7, Kinghorn Subdivision Orient Bay, Ontario". TSB Report Number R94W0101. *Transportation Safety Board Press*, Gatineau, Quebec, Canada.

Transportation Safety Board. (1997). "Interim railway safety recommendations concerning the identification and detection of railway roadbed instability". TSB Recommendation # 05/97. *Transportation Safety Board Press*, Gatineau, Quebec, Canada.

Transportation Safety Board. (1998a). "26 March 1997 – Railway Occurrence Report Derailment Canadian National Train No. Q-102-51-26 Mile 106.15, Ashcroft Subdivision Conrad, British Columbia". Report Number R97V0063. *Transportation Safety Board Press*, Gatineau, Quebec, Canada.

Transportation Safety Board. (1998b). "07 April 1997 – Subgrade Failure Canadian Pacific Railway Train No. 935-06 Mile 44.8, Parry Sound Subdivision Pointe au Baril, Ontario". Report Number R97T0097. *Transportation Safety Board Press*, Gatineau, Quebec, Canada.

Transportation Safety Board. (1998c). "06 May 1997 - Railway Occurrence Report Main-track Derailment Canadian National Train No. E-283-21-05 Mile 34.55, Kingston Subdivision Coteau-du-Lac, Quebec". Report Number R97D0113. *Transportation Safety Board Press*, Gatineau, Quebec, Canada.

Transportation Safety Board. (2000a). "31 May 1998 - Main Track Derailment Canadian Pacific Railway Freight Train No. 981-31 Mile 59.1, Nelson Subdivision, Creston, British Columbia". Report Number R98V0100. *Transportation Safety Board Press*, Gatineau, Quebec, Canada.

Transportation Safety Board. (2000b). "26 June 1999 — Main Track Subgrade Failure / Derailment, Canadian Pacific Railway, Freight Train No. 474-25, Mile 5.3, Keewatin Subdivision, Keewatin, Ontario". Report Number R99W0133. *Transportation Safety Board Press*, Gatineau, Quebec, Canada.

Transportation Safety Board. (2001). "Annual statistics – 2001." *Transportation Safety Board Press*, Ottawa, Canada.

Tratch, D.J., Wilson, G.W., and Fredlund, D.G. (1995). "An introduction to analytical modeling of plant transpiration for geotechnical engineers." *48th Canadian Geotechnical Conference*, Vancouver, Canada, 2: 771-780.

Tsai, C.W. and Franceschini, S. (2003). "An improved point estimate method for probabilistic risk assessment." *World Water and Environmental Resources Congress*, 427-433.

Ugai, K, and Leshchinsky, D. (1995). "Three-dimensional limit equilibrium and finite element analyses: A comparison of results". *Soils and Foundations*, Japanese Geotechnical Society,

35(4): 1-7.

Vanapalli, S.K., Fredlund, D.G., Pufahl, D.E., and Clifton, A.W. (1996). "Model for the prediction of shear strength with respect to soil suction." *Canadian Geotechnical Journal*, Ottawa, 33: 379-392.

Vanmarcke, E.H. (1974). "Decision analysis in dam safety monitoring." *Proceedings Engineering Foundation Conf. on the Safety of Small Dams*, (Henniker, N.H.), Aug.

Veihmeyer, F.J. (1964). "*Evapotranspiration. Handbook of Applied Hydrology*." V.T. Chow (ed.), McGraw-Hill, Inc., New York, USA, 11.1-11.38.

Vu, H.Q. (2003). "*Coupled and uncoupled solution for heave analysis.*" Ph.D. Thesis. University of Saskatchewan, Saskatoon, SK, Canada, 290p.

White, N.F., Duke, H.R., and Sunada, D.K. (1970). "Physics of desaturation in porous materials." *J. of the Irrigation and Drainage Div.*, ASCE, New York, 96(IR2): 165-191.

Whitman, R.V. (1984). "Evaluating calculated risk in geotechnical engineering." *ASCE Geotechnical Engineer Journal*. 110(2): 145-189.

Whitman, R.V. (2000). "Organizing and evaluating uncertainty in geotechnical engineering." *Journal of Geotechnical and Geoenvironmental Engineering, ASCE*, 126(7): 583-593.

Wilson, G.W. (1990). "*Soil Evaporative Fluxes for Geotechnical Engineering Problems*." PhD Thesis, Department of Civil Engineering, University of Saskatchewan, Saskatoon, Canada, 464p.

Wilson, G.W., Barbour, S.L., and Fredlund, D.G. (1997). "The effect of soil suction on evaporative fluxes from soil surfaces." *Canadian Geotechnical Journal*, 34(1): 145-155.

Wilson, G.W., Fredlund, D.G., and Barbour, S.L. (1994). "Coupled soil-atmosphere modeling for soil evaporation." *Canadian Geotechnical Journal*, 31(2): 151-161.

Wright, S.G. (1969). "*A study of slope stability and the undrained shear strength of clay shales*". Ph.D. thesis, University of California, Berkley, California, USA.

Wright, S.G., Kulhawy, F., and Duncan, J.M. (1973). "Accuracy of equilibrium slope stability analysis". *Journal of Soil Mechanics and Foundations Division*, ASCE, 99(SM10): 783-791.

Yamagami, T. and Ueta, Y. (1988a). "Search for noncircular slip surfaces by the Morgenstern-Price method". *In Proceedings of the 6th International Conference on Numerical Methods in Geomechanics*, Innsbruck, 1335-1340.

Yamagami, T. and Ueta, Y. (1988b). "Search for critical slip lines in finite element stress field by dynamic programming." *In Proceedings of the 6th International Conference on Numerical Methods in Geomechanics*, Innsbruck, 1347-1352.

Zapata, C.E., Houston, W.N., Houston, S.L., and Walsh, K.D. (2000). "Soil-water characteristic curve variability". *Advances in Unsaturated Geotechnics*, Denver, USA, Aug. 5-8, 84-123.

Zienkiewicz, O.C., Humpheson, C., and Lewis, R.W. (1975). "Associated and non-associated

visco-plasticity and plasticity in Soil Mechanics". *Geotechnique*, 25(4): 671-689.

Zhou, D.Y. (2001). "A method for locating critical slip surfaces in slope stability analysis". *Canadian Geotechnical Journal*, 38: 328-337.

Zou, J.Z., Williams, D.J., and Xiong, W.L. (1995). "Search for critical slip surfaces based on finite element method." *Canadian Geotechnical Journal*, 32: 233-246.

Appendix A

Probability Density Functions

A.1 INTRODUCTION

Two types of continuous probability density function are used in this thesis to represent different parameters of the W-GHA model. The functions used are the normal and lognormal distributions. This appendix presents these two probability density functions. Integration tables are not presented herein and can be found in statistics books. The integrations required by the W-GHA model have been performed using functions available in Microsoft® Excel 2002.

A.1.1 *Normal Distribution*

The normal distribution and its cumulative form are represented by the following equations:

$$f(x) = \frac{1}{\sigma\sqrt{2\pi}} e^{-\frac{(x-\mu)^2}{2\sigma^2}} \qquad (A.1)$$

$$d(x) = \frac{1}{2}\left[1 + erf\left(\frac{x-\mu}{\sigma\sqrt{2}}\right)\right] \qquad (A.2)$$

where:

$f(x)$	=	probability density function of x;
x	=	parameters being modelled;
σ, μ	=	Parameters of the normal distribution;
erf	=	is the error function.

The parameters of the normal distribution can be estimated using the following equations:

$$\begin{aligned} \mu &= E[X] \\ \sigma &= \sqrt{V[X]} \end{aligned} \tag{A.3}$$

A.1.2 *Lognormal Distribution*

The lognormal distribution and its cumulative form are represented by the following equations:

$$f(x) = \frac{1}{Sx\sqrt{2\pi}} e^{-\frac{(\ln(x)-M)^2}{S\sqrt{2}}} \tag{A.4}$$

$$d(x) = \frac{1}{2}\left[1 + erf\left(\frac{\ln(x) - M}{S\sqrt{2}}\right)\right] \tag{A.5}$$

The parameters *M* and *S* are not the mean and standard deviation of *x* but of *ln*(*x*). The mean, and variance of *ln*(*x*) are given by:

$$\begin{aligned} E(\ln[x]) &= M \\ Var(\ln[x]) &= S^2 \end{aligned} \tag{A.6}$$

The parameters *M* and *S* can be estimated based on the moments of *x*, using the following equations:

$$\begin{aligned} M &= \ln\left(\frac{E[x]^2}{\sqrt{Var[x] + E[x]^2}}\right) \\ S &= \sqrt{\ln\left(\frac{Var[x] + E[x]^2}{E[x]^2}\right)} \end{aligned} \tag{A.7}$$

Tables A.1 and A.2 present a summary of equations for the raw and central moments of the normal and lognormal distribution and a summary of the most important probabilistic measures associated with the normal and lognormal distributions; namely, the mean, variance, skewness, and kurtosis. These equations are required in order to implement the point estimate solution presented in this thesis.

Table A.1 Raw and central moments for the normal and lognormal distributions.

Distribution	Raw moments	Central moments
Normal	$\mu'_0 = 1$	$\mu_0 = 1$
	$\mu'_1 = \mu$	$\mu_1 = 0$
	$\mu'_2 = \mu^2 + \sigma^2$	$\mu_2 = \sigma^2$
	$\mu'_3 = \mu\left(\mu^2 + 3\sigma^2\right)$	$\mu_3 = 0$
	$\mu'_4 = \mu^4 + 6\mu^2\sigma^2 + 3\sigma^4$	$\mu_4 = 3\sigma^4$
	$\mu'_5 = \mu\left(\mu^4 + 10\mu^2\sigma^2 + 15\sigma^4\right)$	$\mu_5 = 0$
Log Normal	$\mu'_0 = 1$	$\mu_0 = 1$
	$\mu'_1 = e^{M+S^2/2}$	$\mu_1 = 0$
	$\mu'_2 = e^{2\left(M+S^2\right)}$	$\mu_2 = e^{2M+S^2}\left(e^{S^2} - 1\right)$
	$\mu'_3 = e^{3M+9S^2/2}$	$\mu_3 = e^{3M+3S^2/2}\left(e^{S^2} - 1\right)^2\left(e^{S^2} + 2\right)$
	$\mu'_4 = e^{4M+8S^2}$	$\mu_4 = e^{4M+2S^2}\left(e^{S^2} - 1\right)^2\left(e^{4S^2} + 2e^{3S^2} + 3e^{2S^2} - 3\right)$
	$\mu'_5 = e^{5M+25S^2/2}$	$\mu_5 = e^{5M+5S^2/2}\left(e^{10S^2} - 5e^{6S^2} + 10e^{3S^2} - 10e^{S^2} + 4\right)$

Table A.2 Probabilistic measures for the normal and lognormal distributions.

Distribution	Variable	Equation
Normal	Mean	$E[x] = \mu$
	Variance	$Var[x] = \sigma^2$
	Skewness $(\gamma_1 = \mu_3 / \mu_2^{3/2})$	$\gamma_1[x] = 0$
	Kurtosis excess $(\gamma_2 = \mu_4 / \mu_2^2 - 3)$	$\gamma_2[x] = 0$
Log Normal	Mean	$E[x] = e^{M+S^2/2}$
	Variance	$Var[x] = e^{2M+S^2}\left(e^{S^2} - 1\right)$
	Skewness $(\gamma_1 = \mu_3 / \mu_2^{3/2})$	$\gamma_1[x] = \sqrt{e^{S^2} - 1}\left(2 + e^{S^2}\right)$
	Kurtosis excess $(\gamma_2 = \mu_4 / \mu_2^2 - 3)$	$\gamma_2[x] = e^{4S^2} + 2e^{3S^2} + 3e^{2S^2} - 6$

Appendix B

FlexPDE Script Files

B.1 MOISTURE FLOW

```
TITLE 'Uncoupled moisture flow'

SELECT
        errlim = 0.0001
        prefer_stability = on

VARIABLES
        uw(0.01)

DEFINITIONS
        width = 0.5 !0.004,  slic = 0.02,  height = 10.0
        bss = 0.01
        Sink = 0.0

        {-------------------------
        *** initial values ***
        -------------------------}
        uw0 = (wt-y)*9.81       ! uw(at y) = (wt elevation - y)*9.81
        Ts0 = 38.0              ! oC
        suc = if uw < -1e6 then 1e6 else if uw > -bss then bss else -uw
        suc0 = if uw0 < -1e6 then 1e6 else if uw0 > -bss then bss else -uw0

        {-------------------------------------------------
        *** Required physical constants ***
        -------------------------------------------------}
        gww = 9.81      !Unit weight of water, kN/m^3
        ga = 9.81       !Gravity, m/s^2
        rww = 1000.0    !Density of water, kg/m^3
        tsb = 5.67e-8   !Stefan-Boltzman constant, W/m^2/K^4
        neta = 0.27     !psychrometric constant, mmHg/oF
```

```
uatm = 101.325 !Total atmospheric pressure, kPa
Wv = 0.018016 !Molecular weight of water, kg/mol
ugc = 8.314       !Universal gas constant, J/(mol.K)
minute = 60, hour = 60*minute, day = hour*24
h = uw/gww+y  !Total Head
gws = 2.65        !Especific weight of solids, unitless

{----------------------------
*** Weather data ***
----------------------------}
!Weather data required by both Penman equation and the limiting function
Ta = 38.0                   !Air temperature, oC
RHair = table("RHair.tbl")

!Weather data required only by the Penman equation
ww = 0.0          !Wind speed, m/s
ra = 0.0          !Solar radiation, MJ/m2
rr = 0.0          !Reflection coefficient
nasnps = 0.0      !Sunshine ratio
PRECIP = 24*3600*10.0e-6

{---------------------------------
*** Vapour Pressure ***
---------------------------------}
uvsat = (0.0000000022*(Ts0^5)+0.0000003985*(Ts0^4)+0.0000174108*(Ts0^3)
+0.0017217473*(Ts0^2)+0.041142732*Ts0+0.6183580754)
RHs = exp(-suc*ga*Wv/(gww*ugc*(Ts0+273.15)))
uv = uvsat*RHs
uvsata = (0.0000000022*(Ta^5)+0.0000003985*(Ta^4)+0.0000174108*(Ta^3)
+0.0017217473*(Ta^2)+0.041142732*Ta+0.6183580754)
uva = uvsata*RHair                          !Air partial vapor pressure

{-------------------------------------
*** Potential evaporation ***
-------------------------------------}
pevap = 0.0                                 ! ** Potential Evaporation, m/day

{-------------------------------------------------------------
*** Actual Evaporation using Wilson, 1997***
-------------------------------------------------------------}
EVAP = if (uv-uva)>0 then pevap*(uv-uva)/(uvsat-uva) else 0.0

{-----------------------------------------------
*** SWCC - Gitirana-Fredlund Equation ***
-----------------------------------------------}
!Gitirana-Fredlund
yb = 10, yres = 100, Sres = 0.3, agg = 0.1, e = 1., e0 = 1.
tb1=(1-Sres)/ln(yres/yb), tb2 = Sres/ln(1e6/yres)
tb1b = (-1+(1+tb1^2)^0.5)/tb1, tb2b = (-1+(1+tb2^2)^0.5)/tb2
dgg = 2*exp(1/ln(yres/yb))
rgg1 = tb1b, rgg2 = (tb1b-tb2b)/(1+tb1b*tb2b),
```

```
thgg1 = -arctan(tb1)/2, thgg2 = -(arctan(tb1)+arctan(tb2))/2

Sr1 = 1+(tan(thgg1)*ln(suc/yb)*(1+rgg1^2)-(1+tan(thgg1)^2)*(rgg1^2*(ln(suc/yb))^2
+agg^2*(1-rgg1^2*tan(thgg1)^2)/(1+tan(thgg1)^2))^0.5)/(1-rgg1^2*tan(thgg1)^2)
Sr2 = Sres+(tan(thgg2)*ln(suc/yres)*(1+rgg2^2)+(1+tan(thgg2)^2)*
(rgg2^2*(ln(suc/yres))^2+agg^2*(1-rgg2^2*tan(thgg2)^2)/(1+tan(thgg2)^2))^0.5)/(1-
rgg2^2*tan(thgg2)^2)
Sr = Sr2+(Sr1-Sr2)/(1+((suc)/((yres*yb)^0.5))^dgg)

Sr10 = 1+(tan(thgg1)*ln(suc0/yb)*(1+rgg1^2)-
(1+tan(thgg1)^2)*(rgg1^2*(ln(suc0/yb))^2
+agg^2*(1-rgg1^2*tan(thgg1)^2)/(1+tan(thgg1)^2))^0.5)/(1-rgg1^2*tan(thgg1)^2)
Sr20 =
Sres+(tan(thgg2)*ln(suc0/yres)*(1+rgg2^2)+(1+tan(thgg2)^2)*(rgg2^2*(ln(suc0/yres))^
2+agg^2*(1-rgg2^2*tan(thgg2)^2)/(1+tan(thgg2)^2))^0.5)/(1-rgg2^2*tan(thgg2)^2)
Sr0 = Sr20+(Sr10-Sr20)/(1+((suc0)/((yres*yb)^0.5))^dgg)

mv = 1e-8
n = e0/(1+e0)+mv*uw
n0 = e0/(1+e0)+mv*uw0
vwc = Sr*n
vwc0 = Sr0*n0

{-----------------------------------------------------------------------------------------------
*** Permeability Function, Power of SWCC or Brooks and Corey ***
-----------------------------------------------------------------------------------------------}
! Brooks and Corey
ksat = 24*3600*5.0e-7, ycr = 3.8, lbd = 3.0, eta = 2+3*lbd, kratio = 1.0
!These are default (global) values that are redefined for each region
kw = ksat*(ycr/suc)^eta
kmin = 24*3600*1e-18
k = if suc<=ycr then ksat else if kw<kmin then kmin else kw
kx = kratio*k
!       kx = ksat !FOR ONE-DIMENSIONAL
ky = k

{-------------------------------------------------
*** Diffusion Coefficient Function ***
-------------------------------------------------}
dbeta = (1-Sr)*n,  dalfa = dbeta^(2/3)
Dvap = (0.229e-4)*((1+(Ts0+273.15)/273.15)^1.75)       !m2/s
Dv = 24*3600*dalfa*dbeta*Dvap*(1000*Wv)/(ugc*(Ts0+273.15))
Dm = ((uatm+uv)/uatm)*(ga/gww)*(Wv*uv/(ugc*(Ts0+273.15)))*(Dv/rww)

{-------------------------------------------------------
*** Net flux boundary condition, m/s ***
-------------------------------------------------------}
LARGE = 100*ksat
WID = 0.1        !kPa
PRECIPN = PRECIP*NORMAL(0,1)
NETF = SWAGE(PRECIPN-EVAP, PRECIPN-EVAP, SWAGE(uw, PRECIPN-EVAP,
```

```
        LARGE*(0-uw), WID), WID)

        {---------------------------------
        *** Flow components ***
        ---------------------------------}
        gradh = (dx(h)^2+dy(h)^2)^.5            !Gradient of h
        gradhx = dx(h)                          !Gradient of h
        gradhy = dy(h)                          !Gradient of h
        graduv = (dx(uv)^2+dy(uv)^2)^.5         !Gradient of uv
        wx = - kx*dx(h)                         !Water velocity, x, m/s
        wy = - ky*dy(h)                         !Water velocity, y, m/s
        vx = - Dm*dx(uw)                        !Vapor velocity, x, m/s
        vy = - Dm*dy(uw)                        !Vapor velocity, y, m/s
        vecfluxw = vector(wx, wy)
        vecfluxv = vector(vx, vy)
        vecfluxt = vector(wx+vx, wy+vy)

        {-------------------------------------------------------------------------------
        *** computing change in moisture using volume integral ***
        -------------------------------------------------------------------------------}
        wc = Sr*(n/(1-n))/gws              !Water content at any point
        wcave = integral(wc)/integral(1)!Average water content in the whole domain
        tvolumew = integral(vwc)           !Volume of water in the whole domain, m3
        tvolumew0 = integral(vwc0)         !Initial volume of water in the whole domain, m3

        {-------------------------------------------------------------------------------
        *** computing flux across the soil-atmosphere boundary ***
        -------------------------------------------------------------------------------}
        mccrateA = -1e3*sintegral(NORMAL(vecfluxt),"soil_atm")/sintegral(1,"soil_atm")
        !Flux rate across soil-atm, mm/day
        mccratewA = -1e3*sintegral(NORMAL(vecfluxw),"soil_atm")/sintegral(1,"soil_atm")
        !mccrate (water portion), mm/day
        mccratevA = -1e3*sintegral(NORMAL(vecfluxv),"soil_atm")/sintegral(1,"soil_atm")
        !mccrate (vapour portion), mm/day
        mccrateV = 1e3*sintegral(NETF,"soil_atm")/sintegral(1,"soil_atm")
        IPRECIPN = 1e3*sintegral(PRECIPN,"soil_atm")/sintegral(1,"soil_atm")
        IRUNOFF = IPRECIPN-mccrateV        !Runoff, mm/day

        {---------------------------------
        *** Error measurement ***
        ---------------------------------}
        acuminoutV = (tvolumew-tvolumew0)*1e6
        acuminoutA = -tintegral(1e6*(sintegral(NORMAL(vecfluxt),"soil_atm")))
        wberr = acuminoutV-acuminoutA

INITIAL VALUES
        uw = uw0

EQUATIONS
        dx[((kx/gww)+Dm)*dx(uw)]+dy[((ky/gww)+Dm)*dy(uw)+ky] + Sink = dt(vwc)
```

```
BOUNDARIES
        Region 1
        yb = 10.0, yres = 500.0, Sres = 0.20, agg = 0.10, e = 0.666, e0 = 0.666
        ksat = 24*3600*1.0e-6, ycr = 10.0, lbd = 0.20, kratio = 1.0
        Sink = 0.0

        start 'internal_bdry' (0,height)
        natural(uw) = 0 line to (0,0)
        natural(uw) = 0 line to (width,0)
        natural(uw) = 0 line to (width,height)
        start 'soil_atm' (width,height)
        natural(uw) = NETF line to (0,height)

TIME
        from 0 to 7 !by 0.1

MONITORS

PLOTS
        for t = 0 by 0.05 to 7

        {--------------------------------------
        *** Output for VisioPlot ***
        --------------------------------------}
        tecplot(uw, suc, uv, h, 100*Sr, 100*vwc, 100*vwc, kx, ky, Dv, Dm, 100*RHs)
        grid(x,y) as "Geometry and mesh"
        contour(uw) as "Pore-water pressure, kPa"
        contour(Sr) as "Degree of Saturation"
        contour(k) as "hydraulic conductvity, m/s"
        elevation(uw) from (width/2,0) to (width/2,height) as "Pore-water pressure distribution"
        export format ' #y#b#1' file="uw.dat"
        history(mccrateA, mccrateV, mccratewA, mccratevA)
        export (100) format '#t#b#1#b#2#b#3#b#4' file="rates.dat"
END
```

B.2 HEAT FLOW

```
TITLE 'Heat flow analysis'

SELECT
    errlim = 0.0001
    prefer_stability = on

VARIABLES
    Ts(0.01)

DEFINITIONS
    width = 0.5,  height = 10.0
```

```
    {-------------------------
    *** initial values ***
    -------------------------}
    Ts0 = 25.0              ! oC

    {-----------------------------------------------
    *** Latent Heat of Vaporization ***
    -----------------------------------------------}
    Lv = 2501000 - 2361*Ts     ! J/kg

    {-----------------------------------------
    *** Volumetric Heat Capacity ***
    -----------------------------------------}
    Ch = 2.9900e6        ! J/(m3 oC)
    Heat = Ch*Ts

    {---------------------------------------
    *** Thermal Conductivity ***
    ---------------------------------------}
    lambd = 1.728e5 ! J/(day m oC)

    {-----------------------------------------------------------
    *** Heat flow boundary condition, m/s ***
    -----------------------------------------------------------}
    Qn = -4.8000e6       ! J/(m2 day)

INITIAL VALUES
    Ts = Ts0

EQUATIONS
    dx[lambd*dx(Ts)]+dy[lambd*dy(Ts)] = dt(Heat)

BOUNDARIES

    Region 1 'body'
    start 'internal_bdry' (0,height)
    natural(Ts) = 0 line to (0,0)
    natural(Ts) = 0 line to (width,0)
    natural(Ts) = 0 line to (width,height)
    natural(Ts) = Qn line to (0,height)

TIME
    from 0 to 7 !by 0.1

PLOTS
    for t = 0 by 0.05 to 7

    {-------------------------------------
    *** Output for VisioPlot ***
    -------------------------------------}
    tecplot(uw, Ts, suc, uv, h, 100*Sr, 100*vwc, 100*vwc, kx, ky, Dv, Dm, 100*RHs)
```

```
    grid(x,y) as "Geometry and mesh"
    contour(Ts) as "Temperature, oC"
    elevation(Ts) from (width/2,0) to (width/2,height) as "Temperature"
    export format ' #y#b#1' file="Ts.dat"
    history(Ts) at (width/2,height)
    export format ' #t#b#1' file="Ts01.dat"
    history(Ts) at (width/2,height-0.5)
    export format ' #t#b#1' file="Ts02.dat"
    history(Ts) at (width/2,height-1.0)
    export format ' #t#b#1' file="Ts03.dat"

END
```

B.3 COUPLED MOISTURE AND HEAT FLOW

```
TITLE 'Coupled moisture and heat flow'

SELECT
    errlim = 0.0005
    prefer_stability = on

VARIABLES
    uw(0.1)
    Ts(0.1)

DEFINITIONS
    width = 0.02,  slic = 0.001,  height = 0.30
    bss = 0.01
    Sink = 0.0

    {--------------------------
    *** initial values ***
    --------------------------}
    wt = 0.30
    uw0 = (wt-y)*9.81 ! uw(at y) = (wt elevation - y)*9.81
    Ts0 = 38.0        ! oC
    suc = if uw < -1e6 then 1e6 else if uw > -bss then bss else -uw
    suc0 = SAVE(if uw0 < -1e6 then 1e6 else if uw0 > -bss then bss else -uw0)
    Tsc = if Ts>0.1 then Ts else 0.1

    {-------------------------------------------------
    *** Required physical constants ***
    -------------------------------------------------}
    gww = 9.81        !Unit weight of water, kN/m^3
    ga = 9.81         !Gravity, m/s^2
    rww = 1000.0      !Density of water, kg/m^3
    tsb = 5.67e-8     !Stefan-Boltzman constant, W/m^2/K^4
    neta = 0.27       !psychrometric constant, mmHg/oF
    uatm = 101.325    !Total atmospheric pressure, kPa
```

```
Wv = 0.018016      !Molecular weight of water, kg/mol
ugc = 8.314        !Universal gas constant, J/(mol.K)
minute = 60, hour = 60*minute, day = hour*24

h = uw/gww+y       !Total Head
gws = 2.65 !Especific weight of solids, unitless

{---------------------------------
*** Vapour Pressure ***
---------------------------------}
uvsat = (0.0000000022*(Tsc^5)+0.0000003985*(Tsc^4)+0.0000174108*(Tsc^3)
+0.0017217473*(Tsc^2)+0.041142732*Tsc+0.6183580754)
!Saturation pore-air vapor vapor pressure, kPa
RHs = exp(-suc*ga*Wv/(gww*ugc*(Tsc+273.15))) !Relative humidity in the soil the soil
uv = uvsat*RHs                !Pore-air partial vapor pressure, Lord Kelvin's Equation

{-------------------------------------------------------------------------
*** SWCC Gitirana-Fredlund ***
-------------------------------------------------------------------------}
!Gitirana-Fredlund
yb = 10, yres = 100, Sres = 0.3, agg = 0.1, e = 1., e0 = 1.
tb1=(1-Sres)/ln(yres/yb), tb2 = Sres/ln(1e6/yres), tb1b = (-1+(1+tb1^2)^0.5)/tb1,
tb2b = (-1+(1+tb2^2)^0.5)/tb2, dgg = 2*exp(1/ln(yres/yb))
rgg1 = tb1b, rgg2 = (tb1b-tb2b)/(1+tb1b*tb2b), thgg1 = -arctan(tb1)/2,
thgg2 = -(arctan(tb1)+arctan(tb2))/2

Sr1 = 1+(tan(thgg1)*ln(suc/yb)*(1+rgg1^2)-(1+tan(thgg1)^2)*(rgg1^2*(ln(suc/yb))^2
+agg^2*(1-rgg1^2*tan(thgg1)^2)/(1+tan(thgg1)^2))^0.5)/(1-rgg1^2*tan(thgg1)^2)
Sr2 = Sres+(tan(thgg2)*ln(suc/yres)*(1+rgg2^2)+(1+tan(thgg2)^2)*(rgg2^2*
(ln(suc/yres))^2+agg^2*(1-rgg2^2*tan(thgg2)^2)/(1+tan(thgg2)^2))^0.5)/(1-
rgg2^2*tan(thgg2)^2)
Sr = Sr2+(Sr1-Sr2)/(1+((suc)/((yres*yb)^0.5))^dgg)

Sr10 = SAVE(1+(tan(thgg1)*ln(suc0/yb)*(1+rgg1^2)-(1+tan(thgg1)^2)*(rgg1^2*(ln(suc0/
yb))^2+agg^2*(1-rgg1^2*tan(thgg1)^2)/(1+tan(thgg1)^2))^0.5)/(1-rgg1^2*tan(thgg1)^2))
Sr20 = SAVE(Sres+(tan(thgg2)*ln(suc0/yres)*(1+rgg2^2)+(1+tan(thgg2)^2)*(rgg2^2*
(ln(suc0/yres))^2+agg^2*(1-rgg2^2*tan(thgg2)^2)/(1+tan(thgg2)^2))^0.5)/(1-
rgg2^2*tan(thgg2)^2))
Sr0 = SAVE(Sr20+(Sr10-Sr20)/(1+((suc0)/((yres*yb)^0.5))^dgg))

mv = exp(ln(1e-10)+ln(1e6/suc)*ln(1e-5/1e-10)/ln(1e6/bss))
n = e0/(1+e0)+mv*uw
n0 = e0/(1+e0)+mv*uw0
vwc = Sr*n
vwc0 = Sr0*n0

{-----------------------------------------------------------------------------------------------
*** Permeability Function, Brooks and Corey (using Hyperbole) ***
-----------------------------------------------------------------------------------------------}
! Brooks and Corey
ksat = 24*3600*5.0e-7, ycr = 3.8, lbd = 3.0, eta = 2+3*lbd, kratio = 1.0
```

```
      kmin = 24*3600*1e-17
      kaa = 0.01  !Bending point of the Hyperbole function
      k  =  MAX(kmin,ksat*EXP(1+TAN(-arctan(eta)/2)*LN(suc/ycr)/(1-TAN(arctan(eta)/2)^2)-
      (1/(1-TAN(arctan(eta)/2)^2))*((TAN(arctan(eta)/2)^2*LN(suc/ycr)^2+kaa^2*(1-
      TAN(arctan(eta)/2)^2))^0.5))/EXP(1))
!     kwx = kratio*k
      kwx = ksat !FOR ONE-DIMENSIONAL
!     kwx = 10*ksat !FOR ONE-DIMENSIONAL
      kwy = k

      {-------------------------------------------------
      *** Diffusion Coefficient Function ***
      -------------------------------------------------}
      dbeta = SAVE((1-Sr)*n)
      dalfa = SAVE(dbeta^(2/3))
      Dvap = SAVE(24*3600*(0.229e-4)*((1+(Tsc+273.15)/273.15)^1.75))          !m2/day
      Dv = SAVE(dalfa*dbeta*Dvap*(1000*Wv)/(ugc*(Tsc+273.15)))
      kv = SAVE(((uatm+uv)/uatm)*(ga*Wv*uv/(ugc*(Tsc+273.15)))*(Dv/rww))

      {-------------------------------------------------
      *** Latent Heat of Vaporization ***
      -------------------------------------------------}
      Lv = SAVE(2501000 - 2361*Tsc)   ! J/kg

      {-----------------------------------------------
      *** Volumetric Heat Capacity ***
      -----------------------------------------------}
      Cs = 3.235e6, Cw = 4.154e6            ! J/(m3 oC)
      Ch = Cs*(1-n)+Cw*n*Sr ! based on volume fractions
      Heat = Ch*Tsc

      {---------------------------------------
      *** Thermal Conductivity ***
      ---------------------------------------}
      lbs = 24*3600*6.0, lbw = 24*3600*0.57,
      lba = SAVE(24*3600*(0.025 + 0.0736*Sr))! W/(m oC)
      g1s = 1/3, g2s = 1/3, g3s = 1/3  !considering absence of preferential particle orientation
      g1a = SAVE(0.015 + (0.333 - 0.015)*Sr), g2a = SAVE(0.015 + (0.333 - 0.015)*Sr),
      g3a = SAVE(1 - g1a - g2a)
      Fs = SAVE((1/3)*((1+(lbs/lbw-1)*g1s)^(-1)+(1+(lbs/lbw-1)*g2s)^(-1)+
      (1+(lbs/lbw-1)*g3s)^(-1)))
      Fw = 1
      Fa = SAVE((1/3)*((1+(lba/lbw-1)*g1a)^(-1)+(1+(lba/lbw-1)*g2a)^(-1)+(1+(lba/lbw-
      1)*g3a)^(-1)))
      lambd = SAVE((Fs*lbs*(1-n)+Fw*lbw*Sr*n+Fa*lba*n*(1-Sr))/(Fs*(1-
      n)+Fw*Sr*n+Fa*n*(1-Sr)))

      {-----------------------------------
      *** PDE coefficients ***
      -----------------------------------}
      K11X = (kwx+kv)/gww
```

```
K11Y = (kwy+kv)/gww
K12 = (kv/gww)*(suc/(Tsc+273.15))
K21 = Lv*kv*(rww/gww)
K22 = (lambd+Lv*kv*(rww/gww)*suc/(Tsc+273.15))

{---------------------------
*** Weather data ***
---------------------------}
!Weather data required by both Penman equation and the limiting function
Ta=table("Ta.tbl")
RHair = table("RHair.tbl")

!Weather data required only by the Penman equation
ww = 0.0            !Wind speed, m/s
ra = 0.0            !Solar radiation, MJ/m2
rr = 0.0            !Reflection coefficient
nasnps = 0.0        !Sunshine ratio

PRECIP = 0.0

{-------------------------------------
*** Potential evaporation ***
-------------------------------------}
PEVAP = table("PE.tbl")/1000                    ! ** Potential Evaporation, m/day

{-------------------------------------------------------------
*** Actual Evaporation using Wilson, 1997***
-------------------------------------------------------------}
uvsata = SAVE((0.0000000022*(Ta^5)+0.0000003985*(Ta^4)+0.0000174108*(Ta^3)
+0.0017217473*(Ta^2)+0.041142732*Ta+0.6183580754))
uva = SAVE(uvsata*RHair)
EVAP = if (uv-uva)>0 then PEVAP*(uv-uva)/(uvsat-uva) else 0.0

{-----------------------------------------------------
*** Net flux boundary condition, m/s ***
-----------------------------------------------------}
LARGE = 100*ksat
WID = 0.1 !kPa
PRECIPN = PRECIP*NORMAL(0,1)
NETF = PRECIPN-EVAP
PRECIPN-EVAP ELSE large*(0-uw)
RUNOFF = SAVE(if NETF>0 then PRECIPN-NETF else 0)

{-----------------------------------------------------
*** Heat flow boundary condition, m/s ***
-----------------------------------------------------}
TSS = table("Tss.tbl")

{---------------------------------
*** Flow components ***
---------------------------------}
```

```
gradh = SAVE((dx(h)^2+dy(h)^2)^.5)                    !Gradient of h
gradhx = SAVE(dx(h))                                  !Gradient of h
gradhy = SAVE(dy(h))                                  !Gradient of h
graduv = SAVE((dx(uv)^2+dy(uv)^2)^.5)                 !Gradient of uv
wx = SAVE(-(kwx/gww)*dx(uw))                          !Water velocity, x, m/s
wy = SAVE(-(kwy/gww)*dy(uw)-kwy)                      !Water velocity, y, m/s
vx = SAVE(-(kv/gww)*dx(uw)-(kv/gww)*(suc/(Tsc+273.15))*dx(Ts)) !Vapor, x, m/s
vy = SAVE(-(kv/gww)*dy(uw)-(kv/gww)*(suc/(Tsc+273.15))*dy(Ts)) !Vapor, y, m/s
vecfluxw = vector(wx, wy)
vecfluxv = vector(vx, vy)
vecfluxt = vector(wx+vx, wy+vy)

{-------------------------------------------------------------------------------
*** computing change in moisture using volume integral ***
-------------------------------------------------------------------------------}
wc = SAVE(Sr*(n/(1-n))/gws)                !Water content at any point
wcave = SAVE(integral(wc)/integral(1))     !Average water content in the whole domain
tvolumew = SAVE(integral(vwc))             !Volume of water in the whole domain, m3
tvolumew0 = SAVE(integral(vwc0))       !Initial volume of water in the whole domain, m3

{-------------------------------------------------------------------------------
*** computing flux across the soil-atmosphere boundary ***
-------------------------------------------------------------------------------}
!Partition of vapour and liquid flow
mccrateA = SAVE(-1e3*sintegral(NORMAL(vecfluxt),"soil_atm")/sintegral(1,"soil_atm"))
mccratewA = SAVE(-1e3*sintegral(NORMAL(vecfluxw),"soil_atm")/
sintegral(1,"soil_atm"))
mccratevA = SAVE(-1e3*sintegral(NORMAL(vecfluxv),"soil_atm")/
sintegral(1,"soil_atm"))
mccrateV = SAVE(1e3*sintegral(NETF,"soil_atm")/sintegral(1,"soil_atm"))

!Average flux rates along the soil-watmosphere boundary, mm/day
INETF = 1e3*sintegral(NETF,"soil_atm")/sintegral(1,"soil_atm")    !Netflux, mm/day
IPRECIPN = 1e3*sintegral(PRECIPN,"soil_atm")/sintegral(1,"soil_atm")
IRUNOFF = 1e3*sintegral(RUNOFF,"soil_atm")/sintegral(1,"soil_atm") !Runoff, mm/day
IPEVAP = -1e3*sintegral(PEVAP,"soil_atm")/sintegral(1,"soil_atm")
IEVAP = -1e3*sintegral(EVAP,"soil_atm")/sintegral(1,"soil_atm")  !Actual Evap, mm/day

!Cumulative fluxes, volumes
cnetf = tintegral(INETF)                   !Cumulative Net flux, mm
cprecipn = tintegral(IPRECIPN)             !Cumulative Precipitation, mm
crunoff = tintegral(IRUNOFF)               !Cumulative Runoff, mm
cpevap = tintegral(IPEVAP)                 !Cumulative Potential Evaporation, mm
cevap = tintegral(IEVAP)                   !Cumulative Actual Evaporation, mm

{-----------------------------------
*** Error measurement ***
-----------------------------------}
acuminoutV = SAVE((tvolumew-tvolumew0)*1e6)
acuminoutA = SAVE(-tintegral(1e6*(sintegral(NORMAL(vecfluxt),"internal_bdry")+
sintegral(NORMAL(vecfluxt),"soil_atm")))) !based on bdr flux
```

```
    wberr = SAVE(acuminoutV-acuminoutA)

INITIAL VALUES
    uw = uw0
    Ts = Ts0

EQUATIONS
    dx[K11X*dx(uw)+K12*dx(Ts)]+dy[K11Y*dy(uw)+kwy+K12*dy(Ts)] + Sink = dt(vwc)
    dx[K21*dx(uw)+K22*dx(Ts)]+dy[K21*dy(uw)+K22*dy(Ts)] = dt(Heat)

RESOLVE (EVAP)

BOUNDARIES
    Region 1 'body'

    yb = 3.8, yres = 8.5, Sres = 0.15, agg = 0.23, e = 0.68, e0 = 0.68
    ksat = 24*3600*3.0e-5, ycr = 3.0, lbd = 3.0, kratio = 1.0       !Brooks and Corey, m/day

    Sink = 0.0

    start 'internal_bdry' (0,height)
    natural(uw) = 0 natural(Ts) = 0 line to (0,0)
    natural(uw) = 0 value(Ts) = 38.0 line to (width,0)
    natural(uw) = 0 natural(Ts) = 0 line to (width,height)
    start 'soil_atm' (width,height)
    natural(uw) = NETF value(Ts) = TSS line to (0,height)

TIME
    from 0 to 40 !by 0.1

PLOTS
    for t = 0 by 0.5 to 40

    {-------------------------------------
    *** Output for VisioPlot ***
    -------------------------------------}
    tecplot(uw, Ts, suc, uv, h, 100*Sr, 100*vwc, 100*vwc, kx, ky, Dv, Dm, 100*RHs)
    grid(x,y) as "Geometry and mesh"
    grid(x,y) as "Geometry and mesh - Zoom in" ZOOM(0, height-width, width, width)
    contour(uw) as "Pore-water pressure, kPa"
    contour(Ts) as "Temperature, oC"
    elevation(uw) from (width/2,0) to (width/2,height) as "Pore-water pressure distribution"
    export format ' #y#b#1' file="uw.dat"
    elevation(uw) from (0.0,height) to (width,height) as "Pore-water pressure distribution"
    elevation(uv) from (width/2,0) to (width/2,height) as "Vapour pressure distribution"
    export format ' #y#b#1' file="uv.dat"
    elevation(Ts) from (width/2,0) to (width/2,height) as "Temperature"
    export format ' #y#b#1' file="Ts.dat"

    history(inetf, iprecipn, irunoff, ipevap, ievap) as "Average flux rates across soil-atmosphere
    boundary, mm/day"
```

```
    export format ' #t#b#1#b#2#b#3#b#4#b#5' file="avflux.dat"
    history(cnetf, cprecipn, crunoff, cpevap, cevap) as "Cumulative fluxex across soil-atmosphere interface, mm/day"
    export format ' #t#b#1#b#2#b#3#b#4#b#5' file="cflux.dat"

    history(mccrateA, mccrateV, mccratewA, mccratevA) as "Flux rate across soil-atmosphere interface, mm/day"
    history(acuminoutV, acuminoutA) as "Total volume across all boundaries (based on both WB and BF), mm3"
    history(wberr) as "Total volume ERROR, mm3"
END
```

B.4 STRESS ANALYSIS

```
TITLE 'Stress analysis - Linear-elastic - Total Stress'

SELECT
    errlim = 1e-5

VARIABLES
    u
    v

DEFINITIONS
    gww = 9.81 ! kN/m3

    !soil properties
    E, mu, gamax, gamay, coes, phi, kk, phib
    K = E/(3.*(1.-2.*mu))
    G = E/(2.*(1.+mu))
    D11 = E*(1-mu)/[(1+mu)*(1-2*mu)]
    D22 = E*(1-mu)/[(1+mu)*(1-2*mu)]
    D12 = E*mu/[(1+mu)*(1-2*mu)]
    D44 = E/[2*(1+mu)]

    !Linear shear strength envelope
    uw = (2-y)*9.81
    gama = 20
    ct = if uw>0 then coes else coes+(-uw)*tan(phib*3.14159265358979/180)

    !strain-deformation
    ex = dx(u), ey = dy(v), exy = dx(v) + dy(u)

    !initial stresses
    sx0 = 0.0, sy0 = 0.0, sz0 = 0.0, sxy0 = 0.0

    !stress-strain
    sx = sx0 + D11*ex + D12*ey,  sy = sy0 + D12*ex + D22*ey, sz = sz0 + mu*(sx + sy)
    sxy = sxy0 + D44*exy
```

```
    k0 = sx/sy

    !principle stress
    s1=(sx+sy)/2+sqrt((sx-sy)^2/4+sxy^2)
    s3=(sx+sy)/2-sqrt((sx-sy)^2/4+sxy^2)
    thet = (180/pi)*(1/2)*arctan(2*sxy/(sy-sx))
    stmax = (s1 - s3)/2.

EQUATIONS
    dx(D11*dx(u)+D12*dy(v)]+dy(D44*[dx(v)+dy(u)])+gamax=0
    dx(D44*[dx(v)+dy(u)])+dy(D22*dy(v)+D12*dx(u))+gamay=0

RESOLVE (sxy)

BOUNDARIES
    region 1
    E = 12000, mu = 0.40, gamax = 0., gamay = gama,
    coes = 2.0, phi = 30.0, kk = 1.00, phib = 20

    start (0,0)
    value(u)=0 value(v)=0      line to (40,0)
    value(u)=0 load(v)=0       line to (40,10)
    load(u)=0 load(v)=0        line to (30,10) fillet(2)
    load(u)=0 load(v)=0        line to (22.5,15)
    load(u)=0 load(v)=0        line to (21.25,15)
    load(u)=0 load(v)=28       line to (18.75,15)
    load(u)=0 load(v)=0        line to (17.5,15)
    load(u)=0 load(v)=0        line to (10,10) fillet(2)
    load(u)=0 load(v)=0        line to (0,10)
    value(u)=0 load(v)=0       line to finish

PLOTS
  contour(sx) as 'X-Stress'
  contour(sy) as 'Y-Stress'
  contour(sxy) as 'XY - Shear stress'
  contour(k0) as 'k0' fixed range(0.1,2.0)
  contour(uw) as 'uw'
  contour(gama) as 'gama'
  contour(ct) as 'total cohesion'

  table(sx) file 'sx.dat' points=(56,81)
  table(sy) file 'sy.dat' points=(56,81)
  table(sxy) file 'sxy.dat' points=(56,81)
  table(ct) file 'coes.dat' points=(56,81)
  table(phi) file 'phi.dat' points=(56,81)
  table(uw) file 'u.dat' points=(56,81)

END
```

Appendix C

A Soil-Water Characteristic Curve Equation with Independent Properties

C.1 INTRODUCTION

Appropriate equations to mathematically represent soil-water characteristic curves (SWCC's) are required for both graphical presentations and for numerical modeling. Leong and Rahardjo (1997) and Sillers et al. (2001) have presented reviews of a range of proposed unimodal equations along with parametric analyses. Difficulties in the application of the available equations exist because the parameters of these equations are not individually related to shape features of the SWCC. As a result, unique values of the soil parameters are difficult to determine and sensitivity analyses become awkward. Statistical assessments of SWCC's and the grouping of soils with typical fitting parameters also become difficult (Fredlund et al., 2000). The lack of physical meaning for the fitting parameters is also undesirable.

This appendix presents a new class of equations based on parameters that are independently related to well-defined features of the shape of typical SWCC's. The selected features possess clear physical meaning. The new equations have been developed for both unimodal and bimodal curves. The mathematical basis for the equations is described and the properties and capabilities of the equations are demonstrated.

C.2 APPROPRIATE SWCC EQUATION PARAMETERS

This section describes SWCC features that can be used as equation parameters and their physical meaning. SWCC's are presented in terms of degree of saturation, *S*, plotted on arithmetic scale. Soil suction, ψ, is plotted on a log scale from 0.1 kPa to 1,000,000 kPa; the later corresponding to the completely dry conditions. The symbol ψ is used herein to describe soil suction for its simplicity, but the term $(u_a - u_w)$ could be used also. The combination of matric and total suctions in the SWCC plot to not interfere with objective of this appendix, which is to present appropriate SWCC equations. The following comments consider only desaturation, but the parameters chosen for the proposed equation are valid for both wetting and drying curves.

C.2.1 *Unimodal curves*

Soils with different textures and/or pore-size distributions have different SWCC's, as illustrated in Figure C.1. Sandy soils, represented by curve 1a, remain essentially saturated up to the so-called, air-entry value, ψ_b, where the largest pores start draining (Brooks and Corey, 1964, White et al., 1970). From this point, the steeper the slope, the narrower the pore-size distribution. Once the second bending point (given by the residual degree of saturation, S_{res}, and residual soil suction, ψ_{res}) is reached, large increments in suction have relatively little effect on *S*. Silty soils, represented in Fig. C.1 by curve 1b, have SWCC's similar to those of sandy soils, but ψ_b and ψ_{res} are usually higher due to the presence of smaller pores.

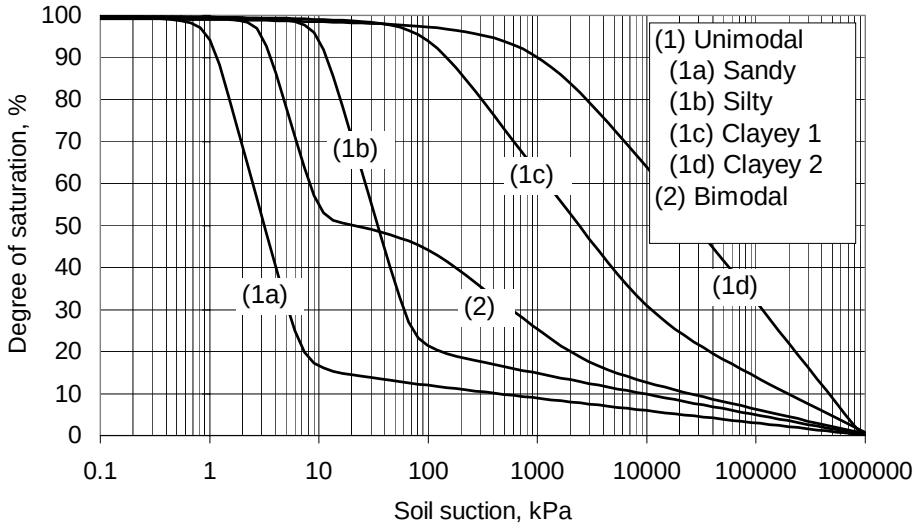

Figure C.1 SWCC's conceptualizations for various soil textures.

Clayey soils (curves 1c and 1d in Fig. C.1) have air-entry values higher than those of silty and

sandy soils and residual points that cannot always be visually identified. Adsorptive forces influence the SWCC for almost the entire range of soil suction (Mitchell, 1976) and vapour flow has an important role on the moisture transfer past the residual point (Barbour, 1998). Therefore, the capillary theory cannot fully explain the SWCC behaviour of clayey soils.

Regardless of the physical meaning of the chosen soil parameters, ψ_b, ψ_{res}, and S_{res} are distinct features of the shape of typical unimodal SWCC's and are therefore appropriate, well-defined soil parameters. A fourth parameter, here called "*a*", defines the sharpness of the transitions at both bending points. This is illustrated by the three curves presented in Fig. C.2, that correspond to the same values of ψ_b, ψ_{res}, and S_{res} but have different sharpnesses, *a*. The type of SWCC's represented in Fig. C.1 by curve 1d require the parameters ψ_b and *a*.

C.2.2 *Bimodal curves*

Curve 2 in Fig. C.1 illustrates a typical bimodal SWCC. According to the capillary theory, the double "hump" can be associated with a bimodal pore-size distribution. Bimodal pore-size distributions are often related to gap-graded grain-size distributions (Durner, 1994), but they are also observed in certain structured soils (Camapum de Carvalho et al., 2002).

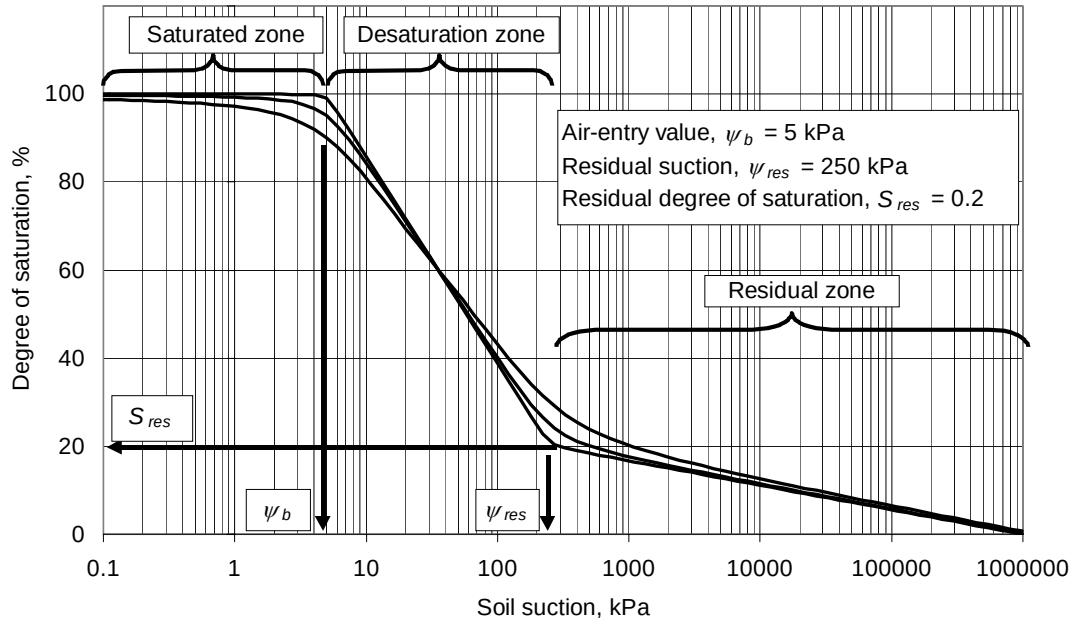

Figure C.2 Idealization of an unimodal SWCC.

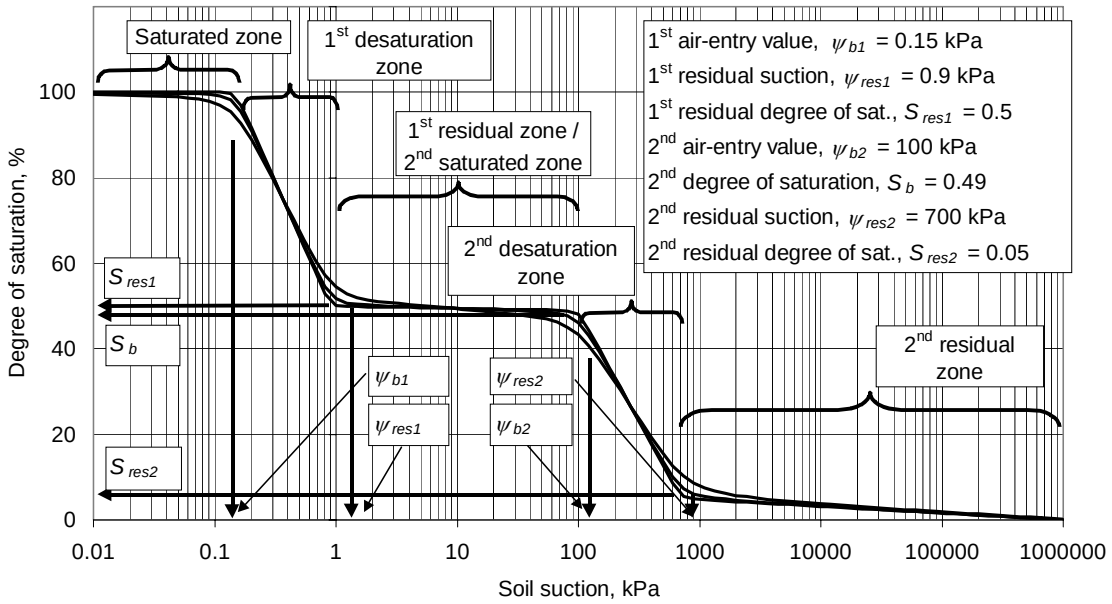

Figure C.3 Idealization of a bimodal SWCC.

Two distinct air-entry values and two distinct residual points can be defined for bimodal SWCC's, giving a total of four bending points. An additional parameter, *a*, is again used to define the sharpness of the transitions at the bending points. The role to be played by parameter *a* is illustrated by the three curves presented in Fig. C.2, that have the same values of ψ_{b1}, ψ_{res1}, S_{res1}, ψ_{b2}, S_b, ψ_{res2}, and S_{res2} but different degrees of sharpness, *a*. In summary, eight parameters are identified to represent bimodal curves: ψ_{b1}, ψ_{res1}, S_{res1}, ψ_{b2}, S_b, ψ_{res2}, S_{res2}, and *a*.

C.3 PROPOSED SWCC EQUATIONS

Three equations are proposed herein; namely, (1) unimodal equation with one bending point; (2) unimodal equation with two bending points; and (3) bimodal equation. The equations are based on the general hyperbole equation in the coordinate system log(ψ)-*S*. The equation parameters are defined as the coordinates where the hyperbolae asymptotes meet. Therefore, a meaningful and consistent geometrical relationship exists between the shape of the SWCC and the equation parameters. Wetting curves that achieve a maximum degree of saturation of less than *S* = 100% can be represented by multiplying the proposed equations by the maximum degree of saturation. SWCC's represented in terms of gravimetric or volumetric water content can be modeled in a similar way.

C.3.1 *Unimodal Equation with One Bending Point*

One rotated and translated hyperbole is used to represent this first type of SWCC curve. The two straight lines defined by (0, 1), (ψ_b, 1), and (10^6, 0) are the hyperbole asymptotes. The equation is written as follows:

$$S = \frac{\tan\theta(1+r^2)\ln(\psi/\psi_b)}{(1-r^2\tan^2\theta)} - \frac{(1+\tan^2\theta)}{(1-r^2\tan^2\theta)}\sqrt{r^2\ln^2(\psi/\psi_b)+\frac{a^2(1-r^2\tan^2\theta)}{(1+\tan^2\theta)}}+1 \quad \text{(C.1)}$$

where:

θ = $-\lambda/2$ is the hyperbole rotation angle;

r = $\tan(\lambda/2)$ is the aperture angle tangent; and

λ = $\arctan[1/(\ln(10^6/\psi_b))]$ is the desaturation slope.

The first derivative of Eq. C.1 with respect to ψ is required to define "water storage" in transient seepage analyses and can be written as follows:

$$\frac{dS}{d\psi} = \frac{1}{\psi}\left[\frac{\tan\theta(1+r^2)}{1-r^2\tan^2\theta} - \frac{r^2\ln(\psi/\psi_b)(1+\tan^2\theta)/(1-r^2\tan^2\theta)}{\sqrt{r^2\ln^2(\psi/\psi_b)+a^2(1-r^2\tan^2\theta)/(1+\tan^2\theta)}}\right] \quad \text{(C.2)}$$

C.3.1 *Unimodal Equation with Two Bending Points*

Two rotated and translated hyperbolae are needed to define an entire unimodal SWCC with two bending points. The three straight lines defined by (0, 1), (ψ_b, 1), (ψ_{res}, S_{res}), and (10^6, 0) are the asymptotes of the hyperbolae. These two hyperbolae are merged through a third equation, producing a continuous equation with a smooth transition. The proposed equation is as follows:

$$S = \frac{S_1 - S_2}{1+(\psi/\sqrt{\psi_b\psi_{res}})^d} + S_2 \quad \text{(C.3)}$$

where:

$$S_i = \frac{\tan\theta_i(1+r_i^2)\ln(\psi/\psi_i^a)}{(1-r_i^2\tan^2\theta_i)} + (-1)^i \cdot \frac{(1+\tan^2\theta_i)}{(1-r_i^2\tan^2\theta_i)}\sqrt{r_i^2\ln^2(\psi/\psi_i^a) + \frac{a^2(1-r_i^2\tan^2\theta_i)}{(1+\tan^2\theta_i)}} + S_i^a;$$

i = 1,2;

θ_i = $-(\lambda_{i-1} + \lambda_i)/2$ are hyperbolae rotation angles;

r_i = $\tan((\lambda_{i-1} - \lambda_i)/2)$ are the aperture angles tangents;

λ_0 = 0;

λ_i = $\arctan[(S^a_i - S^a_{i+1})/(\ln(\psi^a_{i+1}/\psi^a_i))]$ are the desaturation slopes;

S_1^a, S_2^a, and S_3^a = 1, S_{res}, and 0, respectively;

ψ_1^a, ψ_2^a, and ψ_3^a = ψ_b, ψ_{res}, and 10^6, respectively;

d = $2\cdot\exp(1/\ln(\psi_{res}/\psi_b))$ is a weight factor for S_1 and S_2 that produces a continuous and smooth curve.

The first derivative of Eq. C.3 with respect to ψ is:

$$\frac{dS}{d\psi} = \frac{dS_1/d\psi - dS_2/d\psi}{1+(\psi/\sqrt{\psi_b\psi_{res}})^d} - \frac{S_1 - S_2}{[1+(\psi/\sqrt{\psi_b\psi_{res}})^d]^2}\left(\frac{\psi}{\sqrt{\psi_b\psi_{res}}}\right)^d \frac{d}{\psi} + \frac{dS_2}{d\psi} \quad \text{(C.4)}$$

where:

$$\frac{dS_i}{d\psi} = \frac{1}{\psi}\left[\frac{\tan\theta_i(1+r_i^2)}{1-r_i^2\tan^2\theta_i} + (-1)^i \cdot \frac{r_i^2\ln(\psi/\psi_i^a)(1+\tan^2\theta_i)/(1-r_i^2\tan^2\theta_i)}{\sqrt{r_i^2\ln^2(\psi/\psi_i^a) + a^2(1-r_i^2\tan^2\theta_i)/(1+\tan^2\theta_i)}}\right];$$

i = 1,2.

C.3.2 *Bimodal Equation*

Four hyperbolae are needed to model a bimodal SWCC delineated by the five asymptotes that are defined by (0, 1), (ψ_{b1}, 1), (ψ_{res1}, S_{res1}), (ψ_{b2}, S_b), (ψ_{res2}, S_{res2}), and (10^6, 0):

$$S = \frac{S_1 - S_2}{1 + (\psi / \sqrt{\psi_{b1}\psi_{res1}})^{d_1}} + \frac{S_2 - S_3}{1 + (\psi / \sqrt{\psi_{res1}\psi_{b2}})^{d_2}} + \frac{S_3 - S_4}{1 + (\psi / \sqrt{\psi_{b2}\psi_{res2}})^{d_3}} + S_4 \quad \text{(C.5)}$$

where:

S_i, θ_i, r_i, and λ_i	=	where defined in Eq. C.3;
i	=	1, 2, 3, 4;
S_1^a, S_2^a, S_3^a, and S_4^a	=	1, S_{res1}, S_b, S_{res2}, and 0, respectively;
ψ_1^a, ψ_2^a, ψ_3^a, ψ_4^a, and ψ_5^a	=	ψ_{b1}, ψ_{res1}, ψ_{b2}, ψ_{res2}, and 10^6, respectively;
d_j	=	$2 \cdot \exp(1/\ln(\psi^a_{j+1}/\psi^a_j))$ are weight factors, j=1, 2, 3.

The derivative of Eq. C.5 with respect to ψ can be obtained in a manner similar to that above, for Eq. C.3:

$$\begin{aligned}\frac{dS}{d(\ln\psi)} &= \frac{d(S_1 - S_2)/d(\ln\psi)}{1 + (\psi/\sqrt{\psi_{b1}\psi_{res1}})^{d_1}} \\ &- \frac{(S_1 - S_2)(d_1/\psi)}{[1 + (\psi/\sqrt{\psi_{b1}\psi_{res1}})^{d_1}]^2}\left(\frac{\psi}{\sqrt{\psi_{b1}\psi_{res1}}}\right)^{d_1} + \frac{d(S_2 - S_3)/d(\ln\psi)}{1 + (\psi/\sqrt{\psi_{res1}\psi_{b2}})^{d_2}} \\ &- \frac{(S_2 - S_3)(d_2/\psi)}{[1 + (\psi/\sqrt{\psi_{res1}\psi_{b2}})^{d_2}]^2}\left(\frac{\psi}{\sqrt{\psi_{res1}\psi_{b2}}}\right)^{d_2} + \frac{d(S_3 - S_4)/d(\ln\psi)}{1 + (\psi/\sqrt{\psi_{b2}\psi_{res2}})^{d_3}} \\ &- \frac{(S_3 - S_4)(d_3/\psi)}{[1 + (\psi/\sqrt{\psi_{b2}\psi_{res2}})^{d_3}]^2}\left(\frac{\psi}{\sqrt{\psi_{b2}\psi_{res2}}}\right)^{d_3} + \frac{dS_4}{d(\ln\psi)}\end{aligned} \quad \text{(C.6)}$$

where:

$$\frac{dS_i}{d\psi} = \frac{\tan\theta_i(1 + r_i^2)}{1 - r_i^2\tan^2\theta_i} + (-1)^i \times \frac{r_i^2 \ln(\psi/\psi_i^a)(1 + \tan^2\theta_i)/(1 - r_i^2\tan^2\theta_i)}{\sqrt{r_i^2\ln^2(\psi/\psi_i^a) + a^2(1 - r_i^2\tan^2\theta_i)/(1 + \tan^2\theta_i)}};$$

i = 1, 2, 3, 4.

C.4 PARAMETRIC ANALYSIS OF THE PROPOSED EQUATIONS

Parametric studies were used to describe the fitting properties of the proposed equations. Figures C.4 to C.6 show that when changing one parameter while keeping the others fixed, only that feature of the curve related to the parameter being varied is affected. Thus, the curve parameters are mathematically independent. In this way, the new proposed equation is unique amongst all other proposed continuous SWCC equations.

As Figure C.4 illustrates, the larger the value of *a* the smoother the curve. As *a* is increased, the air-entry value might appear to be reduced, but that is not the case. Rather, the apparent reduction should be viewed as a smoothing effect evenly distributed to suction values lower and higher than both ψ_b and ψ_{res}. Ultimately, the bending points are fixed curve parameters that are totally independent on the value of *a*. Limits need to be imposed for the value of parameter *a*. When values of *a* greater than 0.2 are used, the curve limits may start deviating excessively from S = 100% and S = 0%, respectively (see Fig. C.4). For this reason, a range of values of *a* from 0 to 0.15 is suggested. Due to its similar mathematical nature, parametric analyses of the unimodal equations suffice to demonstrate the independence of the parameters of the bimodal equation.

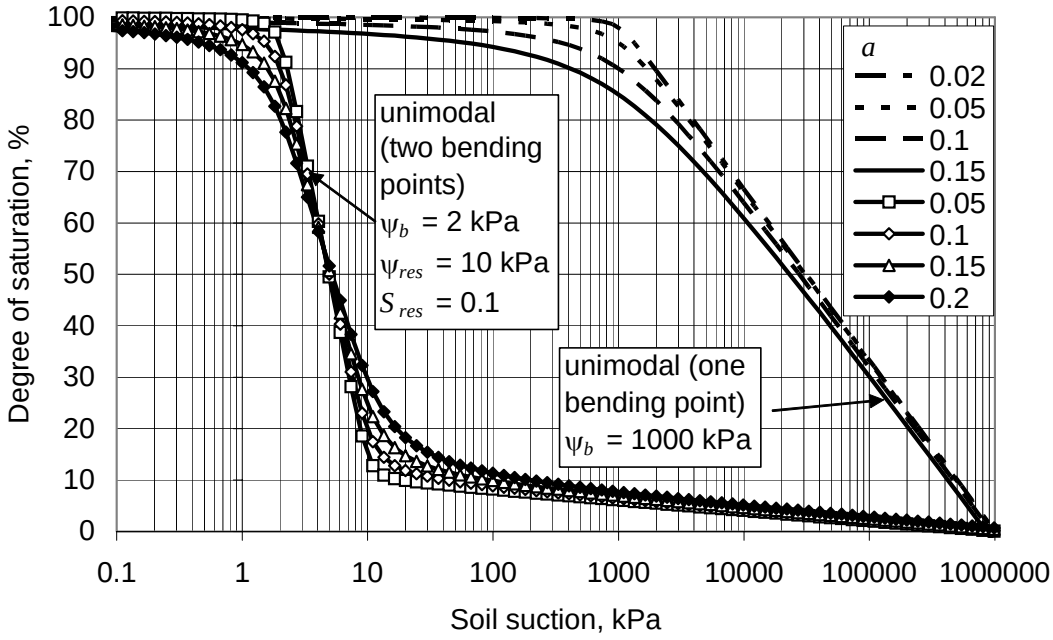

Figure C.4 Effect of changing *a* on unimodal curves.

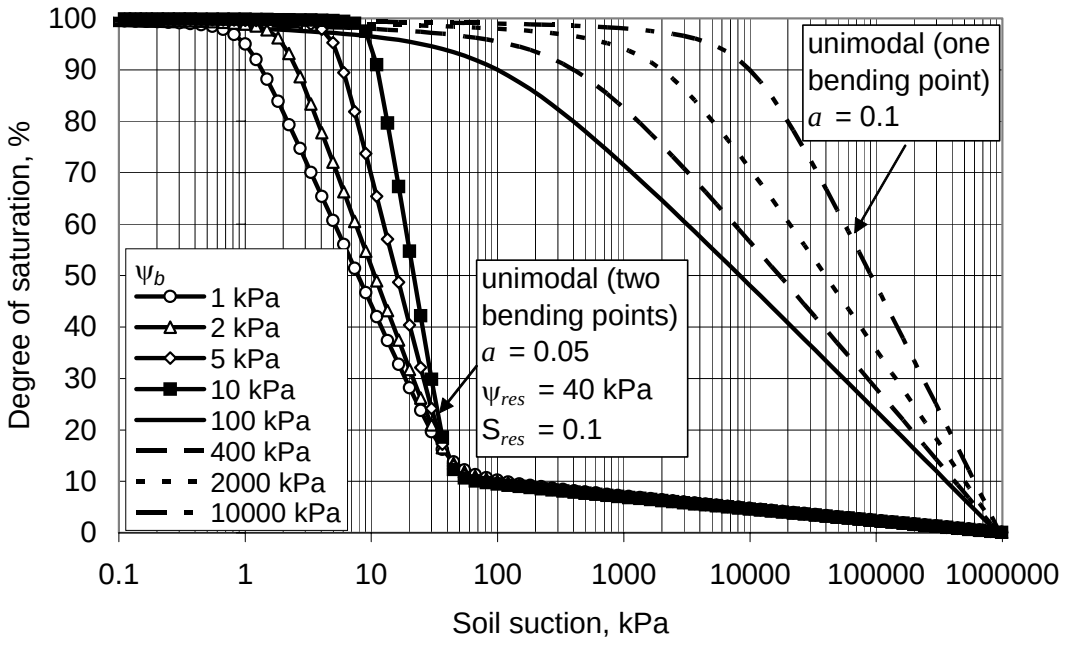

Figure C.5 Effect of changing ψ_b on unimodal curves.

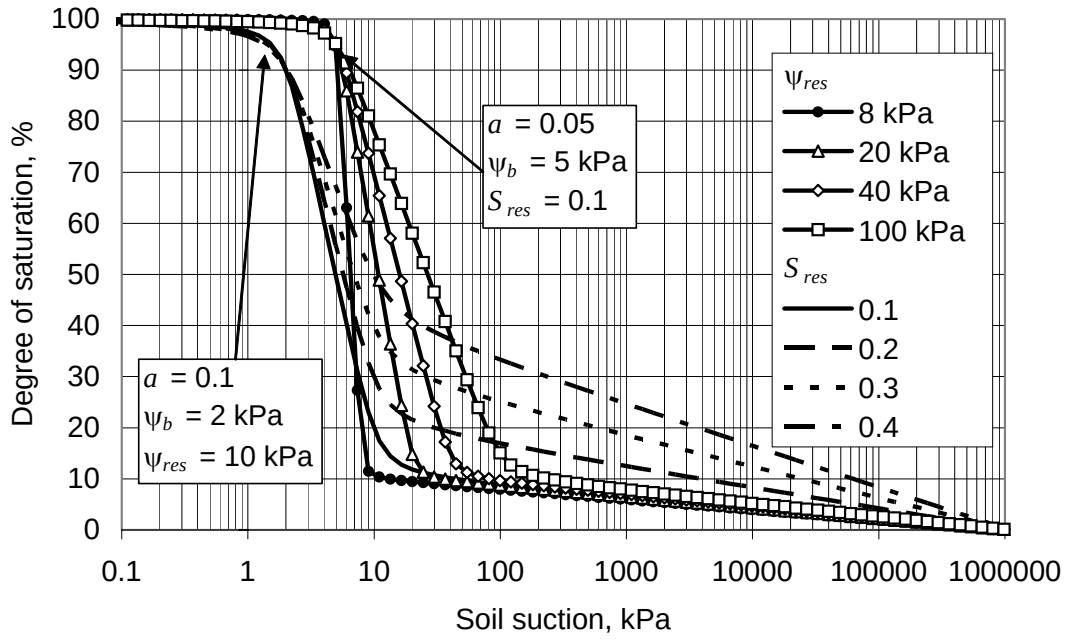

Figure C.6 Effect of changing ψ_{res} and S_{res} on the unimodal curve with two bending points.

C.5 FITTING THE PROPOSED EQUATIONS TO EXPERIMENTAL DATA

Experimental data sets were selected to demonstrate the fitting capabilities of the proposed equations. Since the equation parameters have clear and distinct roles, an eye fitting would be appropriate. However, in order to avoid human bias, a rigorous minimum squares fitting analysis was performed using the minimization solver available in MS Excel 97^{tm}.

Figure C.7 presents the best-fit curves to the experimental data obtained for Regina clay by Fredlund (1964) and for Indian Head till by Vanapalli et al. (1996). A good fit was obtained using the unimodal equation with one bending point. The unimodal equation with two bending points was also used for the Indian head till, giving a slightly better fit. Figure C.8 presents two other data sets, for Patience Lake silt (Bruch, 1993) and Beaver Creek sand (Sillers, 1997) along with the best-fit curve and its parameters. A close fit is observed.

SWCC experimental data for two bimodal soils was used to demonstrate the fitting capability of the proposed bimodal equation. Figure C.9 shows the best-fit curve, the fitting parameters, and the experimental data for a pelletized diatomaceous earth (Burger and Shackelford, 2001) and for a residual, highly collapsible clay from Brasilia (Camapum de Carvalho et al., 2002). Close fits are again observed.

C.6 APPENDIX SUMMARY

Flexible mathematical representations for both unimodal and bimodal soil-water characteristic curves have been proposed. The proposed equations are defined by parameters that have physical meaning and that are independently related to shape features of the SWCC. Parametric analyses and fitting to experimental data sets were used to illustrate the fitting capability of the proposed equations, with excellent results. The proposed equation can make the treatment of SWCC data easier, and statistical analyses on large amount of data will benefit from the use of an equation whose parameters are mathematically independent.

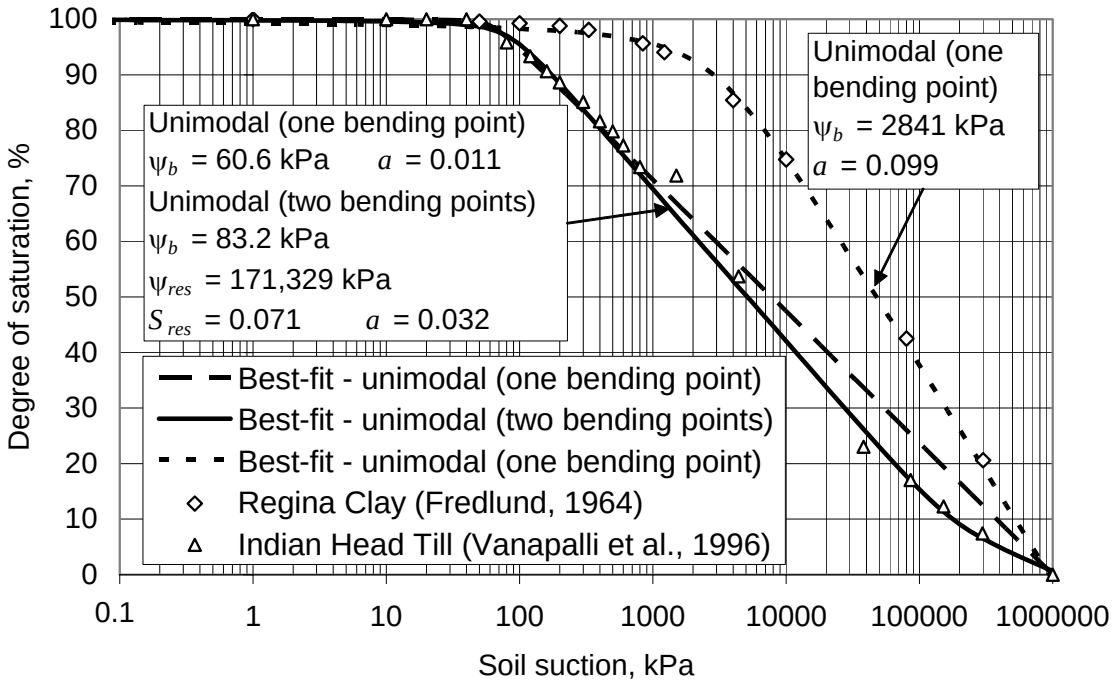

Figure C.7 Best-fit curves to the experimental data of Regina clay and Indian Head till.

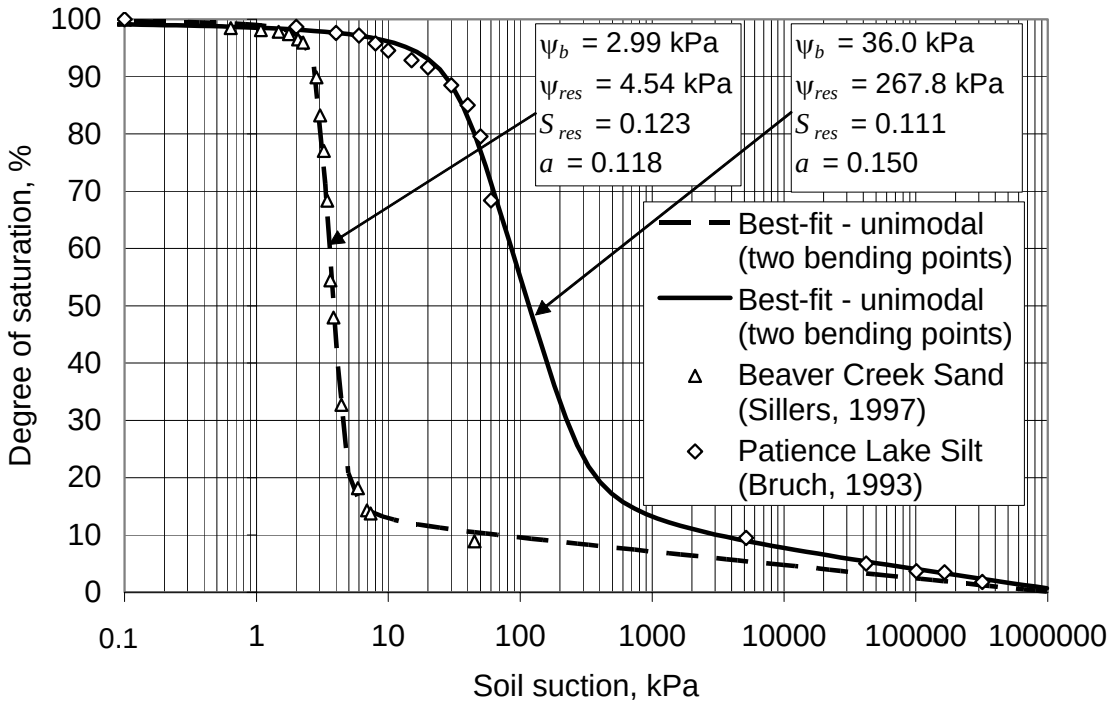

Figure C.8 Best-fit curves to the experimental data of Patience Lake silt and Beaver Creek sand.

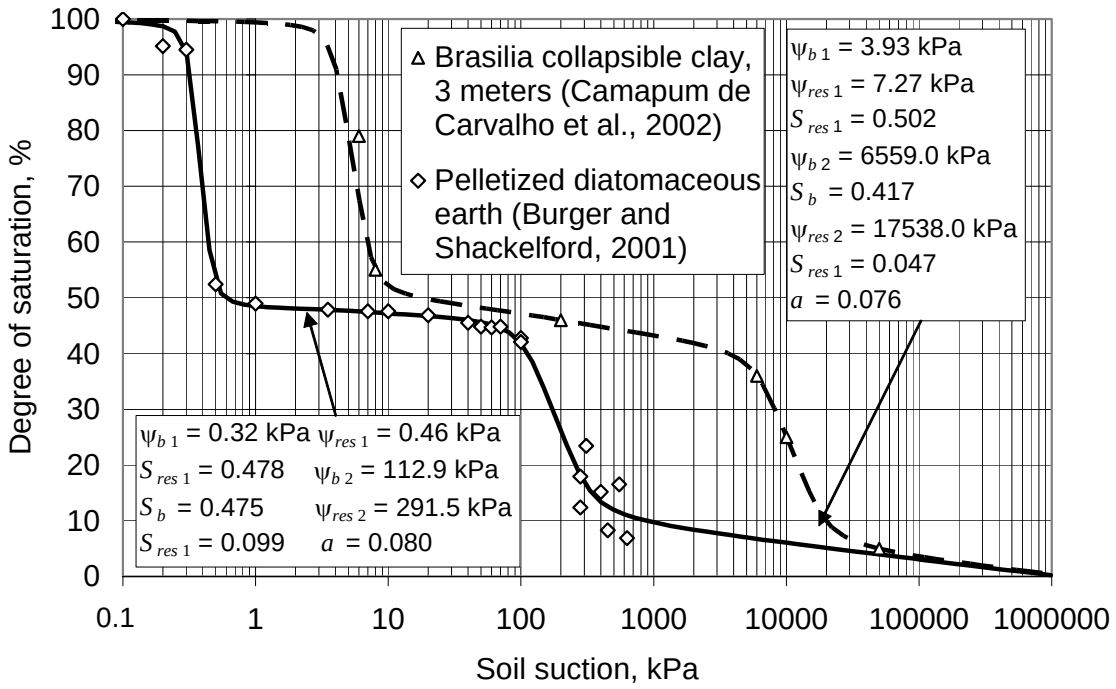

Figure C.9 Best-fit curves to the experimental data of pelletized diatomaceous earth and of the Brasilia collapsible clay.

Appendix D

Records Sampled for the Statistical Analysis of Unsaturated Soil Properties

D.1 SAMPLED DATA

Table D.1 presents the sampled data records used in the statistical analysis of unsaturated soil properties. The data was obtained from the SoilVision database (SoilVision Systems Ltd., 2003). A detailed description of the unsaturated soil parameters associated with the soil-water characteristic curve and the hydraulic conductivity function are presented in Chapter 5 and in Appendix A.

D.2 DESCRIPTIVE STATISTICS

Tables D.2 to D.12 present descriptive statistical measures for the hydraulic properties of unsaturated soils soil-water for all soil groups defined according to the USDA system. Details about the grouping criteria can be found in Chapter 5.

Figures D.1 to D.28 present scatter plots of the variables associated with the soil-water characteristic curve and the hydraulic conductivity function. Some variables are plotted using the natural logarithm. These variables were found to be log normally distributed, as shown in Chapter 5.

Table D.1 Sampled records: the soil-water characteristic curve and hydraulic conductivity function data sampled from SoilVision database along with best-fit parameters.

#	SoilVision ID	USDA Group	% Clay (USDA)	% Silt (USDA)	% Sand (USDA)	Porosity	ψ_b kPa	$\ln(\psi_b)$	ψ_{res} kPa	S_{res}	a	λ_d	$\ln(\lambda_d)$	λ_{res}	$\ln(\lambda_{res})$	k^w_{sat} m/s	$\ln(k^w_{sat})$	ψ_{bk} kPa	$\ln(\psi_{bk})$	η
1	10039	Sa				0.474	2.42	0.882	5.19	0.316	0.075	2.063	0.724	0.060	-2.818	1.83E-05	-10.909	2.30	0.833	5.70
2	10701	Sa	4	12	84	0.430	1.96	0.674	6.98	0.221	0.075	1.412	0.345	0.043	-3.149	3.59E-05	-10.235	2.23	0.803	7.64
3	10977	Sa	0	2	98	0.396	2.14	0.763	7.33	0.338	0.075	1.240	0.215	0.066	-2.719	9.26E-06	-11.590	0.20	-1.609	2.60
4	11061	Sa	0	13	87	0.398	0.32	-1.125	18.93	0.274	0.075	0.411	-0.889	0.058	-2.848	3.50E-04	-7.958	0.56	-0.574	4.40
5	11063	L-Sa	9	10	81	0.567	0.89	-0.119	9.05	0.339	0.075	0.655	-0.423	0.067	-2.698	1.99E-04	-8.522	0.30	-1.204	3.00
6	11065	Sa	4	7	89	0.483	0.91	-0.100	9.39	0.221	0.075	0.767	-0.266	0.044	-3.124	1.86E-04	-8.590	0.21	-1.561	3.00
7	11160	Sa	4	8	88	0.570	2.30	0.831	10.59	0.305	0.075	1.047	0.046	0.061	-2.793	1.80E-06	-13.228	4.00	1.386	5.50
8	11161	L-Sa	6	10	85	0.427	3.49	1.251	9.16	0.410	0.075	1.410	0.343	0.081	-2.509	6.94E-06	-11.878	3.50	1.253	4.70
9	11163	Sa	2	6	92	0.393	3.21	1.167	5.51	0.344	0.075	2.792	1.027	0.065	-2.726	5.21E-05	-9.862	2.50	0.916	5.00
10	11164	Sa	2	3	95	0.400	2.68	0.986	4.55	0.354	0.075	2.810	1.033	0.066	-2.713	5.44E-05	-9.818	2.00	0.693	6.00
11	11167	Sa	2	6	92	0.411	1.96	0.675	8.80	0.254	0.075	1.145	0.135	0.050	-2.990	1.81E-05	-10.922	3.00	1.099	6.00
12	11169	Sa	2	4	94	0.408	2.18	0.779	8.16	0.235	0.075	1.334	0.288	0.046	-3.077	2.20E-05	-10.724	3.00	1.099	7.00
13	11175	Sa	3	6	91	0.423	2.02	0.702	7.05	0.225	0.075	1.427	0.356	0.044	-3.130	1.22E-05	-11.312	3.00	1.099	4.00
14	11177	L-Sa	4	14	82	0.498	3.29	1.191	9.13	0.293	0.075	1.595	0.467	0.058	-2.844	3.63E-05	-10.224	3.00	1.099	4.00
15	11178	L-Sa	2	12	86	0.438	3.42	1.230	9.80	0.274	0.075	1.589	0.463	0.055	-2.906	2.37E-05	-10.650	3.00	1.099	4.00
16	11179	Sa	2	11	87	0.438	3.43	1.232	11.52	0.229	0.075	1.465	0.382	0.046	-3.071	3.13E-05	-10.371	4.00	1.386	7.40
17	11181	Sa	2	11	87	0.396	2.84	1.042	10.33	0.276	0.075	1.289	0.254	0.055	-2.894	2.12E-05	-10.763	3.00	1.099	5.00
18	11274	L-Sa	5	19	76	0.459	6.85	1.924	17.95	0.276	0.075	1.730	0.548	0.058	-2.844	9.40E-07	-13.877	3.00	1.099	4.20
19	11275	L-Sa	6	18	76	0.457	2.16	0.770	32.15	0.240	0.075	0.648	-0.434	0.053	-2.928	1.21E-06	-13.624	3.00	1.099	4.20
20	11276	L-Sa	3	12	85	0.504	2.16	0.770	16.60	0.271	0.075	0.823	-0.195	0.057	-2.870	1.37E-05	-11.197	1.50	0.405	3.00
21	11277	Sa	2	11	88	0.457	1.92	0.651	21.29	0.127	0.075	0.835	-0.180	0.027	-3.607	1.09E-05	-11.423	1.50	0.405	3.00
22	11287	Sa	2	8	91	0.457	2.63	0.965	11.53	0.110	0.075	1.386	0.326	0.022	-3.807	1.94E-05	-10.850	1.00	0.000	2.50
23	11289	Sa	2	10	89	0.438	3.35	1.210	292.92	0.158	0.075	0.434	-0.835	0.045	-3.108	3.81E-07	-14.780	2.00	0.693	2.50
24	11290	Sa	1	6	93	0.366	2.72	0.999	24.09	0.147	0.075	0.900	-0.105	0.032	-3.448	2.81E-06	-12.783	2.00	0.693	2.50
25	11313	Sa	0	5	95	0.385	2.58	0.947	17.15	0.100	0.075	1.093	0.089	0.021	-3.859	1.33E-05	-11.229	1.00	0.000	2.70
26	11315	Sa	1	7	92	0.389	1.40	0.339	281.89	0.067	0.075	0.405	-0.904	0.019	-3.968	9.98E-06	-11.515	1.00	0.000	2.70
27	11316	Sa	1	8	92	0.362	2.72	0.999	46.15	0.141	0.075	0.698	-0.359	0.032	-3.427	4.38E-06	-12.338	0.80	-0.223	2.00
28	11354	Sa	0	1	99	0.385	3.35	1.210	6.32	0.286	0.075	2.595	0.954	0.055	-2.899	4.32E-05	-10.051	3.00	1.099	10.0
29	11396	Sa	9	7	84	0.442	7.89	2.066	11.26	0.348	0.075	4.228	1.442	0.070	-2.656	6.60E-05	-9.626	0.10	-2.303	2.01
30	11399	Sa	5	5	90	0.373	5.31	1.670	10.58	0.152	0.017	2.837	1.043	0.030	-3.492	6.94E-05	-9.575	0.38	-0.970	3.56
31	11401	Sa	2	4	94	0.380	1.20	0.180	8.64	0.140	0.075	1.002	0.002	0.028	-3.585	1.13E-06	-13.691	1.61	0.474	2.40

Table D.1 Continued: Sampled records: the soil-water characteristic curve and hydraulic conductivity function data sampled from SoilVision database along with best-fit parameters.

#	SoilVision ID	USDA Group	% Clay (USDA)	% Silt (USDA)	% Sand (USDA)	Porosity	ψ_b kPa	$\ln(\psi_b)$	ψ_{res} kPa	S_{res}	a	λ_d	$\ln(\lambda_d)$	λ_{res}	$\ln(\lambda_{res})$	k^w_{sat} m/s	$\ln(k^w_{sat})$	ψ_{bk} kPa	$\ln(\psi_{bk})$	η
32	11402	Sa	1	4	95	0.377	0.73	-0.320	9.65	0.210	0.075	0.703	-0.352	0.042	-3.176	2.20E-05	-10.724	0.66	-0.411	2.56
33	11403	Sa	4	6	91	0.463	0.18	-1.701	14.80	0.202	0.075	0.418	-0.872	0.042	-3.173	7.24E-05	-9.533	0.33	-1.110	2.24
34	11404	Sa	3	5	93	0.430	0.26	-1.331	9.86	0.143	0.075	0.545	-0.607	0.029	-3.554	1.32E-04	-8.933	0.35	-1.039	2.47
35	11419	Sa	1	2	97	0.481	1.84	0.608	3.22	0.191	0.075	3.327	1.202	0.035	-3.359	9.60E-05	-9.252	1.80	0.588	10.5
36	11437	Sa	1	6	93	0.438	2.05	0.716	23.83	0.208	0.075	0.743	-0.297	0.045	-3.100	2.78E-05	-10.491	0.57	-0.555	2.65
37	11438	Sa	1	6	93	0.422	5.88	1.772	11.61	0.270	0.075	2.474	0.906	0.055	-2.906	7.78E-05	-9.462	0.10	-2.303	2.63
38	11439	Sa	1	6	94	0.422	4.73	1.554	9.03	0.191	0.075	2.882	1.058	0.038	-3.275	3.33E-05	-10.309	0.38	-0.967	1.93
39	11440	L-Sa	3	12	85	0.365	3.89	1.360	22.49	0.189	0.075	1.064	0.062	0.041	-3.200	1.61E-06	-13.339	1.64	0.492	2.76
40	11441	Sa	1	5	94	0.422	3.70	1.307	12.00	0.200	0.075	1.564	0.447	0.041	-3.203	3.33E-05	-10.309	0.18	-1.736	1.57
41	11442	Sa	1	8	91	0.340	1.61	0.478	41.34	0.114	0.075	0.629	-0.464	0.026	-3.648	2.78E-05	-10.491	0.13	-2.026	1.61
42	11443	Sa	1	5	94	0.385	1.22	0.196	7.88	0.212	0.075	0.971	-0.029	0.042	-3.181	3.89E-07	-14.760	4.61	1.528	4.55
43	11444	Sa	0	3	97	0.359	1.70	0.530	6.18	0.110	0.075	1.587	0.462	0.021	-3.858	1.94E-06	-13.151	4.65	1.536	8.07
44	11445	Sa	0	5	95	0.330	1.99	0.687	11.48	0.220	0.075	1.024	0.024	0.044	-3.113	4.63E-06	-12.283	3.81	1.338	5.31
45	11446	Sa	0	4	96	0.347	1.63	0.486	25.62	0.221	0.075	0.650	-0.431	0.048	-3.032	3.89E-06	-12.457	0.56	-0.573	2.66
46	11447	Sa	1	7	92	0.330	2.73	1.006	19.29	0.104	0.075	1.056	0.055	0.022	-3.817	3.89E-06	-12.457	0.56	-0.573	2.66
47	11448	Sa	0	6	94	0.328	2.60	0.957	23.03	0.102	0.075	0.949	-0.052	0.022	-3.820	9.17E-06	-11.600	0.15	-1.883	1.89
48	11449	Sa	1	4	95	0.377	2.46	0.900	11.04	0.270	0.075	1.119	0.113	0.055	-2.909	2.31E-06	-12.980	2.46	0.898	3.89
49	11450	Sa	1	7	93	0.330	2.53	0.927	12.69	0.151	0.075	1.212	0.192	0.031	-3.480	1.97E-06	-13.136	7.24	1.979	8.05
50	11454	Sa	1	6	93	0.476	12.00	2.485	18.00	0.600	0.075	2.272	0.820	0.126	-2.068	1.94E-06	-13.151	1.56	0.448	2.29
51	11455	Sa	0	3	97	0.374	8.00	2.079	15.00	0.356	0.075	2.358	0.858	0.074	-2.605	9.72E-07	-13.844	4.23	1.442	4.12
52	11456	Sa	0	5	95	0.423	2.34	0.852	12.12	0.433	0.075	0.795	-0.229	0.088	-2.430	1.00E-06	-13.816	1.71	0.535	2.47
53	11457	Sa	0	3	97	0.434	1.95	0.667	6.12	0.467	0.075	1.074	0.071	0.090	-2.413	2.07E-06	-13.090	0.40	-0.916	1.70
54	11474	Sa	1	1	98	0.297	2.11	0.745	8.56	0.141	0.075	1.410	0.344	0.028	-3.580	2.91E-05	-10.446	1.41	0.342	4.38
55	11475	Sa	0	1	99	0.373	2.57	0.943	4.20	0.195	0.075	3.768	1.327	0.036	-3.319	2.31E-04	-8.371	0.72	-0.330	5.34
56	11476	Sa	1	2	97	0.430	2.32	0.841	4.77	0.138	0.075	2.751	1.012	0.026	-3.653	1.16E-04	-9.064	0.77	-0.261	4.50
57	11477	Sa	1	2	97	0.399	2.26	0.817	5.91	0.126	0.075	2.098	0.741	0.024	-3.726	8.01E-05	-9.432	0.10	-2.303	1.28
58	11478	L-Sa	2	15	83	0.384	2.79	1.027	36.21	0.157	0.075	0.757	-0.278	0.035	-3.339	2.79E-06	-12.790	2.40	0.875	3.40
59	11479	Sa	0	6	94	0.414	4.72	1.552	10.80	0.114	0.075	2.467	0.903	0.023	-3.775	2.16E-05	-10.741	5.00	1.609	7.00
60	11480	Sa	4	7	89	0.312	2.19	0.784	96.51	0.157	0.075	0.513	-0.668	0.039	-3.244	1.27E-06	-13.574	0.10	-2.303	1.28
61	11486	Sa	2	7	91	0.333	7.61	2.030	76.95	0.429	0.075	0.569	-0.564	0.104	-2.262	2.94E-05	-10.435	1.13	0.121	4.12
62	11490	Sa	3	11	86	0.430	3.82	1.340	9.80	0.244	0.075	1.848	0.614	0.049	-3.021	6.11E-07	-14.308	4.81	1.570	8.06

Table D.1 Continued: Sampled records: the soil-water characteristic curve and hydraulic conductivity function data sampled from SoilVision database along with best-fit parameters.

#	SoilVision ID	USDA Group	% Clay (USDA)	% Silt (USDA)	% Sand (USDA)	Porosity	ψ_b kPa	$\ln(\psi_b)$	ψ_{res} kPa	S_{res}	a	λ_d	$\ln(\lambda_d)$	λ_{res}	$\ln(\lambda_{res})$	k^w_{sat} m/s	$\ln(k^w_{sat})$	ψ_{bk} kPa	$\ln(\psi_{bk})$	η
63	10036	Si-L				0.478	7.02	1.948	13.88	0.358	0.050	2.166	0.773	0.074	-2.607	4.51E-05	-10.008	7.71	2.043	6.04
64	10037	Sa-L				0.509	5.47	1.699	8.95	0.500	0.050	2.335	0.848	0.099	-2.312	5.88E-05	-9.741	5.66	1.734	5.37
65	10733	Sa-L	7	20	73	0.378	3.26	1.181	7.66	0.470	0.050	1.428	0.356	0.092	-2.388	4.42E-07	-14.633	5.09	1.628	4.71
66	10861	Si-L	17	73	11	0.456	6.10	1.808	791.15	0.383	0.050	0.292	-1.231	0.123	-2.092	1.03E-06	-13.786	1.00	0.000	2.00
67	10933	Si-L				0.430	6.80	1.918	16.34	0.337	0.050	1.743	0.556	0.070	-2.654	2.52E-06	-12.893	7.53	2.019	5.54
68	10934	Si-L				0.493	4.24	1.444	13.39	0.324	0.050	1.353	0.302	0.067	-2.711	6.81E-06	-11.898	4.30	1.459	5.93
69	10935	Si-L				0.463	5.56	1.716	14.41	0.349	0.050	1.576	0.455	0.072	-2.631	3.21E-06	-12.649	6.25	1.833	6.02
70	10936	Si-L	11	57	32	0.458	5.51	1.707	8.65	0.517	0.050	2.471	0.905	0.102	-2.282	6.17E-06	-11.996	5.00	1.610	6.52
71	10937	Si-L	11	57	32	0.496	3.94	1.370	10.01	0.338	0.050	1.631	0.489	0.068	-2.693	7.94E-06	-11.744	4.51	1.507	6.40
72	10938	Si-L	11	57	32	0.544	2.74	1.009	6.86	0.327	0.050	1.691	0.525	0.063	-2.760	2.42E-05	-10.630	2.80	1.028	6.51
73	10939	Si-L	11	57	32	0.518	3.16	1.152	8.24	0.325	0.050	1.624	0.485	0.064	-2.750	1.57E-05	-11.064	3.47	1.245	7.65
74	11036	Si-C-L	38	59	3	0.715	6.24	1.831	48.26	0.596	0.050	0.455	-0.788	0.138	-1.980	3.80E-06	-12.481	0.40	-0.916	3.00
75	11060	Sa-L	9	19	72	0.475	0.49	-0.720	18.43	0.382	0.050	0.392	-0.938	0.081	-2.517	1.33E-04	-8.925	0.56	-0.574	3.60
76	11070	Si-L	18	63	19	0.679	40.00	3.689	900.00	0.438	0.050	0.416	-0.877	0.144	-1.940	5.70E-07	-14.378	1.80	0.588	2.50
77	11073	L	19	33	49	0.529	1.00	0.000	100.00	0.500	0.050	0.250	-1.386	0.125	-2.079	4.73E-05	-9.959	0.30	-1.204	2.10
78	11076	L				0.650	1.00	0.000	400.00	0.380	0.050	0.238	-1.434	0.112	-2.191	5.67E-05	-9.778	0.25	-1.386	2.00
79	11077	L	26	41	33	0.573	1.00	0.000	70.00	0.500	0.050	0.271	-1.306	0.120	-2.117	2.70E-05	-10.520	0.30	-1.204	2.40
80	11080	L	16	38	46	0.453	0.95	-0.057	12.03	0.602	0.050	0.360	-1.021	0.122	-2.101	1.29E-06	-13.560	0.50	-0.693	2.30
81	11081	L	13	40	47	0.419	0.79	-0.236	1049.31	0.226	0.050	0.248	-1.395	0.076	-2.579	7.05E-07	-14.165	0.30	-1.204	1.60
82	11083	L	25	48	28	0.631	1.00	0.000	1000.00	0.380	0.050	0.207	-1.577	0.127	-2.066	4.61E-06	-12.287	0.70	-0.357	2.20
83	11084	Si-L	22	51	28	0.467	25.00	3.219	710.00	0.380	0.050	0.427	-0.852	0.121	-2.115	6.38E-06	-11.962	0.30	-1.204	1.90
84	11090	Sa-C-L	26	19	55	0.533	0.63	-0.463	1000.00	0.200	0.050	0.250	-1.387	0.067	-2.708	8.60E-06	-11.664	0.45	-0.799	2.00
85	11091	Sa-C-L	24	17	59	0.491	0.91	-0.099	1162.64	0.295	0.050	0.227	-1.484	0.101	-2.297	9.80E-07	-13.836	1.00	0.000	2.00
86	11096	L	15	48	38	0.510	0.05	-2.914	1462.57	0.217	0.050	0.177	-1.734	0.077	-2.568	4.25E-05	-10.066	0.04	-3.219	1.70
87	11107	C-L	36	22	42	0.467	1.06	0.060	8.80	0.599	0.050	0.437	-0.828	0.118	-2.133	2.49E-06	-12.904	0.40	-0.916	1.70
88	11120	Si-L	15	59	26	0.651	0.26	-1.349	2913.84	0.096	0.050	0.223	-1.500	0.038	-3.270	1.70E-07	-15.587	1.00	0.000	1.70
89	11122	Si-L	18	57	26	0.406	2.55	0.935	17423.5	0.112	0.050	0.232	-1.463	0.064	-2.752	5.00E-07	-14.509	0.16	-1.833	1.22
90	11126	C-L	31	42	27	0.714	0.74	-0.301	42.91	0.476	0.050	0.297	-1.213	0.109	-2.217	3.70E-05	-10.205	0.14	-1.977	1.02
91	11133	Sa-L	5	31	64	0.525	0.64	-0.449	112.61	0.236	0.050	0.340	-1.079	0.060	-2.816	1.20E-06	-13.633	1.00	0.000	2.00
92	11135	Sa-L	4	28	69	0.509	1.48	0.389	45.82	0.244	0.050	0.507	-0.679	0.056	-2.880	1.95E-06	-13.148	1.00	0.000	1.40
93	11136	Sa-L	3	37	60	0.528	2.05	0.719	857.18	0.152	0.050	0.324	-1.128	0.049	-3.007	2.44E-06	-12.923	0.58	-0.553	1.89

Table D.1 Continued: Sampled records: the soil-water characteristic curve and hydraulic conductivity function data sampled from SoilVision database along with best-fit parameters.

#	SoilVision ID	USDA Group	% Clay (USDA)	% Silt (USDA)	% Sand (USDA)	Porosity	ψ_b kPa	$\ln(\psi_b)$	ψ_{res} kPa	S_{res}	a	λ_d	$\ln(\lambda_d)$	λ_{res}	$\ln(\lambda_{res})$	k^w_{sat} m/s	$\ln(k^w_{sat})$	ψ_{bk} kPa	$\ln(\psi_{bk})$	η
94	11191	L	17	34	48	0.528	2.29	0.828	19.89	0.555	0.050	0.474	-0.746	0.118	-2.137	2.99E-05	-10.419	0.97	-0.030	2.86
95	11196	L	13	24	63	0.533	2.65	0.976	13.50	0.433	0.050	0.803	-0.220	0.089	-2.420	2.11E-06	-13.068	0.12	-2.119	1.65
96	11209	L	21	45	34	0.424	2.74	1.008	11.30	0.595	0.050	0.659	-0.418	0.120	-2.119	1.60E-06	-13.347	2.34	0.850	2.94
97	11262	Si-L	15	78	7	0.420	4.68	1.543	322.75	0.352	0.050	0.352	-1.043	0.101	-2.294	7.64E-06	-11.782	0.27	-1.293	1.95
98	11265	Si-L	12	75	13	0.471	3.85	1.349	1508.57	0.187	0.050	0.314	-1.159	0.066	-2.716	1.35E-07	-15.815	2.30	0.833	1.80
99	11267	Si-L	15	73	12	0.463	1.86	0.623	902.26	0.248	0.050	0.280	-1.273	0.081	-2.508	4.50E-07	-14.615	1.30	0.262	1.90
100	11278	Si-L	12	66	22	0.448	3.06	1.120	357.78	0.302	0.050	0.337	-1.086	0.088	-2.433	3.49E-08	-17.170	10.00	2.303	2.00
101	11279	Sa-L	11	21	68	0.452	1.00	0.004	187.01	0.317	0.050	0.301	-1.200	0.085	-2.466	2.63E-07	-15.152	1.00	0.000	2.00
102	11283	Si-L	9	65	26	0.430	3.39	1.221	362.09	0.256	0.050	0.367	-1.003	0.074	-2.599	3.51E-07	-14.863	3.30	1.194	2.30
103	11285	Si-L	16	60	25	0.433	7.23	1.979	559.44	0.320	0.050	0.360	-1.022	0.099	-2.318	1.42E-05	-11.160	0.10	-2.303	1.61
104	11294	Si-L	14	72	14	0.467	6.23	1.829	936.65	0.259	0.050	0.340	-1.078	0.086	-2.458	3.68E-05	-10.210	0.10	-2.303	1.73
105	11298	Si-L	14	77	9	0.470	0.57	-0.565	500.00	0.250	0.050	0.255	-1.367	0.076	-2.581	9.51E-05	-9.261	0.10	-2.303	2.01
106	11300	Sa-L	11	35	54	0.384	13.27	2.586	759.24	0.343	0.050	0.374	-0.983	0.110	-2.209	4.32E-06	-12.353	0.10	-2.303	1.39
107	11304	Sa-L	12	36	52	0.444	14.49	2.673	815.18	0.367	0.050	0.362	-1.017	0.119	-2.130	2.89E-07	-15.056	0.10	-2.303	1.03
108	11305	Sa-L	15	29	56	0.444	3.02	1.105	54.49	0.459	0.050	0.431	-0.842	0.108	-2.229	5.41E-06	-12.128	0.21	-1.556	1.84
109	11318	Sa-L	11	22	67	0.391	2.66	0.977	104.17	0.368	0.050	0.397	-0.925	0.092	-2.382	3.40E-07	-14.893	4.00	1.386	2.30
110	11319	Sa-L	19	17	65	0.459	2.03	0.707	467.50	0.293	0.050	0.299	-1.206	0.088	-2.431	2.45E-06	-12.919	2.20	0.788	2.10
111	11320	Sa-L	10	22	68	0.449	2.45	0.898	201.59	0.294	0.050	0.369	-0.998	0.080	-2.531	2.04E-06	-13.105	1.20	0.182	2.10
112	11321	Sa-L	11	23	66	0.398	2.48	0.910	183.54	0.314	0.050	0.367	-1.003	0.084	-2.475	1.77E-06	-13.247	0.80	-0.223	2.10
113	11322	Sa-L	19	17	64	0.416	1.99	0.688	268.79	0.243	0.050	0.355	-1.035	0.068	-2.687	1.59E-06	-13.353	0.15	-1.897	1.40
114	11323	Si-L	11	57	32	0.433	7.05	1.954	251.97	0.239	0.050	0.490	-0.714	0.066	-2.711	3.21E-07	-14.952	5.00	1.609	2.40
115	11324	Si-L	11	59	30	0.463	1.52	0.418	373.01	0.200	0.050	0.335	-1.095	0.058	-2.841	3.25E-06	-12.636	0.80	-0.223	2.00
116	11325	Si-L	11	61	28	0.448	1.42	0.350	567.66	0.204	0.050	0.306	-1.185	0.063	-2.767	3.15E-06	-12.669	0.80	-0.223	2.00
117	11405	Si	8	86	7	0.463	3.82	1.339	566.21	0.183	0.050	0.376	-0.978	0.056	-2.874	1.03E-05	-11.483	2.65	0.976	2.38
118	11408	Si-L	14	76	10	0.590	15.00	2.708	459.03	0.372	0.050	0.423	-0.861	0.111	-2.195	2.55E-07	-15.180	4.00	1.386	1.80
119	11415	Sa-C-L	27	10	64	0.600	4.03	1.394	15.10	0.338	0.050	1.154	0.143	0.070	-2.658	4.10E-06	-12.405	3.84	1.346	4.02
120	11416	Sa-C-L	22	12	66	0.542	5.29	1.665	18.98	0.334	0.050	1.200	0.183	0.071	-2.650	6.94E-05	-9.575	1.80	0.590	4.11
121	11417	L	24	42	32	0.700	3.21	1.165	10.93	0.675	0.050	0.610	-0.494	0.136	-1.995	6.11E-06	-12.005	1.68	0.520	2.85
122	11418	L	24	42	32	0.708	3.26	1.182	27.77	0.496	0.050	0.542	-0.612	0.109	-2.218	1.61E-05	-11.036	3.81	1.338	4.08
123	11433	Si-L	22	55	24	0.495	2.00	0.693	26.33	0.483	0.050	0.462	-0.773	0.105	-2.249	9.81E-06	-11.532	1.40	0.336	1.50
124	11489	Sa-C-L	20	17	63	0.547	2.50	0.916	6.10	0.632	0.050	0.951	-0.050	0.121	-2.111	3.61E-07	-14.834	5.00	1.610	3.87

Table D.1 Continued: Sampled records: the soil-water characteristic curve and hydraulic conductivity function data sampled from SoilVision database along with best-fit parameters.

#	SoilVision ID	USDA Group	% Clay (USDA)	% Silt (USDA)	% Sand (USDA)	Porosity	ψ_b kPa	$\ln(\psi_b)$	ψ_{res} kPa	S_{res}	a	λ_d	$\ln(\lambda_d)$	λ_{res}	$\ln(\lambda_{res})$	k^w_{sat} m/s	$\ln(k^w_{sat})$	ψ_{bk} kPa	$\ln(\psi_{bk})$	η
125	10038	C				0.417	0.50	-0.693			0.025					1.23E-07	-15.911	1.08	0.075	1.45
126	10787	C	48	22	30	0.456	0.20	-1.609			0.025					9.64E-07	-13.852	0.80	-0.223	2.24
127	10793	C	40	36	25	0.391	8.66	2.159			0.025					4.63E-06	-12.283	0.35	-1.050	1.80
128	10831	C	55	40	6	0.445	289.22	5.667			0.025					1.16E-07	-15.972	3.44	1.236	4.93
129	10833	Si-C				0.470	1.28	0.247			0.025					2.00E-06	-13.123	0.18	-1.728	1.09
130	10838	C	43	41	16	0.449	16.82	2.823			0.025					4.66E-09	-19.185	2.00	0.693	2.00
131	10839	Si-C	42	41	17	0.438	8.88	2.184			0.025					3.47E-08	-17.177	3.00	1.099	4.10
132	10840	Si-C				0.536	1.43	0.357			0.025					3.28E-07	-14.931	3.04	1.113	4.24
133	10841	C				0.622	2.81	1.033			0.025					7.87E-08	-16.358	1.90	0.642	2.12
134	10842	C				0.428	13.86	2.629			0.025					5.42E-10	-21.336	4.00	1.386	1.30
135	10843	Si-C				0.451	24.01	3.179			0.025					6.59E-10	-21.141	6.00	1.792	1.60
136	10847	Si-C	41	52	7	0.393	23.94	3.176			0.025					5.56E-08	-16.706	3.00	1.099	2.00
137	10851	C	58	31	11	0.463	27.81	3.325			0.025					5.79E-08	-16.665	0.50	-0.693	1.80
138	10864	C	62	34	4	0.732	1.21	0.191			0.025					2.65E-07	-15.143	0.96	-0.045	1.43
139	10865	C	62	34	4	0.671	4.57	1.520			0.025					3.82E-07	-14.778	1.29	0.254	1.95
140	10866	C	62	34	4	0.722	1.77	0.571			0.025					1.54E-07	-15.687	0.56	-0.579	3.50
141	10905	Si-C				0.720	1.96	0.671			0.025					2.10E-07	-15.375	2.35	0.855	2.39
142	10907	Si-C				0.700	1.91	0.648			0.025					3.73E-08	-17.105	4.84	1.576	3.49
143	10908	Si-C				0.570	5.50	1.705			0.025					1.39E-08	-18.092	4.00	1.386	3.50
144	10909	Si-C	41	55.5	3.5	0.790	2.34	0.850			0.025					9.26E-08	-16.195	5.00	1.609	3.10
145	10910	Si-C	49	47.2	3.7	0.790	1.13	0.125			0.025					1.09E-07	-16.034	4.50	1.504	3.70
146	10975	C	52.5	12	35.4	0.593	1.77	0.571			0.025					6.21E-09	-18.898	2.50	0.916	2.00
147	10976	Sa-C				0.421	1.00	0.005			0.025					1.72E-08	-17.881	4.00	1.386	1.80
148	10978	Si-C	43	45	12	0.563	3.08	1.124			0.025					2.47E-08	-17.515	1.30	0.262	1.50
149	10980	C	46	35	19	0.492	13.75	2.621			0.025					5.79E-07	-14.362	1.71	0.536	1.37
150	10981	C	57	38	4	0.557	33.02	3.497			0.025					2.41E-09	-19.845	4.00	1.386	1.60
151	10982	C	63	33	4	0.557	103.64	4.641			0.025					4.63E-08	-16.888	6.00	1.792	1.30
152	11075	Si-C				0.392	7.01	1.947			0.025					7.30E-08	-16.433	1.57	0.450	1.54
153	11084	Si-C				0.467	1.24	0.217			0.000					3.89E-07	-14.760	1.38	0.325	1.75
154	11087	C	48	36	17	0.574	1.00	0.000			0.025					1.73E-07	-15.567	0.80	-0.223	1.40
155	11088	C	50	33	18	0.513	7.26	1.982			0.025					2.95E-08	-17.340	1.00	0.000	1.20

Table D.1 Continued: Sampled records: the soil-water characteristic curve and hydraulic conductivity function data sampled from SoilVision database along with best-fit parameters.

#	SoilVision ID	USDA Group	% Clay (USDA)	% Silt (USDA)	% Sand (USDA)	Porosity	ψ_b kPa	$\ln(\psi_b)$	ψ_{res} kPa	S_{res}	a	λ_d	$\ln(\lambda_d)$	λ_{res}	$\ln(\lambda_{res})$	k^w_{sat} m/s	$\ln(k^w_{sat})$	ψ_{bk} kPa	$\ln(\psi_{bk})$	η
156	11089	C	47	30	23	0.445	14.05	2.643			0.025					1.46E-08	-18.045	1.00	0.000	1.50
157	11099	C	58	27	15	0.623	15.37	2.732			0.025					3.76E-08	-17.098	1.00	0.000	1.90
158	11105	C	40	29	31	0.504	0.10	-2.303			0.025					9.60E-07	-13.856	0.99	-0.011	2.07
159	11143	C	40	27	21	0.571	0.50	-0.693			0.025					1.18E-07	-15.952	4.36	1.473	1.15
160	11148	Si-C	44	54	2	0.457	1.20	0.182			0.025					4.25E-08	-16.974	3.00	1.099	2.00
161	11149	Si-C	45	52	3	0.450	4932.45	8.504			0.025					6.22E-08	-16.594	3.00	1.099	2.00
162	11159	Si-C	44	53	4	0.659	0.50	-0.693			0.025					4.05E-07	-14.719	5.30	1.668	2.15
163	11235	Si-C	49	47	4	0.390	2.67	0.983			0.025					1.19E-08	-18.245	2.50	0.916	2.70
164	11236	Si-C	54	43	3	0.409	4.99	1.607			0.025					1.84E-08	-17.811	3.00	1.099	2.00
165	11306	C	51	38	11	0.541	0.96	-0.043			0.025					5.88E-06	-12.044	0.30	-1.204	1.60
166	11307	C	53	39	8	0.581	3.66	1.298			0.025					1.57E-06	-13.366	0.20	-1.609	1.50
167	11327	C	43	33	24	0.543	2.21	0.794			0.025					4.68E-07	-14.574	2.30	0.832	2.12
168	11328	C	43	33	24	0.543	1.38	0.321			0.025					9.44E-07	-13.873	1.40	0.336	2.00
169	11329	C	43	33	24	0.543	1.56	0.443			0.025					3.33E-07	-14.914	2.10	0.742	2.00
170	11330	C	43	33	24	0.543	1.32	0.277			0.025					4.22E-07	-14.678	2.10	0.742	2.00
171	11331	C	43	33	24	0.544	1.76	0.564			0.025					9.64E-07	-13.852	1.40	0.336	2.00
172	11332	C	43	33	24	0.544	1.49	0.398			0.025					3.69E-07	-14.811	2.20	0.788	1.90
173	11333	C	43	33	24	0.565	0.04	-3.347			0.025					2.05E-07	-15.401	1.90	0.642	1.80
174	11334	C	43	33	24	0.564	0.05	-2.996			0.025					3.14E-07	-14.974	2.10	0.742	2.20
175	11335	C	43	33	24	0.581	0.05	-2.996			0.025					1.54E-07	-15.687	2.50	0.916	2.10
176	11336	C	43	33	24	0.581	0.08	-2.526			0.025					1.72E-06	-13.275	0.80	-0.223	2.10
177	11337	C	43	33	24	0.568	0.20	-1.609			0.025					7.49E-07	-14.105	1.50	0.405	2.50
178	11338	C	43	33	24	0.559	3.86	1.351			0.025					1.12E-07	-16.004	1.35	0.303	2.38
179	11339	C	43	33	24	0.558	0.20	-1.609			0.025					3.17E-08	-17.266	6.00	1.792	2.50
180	11340	C	43	33	24	0.561	0.40	-0.916			0.025					1.19E-07	-15.944	3.50	1.253	2.50
181	11341	C	43	33	24	0.565	2.00	0.693			0.025					3.43E-08	-17.188	4.50	1.504	2.50
182	11382	Si-C	43	48	9	0.351	3.00	1.099			0.025					2.09E-08	-17.681	1.80	0.588	1.50
183	11386	Si-C	43	48	9	0.477	15.44	2.737			0.025					2.27E-09	-19.905	5.00	1.609	1.30
184	11409	C	47	40	13	0.555	9.15	2.213			0.025					1.93E-06	-13.159	0.30	-1.204	2.00
185	11410	C	54	35	11	0.578	23.42	3.154			0.025					5.11E-06	-12.185	0.03	-3.507	1.30
186	11481	Si-C				0.399	9.99	2.301			0.025					3.21E-08	-17.253	2.06	0.721	1.36

Table D.2 Descriptive statistics for the hydraulic properties of unsaturated soils. USDA soils group: All Sands – Sa and L-Sa. (a = 0.075).

Measure	n	ψ_b	$\ln(\psi_b)$	ψ_{res}	S_{res}	λ_{-d}	$\ln(\lambda_{-d})$	λ_{-res}	$\ln(\lambda_{-res})$	k^w_{sat}	$\ln(k^w_{sat})$	ψ_{bk}	$\ln(\psi_{bk})$	η
		kPa		kPa						m/s		kPa		
(1)	(2)	(3)	(4)	(5)	(6)	(7)	(8)	(9)	(10)	(11)	(12)	(13)	(14)	(15)
Min	0.297	0.183	-1.701	3.215	0.067	0.405	-0.904	0.019	-3.968	3.81×10^{-7}	-14.780	0.100	-2.303	1.288
Max	0.570	12.000	2.485	292.917	0.600	4.228	1.442	0.126	-2.068	3.50×10^{-4}	-7.958	7.239	1.979	10.500
Median	0.409	2.438	0.891	10.916	0.220	1.178	0.163	0.044	-3.119	1.82×10^{-5}	-10.915	1.585	0.461	3.484
Mean	0.410	2.937	0.856	24.677	0.231	1.446	0.198	0.047	-3.141	3.88×10^{-5}	-11.336	1.874	0.119	4.037
Range	0.273	11.817	4.186	289.702	0.533	3.823	2.345	0.108	1.901	3.50×10^{-4}	6.823	7.139	4.282	9.212
Std. Dev.	0.055	2.050	0.733	50.874	0.104	0.880	0.592	0.021	0.430	6.34×10^{-5}	1.736	1.582	1.180	2.141
Skewness	0.516	2.150	-1.113	4.718	1.043	1.167	0.079	1.283	0.065	2.990	-0.173	0.959	-0.644	1.144
Kurtosis	0.761	6.178	3.228	22.747	1.520	0.908	-0.705	2.503	-0.392	10.370	-0.900	0.763	-0.659	0.877
CV (%)	13.5	69.8	85.6	206.2	45.0	60.9	299.3	44.7	13.7	163.4	15.3	84.4	988.7	53.0

Table D.3 Descriptive statistics for the hydraulic properties of unsaturated soils. USDA soils group: All loams – Sa-L, Si-L, L, Si-C-L, Sa-C-L, and C-L. (a = 0.050).

Measure	n	ψ_b	$\ln(\psi_b)$	ψ_{res}	S_{res}	λ_d	$\ln(\lambda_d)$	λ_{res}	$\ln(\lambda_{res})$	k^w_{sat}	$\ln(k^w_{sat})$	ψ_{bk}	$\ln(\psi_{bk})$	η
		kPa		kPa						m/s		kPa		
(1)	(2)	(3)	(4)	(5)	(6)	(7)	(8)	(9)	(10)	(11)	(12)	(13)	(14)	(15)
Min	0.378	0.054	-2.914	6.097	0.096	0.177	-1.734	0.038	-3.270	3.49×10^{-8}	-17.170	0.040	-3.219	1.027
Max	0.715	40.000	3.689	17423.5	0.675	2.471	0.905	0.144	-1.940	1.33×10^{-4}	-8.925	10.00	2.303	7.657
Median	0.471	2.697	0.992	185.28	0.338	0.371	-0.991	0.087	-2.446	3.23×10^{-6}	-12.642	1.000	0.000	2.057
Mean	0.501	4.398	0.927	662.84	0.357	0.633	-0.737	0.090	-2.445	1.42×10^{-5}	-12.577	2.032	-0.047	2.792
Range	0.338	39.946	6.603	17417.4	0.579	2.295	2.638	0.106	1.330	1.33×10^{-4}	8.245	9.960	5.521	6.630
Std. Dev.	0.085	6.190	1.090	2224.7	0.133	0.571	0.689	0.025	0.291	2.50×10^{-5}	1.870	2.261	1.391	1.624
Skewness	1.120	3.992	-0.450	7.251	0.422	1.817	1.042	0.207	-0.306	2.792	-0.061	1.461	-0.281	1.468
Kurtosis	0.642	19.269	1.919	55.148	-0.320	2.329	-0.039	-0.962	-0.437	8.992	-0.602	1.816	-0.920	1.064
CV (%)	17.1	140.7	117.6	335.6	37.3	90.2	93.5	27.9	11.9	176.0	14.9	111.3	2962.5	58.2

Table D.4 Descriptive statistics for the hydraulic properties of unsaturated soils. USDA soils group: All Clays – Sa-C, Si-C, and C. (a = 0.025).

Measure	n	ψ_b	$\ln(\psi_b)$	ψ_{res}	S_{res}	λ_{-d}	$\ln(\lambda_{-d})$	λ_{-res}	$\ln(\lambda_{-res})$	k^w_{sat}	$\ln(k^w_{sat})$	ψ_{bk}	$\ln(\psi_{bk})$	η
		kPa		kPa						m/s		kPa		
(1)	(2)	(3)	(4)	(5)	(6)	(7)	(8)	(9)	(10)	(11)	(12)	(13)	(14)	(15)
Min	0.351	0.035	-3.347	--	--	--	--	--	--	5.42×10^{-10}	-21.336	0.030	-3.507	1.094
Max	0.790	4932.45	8.504	--	--	--	--	--	--	5.88×10^{-5}	-12.044	6.000	1.792	4.933
Median	0.544	2.106	0.743	--	--	--	--	--	--	1.17×10^{-7}	-15.962	2.078	0.731	2.000
Mean	0.534	91.397	0.999	--	--	--	--	--	--	5.51×10^{-7}	-16.032	2.363	0.527	2.095
Range	0.439	4932.41	11.85	--	--	--	--	--	--	5.88×10^{-5}	9.292	5.970	5.298	3.840
Std. Dev.	0.100	626.09	2.064	--	--	--	--	--	--	1.16×10^{-5}	2.053	1.614	0.992	0.791
Skewness	0.554	7.829	0.577	--	--	--	--	--	--	3.412	-0.351	0.663	-1.524	1.613
Kurtosis	0.197	61.505	2.173	--	--	--	--	--	--	11.903	0.143	-0.437	3.569	2.763
CV (%)	18.7	685.0	206.6	--	--	--	--	--	--	211.4	12.8	68.3	188.2	37.7

Table D.5 Descriptive statistics for the hydraulic properties of unsaturated soils. USDA soils group: Sa. (a = 0.075).

Measure	n	ψ_b	$\ln(\psi_b)$	ψ_{res}	S_{res}	λ_d	$\ln(\lambda_d)$	λ_{res}	$\ln(\lambda_{res})$	k^w_{sat}	$\ln(k^w_{sat})$	ψ_{bk}	$\ln(\psi_{bk})$	η
		kPa		kPa						m/s		kPa		
(1)	(2)	(3)	(4)	(5)	(6)	(7)	(8)	(9)	(10)	(11)	(12)	(13)	(14)	(15)
Min	0.297	0.183	-1.701	3.215	0.067	0.405	-0.904	0.019	-3.968	3.81×10^{-7}	-14.780	0.100	-2.303	1.288
Max	0.570	12.000	2.485	292.917	0.600	4.228	1.442	0.126	-2.068	3.50×10^{-4}	-7.958	7.239	1.979	10.50
Median	0.399	2.344	0.852	10.796	0.210	1.212	0.192	0.043	-3.149	1.94×10^{-5}	-10.850	1.407	0.342	3.000
Mean	0.402	2.890	0.824	25.800	0.224	1.498	0.221	0.046	-3.181	4.00×10^{-5}	-11.259	1.790	0.022	4.095
Range	0.273	11.817	4.186	289.702	0.533	3.823	2.345	0.108	1.901	3.50×10^{-4}	6.823	7.139	4.282	9.212
Std. Dev.	0.051	2.121	0.758	54.871	0.107	0.928	0.618	0.022	0.442	6.38×10^{-5}	1.731	1.650	1.215	2.299
Skewness	0.428	2.252	-1.079	4.374	1.216	1.043	0.014	1.478	0.256	3.098	-0.284	1.128	-0.485	1.019
Kurtosis	1.066	6.481	3.097	19.267	1.884	0.443	-0.798	2.915	-0.336	11.380	-0.789	0.939	-0.830	0.319
CV (%)	12.7	73.4	92.1	212.7	47.8	61.9	279.9	47.9	13.9	159.6	15.4	92.2	5439.9	56.1

Table D.6 Descriptive statistics for the hydraulic properties of unsaturated soils. USDA soils group: L-Sa. (a = 0.075).

Measure	n	ψ_b	$\ln(\psi_b)$	ψ_{res}	S_{res}	λ_d	$\ln(\lambda_d)$	λ_{res}	$\ln(\lambda_{res})$	k^w_{sat}	$\ln(k^w_{sat})$	ψ_{bk}	$\ln(\psi_{bk})$	η
		kPa		kPa						m/s		kPa		
(1)	(2)	(3)	(4)	(5)	(6)	(7)	(8)	(9)	(10)	(11)	(12)	(13)	(14)	(15)
Min	0.365	0.888	-0.119	9.052	0.157	0.648	-0.434	0.035	-3.339	9.40×10^{-7}	-13.877	0.300	-1.204	2.767
Max	0.567	6.848	1.924	36.208	0.410	1.730	0.548	0.081	-2.509	1.99×10^{-4}	-8.522	3.500	1.253	4.700
Median	0.457	3.291	1.191	16.598	0.274	1.064	0.062	0.057	-2.870	6.94×10^{-6}	-11.878	3.000	1.099	4.000
Mean	0.455	3.217	1.045	18.059	0.272	1.141	0.062	0.056	-2.904	3.18×10^{-5}	-11.789	2.371	0.691	3.696
Range	0.202	5.960	2.043	27.156	0.252	1.082	0.982	0.046	0.831	1.98×10^{-4}	5.355	3.200	2.457	1.933
Std. Dev.	0.062	1.643	0.556	10.357	0.075	0.441	0.404	0.013	0.246	6.39×10^{-5}	1.800	1.028	0.769	0.673
Skewness	0.305	1.200	-0.830	0.890	0.302	0.153	-0.056	0.298	-0.402	2.803	0.562	-1.111	-2.257	-0.096
Kurtosis	0.019	2.994	2.300	-0.563	0.518	-2.069	-2.063	0.837	0.520	8.075	-0.516	0.596	5.487	-1.453
CV (%)	13.7	51.1	53.2	57.3	27.5	38.7	655.6	23.9	8.5	200.8	15.3	43.3	111.3	18.2

Table D.7 Descriptive statistics for the hydraulic properties of unsaturated soils. USDA soils group: Sa-L. (a = 0.050).

Measure	n	ψ_b	$\ln(\psi_b)$	ψ_{res}	S_{res}	λ_d	$\ln(\lambda_d)$	λ_{res}	$\ln(\lambda_{res})$	k^w_{sat}	$\ln(k^w_{sat})$	ψ_{bk}	$\ln(\psi_{bk})$	η
		kPa		kPa						m/s		kPa		
(1)	(2)	(3)	(4)	(5)	(6)	(7)	(8)	(9)	(10)	(11)	(12)	(13)	(14)	(15)
Min	0.378	0.487	-0.720	7.659	0.152	0.299	-1.206	0.049	-3.007	2.63×10^{-7}	-15.152	0.100	-2.303	1.037
Max	0.528	14.491	2.673	857.179	0.500	2.335	0.848	0.119	-2.130	1.33×10^{-4}	-8.925	5.662	1.734	5.374
Median	0.449	2.454	0.898	183.538	0.317	0.369	-0.998	0.085	-2.466	1.95×10^{-6}	-13.148	1.000	0.000	2.000
Mean	0.451	3.785	0.891	272.811	0.332	0.572	-0.789	0.085	-2.497	1.44×10^{-5}	-13.014	1.577	-0.246	2.350
Range	0.150	14.004	3.394	849.521	0.348	2.035	2.054	0.069	0.877	1.33×10^{-4}	6.227	5.562	4.036	4.337
Std. Dev.	0.051	4.278	0.940	303.376	0.096	0.561	0.587	0.020	0.254	3.60×10^{-5}	1.776	1.839	1.326	1.243
Skewness	0.120	2.065	0.363	1.167	0.123	2.793	2.287	-0.159	-0.632	3.063	1.103	1.472	-0.152	1.612
Kurtosis	-1.172	3.314	0.370	-0.123	-0.301	7.583	4.531	-0.557	-0.258	9.501	1.237	0.898	-0.853	1.882
CV (%)	11.3	113.0	105.5	111.2	28.9	98.1	74.5	23.7	10.2	249.4	13.6	116.6	539.3	52.9

Table D.8 Descriptive statistics for the hydraulic properties of unsaturated soils. USDA soils group: Si-L. (a = 0.050).

Measure	n	ψ_b	$\ln(\psi_b)$	ψ_{res}	S_{res}	λ_d	$\ln(\lambda_d)$	λ_{res}	$\ln(\lambda_{res})$	k^w_{sat}	$\ln(k^w_{sat})$	ψ_{bk}	$\ln(\psi_{bk})$	η
		kPa		kPa						m/s		kPa		
(1)	(2)	(3)	(4)	(5)	(6)	(7)	(8)	(9)	(10)	(11)	(12)	(13)	(14)	(15)
Min	0.406	0.259	-1.349	6.860	0.096	0.223	-1.500	0.038	-3.270	3.49×10^{-8}	-17.170	0.100	-2.303	1.228
Max	0.679	40.000	3.689	17423.5	0.517	2.471	0.905	0.144	-1.940	9.51×10^{-5}	-9.261	10.00	2.303	7.657
Median	0.463	3.935	1.370	373.013	0.324	0.376	-0.978	0.074	-2.607	3.25×10^{-6}	-12.636	2.300	0.833	2.000
Mean	0.483	6.466	1.375	1130.52	0.301	0.772	-0.595	0.081	-2.548	1.12×10^{-5}	-12.831	2.888	0.391	3.236
Range	0.273	39.741	5.038	17416.6	0.421	2.248	2.405	0.106	1.330	9.50×10^{-5}	7.909	9.900	4.605	6.430
Std. Dev.	0.065	8.316	1.022	3313.45	0.101	0.696	0.793	0.024	0.291	2.02×10^{-5}	2.013	2.693	1.428	2.089
Skewness	1.871	3.144	-0.324	4.927	-0.032	1.193	0.815	0.826	0.051	3.210	-0.301	1.015	-0.732	0.982
Kurtosis	3.397	10.743	1.759	24.963	0.024	-0.070	-1.045	0.344	0.331	11.718	-0.697	0.446	-0.593	-0.854
CV (%)	13.5	128.6	74.3	293.1	33.6	90.2	133.2	29.8	11.4	180.2	15.7	93.2	365.4	64.6

Table D.9 Descriptive statistics for the hydraulic properties of unsaturated soils. USDA soils group: L. (a = 0.050).

Measure	n	ψ_b	$\ln(\psi_b)$	ψ_{res}	S_{res}	λ_d	$\ln(\lambda_d)$	λ_{res}	$\ln(\lambda_{res})$	k^w_{sat}	$\ln(k^w_{sat})$	ψ_{bk}	$\ln(\psi_{bk})$	η
		kPa		kPa						m/s		kPa		
(1)	(2)	(3)	(4)	(5)	(6)	(7)	(8)	(9)	(10)	(11)	(12)	(13)	(14)	(15)
Min	0.419	0.054	-2.914	10.932	0.217	0.177	-1.734	0.076	-2.579	7.05×10^{-7}	-14.165	0.040	-3.219	1.600
Max	0.708	3.261	1.182	1462.58	0.675	0.803	-0.220	0.136	-1.995	5.67×10^{-5}	-9.778	3.812	1.338	4.083
Median	0.531	1.000	0.000	48.885	0.498	0.316	-1.163	0.119	-2.128	1.11×10^{-5}	-11.521	0.400	-0.949	2.250
Mean	0.555	1.662	0.163	348.11	0.463	0.403	-1.028	0.111	-2.216	1.97×10^{-5}	-11.684	0.943	-0.726	2.392
Range	0.289	3.207	4.096	1451.64	0.458	0.626	1.514	0.060	0.584	5.60×10^{-5}	4.387	3.772	4.557	2.483
Std. Dev.	0.100	1.091	1.114	518.973	0.143	0.208	0.511	0.020	0.197	2.04×10^{-5}	1.579	1.136	1.286	0.710
Skewness	0.222	0.329	-2.031	1.365	-0.524	0.713	0.250	-0.944	-1.135	0.710	-0.255	1.802	-0.195	1.185
Kurtosis	-1.083	-1.476	5.481	0.415	-0.389	-0.815	-1.506	-0.314	-0.037	-1.036	-1.620	2.944	-0.018	1.752
CV (%)	18.0	65.7	684.0	149.1	30.9	51.6	49.6	17.9	8.9	103.7	13.5	120.5	177.2	29.7

Table D.10 Descriptive statistics for the hydraulic properties of unsaturated soils. USDA soils group: Si-C-L, Sa-C-L, and C-L. (a = 0.050).

Measure	n	ψ_b	$\ln(\psi_b)$	ψ_{res}	S_{res}	λ_d	$\ln(\lambda_d)$	λ_{res}	$\ln(\lambda_{res})$	k^w_{sat}	$\ln(k^w_{sat})$	ψ_{bk}	$\ln(\psi_{bk})$	η
		kPa		kPa						m/s		kPa		
(1)	(2)	(3)	(4)	(5)	(6)	(7)	(8)	(9)	(10)	(11)	(12)	(13)	(14)	(15)
Min	0.467	0.629	-0.463	6.097	0.200	0.227	-1.484	0.067	-2.708	3.61×10^{-7}	-14.834	0.139	-1.977	1.027
Max	0.715	6.242	1.831	1162.64	0.632	1.200	0.183	0.138	-1.980	6.94×10^{-5}	-9.575	5.003	1.610	4.116
Median	0.545	1.781	0.488	30.946	0.407	0.446	-0.808	0.105	-2.257	3.95×10^{-6}	-12.443	0.725	-0.399	2.500
Mean	0.576	2.674	0.626	287.849	0.434	0.621	-0.678	0.099	-2.344	1.58×10^{-5}	-12.238	1.630	-0.133	2.718
Range	0.248	5.612	2.294	1156.54	0.432	0.974	1.667	0.071	0.728	6.91×10^{-5}	5.259	4.865	3.587	3.089
Std. Dev.	0.094	2.238	0.933	491.898	0.164	0.412	0.685	0.027	0.286	2.48×10^{-5}	1.748	1.826	1.244	1.195
Skewness	0.746	0.683	0.166	1.470	-0.028	0.608	0.238	-0.066	-0.284	1.884	0.199	1.261	0.136	-0.011
Kurtosis	-0.805	-1.349	-2.118	0.212	-1.790	-1.796	-1.912	-1.666	-1.907	2.963	-0.503	0.192	-1.066	-1.828
CV (%)	16.3	83.7	149.2	170.9	37.7	66.3	101.0	27.4	12.2	156.3	14.3	112.0	937.3	44.0

Table D.11 Descriptive statistics for the hydraulic properties of unsaturated soils. USDA soils group: Sa-C and Si-C. (a = 0.025).

Measure	n	ψ_b	$\ln(\psi_b)$	ψ_{res}	S_{res}	λ_{cl}	$\ln(\lambda_{cl})$	λ_{res}	$\ln(\lambda_{res})$	k^w_{sat}	$\ln(k^w_{sat})$	ψ_{bk}	$\ln(\psi_{bk})$	η
		kPa		kPa						m/s		kPa		
(1)	(2)	(3)	(4)	(5)	(6)	(7)	(8)	(9)	(10)	(11)	(12)	(13)	(14)	(15)
Min	0.351	0.500	-0.693	--	--	--	--	--	--	6.59×10^{-10}	-21.141	0.178	-1.728	1.094
Max	0.790	4932.45	8.504	--	--	--	--	--	--	2.00×10^{-6}	-13.123	6.000	1.792	4.240
Median	0.462	2.837	1.041	--	--	--	--	--	--	3.99×10^{-8}	-17.040	3.000	1.099	2.000
Mean	0.513	229.77	1.507	--	--	--	--	--	--	1.81×10^{-7}	-16.893	3.173	0.978	2.311
Range	0.439	4931.95	9.197	--	--	--	--	--	--	2.00×10^{-6}	8.018	5.822	3.520	3.146
Std. Dev.	0.135	1050.38	1.892	--	--	--	--	--	--	4.24×10^{-7}	1.755	1.508	0.749	0.957
Skewness	0.991	4.690	2.538	--	--	--	--	--	--	4.095	-0.242	0.065	-2.350	0.806
Kurtosis	-0.243	21.998	8.685	--	--	--	--	--	--	17.890	1.075	-0.617	7.708	-0.618
CV (%)	26.3	457.1	125.5	--	--	--	--	--	--	234.6	10.4	47.5	76.5	41.4

Table D.12 Descriptive statistics for the hydraulic properties of unsaturated soils. USDA soils group: C. (a = 0.025).

Measure	n	ψ_b	$\ln(\psi_b)$	ψ_{res}	S_{res}	λ_d	$\ln(\lambda_d)$	λ_{res}	$\ln(\lambda_{res})$	k^w_{sat}	$\ln(k^w_{sat})$	ψ_{bk}	$\ln(\psi_{bk})$	η
		kPa		kPa						m/s		kPa		
(1)	(2)	(3)	(4)	(5)	(6)	(7)	(8)	(9)	(10)	(11)	(12)	(13)	(14)	(15)
Min	0.391	0.035	-3.347	--	--	--	--	--	--	5.42×10^{-10}	-21.336	0.030	-3.507	1.158
Max	0.732	289.218	5.667	--	--	--	--	--	--	5.88×10^{-5}	-12.044	6.000	1.792	4.933
Median	0.557	1.770	0.571	--	--	--	--	--	--	1.89×10^{-7}	-15.484	1.450	0.371	2.000
Mean	0.546	15.292	0.719	--	--	--	--	--	--	7.54×10^{-7}	-15.558	1.918	0.279	1.977
Range	0.341	289.182	9.014	--	--	--	--	--	--	5.88×10^{-5}	9.292	5.970	5.298	3.776
Std. Dev.	0.073	47.729	2.123	--	--	--	--	--	--	1.38×10^{-5}	2.069	1.509	1.029	0.666
Skewness	0.203	5.257	0.006	--	--	--	--	--	--	2.791	-0.653	1.217	-1.376	2.476
Kurtosis	0.874	29.562	-0.276	--	--	--	--	--	--	7.356	0.582	1.042	3.485	9.548
CV (%)	13.4	312.1	295.2	--	--	--	--	--	--	182.9	13.3	78.7	369.2	33.7

Table D.13 Correlation matrix for the hydraulic property parameters of unsaturated soil.

Param. (1)	Group (2)	n (3)	$\ln(\psi_b)$ (4)	$\ln(\lambda_d)$ (5)	$\ln(\lambda_{res})$ (6)	$\ln(k^w_{sat})$ (8)	$\ln(\psi_{bk})$ (9)	$\ln(\eta)$ (10)
n	Sa	1						
	L-Sa	1						
	Sa-L	1						
	Si-L	1						
	L	1						
	C-L	1						
	Si-C	1						
	C	1						
$\ln(\psi_b)$	Sa	-0.058	1					
	L-Sa	-0.616	1					
	Sa-L	-0.424	1					
	Si-L	0.047	1					
	L	0.281	1			*symmetric*		
	C-L	0.301	1					
	Si-C	-0.334	1					
	C	-0.229	1					
$\ln(\lambda_d)$	Sa	0.166	0.591*	1				
	L-Sa	-0.195	0.777	1				
	Sa-L	0.014	0.260	1				
	Si-L	0.017	0.264	1				
	L	0.072	0.783*	1				
	C-L	-0.003	0.785*	1				
	Si-C	--	--	--				
	C	--	--	--				
$\ln(\lambda_{res})$	Sa	0.280*	0.280*	0.113	1			
	L-Sa	0.604	-0.169	0.271	1			
	Sa-L	-0.594	0.638*	0.236	1			
	Si-L	0.025	0.706*	-0.053	1			
	L	0.402	0.549	0.224	1			
	C-L	0.281	0.039	-0.214	1			
	Si-C	--	--	--	--			
	C	--	--	--	--			

(*) indicates the correlation coefficients for which P-value < 5%.

Table D.13 Continued: correlation matrix for the hydraulic property parameters of unsaturated soil.

Param. (1)	Group (2)	n (3)	$\ln(\psi_b)$ (4)	$\ln(\lambda_d)$ (5)	$\ln(\lambda_{res})$ (6)	$\ln(k^w_{sat})$ (8)	$\ln(\psi_{bk})$ (9)	$\ln(\eta)$ (10)
$\ln(k^w_{sat})$	Sa	0.154	-0.223	0.260	-0.109	1		*symmetric*
	L-Sa	0.719*	-0.667	-0.075	0.441	1		
	Sa-L	0.362	-0.175	0.313	0.002	1		
	Si-L	-0.151	-0.013	0.409*	0.028	1		
	L	0.481	-0.290	-0.373	0.166	1		
	C-L	0.357	0.054	0.053	-0.463	1		
	Si-C	0.308	-0.336	--	--	1		
	C	0.119	-0.299	--	--	1		
$\ln(\psi_{bk})$	Sa	0.076	0.126	0.124	0.111	-0.401*	1	
	L-Sa	-0.586	0.794*	0.569	-0.106	-0.613*	1	
	Sa-L	0.115	-0.292	0.549*	-0.122	0.018	1	
	Si-L	0.163	0.174	0.614*	-0.145	-0.320	1	
	L	0.315	0.766*	0.534	0.626*	-0.208	1	
	C-L	-0.367	0.520	0.752*	-0.287	-0.426	1	
	Si-C	0.304	0.122	--	--	-0.540*	1	
	C	-0.043	-0.101	--	--	-0.604*	1	
$\ln(\eta)$	Sa	0.106	0.069	0.366*	0.093	0.076	0.774*	1
	L-Sa	-0.060	0.438	0.519	0.479	-0.217	0.698*	1
	Sa-L	0.048	-0.241	0.738*	0.093	0.460	0.761*	1
	Si-L	0.075	0.153	0.955*	-0.173	0.381*	0.628*	1
	L	0.451	0.588*	0.479	0.623*	0.143	0.886*	1
	C-L	-0.137	0.823*	0.815*	-0.257	-0.206	0.863*	1
	Si-C	0.515*	-0.150	--	--	0.107	0.502*	1
	C	0.102	-0.106	--	--	0.074	0.212	1

(*) indicates the correlation coefficients for which P-value < 5%.

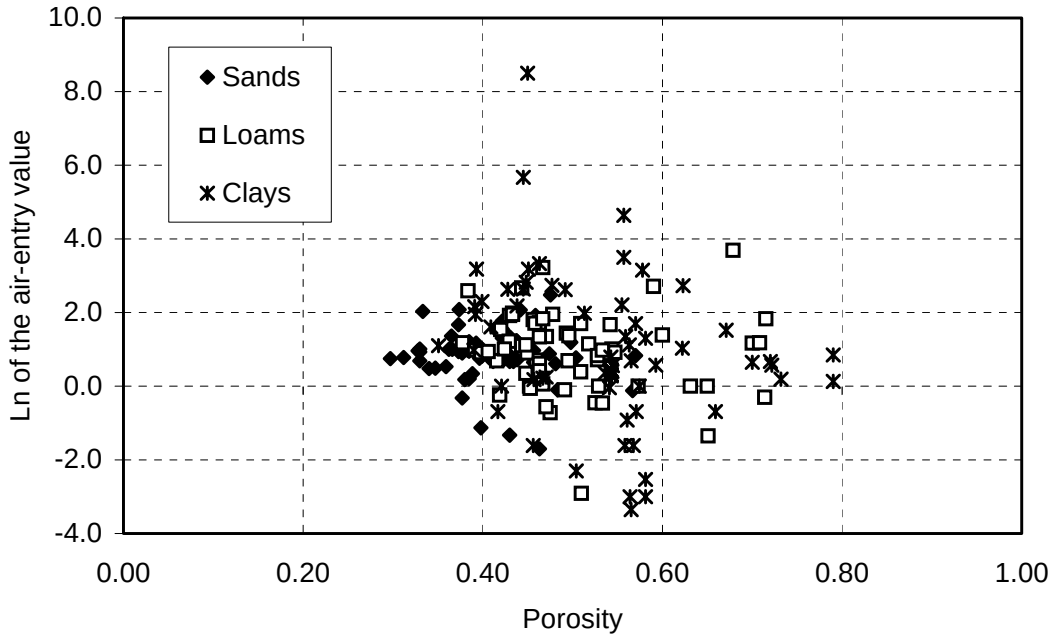

Figure D.1 Scatter plot: porosity versus natural logarithm of air-entry value (kPa).

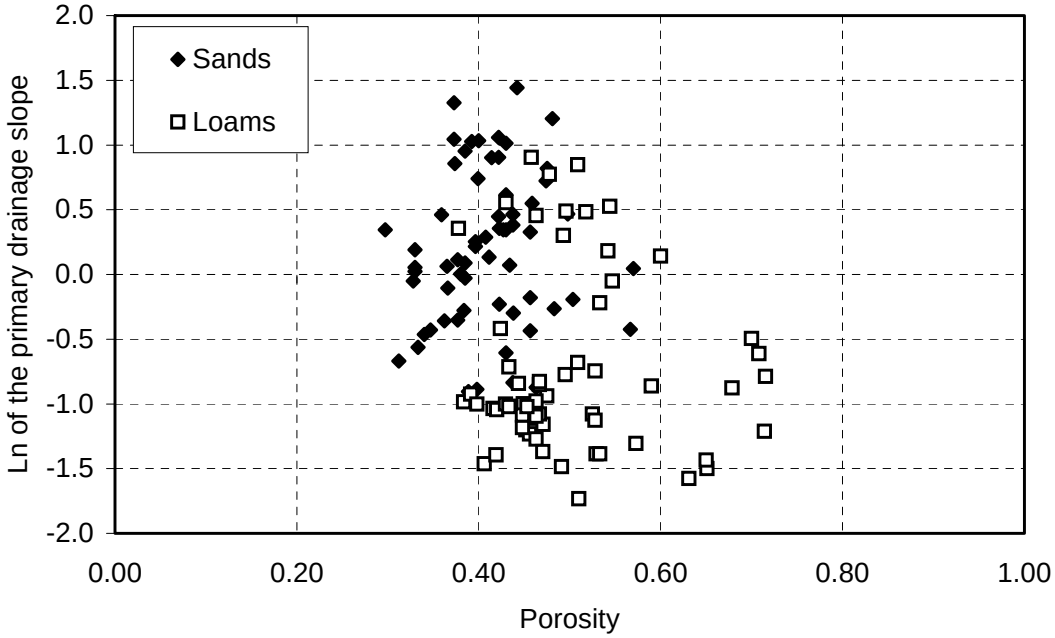

Figure D.2 Scatter plot: porosity versus natural logarithm of the primary drainage slope, λ_d.

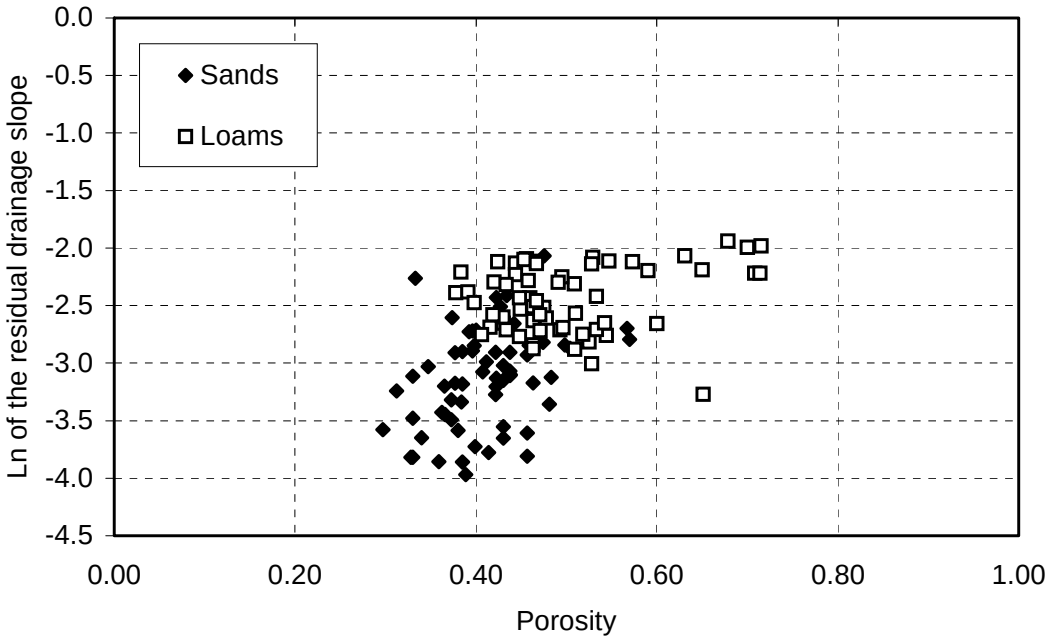

Figure D.3 Scatter plot: porosity versus natural logarithm of the residual drainage slope, λ_{res}.

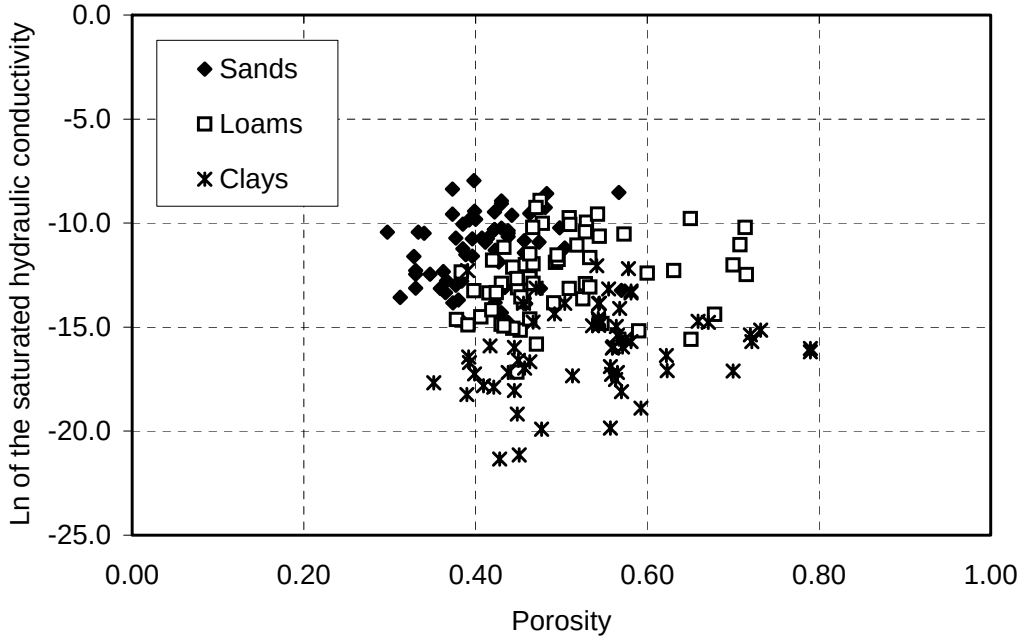

Figure D.4 Scatter plot: porosity versus natural logarithm of the saturated hydraulic conductivity function (m/s).

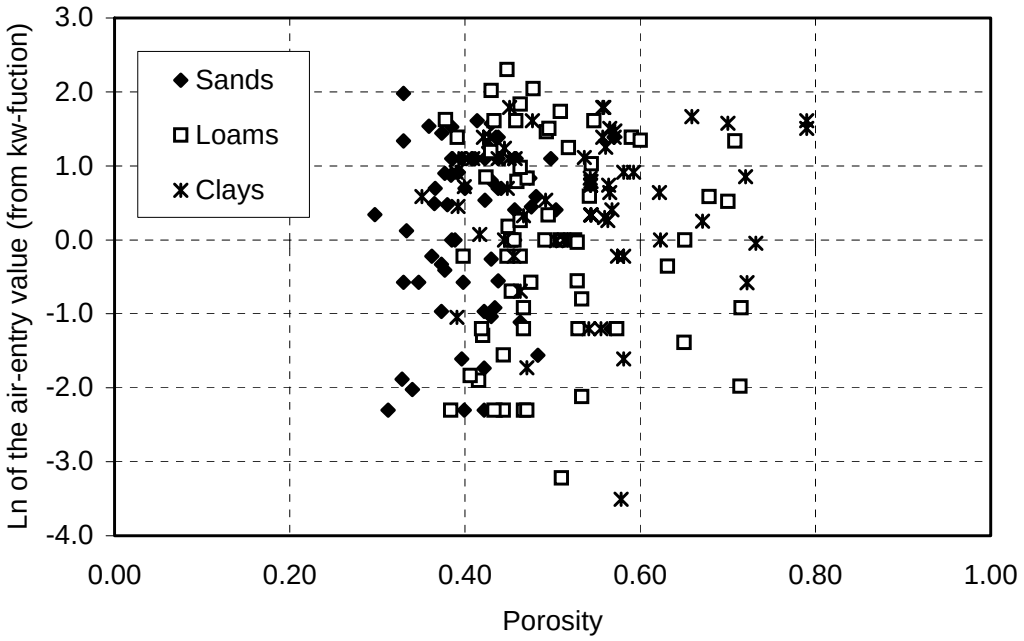

Figure D.5 Scatter plot: porosity versus natural logarithm of the air-entry value (kPa) obtained from the hydraulic conductivity function.

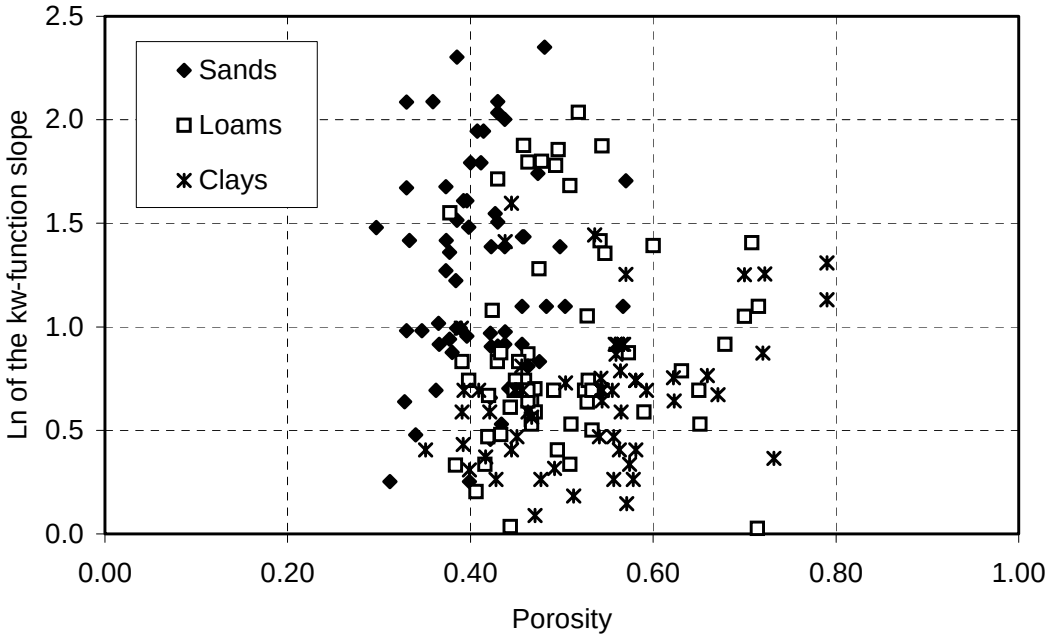

Figure D.6 Scatter plot: porosity versus natural logarithm of the slope of the hydraulic conductivity function.

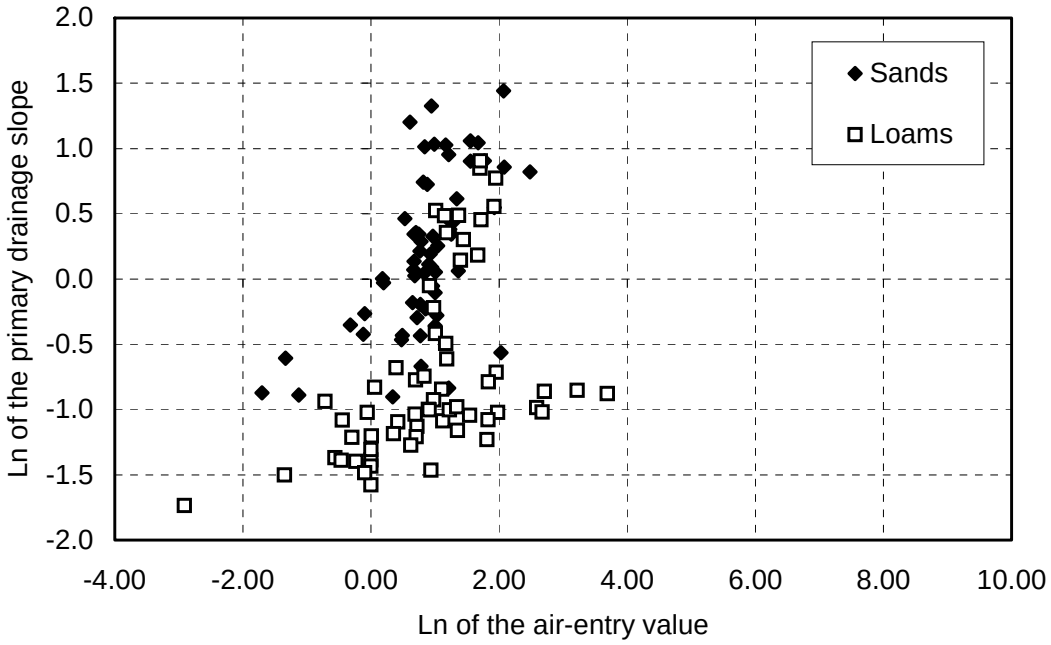

Figure D.7 Scatter plot: natural logarithm of the air-entry value (kPa) versus natural logarithm of the primary drainage slope, λ_d.

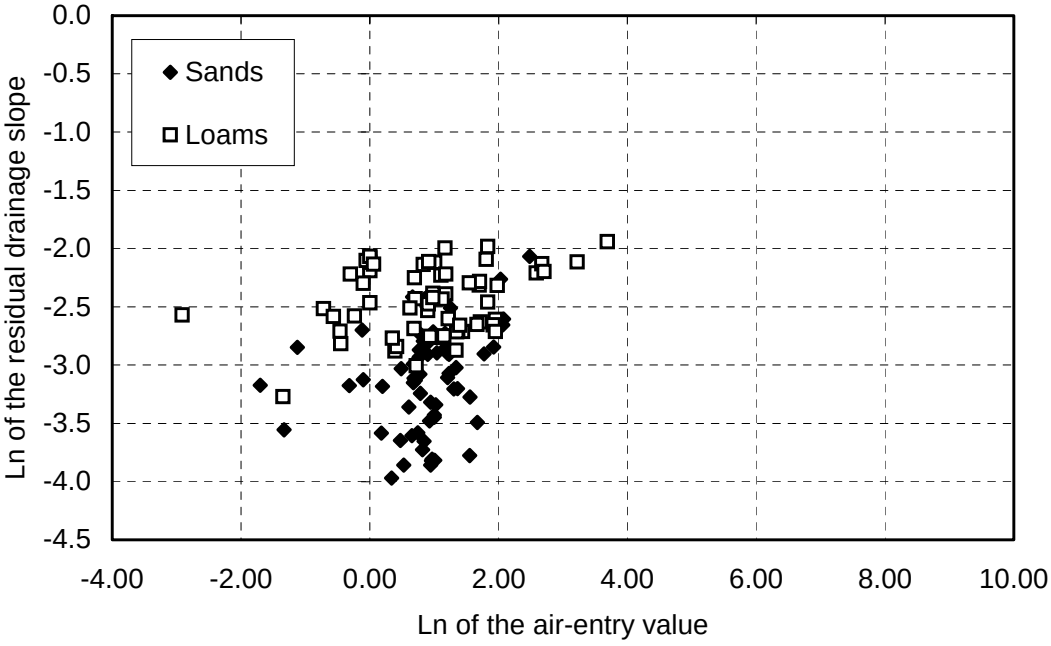

Figure D.8 Scatter plot: natural logarithm of the air-entry value (kPa) versus natural logarithm of the residual drainage slope, λ_{res}.

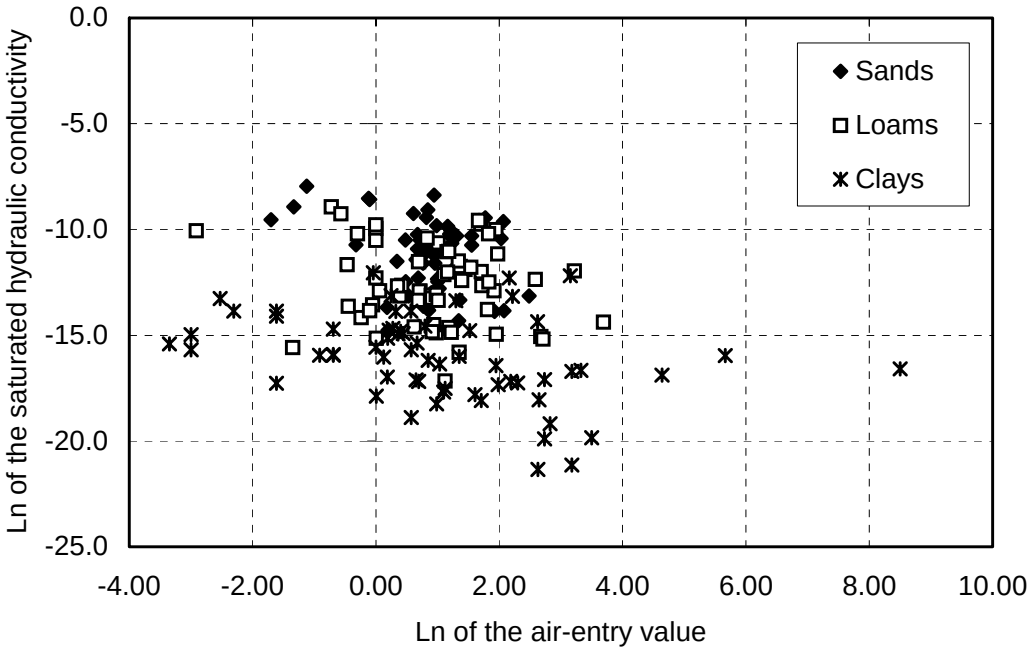

Figure D.9 Scatter plot: natural logarithm of the air-entry value (kPa) versus the natural logarithm of the saturated hydraulic conductivity (m/s).

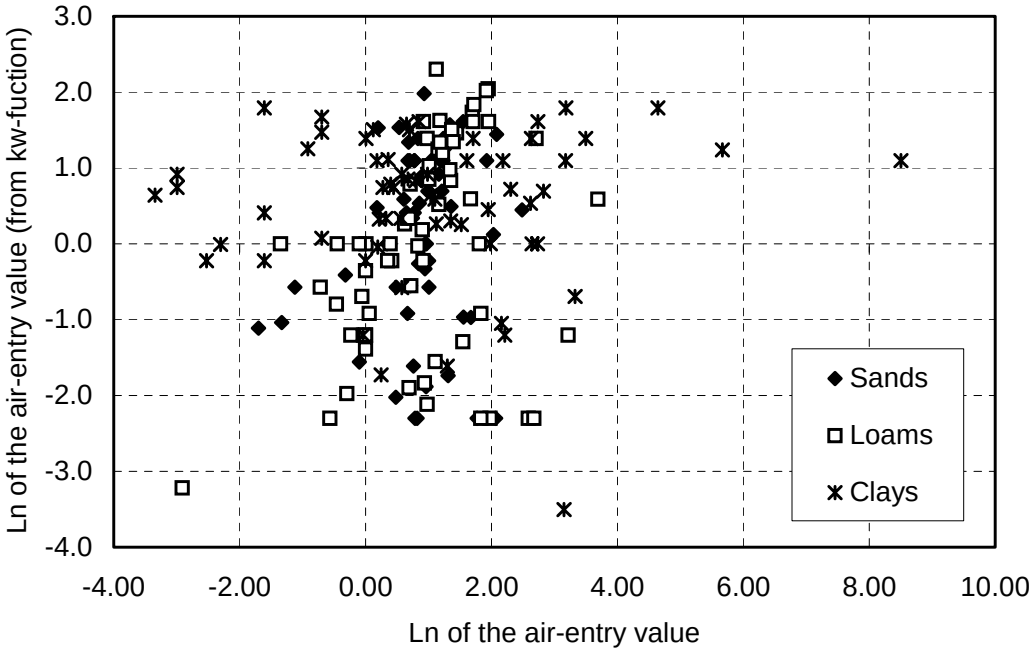

Figure D.10 Scatter plot: natural logarithm of the air-entry value (kPa) versus the natural logarithm of the air-entry value (kPa) obtained from the hydraulic conductivity function.

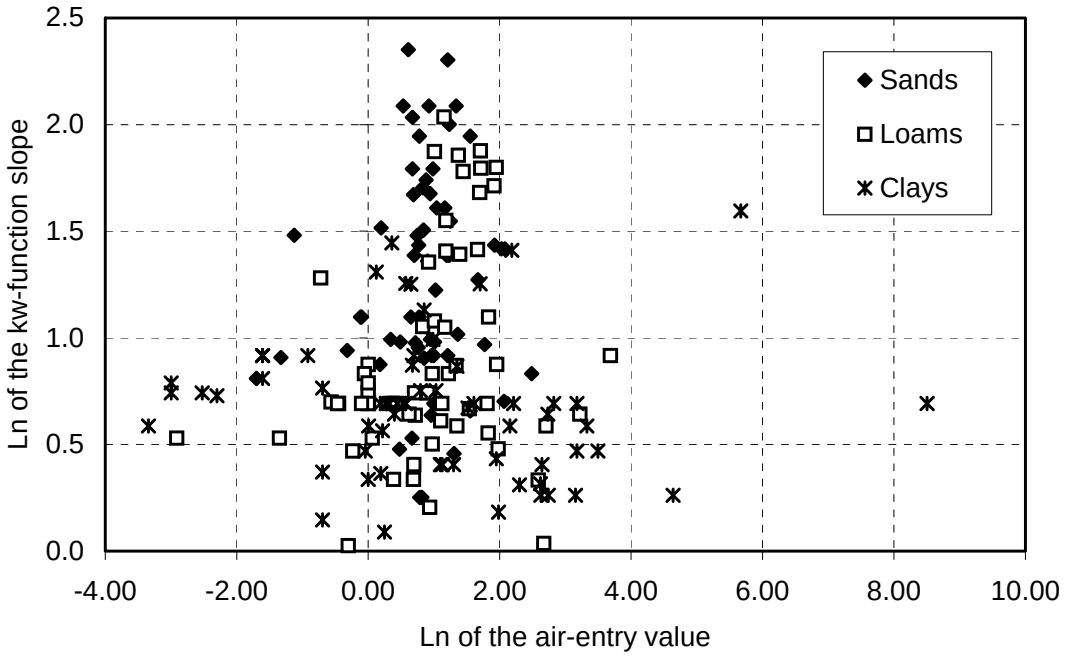

Figure D.11 Scatter plot: natural logarithm of the air-entry value (kPa) versus the natural logarithm of the slope of the hydraulic conductivity function.

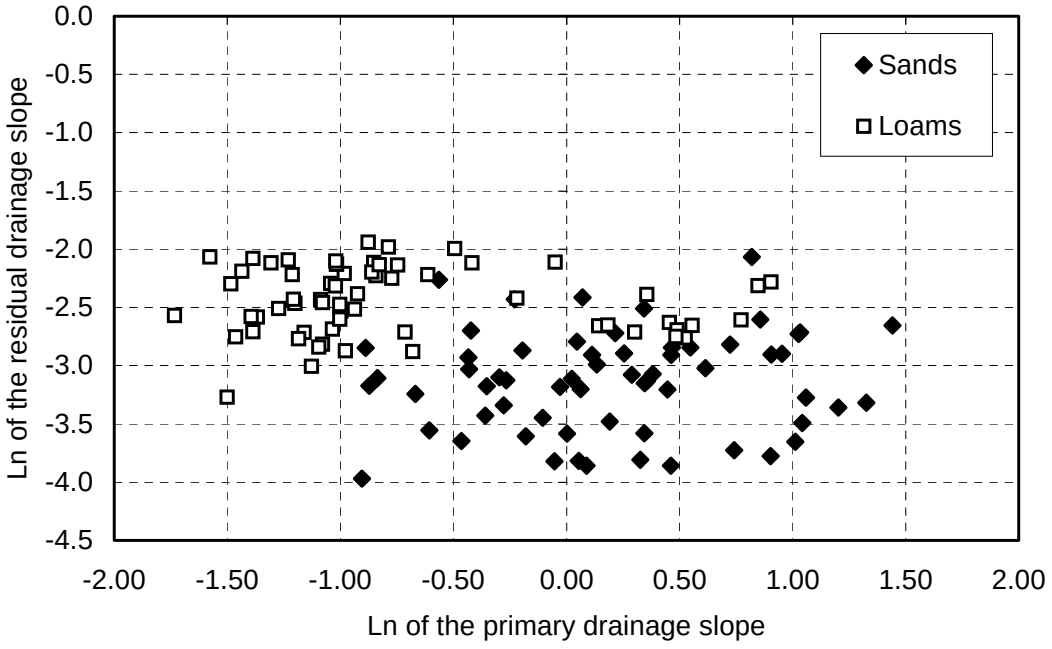

Figure D.12 Scatter plot: natural logarithm of the primary drainage slope, λ_d, versus the residual degree of saturation.

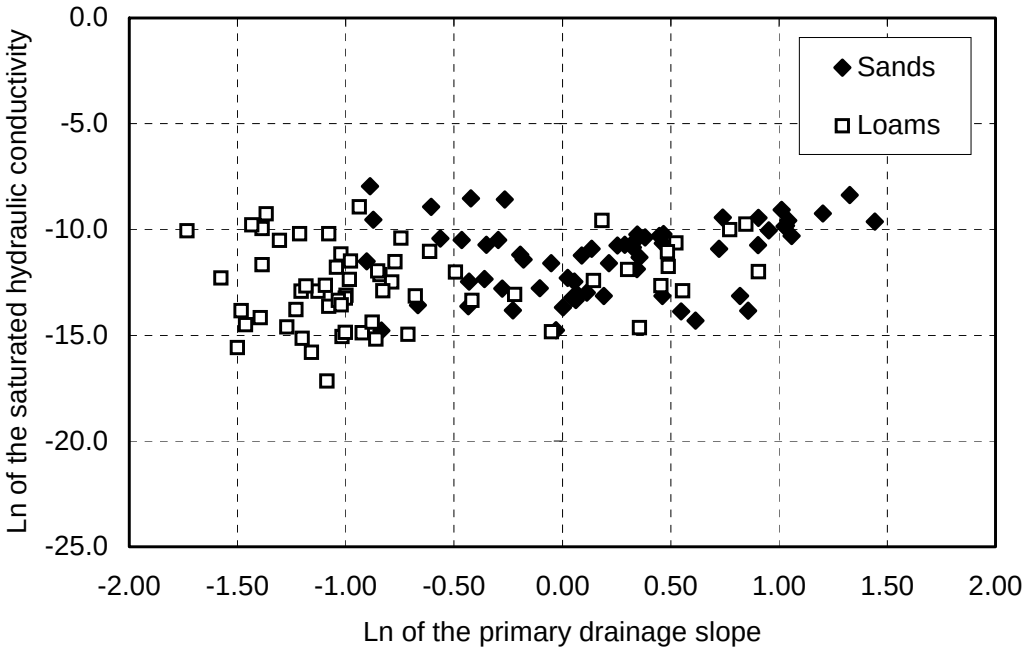

Figure D.13 Scatter plot: natural logarithm of the primary drainage slope, λ_d, versus the natural logarithm of the saturated hydraulic conductivity (m/s).

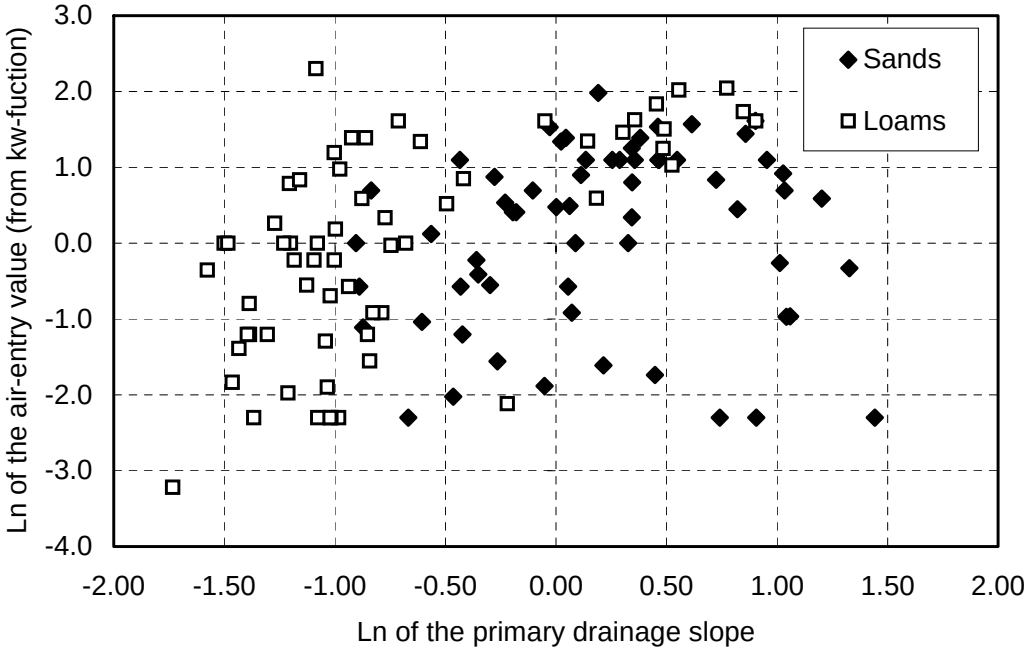

Figure D.14 Scatter plot: natural logarithm of the primary drainage slope, λ_d, versus the natural logarithm of the air-entry value (kPa) obtained from the hydraulic conductivity function.

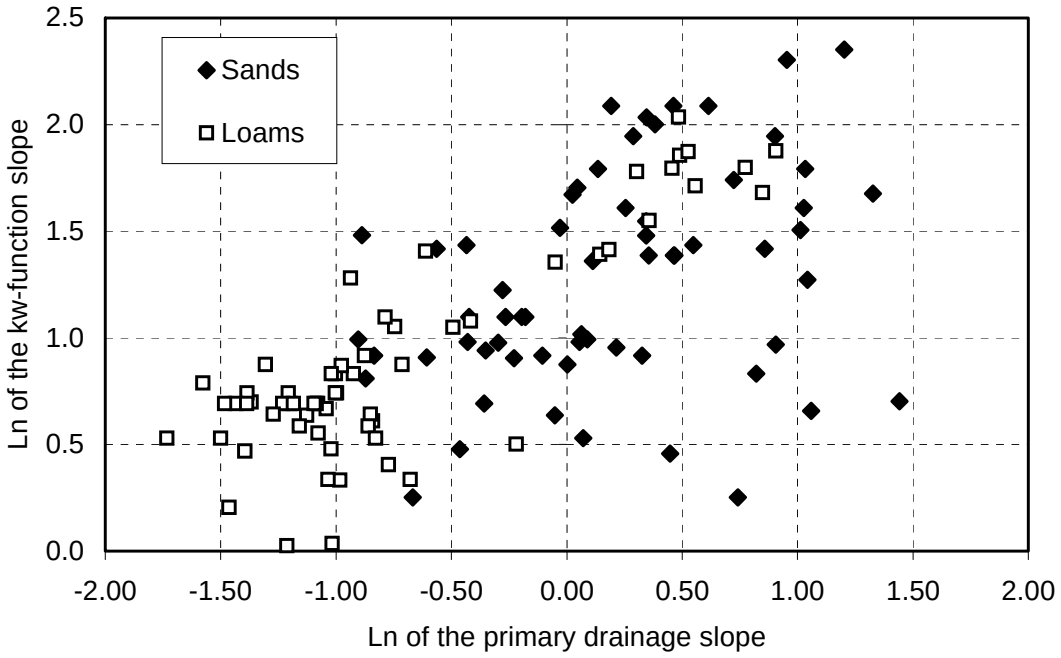

Figure D.15 Scatter plot: natural logarithm of the primary drainage slope, λ_d, versus the natural logarithm of the slope of the hydraulic conductivity function.

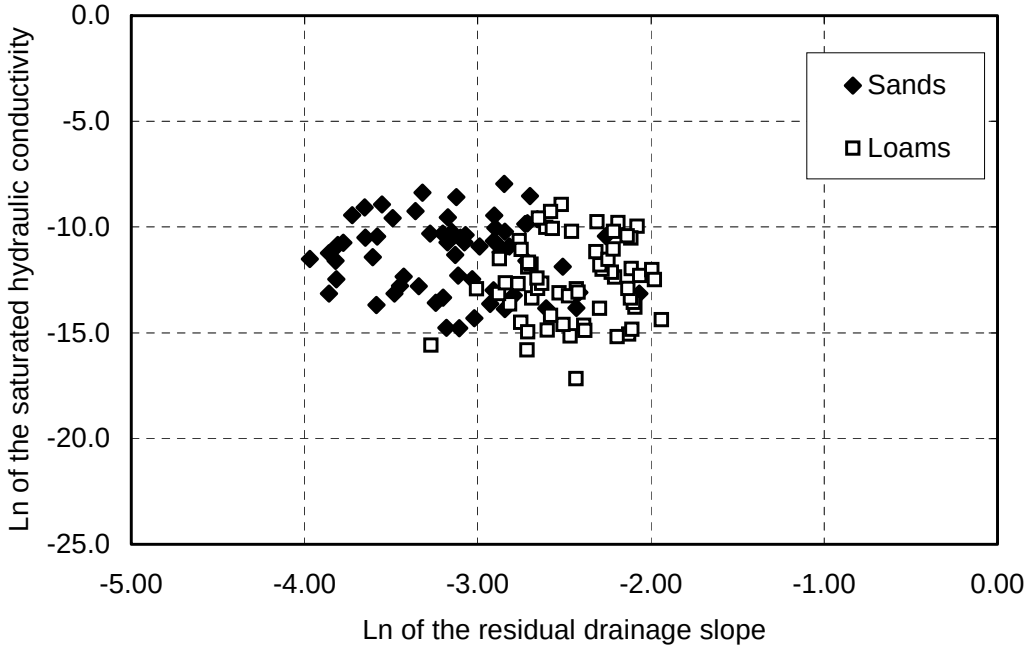

Figure D.16 Scatter plot: natural logarithm of the residual drainage slope, λ_{res}, versus the natural logarithm of the saturated hydraulic conductivity (m/s).

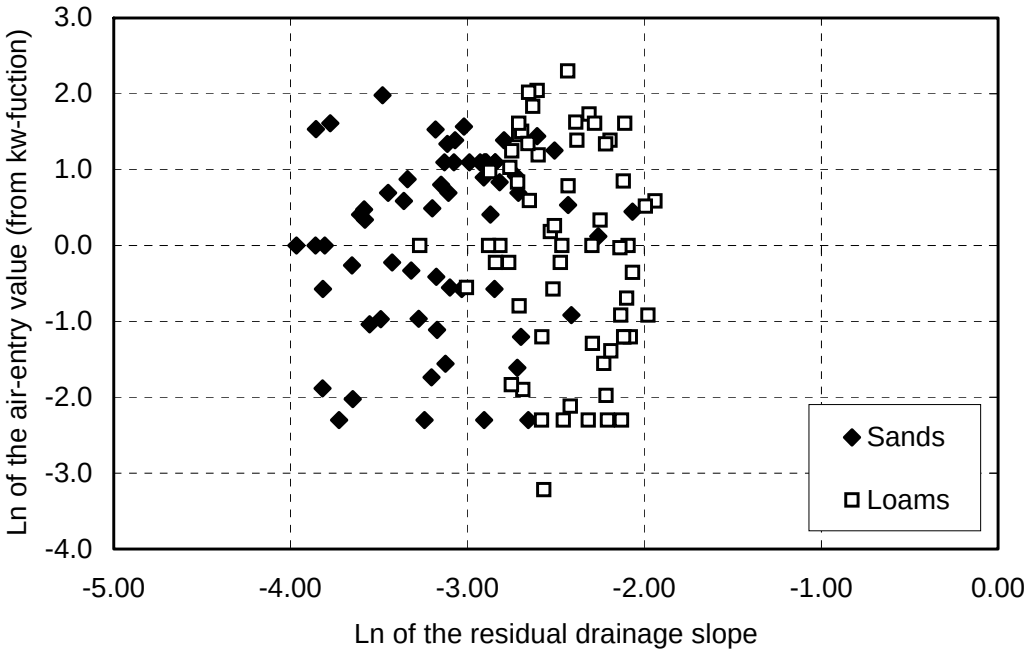

Figure D.17 Scatter plot: natural logarithm of the residual drainage slope, λ_{res}, versus the natural logarithm of the air-entry value (kPa) obtained from the hydraulic conductivity function.

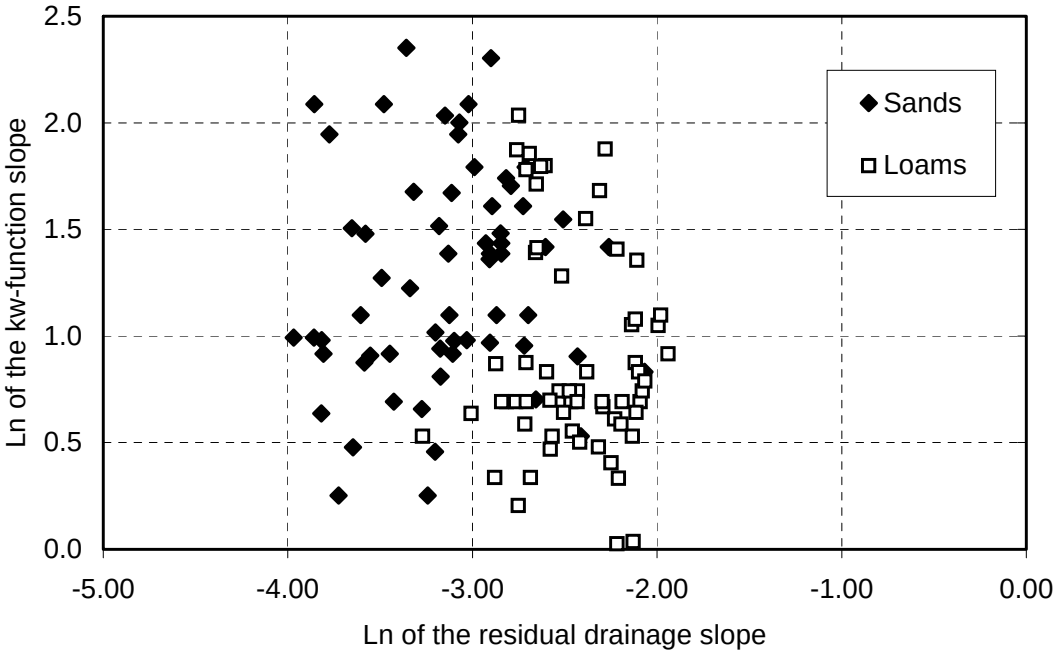

Figure D.18 Scatter plot: natural logarithm of the residual drainage slope, λ_{res}, versus the natural logarithm of the slope of the hydraulic conductivity function.

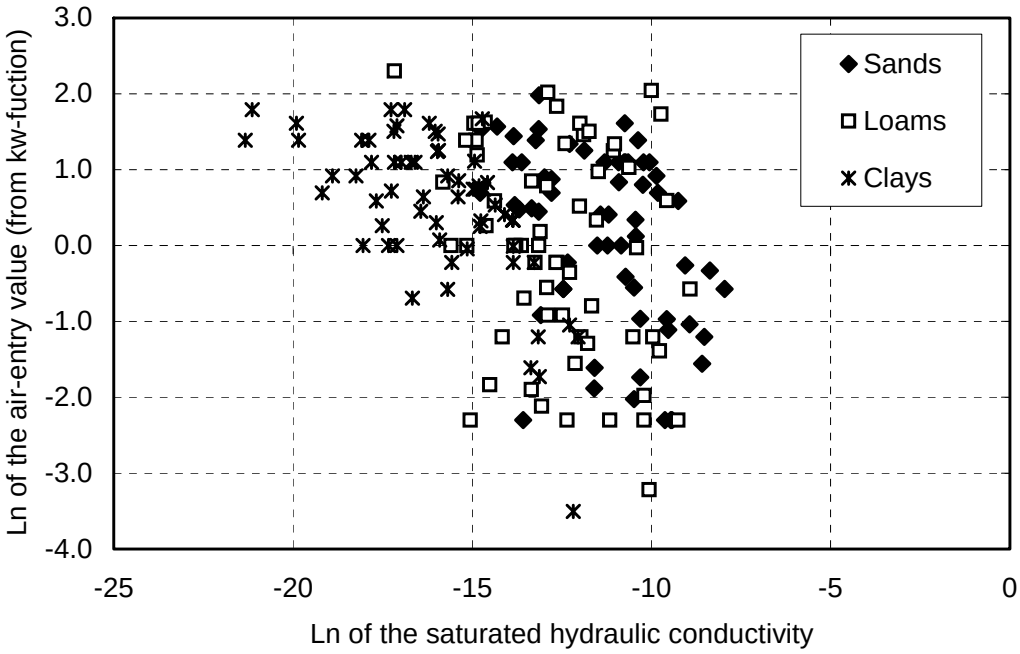

Figure D.19 Scatter plot: natural logarithm of the saturated hydraulic conductivity (m/s) versus the natural logarithm of the air-entry value (kPa) obtained from the hydraulic conductivity function.

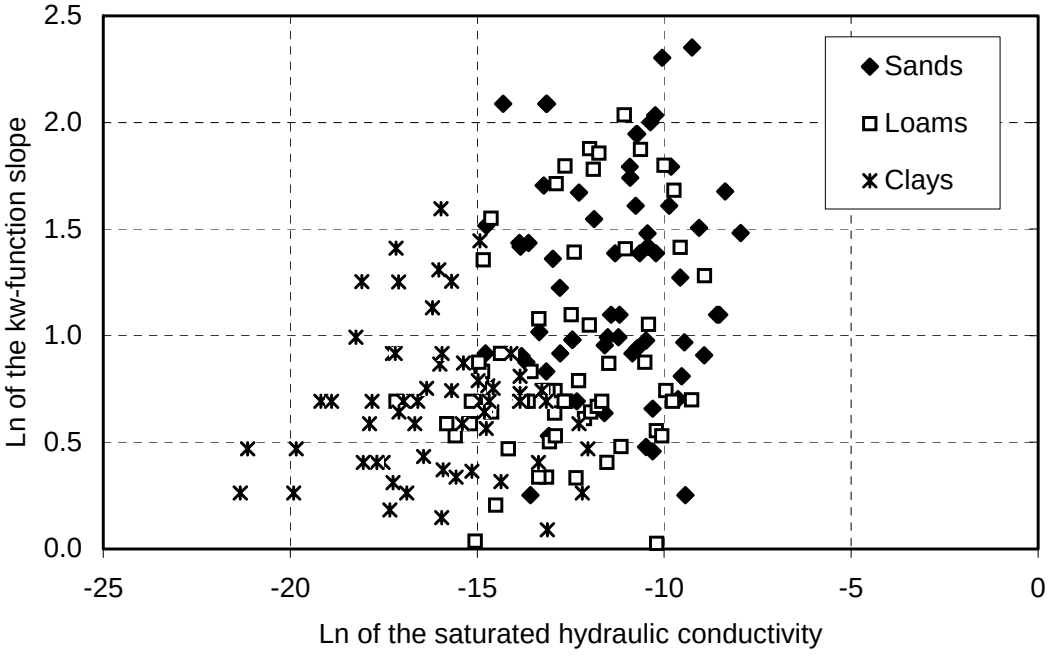

Figure D.20 Scatter plot: natural logarithm of the saturated hydraulic conductivity (m/s) versus the natural logarithm of the slope of the hydraulic conductivity function.

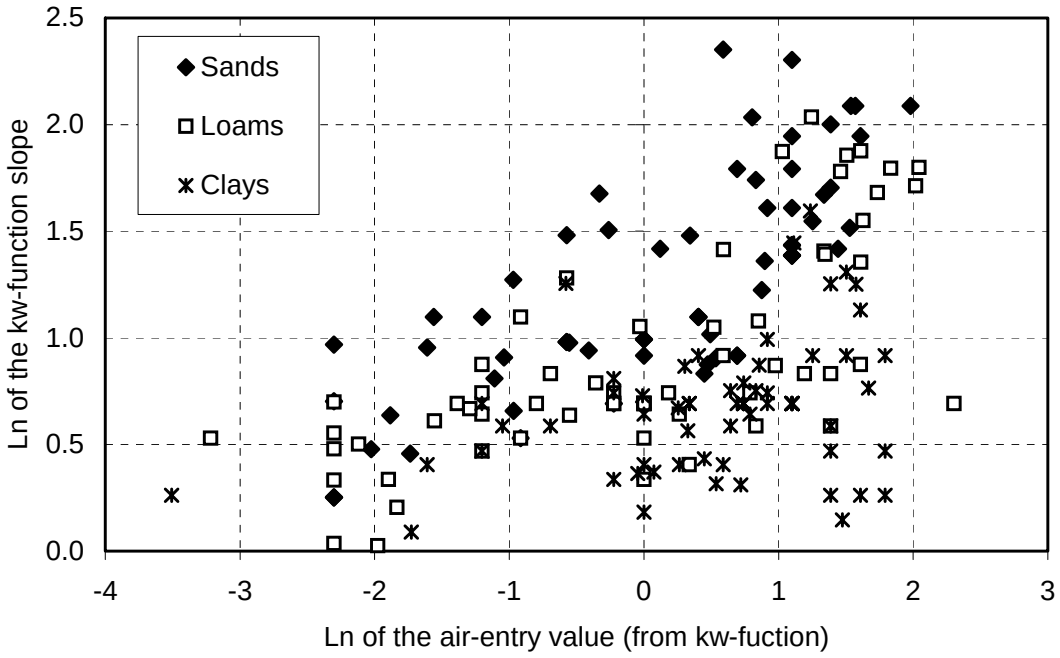

Figure D.21 Scatter plot: natural logarithm of the air-entry value (kPa) obtained from the hydraulic conductivity function versus the natural logarithm of the slope of the hydraulic conductivity function.

Appendix E

Factors of Safety for the Soil Property Case Scenarios

E.1 FACTOR OF SAFETY DATA

This appendix presents the factors of safety computed for all case scenarios shown in chapter 6. The factors of safety are plotted against time. Upper and lower estimate points were separated, for clarity. The case scenario corresponding to the mean parameters is presents in all plots, using a thick, solid line.

E.1.1 *Analyses for the precipitation event*

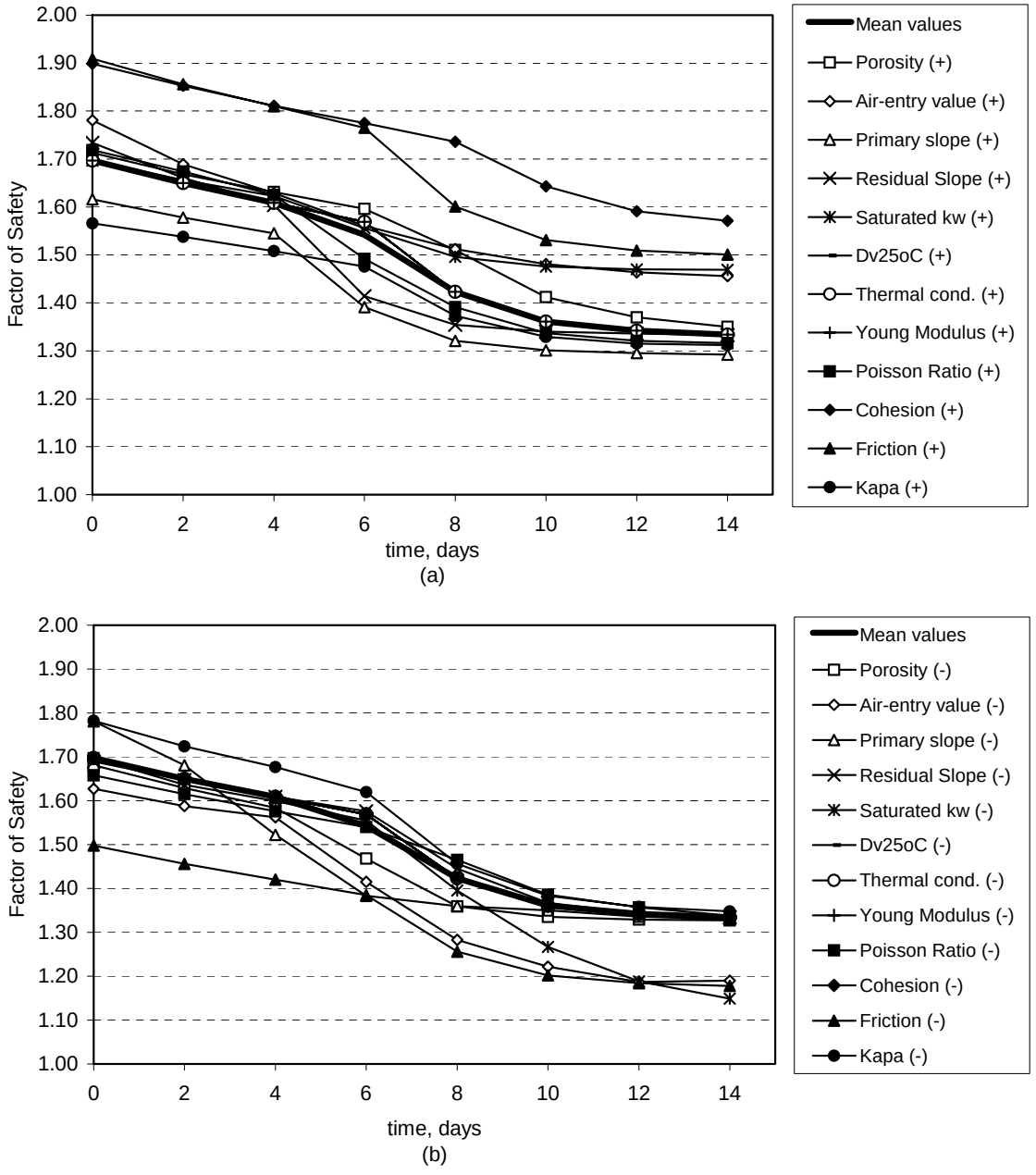

Figure E.1 Evolution of the factors of safety for all case scenarios for the low, loam embankment. Initial conditions: $u_{w\,min}$ = -60 kPa.

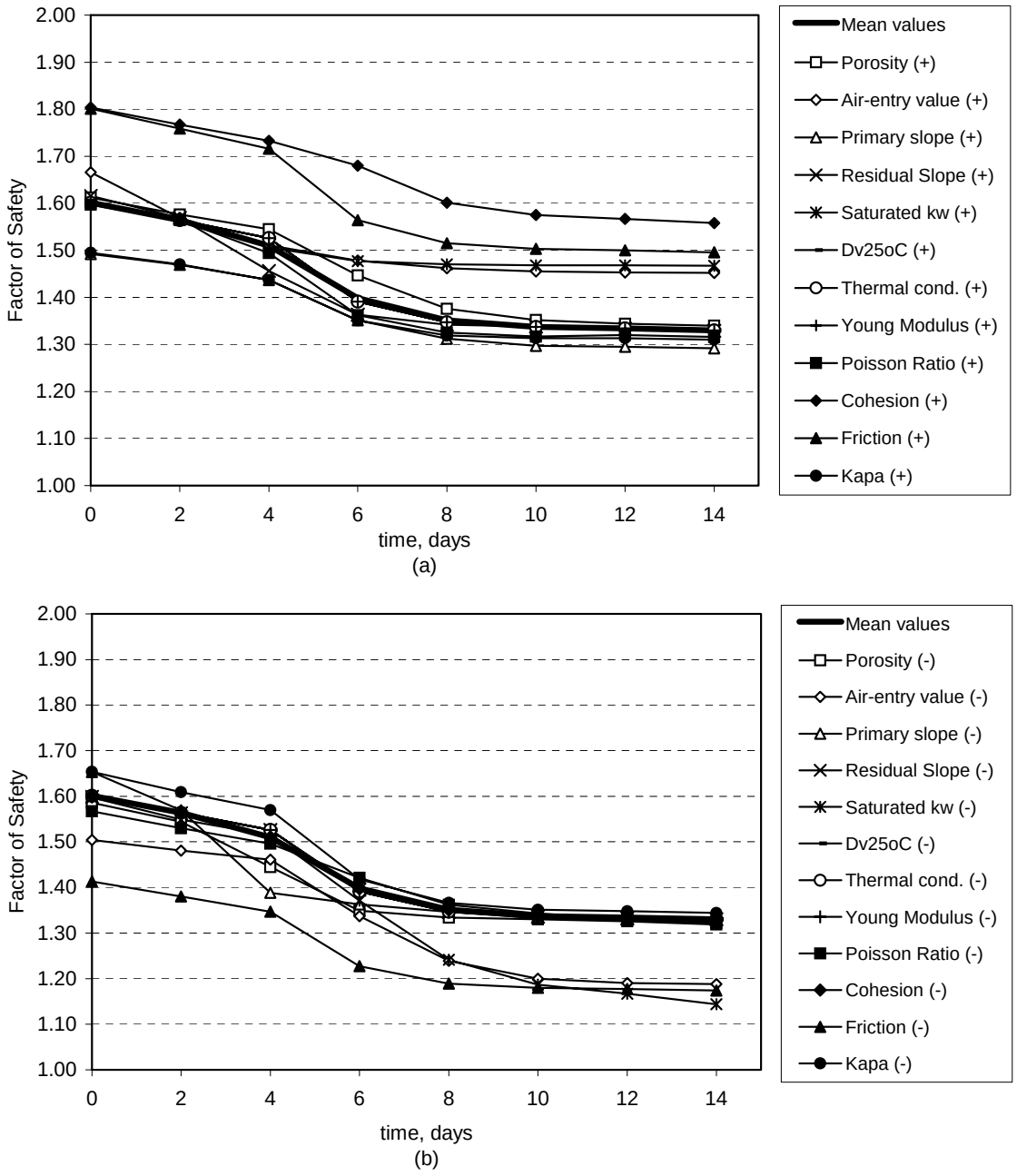

Figure E.2 Evolution of the factors of safety for all case scenarios for the low, loam embankment. Initial conditions: $u_{w\,min}$ = -20 kPa.

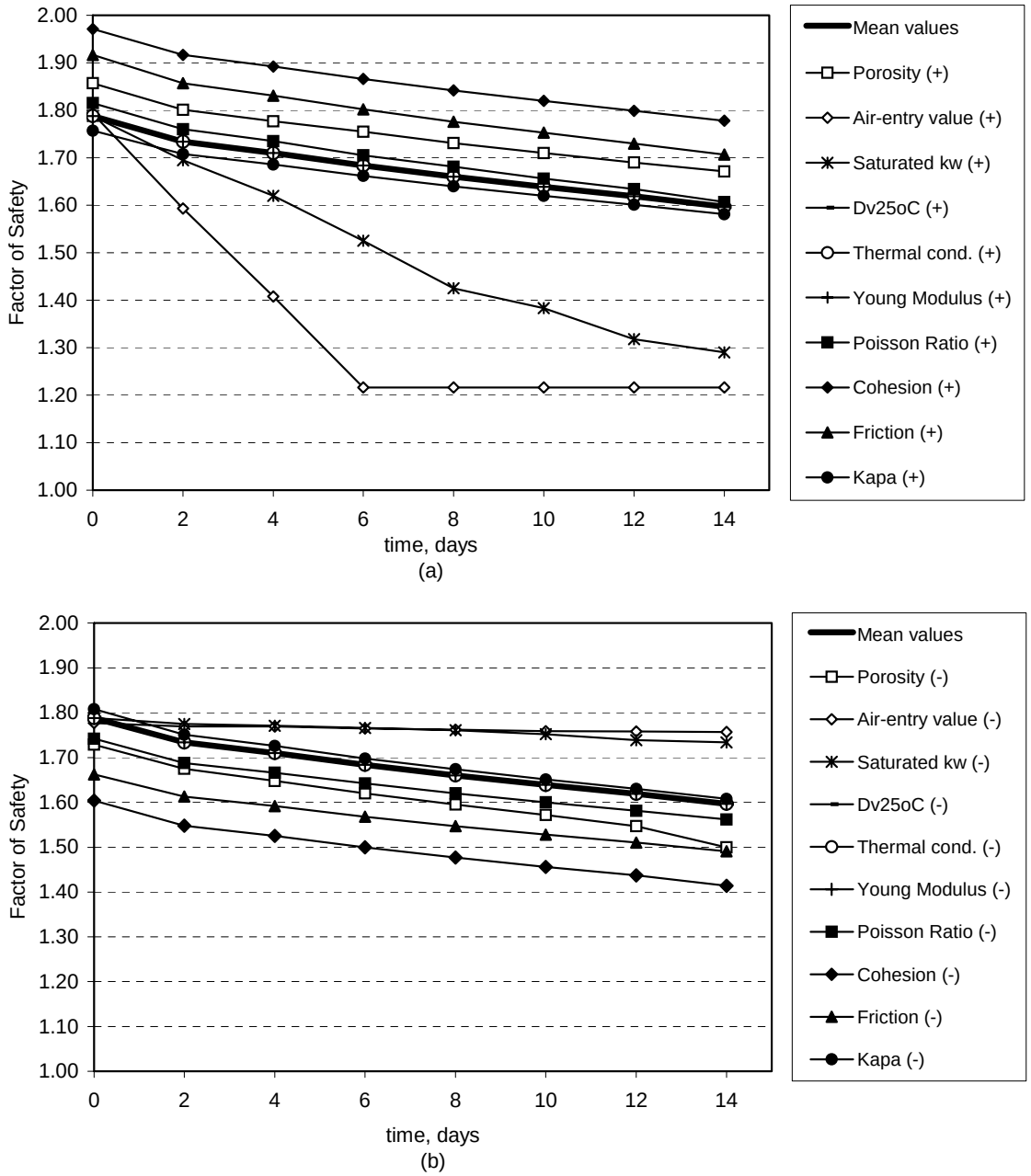

Figure E.3 Evolution of the factors of safety for all case scenarios for the low, clay embankment. Initial conditions: $u_{w\,min}$ = -60 kPa.

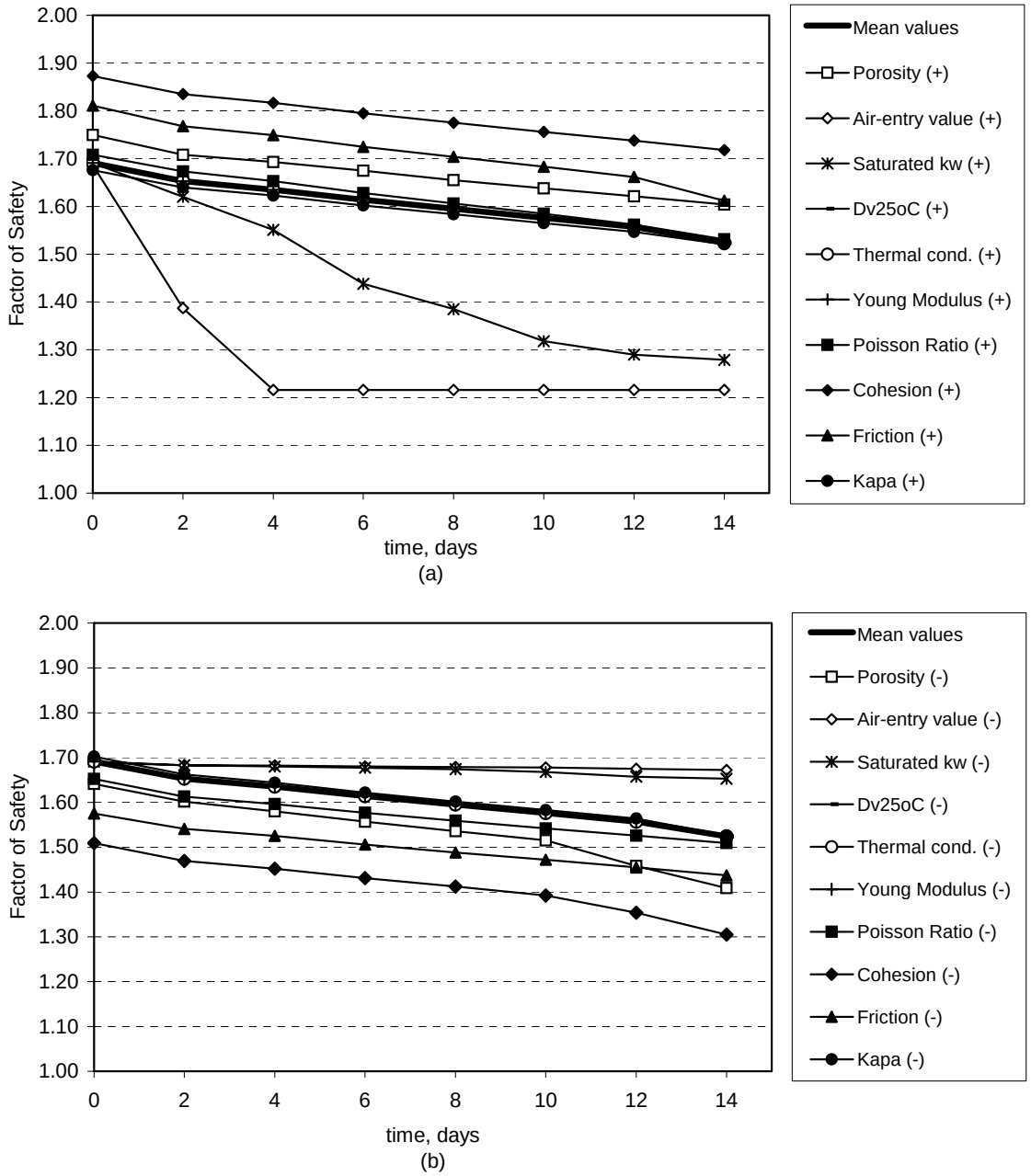

Figure E.4 Evolution of the factors of safety for all case scenarios for the low, clay embankment. Initial conditions: $u_{w\,min}$ = -20 kPa.

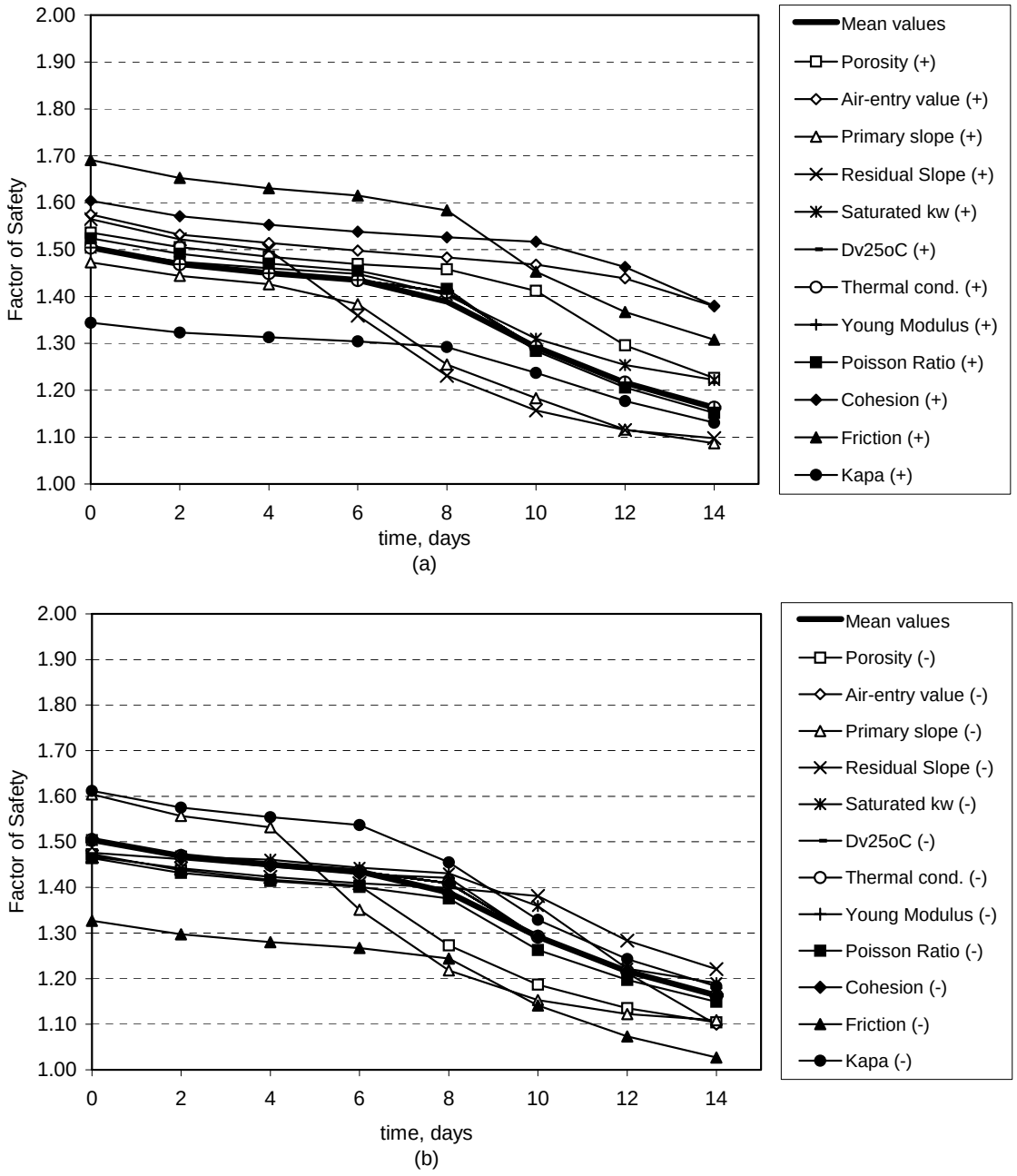

Figure E.5 Evolution of the factors of safety for all case scenarios for the high, loam embankment. Initial conditions: $u_{w\,min}$ = -100 kPa.

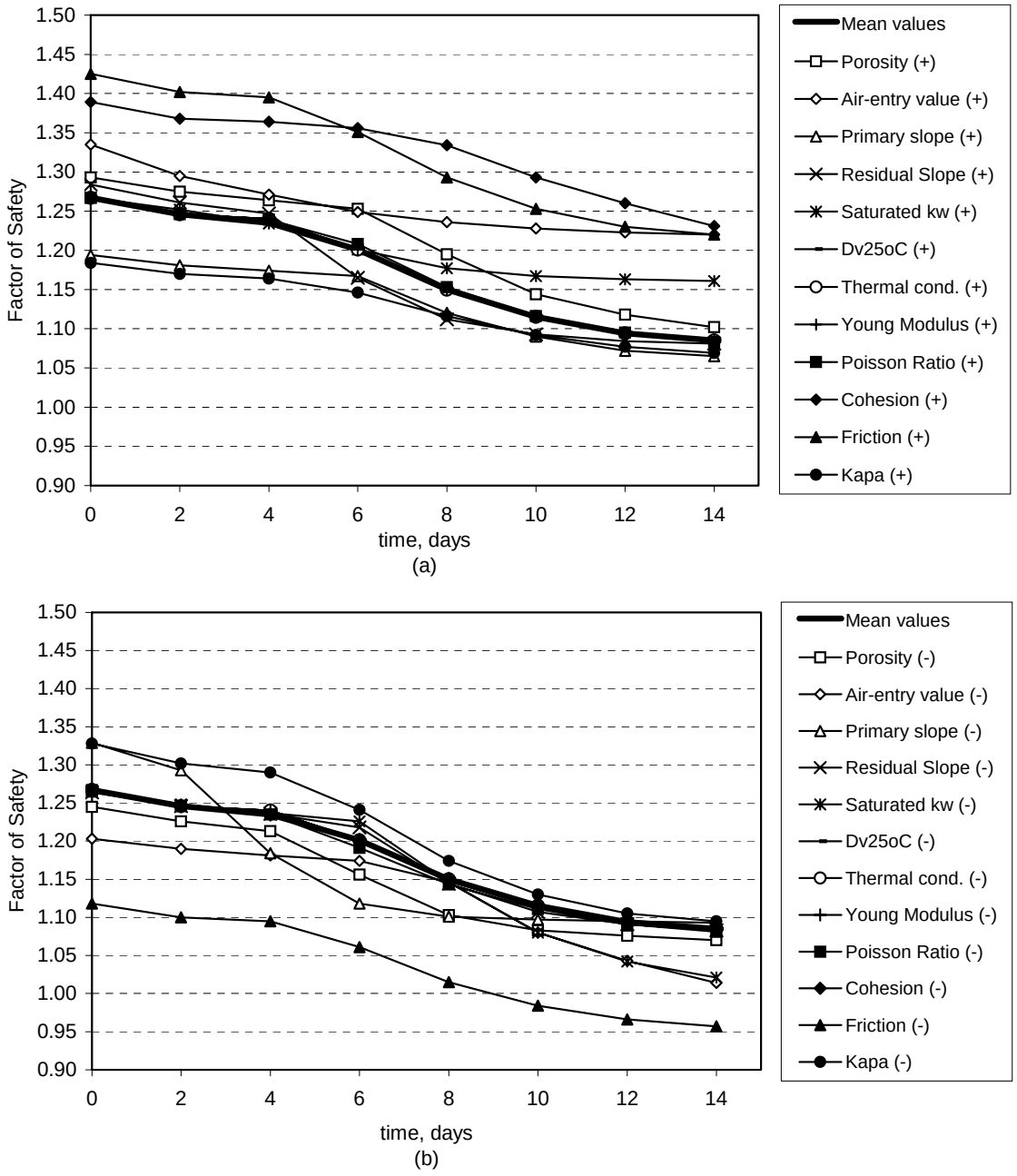

Figure E.6 Evolution of the factors of safety for all case scenarios for the high, loam embankment. Initial conditions: $u_{w\,min}$ = -20 kPa.

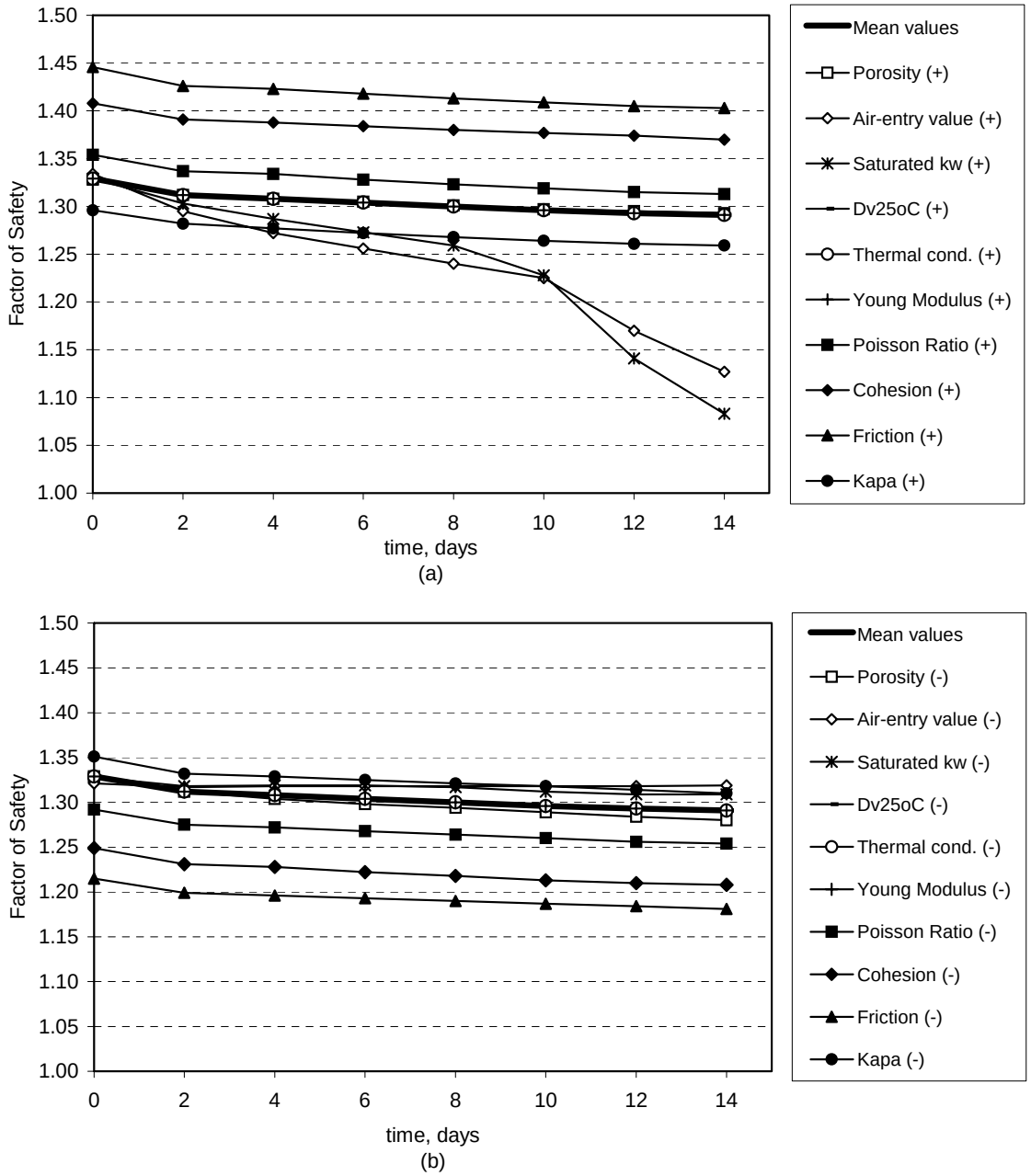

Figure E.7 Evolution of the factors of safety for all case scenarios for the high, clay embankment. Initial conditions: $u_{w\,min}$ = -100 kPa.

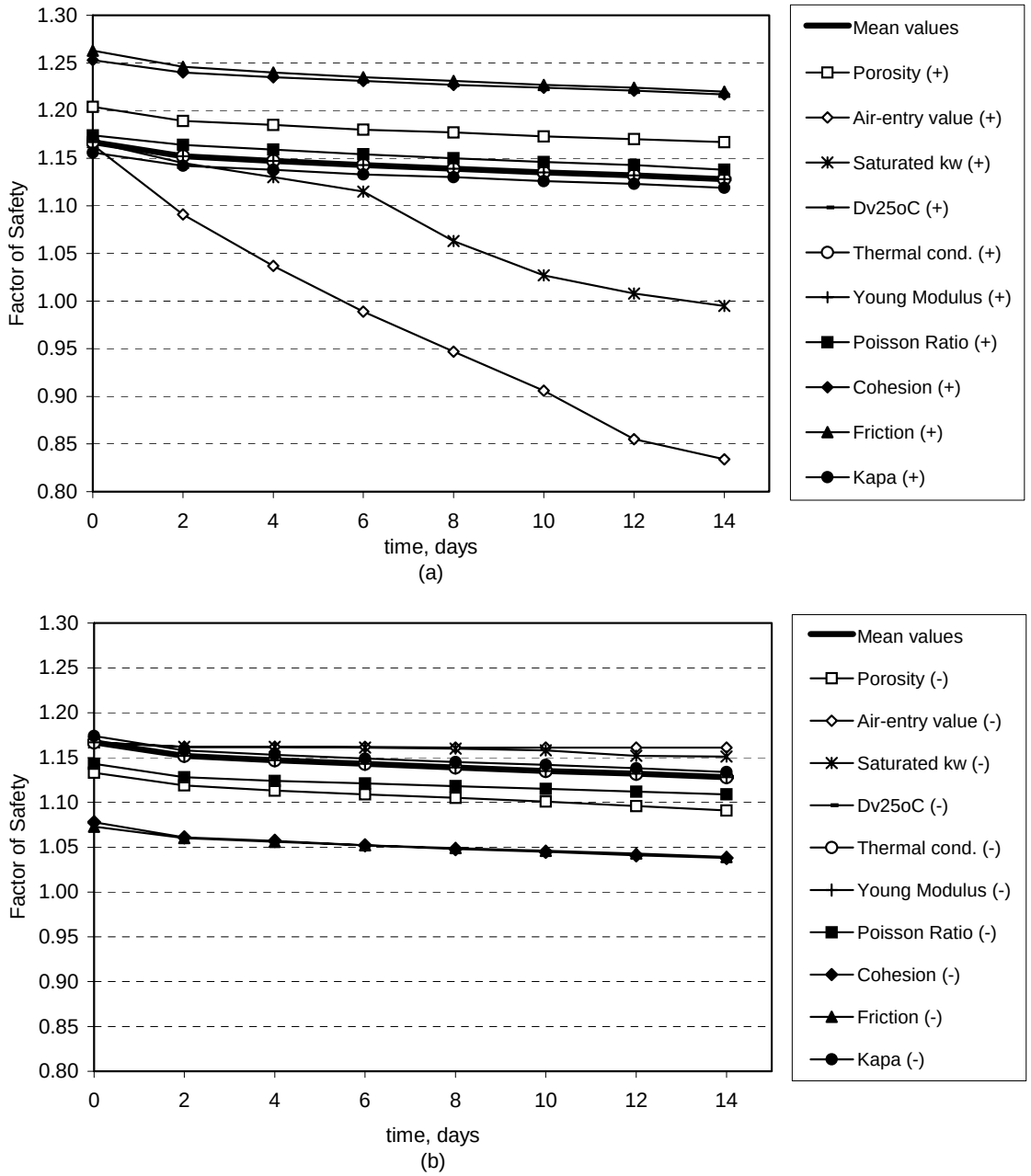

Figure E.8 Evolution of the factors of safety for all case scenarios for the high, clay embankment. Initial conditions: $u_{w\,min}$ = -20 kPa.

E.1.2 *Analyses for the evaporation event*

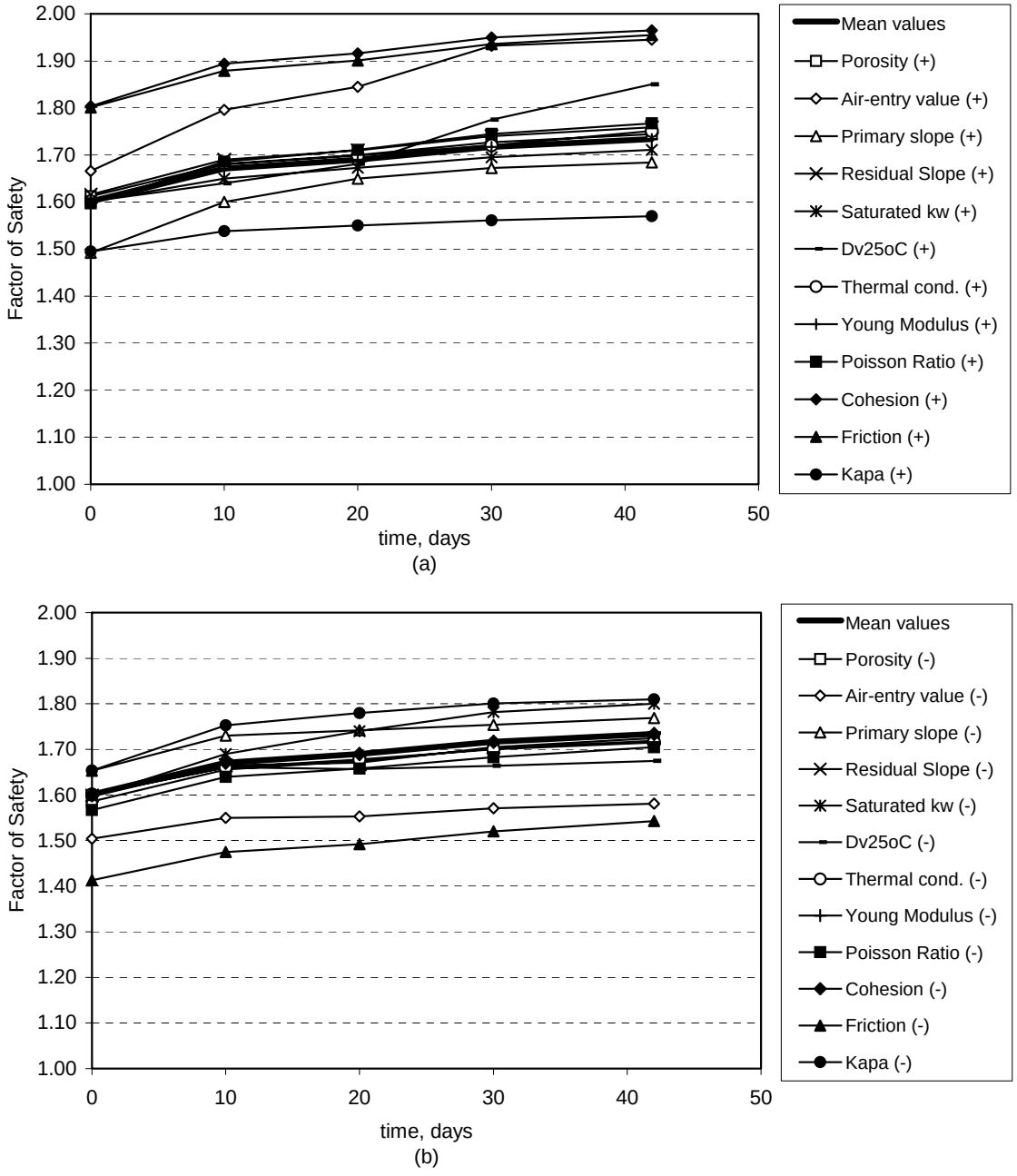

Figure E.9 Evolution of the factors of safety for all case scenarios for the low loam embankment during the evaporation event.

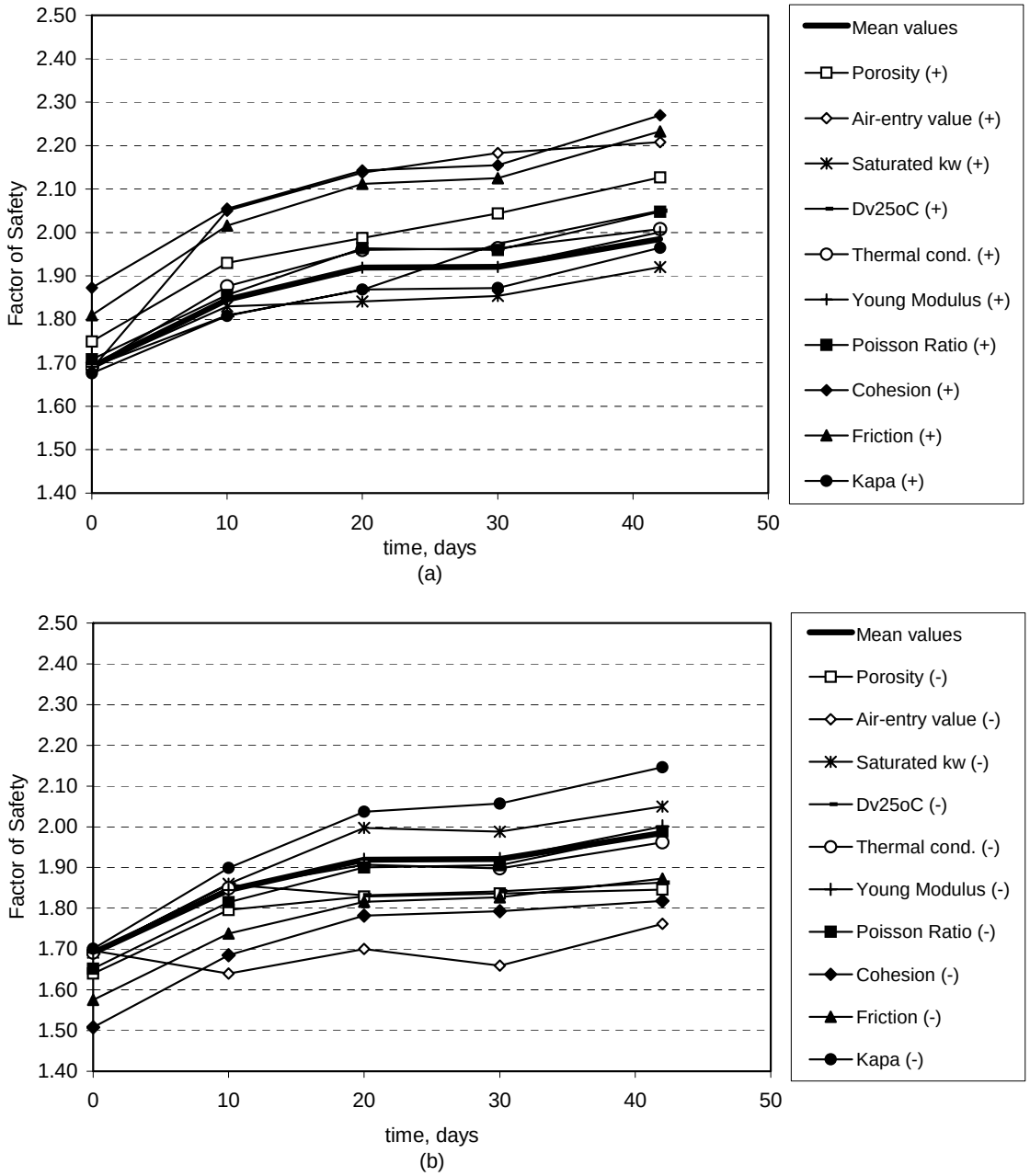

Figure E.10 Evolution of the factors of safety for all case scenarios for the low loam embankment during the evaporation event.